DOE/NV/11718--1245
DOE/NV/25946--022

Nevada Test Site–Directed Research, Development, and Demonstration

FY 2005 Report

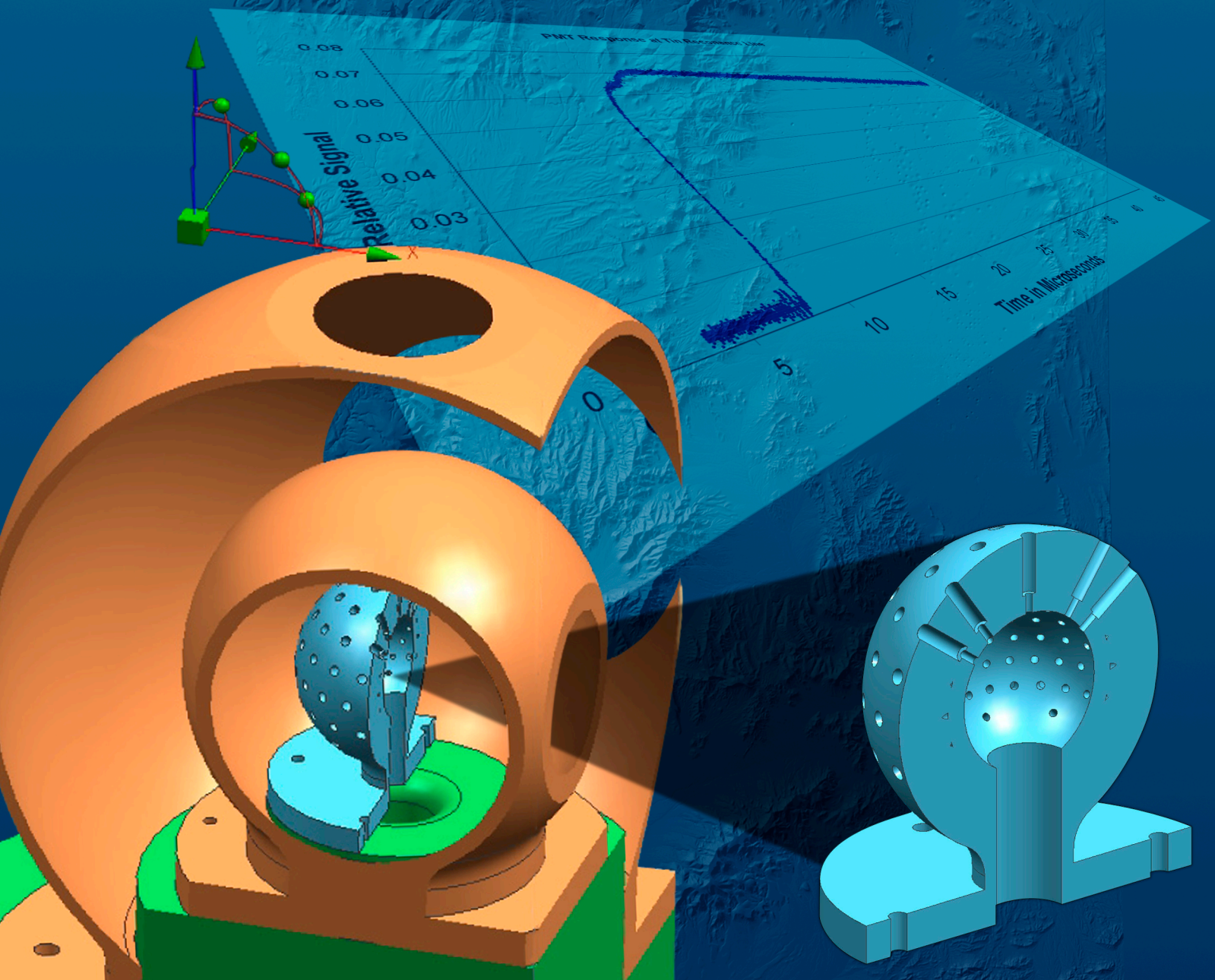

This work was supported by the U.S. Department of Energy, National Nuclear Security Administration, Nevada Site Office, under Contract Nos. DE-AC08-96NV11718 and DE-AC52-06NA25946.

Report Date: September 2006

Disclaimer

DOE/NV/11718--1245
DOE/NV/25946--022

Nevada Test Site–Directed Research, Development, and Demonstration

FY 2005 Report

This work was supported by the U.S. Department of Energy, National Nuclear Security Administration Nevada Site Office, under Contract Nos. DE-AC08-96NV11718 and DE-AC52-06NA25946.

Report Date: September 2006

Detectors and Sensors

Electronics

Photonics

this page intentionally left blank

SDRD FY 2005

The Nevada Test Site–Directed Research, Development, and Demonstration (SDRD) program completed a very successful year of research and development activities in FY 2005. Fifty new projects were selected for funding this year, and five FY 2004 projects were brought to conclusion. The total funds expended by the SDRD program were $5.4 million, for an average per project cost of just under $100,000. Two external audits of SDRD accounting practices were conducted in FY 2005. Both audits found the program's accounting practices consistent with the requirements of DOE Order 413.2A, and one included the observation that the NTS contractor "did an exceptional job in planning and executing year-start activities." Highlights for the year included: the filing of 18 invention disclosures for intellectual property generated by FY 2005 projects; programmatic adoption of 17 FY 2004 SDRD-developed technologies; participation in the tri-lab Laboratory Directed Research and Development (LDRD) and SDRD program review that was broadly attended by NTS, NNSA, LDRD, and U.S. Department of Homeland Security representatives; peer reviews of all FY 2005 projects; and the successful completion of 55 R&D projects, as presented in this report.

In response to a companywide call, authors throughout the NTS complex submitted 151 proposals for FY 2005 SDRD projects. The SDRD program has seen a dramatic increase in the yearly total of submitted proposals, from 69 in FY 2002 to 151 this year, even as the size of the program has remained fairly constant (Figure 1). The quantity and quality of these submissions helped a ensure strongly competitive program and provided a diverse set of innovative ideas, making project selection both challenging and rewarding. Proposals were evaluated for technical merit, including such factors as innovation, probability of success, potential benefit, and mission applicability. Authors and reviewers benefited from the use of a shortfalls list entitled the NTS Technology Needs Assessment that was compiled from NTS, national weapons laboratory, and NNSA sources. This tool proved to be of considerable value in aligning the SDRD program with mission priorities, and it is expected that the Technology Needs Assessment will be updated and expanded in future years. The 50 projects selected for FY 2005 showcase a wealth of creative approaches to innovative technical research with high potential payoff. These endeavors

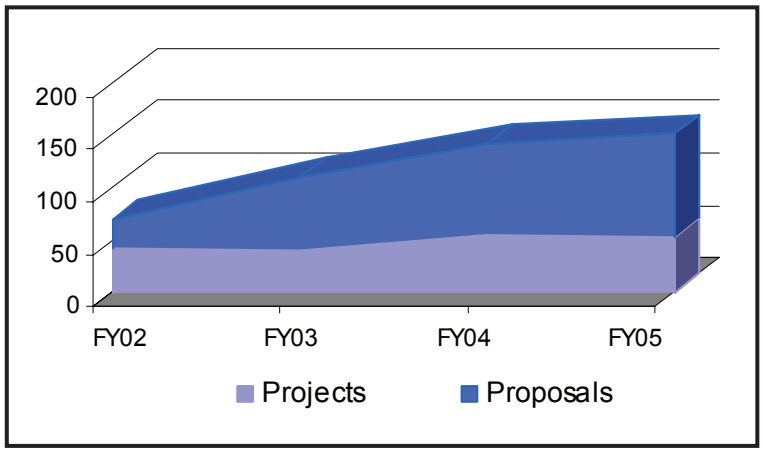

Figure 1. The size of the SDRD program has held fairly steady since its inception, while the number of proposals submitted each year has grown almost threefold

benefited from an impressive cross section of resources and capabilities, and addressed development needs in a variety of technologies, with potential applications to a broad selection of programmatic activities.

Several metrics have been selected to measure the overall effectiveness of the SDRD program's ability to develop innovative solutions to NTS mission technology requirements. The compilated metrics appear in Figure 2. Since the introduction of the SDRD program, more than 90% of the inventions disclosed to the contractor's intellectual property office have been SDRD projects. The number of invention disclosures filed (blue bars in Figure 2) has increased steadily and significantly to an all-time high of 18 in FY 2005—a clear indicator of both the increase in the innovative quality of selected projects and a cultural sea change in the value attached to intellectual property. The red bars in Figure 2 represent a histogram of the number of projects in which developed technologies were subsequently adopted by programs for each fiscal year. In some cases, demonstrated feasibility was sufficient to encourage further research. In other cases, demonstrated innovation has been directly incorporated into new or existing instrumentation or software.

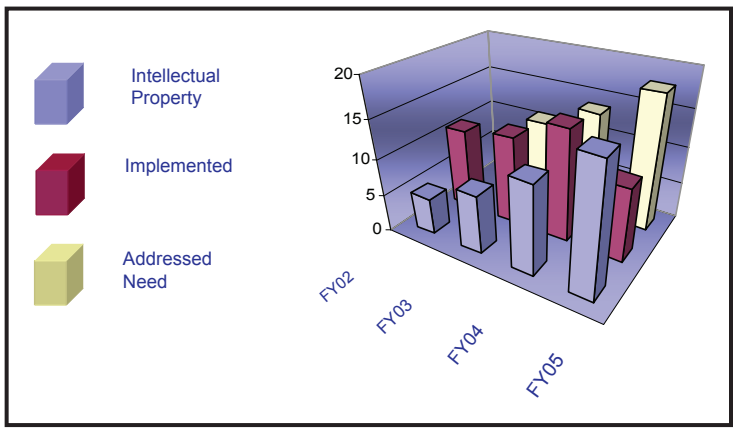

Figure 2. Program effectiveness metrics through FY 2005

It often requires some period of time for SDRD success stories to be communicated to programmatic decision makers, and for funding decisions to be made to implement these technologies. This lag time is evident in the lower number of implemented FY 2005 technologies and by the fact that the data show increases in numbers for all years each time the metric is revised. The third metric shown in Figure 2 indicates how well the SDRD program is strategically aligned with the NTS mission. Each year the NTS Technology Needs Assessment, as foretold by NNSA strategic plans and management, NTS contractor managers and technical staff, and national weapons laboratory management and staff, is updated to identify anticipated technological needs currently under development as well as the "gaps" that remain to be addressed. In the annual process of revising this document, the number of prior-year "gaps" since addressed by SDRD funded projects is tabulated. These addressed needs are presented as the yellow bars in Figure 2.

This final program report covers SDRD project activities that occurred from October 2004 through September 2005. The numerous achievements it describes are a tribute to the skill and enthusiasm that Principal Investigators brought to their projects. While many of the R&D efforts drew to successful and natural conclusions, some spawned follow-on work that may lead to further research. The desired result of all SDRD activities is to develop and/or refine technologies that are implemented by programs. Some of the following project reports clearly identify R&D efforts with those kinds of results. Others, best characterized as feasibility studies, resulted in negative findings; these entirely valid conclusions, often reached in the pursuit of "high-risk" research, reveal that a particular technology is currently impractical. Both types of results help move the NTS toward a more vital technology base by identifying technologies that can be directly related to our programmatic mission.

In conclusion, FY 2005 saw continued evolution of a strong, innovative R&D program that benefited from increased competitiveness and a maturation of the planning and management techniques vital to aligning SDRD with anticipated needs for future NTS mission requirements.

I would like to extend a very special "thank you" to the editing team of Katharine Streeton, Heidi Utz, and Michele Vochosky for compiling, editing, and publishing this report; to Mark Kunish and Project Controls Engineer Pat Herrin for their valuable contributions to tracking progress and costs on the array of FY 2005 projects; to Kim Liu-Bacon and her team for compiling the financial data necessary to fulfill congressionally mandated reporting requirements; and to NTS technical site representatives Warnick Kernan, Chris Hagen, Steve Iversen, Rob Buckles, and Howard Bender, for helping implement and manage a very productive year of R&D at the Nevada Test Site!

Wil Lewis, SDRD Program Manager

SDRD Committee

Robert Braddy, Assistant General Manager, Stockpile Stewardship (Chairman)
Rick Lamison, Assistant General Manager, National Security Response
Nelson Cochrane, Assistant General Manager, Diagnostic and Engineering Operations
Roger Flanagan, Assistant General Manager, Remote Sensing Laboratory
John Manning, Manager, Los Alamos Operations
Tim Sammons, Manager (acting), Livermore Operations
Mike Martinez, Assistant General Manager, Special Technologies Laboratory

this page intentionally left blank

Los Alamos Operations (LAO)
P.O. Box 809
Los Alamos, New Mexico 87544

Livermore Operations (LO)
P.O. Box 2710
Livermore, California 94551-2710

North Las Vegas (NLV)
P.O. Box 98521
North Las Vegas, Nevada 89193-8521

Nevada Test Site (NTS)
P.O. Box 98521
Las Vegas, Nevada 89193-8521

Remote Sensing Laboratory – Andrews Air Force Base (RSL–A)
P.O. Box 380
Suitland, Maryland 20752-0108
(Andrews Air Force Base)

Remote Sensing Laboratory – Nellis Air Force Base (RSL–N)
P.O. Box 98521
Las Vegas, Nevada 89193-8521
(Nellis Air Force Base)

Special Technologies Laboratory (STL)
5520-B Ekwill Street
Santa Barbara, California 93111

this page intentionally left blank

A

ACFM	actual cubic feet per minute
AChE	acetylcholinesterase
ADC	analog-to-digital converter
AGEX	aboveground experiments
ALARA	as low as reasonably achievable
APD	avalanche photodiode
AR	antireflective (coating)
ARG	Accident Response Group

B

BEM	boundary element method
BiMOSFET	bipolar metal-oxide semiconductor field effect transistor
BN	Bechtel Nevada
BuChE	butyrylcholinesterase

C

CAD	computer-aided design
CBRN	chemical, biological, radiological, and nuclear
CCD	charge-coupled device
CFA	color filter array
CFD	computational fluid dynamic
ChE	cholinesterase
CL	cathodoluminescence
CLC	cholesteric liquid crystals
CM	consequence management
CMAS	Consequence Management Assessment Spreadsheet (software)
CMOS	complementary metal oxide semiconductor
CNF	carbon nanofiber
CNT	carbon nanotube
COTS	commercial off-the-shelf
CP	circular polarization
CPO	charged particle optics
CPU	central processing unit
CRT	cathode ray tube
CSDA	continuous-slowing-down approximation
CTIA	capacitive transimpedance amplifier
CVD	chemical vapor deposition

CW	continuous wave
CWA	chemical warfare agents
CZT	cadmium-zinc-telluride

D

DAC	digital-to-analog converter
DARHT	dual-axis radiographic hydrodynamic test machine
DC	direct current
D-D	deuterium-deuterium
DHS	U.S. Department of Homeland Security
DoD	U.S. Department of Defense
DOE	U.S. Department of Energy
DPF	dense plasma focus
DSP	digital signal processor
D-T	deuterium-tritium
DTRA	U.S. Defense Threat Reduction Agency
DXF	Data Exchange Format (file)

E

EBIT	Electron Beam Ion Trap
EDS	energy dispersive spectroscopy
EPA	U.S. Environmental Protection Agency
ESR	equivalent series resistance
ESTAR	(NIST computer program for computing electron interactions with matter)

F

4-D	four-dimensional
FDM	finite difference (method)
FE	field emission
FEA	field emission arrays
FEM	finite element (method)
FET	field-effect transistor
FRMAC	Federal Radiological Monitoring and Assessment Center
FTIR	Fourier transform infrared spectroscopy
FTS	Fourier transform spectrometer
FWHM	full-width (at) half-maximum

G

GC	(gamma) gross counts
GC	gas chromatography
GEANT	Groupe d'experts sur l'accès aux nouvelles technologies
GIS	Geographic Information Systems
GPS	global positioning system

H

HEC	health effect coefficient
HEDP	high-energy density physics
HPAC	Hazard Prediction and Assessment Capability
HV	high voltage

I

IC	integrated circuit
ICE	Isentropic Compression Experiments
ICF	inertial confinement fusion
IDL	Interactive Data Language
IDW	inverse distance weighting (algorithm)
IMETS	Integrated Meteorological Server
IMS	ion mobility spectrometer
IP	Internet protocol
IR	infrared
ITS	injector test stand

J

JPL	Jet Propulsion Laboratory

L

LAACG	Los Alamos Accelerator Code Group
LANL	Los Alamos National Laboratory
LAO	Los Alamos Operations (BN/NSTec)
LDRD	Laboratory Directed Research and Development
LED	light-emitting diode
LET	linear energy transfer
LGA	log departing coefficient
lidar	light detection and ranging

LiF	lithium fluoride
LIFS	laser-induced fluorescence spectroscopy
LIGA	*Lithographie, Galvanoformung und Abformung*
LLR	logarithmic likelihood ratio
LLNL	Lawrence Livermore National Laboratory
LMXG	laser multipulsed x-ray generator
LO	Livermore Operations (BN/NSTec)
LOS	liquid organic scintillator
LP	linear polarization
LPL	Long Pulse Lab (LO)
LSF	least squares fit
LSP	large-scale plasma
LSO	lutetium oxyorthosilicate
LTM	low thermal mass
LVO	Las Vegas Operations

M

MAC	multiply and accumulate
MATLAB	(software package for algorithm development, data analysis and visualization, and numeric computation)
MCA	multichannel analyzer
MCNP	Monte Carlo N-Particle (transport code)
MCNPX	Monte Carlo N-Particle Extended (transport code)
MCP	microchannel plate
MCPI	microchannel plate intensifier
MDA	Minimum Detectable Activities
MFP	microfiber plates
MIXS	multi-imaging x-ray streak camera
MOSFET	metal-oxide semiconductor field-effect transistor
MPCD	multipath communication device
MPP	Multi-Pinned Phase
MS	mass spectrometry
MSP	microsphere plates
M-Z	Mach-Zehnder

N

NARAC	National Atmospheric Release Advisory Center
NASA	National Aeronautics and Space Administration
NBC	nuclear, biological, and chemical
Nd:YAG	neodymium:yttrium-aluminum-garnet

NIF	National Ignition Facility
NIM	nuclear instrument module
NIST	National Institute of Standards and Technology
NLV	North Las Vegas Operations (BN/NSTec)
NNLS	non-negative least squares (fit)
NNSA	U.S. Department of Energy, National Nuclear Security Administration
NOAA	National Oceanic and Atmospheric Administration
NPTEC	Nonproliferation Test and Evaluation Complex
NRC	U.S. Nuclear Regulatory Commission
NREL	U.S. Department of Energy, National Renewable Energy Laboratory
NSTec	National Security Technologies
NTS	Nevada Test Site

O

OEM	original equipment manufacturer
OP	organophosphates
OPCW	Organization for the Prohibition of Chemical Weapons
OTDR	optical time-domain reflectometer
OTT	Optical Tagging and Tracking

P

PAG	Protective Action Guides
PCB	printed circuit board
PDD	polar direct drive
PDF	probability density function
PDV	photonic Doppler velocimeter
PiN (or PN)	(diode structure consisting of a p-doped layer, an n-doped layer, and an i-layer between the two, commonly the depletion zone/layer)
PMT	photomultiplier tube
PNNL	Pacific Northwest National Laboratory
POx	paraoxan
PSD	pulse shape discrimination

Q

QE	quantum efficiency
QR	(mathematical symbols for matrix factorization and solution of linear equations)

R

R&D	research & development
RASCAL	Radiological Assessment System for Consequence AnaLysis (atmospheric dispersion model)
RATS	Radiological Assessment and Training Simulator
RDAD	real-time data acquisition and dissemination
RDD	radiation dispersal device
RF	radio frequency
RIE	reactive ion etching
RSL	Remote Sensing Laboratory (BN/NSTec)
RSL-A	Remote Sensing Laboratory-Andrews Air Force Base
RSL-N	Remote Sensing Laboratory-Nellis Air Force Base
RTIA	resistive transimpedance amplifier
RTN	Radionuclide Temporal Normalization

S

SBC	single-board computer
SCA	single-channel analyzer
SCFM	standard cubic feet per minute
SEM/EDS	Scanning Electron Microscopy/Energy Dispersive Spectroscopy
SEU	single-event upset
SIMION 7	(an electrostatic ion optics modeling program)
SIMS	secondary ion mass spectrometry
SLLED	super luminescent light-emitting diodes
SNL	Sandia National Laboratories
SNM	special nuclear material
SNR or S/N	signal-to-noise ratio
SPL	Short Pulse Lab (LO)
SPME	solid-phase microextraction
SPRT	Sequential Probability Ratio Test
STL	Special Technologies Laboratory (BN/NSTec)
STL	Stereo-lithography Tessellation Language
SV	singular value
SWIR	shortwave infrared

T

2-D	two-dimensional
3-D	three-dimensional
T&E	test and evaluation

TAC	time-to-amplitude converter
TBU	time-base unit
TCC	target chamber center
TDR	time-domain reflectometer
THz	terahertz
TIC	toxic industrial chemicals
TMB	trimethyl boron
TOF	time-of-flight
TTL	transistor-transistor-logic (standard 4-volt logic pulse)
TTS	transit time spread

U

UCLA	University of California, Los Angeles
UCNI	unclassified controlled nuclear information
UCSB	University of California, Santa Barbara
UGT	underground testing
UNLV	University of Nevada, Las Vegas
UNR	University of Nevada, Reno
UTS	universal trigger system
UV	ultraviolet

V

VHOT	Very High Output Tube
VISAR	velocity interferometer system for any reflector
VME	Versa Module Eurocard

W

WFO	Work for Others Program (U.S. Department of Energy)
WMD	weapons of mass destruction

X

XEUV	extreme ultraviolet
XMCP	x-ray microchannel plate

Y

YAG	yttrium-aluminum-garnet

this page intentionally left blank

Accelerators and Pulsed Power

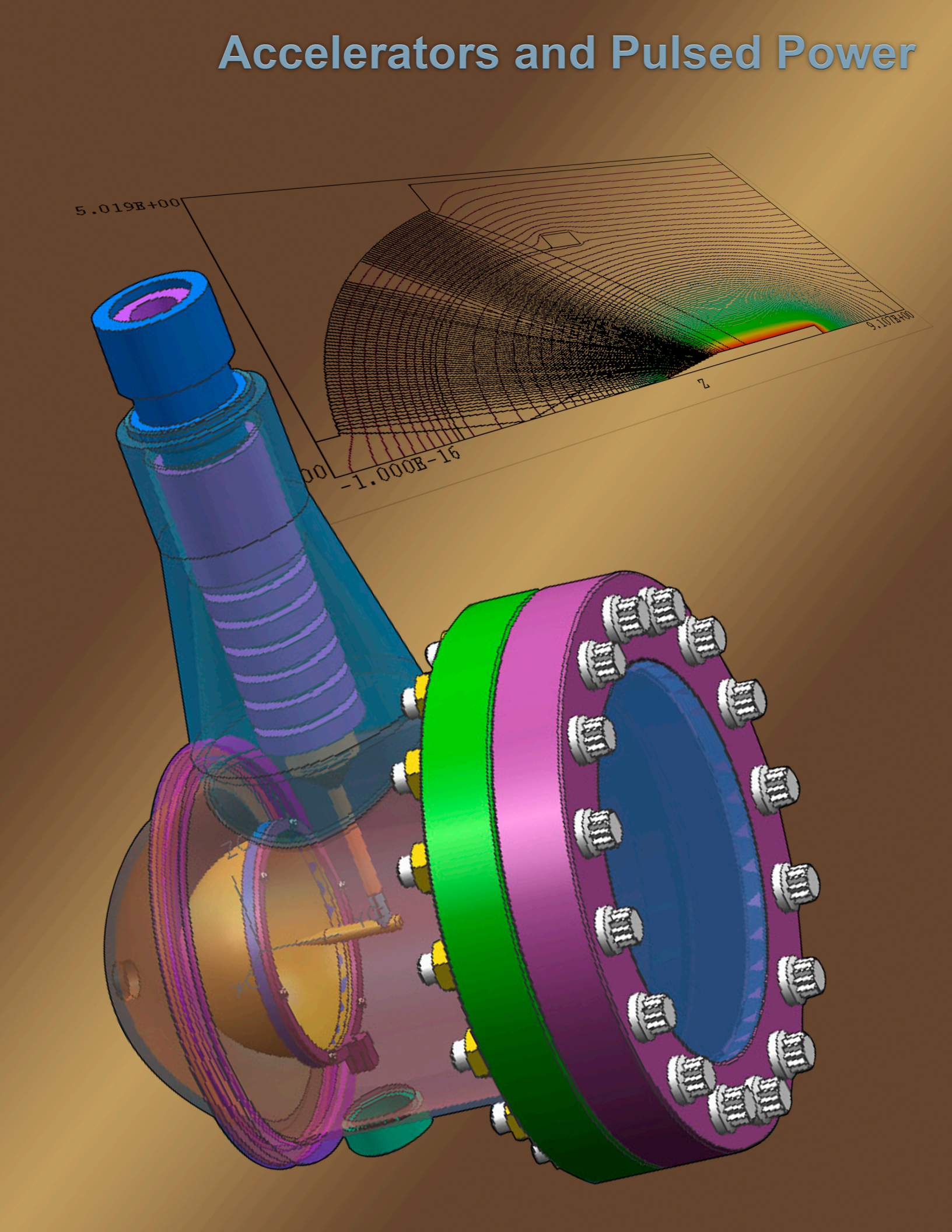

Laser Multipulsed X-ray Generator

Del Anderson, Michael Berninger,[1] Robert Hilko, Morris Kaufman, Craig Kruschwitz, David Schwellenbach, Thomas Tunnell
Los Alamos Operations

Gene Capelle
Special Technologies Laboratory

Brent Davis
North Las Vegas

Donald Ng
Livermore Operations

Our team has constructed a laser multipulsed x-ray generator (LMXG) for dynamic radiography. The tube, which awaits testing, will generate three, 30-ns-long pulses in 1 μs, with a dose of 10 mR per pulse at 15 cm. The x-ray pulses will originate from a single 532-nm laser pulse projected into a fiber-optic splitter and delay-line system. The laser light will illuminate the photosensitive S-20 cathode surface, and the electrons ejected from the S-20 will be accelerated across the diode A-K gap by a 150-kV, high-voltage (HV) bias onto a tungsten (or molybdenum) anode. Collisions between the electrons with the dense target anode will produce a 150-keV endpoint bremsstrahlung x-ray spectrum with a 4-mm-diameter spot size. The LMXG will be tested at STL.

Background

Multiple-exposure, low-energy flash radiographs are currently recorded on a variety of Stockpile Stewardship experiments using a separate source for each exposure. Because the sources do not share a single collinear view of the object, this approach introduces parallax. Our project investigates the feasibility of addressing this limitation through the use of a single anode to be repeatedly pulsed.

Project

Within a conventional multihead x-ray source, the pulsing action is largely defined by switching voltage between the cathode and separate anodes. The LMXG effort sought to develop a technique for generating multiple electron pulses onto the tip of a single anode. The design team researched how to generate these pulses independently from the accelerating voltage source. After evaluating a number of electron-emission schemes, we discovered that the shape and intensity of the electron source could

[1] berninmj@nv.doe.gov, 505-663-2032

be easily controlled by pulsing light onto a photoemissive surface. We also discovered that shining blue-green light onto the S-20 material widely used in photomultiplier tubes would most efficiently generate a repeatable, high-current electron pulse. By defining the pulsing action with a light source, the voltage source could be erected with a single anode, and the pulses could then be accelerated by the voltage onto a single anode.

The LMXG design concept evolved to combine all elements of the photoelectric effect, Child's law, and bremsstrahlung x-ray physics. The light shined onto an S-20 cathode material would transfer sufficient energy to the electrons bound near the surface to overcome the material's work function and be ejected into the gap between cathode and anode. These liberated electrons would be swept away from the surface by the electrical fields erected between the cathode and anode by the voltage source and accelerated onto the conical tip of the anode rod, where they would decelerate because of collisions with the dense anode atoms. The decelerating electrons would then produce the bremsstrahlung radiation used for radiographic imaging.LMXG requirements were defined with the design concept shown in Table 1.

Table 1. LMXG Design (Performance) Requirements

Requirement	Definition
Output Voltage	150 kV, maximum
Current	115 A
Dose at 30 cm	2.5 mR/pulse
Exposure time	25 to 30 ns

The LMXG design effort was divided into five parts: mechanical design, laser source, high-voltage system, anode and x-ray modeling, and fabrication. The resources and expertise to address each part were identified within BN, and independent design teams were created. Each team worked separately and met periodically to report progress and problems.

LMXG

The physical dimensions of the generator were defined in conjunction with its voltage source requirements. The distances between metallic chamber features were determined with the voltage breakdown rule of thumb, 85 keV/cm. Thus, the approximate chamber dimensions were defined as 6 in × 6 in × 11 in (Figure 1). The chamber was constructed with two tubes: a large main body with the nominal inner diameter of 83 mm and a conical HV feedthrough extended at a right angle from the main body. The feedthrough contained a ribbed insulating ceramic piece braised onto a 4-mm-diameter tungsten (or molybdenum) anode rod. The rod extended into the main body and was bent at a right angle concentric with its central axis. The rod terminated with a conical tip 4 cm from the interior surface of the main body's hemispheric endcap. The endcap was the 83-mm-diameter

LMXG cathode coated inside with the photosensitive S-20 material. A hemispherical extraction grid was supported by a holding ring in the gap about halfway between the anode tip and the cathode. The grid was a fine, custom-made, nickel wire mesh that was 95% transparent. The voltage-biased mesh contained a separate HV feedthrough in the main body of the chamber. A porthole for the entrance of the pulsed light source was at the opposite end from the cathode in the tube's main body. The porthole's anti-reflection coating made 532-nm light transmission 97% efficient.

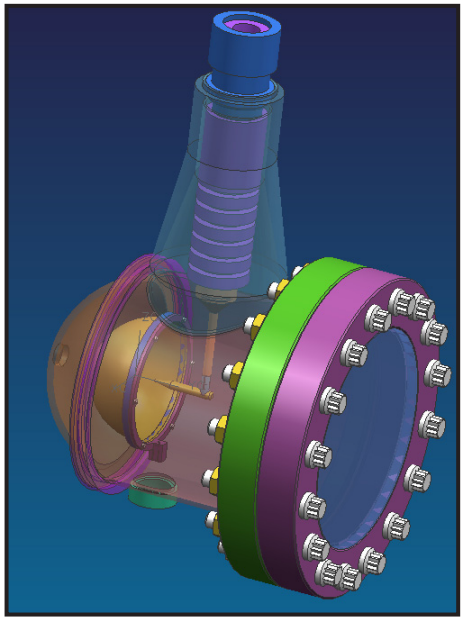

Figure 1. LMXG transparency

High-Voltage System

LMXG voltage was required to be 150 kV, to produce x-rays that would penetrate objects with low areal densities. We used the electromagnetic modeling code E-Stat to calculate the electrical characteristics of the generator and optimize its design (Figure 2). Prior to tube operation, a 350-ft coaxial cable was connected between the HV power supply and feedthrough, then charged to a total tube bias of 150 kV. The extraction grid was biased separately, to 15 kV. With the long charge cable, nominal voltage remained constant throughout pulsing. However, due to voltage division, when the electrical current flowed across the anode-cathode gap, the total high voltage between anode and cathode was 143 kV.

Light Source

To ensure a repeatable, uniform electron pulse, the cathode was required to produce the space-charge-limited current of 115 A for 25–40 ns per pulse. This magnitude of current required that the light source have at least 56 μJ of energy per pulse, to push the current from the cathode to its space-charge-limited saturation. Additionally, the current was required to be pulsed three times in 1 μs. This requirement for the number of pulses per μs was determined through discussions with researchers

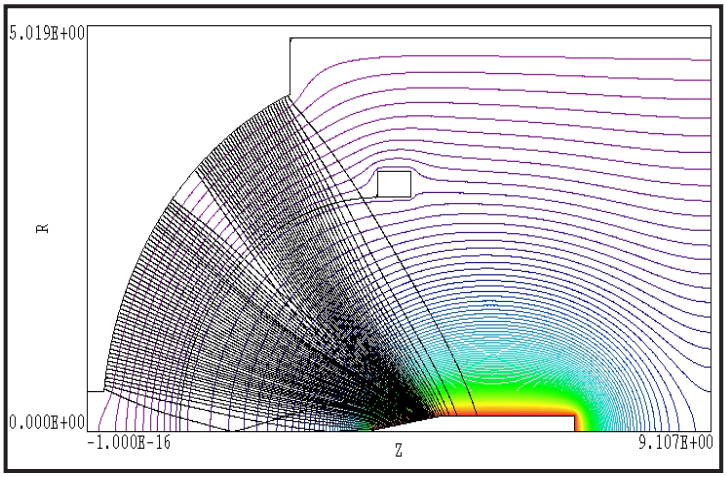

Figure 2. E-Stat calculation of the electron flow within LMXG

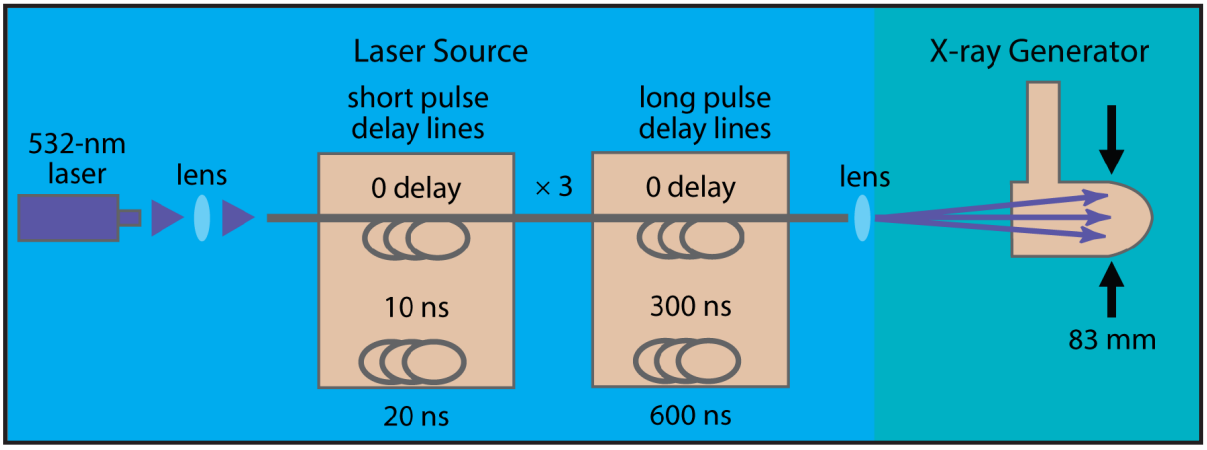

Figure 3. Fiber-optic delay system

in the shock physics field. With numerous light-emitting diodes (LEDs) and lasers on the market, it was relatively easy to identify a light source with adequate energy and pulse length to satisfy tube requirements. However, no laser produced multiple pulses on a μs time scale. Thus, we devised a technique to divide a primary laser pulse into multiple pulses with a fiber-optic splitting system (Figure 3). The fiber delay lines will generate three 30-ns laser pulses in 1 μs. The source of the laser pulses is a pulsed doubled Nd:YAG laser. Pulses are projected onto the cathode through the porthole at the opposite end of the horizontal arm by a fiber-optic splitter and delay-line system.

X-ray Production

The design effort used Monte Carlo N-Particle (MCNP) calculations to identify the x-ray spectrum characteristics created by the collisions between the electrons with the dense target anode. The spectra were required to produce a dose of 10-mR/electron pulse. In this situation, the collisions would create a 143-keV endpoint bremsstrahlung x-ray spectrum with a 4-mm-diameter spot size. The tube would generate a dose of 10 mR/pulse at 15 cm.

It was determined that two anode materials, molybdenum (Mo) and tungsten (W) (Figure 4), met the requirements for the dose. We also discovered that Mo and W produced spectra that could be targeted for specific applications. In the case of Mo, 70% of the x-ray flux was found to reside under the 18-keV K edge peak, making a Mo anode suitable for an application requiring a largely monochromatic x-ray spectrum. The W material produced a spectrum with a larger proportion of high-energy x-rays, and thus would be more suited to imaging dense objects.

Design Process and Fabrication

This effort culminated in a formal engineering design review, in which the full design was examined by a committee of subject matter experts. Upon acceptance, the project moved into the procurement

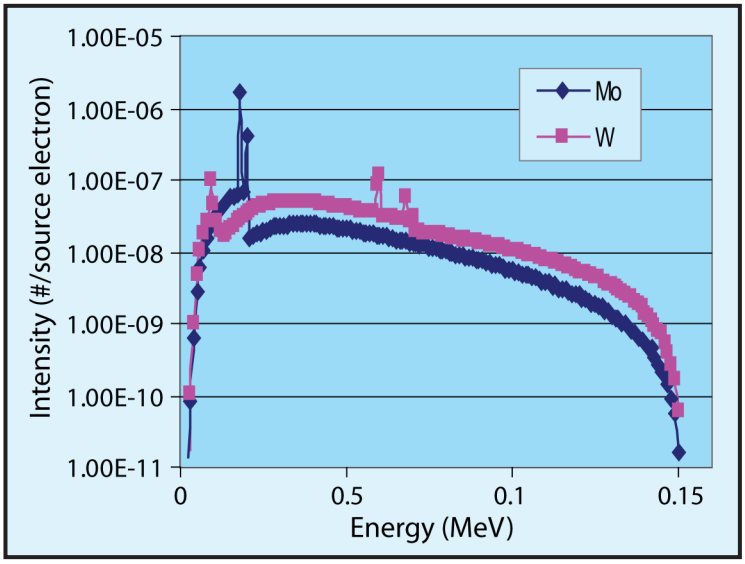

Figure 4. X-ray spectra calculated for collisions of 150-keV electrons with Mo and W

and fabrication phases. After fabrication at the Livermore Operations' processing lab, the tube was ready for delivery to STL, where an experimental team would test and validate the tube against requirements. However, on the eve of the experiments, flaws in the HV system design process were revealed, and the experiments were postponed.

Conclusion

According to the approved design, within the LMXG, a series of 532-nm laser pulses will excite current pulses from the photosensitive S-20 surface onto the cathode S-20-coated surface. The electrons from the S-20 will be accelerated across the gap between cathode and anode by the combined voltage biases of the extraction grid and the total tube bias. The grid will increase the maximum space-charge-limited current flow between cathode and anode to 115 A, by enhancing the velocity of the electrons as they leave the S-20 material. The grid also aids in focusing the electrons onto the cone at the 4-mm-diameter anode tip. After passing through the extraction grid, the electrons will be accelerated by the total tube bias of 143 kV onto a tungsten (or molybdenum) anode. Because the presence of gas within the tube would degrade the current during operations, the tube must be evacuated to a pressure of 1×10^{-5} torr.

A formal engineering design process was followed to design and build the generator. After investigating the HV system, we will test and validate the LMXG at STL. Field tests will then be arranged on the isentropic compression experiments at SNL and at the Atlas facility at the NTS.

this page intentionally left blank

A Tagged Photon Source for Energy-Dependent Radiography

Peter Heimberg[1]
Remote Sensing Laboratory – Andrews

Mike Mendez, Ken Moy, William Quam, Stephan Weeks
Special Technologies Laboratory

During the first year of this project, our primary goals were to generate a design for a "tagged" photon device (phase 1) and to construct an electron beam facility for development and characterization (phase 2). Beam characterization studies were carried out using the STL scattering chamber in parallel with the construction of a larger electron beam apparatus more suited to tagger development. The possibility of using the photoelectric effect to "inject" electrons into the accelerating potential was explored but yielded a mostly negative result. During the beam studies, which used forward bremsstrahlung photons as a diagnostic tool, electron energies of 170 keV, close to the published maximum, were observed. Monte Carlo simulations were carried out to describe and understand the experiments performed at STL. A primary beam current of 100 pA at peak energy was deduced using these bremsstrahlung simulations. A full simulation of the proposed tagger system was not completed.

Background

The first observation of electron beam production from heated pyroelectric crystals was made in 1992 (Brownridge). Since then, nearly monoenergetic beams with energies of up to 170 keV have been produced (Brownridge, 2001). Recently, these crystals have been used to drive fusion reactions by accelerating deuterium ions (Naranjo, 2005). Under the Bechtel Nevada SDRD program, a group at STL has developed a system to study these crystals in detail (Quam, 2004) and used them to produce terahertz radiation (Quam, 2005).

This project sought to design and begin construction on a novel, low-dose, spread-spectrum photon source for radiography, centered around a pyroelectrically generated electron beam. Their extremely compact size and ability to produce high electrical fields (~106 V/cm) make pyroelectrics attractive for applications requiring a portable, tunable, switchable radiation source. Leveraging STL's growing expertise in this area, we planned to use a $LiTaO_3$-based electron source to produce a low-flux (~1–10 K/s), "tagged" photon beam with energies between 20 keV and 500 keV. Roughly monoenergetic electrons with a momentum spread of 10–20% emergent from the $LiTaO_3$ crystal will impinge on a thin foil, leading to bremsstrahlung photons a few percent of the time. The photons and their associated electrons will then pass through a permanent dipole magnet that sweeps the

[1] heimbepc@nv.doe.gov, 301-817-3463

electrons out of the beam and deposits them on a solid-state detector measuring their energy. Since each measured electron with energy less than the initial beam energy must have radiated a photon, we expected to detect the photon downstream in a second detector (e.g., a CsI crystal), in coincidence with the electron. The energy of the downstream photon can be inferred from that of the electron ($E_{photon} = E_{beam} - E_{electron}$). In this way, an energy-selectable, low-dose radiographic image of a sample placed between the magnet and the downstream detector may be constructed.

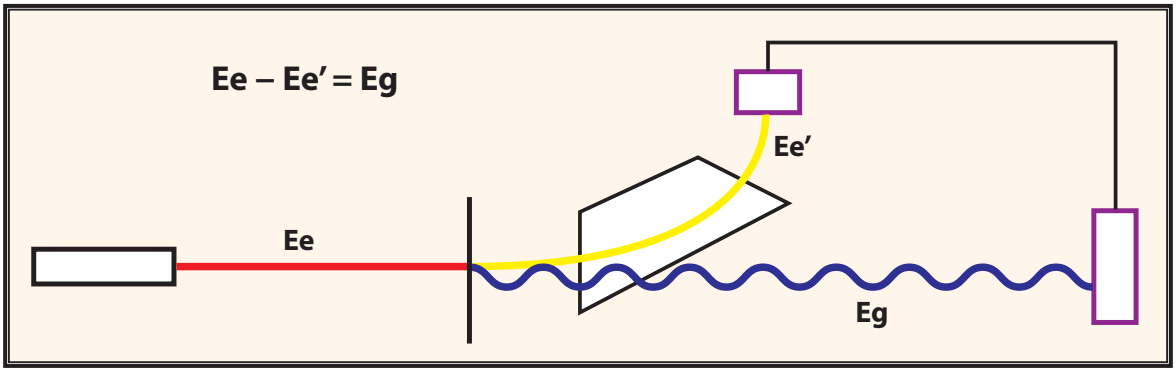

Figure 1. Basic components of a tagged photon system. Incoming electrons of known energy (red) radiate bremsstrahlung photons (blue). The reduced-energy electrons (yellow) are magnetically separated from their associated photons, which are detected in coincidence.

Photon-tagging systems have been used for years in the nuclear and high-energy physics communities. At electron energies relevant for such applications (50–5000 MeV), photon-tagging is a clean process: the electron beam energy spread is generally very small (dE/E ~10^{-4}), and the large Lorentz boost ensures that both the photon and the scattered electron emerge in the very forward direction. At low, almost nonrelativistic, energies (<500 keV), conditions are not nearly as favorable. First, a beam-energy spread no greater than about 10% can be expected from these crystals. Furthermore, the beams' focal length has been on the order of a few centimeters, indicating a huge emittance. The electron beam would thus have to be collimated, reducing the initial flux by a large factor. The final state configuration of the photon and scattered electron could be at much large angles, introducing an energy-dependent efficiency that must be properly accounted for. All these factors represent potential obstacles to developing the tagger. The first step in our approach would be to develop a suitable electron beam: increase the energy as much as possible and operate at a stable energy and current.

Project

The vacuum system built at STL for the terahertz radiation project was configured with a target ladder containing a phosphor screen and several thin bremsstrahlung targets, one of which was ~0.5-mil aluminum. Routine temperature cycling was performed on the crystal, and we observed on the screen

a beam spot at a distance of several centimeters. The thin aluminum target was then placed in the position of the beam spot, and temperature cycling was repeated several times. Gamma-ray spectra were obtained using a cadmium-zinc-telluride (CZT) detector positioned at 0° with respect to the beam direction and downstream of the target at several time intervals throughout the cycle. Figure 2 shows such spectra for a single 1-hour cycle. In this figure, time is increasing left to right and top

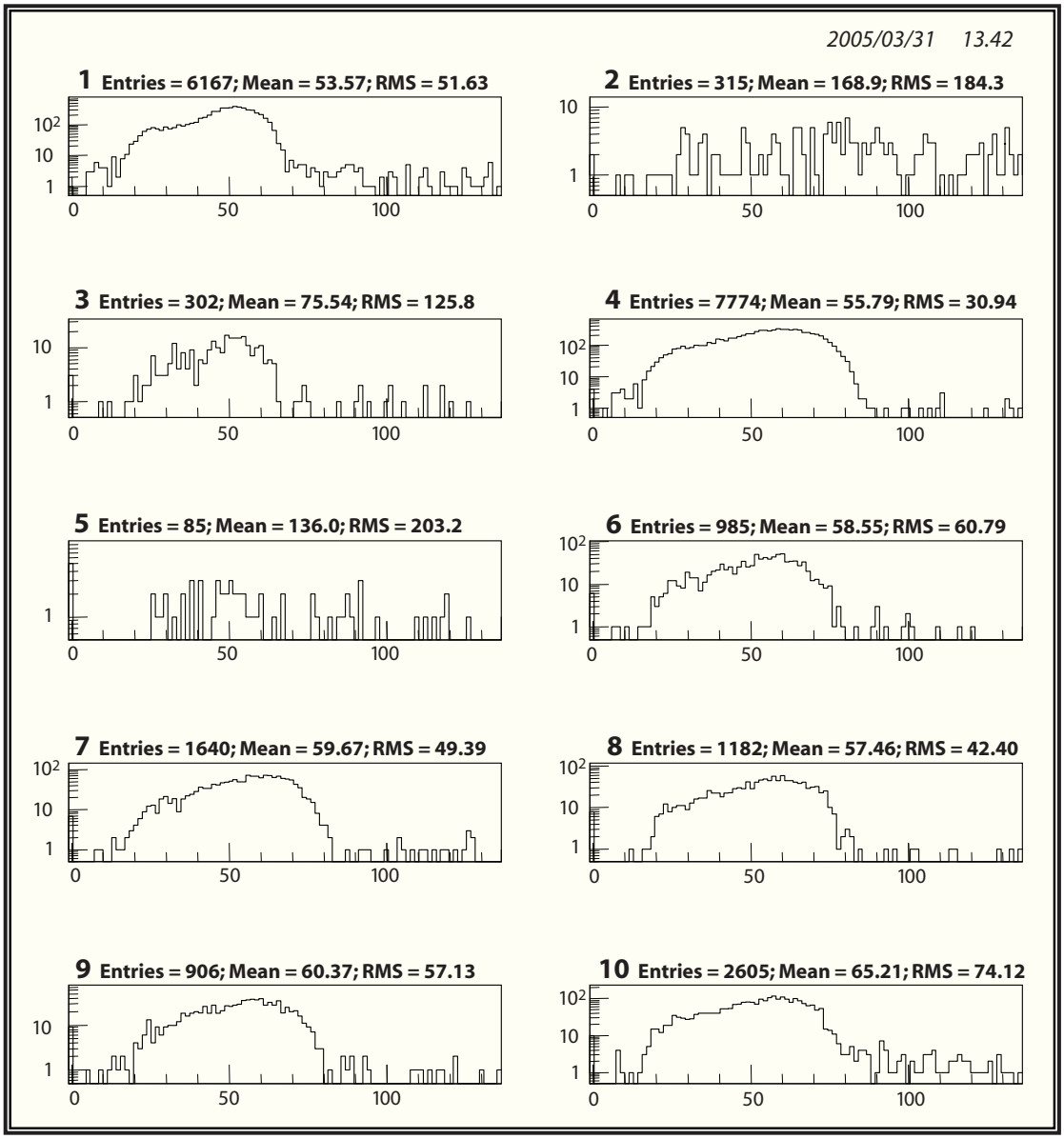

Figure 2. Bremsstrahlung (and x-ray) spectra obtained during a heating-cooling cycle (left to right/top to bottom is time ordinal). The x axis is given in keV. Spectra were obtained by a small CZT detector.

to bottom, with the top two panels taken during a period of heating, and the remaining panels corresponding to the adiabatic cooling phase. The first two and last spectra were collected for 10 minutes; the rest were collected for 2 minutes. Some spectra (#2, 3, 5, 6) appear to have very few counts in them. These measurements immediately follow or contain a discharge event. When a discharge occurs, the crystal tip is momentarily neutralized, and no source of electrons or ions is present to be accelerated. As the crystal continues to change temperature, the supply of free electrons reaches a quasistatic equilibrium. As long as this source (proportional to the temperature change rate) remains below a certain level, discharge is unlikely to occur. The figure also makes clear that the endpoint of the detected photon energy spectrum seems to basically stay constant at ~80 keV. This probably indicates that the change in surface charge density between T = 25°C and 100°C is relatively small compared to its magnitude.

Simulations of the test configuration using the GEANT321 simulation package were performed to bolster the assertion that we were seeing direct bremsstrahlung photons from the target. The scattering chamber itself remained to be added, but the (idealized) beam, bremsstrahlung radiator target, exit window, and shielded detector were included. Figure 3 shows a rendering of the setup being simulated (left) and a spectrum expected in the NaI detector (right). The characteristic 1/E behavior is apparent in this configuration in which the detector subtends a significant solid angle (in contrast to spectra previously obtained with a very small CZT detector).

The green disk is the thin, aluminum bremsstrahlung radiator target. The blue disk is the exit window, and the yellow-green tube is 3/8"-thick lead shielding that houses the 2 × 2" NaI detector (red). The blue tracks belong to photons; the red, to electrons. The simulated spectrum is the result of 20 million

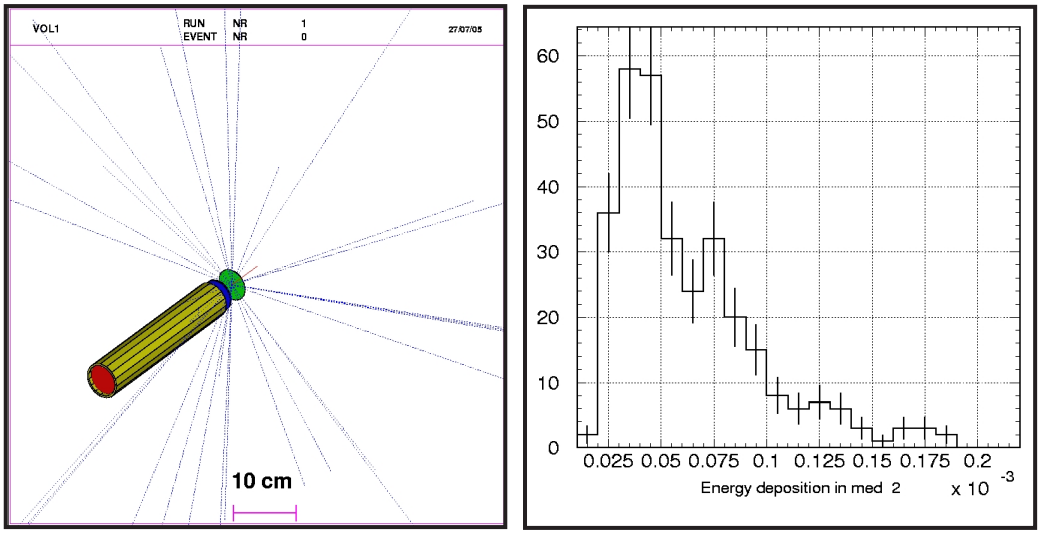

Figure 3. (left) Rendering of the geometry used to simulate the detected bremsstrahlung photons; (right) simulated bremsstrahlung spectrum

electrons striking the target with 200 keV of energy. When compared with the observed rates in the detector, approximately 100 pA is found for the beam current. This is within an order of magnitude of those currents measured in previous STL work (0.2–1 nA).

Figure 4 shows the bremsstrahlung spectrum as a function of time during heating (slice 1 of the left plot is a calibration source). A maximum beam energy of nearly 170 keV was obtained in both runs. A detailed comparison with simulations must be performed to correctly interpret the observed spectral shape. The beam energy and current shown here depends on the rate of temperature change (or thermal gradient, perhaps). This effect is well documented in the literature (Brownridge, 2001; Quam, 2004). Future improvements to these measurements include a feedback loop to maintain constant rates of temperature change. Furthermore, the crystal temperature gradient will be monitored and the electron beam will be measured directly, enabling a reliable determination of the beam energy spread.

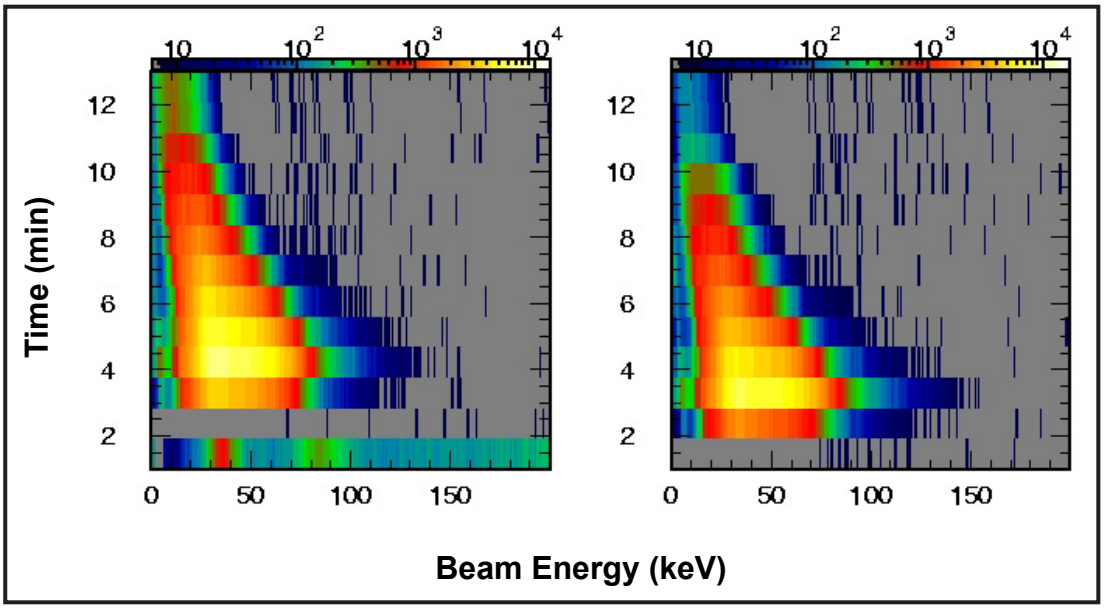

Figure 4. Bremsstrahlung spectrum as a function of time measured during LiTaO3 crystal temperature cycling. The first time slice in the left plot is a calibration spectrum (peaks at 35 and 83 keV).

The literature (Brownridge, 2001) shows that, in direct measurements of electron beam energy, 170-keV beams have about a 10% energy spread, but only when short measurement intervals are used. This drift (or decay) of beam energy as a function of time would make such a device unsuitable for a tagged photon beam that relies on stable beam conditions. Thus, we focused our attention on making this acceleration mechanism work in the steady state, not just during heating or cooling. If part of the

mechanism for acceleration is the potential created at the surface by the neutralizing layer of collected charge, which at long distances is cancelled by the polarization charge within the crystal itself, then a source of zero-energy electrons released or injected at the crystal surface is needed. One idea was to create a source based on the photoelectric effect. To test this concept, we evaporated a thin (~1-μm) layer of aluminum onto the tip of a crystal. An ultraviolet light-emitting diode (UV LED), 265-nm light source was then positioned inside the vacuum chamber within 1 cm of the crystal surface. Figure 5 shows a layout of the apparatus used. The electron beam emergent from the crystal (light blue) will strike the 0.5-mil Al radiator. The resulting photon will exit through a thin, Mylar window to be detected in a 2 × 2" NaI detector (green). The in situ UV LED appears in dark blue.

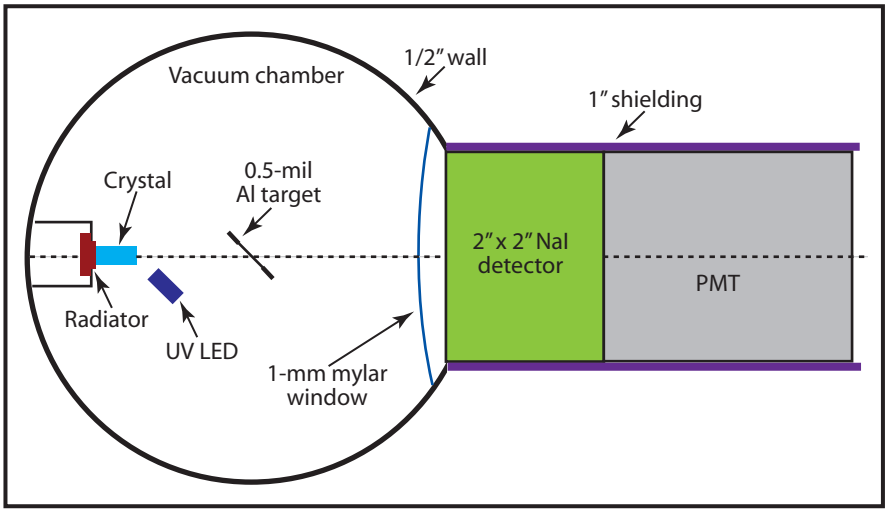

Figure 5. Configuration for photoelectric injection test

Figure 6 shows the components inside the scattering chamber. In these tests, the crystal was heated and allowed to equilibrate at 135°C. The LED was then cycled on and off at 10- and 30-minute intervals, while the NaI-based detector collected counts. Here we attempted to reduce the systematic uncertainties due to changes in temperature and pressure (which were monitored and held constant). Any increase in count rate because of the light source would indicate acceleration of photoelectrons. In Figure 7, the results for approximately 10 hours of data from two separate runs are expressed in terms of a percent asymmetry in the counting rates (dominated by background). The combined result (triangle) shows a 2 ± 1% asymmetry, a 2σ effect statistically. Systematic uncertainties, which are not easy to determine to the 1% level, could easily account for the observed difference. Thus, we consider this to be a null result or, at best, not very encouraging.

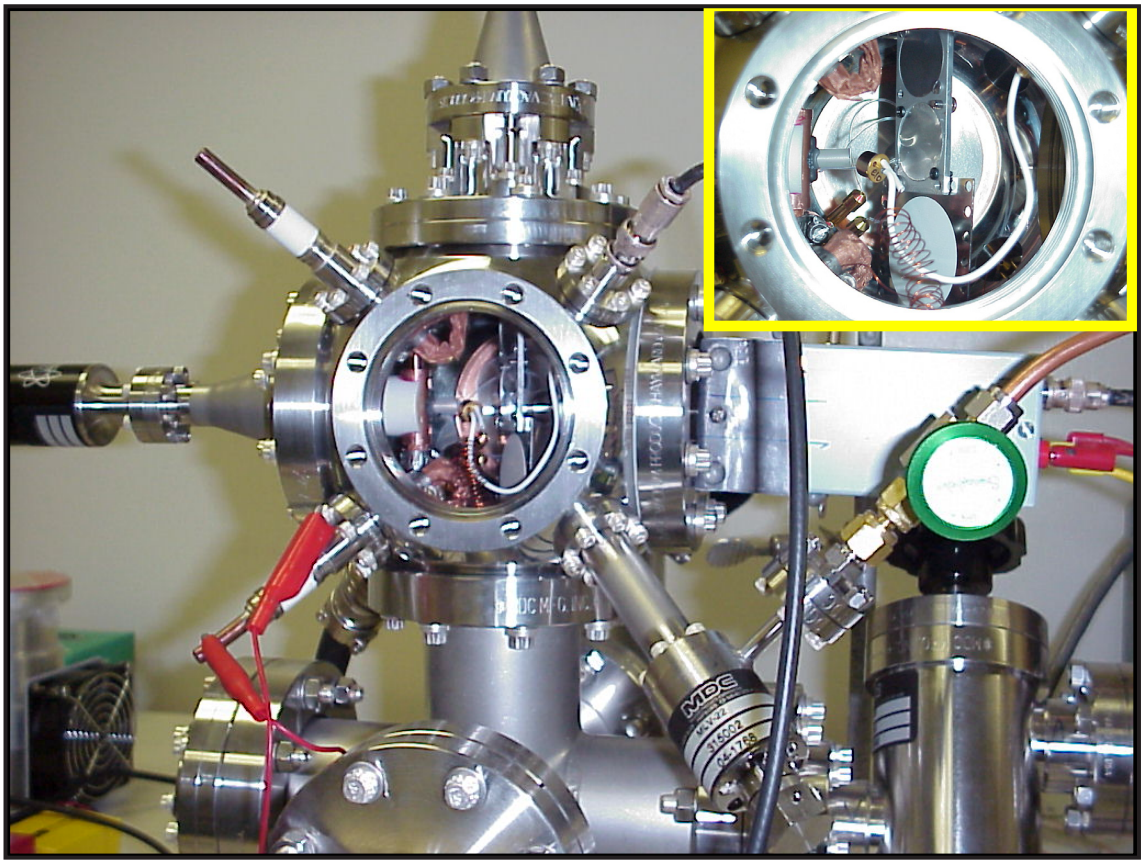

Figure 6. Apparatus used in the injector tests. Inset: crystal, UV LED, and bremsstrahlung radiator.

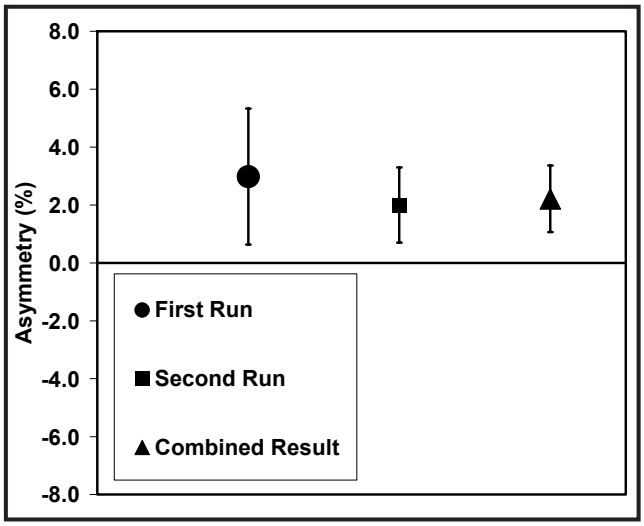

Figure 7. Asymmetries in photon counting rates measured with the LED on and off

This result might be attributable to the buildup of an Al-O layer on the Al coating. A recent measurement of the effect of the buildup on the work function (Magkoev, 2001) shows an increase from 4.2 to 4.9 eV, placing it just out of reach of our LED, which emits 4.7-eV light.

Conclusion

We have begun to develop an electron beam system with the goal of attaining the energies, stability, and currents required for use in a tagged photon device. Simulation of the system has begun, and initial results compare well with the data obtained in beam testing. A full simulation of a tagger, however, was not completed as planned. This work is still in the early stages.

A follow-on proposal to complete the development of the electron beam and implement a coincidence counting system for bremsstrahlung photons has been submitted. Should these experiments be completed, a solid assessment of this technology's use in a tagger system will be reached.

Acknowledgments

The authors would like to thank L. Maximon of George Washington University for providing bremsstrahlung calculations.

References

Brownridge, J. D., "Pyroelectric x-ray generator," *Nature* **358** (July 23, 1992) 287.

Brownridge, J. D., S. M. Shafroth, D. W. Trott, B. R. Stoner, W. M. Hooke, "Observation of multiple nearly monoenergetic electron production by heated pyroelectric crystals in ambient gas," *Appl. Phys. Lett.* **78**, 8 (Feb 19, 2001) 1158.

Magkoev, T. T., G. G. Vladimirov, "Aluminum oxide ultrathin-film growth on Mo(110) surface: a work function study," *J. Phys. Condens. Matter* **13** (2001) L655–L661.

Naranjo, B., J. K. Gimzewski, S. Putterman, "Observation of nuclear fusion driven by a pyroelectric crystal," *Nature* **434** (April 28, 2005) 1115.

Quam, W., S. Weeks, "Heat-Stimulated Lithium Niobate X-ray Source," *Nevada Test Site–Directed Research, Development, and Demonstration*, FY 2003, Bechtel Nevada, Las Vegas, Nevada, 2004, 51–54.

Quam, W., M. Mendez, K. Moy, S. Sawyer, S. Weeks, "Lithium Niobate Terahertz Generator," *Nevada Test Site–Directed Research, Development, and Demonstration*, FY 2004, Bechtel Nevada, Las Vegas, Nevada, 2005, 31–34.

Design and Test of a Fast-Pulsed Assembly for the Dense Plasma Focus

Bernard T. Meehan[1]
North Las Vegas

This project sought to demonstrate that BN's 130-kJ OneSys plasma focus device can be used as a fast-pulsed assembly. The fast-pulsed assembly generates an intense pulse of fission neutrons by irradiating a stack of 238U disks with neutrons from either deuterium-deuterium (D-D) or deuterium-tritium (D-T) fusion. This operational test demonstrated the capability of the dense plasma focus (DPF) to be used in future experiments involving fast-pulsed assemblies and possibly as a pulsed epithermal neutron source.

Background

Using the OneSys DPF as a fast-pulsed assembly would allow BN to participate in experiments that require brief, intense neutron pulses. These experiments include:

- neutron-detection system design, characterization, and calibration
- neutron dose delivering to test objects (damage studies)
- neutron radiography and tomography systems
- neutron resonance spectroscopy
- tailored output through careful selection of neutron multipliers

Project

Very High Output Tube Anode Design and Fabrication

The Very High Output Tube (VHOT) anode was designed to put depleted uranium disks as close to the Z-pinch in the plasma focus tube as possible, while completely protecting the uranium from the energetic deuterium plasma. The VHOT will also allow for samples or detectors to be introduced into the bore of the anode. In Figure 1, below, the uranium disks are shown in the VHOT anode cutaway, secured by a retaining spring. The spring prevents the disks from shifting in the anode bore during installation. Disk insertion required a new mechanical design for the anode base and a new vacuum seal method. The anode carries a pulse of ~1.4 million A and is subject to mechanical shock.

[1] meehanbt@nv.doe.gov, 702-295-0490

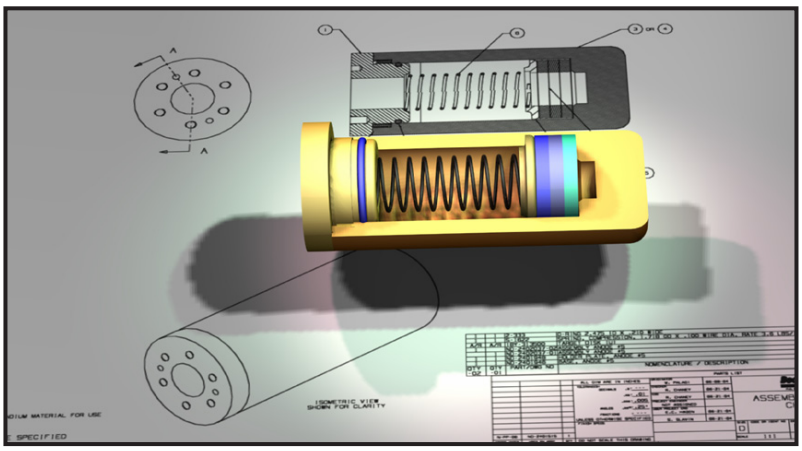

Figure 1. VHOT anode concept drawing

^{238}U Disk Fabrication and Delivery

The team also expended significant effort on determining the safe and proper way to handle depleted uranium disks for this experiment. The procedure preparation, documentation, and staff training will make future fast-pulsed assembly experiments safer and more efficient.

LANL provided the depleted uranium disks to our specification. To prevent uranium oxidation, the disks were wrought, machined, and electroplated with nickel. The blueprint and finished product appear in Figure 2.

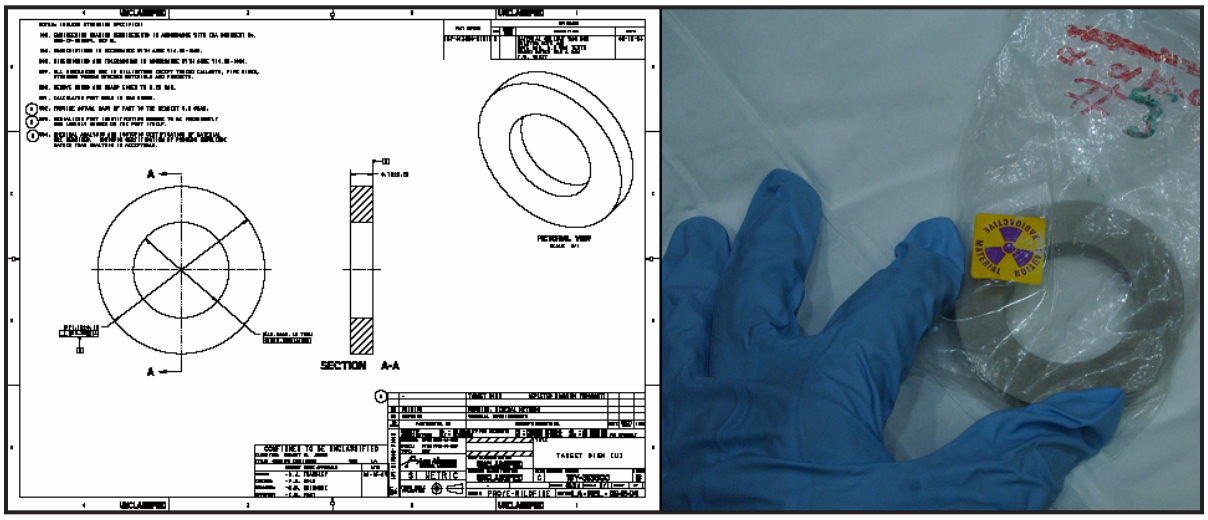

Figure 2. Uranium disk inserts

Optimizing VHOT Tube's D-D Fusion Performance

In order to produce the highest output from the fast-pulsed assembly, neutron output from the deuterium fusion reaction in the plasma focus tube must be maximized. This was most easily accomplished without the uranium disks inside, or even near, the plasma focus tube. Optimization also allowed us to perform background measurements to compare to the neutron output when the uranium disks were installed. The background measurements consisted of:

- gamma/x-ray background levels, with and without the disks installed;
- firing the plasma focus tube with argon for a null measurement, with and without the disks;
- firing the plasma focus tube with deuterium inside but no disks installed.

MCNPx Calculations

Calculations performed using Monte Carlo N-Particle Extended code (MCNPX) at the University of Nevada, Las Vegas (UNLV), super-computer cluster indicated that the fusion neutrons from the deuterium fusion in the plasma focus tube would generate fission neutrons in the uranium disks. The pulse width of the fission neutrons would be much longer than that of the fusion neutrons because of the nature of the two interactions. In the MCNPX-generated neutron energy spectrum (Figure 3), the dark green area indicates the fission neutrons to be produced in the uranium disks. The blue line represents the DPF output, as seen by a detector outside the DPF. The green area represents the additional neutron flux due to the fissioning of the uranium disks.

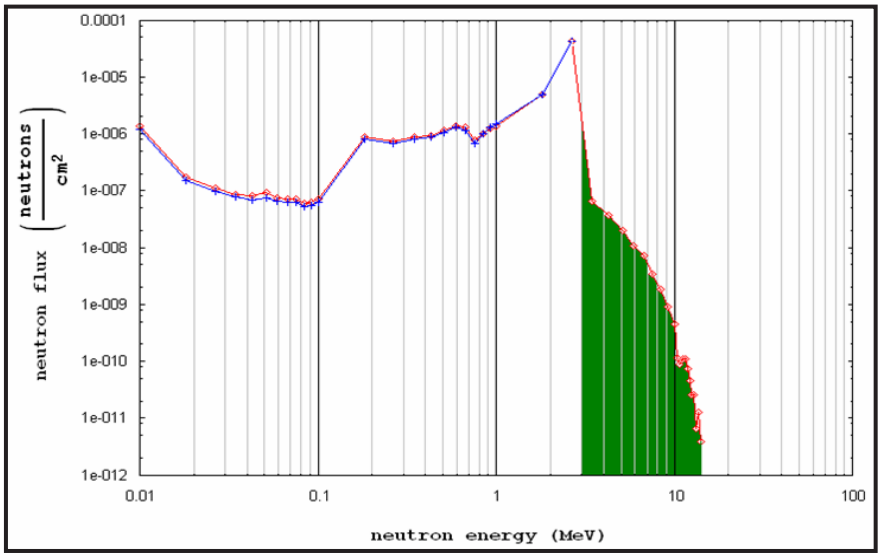

Figure 3. DPF neutron energy spectrum

VHOT Tube Performance with ^{238}U Disks Installed

The primary DPF neutron diagnostics are beryllium-activation detectors. As they quantify neutron output by measuring decay radiation from neutron activation of the detection element, beryllium,

they cannot discriminate between deuterium fusion neutrons and neutrons from fissions induced in the uranium disks. The neutron yield of the plasma focus tube can be inferred from integrating the time history of beryllium-activation detector activity, as shown in this equation:

$$f \int_a^b \lambda N_0 e^{-\lambda t} dt = \left(e^{-a\lambda} - e^{-b\lambda}\right) f N_0 = K N_0, \quad \textbf{(1)}$$

where:

- f is the geometric and efficiency factor between the measured activity and the total activity,
- N_0 is the number of neutrons from the event,
- λ is the decay constant of ^{6}He, and
- K is the calibration constant between the integral and actual number of neutrons.

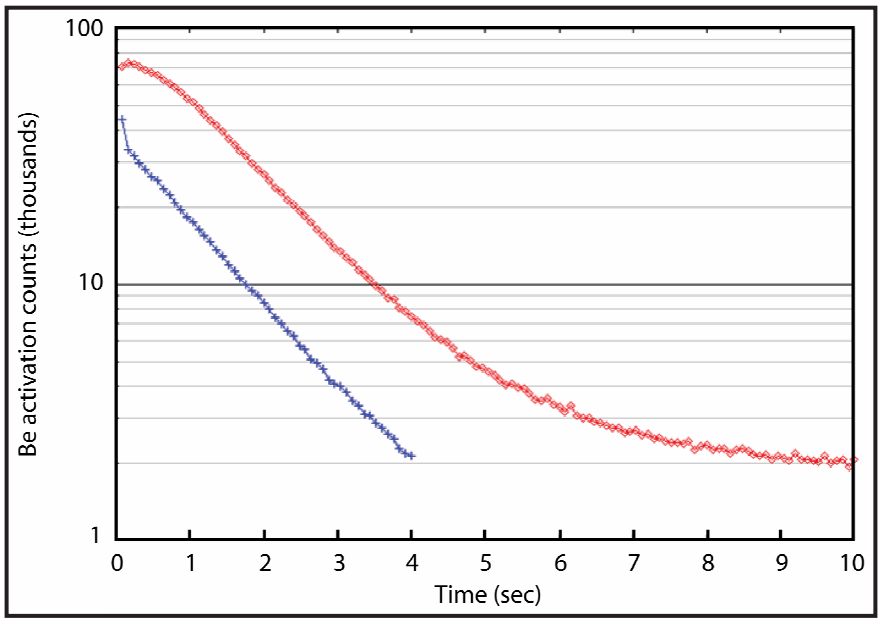

Figure 4. Beryllium activation data

Shown in Figure 4 is the beryllium-activation detector response for two experiments. The blue curve is the activation decay of a deuterium shot with the VHOT anode in the plasma focus tube. The linear decline of the activity on the log-scale plot indicates the normal decay of ^{6}He. The red curve indicates that the total neutron yield increases when the uranium disks are placed halfway between the pinch

in the plasma focus tube and the beryllium-activation detectors. Activation decay also declines at a less than exponential rate of the ^{6}He decay, showing the presence of decaying fission products in the uranium disks.

Conclusion

This research has successfully demonstrated the capability of the OneSys DPF device for:

- **fast-pulsed assembly**
  - As noted, fast-pulsed assemblies allow augmentation of the neutron yield of existing DPF sources by factors of 10 or more, depending on the fissionable mass' geometry, size, and composition.
- **mixed spectrum (fusion-fission) output**
  - When used with D-D or D-T fuel, the DPF generates a monoenergetic pulse. Earlier work, "Tailored Neutron Source" (Pigg, 2004), demonstrated that this monoenergetic spectrum can be modified by moderation and reflection to approximate the broad energy spectrum characteristic of a fission source. This research builds on this earlier work and offers experimenters not only a more powerful source, but a source with a fission-fusion spectrum ideal for many dosing/damage, characterization, and calibration tasks.
- **high-output via pulsed assembly**
  - Many neutron uses demand either high dose or high dose rate. This work has demonstrated the feasibility and practicality of a fast-pulsed assembly driven by a DPF.

and the team's capability to carry out:

- **uranium ordering, shipment, storage, and handling**
  - The processes to receive, store, and use depleted uranium disks have been created, approved, and utilized, allowing further work to proceed efficiently.
- **DPF neutronics modeling**
  - At UNLV, the MCNPX code was used to model output. We have demonstrated not only the utility of modeling and comparing experiment to theory, but also the efficacy of the BN-UNLV collaboration, a resource that will be utilized for future work.

Reference

Pigg, J. L., E. C. Hagen, "Tailored Neutron Source," *Nevada Test Site–Directed Research, Development, and Demonstration*, FY 2003, Bechtel Nevada, Las Vegas, Nevada, 2004, 43–46.

this page intentionally left blank

Novel Anode Cathode Development for Dense Plasma Focus

Bernard T. Meehan[1]
North Las Vegas

This project intended to improve the performance of dense plasma focus (DPF)-type Z-pinch fusion sources by designing, fabricating, and testing novel anode-cathode assemblies. Two possibilities included increasing neutron yield or decreasing pulse width. In this research, we used the BN 130-kJ OneSys DPF. This work sought to broaden the characteristics and types of radiation produced during fusion burn, and to improve the efficiency and reliability of OneSys. The OneSys device was systematically tested under a wide range of voltages, gas pressures, and gas mixtures. Test results were then used to optimize the machine for high neutron yield or narrow pulse width.

Background

This project both broadened and improved the performance of a DPF device constructed in an earlier SDRD project. This knowledge could then be applied to the design of future BN DPF devices, and increase the scope of neutron science that could be accomplished by BN.

Project

Dose Maximization

Dose maximization is achieved by increasing the efficiency of the energy transfer from the capacitor bank to the plasma in the focus tube. Boosting yield through adding efficiency leads to a trade-off with pulse-width minimization, as energy transfer is more efficient when it occurs over a longer time.

Our team increased source efficiency by attempting to concentrate the plasma near the plasma-focus axis before the pinch phase began. Since less plasma escapes, more material exists for the magnetic piston effect to compress, and thus, additional fusion neutrons are generated. Our experiments showed that a tapered anode and cathode (Figure 1) yielded a significantly higher dose than the traditional Mather design.

Pulse-Width Reduction

We believed that reducing DPF pulse width would eliminate multiple pulses and reduce pinch duration. Under some circumstances, the DPF generates several small pulses closely spaced in time,

[1] meehanbt@nv.doe.gov, 702-295-0490

instead of one larger pulse. For most experiments requiring short-duration neutron pulses, this problem may be worse than with long-duration neutron pulses, since the times of interest in the experiment are obscured.

Multiple pulse outputs are thought to happen because of an asymmetry in the plasma shockwave when it arrives on the top of the anode. Our experiments have shown DPF output to be extremely sensitive to any deviations from cylindrical symmetry. An offset of 0.001″ can mean a significant reduction in yield and output, strongly favoring multiple pulses. Another factor that influences the tendency of the anode-cathode assembly to multiple-pulse is how well the anode-cathode assembly contains electromagnetic standing waves. Essentially, the more the area near the top of the anode

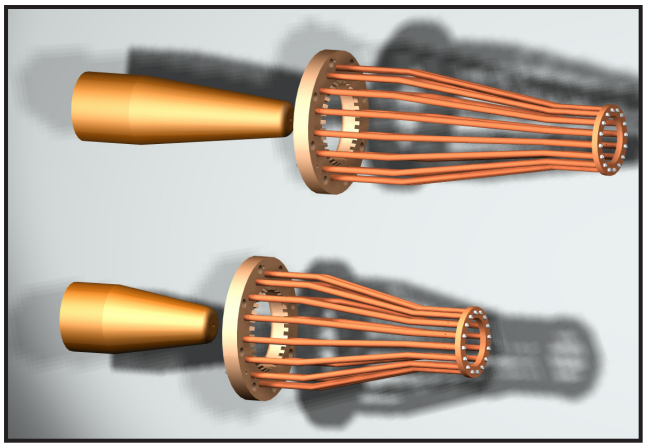

Figure 1. Exploded view of the tapered anode and cathode design, illustrating tapering

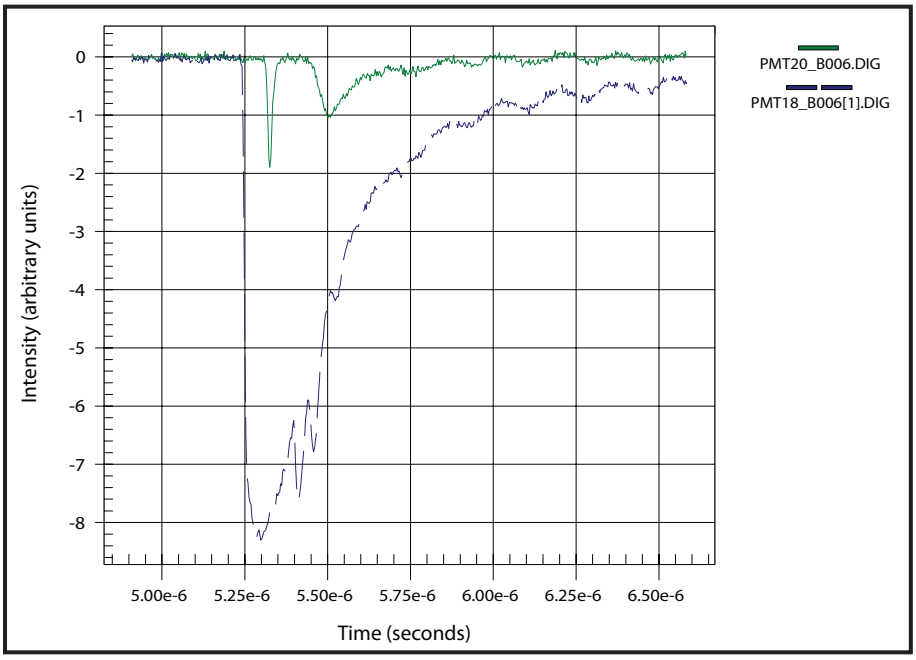

Figure 2. Time-of-flight (TOF) data for single-pulse DPF event

is like a resonant cavity, the more likely the anode-cathode assembly is to pulse multiple times. Experiments have shown that our tapered anode-cathode design has a high yield but also a tendency to generate multiple pulses.

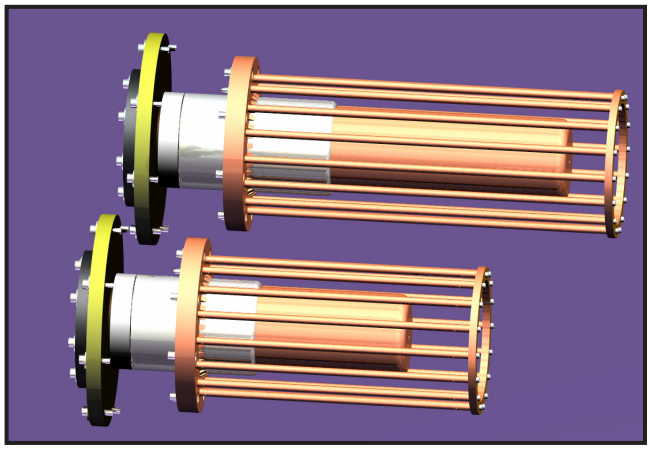

Figure 3. Short and long cathode cages

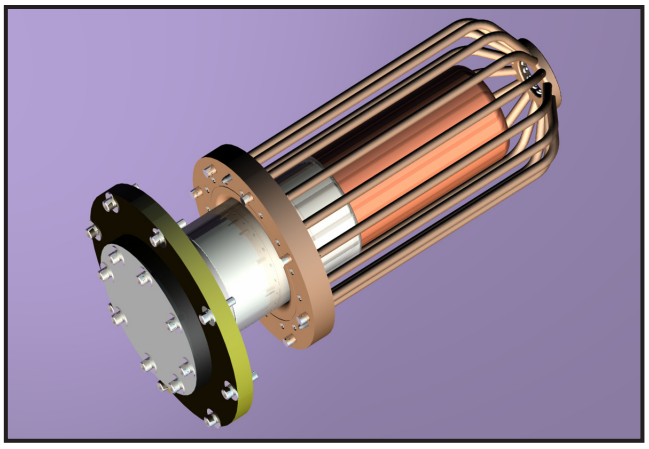

Figure 4. High gamma-neutron ratio tube

The other major effect on neutron pulse duration is the radial stability of the plasma shockwave. This is primarily controlled by operating voltages, experimental gas parameters, and insulator height. These factors combine to determine the strength and stability of the shockwave as it travels down the bore of the plasma focus tube. The height of the cathode cage is an additional factor that determines

shockwave stability as it reaches the anode end in the tube. Figure 3 compares two anode-cathode assemblies with different distances from the tops of the anode to cathode, as well as dissimilar insulator lengths. These assemblies illustrate some parameters under study during this research.

Tailored Output

Used for a variety of research and nonresearch tasks, the DPF device can provide a pulsed neutron output for characterizing neutron detectors for the national laboratories. Tested with this device are many neutron detectors for measuring pulsed neutron outputs in strong gamma and x-ray backgrounds. The ability to produce pulses similar to those clients expect to see in their experiments greatly benefits those using the DPF to operationally test detectors and diagnostic systems. Several candidate anode-cathode assemblies with similar outputs were found, but much room for improvement exists. Figure 4 shows an assembly that yielded a large gamma and x-ray peak compared to the neutron output pulse.

Conclusion

After examining 21 anode-cathode configurations, the team identified plasma focus tube designs that met the design criteria sought at the project's inception. These assemblies delivered neutron pulse widths τ <30 ns, increased neutron yield through greater energy transfer efficiency at constant stored energy, and produced a large gamma-to-neutron output ratio necessary for realistic characterization of some detector systems and useful for characterization and calibration of fast gamma detectors.

Carbon Nanofiber Field Emitter

Ken Moy,[1] *Stephan J. Weeks*
Special Technologies Laboratory

The goal of this project was to develop an electron beam source using field emission (FE) from enhanced carbon nanotube (CNT) structures. Conductive coatings were applied to enhance CNT structures by preventing premature breakdown at relatively low-vacuum operating pressures, and to increase quantum tunneling or emission yield efficiency. During the fiscal year, we entered collaborations for CNT production and coating. First Nano, Inc., delivered two batches of CNT structures. The University of Nevada, Las Vegas (UNLV), coated one batch with a conductive nickel layer, and we achieved a robust FE. Our future goal is to refine the CNT structures to be modulable up to near GHz frequencies.

Background

FE is based on quantum-mechanical tunneling of electrons through the metal-vacuum surface-potential barrier of a conductive solid. An increase in the applied electric field enhances tunneling probability by effectively lowering this potential barrier. This effect was first discovered by Fowler and Nordheim (1928). Earlier efforts to develop an FE-based electron beam source with the ultimate goal of generating pulsed x-rays were unsuccessful due to the ultra-high vacuum requirement of the silicon FE arrays (FEA). If the vacuum is less than ideal, a high FE current emitted by an FEA tip will ionize the residual gas. Gas ions then bombard the FEA tip to create small protrusions that greatly enhance the FE current. Joule heating follows to destroy the tip.

Since the advent of carbon nanofibers (CNF) or CNTs, researchers worldwide have turned to these materials as a more robust candidate to replace silicon FEAs, specifically due to their less stringent requirement for an ultra-high-vacuum operating environment. The application of conductive coatings is expected to enhance quantum tunneling efficiency and increase the structural integrity of CNTs at high-emission-current operations in moderate vacuum. If achievable, these structures promise an electron beam source that can be operated at higher vacuum pressures and produce high currents with low beam emittance, and provide robust and stable emission suitable for photocathodes. These attributes could also help in developing more efficient phototubes and compact, bright-current sources for electron beam accelerators and x-ray devices. These devices form a suite of tools needed by DOE missions and programs in Stockpile Stewardship, Homeland Security, and support to other governmental agencies.

[1] moykj@nv.doe.gov, 805-681-2284

Project

Collaborations

After much research, we found the vendor First Nano, Inc., a division of CVD Equipment Corporation, who was willing to assist us with an R&D effort aimed at producing vertically aligned, multiwall CNT structures well suited for FE. First Nano is local and thus, could provide easy access for onsite consultation and quick response. In addition to CNTs grown on the usual Si wafers, another avenue of research might be to study the feasibility of structures grown on metallic substrates such as Mo, W, or Ni. In addition, we arranged the collaboration of Professor Biswajit Das, director of the UNLV Nanotechnology Laboratory, to help develop and apply coatings to the CNT structures. Candidate coatings are metals (Ni, Mo, W, Ti) to enhance operations in moderate vacuum and low-work-function materials (CsTe, CsI, bialkali, S-20/S-25 mutialkali, Au, Pb) suitable for x-ray and optical photoemission.

CNT Synthesis

First Nano employs the thermal chemical vapor deposition (CVD) process to synthesize CNTs. To prepare the substrate, Fe, Ni, or Co catalyst nanoparticles are formed using Fe3+ solution to interact with the SiO_2 (or Al_2O_3, or MgO) substrate support material (Figure 1). This is a critical step, since the diameter and density of the resulting CNT structures are controlled by the size and nucleation site density of these starting nanoparticles (Cheung, 2002). After preparation, the seeded substrate is placed in a furnace set at 500–1000°C and flowing with precursor gases. By varying the temperature, time, and flow rate of the gas constituents, CNT structures can be tailored to grow up to millimeter lengths. Another technique for growing CNTs, plasma-enhanced CVD, employs a similar strategy to vary these physical parameters.

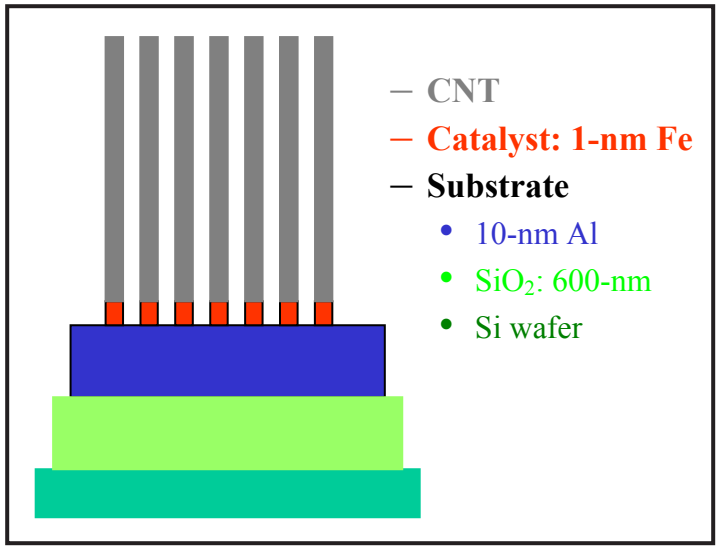

Figure 1. Schematic of CVD growth of carbon nanotubes using Fe catalyst

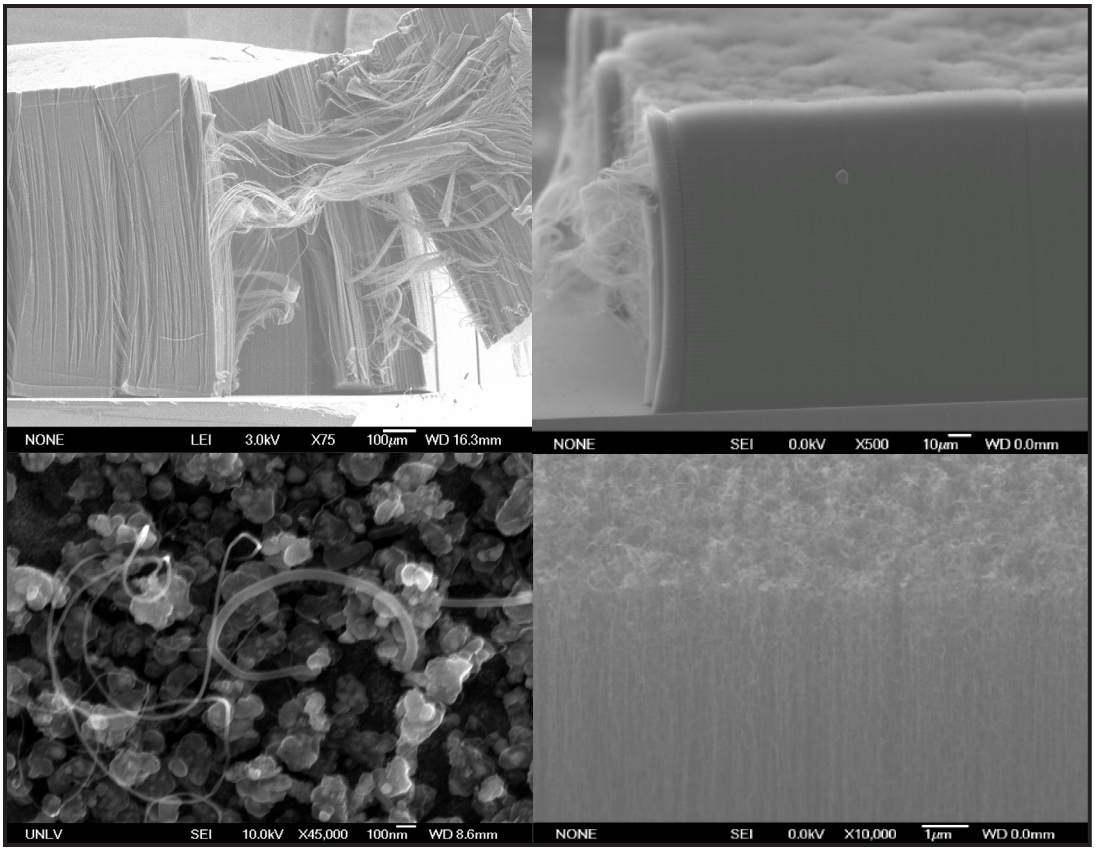

Figure 2. Scanning electron microscope images of CNTs grown by the thermal-CVD process. Counterclockwise from upper left, magnifications are 100 µm, 10 µm, 1 µm, 100 nm.

An example of thermal CVD–grown CNTs is shown in four scanning electron microscope pictures (Figure 2). Note the details of the CNT structures in the four views as the magnification is increased exponentially from 100 µm to 100 nm.

Results

UNLV was contracted to coat the CNT structures with either a metal film to enhance vacuum operations and FE, or with a low-work-function material to enhance photoemission for optical or x-ray radiation. One vertically aligned CNT structure received in the initial batch from First Nano was coated with Ni by UNLV. A second batch of CNTs was delivered and will be forwarded to UNLV for coating with Mo. Laboratory test assembly nears completion but still awaits delivery of a few critical pieces of vacuum hardware.

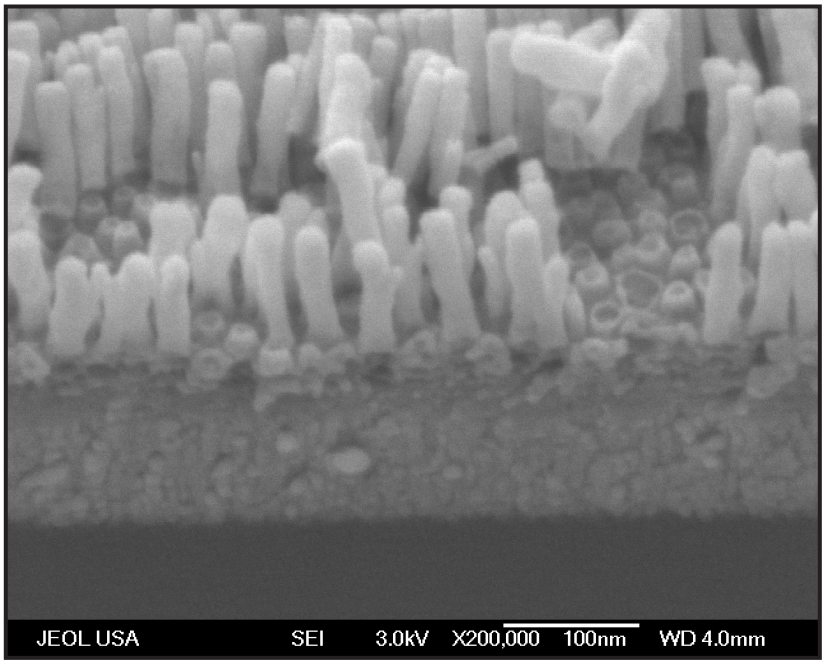

Figure 3. Tantalate pillar arrays are grown and used to develop CNT coating technology. Pillar diameter is on the order of 20 nm.

Test and Evaluation Plan

Coated and uncoated CNT structures will be tested in the completed vacuum vessel to characterize and compare emission properties. These measurements would ascertain the optimal combination of CNTs and coatings, as physical properties are varied during CNT production and coatings are iterated.

An alternate nanoscale structure for FE and/or photoemission may be fabricated from Ta_2O_5. UNLV has made structures with ~20-nm-diameter pillars up to ~μm heights (Figure 3). It would be instructive to test and compare these structures against CNTs. Other potential candidates are nanowires made from ZnO, Si, Cr-Mo, and W.

Conclusion

Our team has found a reliable vendor to develop vertically aligned CNTs and has established an active collaboration with UNLV to coat them with materials that enhance their FE properties. We have also designed a high-vacuum test assembly, and fabrication is nearly complete.

A follow-on SDRD project is planned to complete the test assembly and to study in earnest the variations of the coated CNTs and tantalate nanostructures. Our immediate aim is to create an FE-

based electron beam source. The next step would be to develop a scheme to modulate source current using a low-voltage sinusoidal waveform or pulser. Combining this source with an acceleration structure, the energized electron beam can be used to produce bremsstrahlung radiation, to create a compact, continuous-wave x-ray source for radiography (Sugie, 2001; Haga, 2004). At gigahertz modulation frequencies, this compact FE-based source would become an x-ray comb generator, an ideal calibration source for an x-ray streak camera. By applying a suitable photoemissive coating, a similar nanostructure can provide enhanced response to optical and x-ray radiation, leading to a more efficient photocathode and high-bandwidth response.

As a "cold," room temperature device, the FE-based source provides most of the benefits of a thermionic cathode without the associated high-temperature issues. With the exception of cases that require very high current and low emittance, the compact FE-based source can replace the thermionic cathode in devices and accelerators used for radiation studies and applications, e.g., phosphor characterization and development, detector research, and cathodoluminescence, among others.

Acknowledgments

The authors wish to thank the project collaborators: Yi Tu of First Nano, Inc., a division of CVD Equipment Corporation, for supplying the CNTs; and Professor Biswajit Das, Director of the Nanotechnology Laboratory at UNLV, for coating the materials. The authors further wish to thank Yi Tu and Professor Das for illuminating discussions during the project.

References

Cheung, C. L., A. Kurtz, H. Park, C. M. Lieber, "Diameter controlled synthesis of carbon nanotubes," *J. Phys. Chem. B* **106** (2002) 2429–2433.

Fowler, R. H., L. Nordheim, "Electron Emission in Intense Electric Fields," *Proc. R. Soc. London, Ser. A, Containing Papers of a Mathematical and Physical Character* **119** (1928) 173–181.

Haga A., S. Senda, Y. Sakai, Y. Mizuta, S. Kita, F. Okuyama, "A miniature x-ray tube," *Appl. Phys. Lett.* **84** (2004) 2208.

Sugie H., M. Tanemura, V. Filip, K. Iwata, K. Takahashi, F. Okuyama, "Carbon nanotubes as electron source in an x-ray tube," *Appl. Phys. Lett.* **78** (2001) 2578.

this page intentionally left blank

High-Efficiency, Low-Energy X-ray Source

Donald G. Pellinen[1]
Livermore Operations

We have designed a single high-efficiency, low-energy x-ray tube to replace x-ray sources in three applications: as a monoenergetic source in combination with a monochrometer, as a source of filtered or unfiltered line radiation (much as the Manson source is used now), and as a source of line radiation from that emitted by a fluorescer excited by the high-intensity source. This tube is expected to generate one or more orders of magnitude additional radiation than existing sources and cycle from line to line in seconds, rather than hours. Our tube and mount designs will eliminate several safety issues that the current Henke and Manson tubes pose.

Background

There are two widely employed methods of generating x-rays in the 50 eV–10 keV energy range. The best is the use of a synchrotron radiation source, a number of which exist nationally. Housed in buildings that occupy acres, these sources typically have synchrotron rings ~100 m in diameter. However, such sources have a relatively small beam diameter, and the travel and scheduling involved in using them is inconvenient. For many applications, a relatively small, conventional x-ray source with a better location would be desirable. Two such options are the Henke source, patented by Burton L. Henke (1964), and the Manson source, patented by James Manson (1985). Both were significant when developed but have limitations that we proposed to eliminate in our design.

Project

Our team has designed an x-ray tube that will provide significantly higher x-ray levels and faster operation in the voltage range below 20 keV. The tube is an improvement over the ultrasoft x-ray source. The Henke source was specifically designed to generate low-energy x-rays and to significantly boost low-energy performance with an anode that was not "visible" to the heated filament. This anode converted some of the energy from the electrons into x-rays, by having the electrons emitted from a heated filament directed toward a section of the anode without a direct line of sight to the cathode. Thus, there is no tungsten and/or carbon deposition on the anode to interfere with the x-ray spectrum and conversion efficiency. Our design maintains this feature and also incorporates specific improvements to significantly increase radiation and improve ease and speed of operation and changing x-ray anodes.

[1] pellindg@nv.doe.gov, 925-960-2572

These improvements consist of:

- A rotatable anode, enabling different materials to be exposed to the electrons, to generate a variety of x-ray line radiation characteristic of the material. This line radiation is orders of magnitude greater than the continuous bremsstrahlung. Anodes may be switched in approximately 2 to 3 seconds.
- A single point at which the electrons bombard the x-ray anode, rather than two points, as on the Henke source. Use with a monochrometer permits twice as much radiation as a Henke source.
- The ability to examine the x-ray source at an adjustable, near-grazing angle. This allows a monochrometer to see a larger fraction of the radiation generated. At near-grazing angle, the projected width of the area being hit with x-rays is much smaller than that projected for normal incidence.

This single x-ray tube may be used for the following three applications:

1. As a monoenergetic source in combination with a monochrometer,
2. As a source of filtered or unfiltered line radiation (much as the Manson source is used now),
3. As a source of line radiation from that emitted by a fluorescer excited by the high-intensity source.

A cross section through the center of the ultrasoft, high-efficiency x-ray source appears in Figure 1. As with any conventional x-ray source, electrons are emitted from a heated filament (1). The electrons are accelerated toward a positively charged anode electrode (2) that intercepts only a small fraction of the electrons emitted because of its small cross section. The electrons go past the anode wire (2) and see the electric force from the positively charged, liquid-cooled, x-ray anode with a polygonal cross section (3), where they hit the surface. A fraction of the electron energy is converted to x-ray energy by processes called bremsstrahlung and line radiation. The anode is physically shielded from the line of sight from the filament by a ground electrode (4), as is that of the original Henke x-ray source. The entire unit must operate at a high vacuum of less than 1×10^{-7} atmospheres, so an ultra-high-vacuum "tee" (5) is used to mount the structure and provide a vacuum seal. Electron trajectory follows the approximate track shown (6). The x-rays are taken for use with a monochrometer in the direction indicated by arrows (7) and for use as a monoenergetic source or fluorescer in the direction of the orientation (8). To change the output angle involves rotating the flange that mounts the flange to the next bolthole.

Two unique features characterize the new source. The Henke x-ray anode is fixed. After each use, the system is returned to atmosphere, the flange containing the anode is dismounted and either the anode or the entire flange replaced, and the system is pumped to the high vacuum needed. However, the ultrasoft, high-efficiency x-ray source's anode has a vacuum rotary seal, so that the anode can be

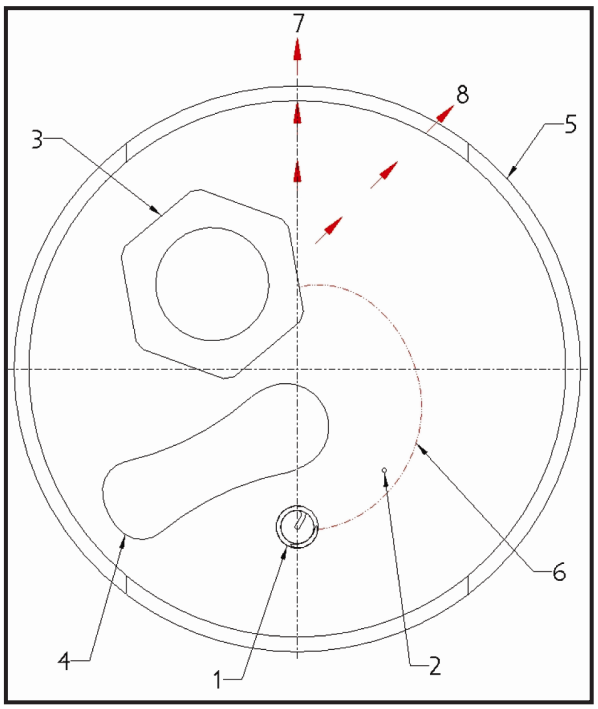

Figure 1. High-efficiency, low-energy x-ray source design

rotated without breaking vacuum. By simply rotating the anode, another material to be used as an x-ray converter is exposed. This feature makes it practical to utilize the much-higher-intensity, characteristic x-ray lines for calibrations and exposures, with the benefit of an anode "change" that takes just seconds instead of hours, as is currently the case.

Also unique is the fact that the face exposed to the electrons, when used with a monchrometer, can have an enhanced area. The source width we view is equal to the geometric width times the sine of the angle. For example, for an angle of 10°, this is 0.174 times the width. Normally, when a monochrometer is used to gain resolution, the slit system restricts the ability to intercept x-rays from the full area of the source. Inclining the system allows the user to view a narrower source without attenuation.

An analysis of our operating angles for a copper line with the maximum energy possible (or 20 kV) is as follows. From the National Institute of Standards and Technology (NIST) program ESTAR, the CSDA range is 1.465×10^{-3} gm/cm^2. Almost all the radiation is created in one-third of the range, or ~5×10^{-4} gm/cm^2, or ~0.55 μm. At 5.7°, which reduces the width by ~10 and increases the path in the material to about 5.5 μm, we have ~80% transmission of the 8.047-keV K-alpha radiation line,

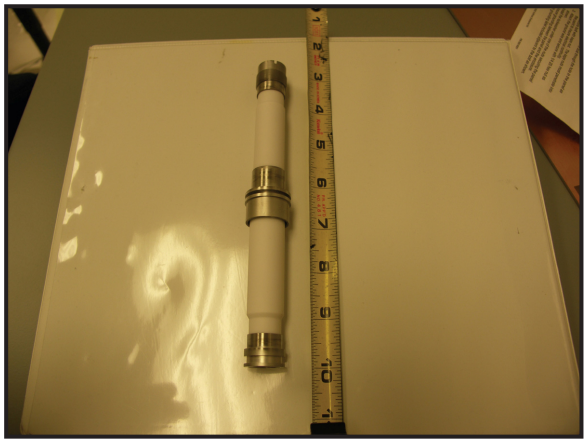

Figure 2. High-voltage insulator/feedthrough

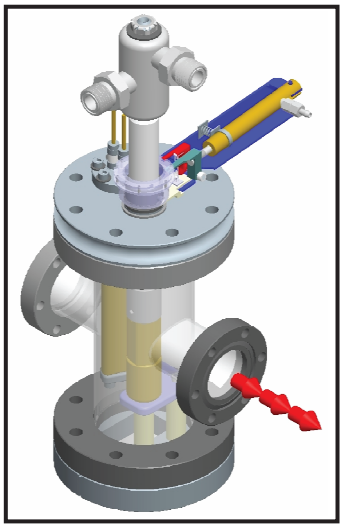

Figure 3. Conceptual model

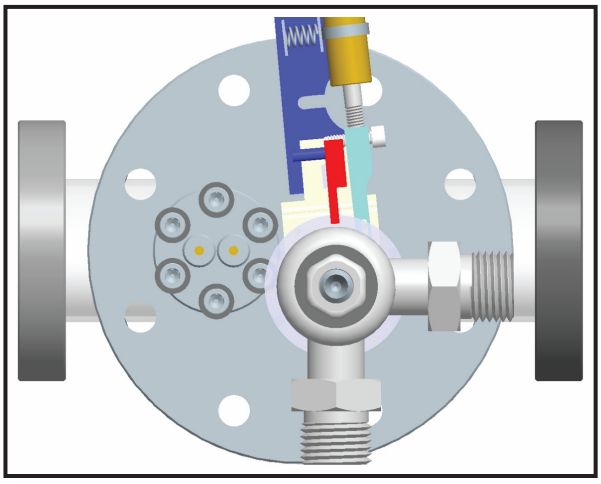

Figure 4. Conceptual model, top view

and at 2.9°, the transmission is approximately 63%. These are worst-case estimates of line radiation attenuation because most of the radiation is produced much closer to the surface and has less material to traverse.

In 1985, James E. Manson patented an x-ray calibration system with a multianode system. The high-efficiency, low-energy x-ray source differs from the Manson source in several major respects:

1. The Manson source has small, convection-cooled anodes that have a direct view of the cathodes. As such, the anodes are susceptible to contamination by carbon and tungsten from the cathode and losses from these effects. The high-efficiency, low-energy x-ray source uses the indirect acceleration similar to that used by the Henke source.
2. The Manson source has a marginal high-voltage insulator design that is not reliable above 10 kV. The high-efficiency, low-energy x-ray source has a design test voltage of 40 kV. Because of the high voltage, it can generate a much higher energy spectrum.
3. The Manson source is limited in x-ray output by a long and tenuous cooling path to ~5-W electron power dissipation in the anode. The high-efficiency, low-energy x-ray source has liquid cooling and a very short cooling path. We anticipate that anode power can exceed 1 kW. If nothing else, if two ideal sources are operated at the same electron energy, x-ray output will be proportional to the power.

Conclusion

The x-ray tube was designed and most of the parts procured, but a unit was not assembled. Future plans include assembling the unit and testing it at LO's current Henke facility.

Acknowledgments

Mechanical design work was excellently performed by Eric Huffman. We acknowledge discussions with Robert LeClair of Elcon, Inc., on details of the design and construction of the ceramic feedthrough.

References

Henke, Burton L., "Ultra-Soft X-Ray Source," Patent Number 3,138,729, U.S. Patent and Trademark Office, June 23, 1964.

Manson, James E., "X-Ray Calibration System," Patent Number 4,506,375, U.S. Patent and Trademark Office, March 19, 1985.

this page intentionally left blank

Lithium Niobate Terahertz Generator

James Capelle, Michael Mendez, William Quam[1]
Special Technologies Laboratory

This extension of FY 2004 work sought to enhance the understanding of mechanisms underlying electron generation from a heated pyroelectric crystal to more completely characterize electron emission. The project benefited from collaboration with a concurrent SDRD project at RSL-Andrews (RSL-A), which designed and built a new vacuum system. This system expanded the options both for experimental configurations of the $LiTaO_3$ (lithium tantalate) crystal and diagnostics instrumentation placement. Experiments with the pyroelectric crystal were limited to studies of heat-cycling effects on electron output. These experiments were complemented by calculations that examined the value of a discontinuous heating method.

Background

The performance of pyroelectric crystals (lithium niobate [$LiNbO_3$] and lithium tantalate [$LiTaO_3$]) was studied in an earlier SDRD project (Quam, 2004). This work was extended in a later SDRD project (Quam, 2005) that examined applications of crystal-generated electron beams, particularly the concept of producing terahertz radiation that might be used to detect airborne chemical or biological materials. Despite progress made in understanding the electron production mechanisms and in characterizing the intensity and spatial extent of the resulting electron beams, our team still lacked a fundamental understanding of pyroelectric crystal performance.

Project

To improve the quality of experiments using pyroelectric crystals, a new vacuum system was designed and built in FY 2004. This system incorporated into the region near the $LiTaO_3$ crystal several ways to introduce sensors, such as temperature and pressure probes, light sources, and other instrumentation. These new sensors facilitated acquisition of physics data of a higher quality than that of the previous system and helped quantify the effects of certain operational parameters that may be key in optimizing the desired crystal effects.

Vacuum Chamber Instrumentation

Using an interface combining analog-to-digital converters and a graphical user interface, we can now record data originating from vacuum chamber experiments as a time record. This user interface (Figure 1) is a hardware/software tool based on National Instruments' LabVIEW software, extended

[1] quamwm@nv.doe.gov, 805-681-2465

Figure 1. LabVIEW interface developed for new vacuum system

by programming performed at STL. In each of the rectangular data records, time is recorded on the x axis, and the data parameter of interest is recorded on the y axis. Presently, the parameters recorded are pressure, two temperatures, heater voltage and current, ion current, and bolometer (for THz) output. This interface was used extensively during collaborative experiments with Peter Heimberg (RSL-A).

Heating Parameter Study

A simple test showed that a square-wave heating current with a 50% duty factor resulted in a greater total electron output current than did heating using a single constant current. This would be a distinct advantage for most pyroelectric crystal applications seeking optimum output intensity.

This heating process was simulated with a finite-element modeling program. A representative result appears in Figure 2. The blue line is the expected temperature at the distal end of the crystal with fixed-rate heating. The red sawtooth gives the proximal end temperature during the 50% duty cycle heating ramps, and the green curve is the distal end temperature that results. Attempts to optimize the heating cycle found that the ideal heating duty factor varied little from the 50% results shown in Figure 2. The total electron current is expected to be a factor of two greater than that from a constant heating current. A vacuum pump failure late in the year prevented checking this result with crystal data.

Incidentally, the $LiTaO_3$ crystal supplier provided a few crystals marked with the wrong polarity. When we tested the incorrectly marked crystals, heating produced an electron current, while subsequent cooling yielded a positive ion current, validating a previous research objective. (Most of our

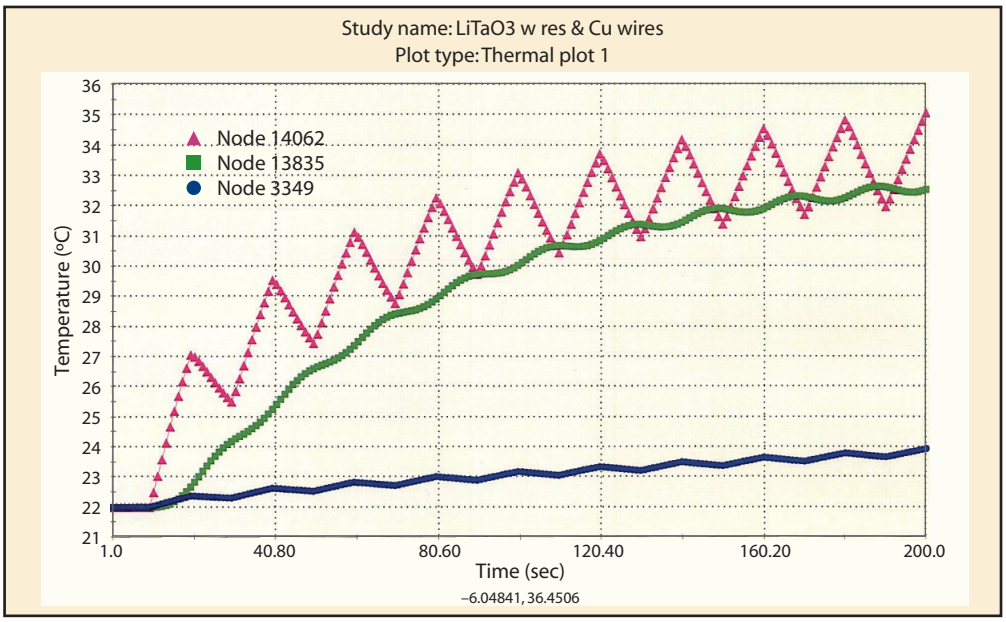

Figure 2. Calculation results of crystal distal end temperature for constant heating (blue) and for sawtooth heating at 50% duty cycle (green). The red sawtooth represents the proximal end crystal temperature, due to square-wave heating

efforts have been concerned with the production of self-focused electron beams that are created upon cooling, a result concomitant with heating the "positive" end of a z-cut crystal. The electrons are then accelerated away from the negative side when heating is stopped.)

Conclusion

Using the new vacuum chamber hardware, we achieved electron endpoint energies of nearly 200 keV, at least 40 keV higher than those seen using the previous simple vacuum system. This indicates the benefit of the higher purity environment in the new vacuum system.

Preliminary tests with a $LiTaO_3$ crystal showed that a sawtooth heating current with a 50% duty factor yielded a higher electron output than achieved with constant-current heating. This finding was confirmed by finite element modeling of the crystal temperature in response to various heating cycles. Further confirmatory experiments on this topic would be quite relevant to better understanding electron generation mechanisms.

Acknowledgments

The authors wish to thank Ken Moy for his contributions to the project.

References

Quam, W. M., S. J. Weeks, "Heat-Stimulated Lithium Niobate X-Ray Source," *Nevada Test Site–Directed Research, Development, and Demonstration,* FY 2003, Bechtel Nevada, Las Vegas, Nevada, 2004, 51–54.

Quam, W. M., M. Mendez, K. Moy, S. Sawyer, S. J. Weeks, "Lithium Niobate Terahertz Generator," *Nevada Test Site–Directed Research, Development, and Demonstration,* FY 2004, Bechtel Nevada, Las Vegas, Nevada, 2005, 31–34.

Nanomaterial-Enhanced X-ray Sources: Materials Study and Compact X-ray Comb Generator

Ke-Xun Sun[1]
Livermore Operations

This project conceptualized a compact, time-modulated x-ray source using nanomaterials to enhance overall efficiency. We propose that microstructured nanomaterials could be used to enhance the efficiency of both photoelectron production and x-ray generation via collision by accelerated photoelectrons. This research effort led to a promising system design for a practical x-ray comb generator capable of instrument calibration.

Background

Laboratory x-ray sources for calibration are in eminent demand, particularly in the form of fast x-ray comb generators for x-ray streak and gated microchannel plate intensifier (MCPI) calibration. A typical comb generator would require a <200-ps-width pulse and a repetition rate of >1 GHz to be used for calibration. Employing existing technology, it is difficult to build such a device, as the x-ray generation efficiency of traditional electron-material interaction is too low (≤0.1%). In addition, it is difficult to modulate a 10-kV electrical drive at high frequencies. X-rays may be generated via direct laser-plasma interaction with an expensive, high-power laser, but the repetition rate is limited.

We intended to generate x-rays in two steps. First, we would use a lower power laser or light-emitting diode (LED) source to excite the temporal packets of photoelectrons. The low-power light source could be electronically modulated to produce a temporal comb. We proposed the use of microstructured nanomaterial collections to enhance the yield of photoelectrons. Second, we would accelerate electrons to produce x-rays through electron-matter interaction. Again, we proposed to use nano materials to enhance x-ray generation from this interaction. Instead of building larger and increasingly expensive machines, this proposal explored the possibility of using nanomaterials, especially nanotube materials, to enhance x-ray generation efficiencies in photon-x-ray, electron x-ray, and multistep intermediate photon-electron interactions.

The idea of x-ray generation in nanomaterials comes from the enhancement of interaction cross section. Indeed, nanotube materials have been reported to increase x-ray generation efficiency by 300% or more, in a simple scheme of laser-target interaction (Nishikawa, 1999). In multistep schemes, where nanomaterials are utilized in each step, we could possibly achieve higher overall efficiency.

[1] sunke@nv.doe.gov, 925-960-2514

Project

System Design

The conceptual system design of a nanomaterial-enhanced x-ray source appears in Figure 1. An optical comb generates periodic optical pulses that are delivered to the photocathode to generate photoelectrons. To enhance the efficiency of the photoelectric effect, the photocathode is made of nanomaterials. The electrons are accelerated by high voltage applied to the anode, where the electron kinetic energy is converted to x-rays. For similar reasons, using nanomaterials at the anode is expected to increase the scattering cross section of the electron converting to x-ray photons, thereby enhancing efficiency for x-ray generation. Nanomaterials could be used in two-step processes: from photons to electrons, and from electrons to x-ray photons.

We researched a number of topics, including selection and availability of nanomaterials for the photo cathode, selection of optical comb wavelength, electron optics, electronics system optimization, and many other details. From a physics perspective, the conceptual framework remains promising.

Optical Comb Generator as Time Base

This conceptual system design (Figure 1) would allow us to take advantage of the optical comb generators continuously developed by STL, thus shortening development time otherwise needed for an

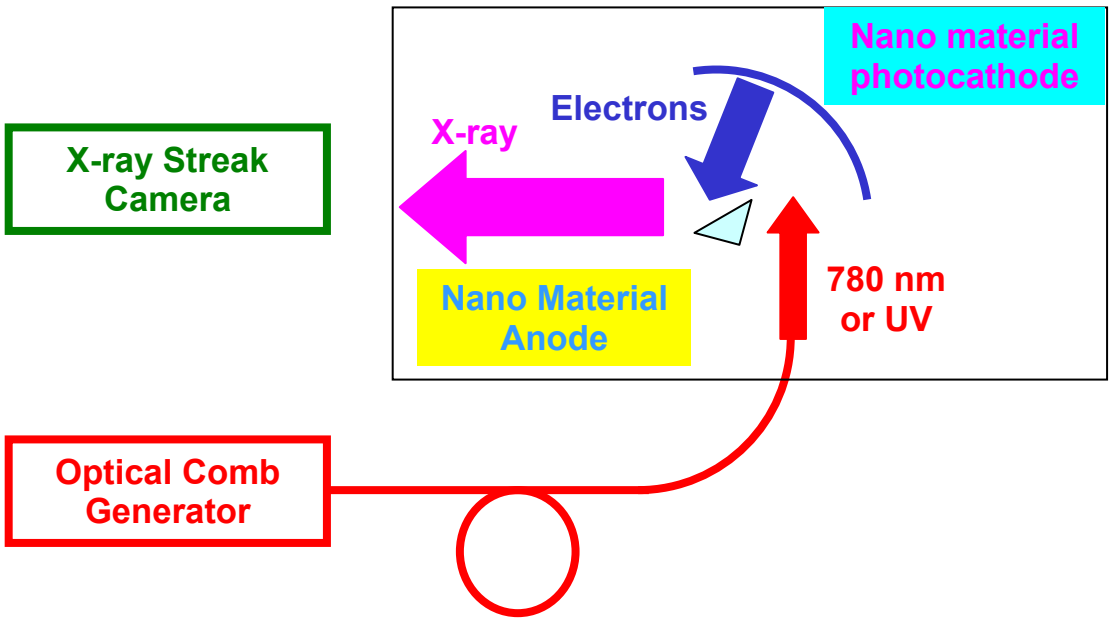

Figure 1. Diagram of the nanomaterial-enhanced x-ray sources

accurate time base. The x-ray comb generator is realized by replicating the periodicity of the optical comb generator. The potential broadening effects in the two-step conversion processes are expected to be small compared to the period of the optical comb pulses. The literature contains reports of <5-ps generation of single x-ray pulses using electrostatic acceleration of electrons, without resorting to a bunching structure (Hinze, 2004). The x-ray comb generator should be able to operate at frequencies of up to 40 GHz with a 5:1 amplitude modulation, covering an upper frequency range of 6 GHz when supported by STL's optical comb generator.

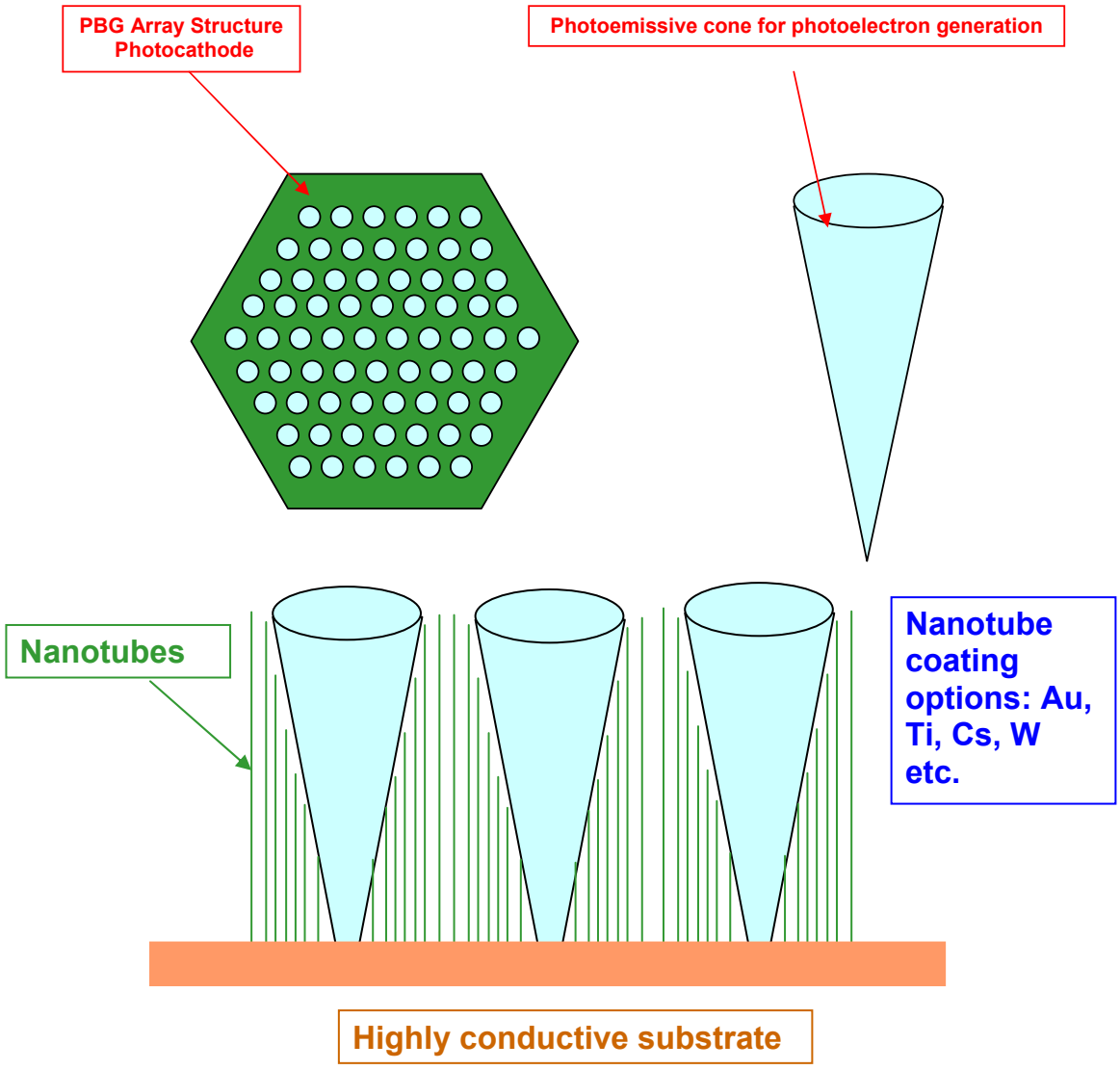

Figure 2. Microstructure for further efficiency enhancement

Wavelength and Photocathode Material

The wavelength of the optical comb generator can be varied according to laser or LED selection. Recently, STL has demonstrated the possibility of ultraviolet comb generation, which extends the choices of the photocathode material beyond the alkali metal compounds. Au- or Al-based photocathodes in the form of nanocylinders could be used. Two factors that could affect photoelectron generation are materials and their geometric shapes. Therefore, to optimize each aspect independently, we have explored substrate nanomaterial coatings as an attractive approach. Substrate nanomaterial coatings on a structurally strong material would allow formation of a geometric shape, which would then be followed by application of a coating that efficiently emits photoelectrons.

Light Trapping by Surface Microstructure

In addition to the enhancement that could be achieved using nanomaterials, proper surface microstructures could further improve the light absorption cross section at the photocathode, thus enhancing photoelectric efficiency. A possible example of this kind, in which cone structures with rough walls made of nanomaterials are used to "trap" incident light, appears in Figure 2. The apex angle of the cone is designed at ~30%, so that incident light will be less likely to be reflected back from the cone.

Conclusion

We have conceptualized nanomaterial-enhanced x-ray sources with several innovative features:

- Two-step nanomaterial enhancement of photon-electron and electron-photon conversions
- Proper selection of coating and wavelength
- Innovative surface microstructures capable of achieving compact, high-efficiency laboratory x-ray sources

The adoption of the optical comb generator as a modulation source could accelerate the development of an x-ray comb generator. Future steps could include development in the area of material growth.

References

Hinze, U., A. Egbert, B. Chichkov, K. Eidmann, "Generation of picosecond hard-x-ray pulses in a femtosecond-laser-driven X-ray diode," *Opt. Lett.* **29** (2004) 2079.

Nishikawa, T., H. Nakano, N. Uesugi, M. Nakao, H. Masuda, "Greatly enhanced soft x-ray generation from femtosecond-laser-produced plasma by using a nanohole-alumina target," *Appl. Phys. Lett.* **75** (1999) 4079.

Computer Sciences

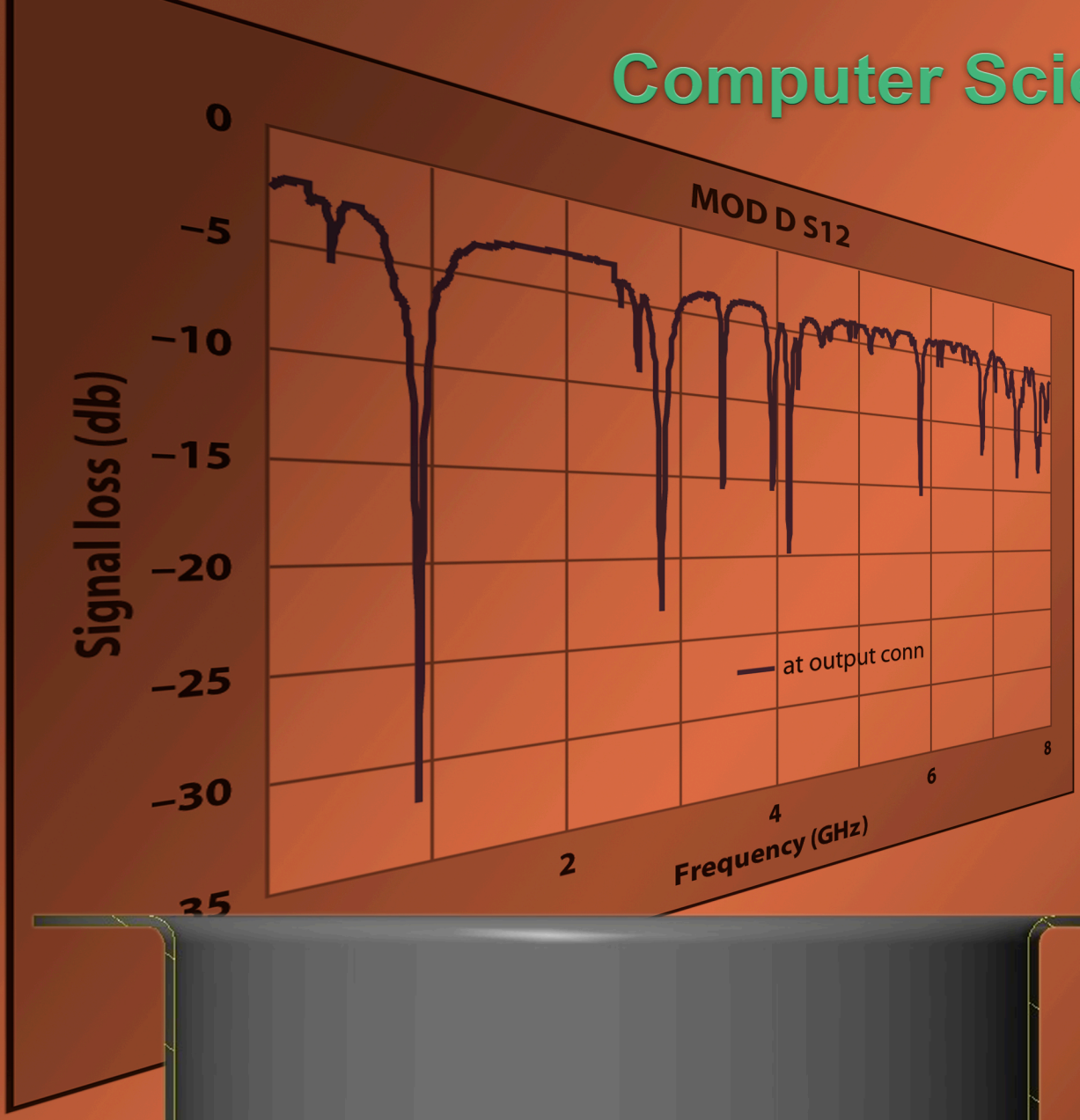

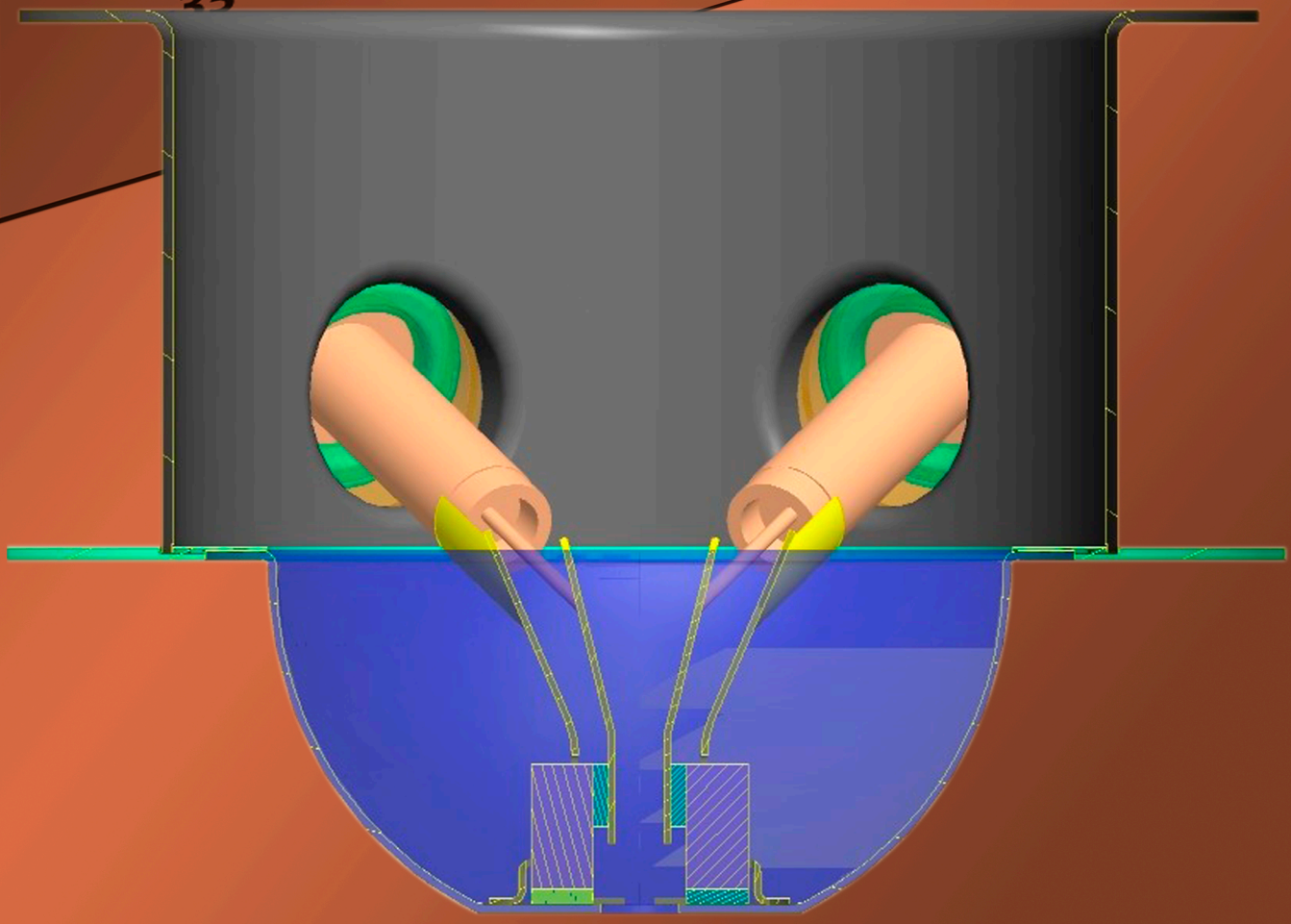

Investigation of Field Effects on Neutron Detection

Rebecca Detwiler[1]
Remote Sensing Laboratory – Nellis

This project used Monte Carlo N-Particle transport code (MCNP) and Monte Carlo N-Particle eXtended code (MCNPX) to model and measure the effects of various natural and artificial surroundings on neutron moderation, scattering, and absorption. A supplemental goal was to more accurately predict these effects on the measured neutron background and neutron source detection in field applications. Modeling would involve neutron detection effects of both land and water, including proximity to ponds or lakes, as well as the variation of effects of air and humidity with source distance. In addition, man-made structures, such as sea and land bridges, overpasses, and tunnels, would be modeled, along with cement rooms, stairways, parking garages, and other enclosures that might increase background counts through neutron scattering. This modeling, combined and compared with field data taken at similar environmental locations with the same type of neutron detector, could help to quantify these background effects on neutron detection in situ.

Background

The effects of structures, both artificial and natural, can include scattering of background neutrons or cosmic ray spallation. The resulting burst or increase in neutron flux near these structures can resemble a neutron fission source. These effects are particularly strong in a maritime environment where neutron scattering and spallation from ship material occur in a lower background sea environment. Modeling these effects with MCNP and MCNPX to predict the amount of background change holds important ramifications for neutron source detection.

Project

UNLV Scope

During FY 2005, preliminary models and geometries were yielded through collaboration with William Culbreth of the University of Nevada, Las Vegas (UNLV), Engineering Department. Culbreth's group has access to a new 225-processor Beowulf cluster with 64-bit Athlon processors to increase speed of low-statistic neutron background-transport simulations. UNLV also has graduate students capable of MCNP modeling; they have been trained in MCNP and MCNPX simulations by the LANL developing team. These students make up a beta test group with access to the latest MCNPX beta version. The group is working toward a platform for carrying out MCNP and MCNPX calculations

[1] detwilrs@nv.doe.gov, 702-295-8613

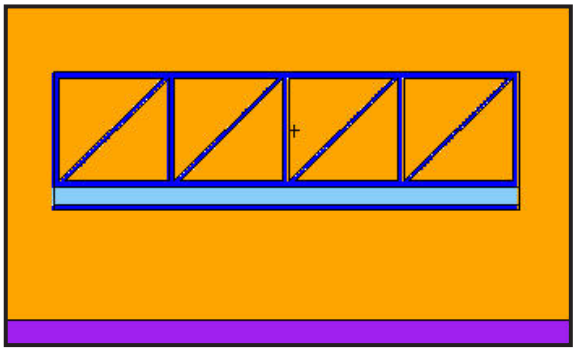

Figure 1. Side view of steel truss bridge

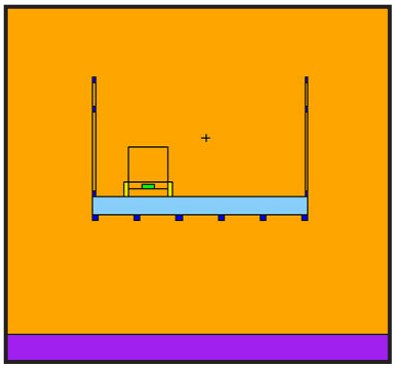

Figure 2. Vertical cross section of bridge and vehicle

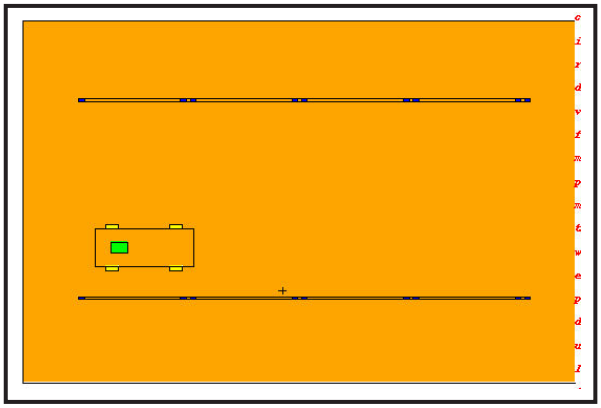

Figure 3. Overhead cross section of vehicle on bridge

for comparison to measured effects from environmental conditions and man-made geometries. Students have begun to model key structures and locations, including elevator shafts, stairwells, and bridges, among others. Initial geometries of a mobile detection system are shown in Figures 1–3.

UNLV students will construct geometries using standard neutron detectors, rather than specific RSL detection geometries for security purposes. Results from the environmental and synthetic structures on these representative detector geometries will then be applied to RSL's detector systems. This work could be extended in the future to modeling of specific RSL systems by building on the UNLV-developed geometries of natural and man-made surroundings that were generated by this project.

Conclusion

Initial collaboration with UNLV has generated some detailed models. In FY 2005, initial geometries of a mobile detection system on a bridge were developed. Continuation to this work and the UNLV partnership have been proposed for FY 2006. Further steps could include running simulations on existing models and developing new geometries. Work completion and a model results summary would help interpret neutron field measurements and would be an asset to RSL nuclear emergency response programs.

Acknowledgments

The author would like to thank William Culbreth (UNLV), who contributed to this work by providing his computing cluster and graduate students to develop MCNP input file geometries.

this page intentionally left blank

Bayesian Inversion of Noisy Spectral Data

Paul O. Frederickson (former employee), Craig A. Kruschwitz[1]
Los Alamos Operations

We have developed a software utility to aid in the inference of a spectrum using data from a small number of detectors. The software assumes that detector sensitivity to photons of various energies is understood and is available as a set of data files. The utility allows the user to choose a low-dimensional space of reasonable spectra, from which it infers the spectrum that best fits the given data in the Gaussian sense. It also infers the number of photons that produced this data. At the user's request, the utility will then make a statistical study of the inferred spectrum, with emphasis on the quantum fluctuations in energy distribution of randomly chosen photons and their effect on accuracy. This study shows how these fluctuations affect the data, and hence, the accuracy of the inferred spectrum. We have used this utility to generate several examples illustrating this sort of statistical accuracy analysis.

Background

We begin with a brief introduction to inverse problems, with focus on the spectral unfolding problem, in which one is to infer the spectrum of a batch of photons that have caused a collection of sensors to produce a spectral data array.

Very briefly, an inverse problem exists whenever a data vector d is produced by sensors in the experimental equipment and the physical phenomena that produced that data must be described as accurately as possible. For example, exploration geophysicists have spent millions of dollars gathering vast amounts of seismological data to use to describe the densities and elastic properties and location of various subterranean rock strata. They are also spending further millions creating parallel computer software and developing the algorithms implemented in this software to solve such an inverse problem accurately and efficiently (Backus, 1968).

The algorithms and software always begin with some assumptions, referred to as Bayesian hypotheses, which allow them to infer a simplified model of the region of interest (Mosegaard, 1999). This model may consist of layers that might be tilted and/or broken by dislocation planes. Using the given model, the inversion software then strives to adjust parameters to approximate the region of interest as well as possible, in the least-squares sense.

[1] kruschca@nv.doe.gov, 505-663-2023

Project

We are particularly interested in an x-ray spectrometer, a device that can infer the spectrum $\mathcal{S}$ of the source of an observed burst of x-rays. The smaller the number of observed particles, the less accurate this inference is, which begs the question of how much accuracy we can reasonably expect (Fehl, 1997).

We begin by conceptually dividing the spectrometer into two parts: a physical part that responds to a number of incoming particles by producing a data vector d and a computational part that uses d to infer the spectrum $\mathcal{S}$ of these particles.

The physical part may, for example, measure the optical density at m regions of a photographic film that, before development, had been located behind a step-wedge in an x-ray spectrometer. Or it may employ a quite different physical mechanism to produce the vector d. The unknown spectrum $\mathcal{S}$ to be estimated using this data vector d might be thought of as a probability density function describing the energies of the observed photons.

The key information used in constructing this estimate is an accurate model of the physical part of the spectrometer, one that describes the expected data vector $d = d(e)$ produced by monoenergetic photons of energy e for all energies in the range of interest. The curves in the screen shot in Figure 1 represent the sensitivities of a set of five x-ray detectors that have been modeled by the software utility.

Our approach to inferring spectrum $\mathcal{S}$ begins with the specification of a set of basis functions B_i, such that $\mathcal{S}$ will be represented as $\mathcal{S} = \Sigma\ w_i\ B_i$ after the weights w_i have been determined. Using our knowledge of detector sensitivities, we then construct a matrix Z. $||Zd||$ is the estimated number of photons, and $(Zd)/||Zd||$ is the estimated vector w of weights. To define the matrix Z, we begin with the matrix $A = [a_{ij}]$, in which a_{ij} is the expected output d_i from the i^{th} detector when hit by a photon chosen randomly from basis function B_j. Then $Z = A^+$, which is the inverse of A when A is nonsingular and the pseudoinverse otherwise.

The two spectra in Figure 2 were inferred from a two-segment time series analysis. The first data vector is the sum of the time series before its peak; the second, after the peak. The software inferred that 13 photons were detected during each of the series' two sectors. We chose to represent the spectrum as a linear combination of three piecewise constant basis functions.

Inference of the number of photons that entered the detectors is important because the smaller the number, the larger the uncertainty on the inferred spectrum due to quantum fluctuations. To make this uncertainty concrete, our software utility will, if requested, perform a short Monte Carlo simulation after a spectrum has been inferred. The simulation consists of repeatedly choosing a photon batch from the inferred spectrum, using the inferred number of photons that produced this spectral inference. Each photon is given to a randomly chosen detector, resulting in a (simulated) data

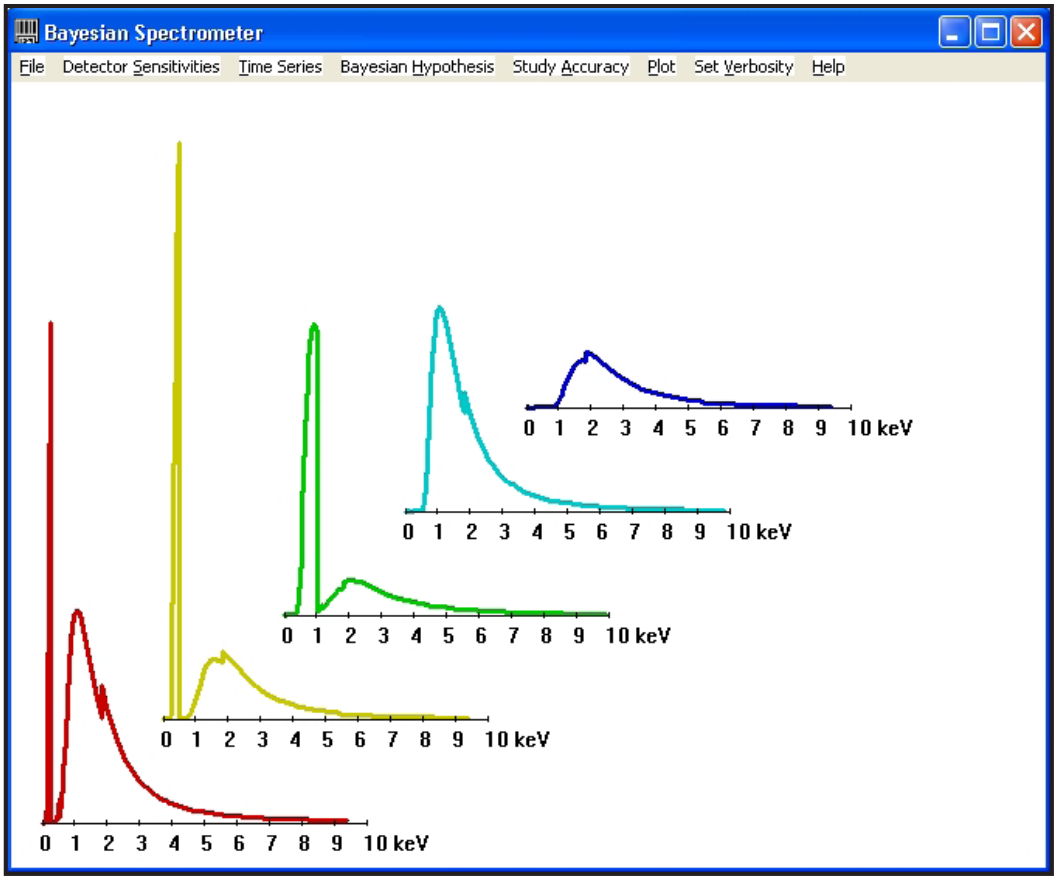

Figure 1. Sensitivities of the five channels of a spectrometer at Sandia National Laboratories

Table 1. Monte Carlo study of data segment 1

Study	Photons	Wt 1	Wt 2	Wt 3
1	12	0.0	0.08893	0.91108
2	21	0.78118	0.08893	0.12989
3	20	0.65238	0.16409	0.18353
4	22	0.76187	0.13505	0.10307
5	17	0.44843	0.20929	0.34228
6	15	0.35034	0.25522	0.39444
7	19	0.64999	0.10749	0.24251
8	14	0.05959	0.36427	0.57614
9	25	0.92241	0.0	0.07759
10	16	0.46252	0.27826	0.25922
	Average	0.50887	0.16915	0.32197

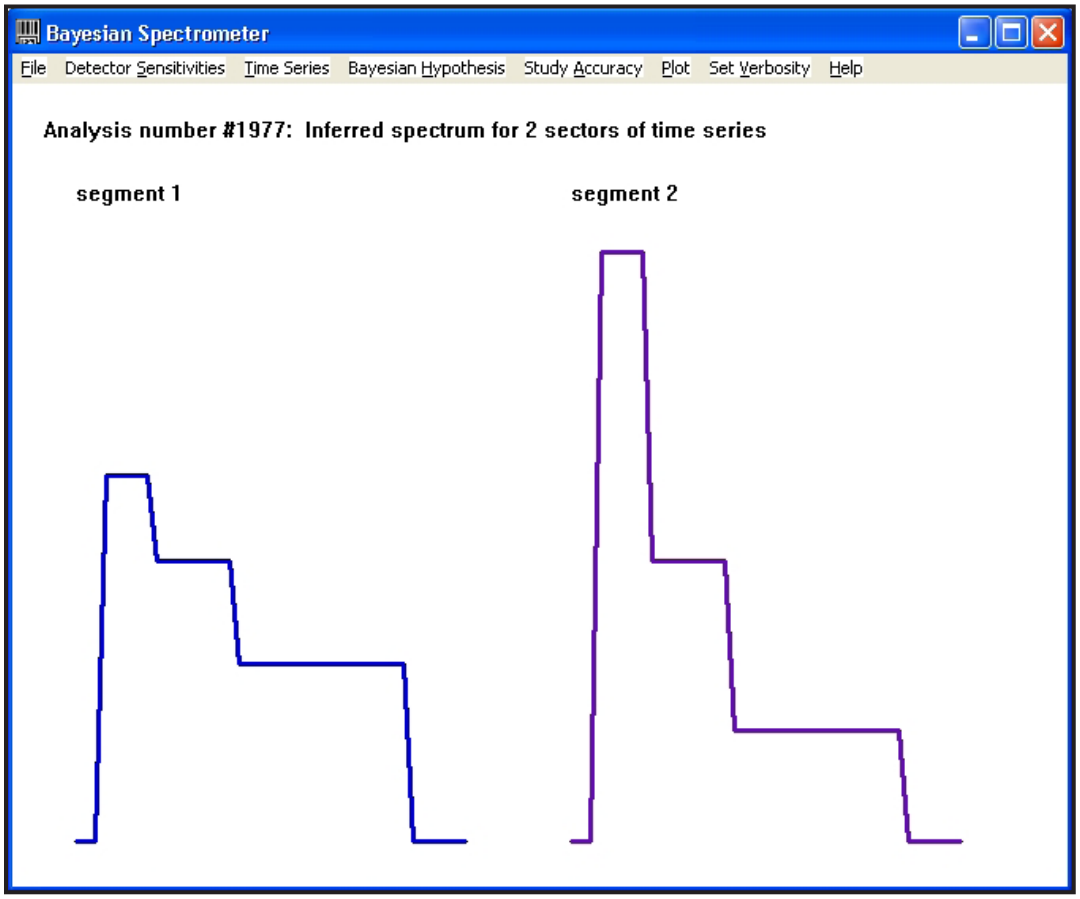

Figure 2. Inferred spectrum for two segments of a time series from the spectrometer at Sandia National Laboratories

vector. This vector will infer a spectrum and a number of photons. As this simulation is repeated multiple times, we can compute the standard deviation of our inferences. The data in Table 1 show the quantum uncertainty on the first of the two spectra in Figure 2.

As we increase the number of basis functions to allow a better approximation to the unknown spectrum S, or if we choose smooth basis functions to accomplish the same purpose, we observe that the condition number of Z worsens. This results in a greater amplification of the quantum fluctuations that are an inevitable component in the data vector d. Development of an optimal Z requires that these two error sources be balanced against each other, so that the total error may be minimized.

The problem faced when attempting to develop an optimal estimation is an old one: optimization requires an estimate of how well the unknown spectrum S can be approximated in our chosen low-dimensional function space, the space spanned by the B_i, and an estimate of the quantum fluctuation vector σ, which requires that we know S and the number of photons.

Conclusion

We have developed an approach to unfolding spectral data in which the number of photons per detector is small enough that quantum fluctuations can cause significant loss of accuracy. We have implemented this approach in a fairly robust software utility.

Acknowledgments

We would like to acknowledge highly beneficial conversations on this topic with David Fehl and Carlos Ruiz of Sandia National Laboratories. The primary author would also like to recognize the support of the Army Research Laboratory while its researchers worked on a similar approach to a rather different inverse problem at Aberdeen Proving Ground.

References

Backus, G., F. Gilbert, "The resolving power of gross earth data," *Geophys. J. R. Astr. Soc.* **16** (1968) 169.

Fehl, D. L., F. Biggs, "Verification of unfold error estimates in the unfold operator code," *Rev. Sci. Instrum.* **68,** 1 (January 1997) 890.

Mosegaard, K., C. Rygaard-Hjalsted, "Probabilistic analysis of implicit inverse problems," *Inverse Problems* **15** (1999) 573.

this page intentionally left blank

Feasibility of Mapping Radiation Distributions Using Measurements Restricted to the Perimeter of an Area

Thomas M. Haard[1]
Remote Sensing Laboratory – Andrews

This project considered the following problem: Given a set of gamma radiation gross-count measurements taken along the perimeter of an arbitrary area, determine the distribution of radioactive material within that area. We report a solution to this problem that uses an algorithm that incorporates linear algebraic techniques and constrained least squares fitting. We developed and tested the algorithm using computer-generated data that simulated either distributions of many point-like sources or areal distributions. The algorithm works well for the point-source case but works poorly for areal distributions. We were unable to develop a solution for a more complicated problem wherein shielding or attenuating materials are included in the simulated area. Although this shortfall limits the real-world applicability of our algorithm, other, more complicated approaches, would likely be possible.

Background

Consider an area that has been contaminated with gamma-emitting radioactive material. The material might be a solution that has spilled from a drum, or it might be numerous fragments from an exploded radiation dispersal device (RDD). Those entering the area risk exposure, may become contaminated, or may spread the contamination outside of the area. This work seeks to demonstrate that the distribution of radioactive material in the area can be determined without entering the area. We will show that it should be possible to take a set of measurements around the perimeter of the area and solve for the activity distribution within. This technique has several potential applications to our work. The ALARA principle states that radiation workers should limit their exposures to levels "as low as reasonably achievable." The perimeter-mapping technique would help to reduce exposure by providing an ex-situ survey technique. It could also provide radiation maps of areas that might otherwise be impossible to map safely.

[1] haardtm@nv.doe.gov, 301-817-3307

Project

Formulation of Problem

We began by developing a formulation of the problem suitable for numerical simulation. In algebraic notation, the problem may be stated as follows:

1. Divide the area into n cells. This need not be a regular array, but for the sake of simplicity we have set up our test cases as square areas divided into symmetric regular arrays. The individual cells will be identified by an index, i, that runs from 0 to n–1. The coordinates of each cell will be stored in the array $R_n(i)$.

2. Define a 1-D array that contains the total activity inside of each cell, i.e.:

$$A = \{a_0, a_1, \ldots, a_{(n-1)}\}. \quad (1)$$

3. Define a 1-D array B that contains the measured values at points around the perimeter. The locations of the measurements will be stored in an array $R_m(j)$. The number of measurements will be m.

4. Consider a detector with a point source spatial response function that is expressed as $F(r)$. For now we only consider azimuthally symmetric response functions so that we do not have to keep track of the detector orientation during each measurement. Then the measured value $B(j)$ at due to a single point source located at $R_m(j)$ should be given by:

$$B(j) = F(R_m(j) - R_n(i))Ai, \quad (2)$$

or, for n sources located at each of the n cell locations:

$$B(j) = \sum_{i=0}^{n-1} F\left(R_m(j) - R_n(i)\right)A_i. \quad (3)$$

The problem is to determine all of the n values of $B(i)$ from the m values of $A(i)$. It should be noted that equation 3 requires that the system have the property of linear superposition, that is, that the signals contributed from all regions of the area contribute additively to the measurement. This is a simplification of the general case in which obstructions would cause varying attenuation of the signals from the different regions.

5. Equation 3 represents a "forward" problem: The value of each measurement B can be determined by evaluating a single sum over the activities A. To set up the desired "inverse" problem we define a rectangular 2-D matrix M that contains the value of the spatial response function evaluated for each measurement j for each cell i, so that

$$M_{ji} = F\,(R_m(j) - R_n(i)). \quad (4)$$

6. We now have a set of m equations and n unknowns which we can express in our notation as:

$$M_{ji}A_j = B_i. \quad \textbf{(5)}$$

The goal of this work was to find a solution to this expression. Our strategy was to apply linear algebraic techniques and constrained least squares fitting.

Algorithm Development

We evaluated several techniques for solving the linear system, including QR factorization, singular value (SV) decomposition, and truncated SV decomposition. These techniques calculate the least squares solution to the $m \times n$ system. We found that these shared a common failing, in that there are unphysical solutions that include some negative source activities which fit the data better than realistic, positive solutions.

The reason the unphysical negative solution gives a better least squares fit (LSF) than the desired, all positive solution is because we are constraining the solution to fixed locations (cell centers) while the sources we are trying to solve for are off-grid. To test this idea we tried constraining the sources to a grid commensurate with the cell locations. Under this condition the QR, SV, and truncated SV algorithms all gave the correct, physical solution. However this approach is not applicable to realistic problems.

The next step was to constrain the solutions to positive values. We identified an efficient algorithm called the non-negative least squares method (NNLS), originally published by Lawson and Hanson (1974). This was translated from the original Fortran 77 to C, and implemented as an extension for the scientific analysis package we used for this work, Igor Pro.

NNLS Performance Testing

The procedure was tested by simulation. Initially, the following assumptions were adopted:

- We only considered point sources.
- We did not consider background, or area distributions.
- We did not consider counting statistics.

These restrictions are addressed later in this project.

The NNLS algorithm immediately yielded improved results compared to the unconstrained results obtained by the QR and SV methods. A typical example is shown in Figure 1, where the simulated sources are shown as circles and the activity distribution determined with the NNLS algorithm are indicated by the colored square pixels. It can be seen that the locations of the colored pixels roughly approximate the locations of the sources. A more quantitative comparison will be described later.

There are nine sources present in the example of Figure 1. Unfortunately, the accuracy of the algorithm worsened as the number of sources was increased. The primary reason for failure derives from fact that we were trying to describe a free distribution of point sources with a solution set of sources constrained to a grid. It seems reasonable that the accuracy of the solution should improve as we increased the density of the grid; however, the computation time increases as a strong function of the number of cells in the grid. This would seem to effectively limit the resolution that can be achieved for a given problem. We address that point in the next section.

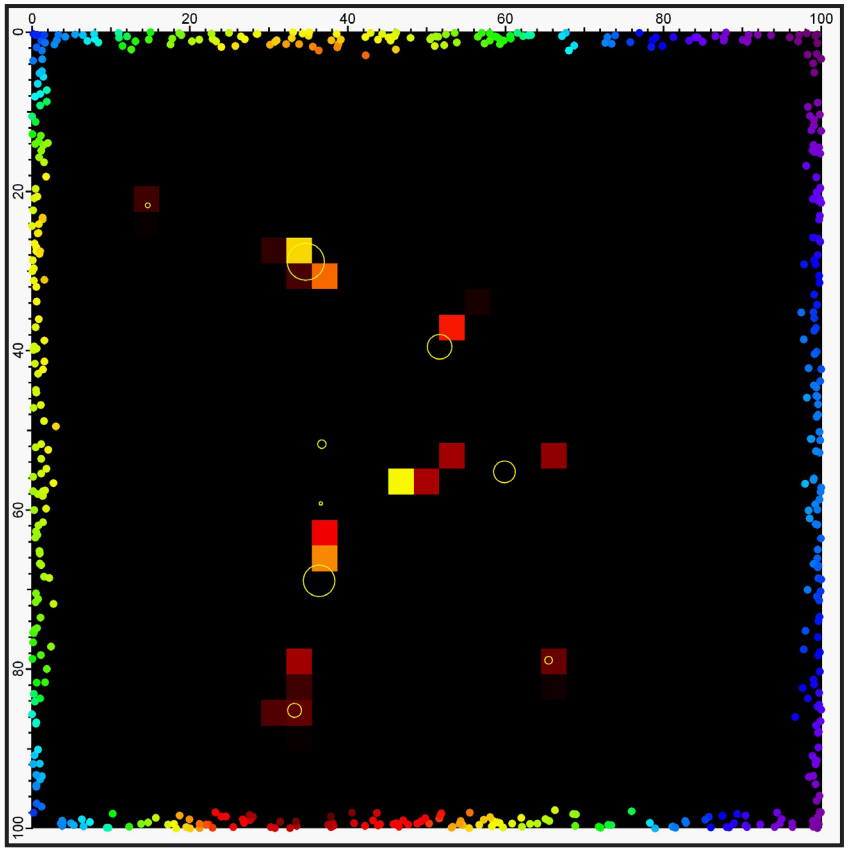

Figure 1. A typical solution obtained with the single-pass NNLS perimeter-mapping algorithm. The grid used here is 31 × 31 cells. The simulated point sources are located at the centers of the yellow circles, the diameters of which are proportional to the source strengths. The colored points around the perimeter show the locations of 1020 simulated measurements. The colored square pixels show the solution of the mapping algorithm.

Improved Resolution by Regridding

We were able to improve the resolution of the solution by using a two-pass method. For the first pass we used a coarse grid to obtain an approximate solution (Figure 1). The result of the first pass was then used to identify the subareas which contained the sources (Figure 2). These subareas were selectively regridded, and a second pass of the NNLS was applied (Figure 3). This method significantly increased the resolution.

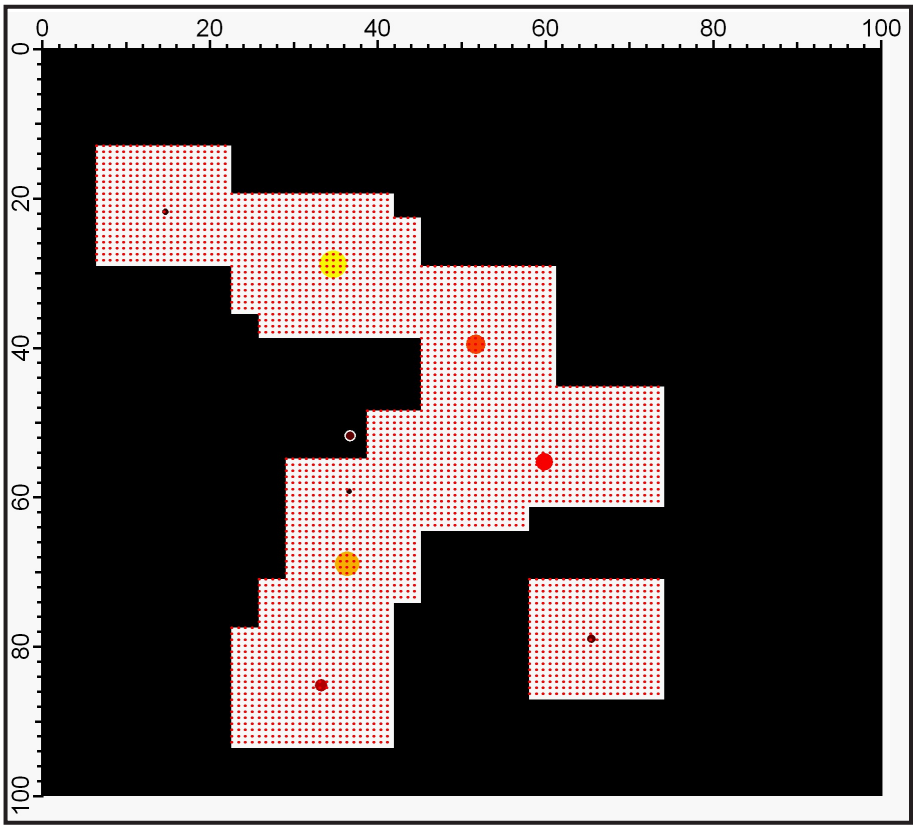

Figure 2. The regridded subareas of Figure 1 that were used for the two-pass algorithm for increasing the solution resolution. The colored circles are the simulated test sources.

To determine the region of interest to regrid, some basic image analysis techniques were used. The solution of the first pass was converted to an image, the image was converted to a binary mask, and then a dilation operation was applied to the mask to grow the masked regions by several coarse grid units in all directions. Dilating the mask simply addressed the inaccuracy of the first pass solution by expanding the region to be regridded into the area surrounding the coarse solution. The masked areas were then regridded. Figure 2 shows the new grid for the same problem shown in Figure 1 and the solution is shown in Figure 3. A visual comparison of Figures 1 and 3 suggest significant improvement in resolving the source locations. The calculated activity is related to the pixel color. A quantitative comparison of the problem and solution are given later.

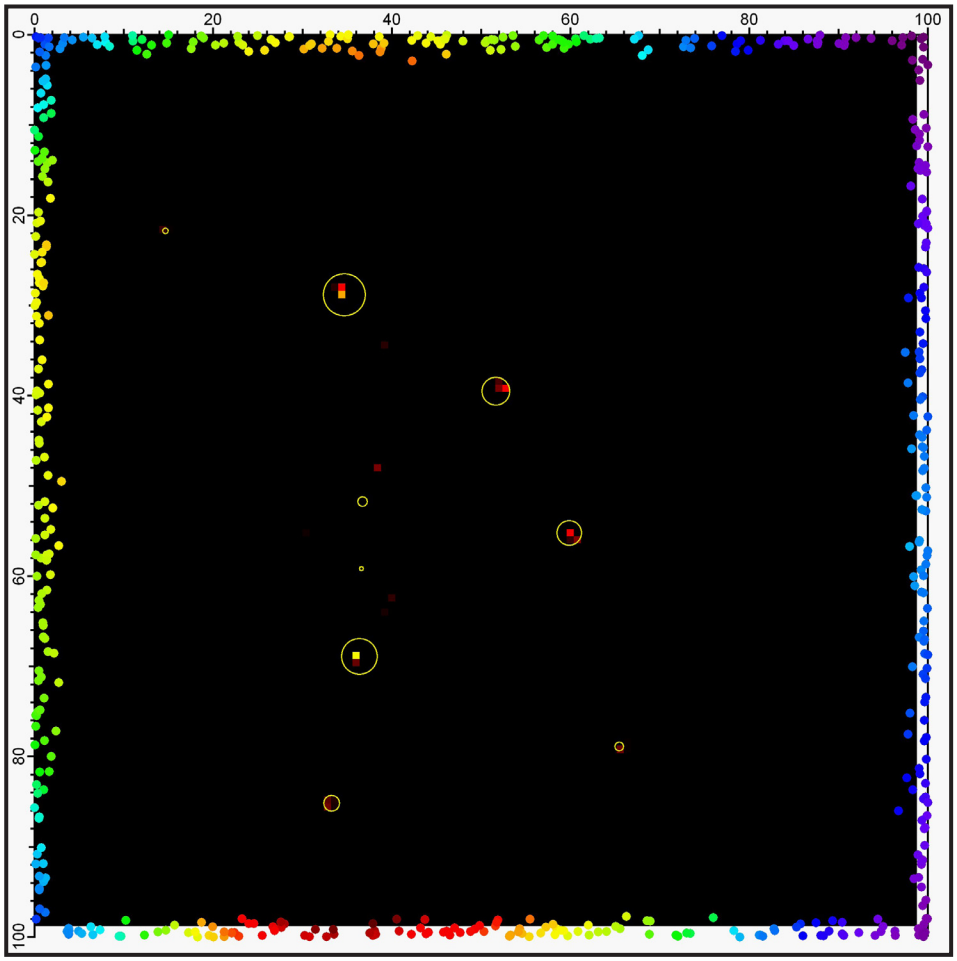

Figure 3. The same problem as Figure 1 after regridding and a second-pass NNLS solution. The source locations are more accurately determined, as can be seen by comparing the positions of the circles (truth) to the colored squares (solution).

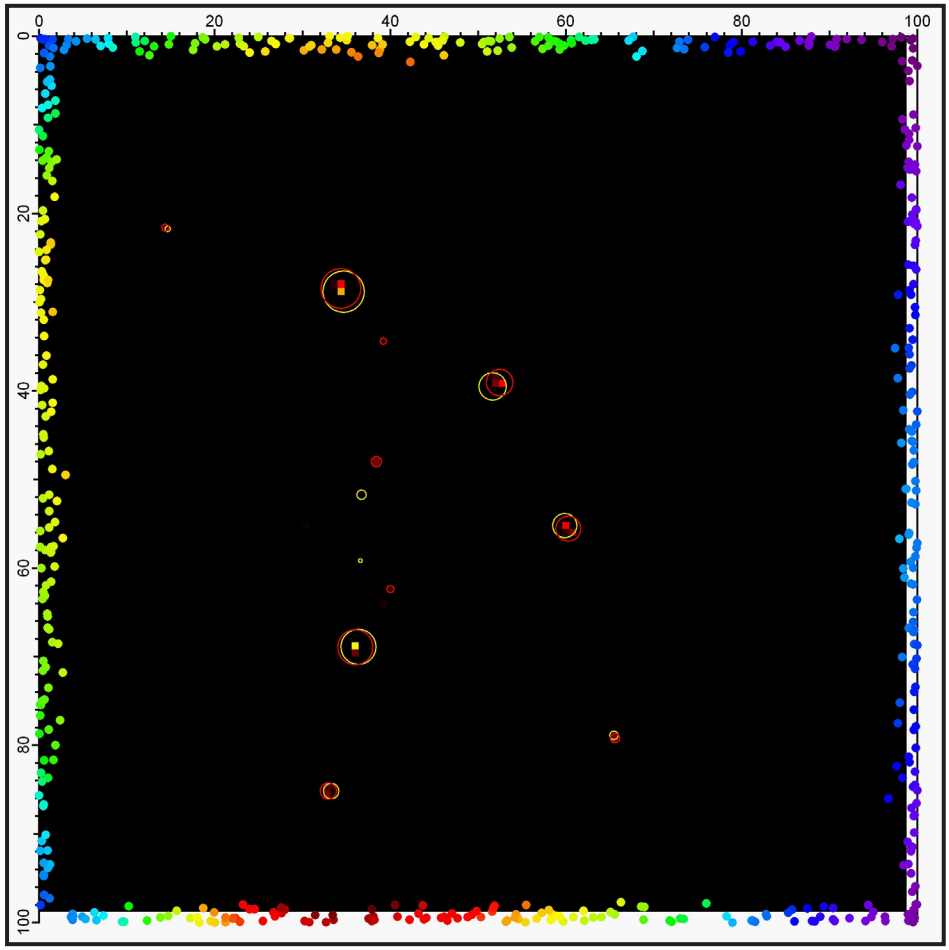

Figure 4. The results from Figure 3, after the particle analysis step. The yellow circles again represent truth—the location and magnitude of the sources. The red circles are determined from the NNLS solution.

Particle Analysis

We developed an interesting post-analysis step to allow a quantitative assay of the algorithm performance. With the second-pass solution represented as an image, a series of image analysis steps collectively called 'Particle Analysis,' were applied to identify each separate clump of pixels. The total activity and centroid of each clump was then calculated. These, now represented as circles, showed the location and magnitude of equivalent point sources. Figure 4 shows the result for the problem shown in Figure 3.

Initial Assessment of NNLS Technique

The approach described so far is only appropriate for 'linear' problems that do not involve shielding. Next, we sought to develop an alternative algorithm that would be able to account for shielding. This method attempted to fit the activity distribution to a set of quasi-orthogonal wave functions. Shielding was introduced as a second field, manifested as another, coarser grid overlapping the area. We hoped to be able to find a way to fit the activity distribution with the wave functions while iteratively adjusting the shielding values. The algorithm quickly became very complicated, work with it ended, and further work with the NNLS technique, which seemed more promising, resumed. Future work along these lines might require collaboration with an expert in computational mathematics.

At this stage in the project the NNLS algorithm had two important limitations:

1. The solution was very sensitive to measurement noise.
2. The solution worked well for point sources, but not well for continuous distributions.

To try to improve the stability of the NNLS technique, two strategies were employed.

1. Implement anisotropic response functions:
   - Simulate a detector with approximately 30° collimation.
   - Extend to model arbitrary detector response.
2. Implement weighting in the NNLS algorithm:
   - The weight w_{ii} for each B_i is $\sqrt{B_i}$.
   - Solve $w_{ii}(M_{ji} A_j = B_i)$.

Anisotropic Response Function

Support for anisotropic detector response functions was added. This allowed the algorithm to represent more realistic detector models, including highly collimated detectors. For the purpose of our simulation we used a simple analytical form to express the dependence of the detector response function on the azimuthal angle.

$$F(r,\phi) = \frac{A}{r^2} \exp\left(-\frac{\phi}{2\sigma^2}\right). \quad \textbf{(6)}$$

We also propagated variables throughout the simulation and algorithm to track the orientation of the detector.

Initial tests compared the solutions obtained for several simulated point source test cases using isotropic and 30° collimated response functions. The solutions were comparable for most tests contain-

ing 5 to 20 point sources. Dependence between the degree of collimation and the quality of the fit seems to exist. Although we did not quantitatively study this effect, we expect that as the response function ranges from totally anisotropic to isotropic the fit 'quality' will increase through a maximum at some value of partial collimation.

Weighted NNLS Algorithm

We assumed that counting statistics were the dominant source of noise in our measurements. The weight that should be assigned to each measurement is approximately the square root of the measured counts. This weight was incorporated in the NNLS routine by computing $M'_{ji} = w_{ii}M_{ji}$ and $B'_i = w_{ii}B_i$, and then evaluating $M'_{jj}A_j = B'_i$.

We compared the performance of the two-pass NNLS method for cases with a range of statistical noise with a signal-to-noise ratio (S/N) between 1 and 25. Two examples are shown in Figure 5. We find that the weighting introduced is effective for obtaining solutions when the average S/N is approximately five or greater (with additional dependence on other parameters).

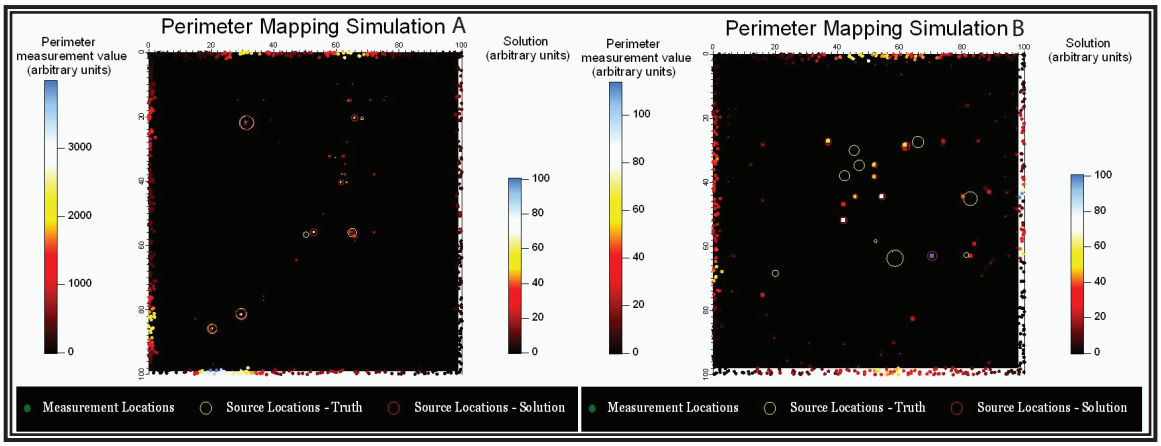

Figure 5. A series of example problems for the weighted NNLS algorithm having average S/N values of 20 (simulation A) and 4 (simulation B)

Continuous Distributions

It proved surprisingly difficult to obtain stable and representative solutions for continuous distributions. The distributions themselves were modeled using a fine-meshed grid of slowly varying values. The distribution grid spacing was smaller than the solution grid spacing by a factor of about 50.

The solutions tended to consist of a few points of high activity, distributed as a rough representation of the true distribution. We attempted to include a gradient penalty term but could not get the modified fitting algorithm to work properly.

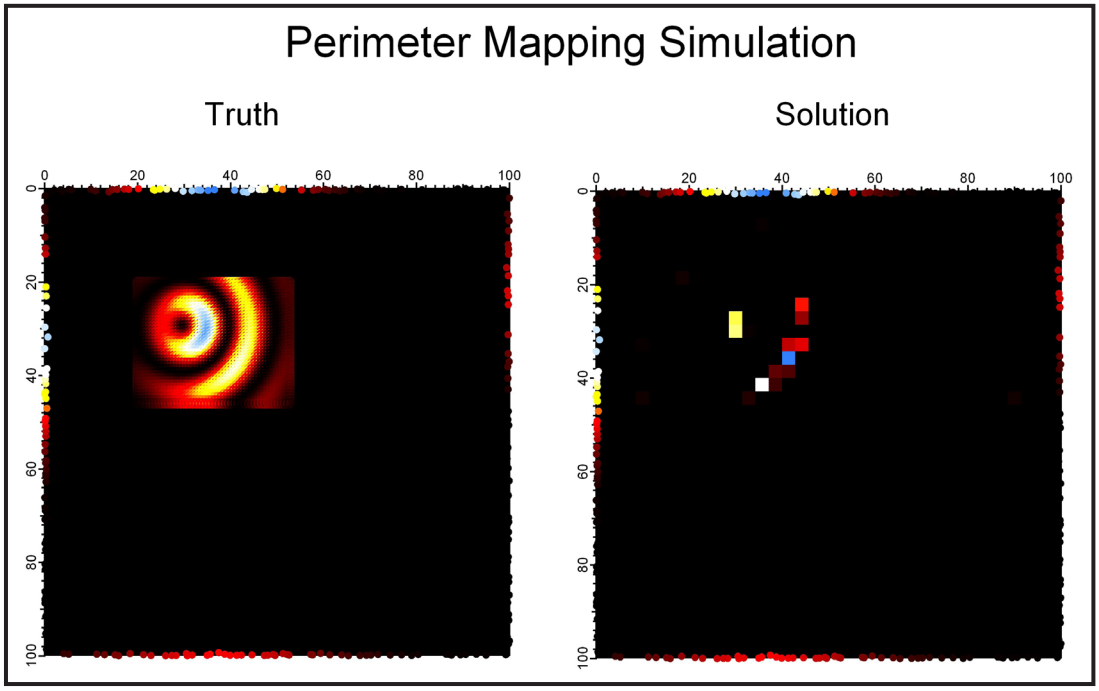

Figure 6. Examples of continuous distribution and solution

Our implementation of the anisotropic response function, and the weighted NNLS routine contributed a moderate improvement to the results. An example of a solution obtained for one test problem is shown in Figure 6. This example incorporates both the 30° collimation and statistical weighting. The dominant parameter affecting the fit quality was the S/N of the measurements.

Conclusion

We have demonstrated that the perimeter-mapping problem is solvable, and developed a working algorithm. The algorithm solves for the unknown activity distribution through use of a constrained LSF, the NNLS. The solution was found to be unstable in general; however, the source of instability (gridding) was identified and the problem lessened by introduction of a two-pass method. The two-pass algorithm works well for distributions of point-like sources, provided that the total number of sources is not too large. We improved the stability of the algorithm for simulations that included statistical noise by adding weighting to the NNLS algorithm. We also added anisotropy to the detector response function and found that it affected the stability as well, particularly for simulations of continuous distributions. We think we have a qualitative understanding of how this feature affects the algorithm performance, but have not made a systematic study to prove it. Overall, the two-pass, weighted algorithm converged nicely for twenty or fewer point sources provided

the average S/N was greater than about twenty. For continuous distributions the results were generally a poor representation of the true solution. In these problems the algorithm tended to "clump" all the activity into a few point-like sources. We were able to improve the solution for any given problem by tweaking parameters, but a universal optimization was not achieved.

Future work on this subject should concentrate on solving the stability problems associated with continuous distributions. We expect that something like the gradient penalty factor, which we were unsuccessful at implementing, would help in this respect. We also feel that the more complicated problem that includes attenuating materials is worthy of future research. That problem cannot be approached with the mathematical formulation used in the present work; however, because attenuation and occlusion are incompatible with the linear superposition property assumed here. That problem might best be approached using a more direct analogy to x-ray tomography and using spectral sensitive measurements.

Reference

Lawson, C. L., R. J. Hanson, *Solving Least Square Problems*, Prentice Hall, Englewood Cliffs, New Jersey, 1974.

this page intentionally left blank

Sequential Probability Ratio Test for Radiation Detection

Warnick Kernan,[1] *Ding Yuan*
Remote Sensing Laboratory – Nellis

This scope of this project was to examine the applicability of the Sequential Probability Ratio Test (SPRT) for field radiation detection, as in a Consequence Management (CM) radiological survey scenario. Our objectives were to develop an SPRT algorithm suitable for handheld devices and to collect data with and without background for performance evaluations. We developed an SPRT algorithm and evaluated it against the default algorithm of an in-house detection device. Preliminary assessment demonstrated that, compared to the default algorithm, the SPRT algorithm has the following advantages: it offers quantitative detection confidence, speeds field operations in high radiation areas, and reduces the rate of false alarms.

Background

Reliable and fast detection of radiation anomalies, with respect to the regional background, is the central focus of many environmental radiological surveys. In a situation where field radiation measurements, such as gamma gross counts (GC), are individually collected with a fixed-length time interval using a handheld device, the objective would be to decide between one of two possible outcomes using the sampled measurements. The first potential outcome, the null hypothesis (H_0), would indicate that the sample was from the background radiation population. The second possible outcome, the alternative hypothesis (H_1), would indicate that the sample was from an anomalous population with higher radiation strength.

The existing algorithm for field radiation detection (using an in-house device) adapts a scheme with fixed sample sizes but cannot quantify decision confidence levels. Moreover, it has a relatively high false-positive rate. On the contrary, Wald's SPRT (2004) works strictly under prescribed confidence levels and dynamically determines needed sampling sizes. For this reason, we determined SPRT worthy of exploration for potential applicability to field radiation detection.

Project

SPRT Details

SPRT provides a means of analyzing multiple measurements to decide among the null hypothesis (H_0), the alternative hypothesis (H_1), or the need for additional measurements. The formalism of

[1] kernanwj@nv.doe.gov, 702-295-8600

SPRT is discussed below. If α and β are the Type I (false positive) and Type II (false negative) errors associated with decisions H_0 vs H_1, respectively:

$$\alpha = P\{\text{Accept } H_1 \text{ when } H_0 \text{ is true}\} = P(H_1|H_0); \quad (1)$$

$$\beta = P\{\text{Accept } H_0 \text{ when } H_1 \text{ is true}\} = P(H_0|H_1); \quad (2)$$

then:

1-α = confidence level of accepting H_0, and

1-β = confidence level of accepting H_1.

Let $\{x_1, x_2, x_3, \ldots, x_n\}$ be an (independently identically distributed) fresh data set collected since the last decision, with a new decision yet to be made. Assuming $f_0(x)$ and $f_i(x)$ are the probability distribution functions for H_0 and H_1, respectively, we can construct a conventional logarithmic likelihood ratio (LLR):

$$\Lambda_n = LLR(x_1, x_2, \ldots, x_n) = Log \frac{\prod_{i=1}^{n} f_1(x_i)}{\prod_{i=1}^{n} f_0(x_i)} = \sum_{i=1}^{n} Log \frac{f_1(x_i)}{f_0(x_i)}. \quad (3)$$

Wald's SPRT has the following forms:

- If $\Lambda_n < A$, then accept H_0;
- If $A \le \Lambda_n \le B$, request an additional measurement be made for the same spot;
- If $\Lambda_n > B$, then accept H_1.

Where A and B are two constants satisfying inequalities,

$$Log \frac{\beta}{1-\alpha} \le £A < B£ \le Log \frac{1-\beta}{\alpha}, \quad (4)$$

a common practice is to simply take:

$$A = Log \frac{\beta}{1-\alpha}, \quad (5)$$

$$B = Log \frac{1-\beta}{\alpha}. \quad (6)$$

Clearly, parameters A and B are related only to the strengths (α, β) or confidences (1 – α, 1 – β) of the test, but are independent of the actual distribution function forms.

In our experiment, we assumed that the gamma GC from a high-radiation anomaly or source follows a Poisson distribution *Poisson* (μ_1). We also assumed that background gamma GC follows a simple Normal distribution $N(\mu_0, \alpha^2_0)$. Using Normal approximation for Poisson distribution *Poisson* (μ_1) → $N(\mu_1, \mu_1)$, we derived the LLR in the following form:

$$\Lambda_n = LLR(x_1, x_2, \ldots, x_n)$$

$$= \sum_{i=1}^{n} \left(\log \frac{\sigma_0}{\sqrt{\mu_1}} + \frac{(x_i - \mu_0)^2}{2\sigma_0^2} - \frac{(x_i - \mu_1)^2}{2\mu_1} \right). \quad (7)$$

The alarm level was calculated using the following formula, which measures the level of deviation of the sample mean from the background mean:

$$AL = Ceiling\left[Log_2 \left[\frac{\mu_1 - \mu_0}{\sigma_0} \right] \right]. \quad (8)$$

An SPRT algorithm with the above distribution details was implemented in a Mathematica platform (Wolfram, 2003) for evaluation.

Experimental Data Sets

We collected experimental data in a laboratory setting, using an in-house handheld detector and a common industrial ^{137}Cs source. The counting interval of the detector was set at 1/2 sec, but was integrated into a 1-sec data stream. We measured the source gamma strength at distances ranging from 1–50 ft, to simulate different source strengths. The background radiation had a mean of μ_0 = 773 (counts/s) and a standard deviation of σ_0 = 33. The integrated 1-sec gamma GC data measured in the lab with and without a source appear in Figure 1.

Results and Interpretations

The default algorithm generated alarms, and the SPRT derived alarms from the experimental data at different strengths or distances (Figure 2). During the experiment, we set α = 0.05 and β = 0.01. These settings (suitable for the average special nuclear material–detection mission) guaranteed that SPRT would have a lower false negative than false positive rate. Notice that the default algorithm does not offer any quantitative estimates for the confidence of the alarm signals.

Comparing the two alarm curves (Figure 2), we drew the following conclusions:

- The SPRT and default alarms have similar ranges and are consistent within the high radiation region ($AL \geq 2$); and
- SPRT reduced the false alarm rate significantly ($AL = 1$).

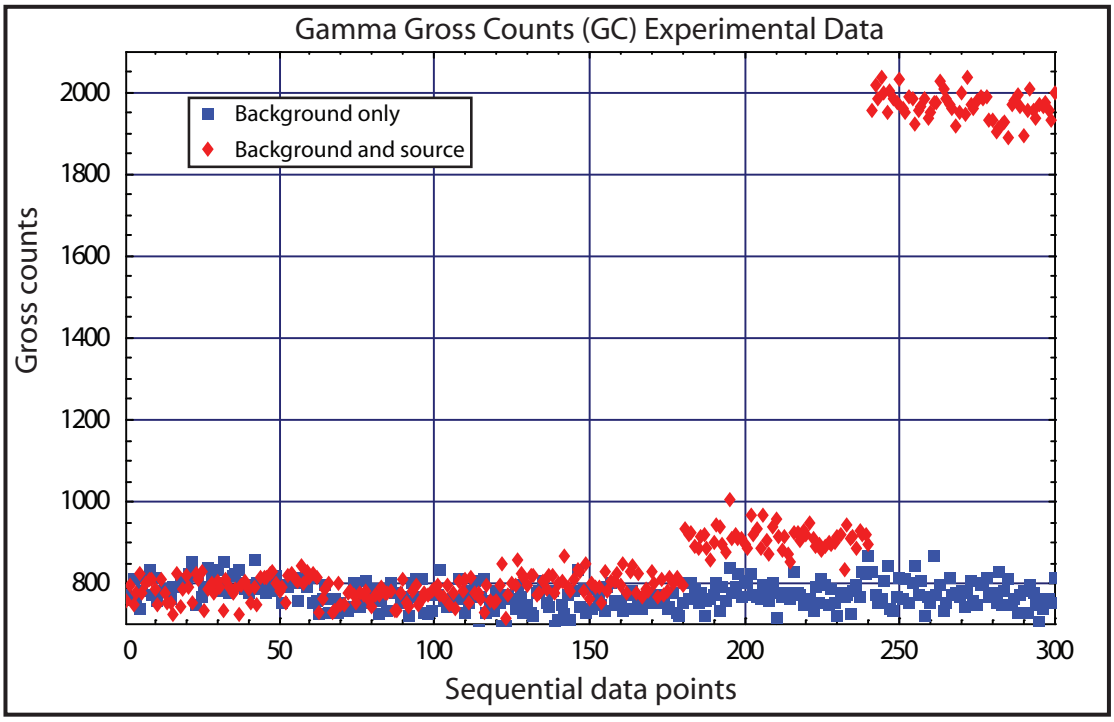

Figure 1. The integrated 1-sec gamma GC data measured in the lab with and without a ^{137}Cs source, where the x axis is the data-point position in the sequence

Although an experienced technician could decrease the false positive rate by moving the alarm threshold to $AL = 2$, additional experience and prior knowledge about background strength would be required.

Further study suggested that for high-radiation anomaly ($LGC \geq 2$), the SPRT requires a minimum of five observations to derive the needed log departing coefficient (LGC) with the given confidence levels. For low-radiation anomaly ($LGC = 1$), the SPRT needs no more than seven observations. For background confirmation ($LGC = 0$), the SPRT may require a longer cycle, anywhere from 6 to 11 observations. We would like a field radiation instrument to be able to minimize the time needed for high radiation source sampling.

Conclusion

Preliminary assessment suggests that the SPRT method described in this paper results in a promising algorithm for field radiation detection. It is compatible with the current default algorithm used by our in-house detector. While maintaining prescribed confidence levels for its estimations, the SPRT

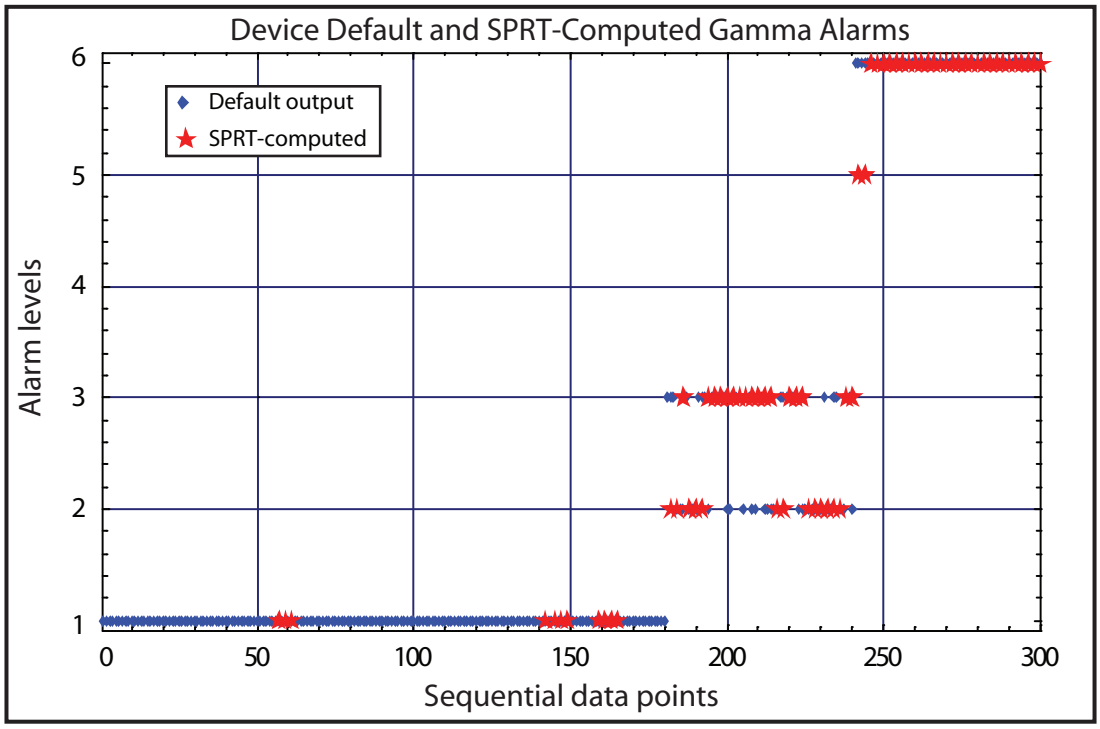

Figure 2. In-house default and SPRT-derived gamma alarms from the experimental data

algorithm reduces the required number of sample measurements for high radiation regions or spots. This implies that it could decrease exposure time for field radiation surveyors. We strongly recommend that SPRT be further investigated for possible CM adaptation.

References

Wald, A., *Sequential Analysis*, Dover Publications, Mineola, New York, 2004.

Wolfram, S., *The Mathematica Book*, 5th ed., Wolfram Media, Champaign, Illinois, 2003.

this page intentionally left blank

Time-Dependent Consequence Management Spreadsheet for Nuclear Weapon Detonation

Warnick Kernan,[1] *Ding Yuan*
Remote Sensing Laboratory – Nellis

Radioactive nuclide measurements vary with time, according to the radioactive decay law. Currently, Consequence Management Assessment Spreadsheet (CMAS) software does not consider the time-dependency of the measurements when computing various Protective Action Guides (PAGs). Through investigation, we proposed the Radionuclide Temporal Normalization (RTN) approach for addressing this issue and derived explicit solutions to the generic radioactive decay systems that are key to the proposed RTN approach. This project extended early work by Bateman (1910) for solving radioactive decay systems.

Background

The Accident Response Group (ARG), the Federal Radiological Monitoring and Assessment Center (FRMAC), and Stockpile Stewardship Test Readiness must be able to rapidly assess health impact from nuclear fallout. Although designed as the assessment tool for all these missions, CMAS software lacks the ability to distinguish the sample measurements made at different times during the survey. Because the fission product mix changes extremely rapidly, this missing feature is critical. The quantity of radioactivity following a nuclear detonation decreases by a factor of ten every seven hours, and this relationship provides a reasonable measure of relative activity from a few hours to several hundred days after detonation (Glasstone, 1977).

This project proposed to investigate methods and explore scientific concepts for improving the CMAS' ability to correlate sampling times and assessment results. Although this work focused on enhancing CMAS software, its underlying concepts could be applied to improving Turbo FRMAC software as well.

Initially we considered two different approaches. The first was to make approximations that captured the time decay of the activity, without attempting to calculate all of the fission nuclide species created in the detonation. This approach would use an empirical decay relationship (Glasstone, 1977) to make time-dependent calculations at a defined time.

The second approach would involve temporal calibration of the different fission nuclides created in the detonation. Using the law of radioactive decay and measurements of fission products taken at

[1] kernanwj@nv.doe.gov, 702-295-8600

different times, one could calculate radionuclide quantities at a common reference time. Subsequently, the dose rates, PAG limits, and other assessment parameters could be uniformly derived, using the calibrated measurements at a preselected reference time (e.g., a seven-hour mark).

The first approach, which omits species-by-species decay calculations, seemed much easier to implement. However, this simplification would have reduced utility for calculating the Derived Response Level (DRL), Dose Conversion Factor (DCF), and other assessment parameters (DOE, 2003). The second approach, which involves only the temporal calibration of the sample radionuclide mixes, would keep all other assessment modules essentially intact. Furthermore, a revised spreadsheet program based on the second approach would be more flexible than a program based on the first approach, by virtue of the common reference time mark. Therefore, we decided to focus on the second approach, hereafter referred to as RTN.

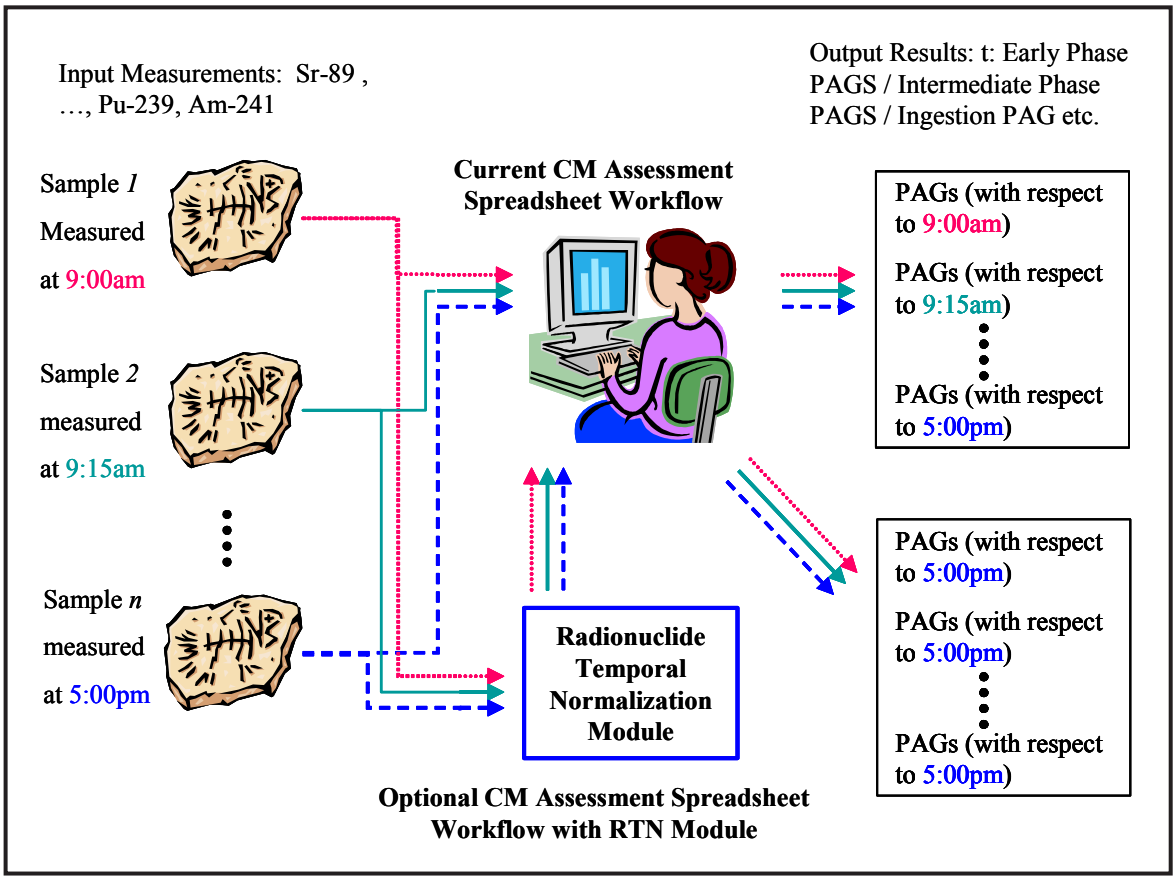

Figure 1. Current CMAS workflow and the optional workflow with additional RTN module

Project

RTN Concept

The RTN concept is quite simple. CMAS currently takes the radionuclide mix measurements and directly computes the derived PAGs from each individual sample (Figure 1). In the end, these PAGs are tied to the measurement times of their associated samples. Derived spatial PAG products, such as contour maps, contain uncertainties caused by temporal nonuniformities (i.e., CMAS makes no allowance for the difference in time at which samples were taken). Such temporal nonuniformities would have a more pronounced effect on the early-phase PAGs.

The RTN approach would add an additional module to the existing CMAS for radionuclide temporal normalization. This module would convert the directly measured radionuclide mix readings to time-corrected values, with reference to a preselected standard time (e.g., 5:00 p.m. of the operation day). In this way, all PAGs and their derived spatial products would carry a unique reference time and would therefore be comparable in time scale. The RTN module would affect no other calculation modules currently existing in the CMAS. Furthermore, RTN could be implemented internally or even externally to the current CMAS software.

RTN Key Issue

The key issue for the RTN module is decay calculation. Suppose we know the radiation strength of a physical sample at 10:00 a.m. What would the same sample's radiation strength be at 5:00 p.m.?

Suppose that the physical sample consists of m radioactive nuclides. At a given time t, the nuclide i in the sample has exactly $N_i(t)$ atoms, and the quantity $N_i(0) (= N_i,0)$ has been measured at the initial time. Therefore, the RTN module should be able to compute

$$\{N_i(t)\}_{i=1}^{m}$$

from

$$\{N_{i,0}\}_{i=1}^{m}$$

for an arbitrary $t > 0$.

Let's define λ_i as the decay constant for nuclide i. Also, let us define $\rho_{i,j}$ as the branching factor or transmutation coefficient from nuclide i to nuclide j. Notice that we have not yet used the genealogy order of the nuclides (i.e., parent to child to grandchild). Obviously, $0 \le \rho_{i,j} \le 1$, $\rho_{i,j} \ne \rho_{j,i}$, $\rho_{i,i} = 0$ and $\rho_{i,j} > 0$ if and only if nuclide i is a parent of nuclide j. Also, if $\rho_{i,j} > 0$, then $\rho_{i,i} = 0$, since the parent-child relationship is one-directional.

Under these notations, the time-dependency of:

$$\{N_i(t)\}_{i=1}^{m}$$

can be described by the following simultaneous differential equations:

$$\frac{dN_i(t)}{dt} = -\lambda_i N_i + \sum_{j=1, i\neq j}^{m} \rho_{j,i}\lambda_j N_j \qquad \text{for } i = 1, 2, \ldots m, \tag{1}$$

where:

$\{N_{i,0}\}_{i=1}^{m}$ = known initial conditions.

These equations extend the radioactive decay law described in many textbooks (Krane, 1988) by introducing the branching factors (also referred to as "transmutation coefficients" in some of the literature).

Current Findings

The differential equations for single-child radioactive decay chains were first solved by Bateman (1910). However, Bateman's solution cannot handle radioactive decay systems with branching and converging chains, such as the ^{238}U – ^{234}U decay chain commonly found in the environment (Figure 2). Thus, we required solutions for more generalized radioactive decay systems.

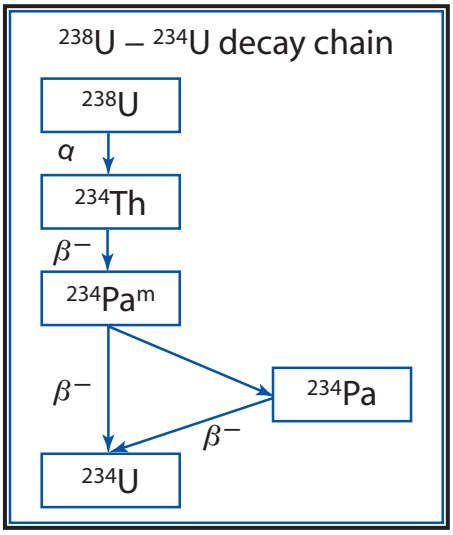

Figure 2. ^{238}U – ^{234}U decay chain

Through our research, we derived the complete solutions to the above decay equations, providing that the radioactive nuclides are arranged in a genealogical order and there is no other uncountable source during the decay. Under these conditions, $N_i(t)$ can be precisely expressed in the following form:

$$N_i(t) = C_{i,1}e^{-\lambda_1 t} + C_{i,2}e^{-\lambda_2 t} + \ldots + C_{i,i-1}e^{-\lambda_{i-1} t} + C_{i,i}e^{-\lambda_i t} \qquad i = 1,2,\ldots m, \tag{2}$$

where the coefficients $\{C_{i,j}\}_{j=1,2,\ldots i-1,i=2,3,\ldots m}$ can be recursively calculated using the following formulas:

$$C_{1,1} = N_{1,0}; \tag{3}$$

$$C_{i,j} = \frac{1}{\lambda_i - \lambda_j}\sum_{k=j}^{i-1}\rho_{k,i}\lambda_k C_{k,j} \qquad j = 1,2,\ldots i-1,\ i = 2,3,\ldots m; \tag{4}$$

$$C_{i,i} = N_{i,0} - \sum_{k=1}^{i-1} C_{i,k} \qquad i = 2,3,\ldots m. \tag{5}$$

Transition Series Example

As illustration, we will consider the decay of the isobar transition series ^{95}Rb – ^{95}Mo. The nuclides, their half-lives, and respective decay constants appear in Table 1. ^{95}Rb, a possible fission product, does not occur naturally and has a very short half-life. ^{95}Rb, ^{95}Sr, and ^{95}Y are short-lived nuclides, from a field measurement point of view. Their measurements are essentially valid only for the moment in which the measurements are made. On the other hand, ^{95}Zr and ^{95}Nb have relatively long half-lives of 64 and 35 days, respectively.

Figure 3 shows the accumulation/decay curves for the ^{95}Rb – ^{95}Mo series, computed with different initial values, using the formulas presented earlier in this paper. Curves in the left column were calculated using initial values of $N_{1,0} = 1$ and $N_{2,0} = \ldots = N_{5,0} = 0$, where one unit is simply the normalized initial population. Similarly, curves in the right column were calculated using initial values of $N_{1,0} = \ldots = N_{5,0} = 0.2$. Essentially, all these curves (with the exception of the ^{95}Rb curve) exhibit three phases: accumulation, quasi-equilibrium, and decay. These lengths vary dramatically. As these curves clearly show, the radioactive measurements are only accurate when initially made. For CMAS-like assessment tasks, samples can only be compared if they are normalized to the same reference time.

Table 1. Isobar transition series, half-life, and decay constants

Isobar	^{95}Rb	^{95}Sr	^{95}Y	^{95}Zr	^{95}Nb	^{95}Mo
$T_{1\,2}$	0.378 s	23.1 s	10.0 m	64.03 d	35.0 d	∞
1 in m^{-1}	1.102×10^{2}	1.801	6.911×10^{-2}	7.517×10^{-6}	1.376×10^{-5}	0

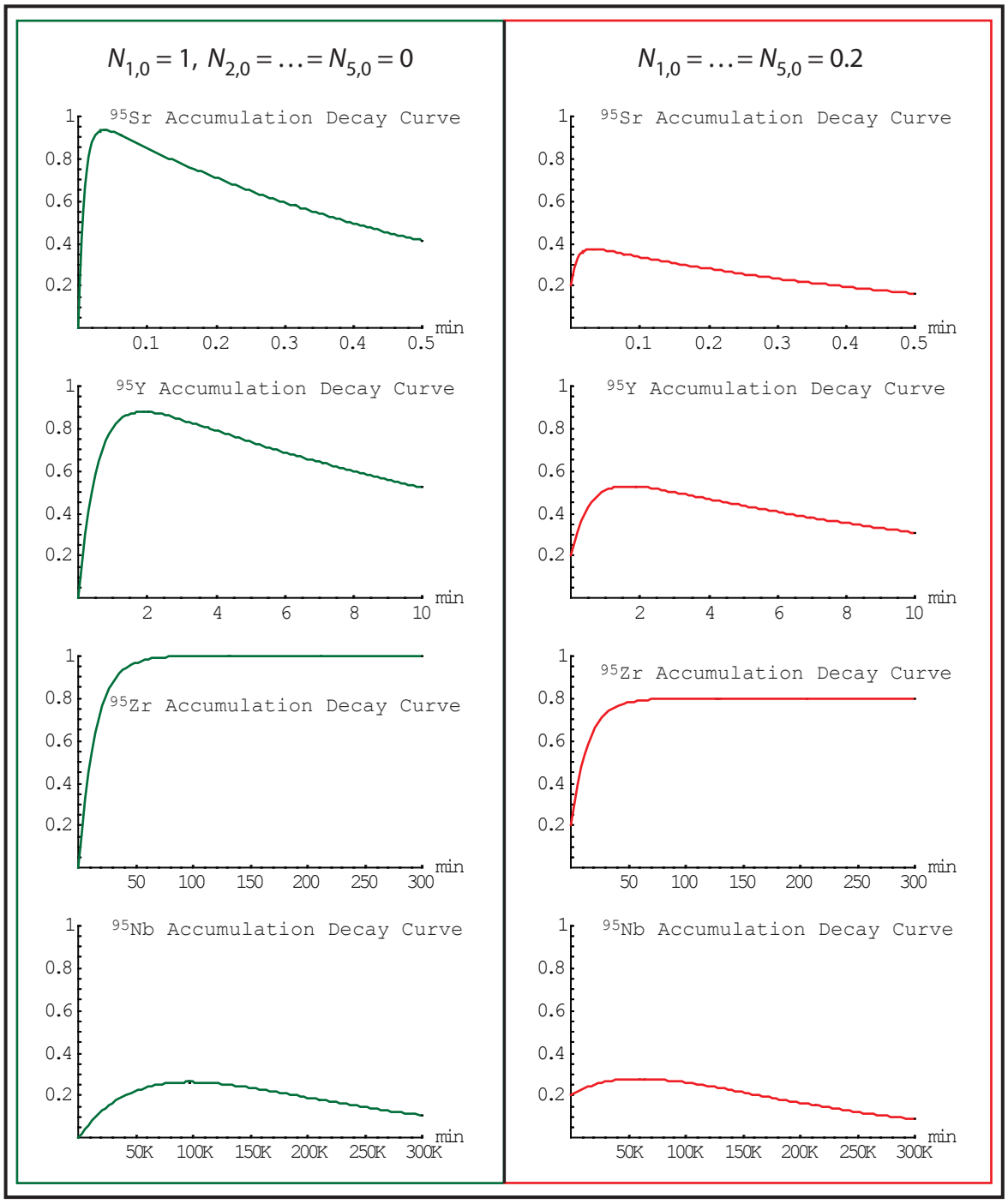

Figure 3. ^{95}*Rb* – ^{95}*Mo* accumulation/decay curves with two sets of initial conditions: (left column): $N_{1,0} = 1$, $N_{2,0} = \ldots = N_{5.0} = 0$; (right column): $N_{1,0} = \ldots = N_{5,0} = 0.2$

Conclusion

We have derived explicitly the quantitative solutions for generic radioactive decay systems, which are key in solving the CMAS time-dependency issue. The proposed RTN module for the CMAS software program could be further studied and usefully implemented by a number of groups, including the DOE's Consequence Management organization.

References

Bateman, H., "The Solution of a System of Differential Equations Occurring in the Theory of Radio-Active Transformations," *Proc. Cambridge Phil. Soc.* **15** (1910) 423–427.

Glasstone, S., P. J. Dolan, *The Effects of Nuclear Weapons*, 3rd ed., U.S. Department of Defense and U.S. Department of Energy, Washington, D.C., 1977, 1.64.

Krane, K. S., *Introductory Nuclear Physics*, John Wiley & Sons, Inc., New York, 1988.

U.S. Department of Energy, National Nuclear Security Administration, Nevada Site Office, Federal Radiological Monitoring and Assessment Center, "FRMAC Assessment Manual; Methods: Volume 1," SAND2003-1071P, http://www.nv.doe.gov/library/publications/frmac/SAND2003_1071P_VOL1.pdf, accessed April 26, 2006.

this page intentionally left blank

Temperature Measurement of Thermal Hot Spots Using SWIR Channels of the Daedalus 1268 Scanner

Alan L. Klawitter[1]
Remote Sensing Laboratory – Nellis

Recent catastrophic thermal events, including 9/11 and western U.S. wildfires, have shown that an airborne instrument capable of quickly and accurately measuring the temperature and location of high-temperature thermal anomalies is critical to decision-making authorities. A novel approach using an airborne reflectance spectrometer has proven effective in providing this information. A shortwave infrared (SWIR) attachment to the Remote Sensing Laboratory's Daedalus 1268 airborne scanner accurately measured the temperatures of hot objects under practical conditions.

Background

This project intended to determine if a Daedalus 1268 multispectral scanner, operated by the RSL during emergency response activities, could remotely ascertain the temperature and location of hot objects with a high degree of radiometric and geodetic accuracy. Part of this project was completed in 2004. However, due to time constraints, all tests were conducted under laboratory conditions in a darkroom, where the scanner recorded only sources of energy emitted from controlled blackbodies at known temperatures. Under these conditions, we were able to evaluate the scanner's ability to accurately resolve temperatures. However, such a controlled laboratory environment does not adequately represent conditions encountered during an actual response to an incident or accident. Therefore, we conducted additional experiments in 2005 to determine if the scanner could radiometrically resolve hot object temperatures in such an environment.

A long-standing problem in determining object temperatures using thermal sensors has been that emission sources smaller than the measuring sensor's field of view result in ambiguous solutions. For example, did the total measured thermal radiation emanate from a hot source of small dimensions or a cooler source of larger dimensions? Spectrometers eliminate this ambiguity because they measure both signal intensity and wavelength. The shape of the resultant thermal spectrum shows the distribution of energy emitted from the source. This shape can then be used to determine a unique temperature, and the intensity yields the area of the emitting source.

A Daedalus 1268 multispectral scanner in the traditional Airborne Thematic Mapper configuration records thermal emissions in the wavelength between 8.28 and 10.67 μm. It is nominally capable of reporting apparent object temperatures from 20°–180°F; however, it cannot determine the much higher temperatures associated with most catastrophic thermal events. RSL maintains and operates

[1] klawital@nv.doe.gov, 702-295-8603

a SWIR attachment to the Daedalus 1268, which records 52 channels of data in relatively narrow bandwidths from 420–2416 nm. In 2001, Clarke et al. documented a novel approach using a visible/near-infrared hyperspectral scanner for determining surface temperatures of fires burning under the collapsed World Trade Center towers. Using similar methodologies and the SWIR attachment, RSL should be able to attain the same goal.

This project is based on Planck's Radiation Law, which relates spectral radiant emittance to temperature. The spectral distribution of the radiation emitted by a blackbody is a smooth curve with a single maximum. Examples are depicted in Figure 1.

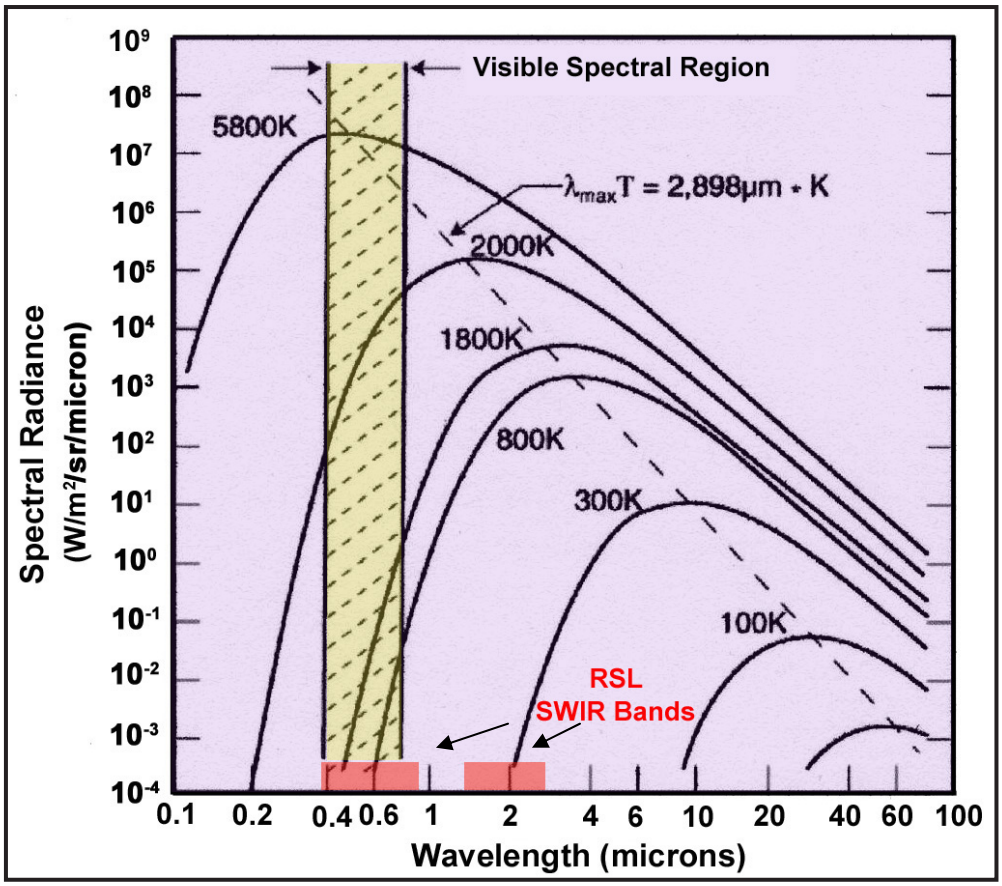

Figure 1. Planck blackbody curves at various temperatures

In mathematical form, Planck's law is stated as:

$$W_{\lambda B} = \frac{c_1}{\lambda^5} \times \frac{1}{\frac{c_2}{e\,\lambda T - 1}}, \quad \textbf{(1)}$$

where:

B = blackbody

W_λ = spectral radiant emittance, w/cm^2 (μm)

λ = wavelength (μm)

T = absolute temperature (°K)

c_1 = first radiation constant (2π h c^2)

h = Planck's constant (6.256×10^{-3} w/s^2)

c = velocity of light (2.9979×10^{10} cm/s)

c_2 = second radiation constant (ch/k)

k = Boltzmann constant [1.3805×10^{-23} w/s(°K)].

Figure 1 shows that, as the temperature of a blackbody increases, the spectral distribution curve changes shape and shifts toward shorter wavelengths. It also indicates that blackbodies with temperatures ranging between approximately 250 and 3500°F can be accurately assessed by determining the slope of spectral emittance curves between 0.4 and 2.5 μm and comparing them to the Planck function. Additionally, equations detailed by Clarke (1979) allow separation of reflected radiance components from emitted components, thereby permitting the use of Planck functions to extract target temperatures.

Project

Primary Instrumentation

RSL's primary airborne imaging spectrometer is the Daedalus 1268 scanner. During normal operation, the scanner records 11 broadband channels of data between 420 and 10670 nm. The SWIR attachment developed for this scanner records 52 narrowband channels, as listed in Table 1.

A Daedalus 1268 can collect data at rates of up to 100 Hz, facilitating the acquisition of high spatial resolution data at low altitudes. Most recently manufactured multi-/hyperspectral scanners are incapable of reproducing the spatial resolutions of the Daedalus 1268. Presently, Daedalus data are

Table 1. Daedalus 1268 SWIR channels, bandwidths, and spectral coverage

Number of Channels	Bandwidth (nm)	Wavelength (nm)
20	24	430–910
16	35	1386–1934
16	32	1925–2416

captured at 8-bit resolution due to limitations of the scanner's digitizing boards. Because the 8-bit limitation affects the system's radiometric properties as illustrated below, we are upgrading the boards to 16-bit digitization.

An Analytical Spectral Devices, Inc. (ASD), portable field spectrometer was employed to independently record the reflectance spectra of targets imaged by the Daedalus scanner. The ASD spectrometer collects visible/near-infrared spectra of an object from 350–2500 nm in 1-nm increments. This instrument was radiometrically calibrated for radiance measurements at ASD's laboratory in spring 2002, and the manufacturer's guidelines were followed during its use.

Data Acquisition

To test the hypothesis that the Daedalus 1268 could accurately record the temperatures of hot objects, our team designed a series of experiments. These included darkroom and outdoor experiments with stationary equipment and airborne tests. However, airborne testing could not be completed due to scheduling conflicts.

Outdoor experiments were performed on clear, sunny days in May, July, and September 2005, on an asphalt apron adjacent to the northeast side of the RSL building at Nellis Air Force Base. Controlled heat sources with surface emissivities of greater than 0.96 were located 4 ft directly below the scanner's collection mirror. Temperatures were monitored by thermocouples/thermometers embedded into the surface of the heat sources and the ASD spectrometer. ASD-derived temperature measurements were gathered using 18° field-of-view fore optics aimed at the center of the heat source. Daedalus 1268 SWIR imagery was recorded for 30-second intervals encompassing the heat sources. Only the images' centermost portions, correlating to the hottest areas of the heat sources, were extracted for statistical analysis.

Results

Clarke et al. (2001) used a ratioing technique named "derived reflectance" to determine the temperatures of hot spots at the World Trade Center following the towers' collapse. In derived reflectance, thermal radiation is the Planck response divided by the solar spectrum. This ratio produces the following effects: 1) data are corrected for atmospheric scattering and absorption, 2) the reflected solar

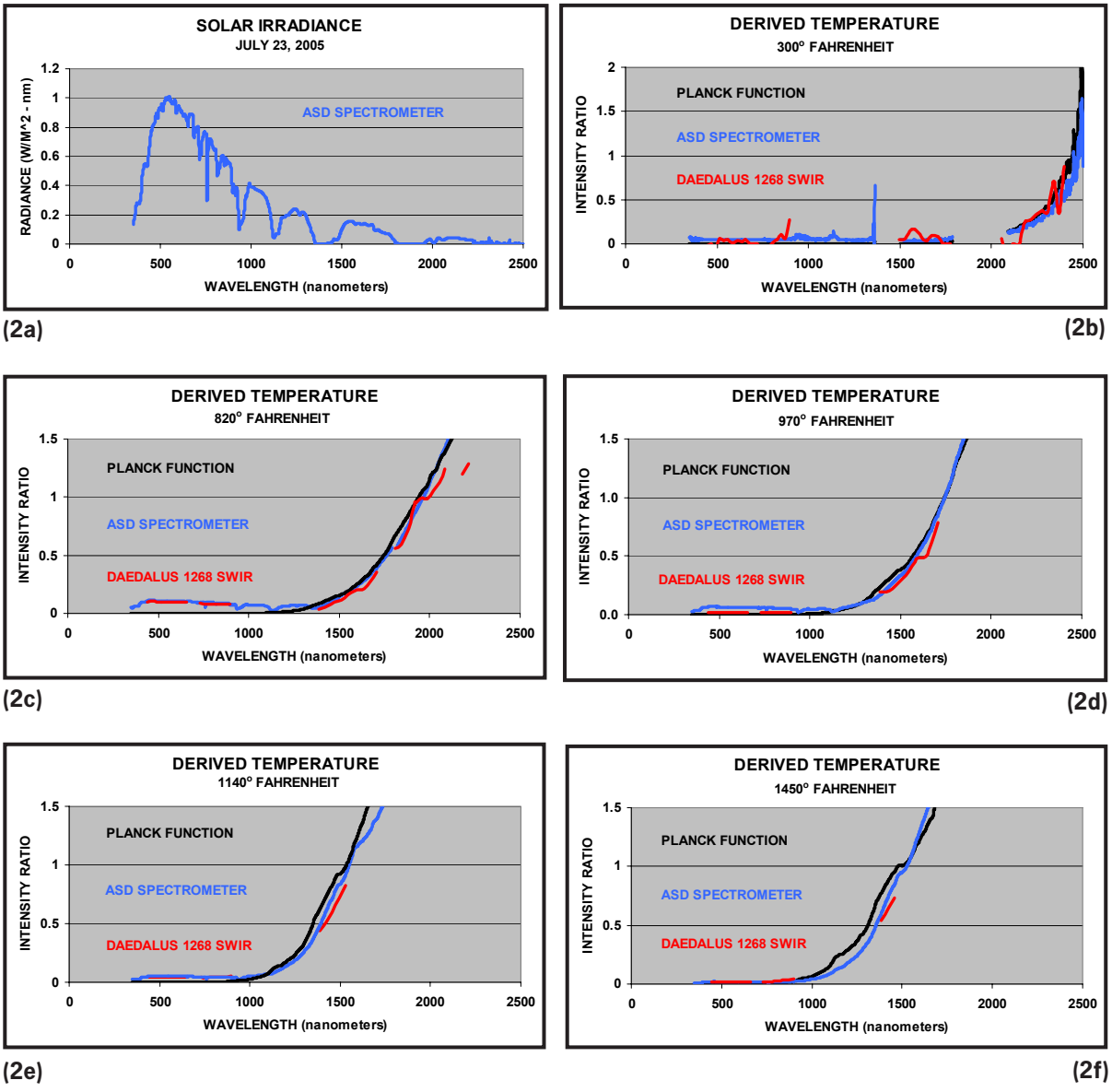

Figure 2. Greybody temperature determinations using derived reflectance curves from Planck functions, an ASD reflectance spectrometer, and a Daedalus 1268 SWIR multispectral scanner

component can be readily assessed and compensated for, and 3) a steep curve that is readily distinguishable from reflected sunlight and surface material reflectance is produced. Comparing the slopes of SWIR spectrometer ratio curves to Planck function ratio curves allows the emitter temperature to be determined.

Daedalus scanner values were converted from digital numbers to radiance prior to ratioing using band gains, band offsets, and calibration coefficients determined at the National Aeronautics and Space Administration (NASA) Ames Research Center. ASD radiance values are internally calculated using lookup tables generated by the manufacturer during instrument calibration. ASD spectrometer data were collected as an independent means to both measure source temperatures and cross-check Daedalus-Planck function relationships. Solar irradiance was also calculated with the ASD portable spectrometer, using a fore optic specifically engineered to measure full hemisphere irradiance. Figure (2a) shows the solar irradiance on July 23, 2005, at 11 a.m. PDT.

Figures (2b)–(2f) illustrate temperature derivation of greybody sources at various temperatures using derived reflectance. Two greybody sources were employed during the experiments. Generally, very good correlations were established between SWIR-recorded values and measured emission source temperatures. Deviations from smooth derived reflectance curves are due to slight variations of atmospheric water vapor content, accentuated by ratioing. The slight separation between the SWIR and Planck curves evident in Figures (2f) and (2g) probably derived from greybody emissivity changes due to temperature and wavelength variations. All Planck function curves were created using an emissivity value of 1.

SWIR temperature-resolution limitations are evident in the graphics. Although SWIR channel gain settings were optimized for each channel at each temperature, the detectors quickly saturated. Data saturation caused by 8-bit digitizing resolution minimized points used to define the curves at elevated temperatures. The data gap between 0.91 and 1.356 μm resulted in underdefined curves at temperatures between about 1400 and 2400°F. Temperatures above 1500°F could not be created using the greybody sources. SWIR and ASD instrument noise is evident in Figure (2b), at 300°F, which is close to the minimum detectable temperature of both instruments. Correlations in Figures (2e) and (2f) indicate that greybody surface temperatures were 30–40°F cooler than temperatures measured by a thermocouple embedded into the ceramic surface, and that it was difficult to maintain constant high surface temperatures during the 30-sec sample intervals.

Conclusion

RSL's Daedalus 1268 multispectral scanner with the SWIR attachment can be used to determine the temperature of hot spots during emergency response and consequence-management surveys. Good correlations were established between emitting source temperature and SWIR response. Data acquired independently with an ASD portable field spectrometer verified experimental results.

Although instrument noise is evident, temperatures as low as 300°F can be resolved. The maximum detection limit has not been established but should exceed 3000°F. Temperatures between 1400 and 2400°F can be determined; however, because no data were recorded between 910 and 1356 nm, few points to define the emission curve are available.

Limitations of the Daedalus 1268 configuration as tested included: 8-bit radiometric resolution, which produced rapid detector saturation and a resultant loss of curve definition; lack of data acquisition between 910 and 1356 nm; and the inability to acquire more than 12 channels simultaneously without replugging cables on the detector head.

Acknowledgments

The author would like to acknowledge the contributions of Marc Rivera, Ed Doak, and Fred Osterwisch to this project.

References

Clarke, R. N., R. O. Green, G. A. Swayze, G. Meeker, S. Sutley, T. M. Hoefen, K. E. Livo, G. Plumlee, B. Pavri, C. Sarture, S. Wilson, P. Hageman, P. Lamothe, J. S. Vance, J. Boardman, I. Brownfield, C. Gent, L. C. Morath, J. Taggart, P. M. Theodorakos, M. Adams, "Environmental Studies of the World Trade Center Area After the September 11, 2001 Attack," USGS Open File Report OFR-01-0429, 2001.

Clarke, R. N., "Planetary Reflectance Measurements in the Region of Planetary Thermal Emission," *Icarus* **40** (1979) 94–103.

Klawitter, A., "Temperature Measurement of Thermal Hot Spots Using SWIR," *Nevada Test Site–Directed Research, Development, and Demonstration*, FY 2004, Bechtel Nevada, Las Vegas, Nevada, 2005, 171–176.

this page intentionally left blank

Atmospheric Dispersion Models

Sanjoy Mukhopadhyay[1]
Remote Sensing Laboratory – Andrews

This project evaluated atmospheric dispersion models currently available in the Department of Energy (DOE) and Department of Defense (DoD) communities to predict urban hazard scenarios. Success of a downwind hazard prediction model depends heavily on the choice of meteorological data with proper atmospheric dispersion models. To address urban dispersion problems, many models exist, offering varying degrees of success. This study sought to identify the most deployable, stand-alone model that could be used in all consequence management scenarios. To assess commonality among the leading atmospheric models (Hazard Prediction and Assessment Capability [HPAC] and National Atmospheric Release Advisory Center [NARAC]), we compared simulated output from the two most frequently used models in predicting count rates in commonly available health physics equipment.

Background

The DOE, DoD, and Department of Homeland Security (DHS) have undertaken a serious effort to create a hazard prediction model that will accurately address terrain and atmospheric dispersion in an urban area. Existing models for point sources are inadequate for treating turbulence above large metropolitan areas, since the turbulence structure is severely altered by the roughness of urban elements and different thermal properties relative to rural areas. These changes lead to a shallow, well-mixed urban boundary layer at night, within which turbulence can grow. As a result, plumes from short or moderately tall stacks disperse more rapidly and can produce high ground-level contamination. Thus, "dirty bombs" would have a larger effect if exploded close to the ground at night. In order to address various incident/ accident scenarios, a greater understanding of the model is needed. This study followed the same radiation dispersal device (RDD) scenario for different atmospheric models and compared outputs under similar weather conditions.

This study examined three atmospheric models:

1. HPAC—developed and supported by the Defense Threat Reduction Agency (DTRA)
2. NARAC—developed at Livermore National Laboratory (LLNL) and supported by the DOE
3. The Radiological Assessment System for Consequence AnaLysis (RASCAL 3.0.3), developed and maintained by the U.S. Nuclear Regulatory Commission (NRC)

[1] mukhops@nv.doe.gov, 808-474-2654

HPAC

HPAC models nuclear, biological, and chemical (NBC) effects concerning military operations. The source term may be defined from chemical, biological, radiological, and nuclear (CBRN) weapons, or from conventional weapon attacks against NBC production and storage facilities. Similar effects may result from industrial accidents/incidents involving the release of hazardous material into the atmosphere. HPAC models transport phenomena over complex terrains and import weather data from the Integrated Meteorological Server (IMETS) maintained by the DoD. However, the micro-MET data required to accurately determine the hazard area from a biological agent release is currently unavailable from IMETS.

HPAC is a Gaussian puff model that uses a second-order closure theory to treat turbulence. HPAC is a forward-deployable disaster-preparedness capability (OFCM, 2004). It provides collateral effects of counterproliferation attacks and exposure information for military and/or civilian populations attacked with CBRN weapons. HPAC also provides exposure information for populations near accidents involving nuclear power plants, chemical and biological production facilities, and CBRN storage facilities/transportation containers. HPAC models atmospheric dispersion of vapors, particles, or liquid droplets from multiple sources. It uses arbitrary meteorological input ranging from a single-surface wind speed and direction up to four-dimensional (4-D) wind and temperature field input in a grid pattern. The model accounts for dynamic plume rise, dense gas effects, and time- and space-dependent boundary layers. It predicts the three-dimensional (3-D) concentration field as a function of time, with integrated inhalation dosage and surface deposition fields. Primary and secondary droplet evaporation algorithms are included.

NARAC

Simulations of the atmospheric dispersion of any type of release start with information about the release itself: its location, time, and the initial size of the cloud or mechanism of the release. Information about the processes that factor in dispersing, transforming, and depositing the material must be incorporated into the data. Various meteorological factors are important in modeling a release. Initially, the wind speed and direction at the release location control the plume's path. Accurately determining the winds at the accident site is crucial to producing a credible result. If the release involves a powerful explosion or fire, winds high above the ground may determine the plume's transport, and its vertical extent may be limited by a temperature inversion in the atmosphere. As the plume travels downwind, turbulence dilutes the plume by mixing the material vertically and horizontally. In addition, local wind systems (such as sea breezes) or terrain may change the plume's path. Mountain ridges can block flows, and valleys can channel wind flows. Furthermore, material may be removed from the plume by being deposited on the ground (resuspension becomes an important issue) or washed out by precipitation (Baskett, 2005).

The NARAC Emergency Response Modeling System accounts for these effects by using a series of codes that represent the third-generation modeling system in its 20-year history. The first code, GRIDGEN (Ermak, 2000), draws on a terrain database covering most of the globe at 500-m resolution to develop the underlying terrain and numerical grid for the dispersion area.

The second code, ADAPT (Sugiyama, 1998), creates 3-D wind fields using worldwide meteorological data obtained from online links to the Air Force Weather Agency or weather forecasts from the U.S. Navy and the National Oceanic and Atmospheric Administration (NOAA). LODI (Hodur, 1997), the third code, simulates the transport, diffusion, and deposition of a release by using numerical marker particles (i.e., the positions in space representative of the released material). Finally, a graphics code converts the data to plots of interest, such as doses for radiological accidents, air concentrations for chemical releases, or ground deposition. The plots are displayed on a map of the model domain (Nasstrom, 2000).

RASCAL

RASCAL (Oak Ridge National Laboratory, 2004) is intended as a screening tool to evaluate potential consequences from nuclear power plant releases. It includes modules to estimate source terms, to evaluate transport and atmospheric diffusion and surface deposition, and to estimate doses from radionuclides in the environment. The code output relates dose estimates to both early health effects and the U.S. Environmental Protection Agency's Protective Action Guides (PAG). This model is limited by the fact that the source term is constant once established. Multiple release points cannot be simulated. Despite using a Gaussian puff model, RASCAL is confined to meteorological data from a single location. In addition, it lacks the ability to model directional wind shears. Building wake is not included, and in-growth of daughters does not exist in the radionuclide decay scheme.

Project

This project worked out the procedures for overlaying the resultant outputs from the three aforementioned atmospheric dispersion models onto geographical information system (GIS) maps. Each model used the same simulated scenario of an RDD consisting of 5000 Ci of ^{90}Sr and 10000 Ci of ^{137}Cs exploded with 1000 lbs of conventional TNT at a location near RSL in Las Vegas, Nevada. We used a single-point wind speed (300° NW at 4.2 m/s). Special attention was devoted to the HPAC model. A conversion algorithm was formulated for the HPAC-predicted radiological data to be presented in a grid pattern so that ArcView mapping software could easily assimilate and overlay the data on a geographical map.

One project goal was to incorporate HPAC radiological data into the Radiological Assessment and Training Simulator (RATS) software package developed at RSL. The package accepts the grid data of surface deposition from a radiological explosion predicted by HPAC, folds in the efficiencies of the radiation-measuring field equipment, and simulates the "readings" on the equipment as would be observed by a deployed radiological technician in a real scenario.

Calculation Methods

Before the inverse distance weighting (IDW) method was chosen, several other methods were tested:

- Spline estimates: Using this algorithm, one calculates field values using a mathematical function that minimizes overall surface curvature, resulting in a smooth surface that passes exactly through the input points. This method is best for gently varying surfaces. There are two spline methods: regularized and tension. The regularized method creates a smooth surface with values that may lie outside the sample data range. The tension method tunes the stiffness of the surface according to the character of the modeled phenomenon.
- Kriging: Kriging is based on statistical models that include autocorrelation (the statistical relationship among the measured points). Some measure of the predictions' certainty or accuracy can also be provided. The basic kriging formula is:

$$Z^*(x_0) = \sum_{i=1}^{n} \lambda_i \, Z(x_i), \qquad (1)$$

where:

x_0 = a location

$Z^*(x_0)$ = estimate at location x_0

n = sample data points

λ_i = unknown weight at the i^{th} location.

There are five functions to model the empirical semivariogram (fitting the model): circular, spherical, exponential, Gaussian, and linear.

- IDW: The IDW calculation estimates cell values by averaging the values of sample data points near each cell. The closer a point is to the center of the cell being estimated, the more influence or weight it has in the averaging process. This method assumes that the variable being mapped decreases in influence with distance from its sampled location. The simplest weighting function is inverse power:

$$W(d) = 1/d^P, \qquad (2)$$

where:

W = weight function

d = distance

P = numeric value of the inverse power law (2.3).

By defining a high power, more emphasis is placed on the nearest points, resulting in greater detail. Specifying a low power will give more influence to points that are farther away, thus yielding a smoother surface.

We have written a Java applet that will accept ASCII data from HPAC and re-bin the data in the form of a 350 × 350 grid data that can be used directly with RATS.

Incorporation of HPAC data into RATS involves three separate steps:

1. The radiological incident scenario is run in the HPAC environment. Exact dispersal mechanism, isotope mix, and individual strengths are defined. Furthermore, the amount of explosives is specified, weather and terrain conditions are defined, and exact GPS coordinates are given. The ASCII data output from HPAC defines a particular field (in this case, surface deposition of isotope ^{137}Cs) and is saved and processed to generate count rates for well-characterized radiation monitors at given GPS coordinates (Figure 1).
2. This HPAC output field distribution is then put in the form of grid data by redefining the region of interest. GPS coordinates are used at the extremities of a square to define the region of interest. This conversion is done by means of the applet shown in Figure 2.
3. By applying IDW estimates, the contours of equal surface deposition points are defined.

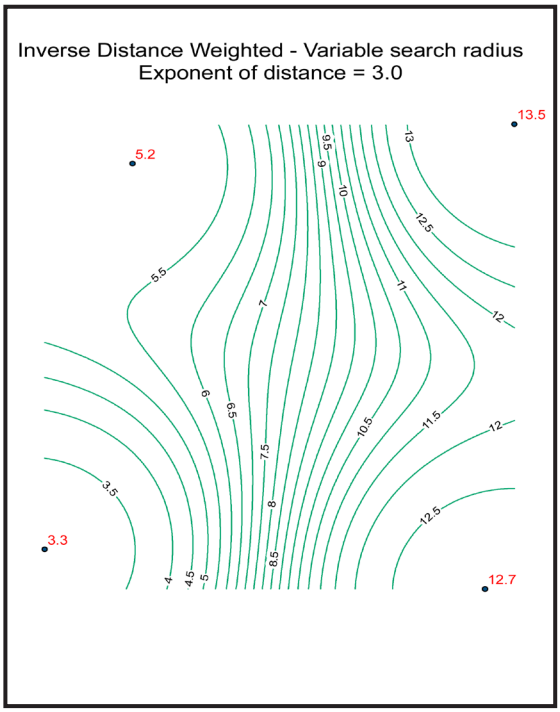

Figure 1. Four discrete data values of a particular field (e.g., radiation dose rate) are shown as red points. Using IDW estimates, the green isopleths (equal dose-rate lines) are generated, and any point in the 2-D space between the four red points is assigned a unique field value.

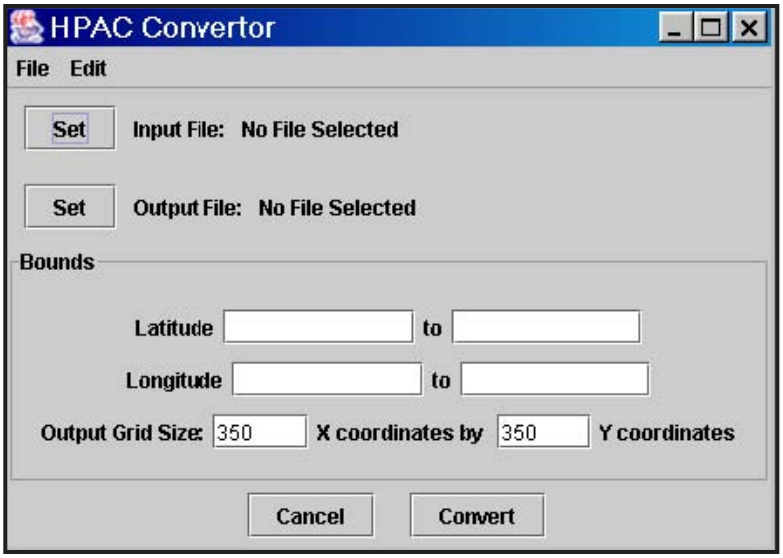

Figure 2. The selectable input file contains HPAC ASCII data (*.avs format). Data could be mean surface deposition in terms of pCi/m2, or average dose rate at 1 m in µR/hr. The package requires a range of longitudes and latitudes over which it bins the relevant data as a 350 × 350 matrix. RATS can readily accept this grid data.

At this point, the data set is ready to be used with RATS, which calculates the response (in terms of counts per predefined time intervals) of any radiation-measuring field equipment, provided its efficiency is known as a function of incident radiation energy.

Results

Two data sets are presented in this article. A set of GIS plots shows successful assimilation of three atmospheric model outputs in ArcView. The first set consists of a surface deposition of ^{137}Cs in pCi/m^2, as predicted by HPAC and NARAC (Figures 3 and 4, respectively). The second set consists of a dose rate (in µR/Hr) generated by the same radiological incident as predicted by RASCAL 3.0.3 (Figure 5).

We developed a GIS application to import RASCAL data in grid format to overlay on GIS maps. A simulated scenario in which 1000 lbs of TNT has been exploded with 10000 Ci of ^{137}Cs and 5000 Ci of ^{90}Sr (in equilibrium with 5000 Ci of ^{90}Y) near RSL is shown in an application plot (Figure 5). RASCAL data is produced on an Alber projection, and cell values contain the dose rate or surface deposition value at the center of equal-area pixels, giving the data a pixelated appearance.

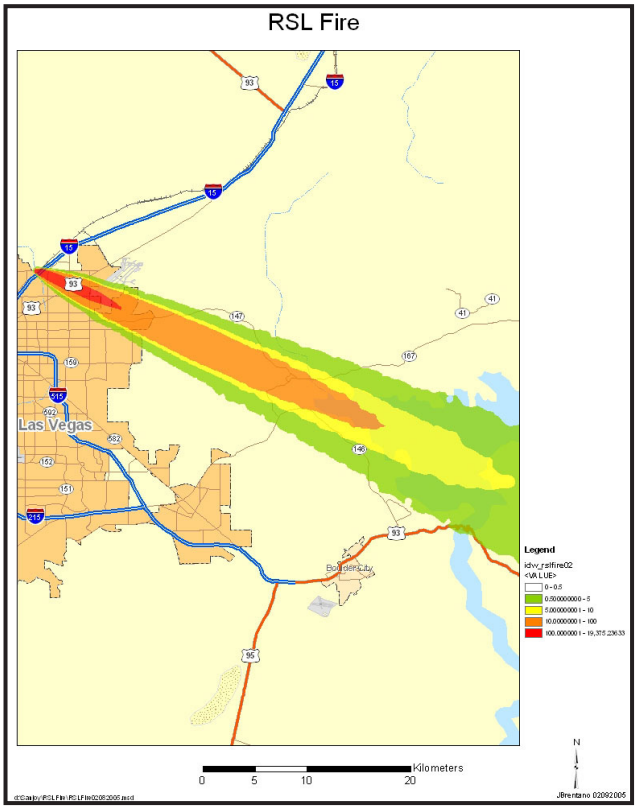

Figure 3. GIS map shows surface deposition (pCi/m2 of ^{137}Cs) data generated from the HPAC model. The same radiological dispersal incident has been modeled by NARAC and appears on the GIS plot in Figure 4.

This project's most important aspect was to be able to use the HPAC simulated data to generate responses from several well-characterized radiation survey meters. BN developed the RATS simulation program to allow users to create various modules of a release scenario: isotopes used, isotope mixes, radioactive source terms, and instruments and georeferenced maps and images. These modules can be easily combined, varied with time, and shifted in position in order to create a high order of variation from a finite number of parameters. A Palm OS–based, field-deployable version of the program interfaces with a GPS and presents the measurements at the current time. RATS is an exciting training tool that simulates realistic real-time field instrument data for consequence management (CM) teams. Traditionally, RATS utilizes NARAC simulation data for surface deposition from a plume. This study has extended RATS' capability to be used with HPAC data as well. An instantaneous snapshot of

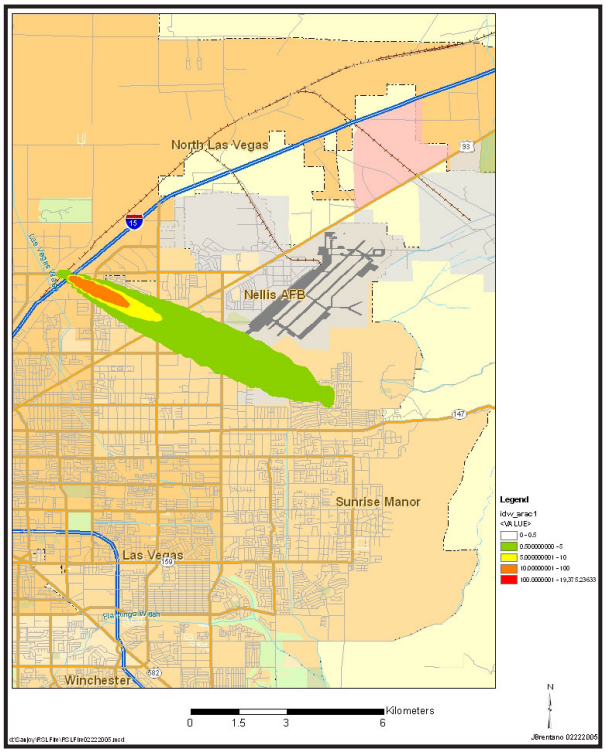

Figure 4. Contoured NARAC plot for surface deposition, from a simulated RDD incident in which 1000 lbs of TNT was exploded with 10000 Ci of ^{137}Cs and 5000 Ci of ^{90}Sr (in equilibrium with 5000 Ci of 90Y) near RSL

RATS output (as it would appear on a laptop screen) appears in Figure 6. As the cursor is moved around on the map, the counts simulated for several radiation meters would change according to the surface deposition strength determined by the atmospheric dispersion model (in this case, HPAC).

Conclusion

A recognized, well-tested atmospheric dispersion model would be extremely useful in all domestic scenarios dealt with by DHS, in addition to potential scenarios under DOE and DoD purview. In this context, weather assessment is so crucial and oftentimes so localized and ambiguous that continuous reliable weather monitoring becomes an integral part of modeling. Much remains to be developed in the realm of simulating buildings, structures, and urban terrain in and around large U.S. cities. Initial ground-zero radiological data is critical in CM scenarios. The accuracy of these initial data, fed back into the precrisis models, will eventually determine the usefulness of the model. Numerous early-phase emergency PAGs and decisions (such as evacuation and relocation, shelter-

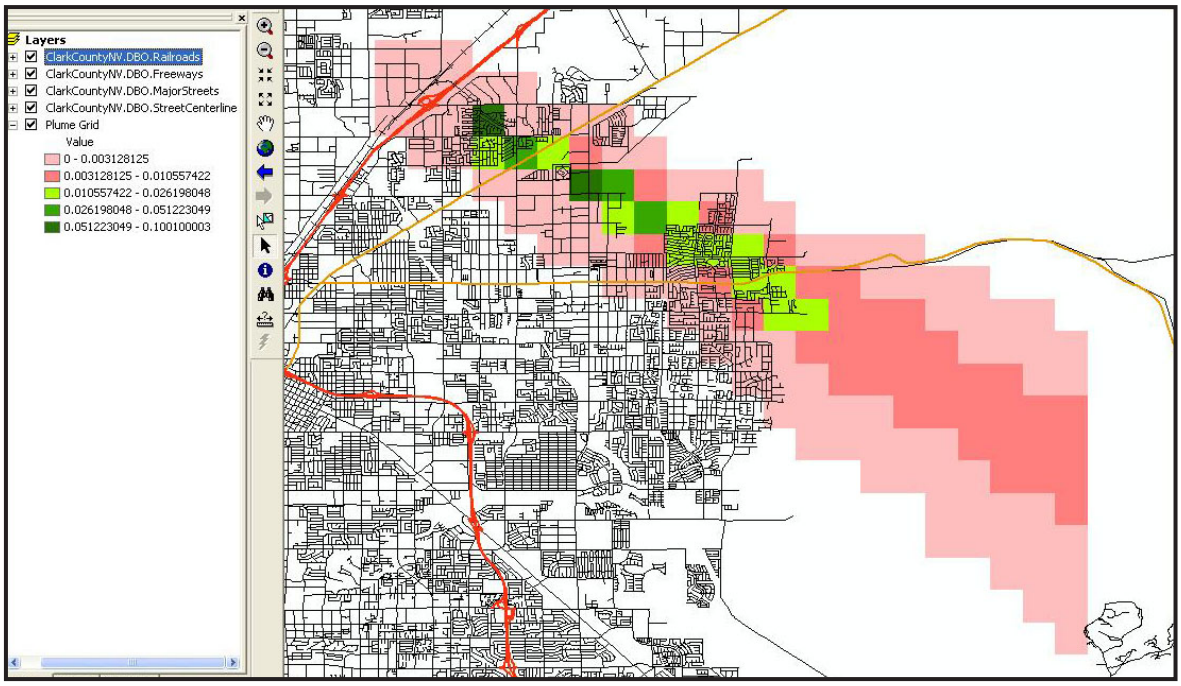

Figure 5. RASCAL dose-rate output from simulated explosion overlaid on a GIS map

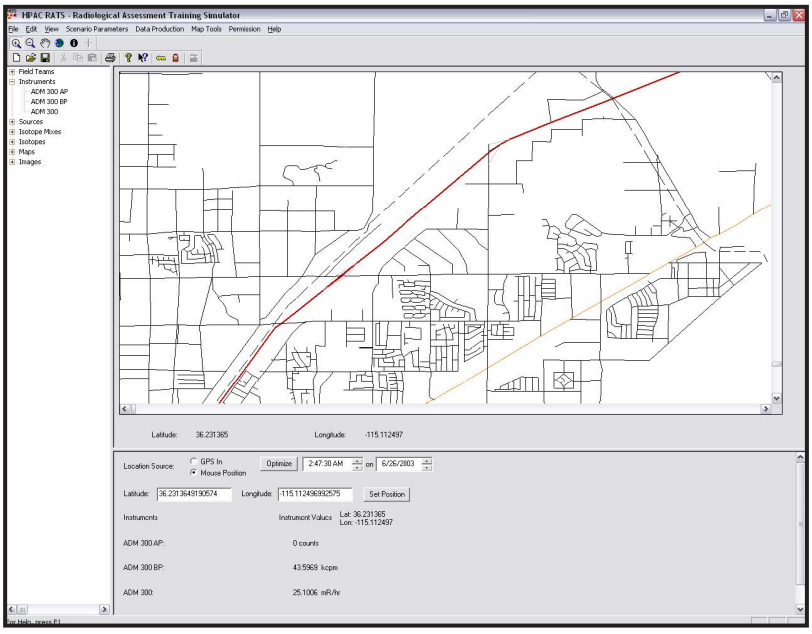

Figure 6. RATS snapshot using HPAC surface deposition data. RATS is completely transportable. Standing alone, HPAC can generate the surface distribution after the plume has passed, and RATS can apply surface distribution data to create counts/min in specific instruments.

in-place) in a catastrophic radiological accident depend on the atmospheric models used. In light of this, on April 15, 2004, DHS established an Interagency Modeling and Atmospheric Analysis Center (IMAAC), which will be the single source for federal atmospheric plume-modeling predictions during an Incident of National Significance (INS). IMAAC will coordinate federal support by DHS and provide effective communication between local, state, and federal emergency response agencies for assessing hazardous atmospheric releases. It will integrate authoritative input from many sources, distribute predictions to all levels of government to assure a common operating picture, and provide expert interpretation of results. It is currently available for modeling assistance on a 24/7 basis in its permanent location at LLNL's NARAC. A Memorandum of Agreement (MOA) between eight federal agencies on the IMAAC, including both the U.S. Environmental Protection Agency (EPA) and DHS, has been signed. An EPA-specific annex to the MOA, now under development, will include information on how EPA can request modeling assistance for an EPA-lead incident that is not necessarily an INS.

References

Baskett, Ronald L., "Forewarnings of Coming Hazards," http://www.llnl.gov/str/Baskett.html, accessed April 10, 2005.

Ermak, Donald L., John S. Nasstrom, "A Lagrangian stochastic diffusion method for inhomogeneous turbulence," *Atmos. Environ.* **34**, 7 (2000) 1059–1068.

Hodur, Richard M., "The Naval Research Laboratory's Coupled Ocean/Atmosphere Mesoscale Prediction System (COAMPS)," *Mon. Weather Rev.* **125**, 7 (1997) 1414–1430.

Nasstrom, J. S., G. Sugiyama, J. M. Leone, Jr., D. L. Ermak, "A real-time atmospheric dispersion modeling system," preprint, 11th Joint Conference on the Applications of Air Pollution Meteorology, Long Beach, California, January 9–14, 2000.

Oak Ridge National Laboratory, Radiation Safety Information Computational Center, "RSICC Code Package CCC-553; RASCAL 3.03: Radiological Assessment for Consequence Analysis for Windows," http://www-rsicc.ornl.gov/codes/ccc/ccc5/ccc-553.html, accessed September 2, 2004.

Office of the Federal Coordinator for Meteorology (OFCM), "General and Specific Characteristics of Model: HPAC," *Directory of Atmospheric Transport and Diffusion Consequence Assessment Models*, http://www.ofcm.gov/atd_dir/pdf/hpac.pdf, accessed December 7, 2004.

Sugiyama, G., S. T. Chan, "A New Meteorological Data Assimilation Model for Real-Time Emergency Response," preprint, 10th Joint Conference on the Applications of Air Pollution Meteorology, Phoenix, Arizona, January 11–16, 1998, 285–289.

Electron Trajectory Codes for Image Tube Design

Jerome M. Richter[1]
Livermore Operations

This project sought to obtain an improved three-dimensional (3-D) electron trajectory computer code to support the design of electrostatic image tubes manufactured at LO. A suite of post-processing routines for measuring image quality would also need to be defined. After conducting an extensive market survey of electron trajectory codes and consulting with vendors and current users, we selected three codes for detailed evaluation: the Lorentz and Charged Particle Optics (CPO) boundary element codes and the Field Precision finite element codes. Testing showed that our needs would be best served by 1) the Field Precision codes, which provide electric and magnetic field solutions with support for space charge, secondary emission, and dielectrics, and 2) the CPO codes, which offer an auto-focus mode but limited support for magnetic fields.

Background

We have designed and manufactured several inverting electrostatic image tubes, including the optical, infrared and x-ray streak tubes; optical and x-ray framing tubes; and several minifier tubes. All tube designs were based on electron trajectory models generated with either EBQ (a code that models electric and magnetic fields and space charge) or SIMION 3D, both of which use the finite difference method with square or rectangular meshes. EBQ (currently nonoperational) was a two-dimensional (2-D) code that interpolated fields to the electrode surface. SIMION 3D simulates curved surfaces with a rectangular mesh which results in irregular extraction fields that compromise the accuracy of the electron image.

Inverting image tubes often use curved photocathodes and phosphor screens. Electron emission energies are normally low, in the range of 1 eV. Accurate electron-trajectory simulation thus requires that extraction fields near the photocathode be smooth and regular. This generally means that the electrode mesh must be conformal to the electrode surface. Moreover, accurate trajectory information must be accessible at or near the screen, to allow the generation of focal-spot diagrams and the calculation of such image parameters as focal length, resolution, magnification, distortion, astigmatism and depth of field, as well as focal surface location and shape. Some image tubes, such as streak and framing tubes, require a 3-D model to properly account for the effect of deflection plates and slot apertures. Design improvements for better resolution and faster sweep speeds, while maintaining dynamic range and avoiding pinch effects at high current densities, can be achieved only with a full

[1] richtejm@nv.doe.gov, 925-960-2511

3-D modeling capability, including space-charge effects. Codes for modeling photomultiplier tubes and other electron tubes that employ field-emission arrays and microchannel plates must also support secondary emission.

During the summer of 2004 the OPERA-3d finite element code from Vector Fields was evaluated. Excellent graphics and plots with user-specified data transforms allowed for the direct generation of several imaging parameters from the calculated trajectories. This code provides excellent control for the conformal mesh generation, but field solutions were slow, temperamental and difficult to achieve, and the price was very high.

Project

Market Survey

The project began with a market survey comprising Internet searches and personal contacts with electron trajectory code users within BN and the national laboratories. Art Paul (LLNL), the author of EBQ, is an enthusiastic supporter of Field Precision's TriComp 2-D codes. I subsequently met with Josh Friedman, Steve Mitchell, and Brent Davis at NLV to discuss their experiences with several electron trajectory codes. Josh demonstrated both the 2-D and 3-D finite element codes from Field Precision. He is satisfied with the code capabilities and the software support. Steve uses the large-scale plasma (LSP) particle-in-cell code from Mission Research. LSP yields good results for high-current beams with strong self-magnetic fields, but the code is expensive and difficult to use. Brent uses the Field Precision 2-D codes for several different projects. He has noted discrepancies in modeling secondary emission from the dynodes in a photomultiplier tube.

Internet searches located more than 200 electromagnetic computer codes from approximately 70 commercial sources. Three large code compilations were found. The Los Alamos Accelerator Code Group (LAACG) lists 141 codes from 22 sources and also provides links to 16 other code libraries. The LAACG codes generally support high-current beams in accelerators, quite a different environment from that of the typical image tube. The Electromagnetic Compatibility Laboratory at the University of Missouri-Rolla lists 96 codes from 54 commercial sources worldwide. EMLIB, the electromagnetics software library at NASA's Jet Propulsion Laboratory, contains 89 entries, pointing to individual codes, code packages, and other libraries. However, many of these codes lack the electron trajectory calculations required for image tube design. Table 1 contains a list of Web sites visited during the market survey, arranged by electron trajectory code.

Code Evaluation

After reviewing the list of available codes and consulting with vendors and current users, we chose three for trial evaluation: the Lorentz and CPO boundary element codes and the Field Precision finite element codes. For the evaluation we used 3-D models of the optical streak tube, for which a large body of laboratory data is available. All three codes successfully modeled the beam-spreading

Table 1. Electron trajectory codes, sources, and links

Code	Source	Site Address
Amaze 3D	Field Precision	http://www.fieldp.com/index.html
(Commercial software)	University of Missouri-Rolla	http://www.emclab.umr.edu/csoft.html
CPO	Scientific Instrument Services	http://www.simion.com/cpo/
(LAACG software)	Los Alamos Accelerator Code Group	http://laacg.lanl.gov/laacg/services/services.phtml
Lorentz	Integrated Engineering Software	http://www.integratedsoft.com/products/lorentz/
LSP	ATK Mission Research	http://www.mrcabq.com/Codes/codes.htm
SIMION 3D	Scientific Instrument Services	http://www.simion.com/ http://www.sisweb.com/simion.htm
SIMION SL Toolkit	Scientific Instrument Services	http://www.simion.com/sl/
Opera 3D	Vector Fields	http://www.vectorfields.com/content/view/19/42/

caused by the accelerator slot, which limits the effective temporal field of view to roughly half the slot width. All of the codes allowed trajectory parameters to be saved at selected test planes, a feature that is required for post-processing analysis of focal properties.

The codes were ranked against a set of standards that are critical in evaluating image quality and such other factors as speed, price, computer requirements, import/export capabilities, and ease of use. Support for ion beams with space charge, dielectrics, dynamic fields, and various emission models was also considered.

The boundary element method (BEM) uses electrode potentials to determine the charge distribution on electrode surfaces. This contrasts with the rectangular-mesh finite difference method (FDM) and the conformal-mesh finite element method (FEM), which solve for the potentials at every mesh point in the model volume. Except for space charge problems, the BEM does not need a mesh in the trajectory space, and thus typically requires three or four magnitudes fewer mesh points than the FDM and FEM. However, BEM trajectory calculations are much slower because the fields must be calculated from the charge distribution on the electrodes at each time step, as opposed to the simple mesh interpolation used by FDM and FEM.

Lorentz is primarily a BEM code, although the 2-D version also supports the FEM. It features a powerful geometry builder and excellent graphics with labeled plots and annotations. However, ray definitions are difficult, trajectory calculations are slow, and the cost is very high. Moreover, trajectories in 2-D cylindrical geometry are restricted to the plane that intersects the rotation axis.

CPO is an inexpensive, electostatic BEM code with limited magnetic capability. Its auto-focus mode minimizes the size of multiple focal spots at a given focal plane by adjusting the potentials up to

20 electrodes. CPO also has a convenient data builder to construct or modify electrodes via a large shape library and to control various process parameters. It provides an extensive online help package to supplement the limited user's manual.

Field Precision provides a full-featured FEM package that offers several suites of codes for both static and dynamic electric and magnetic field solutions. Its volume-based model generator supports linear and rotational fills and cuts, as well as surface-coating options to set boundary conditions. A comprehensive user's manual and two textbooks by code author Stan Humphries are provided in digital format. Program control and model input are almost entirely file-based. Field solutions and trajectory calculations are much faster than Lorentz's, but user control over the graphical display of results is limited.

Figure 1 shows a cutaway view of the optical streak tube from CPO 3D, with a set of rays originating at the photocathode from a point 10 mm off the tube axis and centered on the middle of the 2-mm accelerator slot. The rays cross the tube axis near the blue anode aperture and green deflection plates and terminate on the curved phosphor screen at right.

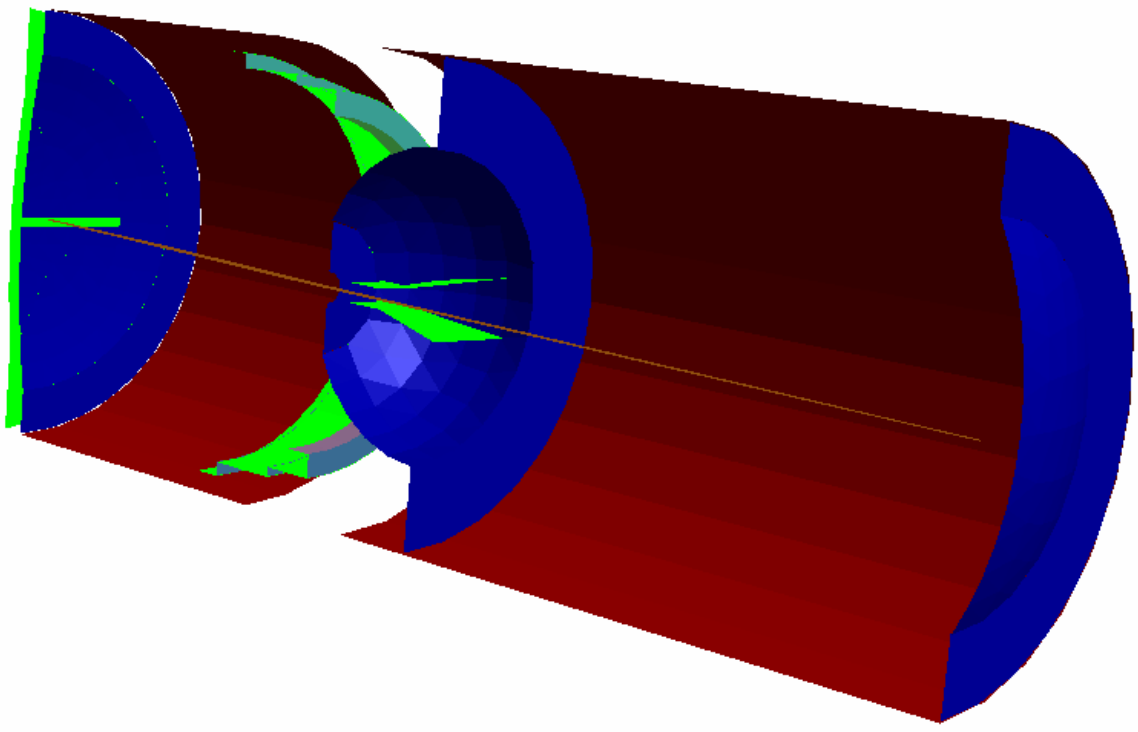

Figure 1. Optical streak tube model from CPO 3D showing rays from 10 mm off-axis

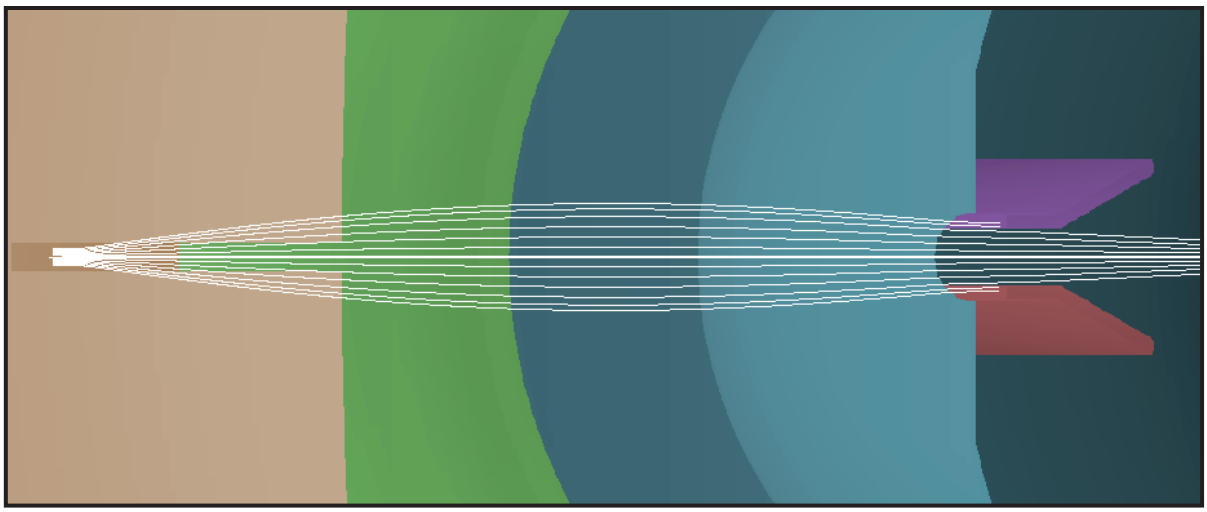

Figure 2. Temporal field of view in an optical streak tube model from AMaze 3D

Figure 2 shows an electron beam emitted from 20 mm left of the tube axis in a streak tube model from Field Precision's AMaze 3D. A set of 13 parallel rays is arrayed across the 2-mm slot width at 0.1-mm increments along the temporal axis. The divergent lens formed by the slot causes the rays to spread so that the outer two rays on each side hit the deflection plates behind the anode aperture thus limiting the effective temporal field of view to 0.8 mm.

Figure 3 shows an overhead view of the streak tube from CPO 3D with two sets of temporal rays originating from 10 and 20 mm off the tube axis. Electron travel time is shown at 1-ns intervals along each trajectory, except for the last point on the right, which represents a test plane 250 mm from the photocathode.

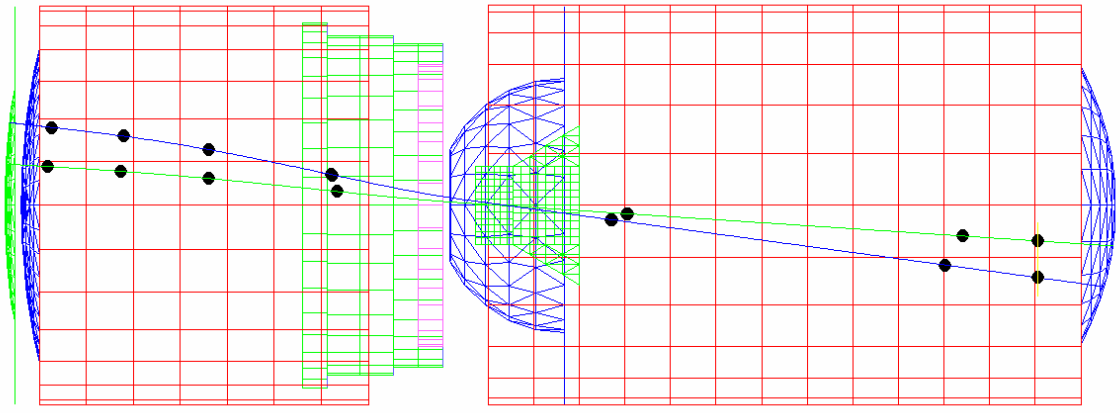

Figure 3. Overhead view of a CPO 3D optical streak tube model showing flight times for two sets of temporal rays from 10 and 20 mm off-axis

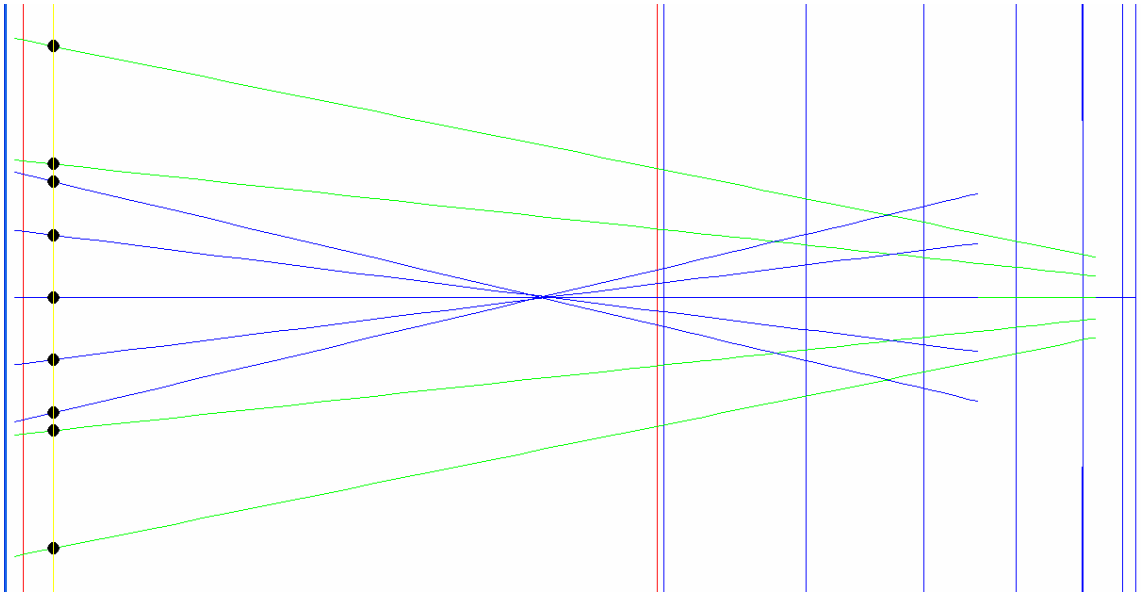

Figure 4. Side view of the temporal rays from Figure 3 near the screen. The rays originating from 10 and 20 mm off-axis are shown in green and blue, respectively.

Figure 4 shows a magnified side view of the temporal rays from Figure 3, from the test plane at 250 mm to the screen. Each set of five rays was emitted from a single point on the photocathode with angular deviations from the photocathode normal of ±10 and ±20 degrees in the temporal plane. The rays end when they hit the curved screen surface. Note that the green rays from the 10-mm offset have not yet come to a focus, while the blue rays from 20 mm have already crossed the focal point. The approximate scale of this zoomed plot from CPO 3D is 20 mm horizontally by 40 μm vertically. This difference in scale, of nearly three orders of magnitude between the axial length and the transverse focus dimension, is typical for all inverting image tubes. This large difference in scale requires special post-processing to generate focal plots for off-axis rays in the spatial plane.

Conclusion

After conducting an extensive market survey of electron trajectory codes and consulting with vendors and current users, we selected three codes for detailed evaluation: Lorentz, Field Precision, and CPO. Based on test results and prior experience with EBQ, SIMION 3D, and OPERA-3d, we purchased the finite element Field Precision codes and the boundary element CPO codes. Both codes support 2-D and 3-D models. Field Precision provides both electric and magnetic field solutions, with support for space charge, secondary emission, and dielectrics. CPO features an auto-focus mode but offers only limited support for magnetic fields.

We also purchased from Field Precision the GamBet radiation transport and scattering code that uses the Monte Carlo method for photon and electron interactions with matter. Because of the large existing base of SIMION models at LO, we procured the SIMION SL Toolkit to provide a computer-aided design (CAD) input and output interface that supports both 2-D Data Exchange Format (DXF) files and 3-D Stereo-lithography Tessellation Language (STL) files. The toolkit also offers a syntax-based text editor and a high-level compiler for generating SIMION user programs.

These new programs provide a powerful, flexible capability for modeling varied image tube designs. However, to generate critical image-quality measurements, further work must be done to provide post-processing trajectory analysis for the new codes.

this page intentionally left blank

Optimization of Streak Tube Temporal Resolution

D. Taner Bilir, Charles E. Diamond, Richard A. Shellman[1]
Livermore Operations

This research intended to test if deflection feedthrough and deflection plate connections imposed limitations on the streak tube. Our team hoped to find, identify, and propose alternatives to signal losses or impedance mismatches in items that may have been limiting the tubes' sweep speed. Using a Hewlett-Packard network analyzer and a time-domain reflectometer (TDR), we tested a representative section and found that, at the feedthrough, the tube resembled a rejection filter tuned at 930 MHz. To eliminate signal loss at this frequency, we were able to change the feedthrough and method of signal-feeding to the deflection plate.

Background

Many experimenters are now using the BN streak tube satisfactorily, and it has reached sweep speeds of up to 5 ns per 30 mm during some experiments. Several experimenters have requested faster sweep speeds, but to date, this has only been achieved by applying additional voltage in the form of higher sweep ramps. When this increase is combined with the need for hold-off voltage and common mode focus voltage, the total can stress the feedthrough, deflection plate insulators, and electronics used to drive the tube. Our team proposed to improve this sensor package by resolving the feedthrough/deflection plate connections.

Project

The existing tube feed through is a 100-Ω unit borrowed from an EG&G cathode ray tube (CRT). The internal connections in both the CRT and streak tube from feedthrough to components is by a 0.005" × 0.020" nickel ribbon. In the potted version of the tube, the deflection lead is a single insulated wire from the center pin of the feedthrough out of the potting compound to the ramp driver board. There is no consistent impedance for the ramp signal to enter the deflection section. The voltage necessary to deflect the beam for a sweep has been consistent until we try to go faster than about 20 ns. The faster sweeps have been achieved, to date, by increasing the voltage applied to the tube. We hope to find out what is limiting the sweep speed of the tube and what may push back the limit to allow faster sweeps.

[1] shellmra@nv.doe.gov, 925-960-2513

This project was divided into the following sections:

- Use the Hewlett-Packard spectrum analyzer to establish a baseline for improvements.
- Review possible connector options.
- Decide how to best connect to the deflection plates.
- Modify a test deflection section, then retest.

Establish Baseline

Until the network analyzer was used to view the signal (Figure 1) at the deflection plate (Figure 2), we did not realize how much of the signal was being lost to reflections and inconsistencies in the signal path. We also learned that RG-174 is not an optimal cable for test measurements, as it becomes lossy at higher frequencies. Therefore, we switched to RG-141 conformable coax, as it has better response and is easier to work with.

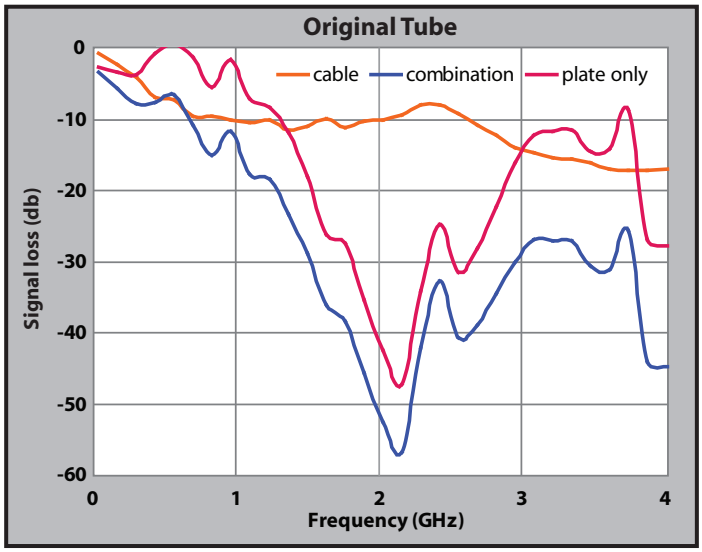

Figure 1. Transmission spectrum of baseline section

Connector Options

Since the streak tube is considered a hostile environment from a material standpoint, the choices for tube body penetrations are limited to items constructed of 300 series stainless, Kovar, or high-alumina ceramic. This is because the tube body must be leak-tight to $<10^{-9}$ cc/sec, and the process cycle subjects the body to pressures of less than 1×10^{-8} Torr and temperatures of 365°C. This, along with the need for very good electrical properties, eliminates most common materials. An

Figure 2. Phosphor end view of deflection section

Internet search for connectors to meet these criteria was fairly brief and revolved around ultra-high-vacuum and high-altitude equipment manufacturers. We finally selected a weldable, high-power microwave feedthrough made by Meggitt Safety Systems, Inc.

Connections to the Deflection Plate

Connecting to the deflection plate was probably the trickiest part of the project, as the workspace is small and located behind the plate to avoid interference with the deflecting electron beam (Figure 4). We tried to attach the signal lead in several different places. However, as long as the signal was injected in only one spot, spectrum response dipped sharply below 1 GHz (Figure 3). The center frequency of the dip could be moved from approximately 830 to 920 MHz, depending on where the lead was attached to the deflection plate.

Another experiment consisted of feeding the signal with one coax at a point on the deflection plate and attaching at another point a second coax to act as a terminator for the plate. This, in effect, made the plate part of the signal path. The dip-short of 1 GHz disappeared (Figure 5). Several different attachment points were tried and tested to gauge their effects in the frequency response. The experimental section now has uniform impedance to and from the deflection plate, but not across the deflection plate itself. To mimic the strip lines used in printed circuit boards (PCBs), we fabricated a conductive plane parallel to and placed behind the deflection plate and spaced to approximate an impedance of 50 Ω (Figure 6). This was tested for frequency response. Although the data above 4 GHz shows more dips, we felt they were too far outside the range of interest to be of consequence. Experimentation to identify the optimum location of the signal leads is nearing completion.

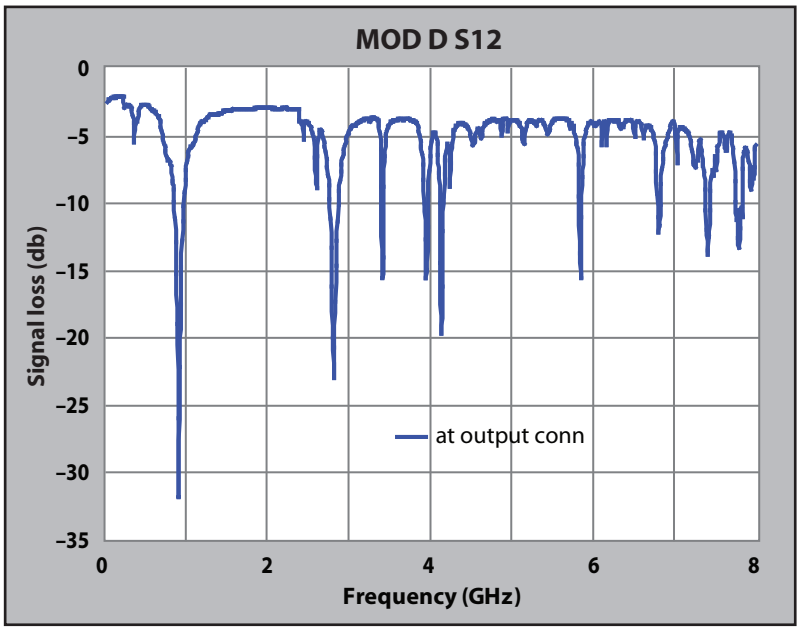

Figure 3. Frequency Spectrum at RG-141 Termination

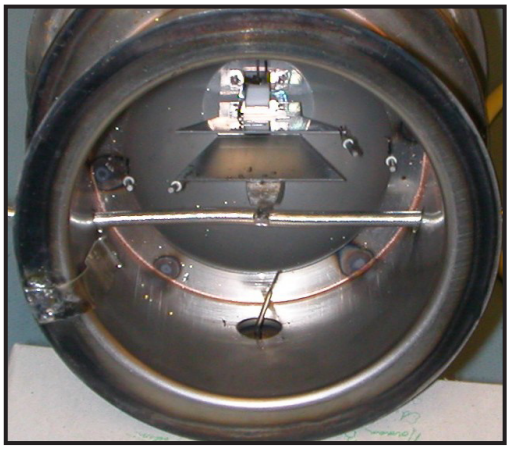

Figure 4. Deflection section with RG-141 tapped

Conclusion

This project has shown that the modified streak tube can accept deflection signals in the 1–2 GHz range. A logical next step would be to build a streak tube incorporating the new parts and test it before and after final tube assembly to validate the test data. Some frequency artifacts have not yet been eliminated. These frequencies are too high to cause trouble with the deflection speeds that we wish to use and will most likely remain until the deflection plate shape can be modified to become a

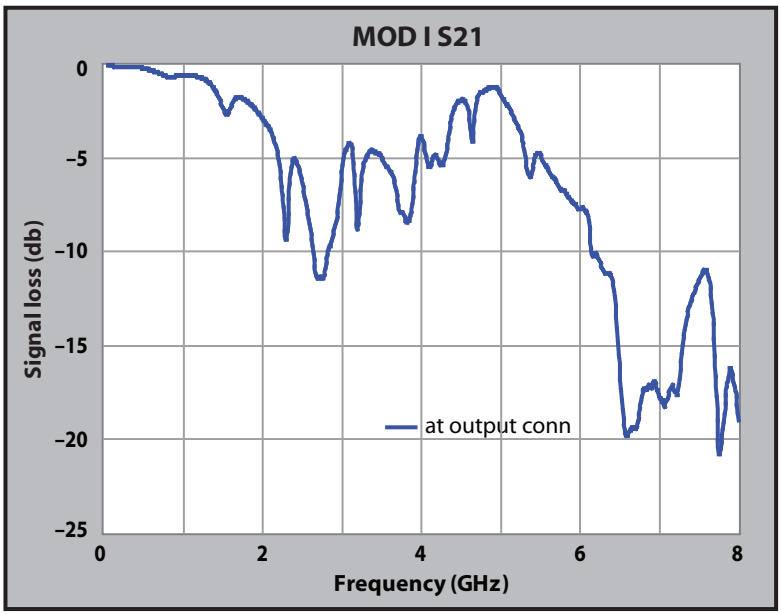

Figure 5. Frequency spectrum at termination with two coax attachment points and backplane

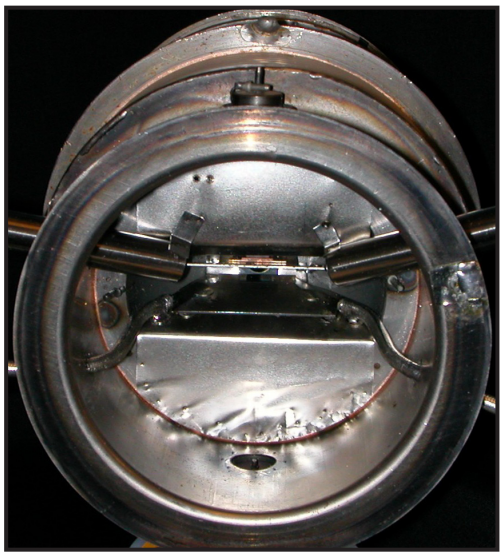

Figure 6. Deflection section with new feedthrough and backplane

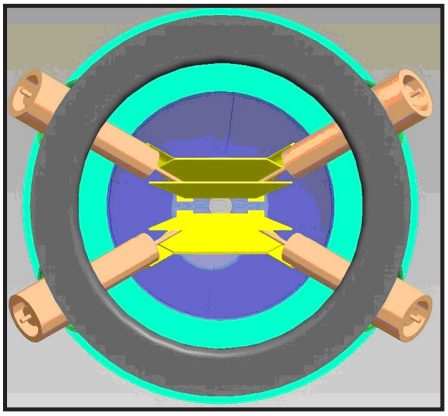

Figure 7. Phosphor end-view with new feed-through and backplane

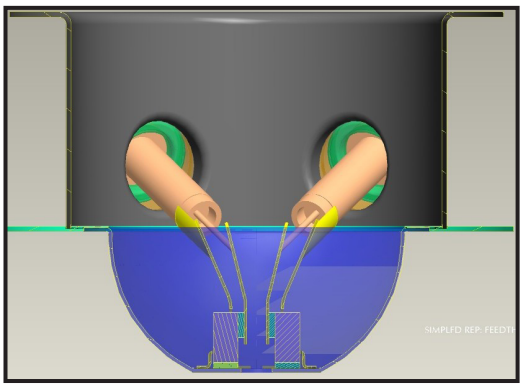

Figure 8. Side view showing back plane to deflection plate spacing

better electrical path for the deflection signals. The new design for the deflection section has two ports (Figure 7) for each deflection plate, separating the biasing and sweep ramp signals, as was impossible with the old deflection section. The newly designed tube section (Figure 8) is interchangeable with the existing section, enabling the streak tube to function as a standard model and a fast model by exchanging one section.

Acknowledgments

I wish to acknowledge all of the people who contributed their time in listening and talking to me about this project. In particular, I wish to thank Vu Tran for advice on setting up and using the test equipment. That was a great help.

Reference

Meggitt Safety Systems, Inc., www.stablecable.com, accessed February 14, 2005.

Monte Carlo Simulation of High-Speed Gated X-ray Detectors

Craig A. Kruschwitz, Dane Morgan, Jiaming Morgan, Ming Wu[1]
Los Alamos Operations

This research intended to develop a Monte Carlo simulation code for modeling secondary electron emission processes and electron dynamics in a microchannel plate (MCP), a key component of many high-speed gated x-ray detectors. We have successfully developed a simulation code to describe nonrelativistic propagation and multiplication of electrons in a single MCP channel. This code contains standard secondary emission models and electron elastic reflection. We have used the code to conduct numerical studies of the sensitivity of an MCP with DC and pulsed applied potentials. Good agreement between the measured and modeled gain was observed.

Background

High-speed, gated x-ray detectors based on straight-channel microchannel plates are a powerful diagnostic tool for two-dimensional, time-resolved imaging and time-resolved x-ray spectroscopy in the field of laser-driven inertial confinement fusion and fast Z-pinch experiments. These detectors consist of a gold photocathode coated on the front of the MCP, a phosphor screen coated on a fiber-optic faceplate, and a film recorder or charge-coupled device (CCD). High-speed gating is achieved by sending a subnanosecond high-voltage pulse through a microstrip transmission line coated onto the MCP. When the high-voltage pulse is propagated along the strip line, MCP gating occurs wherever the voltage is applied.

The gain of the MCP depends in a highly nonlinear way on the applied voltage (gain ~V^9); therefore, the MCP optical gate is much narrower than the voltage pulse width. Furthermore, impedance mismatches between the microstrip and the high-performance pulsers used to supply the gating voltage affect voltage waveforms along the MCP. This presents obvious problems in data interpretation and makes understanding MCP behavior under time-dependent voltages essential. Monte Carlo–based computer simulations of MCP response to a steady-state voltage have been performed (Ito, 1984; Guest, 1971), but these models have not included the important time-dependent effects. We have developed a steady-state voltage simulation using an electron-transport and secondary electron-production model, which we have expanded to include simple pulsed waveforms.

[1] wum@nv.doe.gov, 505-663-2030

Project

A microchannel plate is essentially an array of parallel continuous electron multipliers. Individual MCP channels are typically about 10 μm in diameter, and the plates themselves are generally 450–600 μm thick. Generally, the channels are set at an angle, α, to the normal surface of the MCP. Often, an MCP is characterized by the ratio of its thickness to the channel diameter, or its L/D ratio.

We wrote our program in the Interactive Data Language (IDL) of Research Systems, Inc. It describes the cascade and dynamics of electrons in a single microchannel. For our purposes, it is acceptable to assume that all microchannels in a particular plate are identical, since we are neglecting any cross-talk effects between adjacent channels.

The cascade is taken to be initiated by some number of incident electrons. Their number, incident energy, and direction are determined by the user. Standard equations give the mean secondary emission yield, δ, for each electron as a function of incident energy and angle relative to the surface normal. The actual secondary yield is determined by random sampling of a Poisson distribution with a mean value δ. With the number of secondaries determined, each electron's initial energy is assigned by sampling a Maxwell-Boltzmann distribution with a mean energy of $E_{0.}$ The direction in which each electron is emitted (relative to the surface normal) is sampled from a cosine distribution. The trajectories of the secondary electrons are then calculated using straight-forward, nonrelativistic equations of motion. Since the maximum electron energies are on the order of 1 keV or less, a small fraction of the rest-mass energy, the problem can be safely treated nonrelativistically. By solving the electron equations of motion, the impact energy and angle are ascertained, thereby determining initial conditions for the

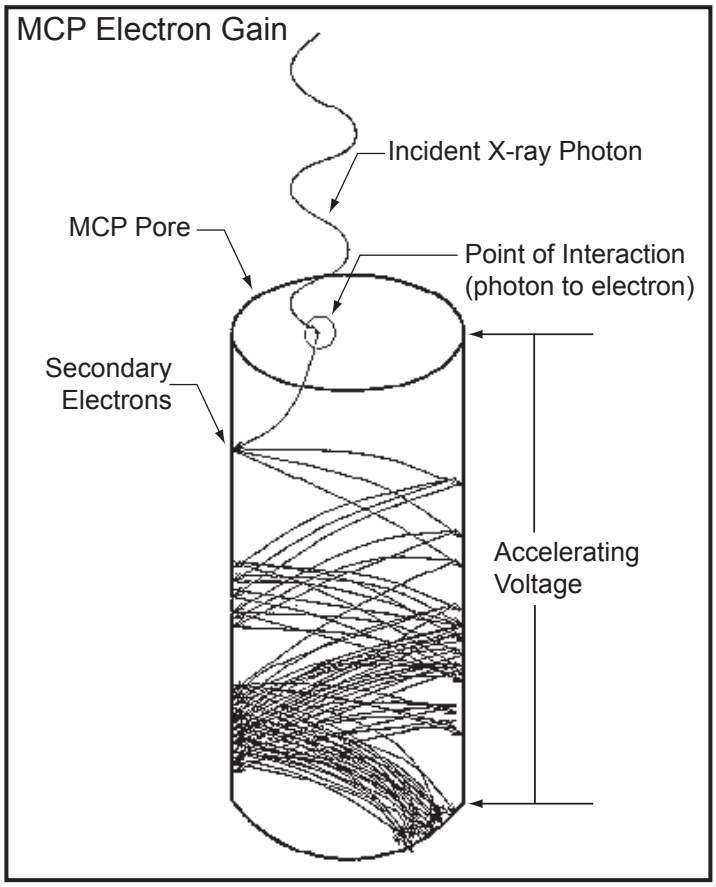

Figure 1. Electron cascade in a straight microchannel

next generation of electrons. This process is repeated until the electrons emerge from the output end of the channel or the cascade dies out, producing a net yield of zero. Figure 1 illustrates the cascade process for a straight ($\alpha = 0$) microchannel.

The basic equations describing secondary electron emission used by Ito (1984) and Guest (1971) assume that each collision produces secondary electrons according to a Poisson distribution. They neglect the possibility of reflection of the incoming electron, which we found to be an important effect for low-bias voltages (less than ~800 V). Scholtz (1996) studied the probability of electron reflections from lead glass at normal incidence as a function of energy. This research found that, for a 10-eV electron, the probability of reflection was approximately 95%, decreasing to about 5% for a 100-eV electron. Unfortunately, the research did not examine any angular dependence for this effect. Nevertheless, we have included the option of using Scholtz's results in the simulations as an elastic scattering approximation.

DC Voltage Simulations

Although the MCP simulation can be adapted to MCPs of almost any geometry, we have concentrated most of our modeling efforts on an MCP with a 10-μm channel diameter and a thickness of 0.46 mm (L/D = 46). For these parameters, we have a large amount of MCP data with which we can compare our model results. Figure 2 shows simulation results for the L/D = 46 MCP with a steady-state bias of 1000 V. The gain histogram for 1000 separate runs (left), shows the average gain is 20911, but a considerable spread in the gain clearly exists. This is a consequence of the statistical nature of the secondary emission process. The transit time distribution for the same 1000 runs (right) looks essentially Gaussian, with a mean transit time of 200 ps and a full-width half-maximum (FWHM) transit time spread (TTS) of 54 ps. We lacked transit time measurements for the MCPs we were simulating (such measurements are difficult to make), but 200–300 ps transit times are consistent with existing measurements (Wiza, 1979).

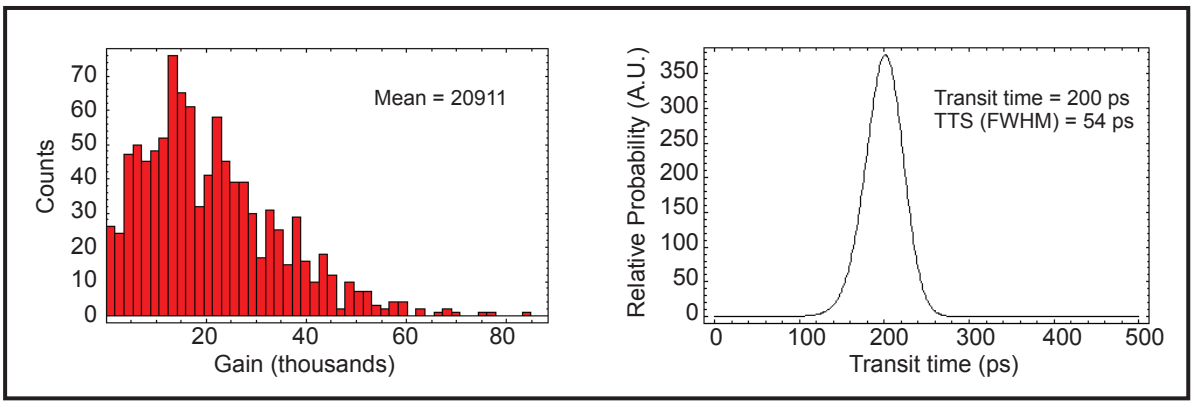

Figure 2. Simulation results for an L/D = 46, 10-μm pore diameter MCP, biased at 1000 V DC, with a bias angle of α = 8 degrees: (*left*) gain histograms; (*right*) transit time distribution

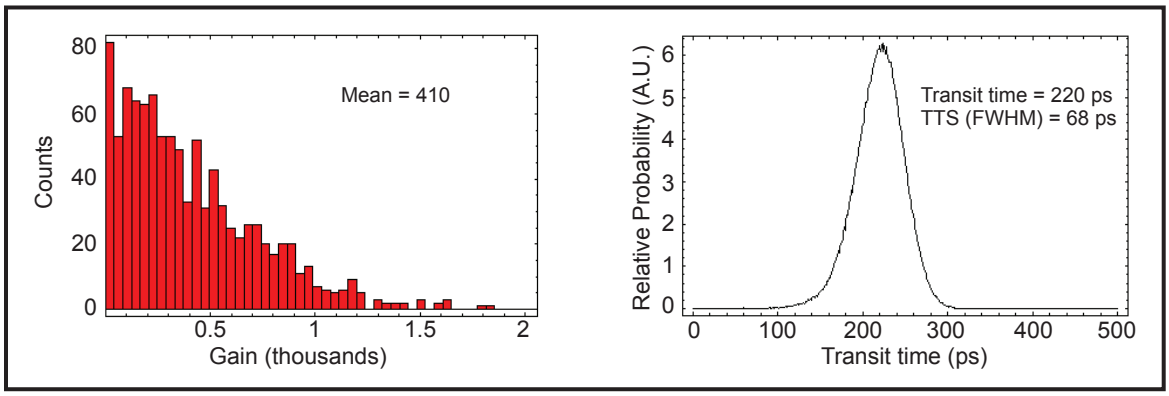

Figure 3. 700-V DC bias on same MCP shown in Figure 2

Figure 3 shows simulation results for an identical MCP, but with an applied voltage bias of 700 V DC. The average gain (left) is 410, nearly two orders of magnitude lower than for the 1000-V simulations, because electron impact energies are smaller, resulting in a smaller secondary electron yield. The mean transit time (right) is 220 ps, 20 ps longer than for the 1000-V simulations. This is a consequence of the decreased acceleration in the 700-V bias case. Because the electrons undergo less acceleration in the channel, they don't travel as far down before colliding with the channel wall. Thus, they require more time to reach the output end of the channel. The TTS for the 700-V case is longer than that of the 1000-V case due to the smaller impact energies: as impact energies become comparable to secondary emission energies, the stochastic nature of the secondary emission process leads to a greater spread in transit times.

Comparison to Experimental Data

To check the validity of our simulation results, we compared the modeled sensitivities (gains) versus measured sensitivities. The measurements were performed with the Manson x-ray source at SNL, on L/D = 46 MCPs with coatings of various thicknesses. Relative sensitivities were measured as a function of voltage for potentials ranging from 450 to 950 V, increased in 50-V increments. Both modeled and measured sensitivities are plotted versus voltage in Figure 4. The simulated gains have been scaled so that the value at 450 V is set to the average of the measured data at 450 V. Clearly, the model reproduces the trend in the measured data extremely well over virtually the entire voltage range. However, the data show some leveling off at 950 V, which is not seen in the simulations. This is probably due to the onset of saturation in the CCD used to collect the data, and is not an effect of the MCP.

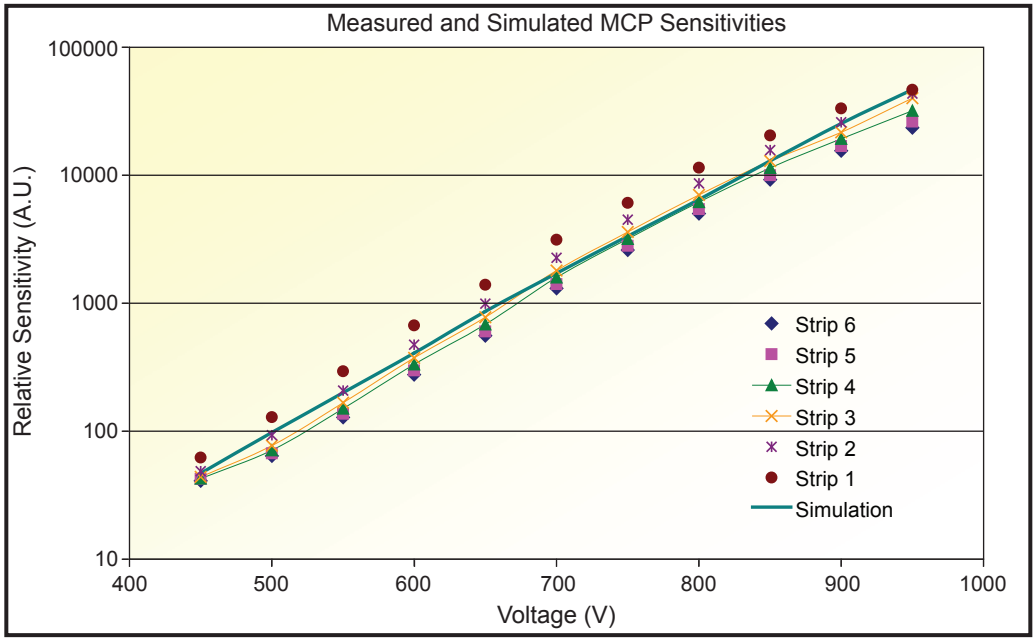

Figure 4. Measured and modeled sensitivity vs. voltage for L/D = 46 MCP

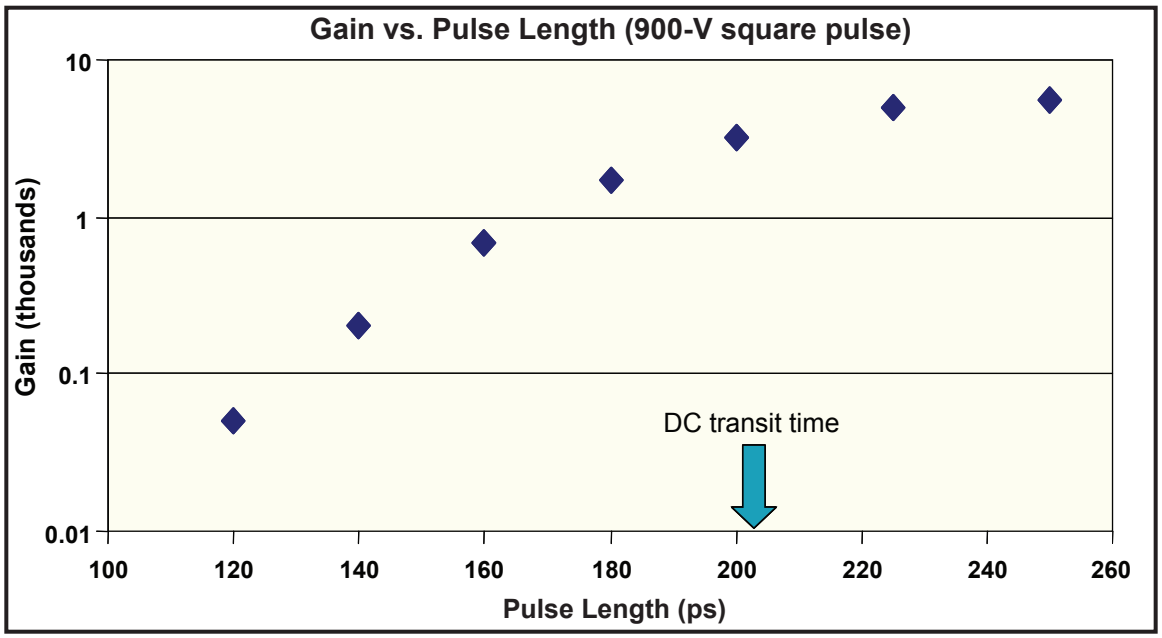

Figure 5. Simulated gain vs. pulse length for a 900-V square pulse

Pulsed Voltage Results

With some measure of confidence in the validity of the DC simulations in hand, our team expanded the simulation to include some simple voltage pulses. For our study, we once again considered an L/D = 46 MCP and chose a peak voltage of 900 V. The mean transit time for such an MCP biased at 900 V DC is 205 ps, while the TTS is 57 ps, and the gain is approximately 6000. We wanted to see how these characteristics would change as we applied voltage pulses with pulse lengths ranging from equal to the mean DC transit time to much shorter than it. For simplicity, we considered a square-wave voltage pulse. Figure 5 shows the simulated gains versus pulse length. Clearly, the gain shows little variation from the DC gain for pulse lengths equal to or greater than the DC transit time. However, gains diminish rapidly for pulse lengths shorter than the DC transit time, with the gain from a 120-ps pulse (60% of DC transit time) decreasing two orders of magnitude from the DC gain. These results indicate that the pulse length should probably be kept to the DC transit time or longer.

Conclusion

We successfully developed a computer code to run Monte Carlo simulations of MCP sensitivity for both steady-state and pulsed voltages. The comparisons of simulation results for a DC-biased L/D = 46 MCP agree well with measured sensitivities of such an MCP. Results for square-wave voltage pulses of various lengths indicate that pulse lengths should be at least the DC transit time. We consider our accomplishments thus far an important improvement on preceding work. We intend to present these results at the American Physical Society Division of Plasma Physics Conference in Denver, Colorado, in October 2005.[2]

It is possible for future research to take several directions. First, the pulsed voltage simulations could be expanded to include more complex, realistic voltage pulse shapes. Also, we would like to include the effects of MCP saturation at high gains. Other important potential considerations include: end spoiling, pore bleaching (due to cross talk between channels), dielectric effects in the MCP glass, and effects of the angular distribution of the incoming x-rays. Finally, to form a more complete picture of overall detector response, the responses of the phosphor, CCD, and photocathode coating should be evaluated.

[2] Bulletin of the American Physical Society, **50,** 8, 358, UP1 48

References

Guest, A. J., "A computer model of channel multiplier plate performance," *Acta Elec.* **14** (1) (1971) 79.

Ito, M., H. Kume, K. Oba, "Computer analysis of the timing properties in micro-channel plate photomultiplier tubes," *IEEE Trans. Nucl. Sci.* **NS-31** (1) (February 1984) 408.

Scholtz, J. J., D. Dijkkamp, R. W. A. Schmitz, "Secondary electron emission properties," *Philips J. Res.* **50** (1996) 375.

Wiza, J. L., "Microchannel plate detectors," *Nucl. Instrum. Methods* **162** (1979) 587.

this page intentionally left blank

Xbox Beowulf Cluster

Thomas Tunnell, Anthony Zukaitis[1] (former employee)
Los Alamos Operations

This project sought to build a Beowulf cluster using off-the-shelf components, specifically the central processing unit (CPU) of a Microsoft Xbox™ gaming system. The project would demonstrate success by loading and executing the Monte Carlo N-Particle (MCNP) radiographic modeling code. Loading Linux onto the gaming system's CPUs proved to be very difficult, and the project did not succeed.

Background

The project proposed to build a small Beowulf cluster using a Microsoft Xbox gaming system, which is essentially a PC specifically designed to run games. It was deemed desirable in this case for its low price (~$150) and the fact that it can serve as a node on a cluster. Our team proposed to develop a Web interface for the cluster, to enable users to submit jobs, upload input files, download output files, and possibly view results via a Web page rather than with Linux, which requires log-in on a terminal session to submit jobs. Using a Web page would eliminate the need for a user to know Linux. The Web submission system could then be copied and used on other clusters.

The project plan was to first build the cluster on a small scale before purchasing the proposed 48 nodes. The Web interface would also be written. The ultimate end product would be a cheap, easy, fast computer that would improve modeling time and enable the use of more complex models for simulations.

Project

The team purchased four Microsoft Xbox gaming systems and extracted the CPUs. Techniques for loading Linux onto the CPUs were researched. Next, the team built a master server for the Web development, and the quest to install Linux began.

Difficulties with the installation were encountered. Apparently, Microsoft had protected the Xbox such that other software could not be loaded. In an effort to circumvent these restrictions, the team reconfigured the computer and attempted a hot-swap install of the Linux. Improved Xbox software was also purchased so that other software-based methods of installing Linux could be attempted.

By the end of January, the team had successfully loaded a Linux kernel onto the Xbox, but unfortunately, this kernel required manual control to boot.

[1] zukaitis@lanl.gov, 505-665-1276

Ultimately, problems persisted that prevented us from successfully installing Linux on the Xbox as desired. The team recommended stopping the project at midyear.

Conclusion

The goal of building a Beowulf cluster using a Microsoft Xbox gaming system is probably achievable but not realistic. The labor effort of trying to install Linux on the Xbox might prove too costly.

Detectors and Sensors

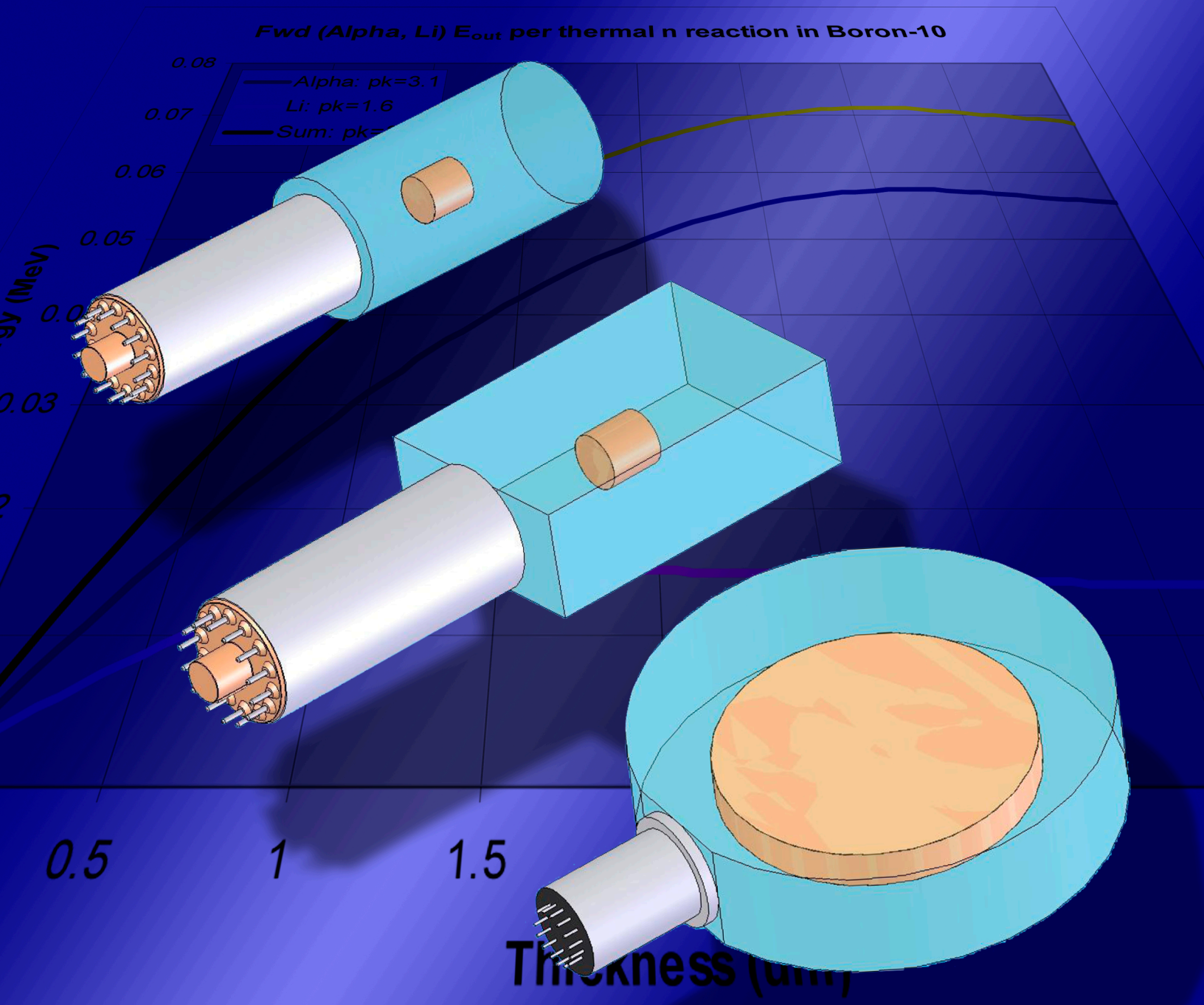

Neutron Diode/Memory Chip

Tondra De (former employee), Robert Fisher, Raymond Keegan,[1] Steven Riedhauser, Eric Schmidthuber
Remote Sensing Laboratory – Nellis

The objective of this project was to find a semiconductor device suitable for neutron detection that could replace the standard ^{3}He tubes. Our team procured for testing and examination potential neutron detectors including solar cells, memory chips, and a neutron diode detector. These tests, combined with a literature review, indicated that the best approach would be to use regular/avalanche photodiodes integrated with a converter, such as a borated scintillator or a ^{10}B layer to convert neutron interactions into electrical pulses.

Background

Portable arrays or layers of semiconductors could be built and deployed to detect smuggling of neutron-emitting material. Although the intrinsic efficiency of a semiconductor may be very low, namely <3%, the detectors could be layered to improve performance.

For this work, we selected the reaction of the capture of thermal neutrons by ${}^{10}_{5}\mathrm{B}$ to form ${}^{7}_{3}\mathrm{Li}$ and ${}^{4}_{2}\mathrm{He}$ fragments. ${}^{10}_{5}\mathrm{B}$ was chosen partly because of its very large thermal neutron cross section of 3840 b, and the fact that it exists in solid form at room temperature. The reaction is:

$$ {}^{10}_{5}\mathrm{B}+{}^{1}_{0}n \rightarrow {}^{7}_{3}\mathrm{Li}+{}^{4}_{2}\alpha \qquad \text{Q–value = 2.792 MeV (ground state), or} \qquad (1) $$

$$ {}^{10}_{5}\mathrm{B}+{}^{1}_{0}n \rightarrow {}^{7}_{3}\mathrm{Li}^{*}+{}^{4}_{2}\alpha \qquad \text{Q–value = 2.310 MeV (excited state).} \qquad (2) $$

When triggered by thermal neutrons (0.025 eV), 94% of all reactions lead to the excited state, while the remainder goes to ground. The fragments are emitted at an angle of 180° with respect to each other, and their flux is isotropic. The natural isotopic abundance of ${}^{10}_{5}\mathrm{B}$ is 19.8% (Knoll, 1999). The ${}^{7}_{3}\mathrm{Li}$ and ${}^{4}_{2}\mathrm{He}$ fragments have energies of 0.84 MeV and 1.47 MeV, respectively. The fragment ranges, calculated (Ziegler, 2003) in both silicon and gallium arsenide, were found to be ~2 μm and 5 μm for the ${}^{7}_{3}\mathrm{Li}$ and ${}^{4}_{2}\mathrm{He}$ fragments, respectively.

Project

In June 2005, we wrote a subcontract for Rama Venkat of the University of Nevada, Las Vegas (UNLV), to perform semiconductor detector sample preparation. The UNLV team provided electrical engineering and microelectronic and material science expertise to solve device preparation problems and assist in the selection, acquisition, preparation, and testing of devices for study.

[1] keeganrp@nv.doe.gov, 702-295-1005

Detector Studies

Semiconductor devices procured for study included solar cells, memory cells, and a neutron diode. These devices had ^{10}B either as a surface layer or incorporated into the atomic structure of the semiconductor material. The goal was to exploit existing devices that could be used as neutron detectors with or without modification. Tests were performed on each device using a ^{252}Cf source with an expected yield of 2×10^5 n/s. The devices studied are described below.

NREL Solar Cells

At Rama Venkat's suggestion, we procured two BGaInAs compound semiconductor solar cells from John Geisz at the National Renewable Energy Laboratory (NREL), Golden, Colorado. The cells are unique because of the unusually high concentration of boron (~10^{21} atoms/cm^3) in the layer adjacent to the PN junction. A natural depletion region is expected to form around the junction. Natural boron was used as a dopant during the cell fabrication process. As stated above, the abundance of ^{10}B in nature is 19.8%; however, we hoped that sufficient ^{10}B would exist to observe a response. We anticipated that, due to the close proximity of the highly borated layer to the PN junction, fragmentation would likely result in the passage of a fragment across the depletion region, thereby forming free charge. This charge would be swept out of the region by the natural junction potential. We predicted that a signal could be sensed between the front and back of the cell. GaAs has a band gap of about 1.4 eV, which indicates that these cells are very quiet, thus facilitating electrical pulse detection.

Since these are solar cells, it is noteworthy that the PN junction is located at ~0.6 μm below the top surface. Sunlight can penetrate to the PN junction and generate free charge, namely holes and electrons in the associated depletion region. This charge is swept out of the region and can form an electric current in an external circuit. The cells have no passivation/protective layer and, therefore, if such cells demonstrated potential as neutron detectors, ^{10}B could be deposited directly onto the cell surface. The fragments would have sufficient range to transverse the PN junction and, thus, the depletion region.

Six independent solar cells were formed on each of two GaAs wafers. Each cell was defined by a 0.1 cm^2 gold grid for electrical connection to an external circuit. The two wafers were labeled MC616 (n-on-p structure) and MC610 (p-on-n structure). Because the wafers were fragile, they were bonded to rigid bases for physical support. The bottom surface of each wafer and each of its cells were wired to pins so that connection to external circuitry could be made. Each base was fitted with a lid to keep out light. The cells on each wafer were tested in turn with the lids removed, to check their response to regular laboratory light. The maximum reverse bias that could be applied would be ~ –1 V before breakdown would be expected. We decided that no bias would be provided to the cells in order to prevent damage.

Neutron irradiations were carried out using the ^{252}Cf source described above. Neutron irradiation tests were performed whereby the above source located in its 10.4 cm-diameter polyethylene cylindrical holder was placed on its side centered on top of the test fixture. This was to provide a field of thermal neutrons to induce ^{10}B boron fragmentations. The distance between the source and cell was ~5 cm. The wafer chip box was grounded to the test fixture. The dark current was measured for wafer MC610 using the above pA meter, and was found to be 4 pA before, during, and after irradiation. The cell was irradiated with a $^{59}_{27}Co$ gamma source of activity 2 μCi. No change in response was observed.

A preamplifier was built using a commercial Ultra-Low-Input Current Amplifier, manufactured by the National Semiconductor Corporation. The gain bandwidth of this amplifier was 1.3 MHz. Neutron irradiation of both wafers was carried out as described above, except with the neutron source located in its polyethylene holder placed to the side of the test fixture centered on the cell. Exposure time was about 10 mins in each case. Pulses were observed both with and without the neutron source present, at about the same rate. It could not be concluded that the pulses were due to neutron fragmentations. Microphonic noise and coincident electromagnetic interference from other activities in the area were observed during the irradiations.

We anticipated that alpha particles from a $^{239}_{94}Pu$ electroplated source would have sufficient energy to penetrate through the top surface to the PN junction. If pulses could be seen from alpha particles, then placement of a $^{10}_{5}B$ layer on the top surface would result in pulses due to helium fragments that would transverse the PN junction. The average range of a 4.5-MeV alpha particle from $^{239}_{94}Pu$ in GaAs is ~16 μm. An irradiation using wafer MC616 was performed under laboratory lighting. The 276 μCi $^{239}_{94}Pu$ source was placed at ~1 cm from the cell surface at normal incidence. The above preamp was used with an exposure time of ~10 mins. The laboratory lights were dimmed or turned off to minimize interference. We used an oscilloscope to view the signal from the preamp. No pulses were observed due to alpha particle passage through the PN junction. We concluded that a more sensitive preamp with as wide a bandwidth as possible was required.

Silicon Storage Technology (SST) Memory Chips

The principle behind using a memory chip as a radiation detector is that a highly ionizing particle, such as an alpha particle or heavier ion, passes through a memory cell and causes it to flip from one binary state to another (Li, 2005). Such a state change is called a "single-event upset" (SEU). The chip would need to have a conversion layer, such as ^{10}B, placed on its top surface in close proximity to the memory cell–sensitive volumes so that fragments could penetrate and produce free charge to trigger SEUs. The chip would be used by first writing either 0s or 1s to all cells on the chip, then exposing it to a thermal neutron field for a known period of time. The chip would then be read to see how many cells had flipped state, i.e., count SEUs. This count is directly related to the magnitude of the thermal neutron flux.

This idea poses two problems. Memory chips are notoriously radiation hard, and the $^{10}_{5}\mathbf{B}$ fragments have expected ranges of between 2 and 5 μm. Chips normally have a silicon dioxide passivation layer of at least 2-μm thickness beneath a very thick epoxy layer likely to be a few millimeters thick. The technique requires that the epoxy layer be removed and that the passivation layer be thinned as much as possible to a thickness of preferably less than 2 μm. The topmost zone of the chip is expected to have a "dead layer" a few microns thick that will not respond to ionizing radiation. Placement of boron within microns of the cell's active volumes is vital to success.

The memory chips chosen for this study were procured from SST. Venkat's contact at SST obtained suitable samples for us and could have epoxy/passivation layers removed or thinned. The model number for the chip type was SST39VF040. The chips were manufactured with the vendor's proprietary, high-performance CMOS SuperFlash technology (Silicon Storage Technology, 2005) and are organized as 512K × 8 bits.

The memory chip test interface was designed to facilitate testing with the flash memory chips. Simple push-buttons allow the user to erase an entire chip, read each of the memory locations on the chip, check for SEUs, and display the results to a computer via the serial port. Colorful LED indicators designate completion of each step in the process.

Testing was performed using the test interface as follows. Three chips were tested, one with the full epoxy layer, and the other two with those layers removed. The chips were all cleared with the cells set to binary 1 and were mounted side-by-side for exposure with 28 mm spacing on a foam base. We placed the chips in front of the neutron source (same as used previously), with the center chip (no epoxy layer) at 3.0 cm in front of the source. The exposure time was 1 hr, 50 mins. When we read out the chips, no SEUs were found.

A second test was carried out using the chip that had a full epoxy layer. The chip was cleared as before, with all the cells set to binary 1. The source was then placed in contact with the chip epoxy surface for 4 hrs. Again no SEUs were found during readout.

Activities at UNLV primarily involved the modification of a sputtering system to place layers of ^{10}B on the surface of memory chips. The original plan was to deposit ^{10}B using sputtering and to utilize a sputtering system under development that used a standard disk-type ^{10}B target. Several detailed discussions with sputter target manufacturers indicated that the ^{10}B targets (5.0 cm diameter and 1.3 cm depth) would be exorbitantly costly ($20–30K). In the meantime, BN obtained a 94% pure hemispherical shell of ^{10}B (25 mm inner diameter; 46 mm outer diameter), which was developed for a different application. Thus, we decided to design and build a magnetron sputter system around the hemispherical target.

Since the sputter efficiency of the magnetron sputtering system critically depends on magnetic field lines, we performed a theoretical simulation and analysis of field lines using Field Precision's TRICOMP4 software (version 4). A cylindrical rare earth permanent NdBFe35 magnet (18.5-mm

diameter, 17.9-mm height) was assumed for simulation and design. Several simulations using various geometries and dimensions were carried out. The best design was chosen and built using conclusions drawn from the shape and strength of the magnetostatic field lines at the ^{10}B target. At report time, ^{10}B has been successfully coated onto a glass substrate, and the system is functioning correctly. Due to time constraints, ^{10}B coated memory chips have not been exposed.

SOLTEC Neutron Diode Dosimeter

A neutron-sensitive electronic dosimeter was purchased from the SOLTEC Corporation in San Fernando, California. Manufactured by Fuji Electric Company, the dosimeter is distributed in the U.S. by SOLTEC. This model NRY21222-1 simultaneously measures gamma and neutron dose equivalent. Energy response ranges between 0.025 eV and 15 MeV. Information from Fuji (Aoyama, 2000) indicates that the dosimeter has two neutron detectors: one measuring fast neutron flux and the other, thermal neutron flux.

The dosimeter was tested by placing the same 2×10^5 n/s ^{252}Cf source previously mentioned at a distance of ~3 mm from the front face of the dosimeter, at the point indicated on the face where the neutron detectors were expected to be located. A 5-cm-thick polyethylene slab was placed behind the dosimeter to generate the albedo flux of thermal neutrons required to make the thermal neutron detector function. The exposure was carried out over 38 mins. The neutron detectors indicated a dose equivalent of 30 mrem neutron and 1.01 mrem gamma. We assume that most of the neutron component is due to recorded thermal neutrons.

Following this exposure, the dosimeter was opened to determine detector location. Three detectors were found enclosed within a grounded metal box, which indicated on the outside where the detectors were located. We believe that one is the gamma detector, and the other two are neutron detectors. Component labels ("NAF" and "NAT") were assumed to indicate "fast" and "thermal." The most interesting finding was that the neutron detectors were light-sensitive and behaved like solar cells/photocells. Thus, the best approach may be looking at solar cell/photo diode type devices. These devices' PN junctions are very close to the top surface (for our NREL devices, it is within 0.6 μm of the top surface), and $^{10}_{5}B$ fragments can easily penetrate to the active volume.

Conclusion

We expected the solar cells procured from NREL to have potential. The physics indicates that about six ^{10}B fragmentations occur per minute in the combined six cells; however, none were observed. Irradiations using an alpha-emitting source in which the alpha particles could penetrate through the PN junction showed no pulses. We concluded that the preamplifier was not sensitive enough and that the cells' internal capacitance could have been hindering pulse detection. The main advantage of using cells of the type studied in this work is that the PN junction was within 1 μm of the top surface of the cell, so that ^{10}B fragments could penetrate and deposit energy in the depletion region.

The study of the dosimeter indicates that these silicon-based diode detectors are light sensitive and structurally very similar to solar cells or photodiodes. We know that a ^{10}B layer placed near the diode is used to irradiate the PN junction. Despite the fact that we saw no pulses with the NREL cells, we believe that solar cells/photodiodes have significant potential as neutron detectors.

Exposure of SST39VF040 memory chips resulted in no SEUs. Success with memory chips is considered to be less likely due to the thickness of the epoxy and passivation layers. The chip is considered to have a dead layer on top where junctions, etc., formed are insensitive to ionizing radiation. Fragments are less likely to penetrate through to the sensitive volumes, and when they do, the linear energy transfer (LET) may be too small to trigger an SEU. The fragments are produced on their Bragg peaks, and the LET is falling off rapidly as a function of path length as the stopping point is approached. A passivation layer will always be required to isolate the boron from the underlying circuitry. With current technologies, there will always be a few microns between the conversion layer and the cell-sensitive volumes. Greater success is likely if the boron can be incorporated into the chip volume, either as layers or boron-filled holes, or distributed throughout the volume of the semiconductor.

The best approach to neutron semiconductor detector design would likely be to use existing photodiode technology, as developed for the optoelectronics industry, and form a conversion layer on top of its active surface. This layer could be ^{10}B on the photodiode surface, or it could be a borated scintillator. These photodiodes are designed specifically for very-high-speed applications, namely pulse widths on the order of nanoseconds, and have quantum efficiencies on the order of ~90%. These devices have antireflection and protective coatings on top of the active area that likely would need thinning before boron deposition. Large numbers of such devices could be formed in isolation from each other, in arrays on wafers and/or mounted in layers to increase efficiency.

The same argument applies to avalanche photodiodes, which are more sensitive to low levels of light energy. Rather than attempt to remove antireflection coatings, it may be better to place a neutron-sensitive scintillator in contact with the photocell, to act as a converter. One example would be a gadolinium-loaded liquid scintillator, such as Eljen Technology's EJ-331 or EJ-335. This would be a natural gadolinium, with 15.7% ^{157}Gd that has a cross section of 255,000 b. These products' flash points are 44°C and 64°C, respectively, meaning that they would need to be sealed away from air and temperature-controlled within an optical chamber.

Another example would be the use of lithium glass scintillator types GS20 or KG2, sold by Saint-Gobain. The glasses are enriched to about 7.0% ^{6}Li, which has a thermal neutron cross section of 940 b. The key advantage to using glass would be physical stability over a wide range of temperatures, which would likely not be possible with liquid scintillators. In both cases, the total energy of the nuclear reaction is deposited in the scintillation medium, which is likely to yield a higher efficiency than using a ^{10}B conversion layer on top of a sensitive volume. Established optoelectronic photodiode receivers that integrate a photodiode with an amplifier could be purchased off the shelf and used with a borated scintillator.

Acknowledgments

The authors would like to thank John Geisz from the National Renewable Energy Laboratory for making the two solar cells used in this work available to the RSL team. We express our gratitude to David Nigg at the Idaho National Laboratory for making available the ^{10}B samples. We would also like to thank Rama Venkat and his staff at UNLV, and all of the RSL staff, including Dave Mitchell and Kevin Forcade, for their help and many useful discussions.

References

Aoyama, K., N. Yoshiyuki, T. Suzuki, "The development of new generation electronic personal dosimeters," Proceedings of the International Radiation Protection Association Conference #10, Hiroshima, Japan, May 2000.

Knoll, G. F., *Radiation Detection and Measurement*, 3rd edition, John Wiley and Sons, 1999, 507.

Li, H., J. Y. Deng, D. M. Chang, "Monte Carlo calculation of the cross-section of single event upset induced by 14-MeV neutrons," *Radiation Measurements* **39** (2005) 401–407.

Silicon Storage Technology, SST39VF040 data sheet, September 2005.

Ziegler, J. F., J. P. Biersack, SRIM computer code version SRIM-2003.26, 2003.

this page intentionally left blank

Reactive Optical Diffracting Materials for Sensing Organophosphates

Clare Kimblin,[1] *Roderick Tiangco*
Special Technologies Laboratory

A new method amenable to the remote sensing of organophosphates (OP) is reported here. The method pairs an enzyme inhibited by OPs with a reactive, reflective holographic material. The material is affected by the production of charge within it and swells due to protonation by an acid generated from enzyme activity. Swelling results in a red shift of light reflected from the material. The ability of the material to colorimetrically indicate the presence of OPs is demonstrated using the OP enzyme inhibitor paraoxon (POx). In the absence of POx, a 60-nm visible shift in Bragg-reflected light is observed, but in the presence of POx, the red shift is rapidly quenched. The optical change exhibited by the reflective holographic material is particularly promising. The color change allows for simplified detection and enables reflective materials to be applied to remote detection. The current system does not require power and does not emit a radio-frequency (RF) signature.

Background

Much research has been devoted to the detection of certain classes of OPs, and a variety of detection methods exist. Ideally, these methods would be amenable to remote detection. In an effort to create a simple sensor that detects OPs remotely, a cholinesterase enzyme that is inhibited by OPs was paired with a reflective holographic material.

Cholinesterases

Cholinesterases (ChE), such as acetylcholinesterase (AChE) and butyrylcholinesterase (BuChE), catalyze the hydrolysis of the neurotransmitter acetylcholine (ACh^+) (Equation 1). By removing residual acetylcholine, the nerve impulse triggered by the molecule is "turned-off" until the next impulse is caused by a subsequent initiation. One of the hydrolysis products is acetic acid; thus, in the presence of excess ACh^+ substrate, the solution pH decreases as the reaction proceeds. This reaction progresses at about 50 μs/turnover (Millard, 1999).

$$ACh^+ + H_2O \xrightarrow{AChE} acetate^- + H^+ + choline^+. \quad \textbf{(1)}$$

[1] kimblicw@nv.doe.gov, 805-681-2257

Certain OPs inhibit the active sites of ChEs and prevent the breakdown of ACh^+, thereby interfering with nerve impulse transmission (Rand, 2004). The molecular structures of the substrates ACh^+ and acetylthiocholine (ATC^+), and the OP ChE inhibitor POx are presented in Figure 1.

In the presence of OP inhibitors, the active site of AChE is blocked and ACh^+ is not converted to acetic acid (Equation 2); therefore, the pH of the reaction solution is not altered.

$$ACh^+ + "OP" \xrightarrow{ChE} ChE - "OP" + ACh^+. \quad \textbf{(2)}$$

The assembled detection system relies on pairing a pH-sensitive holographic material that responds optically to changes in pH with a ChE that reacts with excess choline substrate (ACh^+ or ATC^+) and produces acetic acid when *not* inhibited by OP.

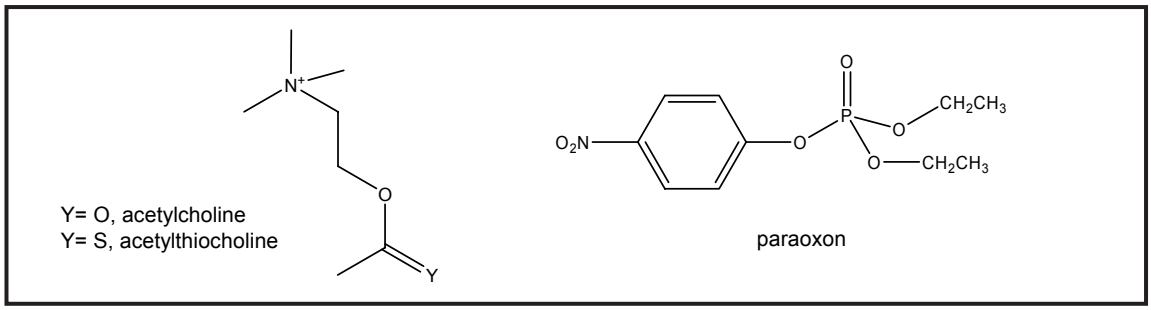

Figure 1. Molecular structures of the choline substrates (left) and the OP ChE inhibitor POx (right)

Reactive Hologram

The group led by Chris Lowe (University of Cambridge, England) has demonstrated that pH changes and other solution reactivity can be monitored by observing changes in the wavelength of light reflected by holographic gratings embedded in reactive, swellable hydrogel films (Marshall, 2003). To help minimize charge repulsion, and as a result of osmotic effects, a charged hydrogel absorbs more water into its pores than a neutral hydrogel (Mayes, 2002). Solvent migration into or out of the hydrogel results in swelling or shrinking. This solvent migration also affects the grating spacing. Volume changes within the material result in a decrease or increase in the spacing (d in Equation 3) between silver fringes and bring about a color shift of Bragg-reflected light. The wavelength of light diffracted by the grating, and thus, the apparent color of the hologram, is directly proportional to the fringe spacing, in accordance with Bragg's law:

$$m\lambda_{max} = 2nd \sin\theta, \quad \textbf{(3)}$$

where:

m = order of diffraction

λ_{max} = wavelength of diffracted light

n = average refractive index

d = spacing between diffracting planes

θ = angle of light incident on, and reflected from, diffracting planes.

Light diffracted by the holographic material will be blue-shifted in the case of solvent migration out of the hydrogel (decrease in *d*: hydrogel shrinkage) and red-shifted in the case of solvent migration into the hydrogel (increase in *d*: hydrogel swelling).

Project

To colorimetrically indicate the presence of OP ChE inhibitors, a ChE enzyme, BuChE, and a substrate, acetylthiocholine iodide (ATCI, which is hydrolyzed to acetic acid and thiocholine), were used in conjunction with a swelling holographic material, H-poly[HEMA-co-DMAEM(6 mol%)-co-EDMA(5 mol%)], (H-poly[HDE]). The H-poly[HDE] was synthesized by STL scientists based on a procedure by the Lowe group (Marshall, 2003; Mayes, 2002). The hydrogel polymer, poly[HDE], contains basic amine groups (DMAEM (6 mole %)) that are protonated by acid, causing material swelling. It was proposed that in the absence of an enzyme inhibitor, ATC^+ would be hydrolyzed to acetic acid and thiocholine, and that the hydrogel amine groups would be protonated, causing swelling of the hydrogel and a red shift. With the addition of POx, a powerful OP ChE inhibitor, the color change should be halted.

Synthesis of H-poly[HDE] relies on basic holographic principles (Unterseher, 1996) but employs a custom polymer emulsion. Steps performed at STL included:

- Synthesis of a poly[HDE] thin film as a grating matrix
- Impregnation of the film with silver bromide
- Exposure of the photosensitive emulsion to coherent light (neodymium:yttrium-aluminum-garnet [Nd:YAG] laser)
- Development of the latent image.

The pH-sensitive hydrogel was fabricated by incorporating the amine base dimethylaminoethyl methacrylate (DMAEM) into a 2-hydroxyethyl methacrylate (HEMA) polymer chain with ethylene glycol dimethacrylate (EDMA) cross-links to provide support (Figure 2). Thin films were created on glass microscope slides by applying pressure to a controlled volume of monomer solution.

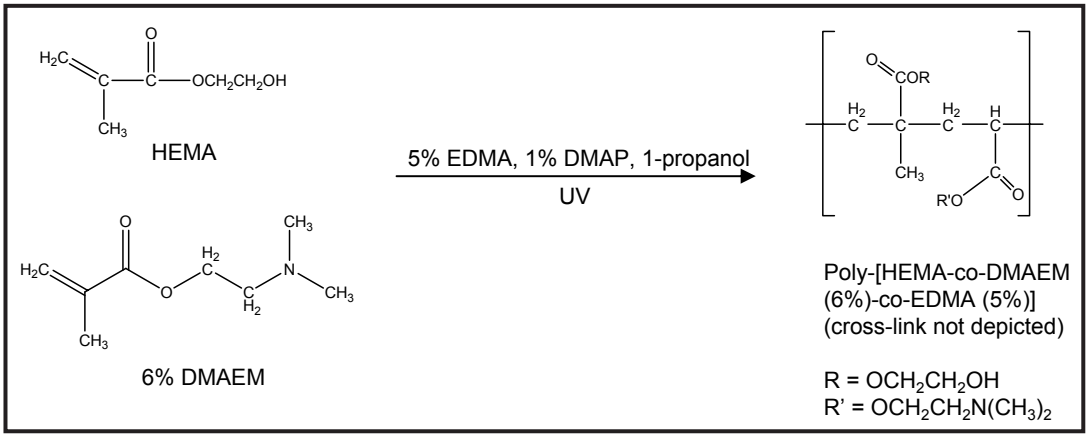

Figure 2. Synthesis of hydrogel (Poly[HDE]) consisting of basic dimethylaminoethyl methacrylate (DMAEM) units in a 2-hydroxyethyl methacrylate (HEMA) backbone, with ethylene glycol dimethacrylate (EDMA) cross-links

Polymerization was initiated using a sensitizer 2-dimethoxy-2-phenyl acetophenone (DMAP) and ultraviolet (UV) light (254 nm). The hydrogel film was then treated to create light-sensitive silver bromide grains within its pores. Following immersion in a sensitizer bath, slides were submerged in a solution of sodium nitrate (3 M) and exposed using a continuous wave Nd:YAG laser (λ = 532 nm, 3.5–25 mW, ~250 ms). As shown in Figure 3, slides were exposed at a 4° angle relative to a mirror that is imaged in the hologram and sits at the base of the dish where the slide is positioned. Constructive interference between incoming light waves and those reflected from the mirror results in silver ion being reduced to silver metal at $\lambda/2$-nm intervals.

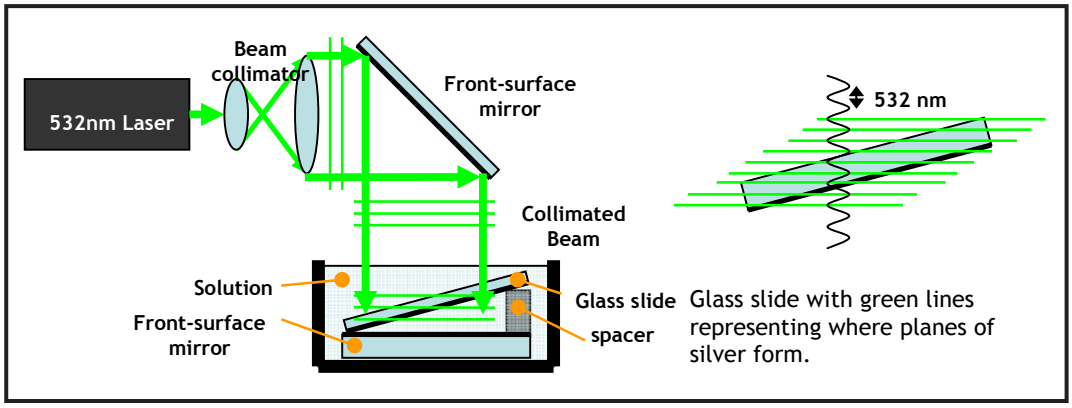

Figure 3. Setup for slide exposure: arrows indicate the path followed by the laser beam (left); enlargement of glass slide with regions of constructive interference by 532-nm light indicated with green lines at $\lambda/2$ apart (right). Planes of silver metal form at these sites.

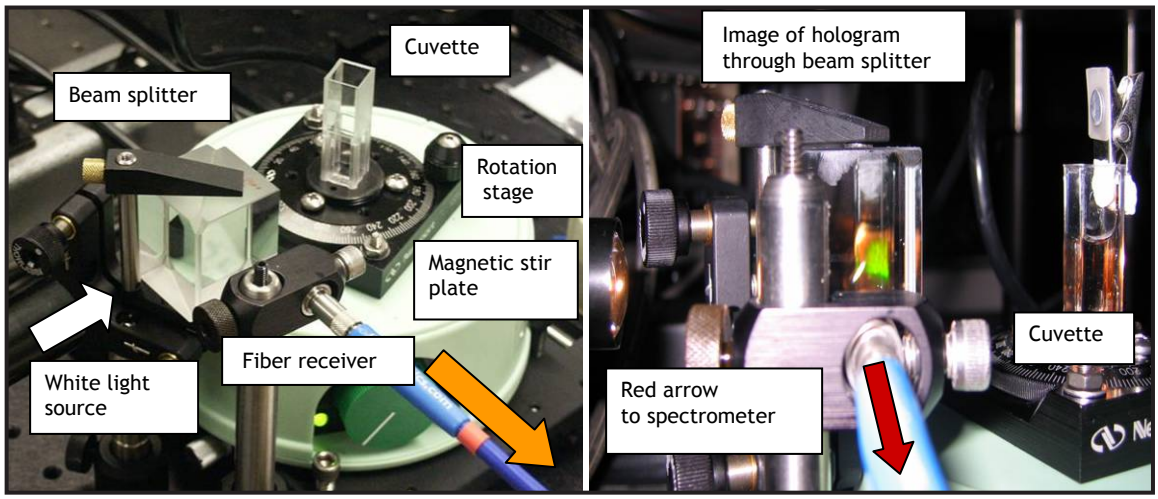

Figure 4. (left) The empty cuvette for holding hologram and reaction solution. The white arrow indicates white light, which passes through the beam splitter and would hit a hologram in the cuvette. Bragg-reflected light (orange arrow) is sent back through the beam splitter to the fiber receiver and detector (not shown). (right) The cuvette contains a hologram; the view is from the fiber receiver input. The red arrow indicates diffracted light, which will reach the spectrometer.

Standard photography protocols were followed to develop slides (Foto Info, 2005). Poly[HDE]-based holograms exposed in a nitrate solution diffracted green light (~550 nm) when submerged in water. To quantitatively measure diffraction wavelength from the slides, the setup shown in Figure 4 was used with an Ocean Optics spectrometer (HR2000CG-UV-NIR). A cuvette sits on a rotation stage adjusted such that Bragg-reflected light is returned without simultaneously back-reflecting the white light source. In Figure 4 (right), the cuvette contains a hologram that reflects green light, as seen through the beam splitter. Holographic images are also presented on the right side of the plot in Figure 5.

To demonstrate the ability of a Poly[HDE] holographic slide to differentiate between uninhibited BuChE and enzyme inhibited with an OP, a comparison was made. A holographic slide was positioned with the emulsion side facing into a buffer solution (5 mM phosphate buffer [PB], pH 7.1) with an excess of the substrate, ATC^+ (0.68 mM). Prior to enzyme addition, light reflected from the hologram was green (~556 nm). After the addition of BuChE (equine, 6 units/2.66 mL) a 48-nm red shift, $\Delta\lambda_{max}$, was observed over a 7-min period, giving the hologram an orange/red appearance. A second shift to 622 nm (total shift: 66 nm) was observed after the addition of more substrate (1.1 mM total ATC^+). Results are plotted in navy blue in Figure 5. The hologram was then washed with water and ethanol (to denature residual protein), and the experiment was repeated. A red shift was observed for 1.5 min, indicating that the assembly was not degraded by regeneration and was functioning as before. Following 1.7 min, when λ_{max} was ~573 nm, the OP POx (0.11 mM) was added to the sample.

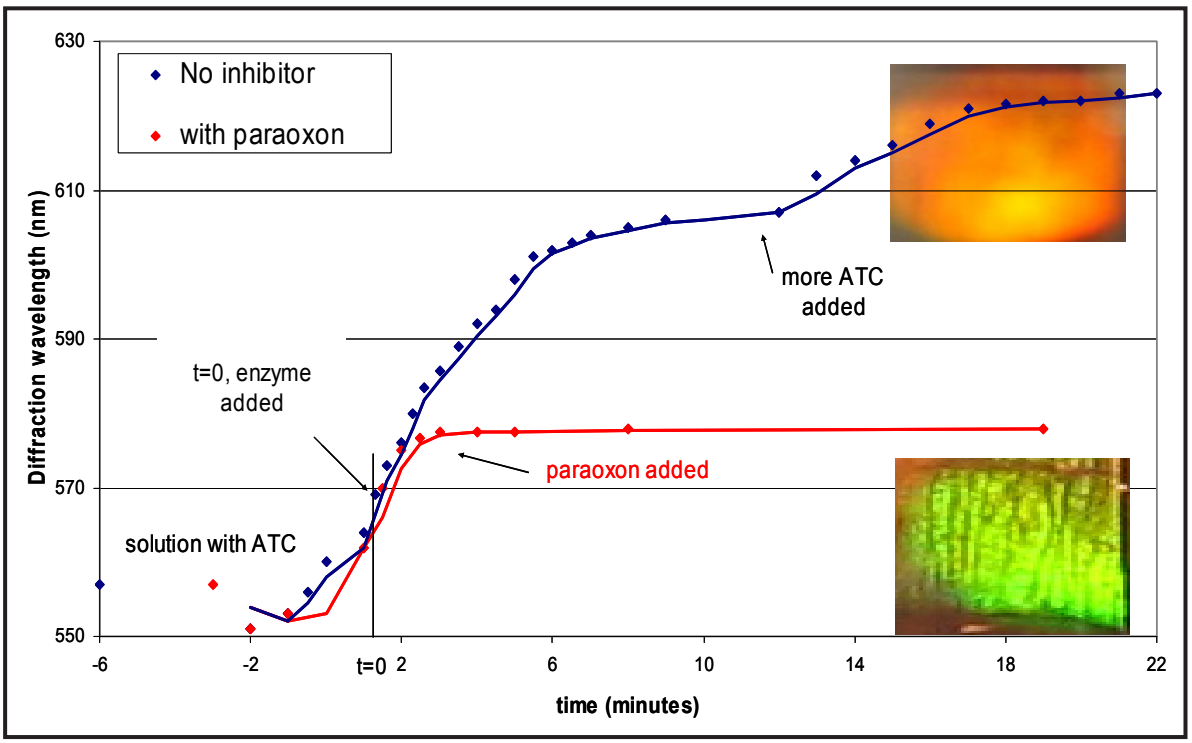

Figure 5. Time versus diffraction wavelength: diffraction shift without inhibitor (blue line) and diffraction shift quenched when POx added (red line). Quenching observed within ~1 min.

Within ~1 min, the rate of red-shifting had diminished (λ_{max}= ~577 nm), and 1.5 min later, λ_{max} was stable at 578 nm. A similar series of tests was performed using 6.5 times less POx (17.2 μM) with ATC^+ (1.55 mM) and BuChE (2.5 units/2.09mL). Addition of POx again quenched the reaction of BuChE with substrate but this time less rapidly, presumably due to the use of less inhibitor. Within the 4 min following the POx addition, the red shift was not more than 5 nm (571 to 576 nm). Within the same 4-min time period, in the *absence* of an inhibitor, $\Delta\lambda_{max}$ was 15 nm (571 to 586 nm). These experiments demonstrate proof of principle but were not optimized for rapid response and optimal sensitivity.

In the current setup, with no inhibitor, the rate-limiting step is expected to be the time required for the concentration of acid produced to override the buffering capacity of the buffer, and for the acid to diffuse into the hydrogel. In the presence of the inhibitor, dilution of the inhibitor and enzyme likely prolongs response time. By limiting the volume of the sample solution to just that which is required to wet the hydrogel, we predict that the response rate will be greatly enhanced, since protons generated would be in closer proximity to the amine functionalities of the hydrogel. In order to keep the acid produced by the uninhibited enzyme in the vicinity of the hydrogel, collaborators at the

University of Nevada, Reno (UNR), covalently attached BuChE to the hydrogel surface (procedure based on Kok, 2001). However, tests indicate that the attachment procedure alters the acid sensitivity of the hydrogel material.

Conclusion

A reflective material that relies on the inhibition of a cholinesterase (BuChE or AChE) and the diffractive and swelling properties of holograms in a flexible polymer framework was fabricated for the detection of OPs. The ability of the holographic material to colorimetrically indicate the presence of OPs was demonstrated using the ChE-inhibitor POx. To optimize response, we propose a miniaturized system that would not require enzyme attachment. While optimization is required, this research demonstrates a new technology for sensing OPs, which, in its current form, does not require power and does not emit an RF signature. Reflective holographic materials are promising because they may be applied to remote detection. A longer report will be generated and submitted for publication in a scientific journal.

Acknowledgments

The authors would like to thank Professors Suk-Wah Tam-Chang and Ken Hunter of UNR for exploring enzyme immobilization procedures and alternative methods of hydrogel film application, and for helpful discussions and advice regarding enzyme use.

References

Foto Info, "Black and White Chemistry Info," http://www.fotoinfo.com/bandw.html, accessed May 4, 2005.

Kok, F. N., F. Bozoglu, V. Hasirci, "Immobilization of acetycholinesterase and choline oxidase in/on pHEMA membrane for biosensor construction," *J. Biomat. Sci., Polymer Ed.* **12** (2001) 1161–1176.

Marshall, A. J., J. Blyth, C. A. B. Davidson, C. R. Lowe, "PH-Sensitive Holographic Sensors," *Anal. Chem.* **75** (2003) 4423–4431.

Mayes, A. G., J. Blyth, R. B. Millington, C. R. Lowe, "Metal ion sensitive holographic sensors," *Anal. Chem.* **74** (2002) 3649–3657.

Millard, C. B., G. Kryger, A. Ordentlich, H. M. Greenblatt, M. Harel, M. L. Raves, Y. Segall, D. Barak, A. Shafferman, I. Silman, J. L. Sussman, "Crystal structures of aged phosphonylated acetylcholinesterase: nerve agent reaction products at the atomic level," *Biochem.* **38** (1999) 7032–7039.

Rand Corporation (W. Augerson), "A Review of the Scientific Literature as it Pertains to Gulf War Illnesses; Chapter 5: Nerve Agents," http://www.rand.org/pubs/monograph_reports/MR1018.5/, accessed December 15, 2004.

Unterseher, F., J. Hansen, B. Schlesinger, *Holography Handbook,* Ross Books, Berkeley, California, 1996.

Liquid Organic Scintillator for Special Nuclear Material Detection and Improved Minimum Detectable Activity

Ronald E. Guise, Jon G. Leander,[1] Thomas G. Stampahar
Remote Sensing Laboratory – Nellis

This project sought to achieve satisfactory neutron-gamma discrimination of output pulses from a liquid organic scintillator when excited by a fast neutron source typical of special nuclear material (SNM). Laboratory testing indicated that a high-speed transient digitizer could be programmed to yield excellent neutron-gamma discrimination.

Background

A liquid organic scintillator could be a valuable SNM detector if it could generate the energy spectrum of a fast neutron source characteristic of SNM. Since the liquid organic scintillator is responsive to both gammas and fast neutrons, some means must be developed to discriminate between these two at moderate to high pulse count rates over a 1–8-MeV energy range. If neutron/gamma discrimination can be achieved, the fast neutron source spectrum can be derived from the proton recoil pulse output of the photomultiplier tube (PMT) dynode by deconvolution techniques.

Project

Five methods of analog and digital neutron/gamma pulse shape discrimination (PSD) were evaluated:

1. The originally proposed zero-crossing method per Sperr (1974) using an ORTEC Model 552 Pulse Shape Analyzer Nuclear Instrument Module (NIM).
2. A similar zero-crossing method per Marrone (2002) using a Canberra model 2160A and Tennelec TC453 Constant Fraction Discriminator.
3. Digital current integration method per Jastaniah (2002).
4. Digital signal processing using time-over-threshold and slew rate techniques similar to Sperr (1974). Timing information was derived directly from the anode fall time characteristic of the liquid organic scintillator PMT, while energy information was obtained from the conditioned dynode pulse of the liquid organic scintillator PMT. An analog time delay, typically 450 ns, of the dynode energy pulse was required to utilize this method. That delay function was performed by an ORTEC Model 427A delay amplifier.

[1] leandejg@nv.doe.gov, 702-295-8083

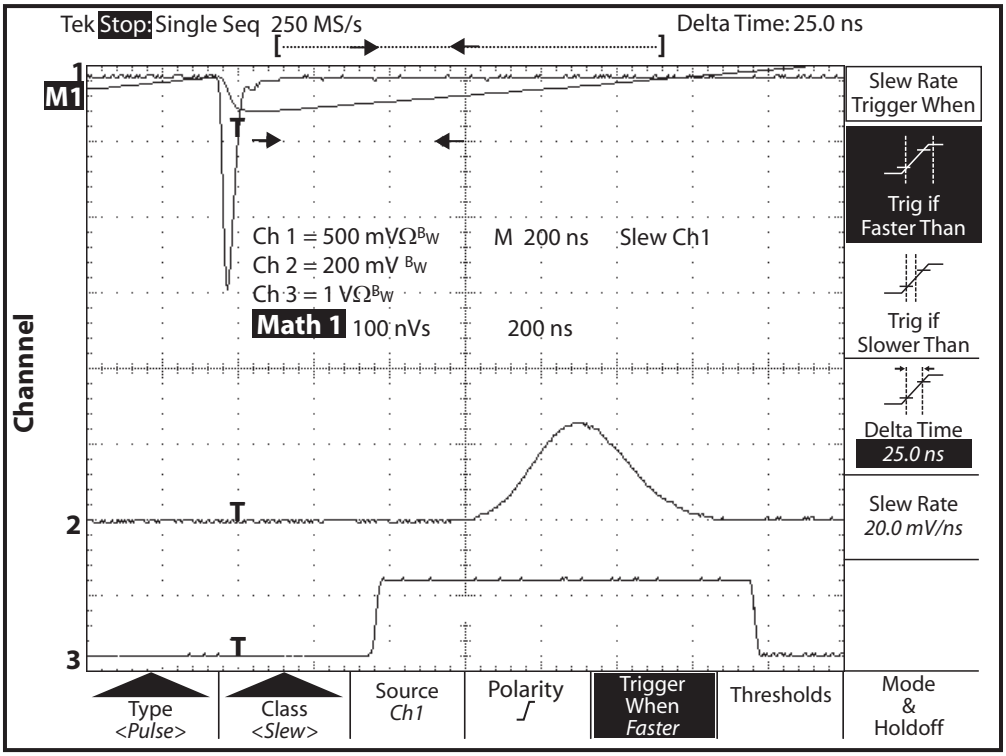

Figure 1. Gamma response – digital current integration. The top trace is the PMT anode pulse. The middle trace is the digitally integrated anode pulse. The bottom trace is the threshold detector output.

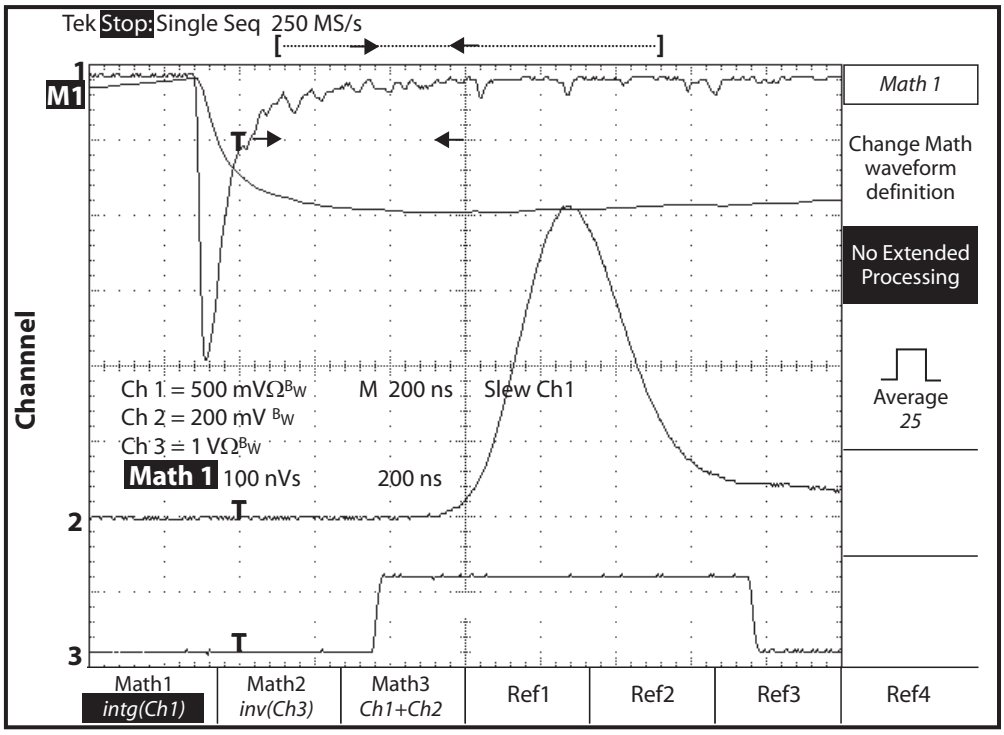

Figure 2. Neutron response – digital current integration. The top trace is the PMT anode pulse. The middle trace is the digitally integrated anode pulse. The bottom trace is the threshold detector output.

Additionally, a commercial neutron spectroscopy system based on an analog charge comparison method was purchased from Bubble Technologies, Inc., for evaluation and comparison purposes.

Methods 1 and 2 failed to exhibit acceptable neutron/gamma discrimination characteristics, and their exploitation was discontinued in favor of the digital techniques of methods 3 and 4. Method 3 exhibited acceptable neutron/gamma discrimination (see Figures 1 and 2). Method 4 provided very good discrimination when operating in the slew-rate mode (Figures 3 and 4).

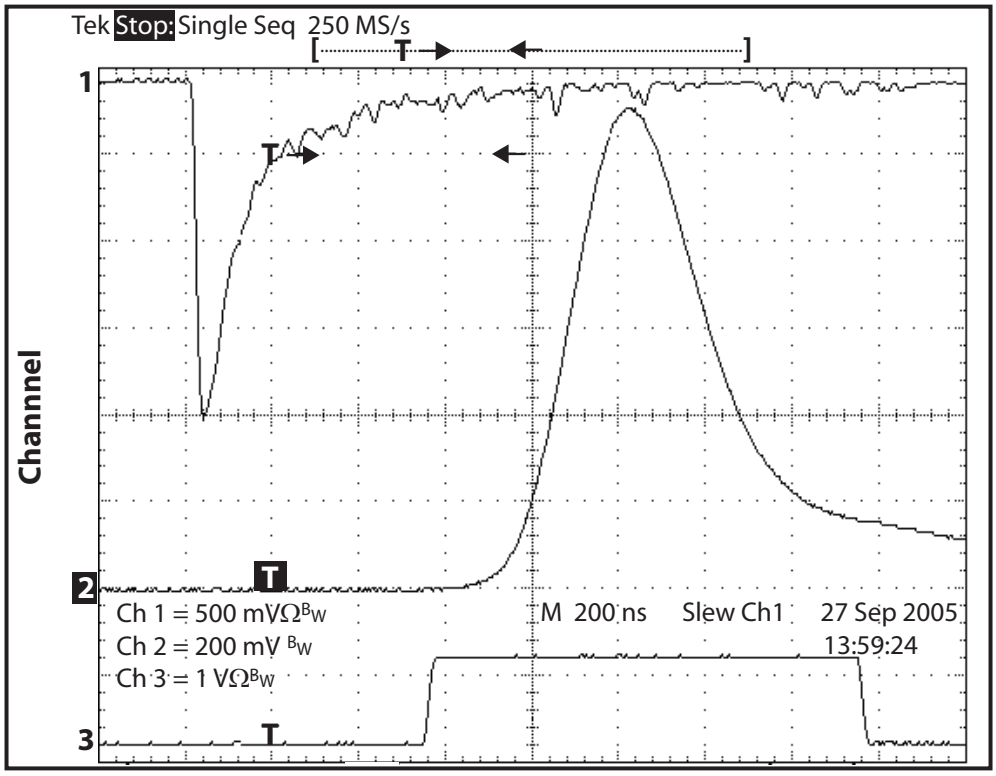

Figure 3. Gamma response – slew rate discrimination. The top trace is the PMT anode pulse. The middle trace is the integrated anode pulse. The bottom trace is the threshold detector output.

Conclusion

Both of the zero-crossing techniques failed to provide satisfactory neutron/gamma discrimination characteristics, while all three of the digital signal–processing methods yielded quite satisfactory discriminator performance. The commercial spectroscopy system initially performed satisfactorily but developed application software problems after about three weeks of intermittent operation. Corrections are currently being implemented. Because the digital signal processor used was an

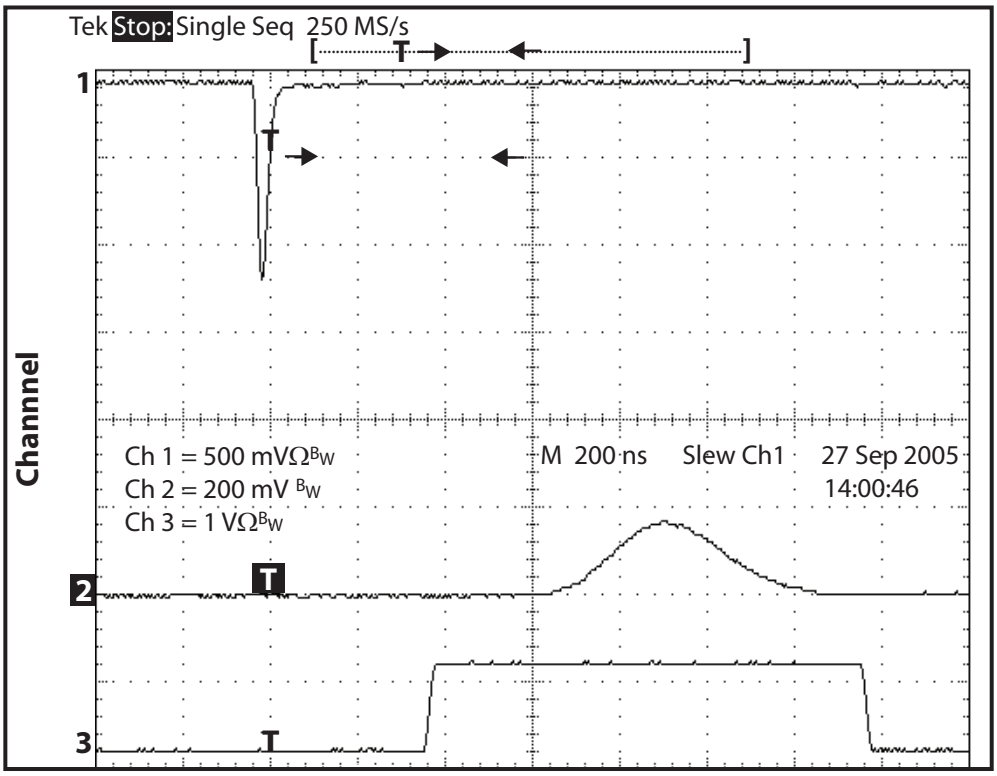

Figure 4. Neutron response – slew rate discrimination. The top trace is the PMT anode pulse. The middle trace is the integrated anode pulse. The bottom trace is the threshold detector output.

expensive, laboratory-grade digital oscilloscope, it is suggested that a commercial 8-bit, 2 Gs/sec, dual-channel waveform digitizer be purchased and programmed as required to implement the discrimination algorithms of Methods 3 and 4.

References

Jastaniah, S. D., P. J. Sellin, "Digital techniques for neutron/gamma pulse shape discrimination and capture-gated neutron spectroscopy using liquid scintillators," *Nucl. Instrum. Methods in Phys. Res. A* **517** (2004) 202–210.

Jastaniah, S. D., P. J. Sellin, "Digital pulse-shape algorithms for scintillation-based neutron detectors," *IEEE Trans. Nucl. Sci.* **49**, August 2002.

Marrone, S., D. Cano-Ott, N. Colonna, C. Domingo, F. Gramegna, E.M. Gonzalez, F. Gunsing, M. Heil, F. Kappeler, P.F. Mastinu, P.M. Milazzo, T. Papaevangelou, P. Pavlopoulos, R. Plag, R. Reifarth, G. Tagliente, J.L. Tain, K. Wisshak, "Pulse shape analysis of liquid scintillators for neutron studies," *Nucl. Instrum. Methods in Phys. Res. A* **490** (2002) 299–307.

Sperr, P., H. Spieler, M. R. Maier, "A simple pulse-shape discrimination circuit," *Nucl. Instrum. Methods* **116** (1974) 55–59.

Multilayer Solid-State Neutron Detector

Harry McHugh,[1] *Ken Moy*
Special Technologies Laboratory

The technical goal of this project was to prove the feasibility of developing a cost-effective multilayer solid-state neutron detector. The basic detector consists of amorphous silicon PiN diodes applied to a boron-10 (^{10}B)-coated substrate. Multiple layers of this construction were to be used to obtain the desired sensitivity. Working with the National Renewable Energy Laboratory (NREL), PiN diodes were developed and tested. These diodes, mounted on microscope slides, were very sensitive to alphas, as required. The leakage currents were measured to be very low, exceeding design goals. The sputtering of ^{10}B, however, has proven difficult and has prevented the fabrication of the completed device. A concept has evolved from this effort to adapt new video display technology to construct large area detectors with excellent signal-to-noise levels. Additional advantages of this new approach are highly pixelated neutron detectors with fast (<100 ns) rise times that will be useful for other applications.

Background

Helium-3 (^{3}He) tubes have been the predominant neutron detector for many years. While quite reliable and accurate, they are very expensive and relatively large. The cost of ^{3}He tubes, approximately $40/sq. in. (cross-sectional area), is the principal reason that they are not widely employed in portal detectors. New solar cells, which are themselves multilayer semiconductors, can be purchased at retail prices of less than $0.40/sq. in. Adapting this solar cell technology—based on amorphous silicon PiN diode technology—to neutron detection should yield detectors that can be fabricated for a price lying between these two extremes, thus making them more economical to widely install in critical applications.

Project

Device Design

The basic PiN diode configuration is illustrated in Figure 1. It relies on the alpha particles—generated by a neutron interaction with the ^{10}B—reaching the diode material and producing electron-hole pairs. As an alpha-particle generator, the ^{10}B layer has an optimum thickness of about 1.5 μm. Figure 2 shows the peak of the energy curve, as realized at a thickness of 1.5 μm. Too thin a layer will

[1] mchughhr@nv.doe.gov, 805-681-2454

produce fewer neutron interactions that lead to alpha particles, while too thick a layer will stop most of the alpha particles within the boron, so they do not reach the adjacent diode detector layer. For the optimized boron thickness, the average outgoing alpha-particle energy is around 1 MeV.

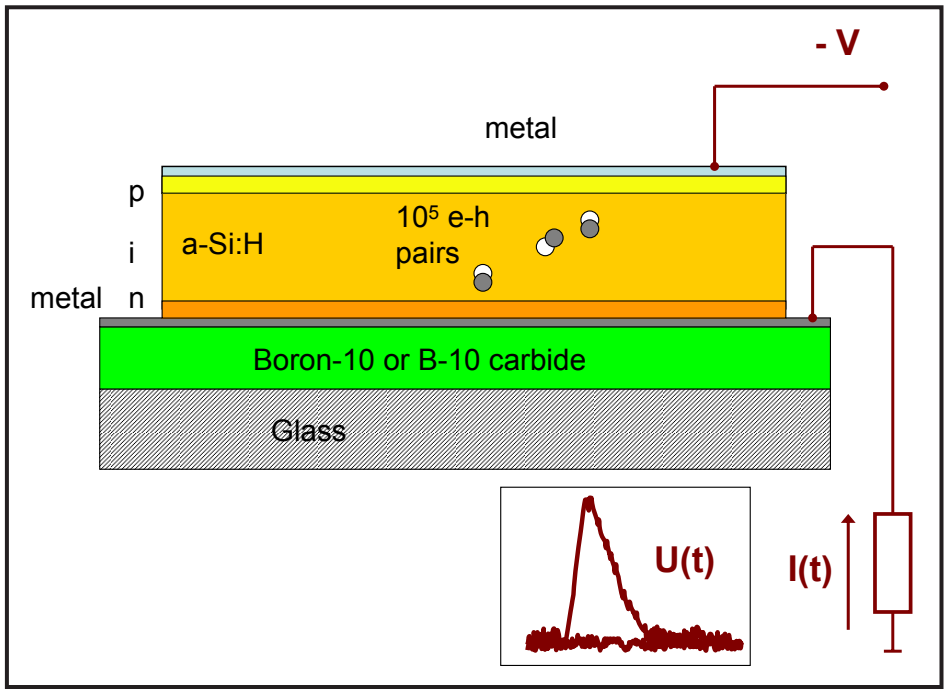

Figure 1. Illustration of the PiN diode structure being utilized

With this value in mind, the diode detector i-layer (the depletion layer in a basic PiN diode structure) thickness was determined to be about 2.4 μm by averaging the incident alpha particles over all incident angles. After approximately determining the diode thickness, it was evaluated whether such a diode can perform successfully as an alpha-detector. First, it was estimated whether a 2.4-μm-thick diode is fully depleted and thus has a uniform field in the i-layer. The depletion width in an a-Si:H (hydrogenous amorphous silicon) diode is given by:

$$W = \sqrt{\frac{2\varepsilon\varepsilon_o V}{eN_i}} = \sqrt{1.3\times10^7 V/N_i}(cm), \quad (1)$$

where:

W = depletion width

ε = permeability of free space

ε_o = relative permeability

V = voltage

e = charge of a single electron

N_i = defect concentration of atoms/cm^3.

Taking the midgap defect concentration $N_i \approx 1/3\ N_D \approx 10^{15}cm^{-3}$, we obtain for an applied voltage V = 10 V, a depletion width W ≈ 3.6 μm. Therefore, the depletion condition indeed is fulfilled at 10 V reverse bias. This diode also has high collection efficiency, as the drift lengths under 10 V reverse bias are about 100 μm for electrons and 20 μm for holes. Electron collection time is sufficiently short to produce individual rise times due to alpha particles as:

$$t_e = \frac{d}{v_{drift}} = \frac{d^2}{\mu V} \approx 10 - 100\ ns, \quad \textbf{(2)}$$

where:

t_e = electron collection time in ns

d = film thickness

v_{drift} = drift velocity in cm/s

μ = drift mobility

V = applied voltage.

One alpha particle produces about 10^5 electron-hole pairs in the i-layer, which amounts to Q = 16 fC charge of each type of carrier. This charge will most likely be collected by the diode capacitance C at first, giving rise to a voltage spike of $\delta U \sim \delta Q/C$. For the diode area of 4 mm^2, the capacitance of the diode (mostly geometrical, since it is fully depleted) is about 160 pF, and thus the voltage spike will be about 0.1 mV. At later times, the charge will dissipate through a load resistor or an external electronics circuit. Detection can be further improved by optimizing the external electronics.

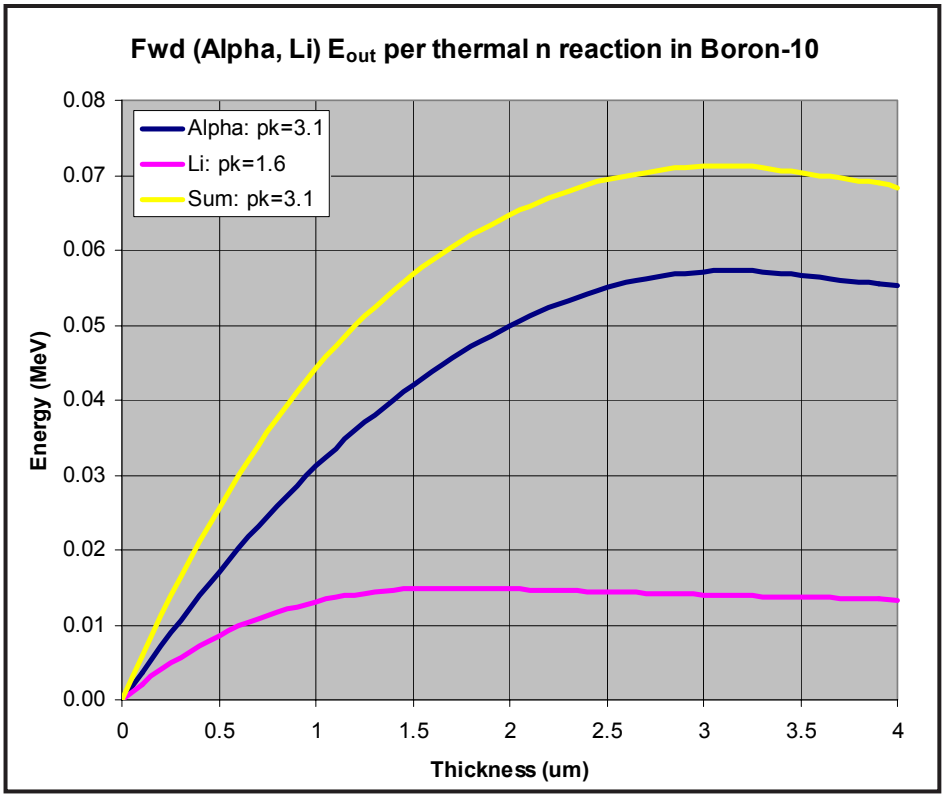

Figure 2. Escape energy of forward-directed alpha particle and Li ion per normally incident thermal neutron as a function of ^{10}B thickness

Device Preparation and Optimization

The device consisted of a-Si:H–based thin-film diode on metal-coated glass substrate. At the first stage, the boron layer was absent because the diode needed to be optimized as an alpha detector. The bottom metal contact was Cr, due to its good adhesion to glass and contact properties, and the top contact was Pd, known for its good contact properties to p-type a-Si:H and chemical/mechanical resistance. Electrode masks were designed and ordered for appropriately sized contacts. In addition, diodes of different contact area as well as series-connected diodes were produced.

Optimization Steps

We chose the value of diode dark current at a reverse bias of 10 V as the principal measure of the diode quality. We started from a standard n-i-p a-Si:H diode structure with standard trimethylboron (TMB) dopant gas used for p-layer deposition. This diode deposition mode yielded dark current densities (I_d) at –10 V that exceeded 10^{-9} A/cm^2, even though the i-layer was deposited at temperatures that minimized the midgap defect concentration (Figure 3, curve A). Two possible sources

of higher currents were considered: current spreading in the top p-layer (increasing the effective area of the diode), and a nonoptimized p-layer and p-i layer interface. The first possibility was addressed by reactive ion etching (RIE) of the diode using the top Pd contact as a natural mask to etch away any exposed conductive p-layer. This led to some improvement in dark current (Figure 3, curve B), but as the results were not consistent, we stopped using RIE. Therefore, we concentrated on the p-layer properties and, as the next step, introduced a carbon-graded buffer layer of a-SiC_x:H as a carrier diffusion barrier. This decreased the dark current (I_d) at –10 V to around 5 × 10^{-10} A/cm^2 (Figure 3, curve C). Finally, a carbon-alloyed p-layer deposited from a TMB and CH_4 mixture was introduced, and its thickness was increased to 25 nm. This optimization (C-graded a-SiC_x:H layer plus carbon-alloyed a-SiC_x:H p-layer) finally led to I (–10 V) values of 10^{-10} A/cm^2 (Figure 3, curve D). This result was similar to the best reported in the literature. These optimized diodes (without ^{10}B) were experimentally tested as alpha-detectors, and proved to be successful.

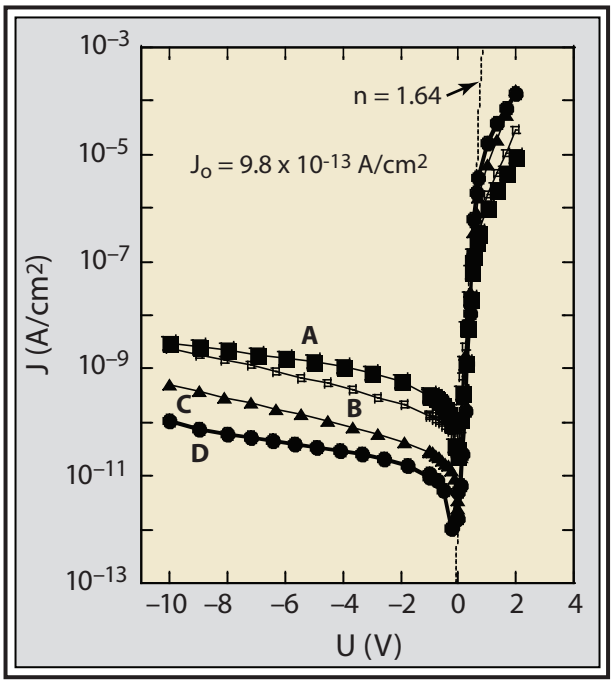

Figure 3. Diode I-V curves in different stages of optimization: (A) a standard n-i-p structure; (B) same, after reactive ion etching; (C) with graded a-SiC_x:H buffer layer between i- and p-layers; (D) with both a-SiC_x:H buffer layer and SiC_x:H B-doped p-layer

Boron Layer Depositions

Boron layer deposition was done by Thin Film Research, Inc., a company that specializes in sputtering. The first boron films on Corning 1737 glass had pinholes and cracks. It was established that most of these defects develop after sputtering, due to reaction of the sputtered layer with atmosphere, particularly with water vapor. Even packing the films in inert-gas-filled bags for shipping to NREL did not solve the problem. Figure 4 is a microscope photo of a ^{10}B-coated glass slide illustrating the poor surface quality. The next deposition involved capping the ^{10}B layers with a thin Cr layer while still inside the deposition chamber. Those films are much more stable and have no pinhole defects. Nevertheless, they still have cracks, likely from too high a deposition rate of nonoptimized substrate temperature, so depositing diodes on those films might be problematic.

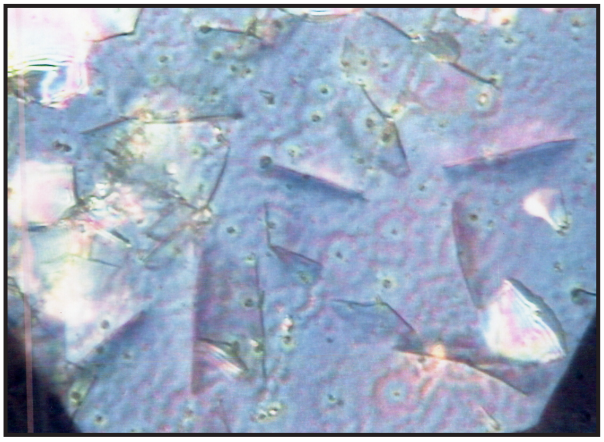

Figure 4. Microscope photograph of boron surface

A possible future step would be to evaluate ^{10}B carbide for sputtering because it is quite inert. The loss of density of boron atoms is fairly small since there are four boron atoms per every carbon atom. Dr. James Maxwell of LANL has successfully sputtered boron films for the National Aeronautics and Space Administration (NASA) that exceed the surface requirements for amorphous silicon deposition.

Diode Size Considerations

The absolute value of the leakage current of the diodes is proportional to the area of the diode. The induced noise current is proportional to the square root of the leakage current. Therefore, it becomes increasingly difficult to fabricate larger diodes with acceptable operating parameters. Sensitivity to neutron flux is directly related to the diode cross-sectional area. The use of many small diodes solves the problem of noise and capacitance that are directly related to diode area. However, every individual diode requires a separate preamplifier and comparator, creating a need for a very large number of circuits and connections. This requirement precludes the use of discrete circuitry except for small demonstration projects. Fortunately, there are some new technologies that can be utilized to produce large numbers of individual diodes with on-board integrated electronics at a very reasonable cost.

New video displays have been developed (but have not yet been mass marketed) using NREL's amorphous silicon technology that utilizes large, continuous-vapor-deposition processes to create video

displays that can be modified to become single-layer detectors. These displays can be made very large, exceeding one square meter, and can be fabricated for a few hundred dollars each. The fill factor for these arrays is very high; they are highly pixelated arrays with integrated electronics. By substituting a ^{10}B-coated substrate for the present one and modifying the integrated electronics, a single-layer neutron detector can be fabricated. The optical components could be eliminated and replaced with the amorphous silicon PiN diodes developed from this project. Multiple layers of these sheets could be laminated to produce a very sensitive neutron detector.

Conclusion

High-quality amorphous silicon PiN diodes have been developed in this project, and have been shown to be very good alpha detectors. Difficulties with sputtering ^{10}B have prevented the fabrication of a complete neutron detector to date. These diodes are compatible with large-scale continuous-vapor-deposition processes that have been developed for the next generation of video displays. Lamination of multiple layers of these sheets will create sensitive, low-cost neutron detectors of large area to meet the needs of many government agencies. The fast time response and fine pixelation will undoubtedly provide solutions for other problems, such as neutron imaging, that have not been supported by existing technology.

Acknowledgements

The authors would like to thank Paul Stradlins and Howard Branz of the NREL for their significant contributions in the design and fabrication of the amorphous silicon detectors.

this page intentionally left blank

Microchannel/Microsphere Plate (MCP/MSP) Detector to Measure Gamma Rays and Neutrons

Namdoo Moon[1]
Remote Sensing Laboratory – Andrews

Microchannel plate (MCP) technology has previously been used to detect ions, electrons, soft x-rays, ultraviolet photons, and neutrons. However, it is not an efficient detector for high-energy gamma-rays since the detector is very thin (about few hundred microns). This project focused on using a gadolinium-doped MCP with an attached NaI detector to develop a dual detector system to measure gamma and neutrons.

Background

MCP technology has continuously evolved, the latest innovations being microsphere plates (MSP) and microfiber plates (MFP). NOVA Scientific, Inc. (Sturbridge, MA), developed MCP technology using ^{10}B-enriched spheres, to sense neutrons more efficiently than a comparably sized ^{3}He detector (Tremsin, 2004, 2005). In neutron-imaging techniques, this technology has proven to offer higher resolution and greater efficiency than existing detectors. Our proposal adapts this technology to enhance combined neutron- and gamma-detection ability in an MCP/MSP system that includes a coupled NaI crystal. The prototype detector was designed, manufactured, and tested with nuclear instrument module (NIM) electronics (Figure 1). NOVA Scientific provided the MCP detector coupled with the NaI detector.

In this project, we proposed an initial study of an MCP/MSP system, mainly to measure gamma rays, but also to detect gamma rays and neutrons in one unit. Featuring a detector size of up to 10" diameter, this system would enable both gamma and neutron detection by a single system. Benefits include small size and light weight, possible cost savings over existing detector systems, ruggedness, and flexible shape. Differentiating gamma rays from neutron signals poses a challenge. In order to enhance the system's ability to detect high-energy gamma rays, scintillating material would need to be attached to it.

[1] moonn@nv.doe.gov, 301-817-3353

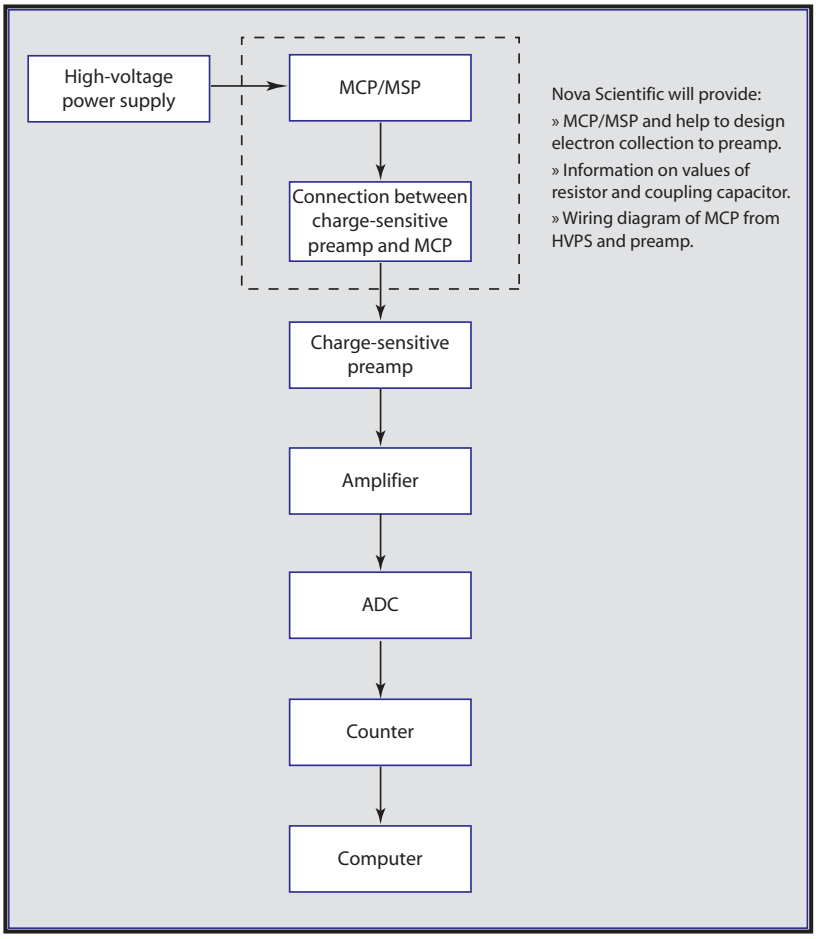

Figure 1. Overall electronics configuration

Project

For this project, we purchased and tested several NIMs (preamplifier, Canberra model 2005; spectroscopy amplifiers, ORTEC models 671 and 572A). NOVA Scientific, Inc., created a prototype detector assembly with the following features:

- The standard chevron MCP is replaced by a 25-mm-diameter, Gd-doped chevron
- A standard photocathode is included
- A 1" × 1" NaI(Tl) crystal is attached to the input window
- A high-voltage power supply can operate the tube to at least 2500 volts with 12-volt input
- The photocathode can be switched off with a high-voltage gating circuit
- Housing is made from Delrin plastic, FR-4 glass epoxy, and some metal screws and wire.

The detector assembly appears in Figure 2. The circuit board is designed to collect one signal (black wire) in the middle from 64 × 64 anodes from the MCP. The red wires are high voltages to the MCP and photocathode.

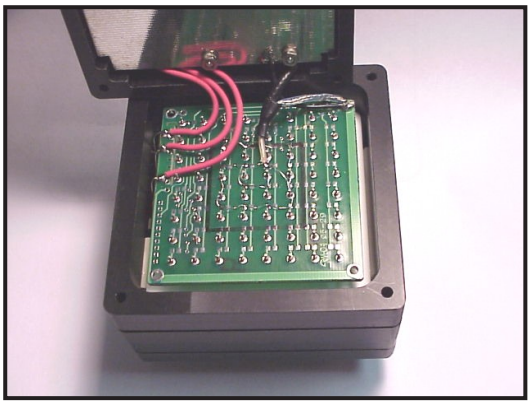

Figure 2. Circuit board inside detector

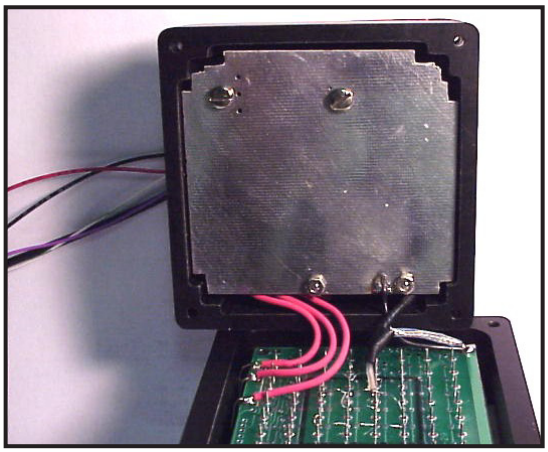

Figure 3. Behind the metal plate is high-voltage circuitry

The detector's high-voltage power supply (3500-V maximum) is behind the metal plate (Figure 3). The completed detector (Figure 4) has a 1" × 1" NaI crystal attached to the MCP through a photocathode gated by high voltage.

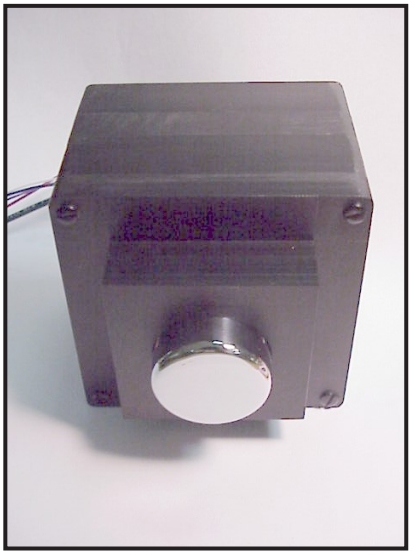

Figure 4. Front view showing 1" × 1" diameter NaI crystal mounted in the center of the package. Package size is 3.1" × 3.1" × 3.42" deep.

In Figure 5, the oscilloscope measured a typical signal at ~0.6 mV, with a 100-µsec pulse width at the preamplifier output. This signal is amplified by the spectroscopy amplifier (ORTEC 572A) to the multichannel analyzer (MCA).

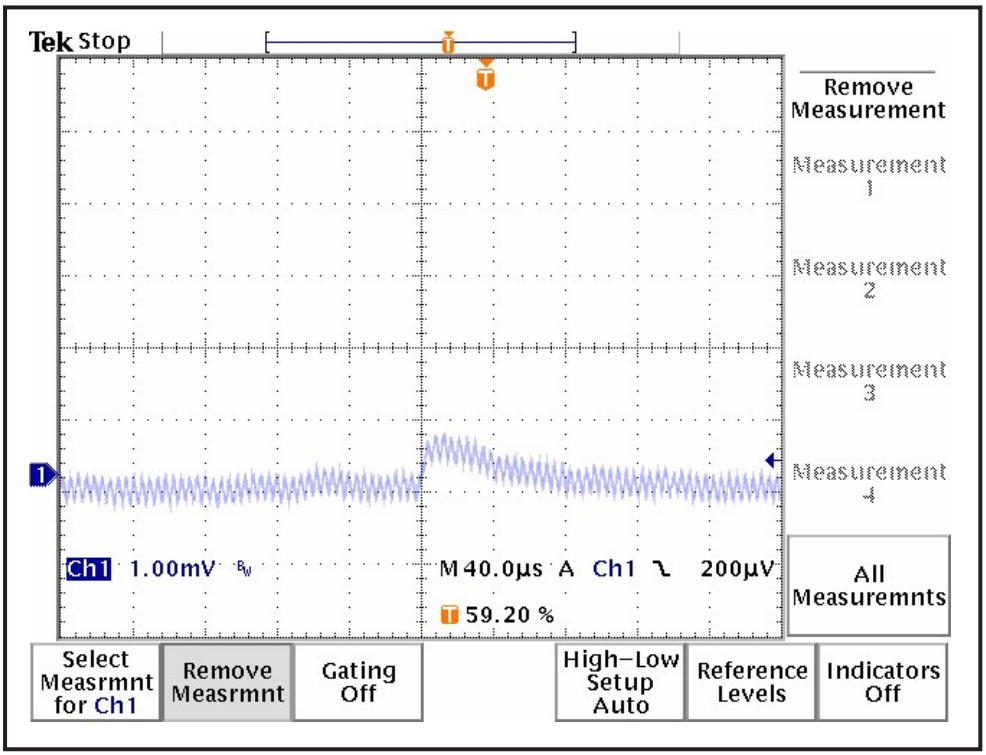

Figure 5. Preamplifier output signal at the oscilloscope

MCP gain was measured over a range in which the tube showed a gain of ~100,000. Although the voltage applied was above the usual level, the signal was shown without any distortion (Figure 6).

The MCP with the NaI crystal shows reasonable resolution at the ^{137}Cs peak (Figure 7). The typical photomultiplier tube (PMT)-based NaI crystal has been measured at about the same resolution range. Figure 8 shows the separate peaks of ^{57}Co signals at 122 and 136 keV.

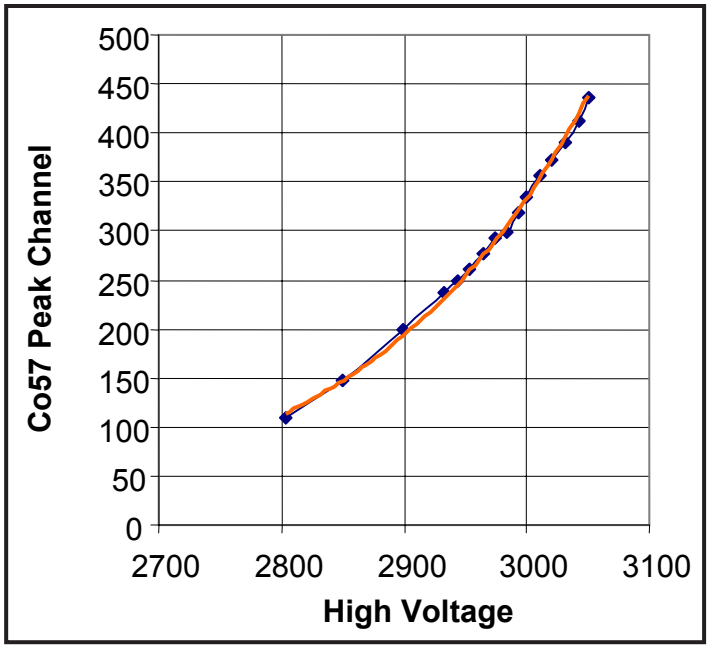

Figure 6. Gain vs. high voltage to the detector (^{57}Co peak channel)

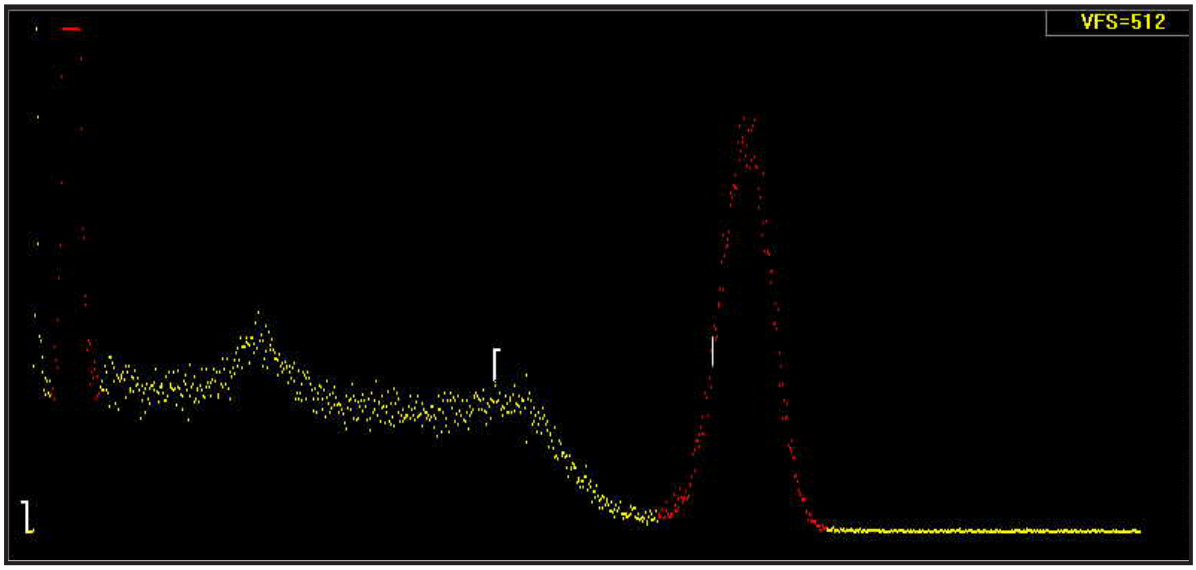

Figure 7. ^{137}Cs spectrum with resolution at 9.7%

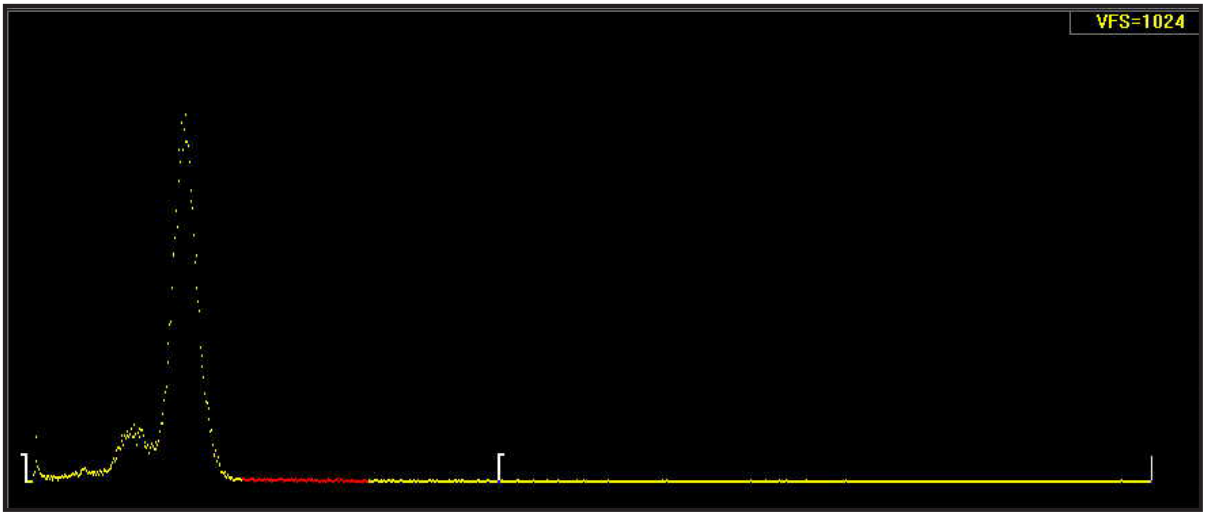

Figure 8. ^{57}Co spectrum with resolution at 16.5%

Conclusion

This MCP detector shows promising results with its spectra; however, it still must be characterized. The detector can be improved by using a Z-type MCP to raise additional gain. For neutron measurement, we did not complete testing because of time constraints and the lack of a strong neutron source at the laboratory. The next generation detector (MFP, ^{10}B-based) will soon be available from NOVA Scientific.

Acknowledgments

I greatly appreciate Ethan Smith for his efforts in measuring the spectra and Richard Maurer for his helpful advice.

References

Tremsin, A. S., W. Bruce Feller, R. Gregory Downing, "Efficiency optimization of microchannel plate (MCP) neutron imaging detectors. I. Square channels with ^{10}B doping," *Nucl. Instrum. Methods* **A539** (2005) 278–311.

Tremsin, A. S., W. Bruce Feller, R. Gregory Downing, David F. R. Mildner, "The efficiency of thermal neutron detection and collimation with microchannel plates of square and circular geometry," IEEE Nuclear Science Symposium, Rome, Italy, (October 2004) 1020.

Wide-Area Sensor Network

Sanjoy Mukhopadhyay,[1] *Andrew Murphy, Tricia Nix*
Remote Sensing Laboratory – Andrews

The technical concept for this wide-area sensor network has existed since the 1986 Chernobyl accident, which led a host of eastern European nations, including Hungary and Belarus, to develop a countrywide grid of sensors to monitor airborne radiation. Our team's objective was to build a fully developed radiological sensor network for real-time monitoring of environmental radiation levels, to provide data that would warn of and assess a nuclear event. Data communication among four sensor nodes, a prototype sensor node system, and an interface to map the sensors with a plume model were planned. Initially, we proved the concept that by connecting the nodes on a particular measured isopleth, one can accurately define the plume. Then we equipped four sensor units, each assigned a health-based risk factor, with a weather station and radiation-measuring equipment consisting of gamma, neutron, alpha, and beta counters.

Background

The advent of low-cost, low-power sensors; powerful, programmable sensor nodes; and maturing interconnection technology has led to an explosive growth in the use of sensor networks targeting a variety of distributed or remote sensor applications. One of the most important potential uses for such networks is in environmental monitoring.

Traditionally, this monitoring has been accomplished by either manual visits to the sensors or by constructing a custom network to automatically retrieve the data. Primitive by networking standards, these networks usually consist of a strict client-server model with unsophisticated protocols or interfaces. Since these networks are generally only utilized by a single researcher, other researchers cannot easily use established networks to transmit their own data. Therefore, one researcher's substantial time and equipment investment in building his/her own system is useless to his/her colleagues.

To address these problems with current sensor networks, we proposed to design and prototype a network that would deliver mobility, scalability, and extensibility, to service both a large geographic range and a broad variety of sensors and users. This network would permit environmental and agricultural researchers to easily link their distant sensors to our network, allowing them remote, reliable, real-time data access without concern for the underlying network.

[1] mukhops@nv.doe.gov, 808-474-2654

Project

Each sensor unit consisted of the following:

- Aware Electronics RM-80 radiation monitor with add-on fan
- Aware Electronics PMI-30 gamma ray counter connected to a NaI detector
- Aware Electronics PMI-30 neutron counter connected to a ^{3}He detector
- Sun Nuclear 1027 CRM radon monitor
- Aware Electronics LCD-60 module displays (3)
- Scientific Scales Vantage Pro Weather Link Station
- IBM ThinkPad T42 laptop installed with Windows XP
- Sierra Wireless AirCard 775.

Figure 1. Bottom layer of one sensor unit displaying two PMI-30 interfaces to NaI and neutron sensors containing ^{3}He

The RM-80 monitored the external add-on fan and detected alpha, beta, and gamma radiation, as well as x-ray radiation. The fan enabled radon gas detection. Using the Aw-Radw software provided by Aware Electronics, we set the time-base unit (TBU) to 60 sec and the Fact. Rad Calibration to 354. The PMI-30 was connected to both the NaI and ^{3}He detectors. The 1400-VDC PMI-30 was used with the 3" x 3" NaI detector to measure gamma counts. The 2000^{+}-VDC PMI-30 was paired with the ^{3}He to measure neutron counts. For both PMI-30 units, the TBU was set to 60 sec, and the Fact. Rad Calibration was set to 30000 for the 60-sec TBU with the Aw-Radw software. Figures 1 and 2 show the bottom and top layers of the assembled sensor unit. Figures 3 and 4 show the sensors' display of raw data, converted into dose rates.

Figure 2. Top layer of sensor unit displaying the 1027 CRM radon monitor (large box), three LCD-60 displays for PMI-30 and RM-80 sensors (L to R:) gamma, neutron, beta, and the RM-80 interface sensor (lower right)

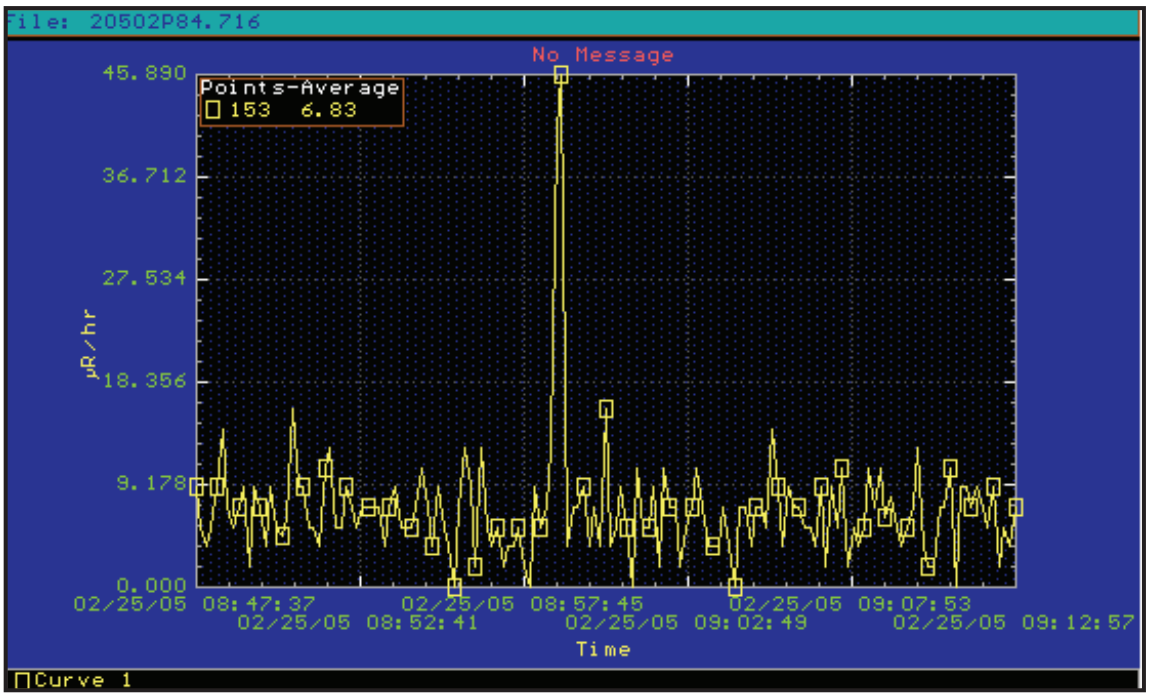

Figure 3. Gamma counts from ^{137}Cs converted into dose rate shown as a function of time, as a calibration source was moved in front of the 3" × 3" NaI:Tl crystal attached to the PMI-30 and a laptop. Background was recorded at ~7 µR/hr.

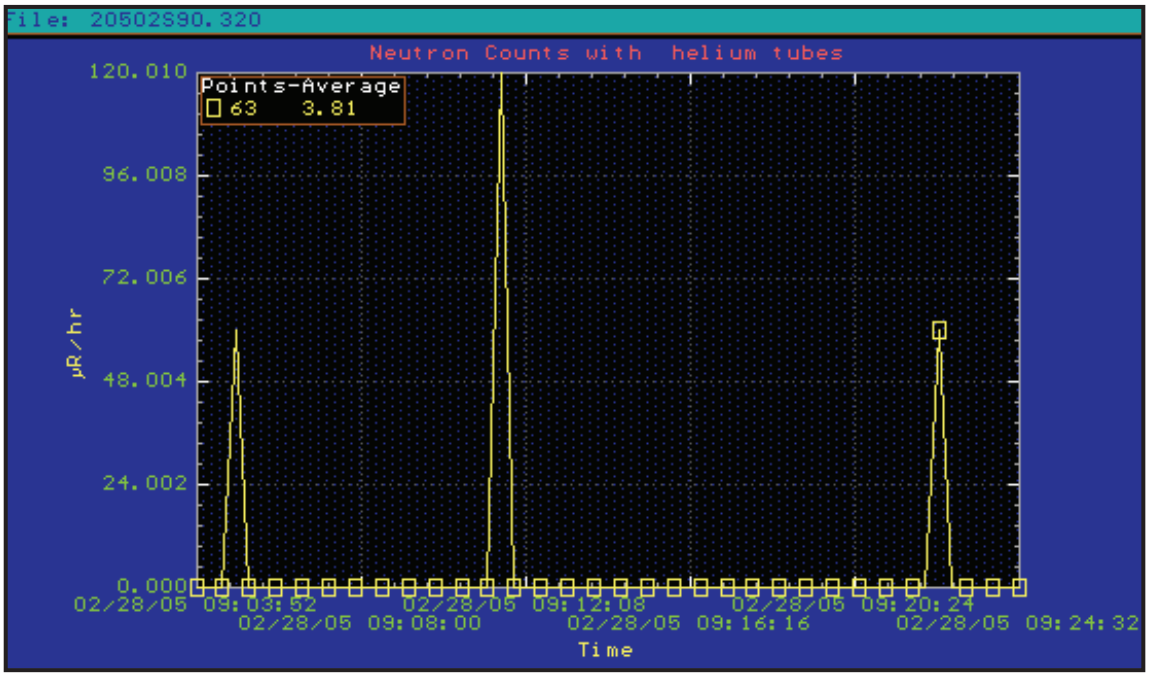

Figure 4. Neutron counts from a weak ^{252}Cf fission neutron source converted into dose rate shown as a function of time, as the calibration source was moved in front of the ^{3}He tube attached to the PMI-30 and a laptop

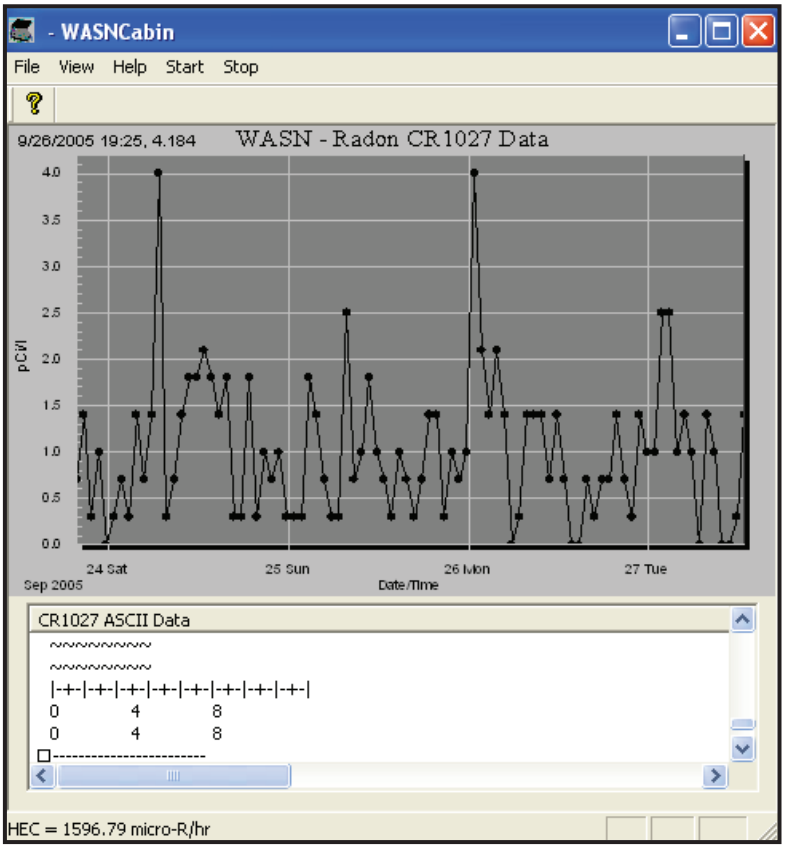

Figure 5. HEC of RSL office background

The Scientific Sales Vantage Pro Weather Link Station was selected to provide ambient temperature, wind speed and direction, humidity, and barometric pressure. It displayed inside and outside temperatures in degrees Fahrenheit or Celsius; inside/outside humidity in percentage; rain in inches or millimeters; barometer in inches, millimeters, millibar, or kiloPascal; elevation in feet or meters; and wind speed in miles per hour, knots, kilometers per hour, or meter/second.

We wrote a custom application to log and display data from the Sun Nuclear radon monitor. This application also allowed the user to input global positioning system (GPS) coordinates, and calculated, logged, and displayed the health effect coefficient (HEC).

Figures 5 and 6 are two snapshots of the interface. Figure 5 shows a background HEC of ~1500 µR/hr. Figure 6 shows an HEC of ~5400 µR/hr, with a small ^{137}Cs source, which was placed ~1 ft from the sensor unit.

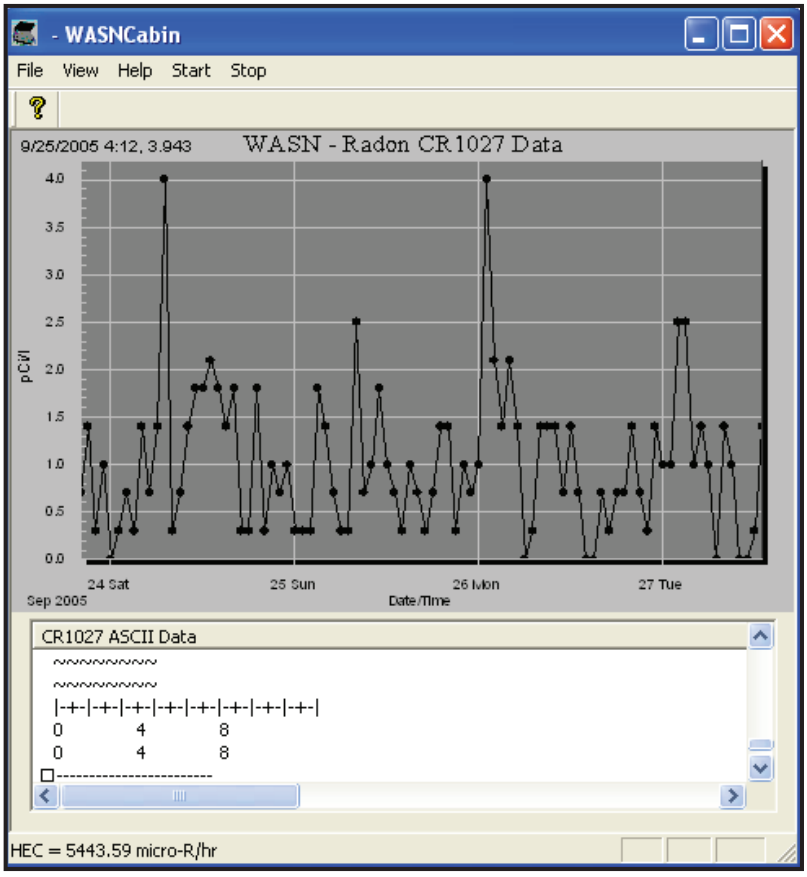

Figure 6. HEC in same office location, with 10 µCi ^{137}Cs source placed ~1 ft from sensor

Network Selection

A hybrid cluster-tree configuration combines mesh and star topologies. It is frequently the best solution for low-data-rate applications that require both long battery life at the node and high network reliability. Battery-powered sensors in a home or on one floor of a commercial building could be connected in a star topology to line-powered wireless appliances on each floor or in each home, then linked in a mesh topology.

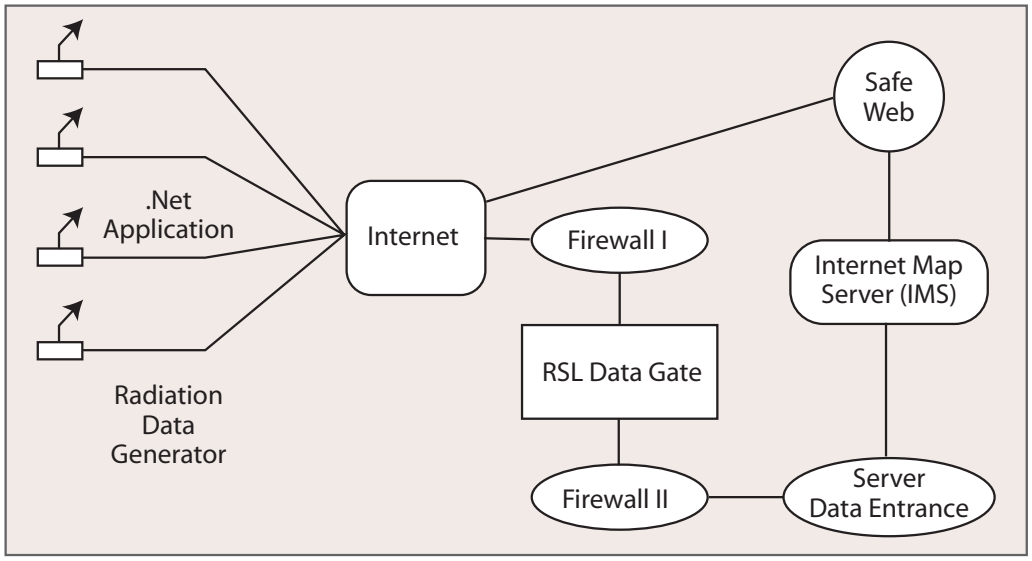

Figure 7. Radiation data presentation on SafeWeb.Net applications

A typical .Net application appears in Figure 7. Here, radiation data were brought into a data server outside the RSL Data Gate and moved through the firewalls using SafeWeb.

GIS-based Software

Our contouring algorithm, Inverse Distance Weighted (IDW), estimates cell values by averaging the values of sample data points in the vicinity of each cell. The closer a point lies to the center of the cell being estimated, the more influence, or weight, it has in the averaging process. This method assumes that the variable being mapped decreases in influence with distance from its sampled location. The simplest weighting function is inverse power: $w(d) = 1/d^P$, with P a user-specified value >0. By defining a high power, greater emphasis is placed on the nearest points, resulting in better detail. Specifying a lower power gives more influence to points further away, resulting in a smoother surface. Figure 8 shows contours from four discrete points.

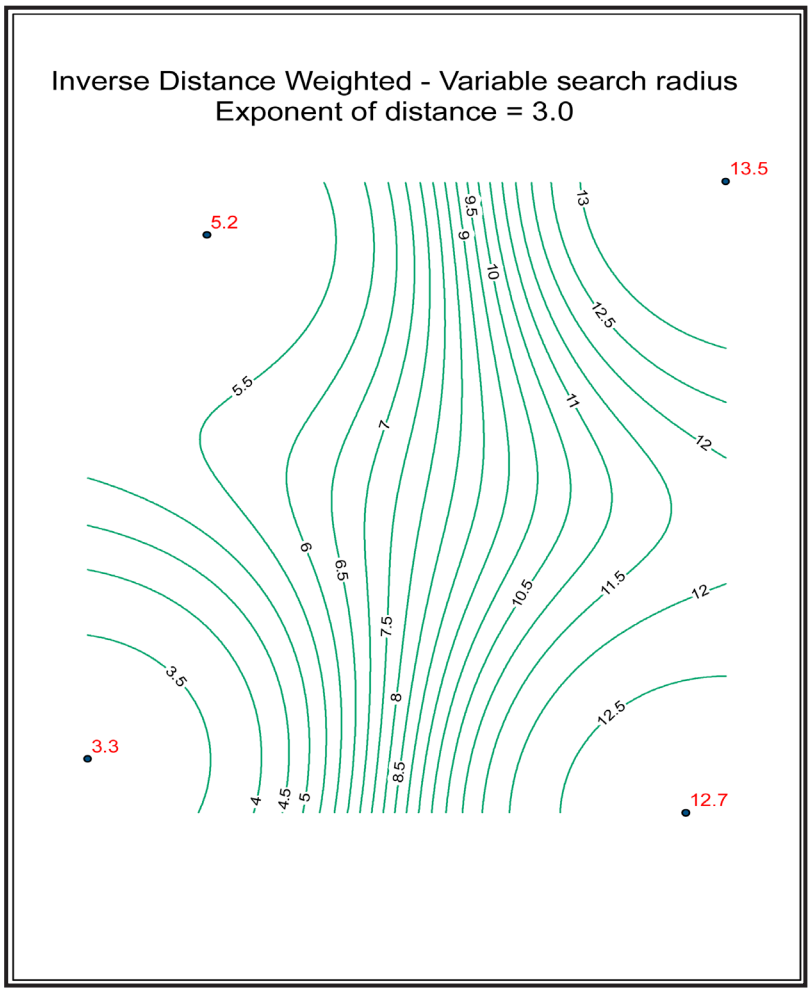

Figure 8. Contouring technique to draw isopleths over a region in which only discrete data points exist

Results

To prove the concept that collecting and analyzing radiological data acquired with a set of distributed sensors can define the plume from a localized or widespread release, we applied a National Atmospheric Release Advisory Center (NARAC) point grid to our contouring algorithm, IDW. This algorithm assumes that each measured point has a local influence that diminishes with distance. It weights the points closer to the prediction location greater than those further away, hence the name "Inverse Distance Weighted." Figures 9 and 10 show the original NARAC-generated contours and the contour map produced using the original NARAC data grid points.

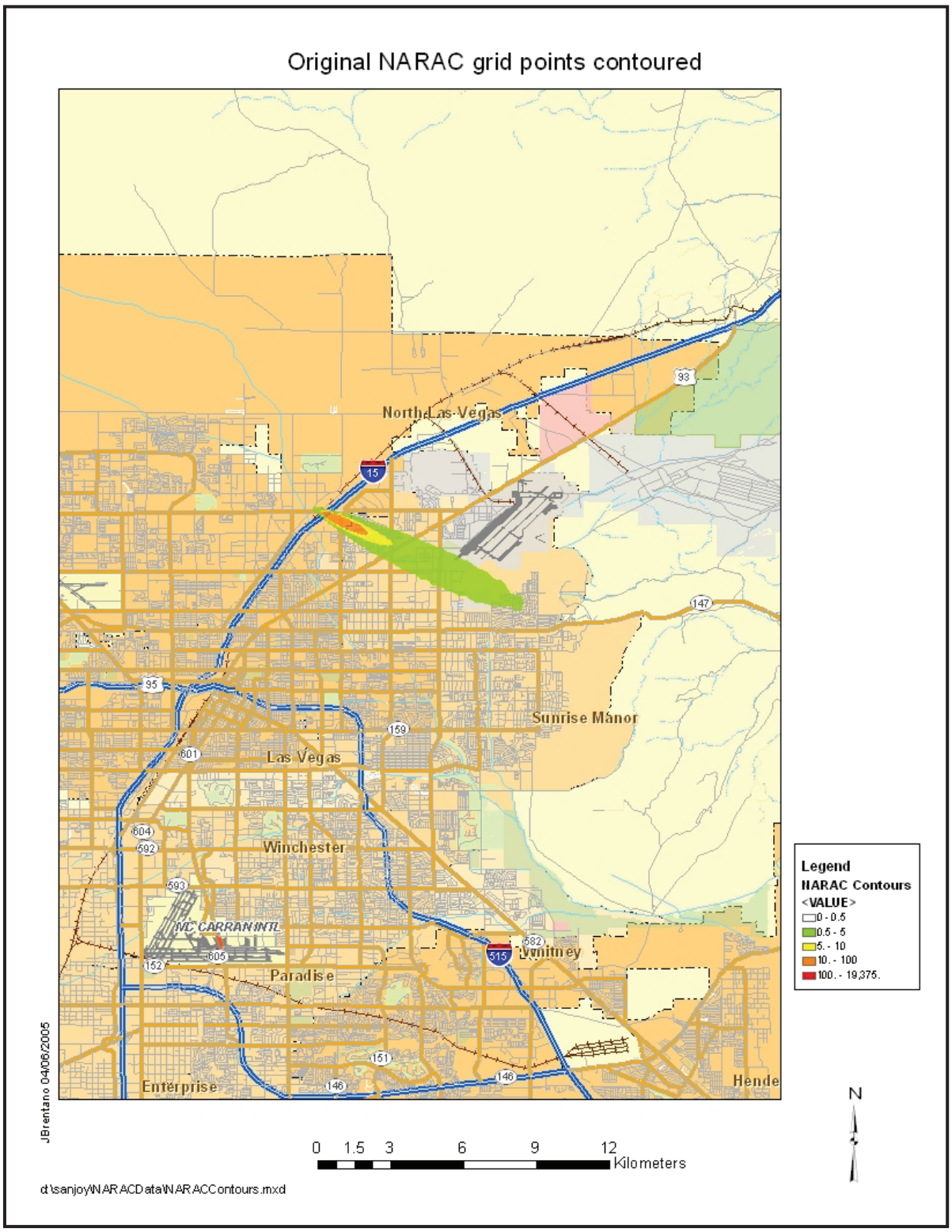

Figure 9. Contour map generated from NARAC grid points

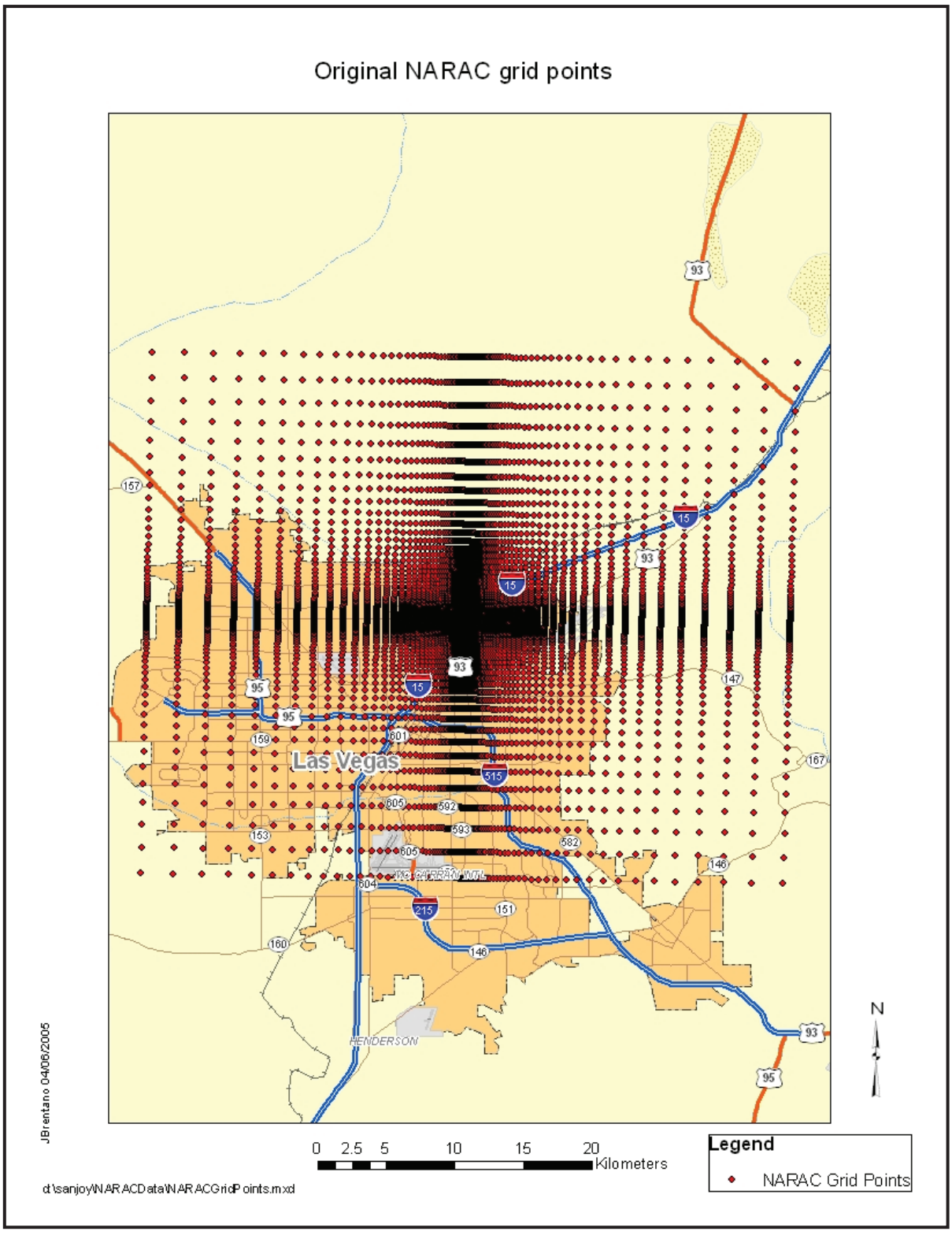

Figure 10. Original 19,600 NARAC grid points

Next, a small subset of 1148 data grid points was extracted from the original NARAC data grid points (~6% of original data). This subset was then contoured using the same IDW algorithm as applied to the original NARAC data grid points.

Conclusion

Our objective was to develop four sensor packages consisting of alpha, beta, gamma, neutron, and radon counters, and a weather station at different locations in remote areas. The data from each package would be continuously collected using a laptop. Each unit's HEC and GPS coordinates would be sent over air cards to a central fifth laptop. This laptop would display, analyze, and demonstrate results on a Geographic Information Systems (GIS) map, to define the plume from a localized or widespread release.

Our work proved that collecting and analyzing radiological data acquired with a set of distributed sensors can define the plume from a localized or widespread release. We assembled four complete units, each consisting of three radiation monitors, a radon monitor, and a weather station. Each node was assigned an HEC. HEC and GPS coordinates for each node would define one discrete grid point in the plume description. As shown previously, many sensor arrays (~1000) are needed to define the plume very well; but even with 50 units, a target area of one square mile can be monitored.

Acknowledgments

We would like to thank the following former BN employees for their work on this project: Josef Brentano, Ninfa (Lille) Guarrella, Robert Junker, and Dhiren Khona.

Germanium-Based, Near-Infrared Photocathode

Donald Ng[1]
Livermore Operations

Development of an infrared-sensitive photocathode based on germanium (Ge) was attempted. It was hoped that a narrow band-gap semiconductor such as Ge would yield sensitivity in the visible and near-infrared wavelengths to 1500 nm. Several photocathodes of varying thicknesses were deposited onto glass faceplates, but photosensitivity proved very low. After further testing, we have concluded that the deposited Ge photocathode is too thick for sufficient light transmission to the vacuum-photocathode interface. Further experimentation with thinner Ge photocathodes might yield more promising results.

Background

Image intensifiers, used in physics experiments to record data, can be made to operate in the visible, x-ray, and infrared spectra. The conventional infrared photocathode used in phototubes is the S-1 photocathode, based on AgO. However, this photocathode is sensitive only to 1100 nm and has a quantum efficiency (QE) of less than 1%. If a photocathode sensitive to 1500 nm existed, commercially available lasers operating in this longer wavelength would become viable in various physics experiments. Were the QE of such a photocathode a few percent, sensitivity over the S-1 would improve by an order of magnitude. Such photocathodes could be incorporated into phototubes used in optical pyrometry, VISAR laser calibration, temporal recording of events, and other applications requiring near-infrared sensitivity.

Inspiration for this project derived from the solid-state physics of Generation 3 photocathodes commercially available in image intensifiers (Csorba, 1985). These GaAs-based photocathodes achieve a high QE by lowering the electron affinity, the energy difference between the vacuum level and the bottom edge of the conduction band. This is accomplished by depositing a layer of Cs_2O several atomic layers thick onto a p-type GaAs substrate. The subsequent band-bending lowers the vacuum level to below the bottom edge of the conduction band of the GaAs substrate and creates a negative electron affinity, increasing the probability of electron emission into the vacuum. This augmented probability of electron emission increases the effective photoelectron diffusion distance from the surface of the photocathode surface and, subsequently, the QE. However, the band gap of GaAs is too wide to allow light detection with wavelengths longer than the visible spectrum. If a semiconductor with a narrower band gap can be selected, a photocathode with sensitivity in the near-infrared can be constructed. Germanium, with a band gap of 0.6 eV, can be excited with near-infrared radiation

[1] ngdp@nv.doe.gov, 925-960-2500

out to 1500 nm (Kittel, 1996). A drawback to using Ge is the high work function, the energy difference between the vacuum level and the Fermi level. Hopefully, a thin layer of Cs_2O on a p-type Ge substrate can lower the electron affinity sufficiently to allow photosensitivity with a QE higher than that of the S-1 photocathode.

Project

To fabricate our photocathode, a p-type Ge substrate had to be deposited onto a glass phototube window and coated with a thin Cs_2O layer. Since Livermore Operations does not have semiconductor processing facilities, a method was devised to accomplish the requirements of the photocathode with available deposition equipment. Pure Ge was deposited onto a glass window with a 1-A layer of Al embedded in the middle of the Ge. We originally planned to heat the deposited film in the evaporation machine under vacuum to allow diffusion of the Al throughout the Ge film thickness. However, procurement problems prevented us from following this plan. Instead, the photocathode substrate was placed in a processing oven and baked in vacuum at 375°C for 30 hours, our usual bakeout cycle. We hoped this would be sufficient to allow Al diffusion across the Ge film thickness. Since it was not possible to deposit Cs_2O directly onto the Ge film, we formed this layer by first oxidizing the film's top surface, then reacted this oxide with Cs to form Cs_2O and reduce the GeO_2 to Ge. We performed oxidation by heating the photocathode substrate in the presence of oxygen. Cs was deposited onto the oxidized surface of the Ge, and photoemission was monitored while the photocathode was illuminated with white light. Figure 1 illustrates the processing steps.

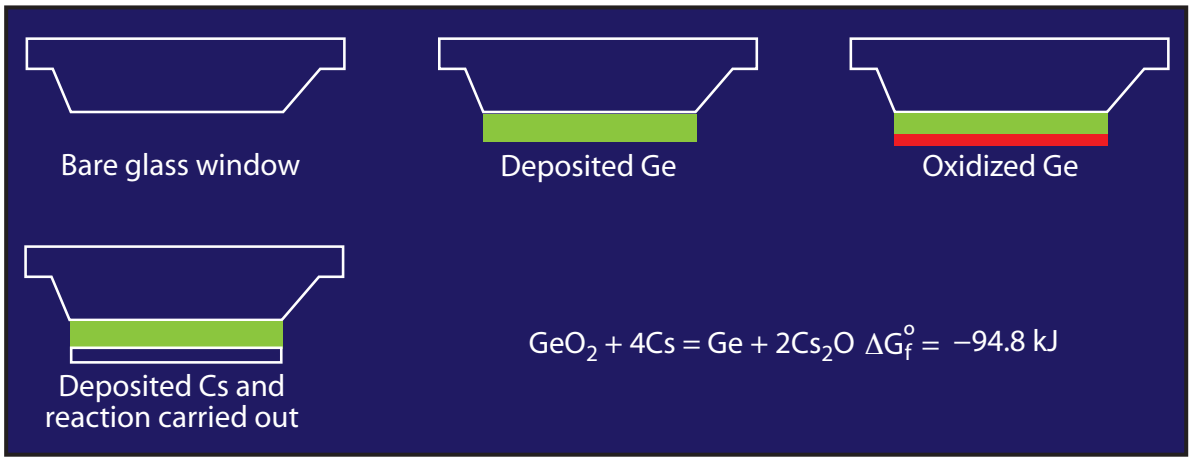

Figure 1. Germanium deposition and processing

To control oxidation of the Ge top surface, temperature and time at temperature must be controlled. This proved to be difficult with our equipment because of the large thermal mass of the vacuum chamber and oven used for photocathode processing. Nevertheless, a 500-A layer of GeO_2 was successfully grown, consuming half of the 1000-A Ge base in a trial with pure Ge. Figure 2 shows a secondary ion mass spectrometry (SIMS) analysis of an oxidized Ge layer.

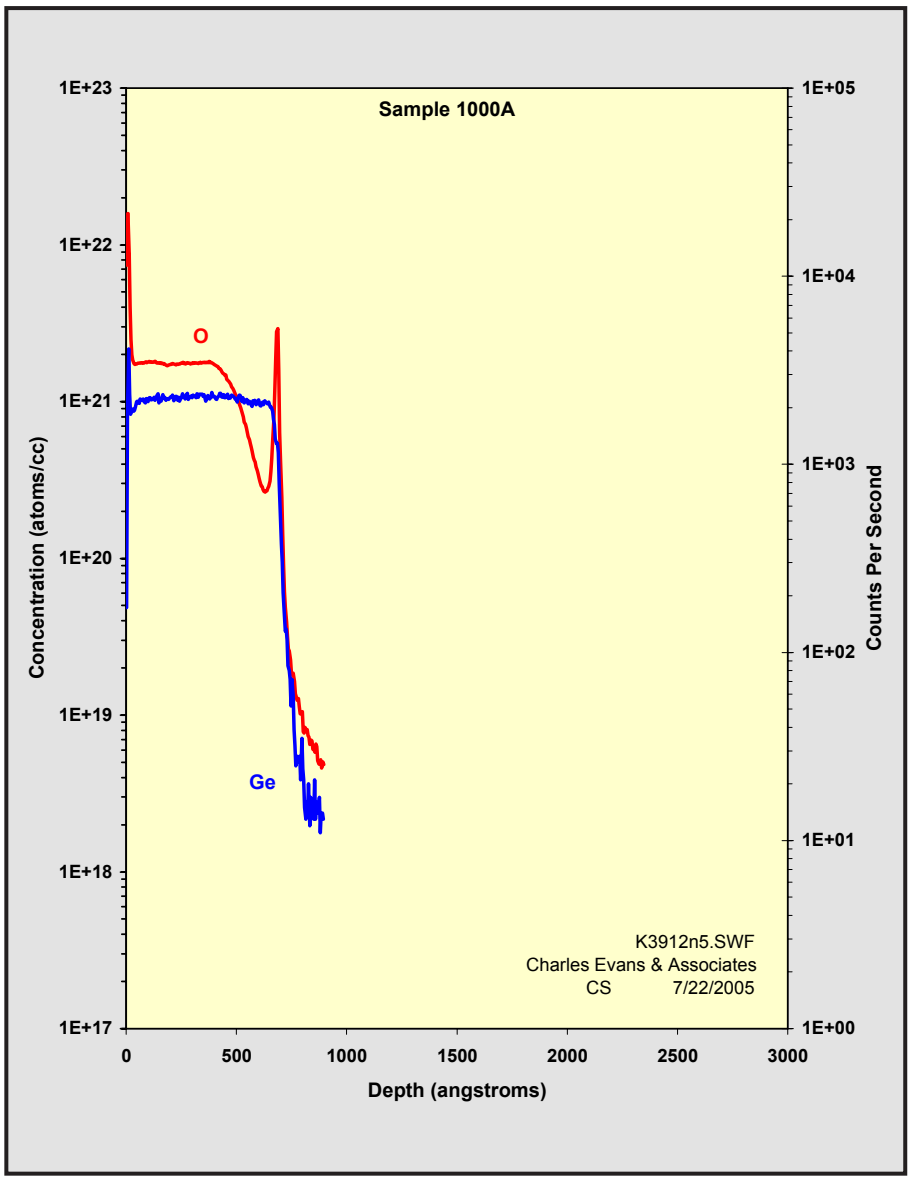

Figure 2. SIMS profile of oxidized 1000-Å Ge film

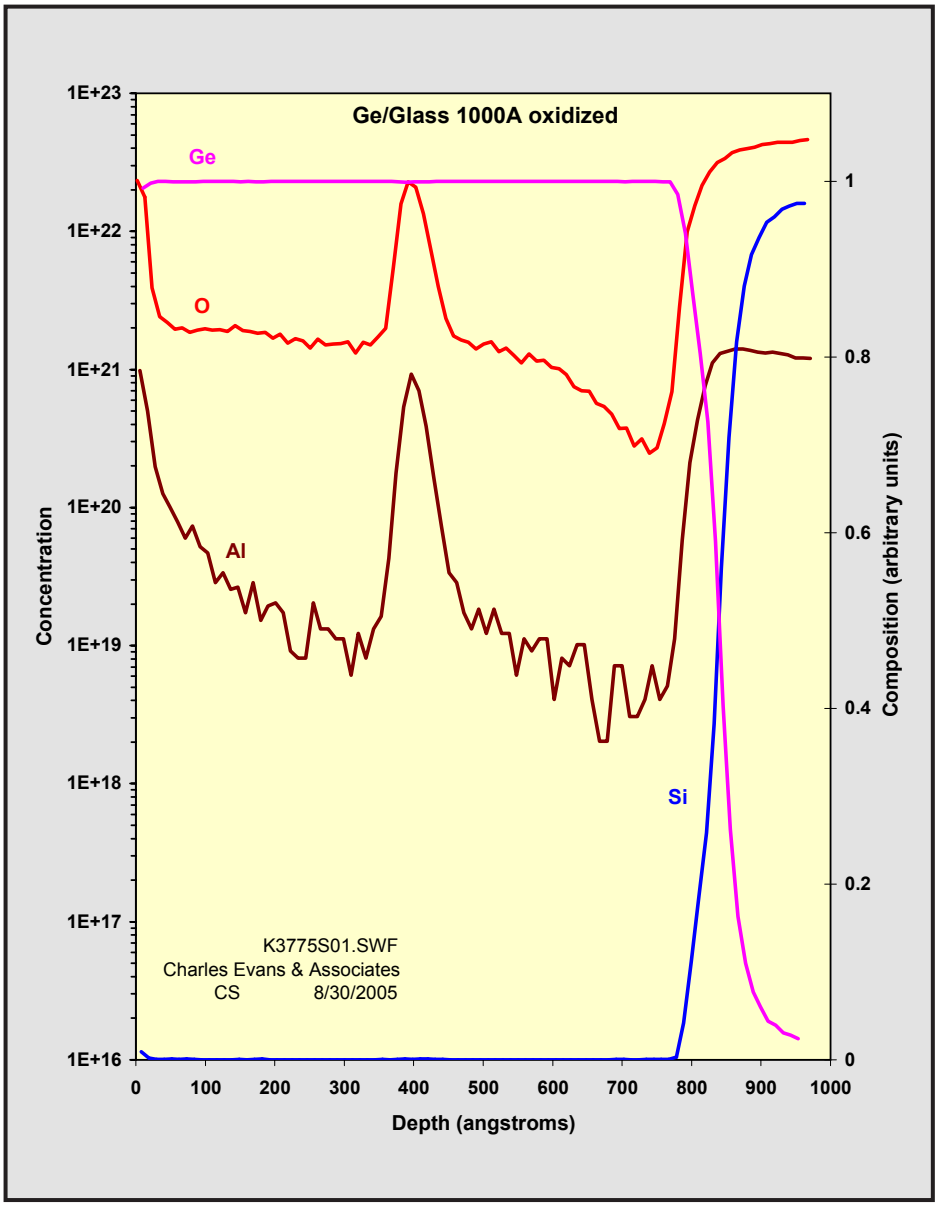

Figure 3. SIMS analysis of Al diffusion in Ge layer

Initial attempts at processing a photocathode used a Ge thickness of 1500 A, sandwiching a 1-A layer of Al in the middle of the Ge films. The photocathodes were oxidized in a low-pressure, ~250-mtorr oxygen atmosphere heated to ~300°C, then allowed to cool overnight. Cs was deposited at 140°C the following day and the reduction of GeO_2 proceeded, while photoemission was monitored as the photocathode was illuminated. The reduction reaction (Brandes, 1999; Lide, 2004) is:

$$GeO_2 + 4Cs = Ge + 2Cs_2O \quad \Delta G_f^\circ = -94.8 \text{ kJ}. \qquad (1)$$

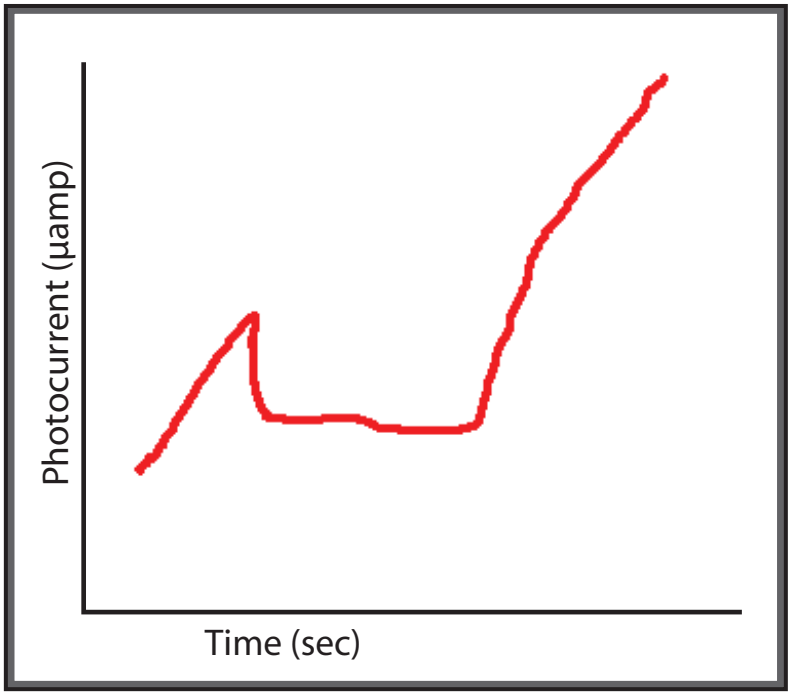

Figure 4. Photocurrent as reaction proceeds during Cs deposition

The photosensitivity of the resulting photocathodes was almost nonexistent. The thickness of the Cs_2O layer depends on the thickness of the GeO_2 layer, over which we had little control. Another potential problem was realized in the form of the Al dopant. Ideally, ion implantation would be used to dope the Ge with Al or B to produce a p-type semiconductor. Such equipment was not available, however, so a more primitive doping method was performed: depositing Ge and Al in sequence to sandwich a 1-A Al layer in the middle of the Ge photocathode layer. Heating at a high temperature for a long time would allow diffusion of the Al across the thickness of the Ge film, lowering the concentration of the Al in the Ge to dopant levels. If sufficient diffusion did not occur, small pockets of high local Al concentrations could adversely affect Ge oxidation because the Al would behave as an oxygen-getter. SIMS analysis of a 1000-A-thick photocathode confirmed that the Al did not diffuse sufficiently across the thickness of the Ge layer in our processing oven (Figure 3).

Lacking the capability of doping a Ge thin film with Al by diffusion, the experimenters located a source of doped Ge material that could be applied evaporatively. A 1200-A thin film of Ge doped with 0.05% boron was evaporated onto a glass window and processed according to the procedures developed. After oxidation, Cs was deposited and allowed to react with the germanium oxide. After sealing the photocathode in vacuum to a phototube body used for testing, light sensitivity was observed with white light. The 50-mm window yielded a photocurrent of about 0.25 µA when illuminated with white light from a tungsten halogen lamp bulb. However, when tested with a

Gamma Scientific GS4100 radiometer, no photo response was detected. We determined that the light source for the GS4100 was less intense than the lamp used for photocathode illumination during Cs deposition and reaction, indicating that the Ge layer is too thick for good transmission of light through the photocathode to the photoemissive surface. For an opaque photocathode, this would not be a problem, but for a transmissive photocathode, light must travel through the thickness of the photocathode film to produce photoelectrons near the vacuum-solid interface of the photocathode. Experiments with thinner Ge layers were not performed, but photosensitivity was demonstrated, and photocurrents of less than 1 μA were measured with white light.

In all the photocathodes processed and reacted with Cs, we found one surprising result. While depositing Cs onto the germanium oxide surface and allowing the reduction reaction to occur, we shone light onto the photocathode through the glass window substrate on which the Ge was deposited. A metallic ring near the photocathode surface was biased with a positive voltage; any photoelectrons emitted during the reaction were collected and measured. As the deposition of Cs onto the photocathode began, the photocurrent began to rise, then fell and stayed constant for a short time, then began to rise again (Figure 4). This response is very similar to the photocurrent measured during the processing of a silver-based S-1 photocathode. Unlike an S-1 photocathode, the endpoint to stop the deposition of Cs onto the germanium oxide is unknown, and several experiments were carried out to determine an appropriate endpoint, but the results were inconclusive.

Conclusion

A photosensitive photocathode based on Ge was fabricated and demonstrated submicroamp photocurrents. However, several problems experienced during the development of this photocathode must be overcome before its sensitivity will be adequate for use in a phototube. The controlled oxidation of the Ge layer or the ability to deposit a thin layer of GeO_2 must be resolved. An optimal thickness of the base Ge layer must be determined to allow sufficient light transmission through the photocathode to produce photoelectrons near the photocathode-vacuum interface, but still sufficiently thick to absorb most of the light incident on the glass window. Finally, the optimal endpoint at which to stop Cs deposition and the period of bakeout required after Cs deposition need to be determined. Once these parameters are investigated, a repeatable process can be employed to produce photocathodes that can be used in existing and future phototubes.

References

Brandes, E. A., ed., *Smithells Metals Reference Book*, 7th ed., Butterworth-Heinemann, Boston, 1999.

Csorba, I. P., *Image Tubes*, Howard W. Sams, Indianapolis, Indiana, 1985.

Kittel, C., *Introduction to Solid State Physics*, 7th ed., John Wiley & Sons, New York, 1996.

Lide, D. R., ed., *Handbook of Chemistry and Physics*, 85th ed., CRC Press, New York, 2004.

Production and Calibration of an Improved, Wide-Band X-ray Detector

Donald G. Pellinen[1]
Livermore Operations

Large fusion facilities, including the National Ignition Facility (NIF) and Omega, use a time-resolved x-ray spectrometer to provide information on energy coupling, radiator efficiency, and energy yield from fusion shots. Accurate interpretation of this data depends critically on x-ray diagnostics in the 200–500-eV energy range. There is a need for a simple, accurate, and absolutely calibrated x-ray detector for measuring this energy range (where the majority of energy transfer occurs in a fission reactor). Cross-checks of a National Institute of Standards and Technology (NIST)–calibrated detector with units calibrated at the National Synchrotron Light Source yielded 10–20% discrepancies in the energy range below 500 eV. This project designed a microcalorimeter according to microelectronic manufacturing methods that could potentially provide accuracy and capability in this limited shot range, and possibly reduce the range of uncertainties to <2%.

Background

Most radiation detection work is directed toward medical or biological applications. Such applications measure "dose," or energy absorbed per unit mass. This is significant within the context of biological applications, since tissue damage to a first order is proportional to dose. However, dose measurements supply little or no information about the nature of the radiation. For scientific applications, it is more important to measure the incident power or energy-per-unit area—also called flux, or fluence. The most direct way to gauge fluence is to put an isolated absorber with a known heat capacity in a given beam and measure the temperature rise. The only requirement is that the energy be fully absorbed. Calibration simply involves calibrating the voltage output of the sensor-versus-power input. The most accurate and sensitive instrument for this measurement is a "cryogenic calorimeter," which operates very close to absolute zero (Jochum, 2006; Preztl, 2005). Several such calorimeters have been built for measuring low-energy x-rays but, judging from the infrequency of use, are very difficult to operate. Thus, they are not a useful working standard for everyday use.

A silicon (Si) diode detector is currently the most used reference standard for measuring low-energy x-rays, with sensitivity quoted at 1 electron-hole pair at ~3.7-eV energy losses. However, a number of trade-offs in its manufacture can affect accuracy, especially at low energies or near absorption edges. For example, a window is required to protect the Si from radiation contamination that can change

[1] pellindg@nv.doe.gov, 925-960-2575

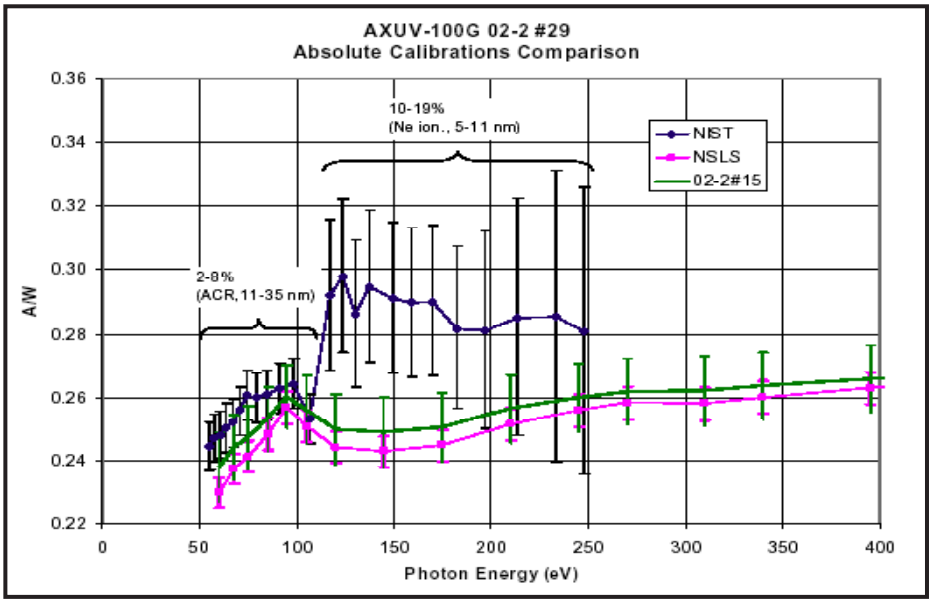

Figure 1. NIST calibration responsivity for AXUV-100G 02-2 #29, compared with #29 and #15 diodes from the same batch (Keister, 2004)

its characteristics. One such detector was calibrated by NIST, with an accuracy quoted at ±3–16% (Figure 1). This project intended to build a calorimeter that had high sensitivity, operated at room temperature, and was simple and straightforward to calibrate and run.

Project

Previous work generated a combination x-ray calorimeter to measure the fluence from a flash x-ray machine (Pellinen, 1972). For this project, I decided to build a very thin, small calorimeter detector using integrated circuit manufacturing techniques. A small design would increase accuracy and ease production in quantity. A few rules of thumb are useful in designing a calorimeter system. The lowest heat capacity that will still absorb x-rays will yield the highest sensitivity, since there is less material to heat. When a thermistor-type sensor is built, semiconductors have a higher temperature coefficient of resistivity than metals. Also, a semiconductor diode has a temperature coefficient of ~2 mV/°C (Guru, 2006). If diodes were built into a temperature sensor, and the bias voltage only slightly exceeded the diode voltage of 0.6 V at room temperature, little self-heating would occur. Also, heat capacity on most materials (~0.6 cal/ml) is proportional to volume. X-ray absorption is proportional to the mass per unit area and is a strong function of atomic number. Therefore, the absorber should have a high atomic number (e.g., Au), and material thickness should be as thin as possible while still completely absorbing radiation at the energy of interest.

Accordingly, a microcalorimeter design was reached with the following characteristics:

- Mounting was to be in a CERQUAD header (identified and purchased before design was started).
- Sensor was to be Si; first try was as a thermistor on a silicon dioxide–insulated wafer coated with polysilicon, with a layer of Au ~4 μm thick for the contacts. The readings were erratic, probably because the coating was not diffused into the polysilicon at the interface. In the future, a diode could be built as the temperature sensor.
- Device was configured as two identical detectors: one exposed to radiation, the other a reference.
- Device would be mounted on silicon dioxide film.
- Si diode would be used as the temperature sensor; further testing could confirm or deny this supposition.
- Each detector would have two loops of polysilicon, one as the temperature sensor, the other as a resistor over which an accurately measured current would flow. This would allow in situ calibration to be performed before and after exposure. It was anticipated that this calibration would be accurate to a small fraction of 1%.

Semiconductor manufacturing procedures differ from those of normal, macroscopic, large-scale manufacturing. Part of the semiconductor manufacturing procedure is defining process flow and designing photomasks to pattern the various layers. To build a device, one specifies a step. If a deposition is required, one specifies film type, thickness, and characteristics. Film shaping is a multistep process. A film of photoresistant material is put on the wafer with the area beneath unprotected. The film is exposed to light through a photomask that leaves a pattern. If a "positive" photoresist is used, the photoresist will be removed by the developer in the areas where it is exposed to light. If an etch chemical or plasma is applied to the wafer, areas unprotected by the photoresist will be etched away. If a LIGA (Lithographie, Galvanoformung, und Abformung) lithography and electromechanical forming process is used, material will be electroplated into the area unprotected by the photoresist.

After conferring with the vendors who would convert the Si wafers into microcalorimeters, we agreed to the process steps illustrated in Table 1. Starting materials were wafers with 2, 5, and 10 μm of silicon dioxide on the front and back surfaces.

Table 1. Advanced x-ray detector process steps

STEP	PROCESS	MASK NO.	MASK TITLE
1	Polysilicon deposition 1 µm		
2	Spin photoresist both sides		
3	Mask backside	6	Backside opening
4	Etch poly to clear		
5	Etch oxide to clear		
6	Strip photoresist***		
	Etch 3 wafers with 2, 5, and 10 µm silicon dioxide; etch through with KOH and check film integrity; do not process rest of wafers until each film is checked		
7	Spin photoresist front side		
8	Mask temperature sensors	1	Temp sensors
9	Etch poly to clear		
10	Strip photoresist		
11	Spin photoresist		
12	Mask, Temp sensor traces	2	
13	Implant 5×10^{14} Phosphorus/cm^2 @ 40 KeV		
14	Hf dip		
15	Evaporate 2000 Å Al		
16	Strip resist and excess metal		
17	4000 Å, CVD oxide		
18	Anneal 450 deg 1/2 hrs		
19	Spin photoresist		
20	Mask 3	3	Temp sensors pads
21	Etch pads open, plasma		
22	Strip photoresist		
23	Mask 4	4	
24	Evaporate 200 Å Ti, 2000 Å Au		
25	Strip photoresist and Au		
26	LIGA Mask	5	LIGA mask
27	Electroplate 4 µm Au	****	
28	Etch backside with KOH to silicon dioxide		
	***Etch 3 selected wafers through to demonstrate device functionality		
	****Other vendor		

Conclusion

The full photomask set and manufacturing process flow were designed for a thermistor-type temperature sensor. Calculations indicate that a diode sensor would be more sensitive and have lower self-heating than a thermistor sensor. Silicon dioxide–coated Si wafers were purchased and deposited with polysilicon to form the temperature sensor and heater for a diode detector. The ceramic housing for a microcalorimeter and a nanovoltmeter to read output were located and purchased. Process steps were agreed to by potential vendors, who would convert Si wafers into microcalorimeters.

References

Guru. B. S., "Notes on Semiconductor Diodes," Kettering University, Flint, Michigan, http://www.kettering.edu/~bguru/DIODE/Diode-02.pdf, accessed May 2, 2006.

Jochum, J., "Cryogenic Calorimeters: Principles and Applications," Technical University, Munich, Germany, http://lappweb.in2p3.fr/Calor2000/Contributions/Bolometry/J_Jochum.PDF, accessed January 5, 2006.

Keister, J., "Silicon Diodes, Experiences and Guidelines," Brookhaven National Laboratory, Upton, New York (2004). Copies of unpublished report available by contacting jkeister@bnl.gov.

Pellinen, D. G., "Small Combination X-Ray Calorimeters," *Rev. Sci. Instrum.* **43**, 8 (August 1972) 1181–1184.

Preztl, K., "Calorimeters in astro and particle physics," *J. Phys. G* **31**, 7 (July 2005) R133–R149.

this page intentionally left blank

Neutron Directional Detector

Michael Mendez, William Quam[1]
Special Technologies Laboratory

This project explored the concept of a directional detector based on self-absorption in a closely packed array of square, gas-filled proportional counters. Each counter was filled with a mixture of xenon (Xe) gas and ^{3}He, resulting in sensitivity to both gammas and neutrons. An array of counters was fabricated and tested for angular response. Neutron response was measured in a highly scattering environment, similar to that of an office building. This array was also modeled with Monte Carlo N-Particle (MCNP) code, and the results compared to the measured values. The angular responses for gammas and neutrons were found to be simple functions of angle over a 45° range. Since the array is symmetrical, this function can be readily translated into other quadrants. The angular errors found were approximately ±7°. Additionally, the minimum detectable activities (MDA) were determined for both gamma and neutron sources.

Background

In an FY 2003 SDRD project (Quam, 2004), a proportional counter filled with Xe and ^{3}He gas was examined to determine if it could provide signals easily separable into gamma and neutron responses. This successful attempt also showed that the low-energy gamma resolution was sufficient to enable identification of some SNM (^{235}U) and most medical isotopes. Surprisingly, neutron sensitivity was enhanced by the addition of Xe gas.

Concurrent research activities resulted in the development of a gamma directional detector based on cesium iodide (CsI) scintillators. Soon after this technique was proven, we proposed adding a neutron array around the square CsI scintillator array to provide both gamma and neutron directionality. This became the basis for the present study, with the added innovation of dropping the CsI and using rectangular proportional counters with dual gas fill for detecting both gammas and neutrons. This form factor minimizes the number of counters and electronics needed for adequate angular sensitivity.

[1] quamwm@nv.doe.gov, 805-681-2465

Project

Mechanical Arrangement of Detector Tubes

As shown in Figure 1, twelve 1-inch-square detectors filled with Xe and ^{3}He gas were assembled in an array of four tubes on each side with a hollow core in the middle. These tubes were used without a neutron moderator. The hollow 12-detector array weighed 2500 g (5.5 lbs) complete with all electronics, except for batteries and digital recorder. The array is ~4 in. square and 12 in. tall (including the electronics).

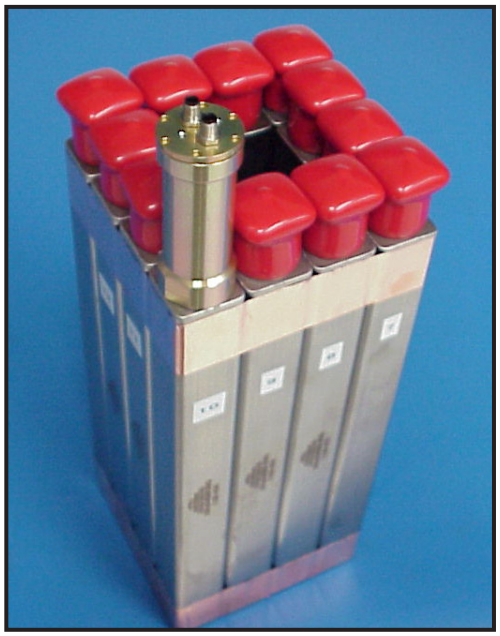

Figure 1. Array of 12 detectors with electronics module attached to one

Figure 2 shows the array in plan view, as though one were looking down on the detectors. The detectors are numbered clockwise from 1 at the upper left, with the 0° direction between detectors 5 and 6. The neutron source is 2 m from the array center.

Since the array is symmetrical, measurements and calculations were performed only for the 45° sector between the source direction and detector 4 on the upper right corner. During testing, the array was rotated clockwise from the 0° position shown above. In practice, the correct sector is determined from the corner detector having the largest counting rate. Once this sector is known, the directional determination follows the simple methods outlined later in this report (e.g., Figures 3 and 4).

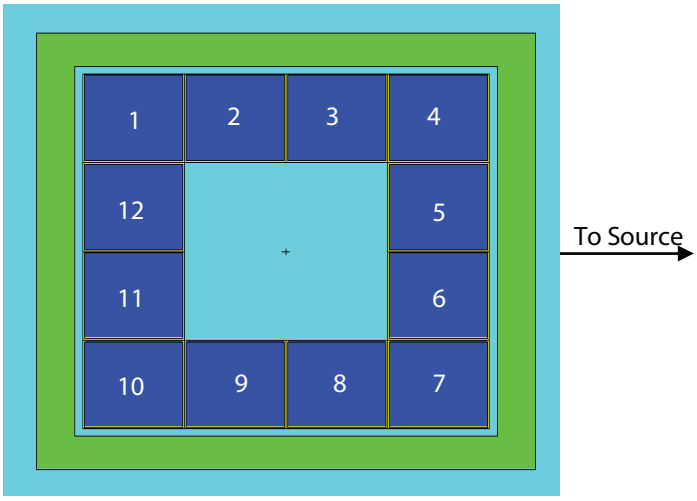

Figure 2. Test geometry and numbering scheme for 12-detector array

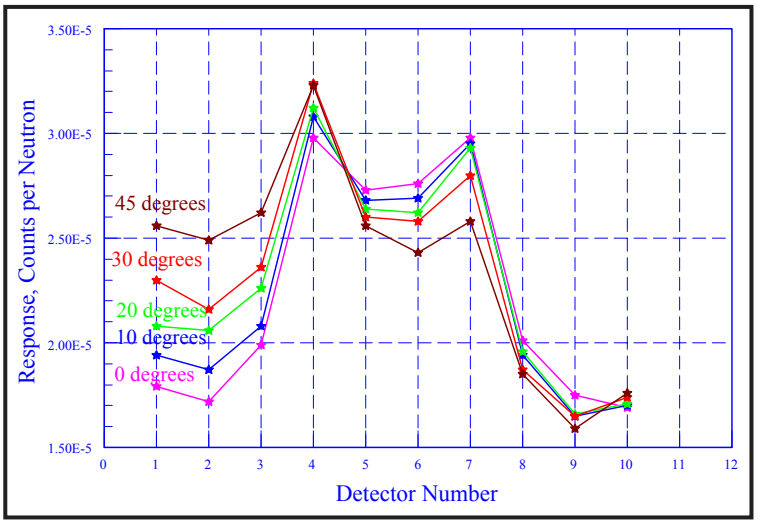

Figure 3. Measured neutron angular response to a source 2 m away

Experiment

The array was placed on a Styrofoam support in a crowded laboratory setting. This choice of area was intended to demonstrate the utility, if any, of this directional detector concept in a typical office environment. For the neutron work, a ^{252}Cf source emitting 2.87×10^5 n/s was placed at 2 m

behind 8 cm of polyethylene to approximate a ^{240}Pu fission source surrounded by hydrogenous material. This is equivalent to 800 g of weapons-grade plutonium. A ^{57}Co source was used at 40 cm for the gamma work.

Calculational Methods

The MCNP code was used to determine the neutron directional effects of a ^{240}Pu-shell source surrounded by hydrogenous material and other high-Z components. This was an attempt to mimic a possible terrorist-deployed weapon. The MCNP code does not permit easy calculation of the actual counting process within the ^{3}He detector tubes. Instead, we used an approximation that tallies the heating within the tube caused by the various neutron reactions with the helium gas. As will be seen, this calculation, while qualitatively accurate for angular effects, is too low by a factor of ~100 compared to measured reaction rates.

The gamma source was accurately simulated by MCNP, but the heating tally was used to enable variance reduction. In this case, the calculated data were greater than the measured values by a factor of ~2.

Neutron Results

The measured data for neutrons are shown in Figure 3. Each data point has an uncertainty (σ) of about ±2%. Thus, there is little difference in the responses of detectors 9 and 10 for all angles measured. A marked difference does exist in the responses of the other detectors, with the angle depending on the self-shielding of one tube to another. This is the basis for angle determination of the source direction.

Results of MCNP calculations, with uncertainties (σ) of ±3%, appear in Figure 4. The response values in both graphs are given in terms of source neutron emitted, but, as noted earlier, the calculations are lower by a factor of ~100. However, the curve shapes are similar and show the same dependence on angle and detector. Thus, the MCNP calculations can be used to interpolate between angles if needed.

Simple Angular Determination for Neutrons

Both the measured and calculated variations of detector response versus angle suggest that a simple detector response ratio could be used to unambiguously determine the source direction (Figure 5). This figure presents the ratio of detector 3 to detector 6 (Det 3 / Det 6) for both the measured and the calculated neutron data sets. The errors in these ratios are about the size of the symbols plotted, suggesting that the angular error can be determined within ±5–7°. In either case, the ratio is monomodal and can thus yield a source direction with no ambiguity. The measured data seem to fit a linear approximation adequately over the 45° range considered.

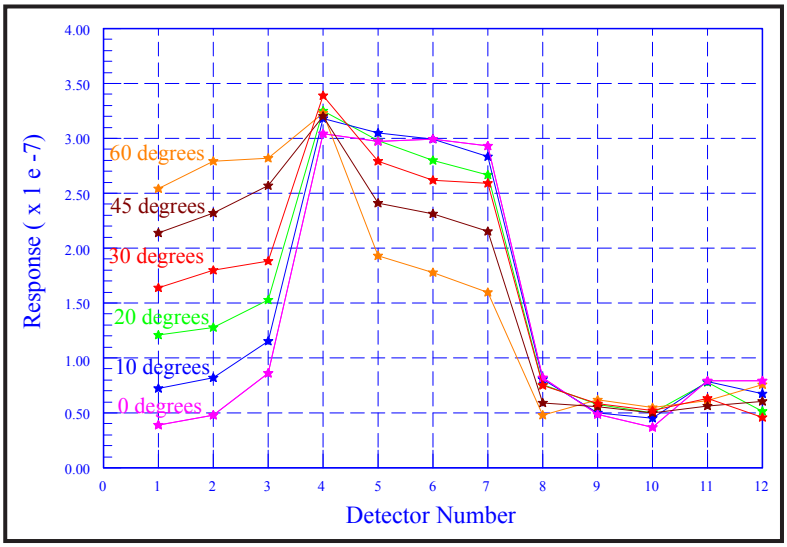

Figure 4. MCNP-calculated neutron angular response for a source 2 m away

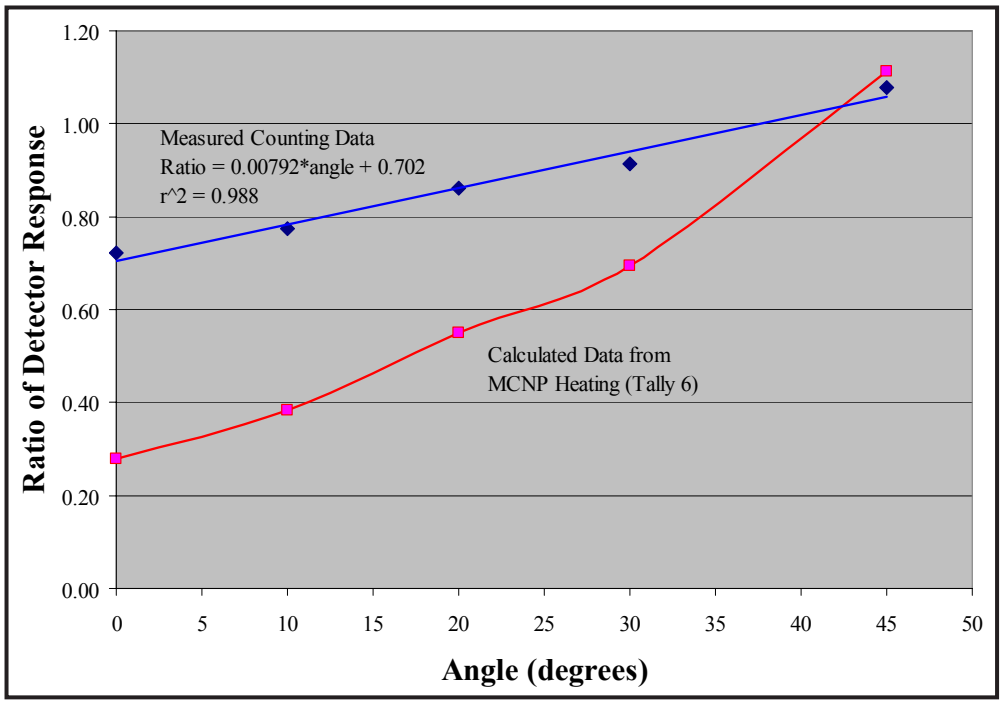

Figure 5. Ratios of detector 3 to detector 6 from neutron measurements (blue) and calculations (red)

This simple analysis could be carried out via logic circuits in real time if needed. A mobile application using much larger detectors is possible using this concept. The steeper slope for the free-field calculations implies that measurements taken in a highly scattering laboratory environment have somewhat degraded angular sensitivity, making the measured curve less steep.

Minimum Detectable Neutron Activity for Directional Purposes

The background counting rates recorded during the experiment were low: 0.024 counts/s per tube over 30 min. These data permitted determination of the MDA for the polyethylene-moderated neutron source configuration studied. One way to express this data is in grams of Pu equivalent, assuming a weapons-grade content of about 6% ^{240}Pu. Thus, we expect an MDA of 90 g Pu at 2 m for a 1-sec count at an error bound of 5 σ.

Gross Counting Sensitivity for Neutrons

On average, seven detectors can "see" the source at 45°. This suggests that the 800-g Pu-equivalent source would produce 49 net counts/s at 2 m from all seven detectors. This is more than 2000 times background. It may be feasible to use this ^{3}He array to search for neutron sources, and to determine the source direction, once an elevated source count has been found.

Gamma Data

The source strengths available (and allowed) did not permit measurements at 2 m. Instead, the 4.1-μCi ^{57}Co source was positioned at 40 cm. MCNP was used to calculate the angular response for this configuration and produced a set of curves similar to that found for the neutrons. Response ratios for two detector pairs appear in Figure 6. This figure shows that better angular discrimination can be obtained using the ratio of Det 2 / Det 7. The errors are smaller than the symbols used for plotting. The steeper curve for Det 2 / Det 7 is approximately the same slope as that for the neutrons (shown as the measured data in Figure 5). Thus, both neutrons and gammas can be detected with good angular resolution.

Minimum Detectable Gamma Activity for Directional Purposes

The gamma background was ~3 counts/s per tube in the pulse-height window centered on the ^{57}Co peak (channel 80). The 4.1-μCi source produced a net counting rate of 27 counts/s in a tube facing the source. For this energy gamma (122 keV), this represents an efficiency of about 0.088 counts/gamma. In past work, the 185-keV gamma from ^{235}U has shown an efficiency similar to that from ^{57}Co. Each detector has an area of 41.9 cm^2. Using these data, the 5-σ MDA at a 2-m distance is approximately 28 g of ^{235}U for one detector tube during a 1-sec counting time. This should be a useful predictor for angular sensitivity. Note that no absorption of the 185-keV gammas is included (as would be seen from ^{235}U).

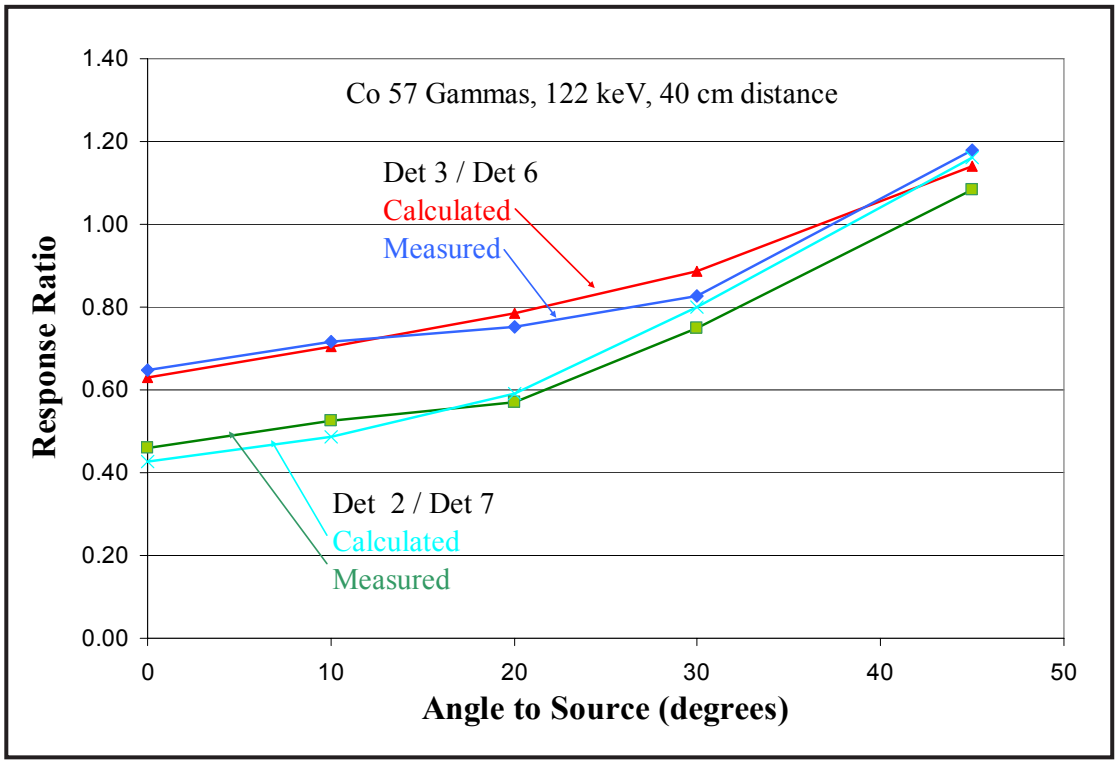

Figure 6. Measured and calculated gamma response ratios for two detector pairs

Gross Counting Sensitivity for Gammas

On average, seven detector tubes will face the source at 45°. This suggests that the MDA for ^{235}U without regard to direction will be about 2 g at a 2-m distance at 5 σ.

Conclusion

Using MCNP code calculations verified with laboratory measurements, we have shown that square-cross-section proportional counters filled with a mixture of Xe and ^{3}He gas can be used to determine the direction of neutron and gamma sources. From the measured data, MDA have been estimated for shielded neutron and unshielded gamma sources, for both directional detection and gross counting modes of operation.

These gas-proportional counters can be made longer with little, if any, effect on performance. This improves counting efficiency and thus reduces the MDA. Current counters have an active length of 6.5 in; counters 10 times longer should be feasible for vehicular applications.

A horizontal array of counters could be used to sense source location above or below the detector position using similar logic to that demonstrated in this work.

References

Quam, W. M., "Gamma and neutron counter," *Nevada Test Site–Directed Research, Development, and Demonstration,* FY 2003, Bechtel Nevada, Las Vegas, Nevada, 2004, 111–113.

CMOS X-ray Color Camera

Robert Buckles, Shaun Hampton, Russell Knight, Donald Pellinen, Travis Pond, Peter Torres III,[1]
John Yuhas
Livermore Operations

Robert Malone
Los Alamos Operations

This project intended to demonstrate the spectroscopic imaging capability of a Foveon, Inc., complementary metal oxide semiconductor (CMOS) sensor for extreme ultraviolet (XEUV) and soft x-rays. We proposed attaching a gold mask onto the face of the CMOS sensor, to shield on-chip electronics from x-rays. The camera was proven to see x-rays in the laboratory, but questions remain about how the x-rays affected the unshielded chip. To date, the camera has not been tested with the gold electronics mask in place.

Background

The Foveon camera chip is a novel CMOS imager that sees true color. No color filter array (CFA) is used. Each pixel collects photocurrent at three distinct depths, thereby employing the electrooptical properties of silicon to assign a unique RGB value. The "blue," "green," and "red" depletion zones are located at the respective range depths of 450-, 550-, 650-nm light (approximately 0.2, 0.6, and 1.5 μm). This layered pixel structure could also be employed to acquire spectrally resolved images in the 100 eV–25 keV energy range. The above-listed sensor depths correspond with the respective range depths of 1.0-, 3.3-, and 10-keV x-rays. Since the sensor is fabricated with reproducible, lithographic precision and silicon's optical properties are well known (good spectral overlap of the various layers), color ambiguity should not exist for the usable energy range.

Once calibrated, this instrument could feasibly resolve spectra as accurately as the instruments used to calibrate them, without employing a nontrivial array of filters and data sets. This would simplify a complicated measurement. Many programs would benefit from simplified x-ray spectroscopy and imaging applications, and could replace their film-based diagnostics with this Foveon technology. Potential beneficiaries include such Campaign 4 projects as High-Energy Density Physics (HEDP), the National Ignition Facility (NIF), and aboveground experiments (AGEX), as well as Campaign 2 projects such as Atlas and Jasper.

[1] torresp@nv.doe.gov, 925-960-2657

Figure 1. Sigma camera in Manson source reference box

Project

The camera was tested on a DC Manson x-ray source without a shield to protect the on-chip electronics from incident x-rays. To operate the camera (Figure 1) from within the vacuum system, an optical triggering system and power and video cables were developed to pass through to the vacuum system.

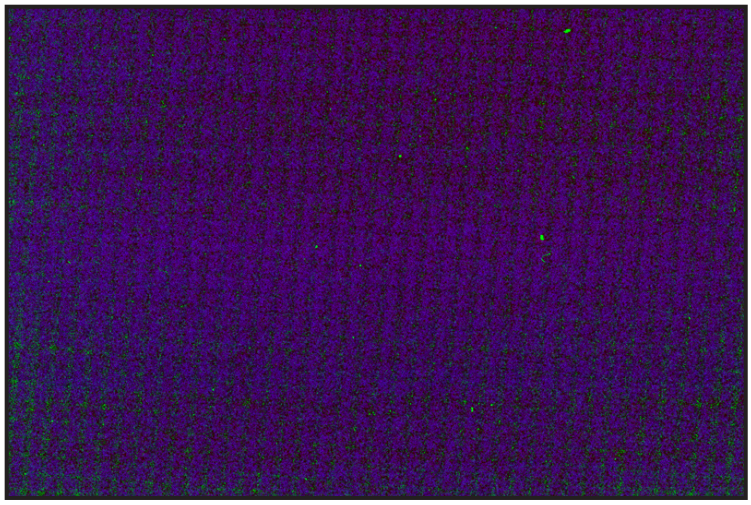

Figure 2. Ni mesh structure supporting a thin film/1500-Å Al x-ray window. The Ni mesh spans 2268 × 1512 pixels of the CMOS chip. Each pixel is 9.12 µm.

First we captured flat-field images utilizing Ti $K_{\alpha 1}$ 4.5-keV x-rays. These images lent insight into the camera's x-ray imaging capabilities; they clearly showed the nickel grid structure supporting the 1500-Å Al window that blocked optical light produced by the source. The window is shown at the center-top of Figure 1. The captured image appears in Figure 2. The grid is 70 lines per in; the nickel wire diameter is 17.8 µm.

Our second data set was taken with a stainless-steel, line-spread function mask positioned just in front of the chip. This test was intended to gauge if the camera was imaging x-rays to reveal differences in energy among the red, green, and blue silicon layers without shielding. We could not determine if the absorption at different depths in the silicon acted as continuous or isolated depletion zones. Figures 3 and 4 show absorption differences between these zones, based on the Foveon's silicon layers.

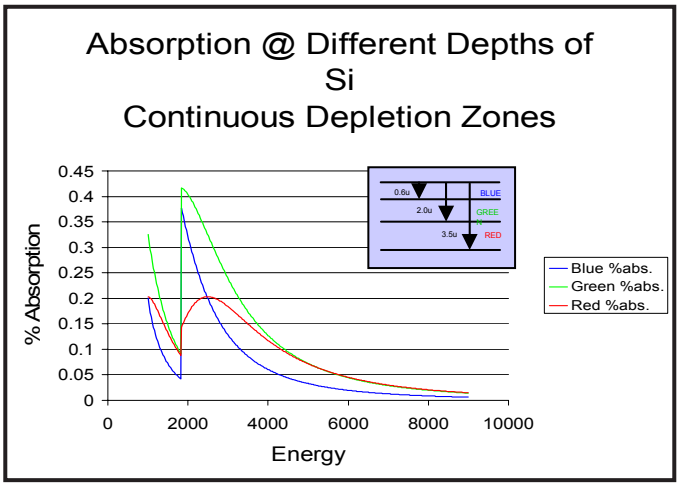

Figure 3. Continuous depletion zone between silicon layers

Given the data taken with Ti 4.5-keV line radiation, it should have been apparent which model was correct by looking for red dominance. However, since the camera response appeared random and nonsystematic, a clear answer was not obvious.

We believe that because the shielding was not in place, the chip responded randomly from shot to shot, such that three layers never worked at once in a single image. One of the layer's signals was inverted as compared to the other two. This inverted response occurred randomly from red to blue to green, from image to image. Figure 5a shows an image of the line-spread function mask taken with 4.5-keV Ti line radiation. The bright green horizontal strips are the 20-µm slits in the mask. The

slits are green because the red and blue channels are not working properly in this image. In Figures 5b, c, and d, the red and blue channels are inverted even though the green channel is working but saturated.

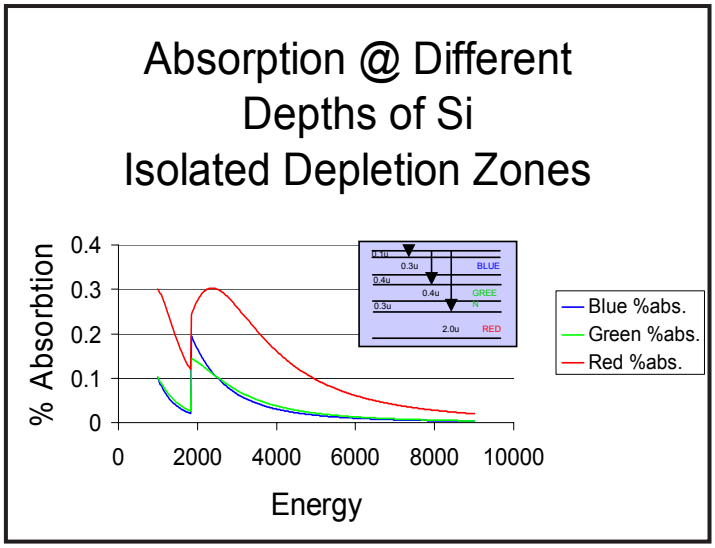

Figure 4. Isolated depletion zone between silicon layers

Because of the inconclusive data, we did not complete calibration of channel absorption to a given input energy.

The gold mask necessary to shield the on-chip electronics was being fabricated using semiconductor processes, but the vendor could not deliver the product before the end of FY 2005. The mask was designed to provide a 5-µm square hole centered on each pixel well while shielding the surrounding read-out circuitry from incident x-rays. This mask is believed likely to solve the issues of inverted signals, thus answering the question of isolated or continuous depletion zones. Once the correct absorption model is determined, further measurements could be obtained to build a color map associating color response to incident x-ray energies.

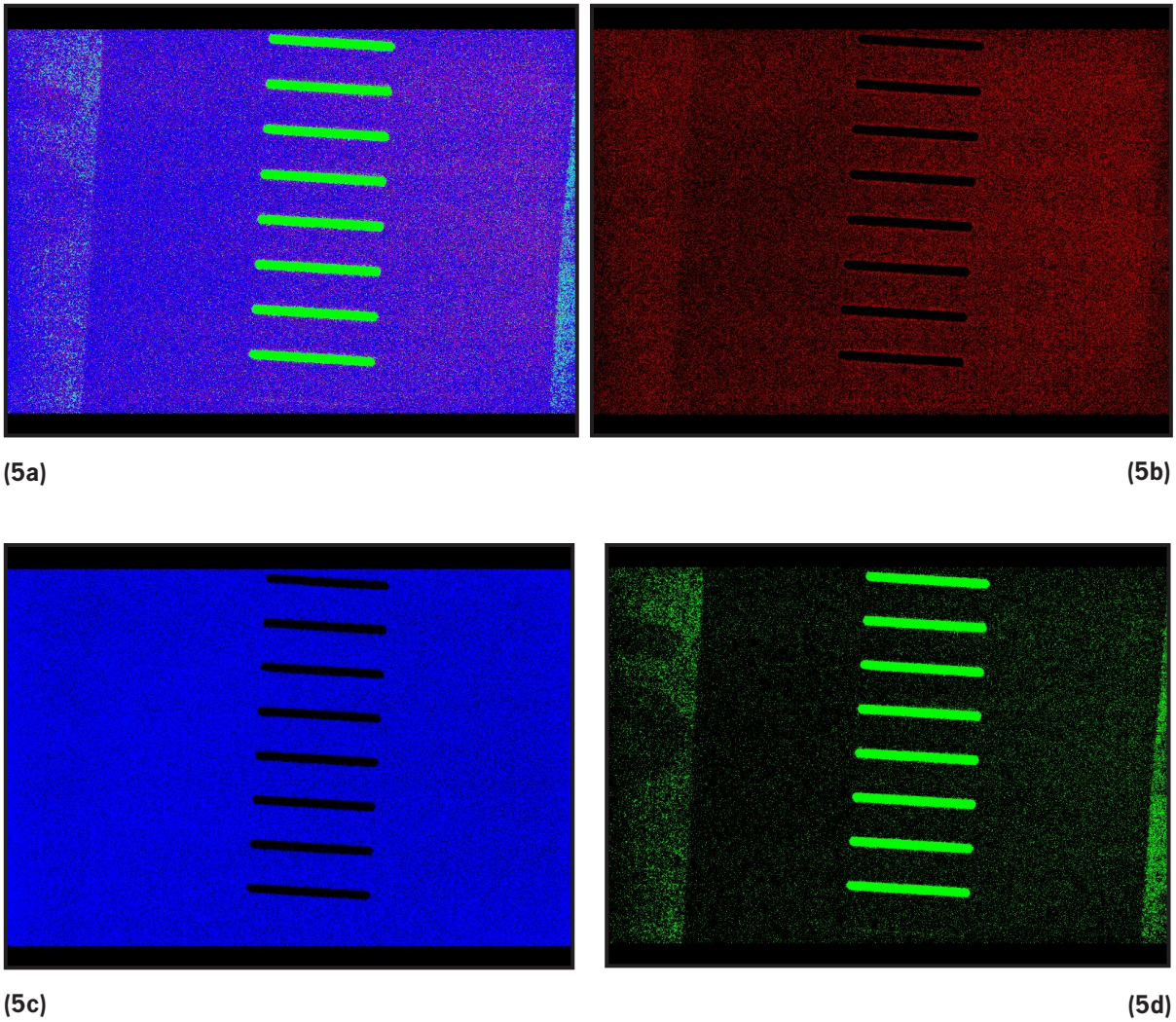

(5a) **(5b)**

(5c) **(5d)**

Figure 5. (5a) Line-spread function mask; (5b) red channel of Figure 5a; (5c) blue channel of Figure 5a; (5d) green channel of Figure 5a

Conclusion

The camera survived the vacuum environment, and its performance hinted at its capabilities as an x-ray imager. However, since it was a consumer-grade camera, it lacked the acquisition control presently used in most diagnostics. With additional time, a suitable platform could be developed to support the Foveon chip. Once the gold mask shields the chip's read-out electronics and the camera's x-ray spectroscopic performance is verified, it could become a very desirable tool for x-ray spectroscopy and medical x-ray imaging.

Acknowledgments

We would like to thank Dick Merrill and Foveon, Inc., for the engineering samples and time during our phone and e-mail conversations.

References

Carr, W., "Multi-spectrum photodiode devices," U.S. Patent 4,238,760, filed Oct. 6, 1978, and issued Dec. 9, 1980.

Gilblom, D. L., S. K. Yoo, P. Ventura, "Operation and performance of a color image sensor with layered photodiodes," *Alternative Vision* (www.alt-vision.com/documentation/5074-35.pdf), accessed October 5, 2004.

Merrill, D., "Color separation in an active pixel cell imaging array using a triple-well structure," U.S. Patent Number 5,965,875, U.S. Patent and Trademark office, Oct. 12, 1999.

Merrill, D., "Method and apparatus for biasing a CMOS active pixel sensor above the nominal voltage maximums for an IC process," U.S. Patent Number 6,246,043 B1, U.S. Patent and Trademark Office, June 12, 2001.

Merrill, D., "The next-generation digital camera," *Optics & Photonics News* **14** (2003) 26–33.

Merrill, D., "Vertical color filter detector group and array," U.S. Patent Application Publication Number U.S. 2002/0058353 A1), U.S. Patent and Trademark Office, May 16, 2002.

Savage, N., "Seeing Red (and Green and Blue)," *OE Magazine* **4** (2004) 37.

Compact Penning Mass Spectrometer

Clifford P. Trainham[1]
Special Technologies Laboratory

A benchtop, Penning-trap mass spectrometer was constructed in an FY 2004 SDRD project. The objective of the FY 2005 continuation was to demonstrate operation and test several detection schemes. Successful operation would then be used to help define final design parameters of a smaller, portable Penning-trap mass spectrometer. The benchtop system constructed here utilizes small permanent magnets mounted within the vacuum system that produce a trapping field of 4.6 kG. The characteristic length parameter for the trap is z_0 = 0.1 cm, and the trap is mounted within standard 2.75-inch ConFlat vacuum hardware. The system uses a 20-l/s vacuum ion pump.

Background

In the Penning geometry, a constant magnetic field is used to constrain ion motion into cyclotron orbits. This forms a pseudotrap in two dimensions. The magnetic field, however, does not constrain the motion along its axial direction, so a colinear electric field is imposed in order to create an axial restoring force. To localize the trapping region, the electric field needs to reverse sign upon transiting the origin, meaning that the electric field must be at least quadrupolar in character. The resulting arrangement of magnetic and electric field creates a three-dimensional pseudotrap at the origin, which is a potential energy saddle point.

The ion motion in this geometry is a combination of linear oscillations in the axial direction and cyclotron orbits in the transverse plane. Because the electric field is quadrupolar, it cannot be entirely colinear with the magnetic field; thus, there is an **E**×**B** force that causes the cyclotron orbits to precess. This precession is called the "magnetron motion", and it is inherently unstable because the potential energy associated with it is a maximum, rather than a minimum, at the origin. Ions are lost from the trap primarily via radial diffusion associated with the magnetron motion (Brown, 1986).

[1] trainhcp@nv.doe.gov, 805-681-2248

The oscillation frequency of the axial motion is:

$$f_z = \frac{1}{2\pi}\sqrt{\frac{qV}{mz_0^2}}. \quad (1)$$

where:

q = ion charge

V = trapping potential

m = ion mass

z_0 = characteristic trap length,

which, for the purpose of experiments, can be simplified to:

$$f_z = 1.56\sqrt{V/M}\ \text{MHz}, \quad (2)$$

where V is expressed in volts, and M is expressed in atomic mass units (AMU). For the benchtop trap, z_0 = 0.1 cm. For atomic hydrogen and a trapping voltage of a few volts, this implies a driving frequency of about 1–4 MHz.

The cyclotron frequency is:

$$f_c = \frac{1}{2\pi}\frac{qB}{mc}, \quad (3)$$

where:

q = ion charge

B = magnetic field

m = ion mass

c = speed of light,

which simplifies to:

$$f_c = 1.53\frac{B}{M}\ \text{MHz}, \quad (4)$$

where B is expressed in kG, and M is expressed in AMU. For our trap, B = 4.6 kG, which yields a cyclotron frequency of about 7 MHz for hydrogen. Because of the magnetron motion, however, the

ions do not respond to the bare cyclotron frequency. This is because the guiding center of the cyclotron motion precesses at the magnetron frequency, and the orbits do not close. The actual frequency of the cyclotron resonance is shifted down from the theoretical value by the magnetron frequency.

The magnetron frequency is related to the other two frequencies by:

$$f_m = \frac{f_z^2}{f_c}. \quad \textbf{(5)}$$

If we choose a trapping voltage of about 3 V for hydrogen, this yields a magnetron frequency of about 1 MHz. Since the magnetron motion is truly unstable, one would ideally want this to be a small perturbation to the cyclotron motion. Because, in our case, the magnetron motion is nonnegligible compared to the other characteristic motions, the trapping time will be very sensitive to collisions with the background gas. Radial ion diffusion occurs because of collisions with the background gas, which displace the radius of the cyclotron orbit's guiding center. This phenomenon underlines the importance of operating the Penning trap at very high vacuum.

Project

The first attempted detection scheme was to apply a radio-frequency (RF) voltage to the trap endcaps, to drive the ion motion and then measure the induced signals in the ring electrode. If the trap is populated with ions, it should act as a nonlinear mixer and create sideband structure at the ion characteristic frequencies. An Agilent 8648C synthesizer supplied the RF signal, and it was applied to the endcap electrodes via a phase-splitting toroidal transformer having a center tap on the secondary winding. This allowed the RF drive to be superimposed on the DC bias of the endcaps.

The ring electrode was grounded through the input amplifier of an Agilent E4402B spectrum analyzer. We initially attempted the RF driving frequency of the axial resonance. The detection windows were placed at the doubled axial frequency, the magnetron frequency, and the shifted cyclotron and axial difference frequency. Bias ramping of the endcaps and ramping of the RF driving frequency were both tried to search for the resonances. Since the effective z_0 of the trap is known to a precision of only about 10%, the drive and detection windows need to be systematically scanned. During the experimental runs that have been conducted so far, the filament was left turned on throughout the cycle. The filament delivered an electron beam with energies ranging up to 60 eV, and the electron current through the trap was on the order of 1 μA. Searches were made for the induced signals of hydrogen, nitrogen, and water. We also attempted to trap electrons.

A series of technical problems has made the detection efforts unsuccessful. An ion pump failure earlier in the year and oil contamination of the vacuum system put the trap out of commission for several months. Once the vacuum system was operative, several problems occurred with the in-vacuum filament connections. Typically, the ion trap would be in operation for only a day or two before some

new failure occurred that required breaking the vacuum and removing the trap. The system never had sufficient pumping time to reach a background pressure of 1×10^{-8} torr or below, so the detection was never optimal. The design of the trap mounting is currently being modified to correct these problems.

Conclusion

A benchtop, Penning-trap mass spectrometer was constructed, and first attempts at signal detection of trapped ions were begun. Unfortunately, a number of technical difficulties occurred, and successful operation has not yet been demonstrated. The vacuum mounting redesign should correct the aforementioned problems. Once successful trap operation has been demonstrated, the survey of detection schemes will resume. If the results are promising, parameters for the design of the portable mass spectrometer should be obtainable.

References

Brown, L. S., G. Gabrielse, "Geonium theory: Physics of a single electron or ion in a Penning trap," *Rev. Mod. Phys.* **58** (1986) 233.

Small, Compton-Suppressed Gamma Detectors

Eric C. Wagner[1]
Remote Sensing Laboratory – Andrews

In this project, our team collaborated with a scintillation crystal manufacturer to produce single-output, aluminum-encapsulated crystal geometry. The geometry consists of one crystal surrounded on all faces by a larger crystal of different material. The goal was to produce a crystal with equivalent or better gross count collection compared to an equivalent size of sodium iodide, with the additional capability to extract spectral information from each crystal with one output. Our team conducted gross count collection (from both crystals), spectral collection (from each crystal), and Compton suppression (counts of one crystal collected in a delayed anticoincidence arrangement).

Background

Commercially available identification equipment, such as the Exploranium GR-135 and the Thermo Electron IdentiFINDER, utilizes a single-detection element for collecting spectra for analysis by their isotope-identification algorithms. Unfortunately, identification becomes far less reliable for spectra generated by multiple sources, especially when one isotope has a much stronger signal than others in the sample. In sample geometry with respect to the detector element, a significant Compton continuum exists for each gamma energy peak. Thus, lower peaks have a much greater likelihood of being lost in the noise of the Compton continuum from higher peaks.

Project

Our first effort was to identify the materials to be used to compose the detection element. Sodium iodide (NaI) was selected as the bulk material due to its availability in quantity and well-known characteristics. For the second element, we wanted a material with superior energy resolution.

Table 1 lists several selected scintillators and their energy resolutions for ^{137}Cs. The resolution is a measure of the photopeak width divided by its energy (here, 662 keV). Therefore, the lower the percentage, the better the energy resolution.

Initially, we proposed to utilize two photomultiplier tubes (PMTs) to measure light output of each crystal. But the crystal with the best energy resolution, $LaBr_3(Ce)$, had a significantly different decay time than NaI(Tl). In addition, the material's wavelength emission was assumed to be compatible with the NaI. Therefore, we made three designs with a single PMT (Figures 1–3).

[1] wagnerec@nv.doe.gov, 808-474-2654

Table 1. Expected energy resolutions (662 keV)

Crystal	Resolution (%)
NaI (Tl)	7.4
LaBr3	3.7
LaCl3	4.7
CsI(Tl)	5.5–5.8
BGO	16
Plastic	Essentially none

As seen in Figures 1–3, only one PMT exists, which makes these designs a type of phoswich detector, or "phosphor sandwich." These designs differ from previous phoswich detectors in that one scintillation material completely encapsulates the other, rather than being simply layered. In addition, how both the proposed designs and the phoswich detectors are used is also different. These detectors were designed to measure the penetrating strength of an energetic particle or photon through one material into another, whereas the crystal complex designs are to be used as Compton-suppression elements.

Utilizing a pulse-processing analysis (Figure 4), the pulses from the individual crystal elements can be separated. The amplifier generates a pulse directly proportional to the rise time of the PMT-generated pulse. The time-to-amplitude converter (TAC) changes the pulse's temporal width into a voltage signal. The single-channel analyzer (SCA) can then select for pulses from the TAC that are specific to a crystal type. The SCA output can then drive the multichannel analyzer's (MCA) gate input. Assuming the delay amplifier is properly configured, the SCA will open the input to the MCA just as the appropriate pulse arrives.

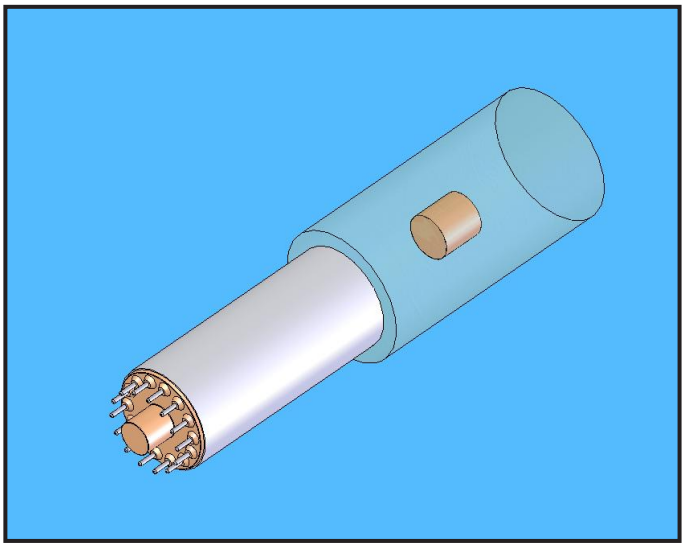

Figure 1. Proposed cylindrical design

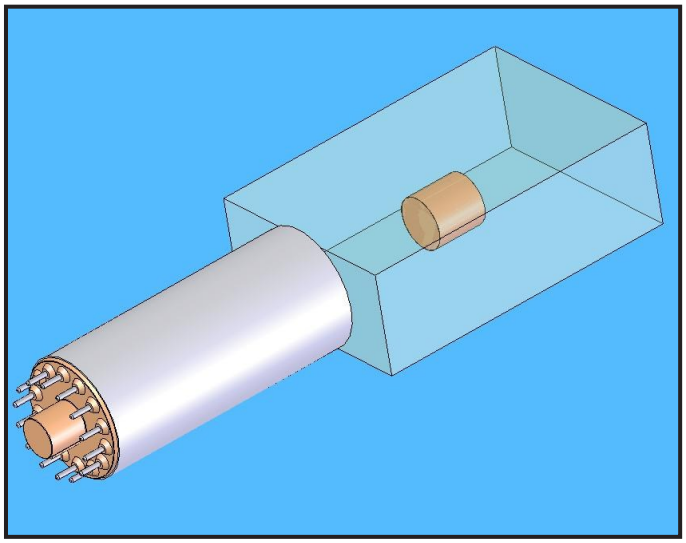

Figure 2. Proposed rectilinear design

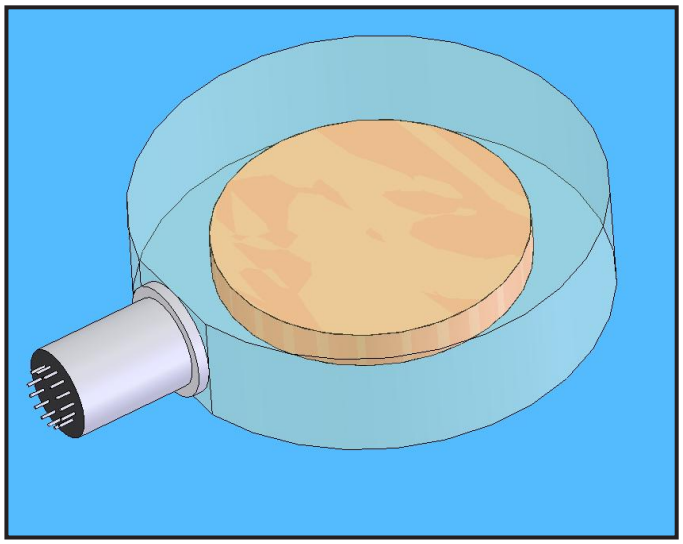

Figure 3. Proposed “pancake” design

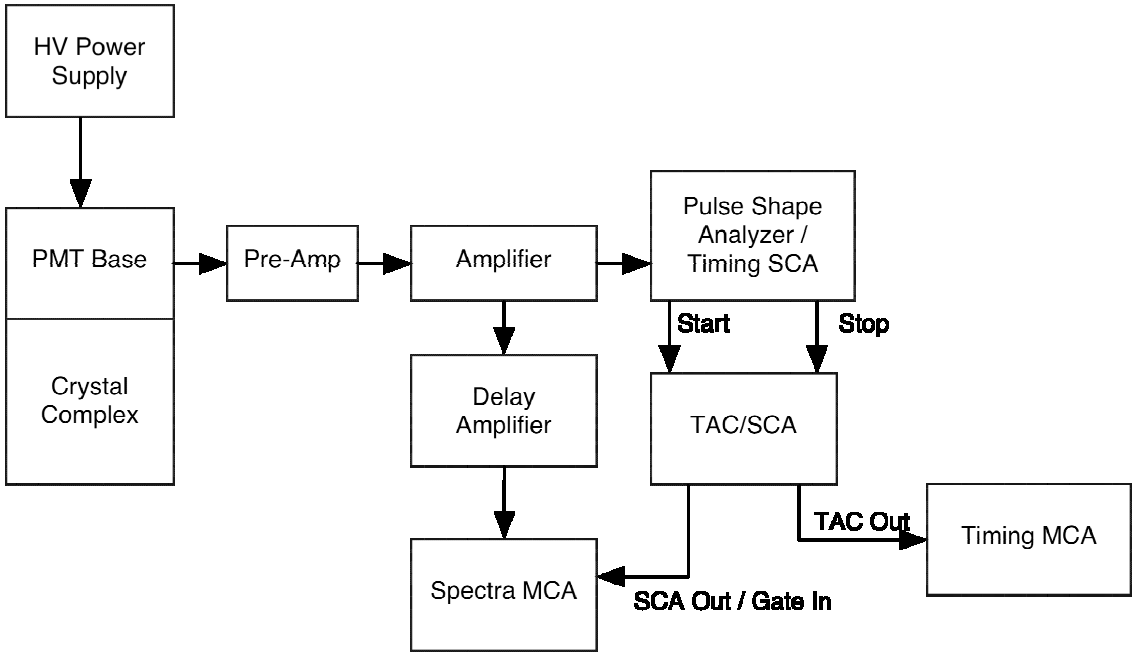

Figure 4. Nuclear instrumentation configuration (adapted from ORTEC online catalog [http://www.ortec-online.com/pdf/neutron_w_stilbene.pdf])

At this point, we established a working relationship with Saint-Gobain Crystals to manufacture one of these composite crystal complexes. At the time, only the 1" x 1" $LaBr_3$ crystals were readily available, making the design in Figure 3 impossible. Manufacturing began on the cylindrical (Figure 1) and rectilinear (Figure 2) designs, but unfortunately, the process proved more difficult than anticipated. The first issue to arise was that chemical interactions occurred between the two crystal types at their coupling. The second, more significant, issue concerned the extreme difference in the thermal expansion coefficients of the two materials: 47.4×10^{-6} /C for NaI versus 8×10^{-6} /C for $LaBr_3$. Thus, the crystal complex was highly sensitive to temperature. A product that is not extremely susceptible to thermal shock during shipment is not yet available.

Fortunately, measurements had been made before any significant damage to the prototypes had occurred. Saint-Gobain collected the data in Figures 5–7 from the rectilinear crystal design with a ^{60}Co source to the side of the crystal. The vendor also collected data in Figures 8 and 9 but with a ^{137}Cs source on axis with the crystal's PMT.

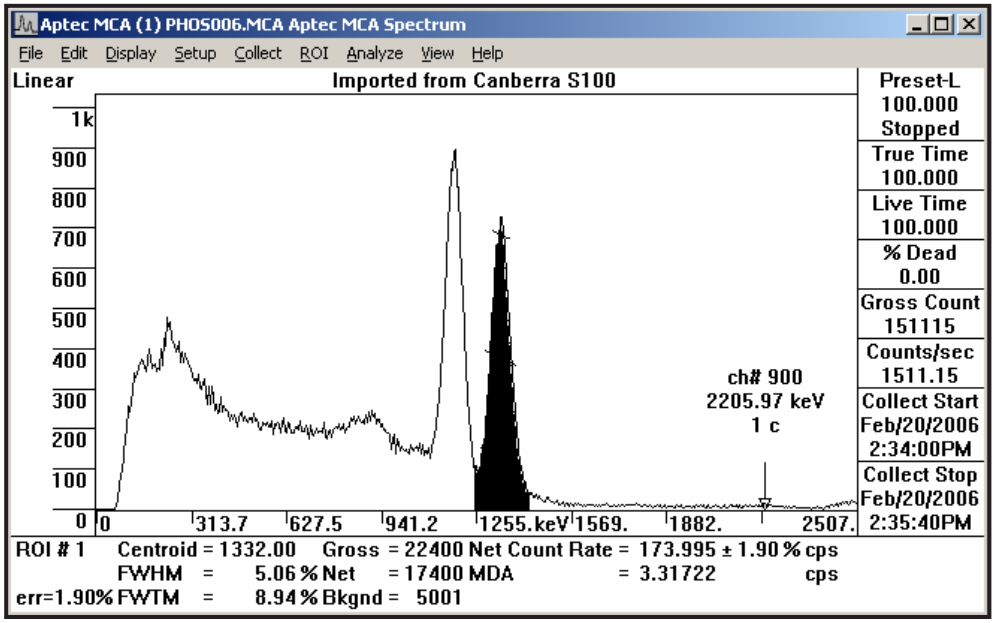

Figure 5. Extracted $LaBr_3(Ce)$ ^{60}Co spectra from rectilinear crystal complex

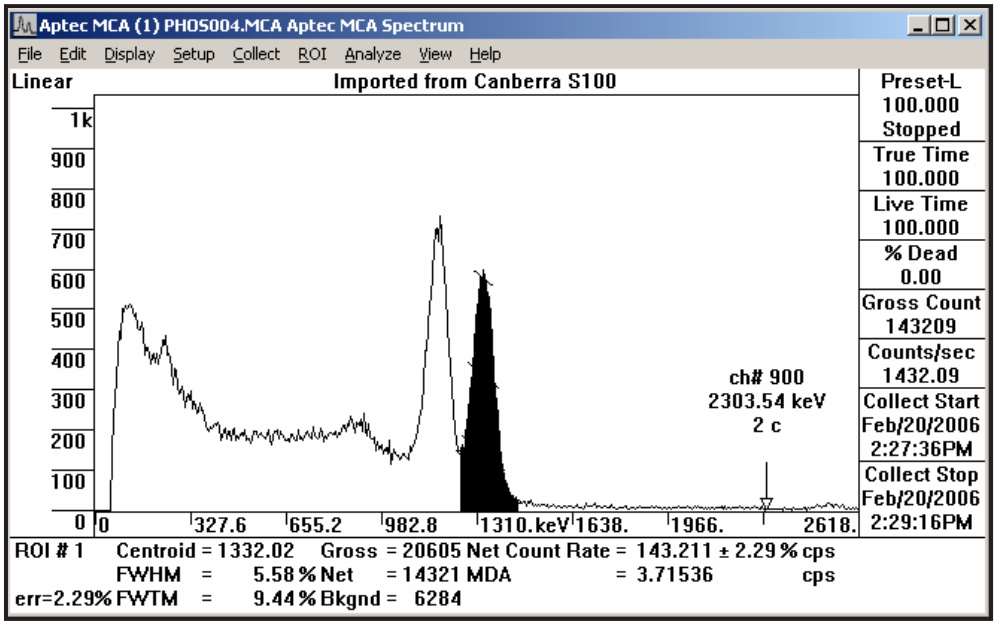

Figure 6. Extracted NaI(Tl) ^{60}Co spectra from rectilinear crystal complex

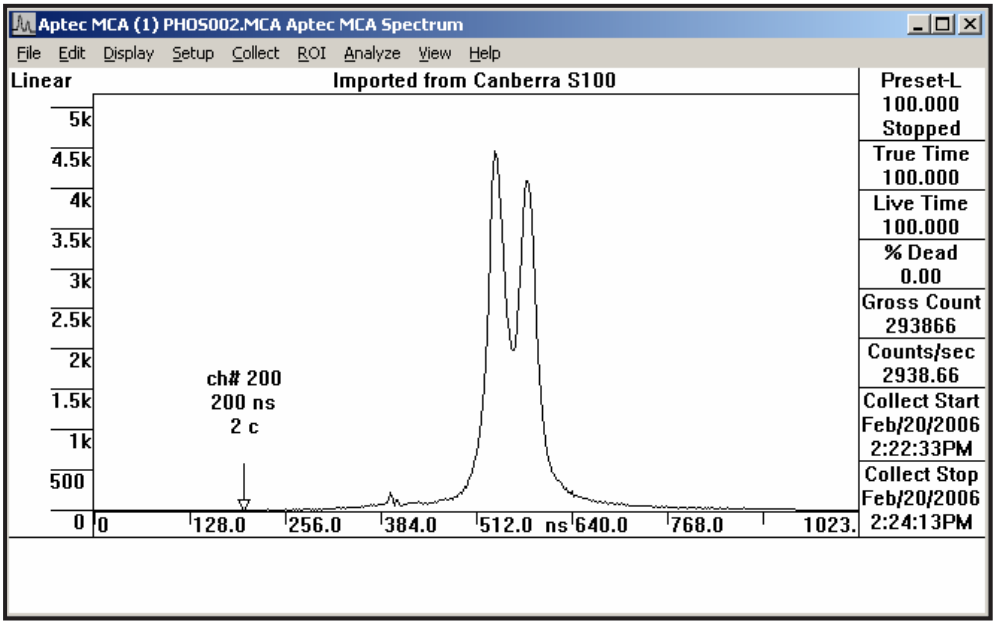

Figure 7. TAC output showing the distinction between pulse shapes from ^{60}Co

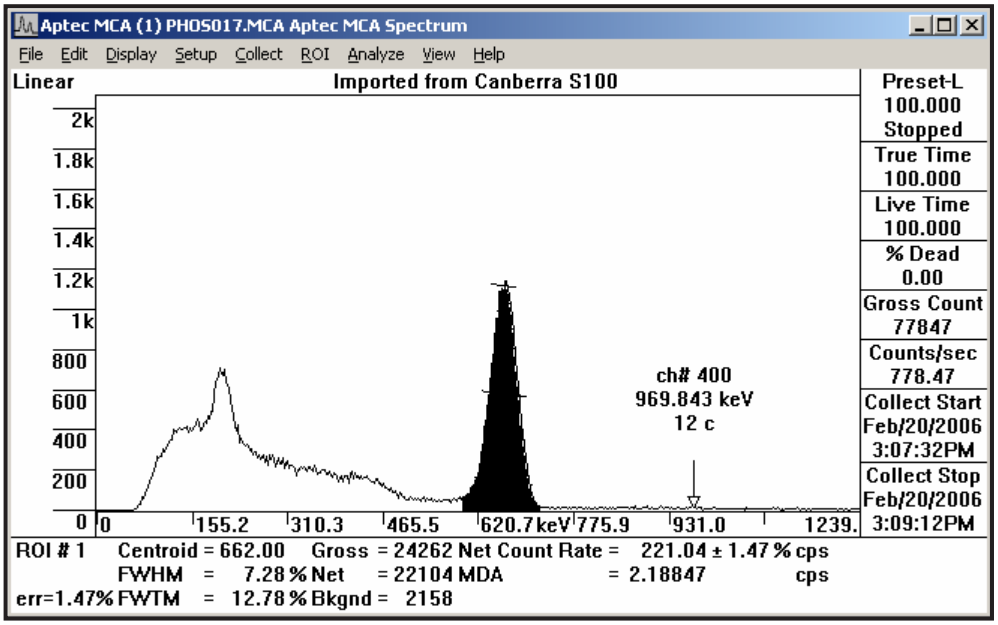

Figure 8. Extracted $LaBr_3(Ce)$ ^{137}Cs spectra from rectilinear crystal complex

The most noteworthy feature is that $LaBr_3(Ce)$ spectra resolution is nearly that of NaI(Tl) (Figures 5 and 8). The timing characteristics shown in Figure 7 indicate that the separation of decay time between the two crystal types is not nearly as great as expected, given the 250-ns decay time of NaI(Tl) versus the 26-ns decay time of $LaBr_3(Ce)$. However, the lack of the impurity signal generated by radioactive material in the $LaBr_3(Ce)$ indicates that the pulse-type separation is functioning (Figures 8–9).

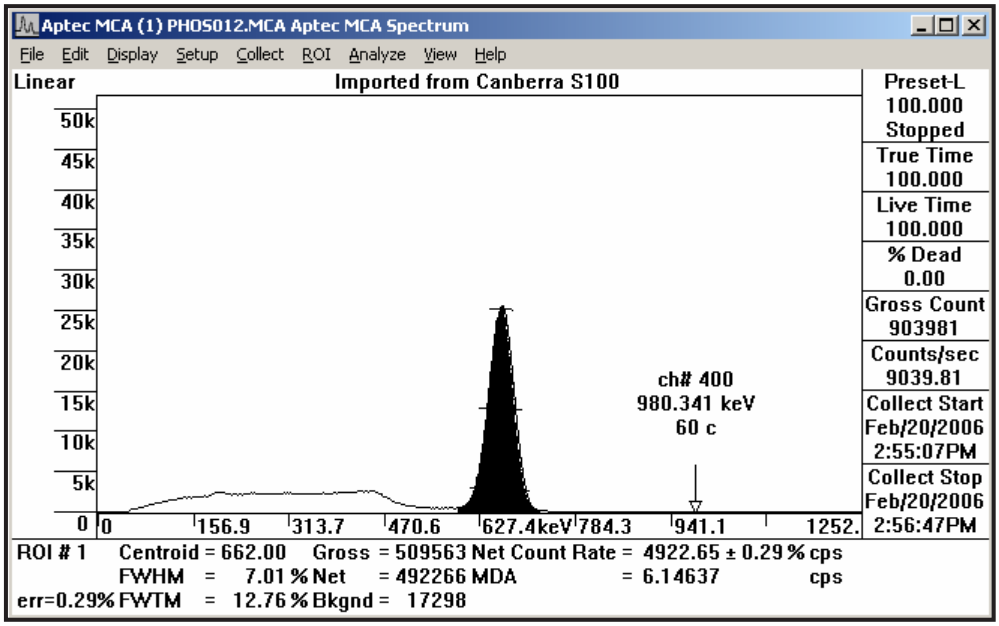

Figure 9. Extracted NaI(Tl) ^{137}Cs spectra from rectilinear crystal complex

Conclusion

Further research must be accomplished. The demonstration of the capability to extract pulses from each crystal type shows that Compton continuum suppression is possible with the crystal complex. However, this would require additional pulse processing equipment (i.e., another delay line to determine if there is a following pulse from the second crystal, then shutting off the MCA's gate). As for the greatly reduced resolution, we can only theorize that, given that resolution in a scintillator is in direct relation to the number of photons reaching the PMT, a significant loss of photons exists. The one indicator that another mechanism is occurring is the extreme similarity between the energy resolution on both crystals. There could be some absorption and reemission by the NaI(Tl), or the overlap between the two pulse durations (Figure 7) could be allowing enough NaI(Tl) counts into the $LaBr_3(Ce)$-extracted spectra. Another remaining question is why the timing shown in Figure 7 is so similar between the pulses.

Overall, the prototype is an interesting design with much room for optimization in successive generations and for further investigation of the discovered enigmas. Future design variations include moving the inner $LaBr_3$(Ce) crystal closer to the PMT; wrapping it with reflective material to help steer the photons directly toward the PMT, thus reducing the average photon path length within the NaI; and utilizing the larger $LaBr_3$(Ce) crystals now available. However, before proceeding to further modifications, the current prototype should be completely characterized.

Acknowledgments

Saint-Gobain Crystals has been a pleasure to work with, especially given the unexpected difficulties that have occurred in what was thought to be a simple design.

References

ORTEC, "Neutron-Gamma Discrimination with Stilbene and Liquid Scintillators," http://www.ortec-online.com/pdf/neutron_w_stilbene.pdf, accessed June 15, 2005.

Portable Fast Gas Chromatography for Field Work: Chemical Agent Detection

Stephan J. Weeks[1]
Special Technologies Laboratory

The fast gas chromatography (GC) project sought to design, construct, and test a smart sampling system to be used with the field-portable, fast GC chemical sensor system developed in FY 2004. A further goal was to demonstrate the system's ability to provide laboratory-quality data. The sampling system was researched, designed, and partially constructed. This system and a preconcentrator will be interfaced with the fast GC and tested under programmatic funding in FY 2006.

Background

Terrorism with chemical warfare agents (CWA) and suicide bombers presents challenging and urgent needs for rapid sampling and analysis using portable field instruments. CWAs and toxic industrial chemicals (TIC) remain the preferred weapons of mass destruction (WMD) for terrorist attacks simply because they are relatively easy to obtain, conceal, and disseminate (Sun, 2005).

To detect CWAs or explosives in a nonintrusive yet effective manner, methods for sampling air, preconcentrating targeted analytes, then delivering the sample for analysis must be representative, rapid, and automated. In FY 2004, a prototype, field-portable, fast (<90 s) GC for chemical-agent-specific analysis was developed. Prior to creating an advanced engineering prototype, we needed to develop a sampling and preconcentration system suitable for field use. Although GC/mass spectrometry (GC/MS) is specified by the Organization for the Prohibition of Chemical Weapons (OPCW) as the preferred test method at suspected sites of chemical agent contamination (Mesilaakso, 2005), OPCW air-sampling procedures and equipment do not currently exist. However, GCs are particularly capable of employing sampling interfaces that trap gas-phase CWAs and preconcentrate them prior to injection, due to the cyclical nature of the analysis. Rhykerd asserts that, with the appropriate detector, GC "will have the fewest false positives and the most sensitive detection levels" (1999).

Existing hand-portable detection technologies for explosives have inherent limitations, including low sensitivity and specificity, high false-alarm rates, high test costs, high consumables use, slow processing times, and limited information displays. Current chemical sensors that are sufficiently small and lightweight with low power and maintenance requirements are often marginally useful, as the dynamic molecular backgrounds encountered in real-world applications often trigger false alarms. Ideal systems would combine the rapid response of a dog's nose (without their saturation

[1] weekssj@nv.doe.gov, 805-681-2262

effects or care and training!) with the highly selective identification and quantitation capability of laboratory GC/MS. To begin to approach the ideal system, technologies are available to develop an effective air-sampling system that may be combined with a handheld fast GC unit.

Explosive detection is complicated by:

- The fact that explosives may consist of chemicals with different volatilities, whose detection depends on sampling conditions.
- Major chemical components in explosives may also have legitimate commercial use; thus, detection of a particular chemical does not necessarily indicate the presence of explosives.

The principal problem in explosive vapor detection is that some explosives have very low vapor pressures, which directly relate to the amount of explosive present in the air for vapor sample collection. The amount collected in real-world situations, with uncontrolled air currents, temperature fluctuations, etc., can be orders of magnitude less. This property combines with others, such as high electronegativity, thermal instability, and a pronounced affinity for adsorbents (stickiness), to present a real challenge in the successful detection of these molecules (Mustacich, 2001).

The goal of this project was to develop and demonstrate a low-power, high-volume, miniature air-sampling apparatus that would integrate with a similarly small, low-power GC instrument for analysis. This approach is also intended to be "adaptive" to the vapor concentrations sampled, in that the sampling and injection processes can both be controlled to quickly scale upward or downward the preconcentration process, as separation and detection results warrant.

Project

The designed field chemical–sampling system for the fast GC significantly enhances target analyte detection within a given sampling time, typically reducing sampling time from ~30 min to ~1–2 min for the same air volume. The sampling system utilizes a self-heating, annular, solid-phase microextraction (SPME) device for high-volume air sampling and preconcentration. It then thermally delivers the extracted analytes to an automated, valveless, sampling-focusing preconcentrator. The preconcentrator then injects the sample into the fast GC unit for target chemical verification. Technical innovations include:

- A pencil-sized, high-volume, low-power SPME preconcentrator
- A nail-sized, valveless, direct-sampling, low-power preconcentrator.

These innovations are then added to a hockey puck–sized, low-thermal-mass (LTM) GC column and a miniature helium-ionization detector. Further preconcentration may also be enhanced in the field by using advanced SPME devices in parallel or employing various SPME coatings in different elements.

The fast GC sampling and analysis system has been designed to incorporate a general or selective detector, such as an ion mobility spectrometer (IMS), which would serve to trigger the fast GC sampling and analysis. This methodology not only provides highly specific chemical analysis to minimize false positive/negative alarms, but also minimizes expendables and power requirements, thus maximizing field use. The sampler may also operate independently, collecting verification samples for later GC/MS analysis.

The FY 2005 work continued to leverage collaboration with RVM Scientific, Inc. The unit and protocol were designed to enhance field operation, including fast response, measurement confidence, minimum maintenance and expendables, and maximum target analyte detection resolution. RVM Scientific, Inc., has patented a preconcentrator concept and breadboarded a pencil-size unit. Further preconcentration was incorporated by using advanced SPME technology.

The approach developed for air sampling uses absorption followed by adsorption, then focused injection onto the front of a temperature-ramped chromatographic column. The analyte is first absorbed into a permeable medium for collection and preconcentration using SPME devices. The absorption of vapors into the SPME film results in a "microextraction." By integrating SPME films with standard syringe parts, the films can be inserted into GC injectors and thermally desorbed to release the extracted vapor components.

Besides faster sampling speed and lower detection limits, yet another aspect of sampling is important for many applications: uncertainty in the amount collected may severely overload a particular detection scheme. Thus, a means of controlling the sampling process is desirable. While the concentration can only be determined after GC injection, the sampling process can be conducted so that the sampling and/or injection process can be controlled to diminish subsequent or secondary injections of the same sample collected on tandem sampling elements.

The adaptive sampling approach we developed is also an inherently multielement approach; different extractive phases based on SPME can be used in parallel. Because of the large surface volume of SPME elements, one challenge is to capture the desorbed vapors into a volume small enough to perform an injection. To achieve this goal, we used a miniature, valve-based microtrap device (Mustacich, 2001) packed with conventional adsorptive polymer materials. This focusing preconcentrator collected the vapors released from a large surface-area SPME device and rereleased them as a small injection band directly onto the GC column for separation and detection. Because GC is one of the most useful tools for chemical analysis of vapor mixtures, the focusing preconcentrator was integrated with a small GC designed for this purpose. This GC was equipped with a small, low-power detection technology based on discharge ionization to provide a miniature GC with greatly reduced consumables requirements compared to a flame-ionization detector. For miniaturization with full chromatography performance of laboratory GC instruments, LTM column-heating technology was used for temperature programming. We separately developed a full-performance chromatography software with a simplified user interface by working with a commercial GC software vendor.

Conclusion

An air-sampling system was designed to prominently enhance the detection of CWAs, TICs, and explosives in a significantly reduced time. The sampling system is integrated with a fast GC analysis unit that employs LTM technology to provide rapid heating and cooling while maintaining use of standard GC capillary-analysis columns. Technical challenges remain, including:

- Minimization of false-positive and elimination of false-negative chemical agent alarms currently plaguing handheld chemical sensors
- Design of a rugged field instrument that reduces power, size, and weight, while still providing laboratory-quality data
- Development of optimized protocols for each of the many applications.

LTM technology provides the advantage of full GC capabilities in the field. Additionally, automated sampling and preconcentration allow field collection of near-real-time, decision-quality data.

Acknowledgments

The author thanks RVM Scientific, Inc., for their cooperation in adapting their hardware to the requirements of this project.

References

Mesilaakso, M., ed., *Chemical Weapons Convention Chemicals Analysis: Sample Collection, Preparation and Analytical Methods*, John Wiley & Sons, Ltd., West Sussex, England, 2005, 73, 82.

Mustacich, R., J. Richards, "Systems and Methods for Vapor Constituent Analysis," Patent Number 6,223,584, U.S. Patent and Trademark Office, May 1, 2001.

Rhykerd, C. L., D. W. Murray, D. W. Hannum, J. E. Parmeter, "Guide for the Selection of Commercial Explosives Detection Systems for Law Enforcement Applications: NIJ Guide 100-99," NCJ 178913, National Institute of Justice, September 1999.

Sun, Y., K.Y. Ong, *Detection Technologies for Chemical Warfare Agents and Toxic Vapors*, CRC Press, Washington, D.C., 2005, 227–228.

Investigation of Interferometric Synthetic Aperture Radar (IFSAR) Mapping Capability

Heather Gledhill, Sherman S. C. Wu[1]
Remote Sensing Laboratory – Nellis

Wil Lewis
Special Technologies Laboratory

This project evaluated the accuracy of elevation data acquired by space-borne interferometric synthetic aperture radar (IFSAR) for application to orthophotography and generation of digital elevation models. Data collected from the Shuttle Radar Topographic Mission were processed and compared to ground truth data for the National Imagery and Mapping Agency (NIMA) camera calibration range and for other areas on the Nevada Test Site (NTS) that had been mapped using digital photogrammetry. The root-mean-square error of elevation was calculated at 4.4–5.5 m.

Background

Previous research on the applicability of airborne metrology to the generation of digital elevation models and orthophotography has been conducted. These technologies, including visible framing cameras (Wu, 2004) and lidar (light detection and ranging) (Wu, 2005), showed both strengths and limitations. Airborne digital framing cameras yield fairly high resolution but are easily blinded by atmospheric conditions. Lidar has very high elevation resolution (~0.1 m) but limited visibility through atmospheric moisture. In addition, lidar does not produce imagery of ground objects.

This research project investigated the relative merits of applying a space-borne technology, IFSAR, to the generation of digital elevation models. This technology is relatively impervious to atmospheric conditions and has a large field of view. However, careful evaluation of the effective elevation resolution is important in understanding the comparative value of the space-borne technology relative to the aforementioned airborne technologies. The goal of this project was to carry out such an evaluation.

Project

An IFSAR instrument comprises two antenna systems. Typically, one system transmits and receives like traditional radar, while a second antenna some distance away from the first acts as just a receiver. The phase difference between the two return signals contains information on path-length differences that can be used to build up an interferogram of the interrogated surface. When deployed above a landscape, this interferogram contains elevation data.

[1] askdrwu@yahoo.com

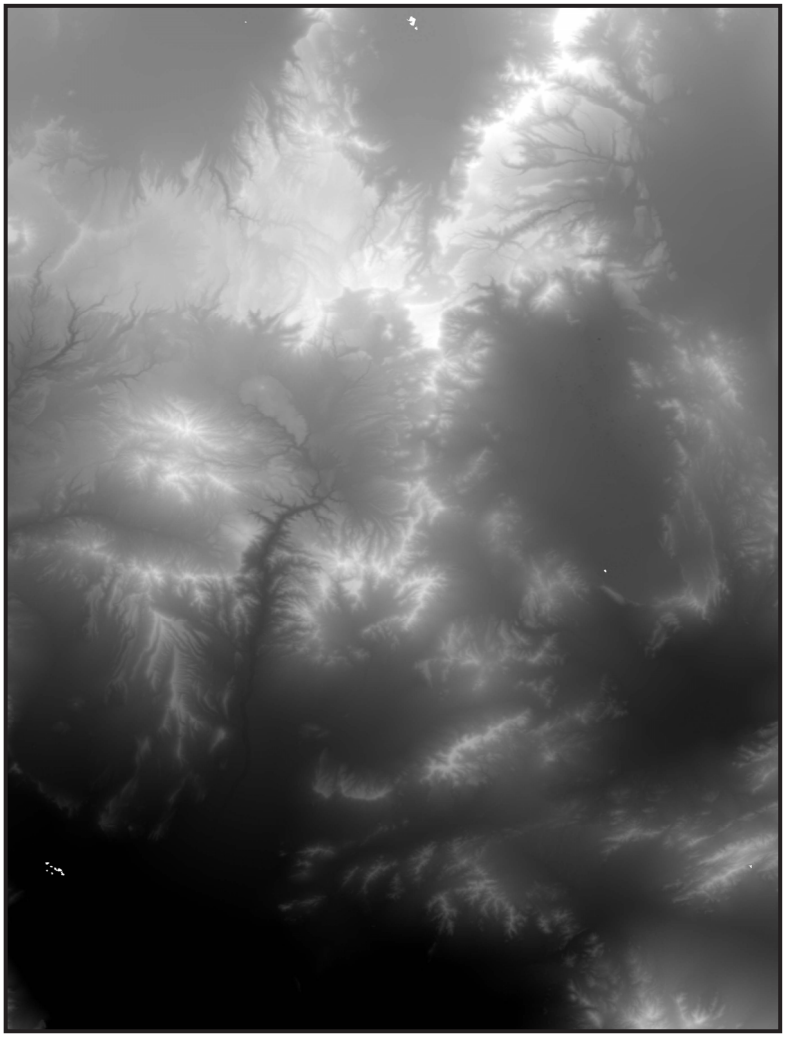

Figure 1. Digital elevation model of the NTS using data from the Shuttle Radar Topographic Mission

In February 2000, the space shuttle Endeavor flew an 11-day, joint National Aeronautics and Space Administration (NASA)–National Geospatial-Intelligence Agency (NGA) mission called the Shuttle Radar Topographic Mission. The mission sought to survey 80% of the earth's land surface between 60 N and 56 S latitude using an IFSAR instrument deployed from the shuttle payload bay. To obtain separation between the two C- and X-band radar receivers, a 60-m boom was extended from the spacecraft while in orbit (California Institute of Technology, 2006).

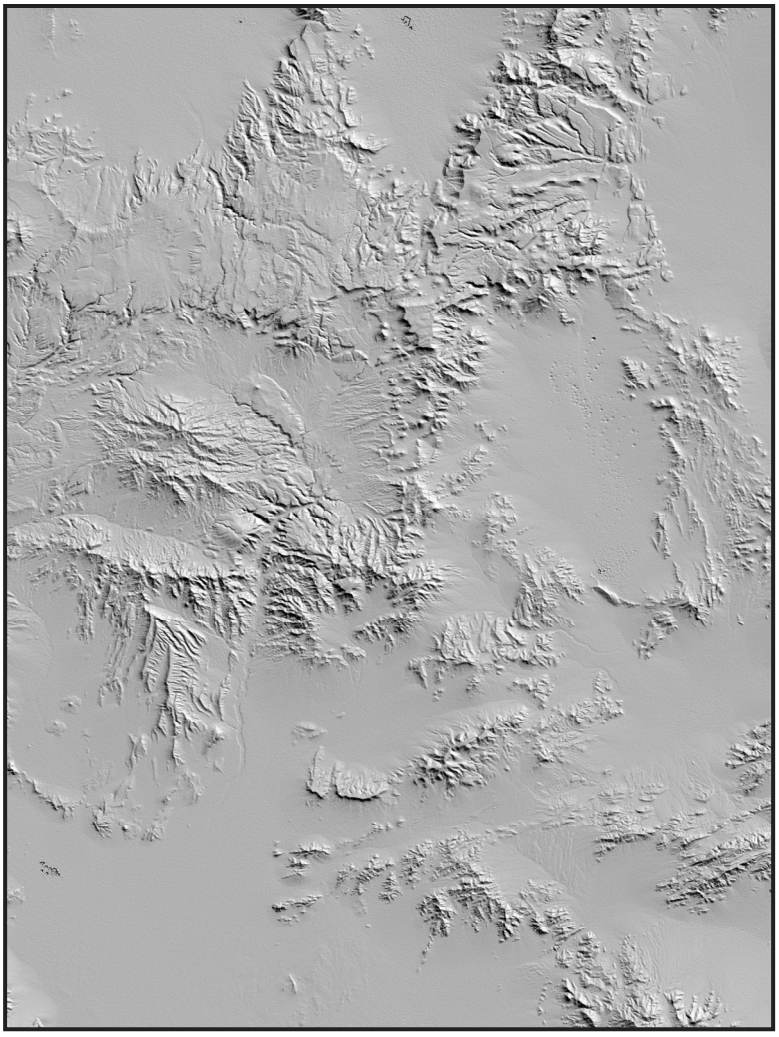

Figure 2. Shaded-relief image of the NTS using data from the Shuttle Radar Topographic Mission

From the Shuttle Radar Topographic Mission, the project team negotiated access to data that covered the NTS and NIMA camera calibration range (two areas that have reliable ground truth data and for which the team had already developed digital elevation models). The shuttle data were supplied in the form of 133 cells of digital terrain elevation data, each cell representing 1 arc sec × 1 arc sec, with a nominal 30-m post spacing. Data relevant to the areas of ground truth were down-selected and processed to generate digital elevation models and shaded-relief images (Figures 1 and 2, respectively). Similar digital elevation models were generated for the NIMA camera calibration range. These

Table 1. Statistical analysis for RMS error of elevation

NIMA camera calibration range (120 ground points)	±4.4 m
NIMA camera calibration range (37.5-megapixel digital elevation model)	±5.5 m*
NTS (50 ground points)	±4.6 m
*arithmetic mean difference: 3.6 m; absolute mean difference: 5.2 m	

models were then evaluated against ground truth data and previously generated models to determine the accuracy of elevation data obtained for the same areas. All in all, 120 ground points and 37.5 × 106 digital elevation model data points were used to evaluate the camera calibration range IFSAR data, and 50 ground points were used to evaluate the NTS data. For RMS error of elevation, statistical analysis yielded the results shown in Table 1.

Conclusion

The team conducted an evaluation of IFSAR mapping capability using digital terrain elevation data for the NTS and NIMA camera calibration range. Based on ground truth data for these areas, we determined that the RMS elevation error was between 4.4 and 5.5 m in maps generated from IFSAR data. IFSAR is a viable technology for generating digital elevation models, with strengths that include all-weather mapping capability and a large field of view. However, characteristics such as its unpredictable data collection schedule and the fact that it achieves a lower resolution than airborne lidar (on the order of one magnitude less) might favor consideration of an airborne IFSAR platform. Such a platform would probably be a much less expensive instrument when scaled down for more proximate imaging (phase information could be obtained with much smaller antenna separation), but the field of view would also be significantly reduced.

Acknowledgments

The project team would like to acknowledge the cooperation and generosity of the Jet Propulsion Laboratory and the National Geospatial-Intelligence Agency for sharing the data acquired from the Shuttle Radar Topographic Mission.

References

California Institute of Technology, Jet Propulsion Laboratory, "Shuttle Radar Topography Mission," http://www2.jpl.nasa.gov/srtm/instr.htm, accessed April 13, 2006.

Wu, S. S. C., "Real Time Photogrammetric Mapping System," *Nevada Test Site–Directed Research, Development, and Demonstration*, FY 2003, Bechtel Nevada, Las Vegas, Nevada, 2004, 149–154.

Wu, S. S. C., "Lidar Experiment for City Models," *Nevada Test Site–Directed Research, Development, and Demonstration*, FY 2004, Bechtel Nevada, Las Vegas, Nevada, 2005, 271–276.

this page intentionally left blank

Optimized Neutron Response Beryllium Activation Detector

Lee H. Ziegler[1] (former employee)
North Las Vegas

A new configuration of a beryllium activation detector consisting of ¼" beryllium rods inserted into a 1½"-diameter BC-418 scintillator has been built, modeled using Monte Carlo N-Particle Extended (MCNPX) code, and tested. MCNPX calculations show that 74% of the beta particles are absorbed in the first 3 mm of the scintillator, and that 84% of the beta particles are captured in the first 4 mm. Detector sensitivity as a function of discriminator setting was measured and compared to the sensitivity of a much larger, beryllium "layer cake" detector.

Background

Beryllium activation detectors have been used to measure neutron yields from several pulse-power devices, such as the Sandia Z machine, the Texas A&M dense plasma focus machine, and the Bechtel Nevada One_sys_70 dense plasma focus (DPF) machine (Rowland, 1984; Nelson, Baltimore, 2004). These detectors are used with other activation detectors and methods to measure the neutron yield of these pulsed neutron generators. Other activation detectors and methods have utilized copper (Cooper, 2001), indium (Ruiz, 1992), arsenic (Jacobs, 1979, 1983), lead (Jacobs, 1965; Lanter, 1966, 1968), and rhodium (Ekdahl, 1979). For the activation methods, each material has properties that are preferred for different yield determinations. These properties include cross-section shape and size, half-life of the activated medium, activated-material radiation, and material response to other radiations generated by the pulse-power machine. In particular, the Z machine produces strong electromagnetic pulses (EMP) and very intense, high-energy bremsstrahlung radiation as well as a neutron pulse during inertial confinement and gas puff experiments. Since beryllium activation detectors are employed extensively at Z, and hopefully will be used at other equally demanding environments such as NIF, we undertook a project to optimize detector response to such environments.

Historically, lead has been used extensively for measuring d-t neutrons (Jacobs, 1965). Spencer and Jacobs have developed a lead-based activation detector called a "lead probe." At Sandia National Laboratories, this detector became a laboratory standard for measuring d-t neutrons. The lead probe was also used extensively to calibrate d-t neutrons in the weapon-testing programs. Previous effort (Nelson, 2003; Nelson et al., 2004) to optimize the response of a lead activation detector resulted in the development of a lead "layer cake" detector (Figure 1). This detector has a figure of merit three times better than that of the standard "lead probe." This project's primary scope was to optimize the response of a similar detector using beryllium as the activation medium.

[1] aziggy@earthlink.net, 702-295-3092

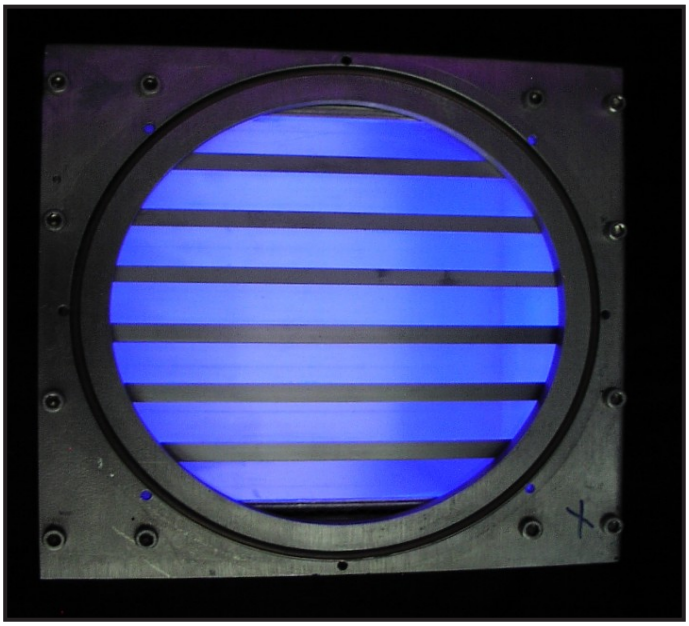

Figure 1. Detector head of a beryllium layer cake detector. Beryllium layers are interlaced between sheets of BC-418 scintillator.

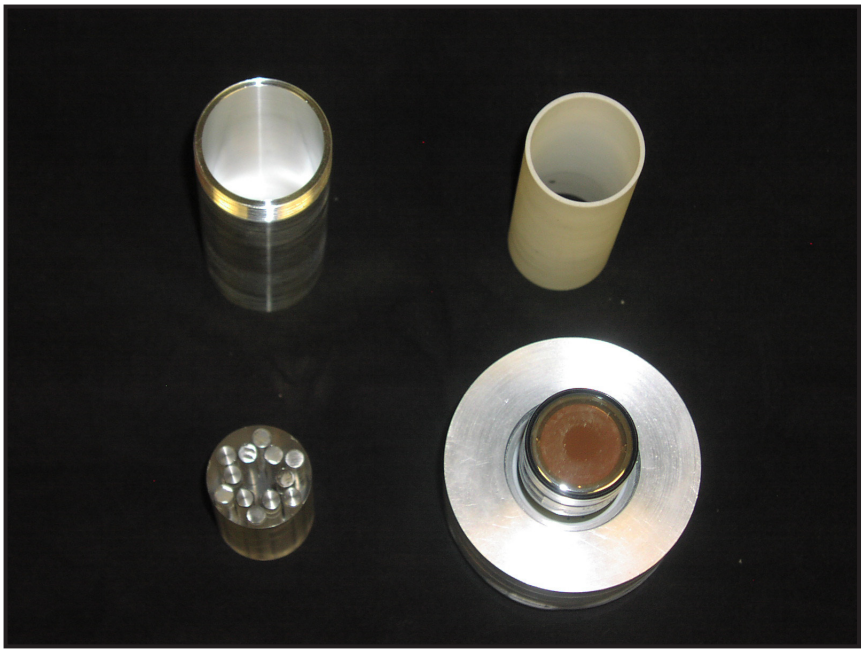

Figure 2. Beryllium rod detector components

Another previous effort incorporated beryllium rods surrounded by a liquid scintillator (Ziegler, 2004). Testing this detector on the Z machine showed a nonexponential component in the decay measurement due to motion generated in the liquid by the accompanying ground motion produced by machine fire. Other tests using a beryllium layer cake modeled after the optimized lead layer cake showed sensitivity to the bremsstrahlung environment at Z. MCNPX calculations indicated that there is an overabundance of scintillator in the layer cake design. Using some spare beryllium rods, we built a small detector with a smaller ratio of activation material to solid scintillator (Figure 2). This project evaluated and compared the response of this beryllium rod detector with the layer cake detector.

Project

The following reactions are of primary interest in measuring the neutron yield:

$$^{2}H + {}^{2}H \rightarrow {}^{3}He\ (0.82\ MeV) + n\ (2.45\ MeV)\ \text{Equally.} \quad \textbf{(1)}$$

$$^{2}H + {}^{2}H \rightarrow {}^{3}H\ (1.01\ MeV) + p\ (3.04\ MeV)\ \} \text{Probable.} \quad \textbf{(2)}$$

$$^{2}H + H \rightarrow {}^{4}He\ (3.5\ MeV) + n\ (14.1\ MeV). \quad \textbf{(3)}$$

These are the primary reactions on all devices used in thermonuclear fusion attempts. Since the neutrons transport efficiently, they are typically employed to measure these devices' performance. Beryllium is an excellent choice for an activation medium for many reasons. It has an exceptional cross section for both d-d and d-t neutrons, being 90 mb at 2.5 MeV and 10 mb at 14.1 MeV (Figure 3).

Beryllium undergoes an (n,alpha) reaction when exposed to neutrons with energies greater than 0.670 MeV, as shown in Equation 4:

$$^{9}Be + {}^{1}n \rightarrow {}^{6}He + {}^{4}a. \quad \textbf{(4)}$$

The ^{6}He decays by beta emission with an endpoint energy of 3.51 MeV. This ^{6}He decay has a 0.8-sec half-life, which is easily measured using conventional nuclear instrument module (NIM) electronics and organic scintillators.

The initial effort was to use MCNPX to optimize the thickness of the combined layers of beryllium and scintillator for d-d neutrons. Previous works (Nelson, 2004; Rowland, 1984) have determined that the ¼"-thick beryllium sheets or rods are the optimum thickness for transporting beta particles emitted from the ^{6}He. Calculations show that 74% of the beta particles are absorbed in the first 3 mm of the scintillator, and that 84% of the beta particles are captured in the first 4 mm (Figure 4). We ordered three sets of BC-418 scintillator to test using the BN DPF neutron generator. Unfortunately, because the DPF has not been operational since the scintillator material was received, we do not have this experimental data to compare with MCNP calculations.

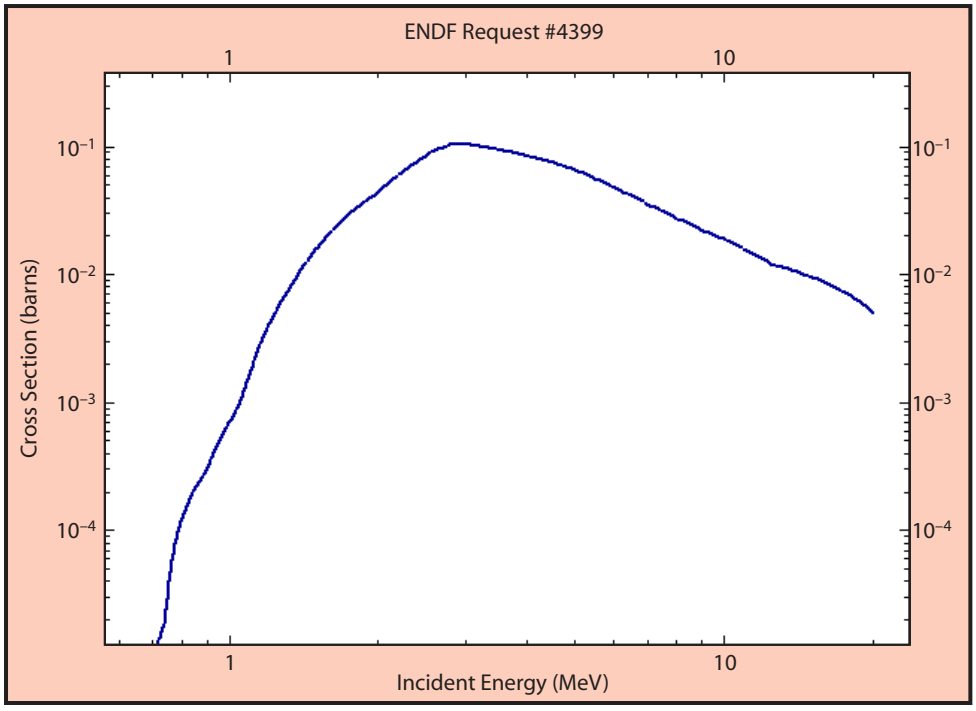

Figure 3. Be(n,a) cross section

The other experiment would determine a detector calibration procedure. The electronics currently used with these activation detectors employ a constant fraction discriminator. To ascertain a stable operating point, the low-level discriminator was varied for the different high voltages applied to the photomultipliers (Figure 5).

Data collected with the beryllium layer cake on a casual shot at Z showed a typical response from activation detectors using counting mode bias strings on the photomultiplier. These responses usually show a dip in the count before the exponential decay becomes dominated by a single component. When the long-lived components are stripped out, data looks like those shown in Figure 6.

From this data, a least-squares fit can be made to determine the half-life of the main decay and the initial count rate A_0. The closeness of agreement with the known decay constant gives a measure of the accuracy of the measurement. A comparison of the sensitivity of the beryllium rod detector to the sensitivity of the beryllium layer cake appears in Figure 7.

Using a discrimination setting of 200 at 6" from a source, rod detector sensitivity compares very well with that of the layer cake with a 400 discrimination setting at 50" from the source.

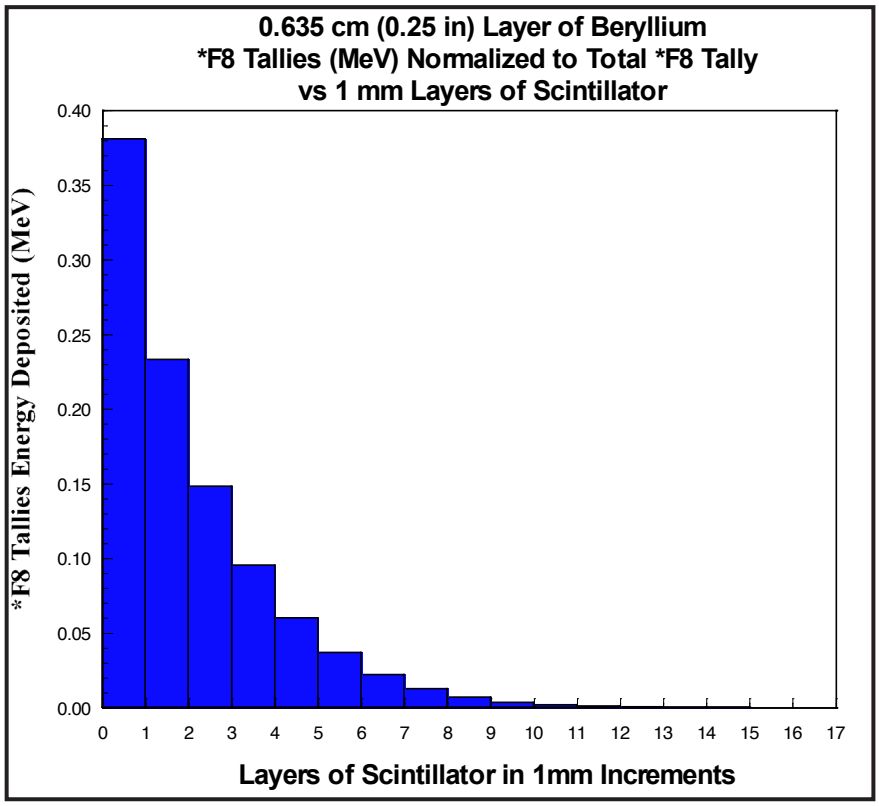

Figure 4. Fraction of beta particles counted vs. scintillator thickness

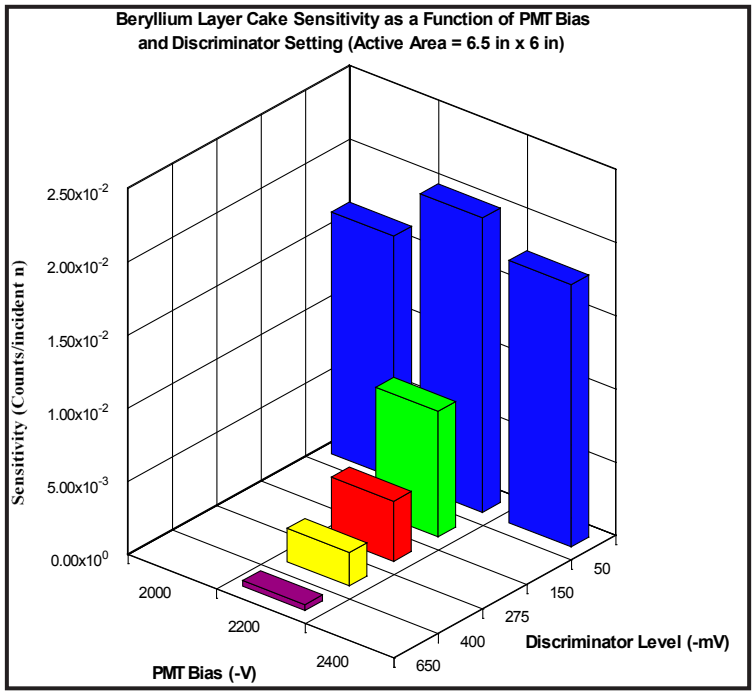

Figure 5. Sensitivity of beryllium layer cake detector as a function of PMT bias and discriminator setting

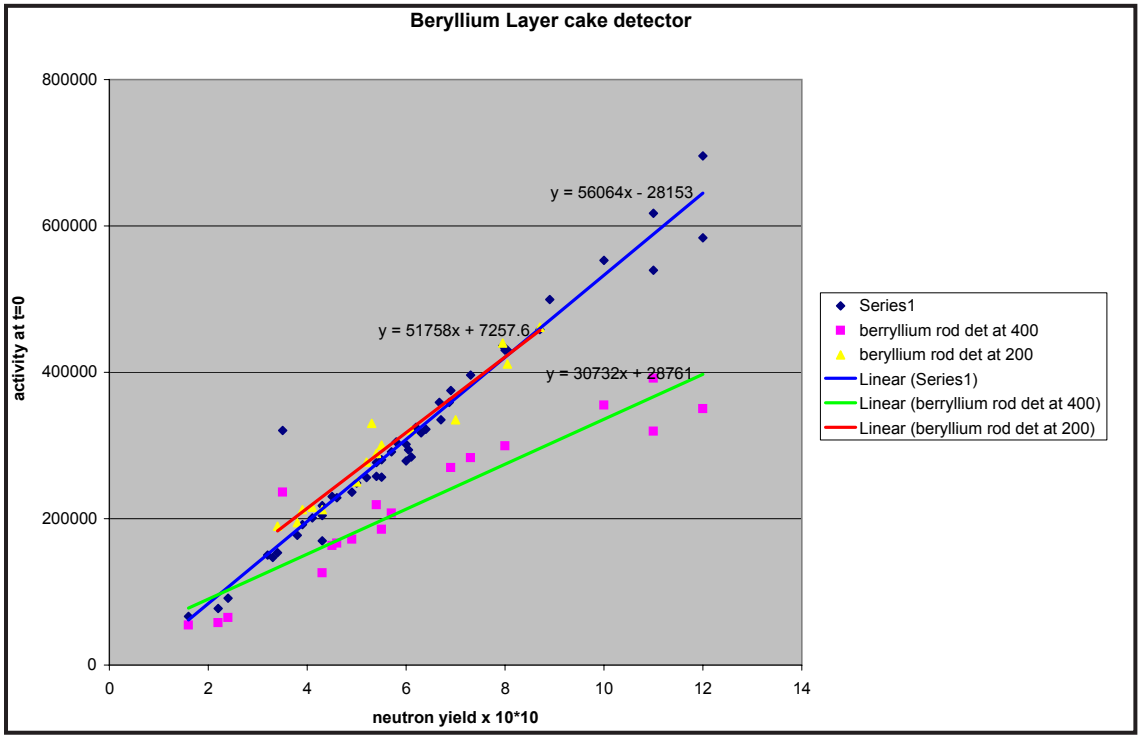

Figure 6. Response of a beryllium layer cake detector vs. channel from an experiment on the BN DPF neutron generator

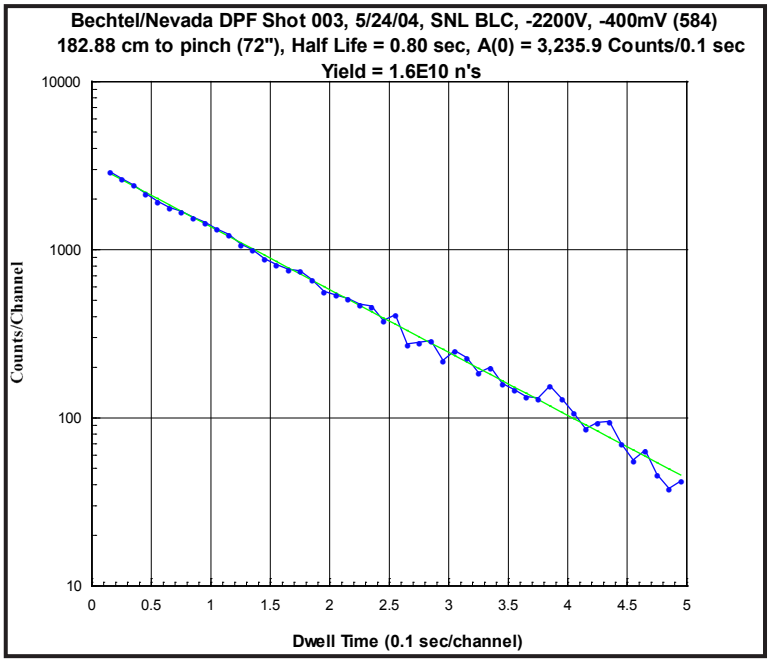

Figure 7. Response of the beryllium rod detector to neutrons as a function of discriminator setting. Series 1 is the response of a beryllium layer cake with a bias of 400 with the detector 50" from the source. The beryllium rod detector was 6" from the source.

Conclusion

The beryllium layer cake shows promise in measuring neutron yields on several pulse-power devices. Special attributes of the beryllium layer cake and rod detectors include:

- High sensitivity (1 count per ~50 incident neutrons)
- Low yield-detection level of 104 neutrons/pulse at 5 cm
- Energy threshold of 0.670 MeV (insensitive to thermal ns)
- 10% accuracy
- Data obtained in real time, ~3 sec
- When multichannel scaling is employed, decay curve appears as a straight line on a semilog plot.

Further research is necessary to determine optimum scintillator thickness for these detectors.

Acknowledgments

I wish to thank Carlos Ruiz, of Sandia National Laboratory, and Alan Nelson, of the University of New Mexico, for contributing most of the data and all the modeling referenced in this report.

References

Cooper, G. W., C. L. Ruiz, "NIF total neutron yield diagnostic," *Rev. Sci. Instr.* **72**, 1 (2001) 814–817.

Ekdahl, C. A., "Neutron diagnostics for pulsed high-density thermonuclear plasmas," *Rev. Sci. Instr.* **50**, 8 (August 1979) 941.

Jacobs, E. L., "An Arsenic-Activation Detector for Bursts of 2.5 MeV Neutrons," SAND79-1831, Sandia National Laboratories, Albuquerque, New Mexico, 1979.

Jacobs, E. L., S. D. Bonaparte, P. D. Thacher, "An arsenic-activation detector for bursts of 2.5 and 14 MeV neutrons," *Nucl. Instrum. Methods* **213** (1983) 387–392.

Jacobs, E. L., C. E. Spencer, "The lead activation technique for high energy neutron measurement," *IEEE Trans. Nucl. Sci.* **NS-12** (February 1965) 407–414.

Lanter, R. J., D. E. Bannerman, "Silver counter for bursts of neutrons," *Rev. Sci. Instrum.* **39**, 10 (October 1968) 1588–89.

Lanter, R. J., D. E. Bannerman, "The Silver Counter, a Detector for Bursts of Neutrons," LA-3498-MS, Los Alamos National Laboratory, Los Alamos, New Mexico, 1966.

Nelson, A. J., "Optimization of the Lead Probe Neutron Detector," Masters of Science thesis, University of New Mexico, Albuquerque, New Mexico, 2003.

Nelson, A. J., C. L. Ruiz, G. W. Cooper, J. K. Franklin, L. Ziegler, "Optimization of the Lead Probe Neutron Detector," SAND2004-1163, Sandia National Laboratories, Albuquerque, New Mexico, 2004.

Nelson, A. J., "Calibration of a detector for measuring D-D fusion neutrons based on the $^{9}Be(n,a)^{6}He$ reaction," 31st IEEE International Conference on Plasma Science, Baltimore, Maryland, June 28–July 1, 2004.

Rowland, M. S., "A novel fast neutron counting system for short bursts," Ph.D. thesis, University of New Mexico, Albuquerque, New Mexico, 1984.

Ruiz, C. L, R. J. Leeper, F. A. Schmidlapp, G. Cooper, D. J. Malbrough, "Absolute calibration of a total yield indium activation detector for DD and DT neutrons," *Rev. Sci. Instrum.* **63,** 10 (October 1992) 4889–4891.

Ziegler, L. H. "Particle-discriminating neutron detectors," *Nevada Test Site–Directed Research, Development, and Demonstration*, FY 2003, Bechtel Nevada, Las Vegas, Nevada, 2004, 117–121.

Electronics

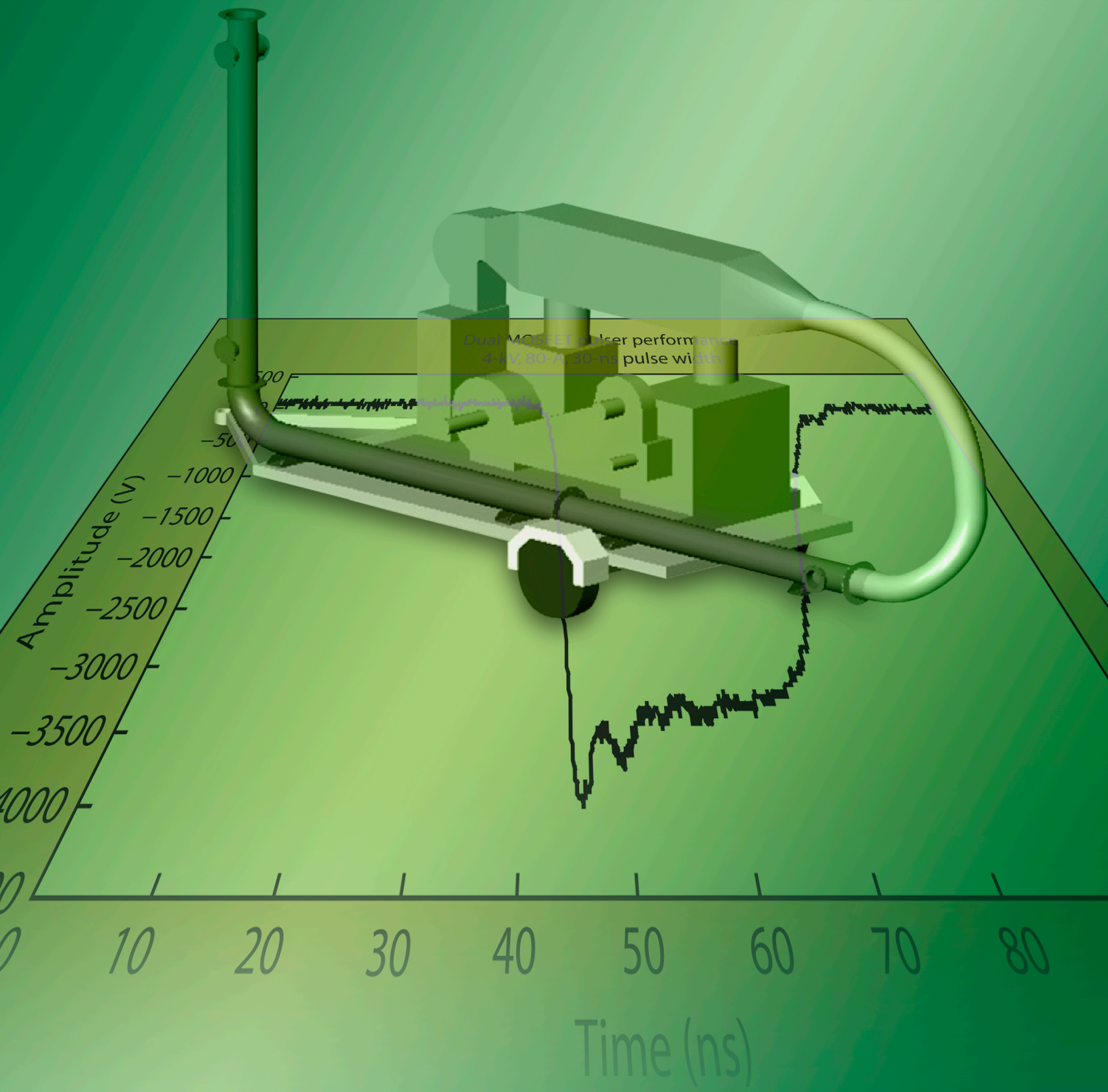

High-Power Pulser

D. Taner Bilir,[1] *William A. Warthan*
Livermore Operations

This research intended to build on previous work to determine suitable solid-state technology for high-power pulsers. In FY 2004, several solid-state devices were identified as potential candidates for such work. Feasibility requirements were chosen based on three criteria: voltage rating, current-handling capability, and rise time. The solid-state pulser may be used to drive 75-mm image intensifiers, and for this platform, we set a design goal of 10 kV into 50 Ω at a 5-ns rise time. First-level prototypes have yielded a 4-kV pulser into 50 Ω at 2.5 ns and an 8-kV pulser into 50 Ω at 2 ns. For demonstration of a typical pulser application, pulse widths were set to 30 ns.

Background

The DOE/NNSA community has always required high-voltage, high-current pulsed electronics. For years, numerous applications have incorporated krytron gas tubes, which are no longer commercially available. Replacement devices with similarly impressive specifications are not yet available. However, great improvements in solid-state semiconductor technology have been realized, thus suggesting that, using solid-state devices, we could build a circuit that mimicked, or even surpassed, the performance of gas tube–based pulsers. While pulser designs using solid-state technology have been around for many years, none has achieved 10 kV or higher pulses with square waveforms and short (<50-ns) pulse widths.

Project

This project began as a follow-on to our previous research, which identified several solid-state switching devices as potential candidates for a high-power pulser circuit. One of the most common applications of the now-obsolete krytron tubes is in the BN image converter (IC) camera, which uses krytrons to send 10 kV into a capacitive load that draws about 200 amps of pulsed current in an approximately 5–15-ns rise time and 30–50-ns pulse width. We designed our circuits to drive 10–12 kV into a 50-Ω load, to exceed the current output requirement of the IC camera pulser.

[1] bilirdt@nv.doe.gov, 925-960-2626

The project consisted of four parts:

- Review of FY 2004 work,
- Development of circuitry design,
- Development of printed circuit board layout design, and
- Fabrication and testing.

Except for part 1, these were iterative stages, whereby circuitry led to layout that was then built and tested, creating design changes in the circuitry and/or layout.

In FY 2004, we identified the following device candidates to put through the four project stages:

- A BiMOSFET: IXYS IXBH40N160
- A thyristor: Solidtron (Silicon Power) SMCT TA3214A10
- A dual MOSFET: DEI (IXYS RF) DE275X2-102N06A.

This report will address issues and results for each device.

BiMOSFET

Because of its combination of speed, voltage, and current, the bipolar metal-oxide semiconductor field effect transistor (BiMOSFET) seemed the most promising device. We initially designed the BiMOSFET circuit with respect to datasheet specifications of 1600 V, 65 A (pulsed), and 5-ns rise time. Since our design goal was 240 A, we paralleled five stacks of six BiMOSFETs to ideally allow 9.6 kV at 325 A. However, the pulsed current specification was for a 1-μs pulse. Since we were aiming for a 5-ns fall time and approximately 30-ns pulse width, we believed that this circuit would be capable of much higher current. According to the specification,

$$65\ \text{A} \times 1\ \mu\text{s} = 65\ \mu\text{C}, \text{ and} \quad (1)$$

$$65\ \mu\text{C} \div 30\ \text{ns} = 2167\ \text{A}.$$

In terms of energy, this is:

$$65\ \text{A} \times 1600\ \text{V} = 104\ \text{kW} \quad (2)$$

$$104\ \text{kW} \times 1\ \mu\text{s} = 104\ \text{mJ}$$

$$104\ \text{mJ} \div 30\ \text{ns} = 3.47\ \text{MW}$$

$$3.47\ \text{MW} \div 1600\ \text{V} = 2167\ \text{A}.$$

Needless to say, this BiMOSFET pulser design should be capable of driving 50 Ω with pulse widths from our 30-ns design point, up to 1 μs.

This flexibility with respect to pulse width was a key design element, since a flexible piece of equipment has more inherent value to BN and our customers. We designed the circuit drive to trigger each stack of BiMOSFETs simultaneously, thus coupling into our load through a large capacitor. The electrical charge was supplied via an EMCO F101 10-kV DC/DC converter. This allowed us to run a low-voltage power supply to the board and increased safety in the design. High-voltage lines were kept short, thus keeping ground loops very short and preventing oscillations. Our initial printed circuit board (PCB) design was fabricated and populated with components for testing.

In January 2005, management decided to discontinue work on this mature BiMOSFET circuit design, in favor of spending research funds on the two less-proven devices.

Thyristor

While the FY 2004 work suggested the use of the Solidtron SMCT TA3214A10, in April 2005, Solidtron launched the VCSFF05N14A10. The new device promised a faster switching time (50-ns vs 100-ns) with decreased current capacity (2000 A vs 4000 A) in a sleek, surface-mounted package. Since the current capability well-exceeded our requirements, we chose to develop a design using this new device and the original thyristor. Thyristors have an interesting property that differs from most semiconductor switches: they latch on and must be actively switched off. Most transistors, including bipolar transistors and field-effect transistors (FETs), will turn off as soon as one removes the switching charge. However, the thyristor latches on via current flow in the device. Thus, switching it off poses a challenge, as both an on- and off-trigger must be provided to turn off the device quickly. Otherwise, the device turns off when the supply charge is depleted, hence reducing the electrical field from anode to cathode to zero. The anode (and its associated charge well) can then recharge through the external power supply.

Although the thyristors were slower than either the BiMOSFETs or MOSFETs, we believed that if we charged the gate as quickly as possible, we would push the limit of the device-switching speed. Thus, in our circuit design, our on-trigger was an avalanche-mode bipolar transistor (the Zetex FMMT417) running at 320 V. This avalanche transistor can switch 320 V in less than 100 ps. Thus, we decided to transformer-couple the trigger signal to decrease gate voltage (to avoid overvoltage damage) without losing speed. Rather than provide a direct off-trigger, we attempted to bias the gate at –5 V, so that when the trigger signal was removed, the gate would see a –5 V potential and switch off. In initial circuit testing, the avalanche drive successfully switched the thyristor on in 40 ns, much faster than the 100 ns quoted on the datasheet. We were encouraged to pursue further designs. However, the –5 V bias potential did not suffice to switch the device off, and we had to rethink our approach (Figure 1).

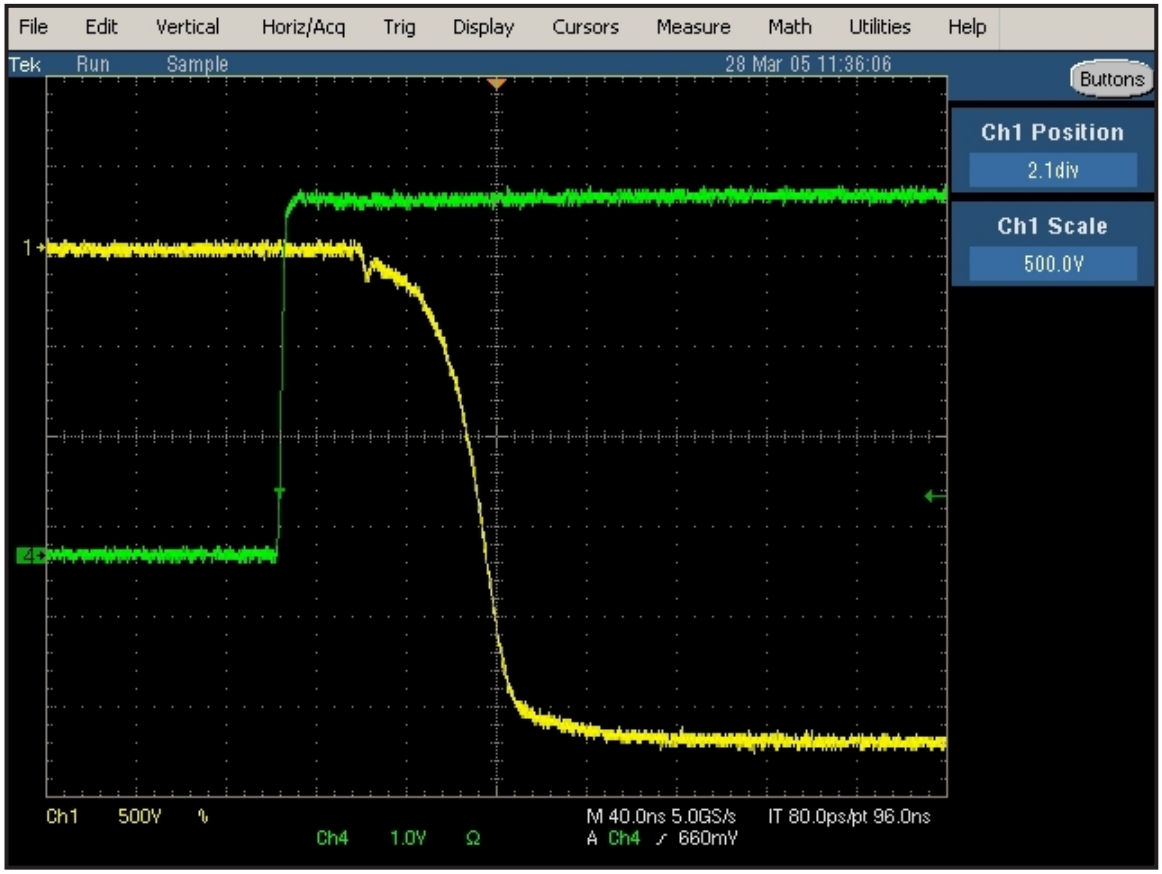

Figure 1. Yellow trace: thyristor switch oscilloscope trace (2.7 kV in 40 ns); green trace: TTL positive-going trigger signal (4 V)

The team decided to pursue a new design, incorporating a coaxial delay line between two thyristor gates. The first device would be switched off by firing a second thyristor to remove the supply charge feeding the current in the first device. In the same way that a charge line can snap a device off, we believed that this circuit would also snap off the device, and it would remain off due to the –5 V bias. We attempted to accelerate fall time by switching to the VCSFF05N14A10 surface-mount package. However, we could only increase the switching speed to a 15-ns fall time. While this was a 62.5% improvement over the previous devices, it was not fast enough for us to incorporate into a pulser for 75-mm image tubes. Additionally, the method of switching the first thyristor off via delay line was unsuccessful. We believed we could modify the circuit to achieve success on this design point. However, because of the thyristor's relatively slow fall time, we chose not to pursue it further.

These thyristors seem too slow to be useful in a krytron-replacement effort. However, the devices' high current capacity and latching ability suggest that they would be well-suited for 15 ns/40 mm or slower ramp-generator circuits because they would have a built-in hold-off.

Dual MOSFET

The dual MOSFETs identified in FY 2004 were part number DE275X2-102N06A from Directed Energy, Inc. (now IXYS RF). With a datasheet rise time of 2 ns and pulsed current specification of 96 A, the dual MOSFET seemed ideally suited to our design goals. The 1-kV devices would stack 12 high to achieve 12 kV, and as with the BiMOSFET current calculation, these devices should be able to switch 3200 A. While these devices' internal resistance would limit the actual current maximum, we believed we could readily achieve the 240-A design goal. We selected was a totem-pole design MOSFET driver, also manufactured by IXYS RF, the DEIC420. This driver was chosen over the avalanche transistor because of the active control of the off-time. Pulse width could be controlled by varying the width of the trigger signal into the pulser. Such a dynamic pulser could have varied applications beyond driving 75-mm image tubes.

While a design using a series/parallel configuration shown with the BiMOSFETs was conceivable, we chose a different route. To eliminate the pulser's high-voltage power supply requirements, we pursued a Marx bank design, in which each stage is capacitively coupled to the next, such that any device in the stack needs to only see a comparatively low voltage (1 kV) with respect to ground. Using a 1-kV instead of a 10+ kV power supply simplifies some printed circuit board considerations because the high voltage (10+ kV) is only present for the duration of the short pulse. Many devices, including passive capacitors and resistors, can deal with much higher pulsed voltages and currents than at DC.

The first prototype was designed to incorporate 4 devices, rather than 10 or more, in order to validate circuit design and resolve triggering issues. The totem-pole trigger was much more fragile than the avalanche designs of the BiMOSFET and thyristor circuits. The DEIC420 claimed a 30-V operating maximum but was only able to drive a MOSFET gate at 15 V without causing an oscillating retrigger. Since the drive's operation at 15 V was significantly slower than the desired 2-ns rise time, we attempted to dampen oscillation via series gate resistance. With less than 1 Ω of resistance, the associated rise time dropped to 3 ns. By placing fast Schottky diodes to shunt negative voltage spikes, we achieved 5 ns on the rising edge of the trigger pulse. Staging through the four circuit devices, we achieved a 2.5-ns fall time and a 9 ns rise time, for a 4-kV pulse into 50 Ω (Figure 2).

This result encouraged us to push the design to 10 devices, from which we expected 10 kV into 50 Ω. However, in testing this pulser, we saw only about 8 kV at the output. Initially we suspected that our capacitors' equivalent series resistance (ESR) was too high, since we could see a voltage drop across them. However, after further testing, we determined that the MOSFETs' internal resistance was also contributing. The devices were specified to have internal resistance on the order of 0.8 Ω. For the approximately 160 A running through them, this would yield a voltage drop of 128 V across

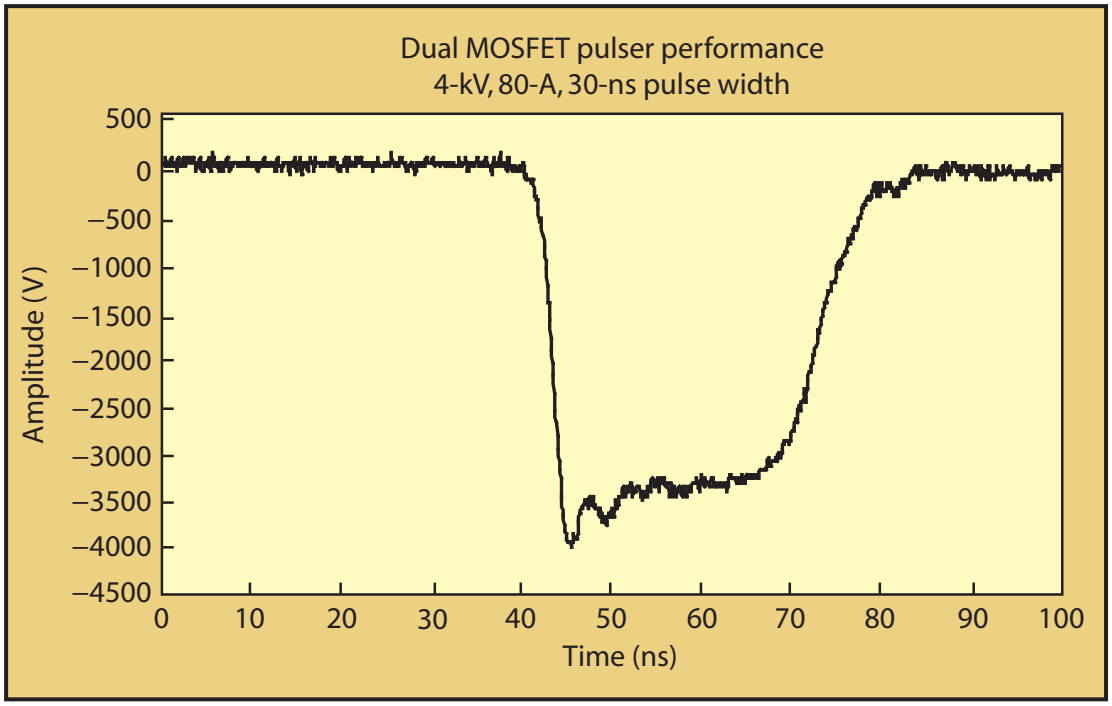

Figure 2. Dual MOSFET pulser waveform

each stage. Since the per-stage drop was approximately 200 V, we attribute much of the remaining 72 V/stage to the capacitors' ESR. If the entire drop were due to ESR, it would imply an ESR of 0.45 Ω, which seemed a bit high but not unreasonable for surface-mount ceramic capacitors at high frequency. Inductance and stray capacitance and resistance were also likely to be factors, but we believe that the ESR and internal device resistance were the greatest contributors.

Thus, the team redesigned the circuit to include four additional 1-kV stages and modified circuit board design to decrease signal path distances as much as practically possible. While we have not yet tested this new circuit and layout, it would be an excellent point at which to pursue further development.

Conclusion

Our team has shown that several different solid-state devices can be implemented into a pulser circuit for high-power applications. While it is still unclear which device and design methodology would best suit any particular application, a DOE/NNSA NTS contract effort could use this work to develop successful high-power pulsers. Additional research and development remains to be conducted, particularly on the BiMOSFET, but initial findings are promising. Some of the circuit designs are company-private but probably not patentable because new circuit design methodology is lacking.

Acknowledgments

The following team members were essential in the success of this research project: Charles Diamond, for his circuit design and testing expertise; Eric Hillenga, for his efforts in fabrication and testing; and Jim Mirador, for his circuit board design and prototype fabrication efforts.

References

Baker, R. J., "Applying Power Metal-Oxide Semiconductor Field-Effect Transistors (MOSFETS) to the Design of Electronic and Electro-optic High-Speed Instrumentation," EG&G Energy Measurements, Aug. 4, 1993.

Baker, R. J., B. P. Johnson, "Stacking power MOSFETs for use in high-speed instrumentation," *Rev. Sci. Instrum.* **63,** 12 (1992) 5799–5801.

Dymoke-Bradshaw, T., "Design of Solid State Pulsers, University of Cardiff, 11 April, 2000," Kentech Instruments Ltd., http://home.btconnect.com/akldb/PDF/CU_talk.pdf, (accessed September 20, 2005; link discontinued).

this page intentionally left blank

Multipath Communication Device

Paul Ainsworth, Kuan Chin, Ben Davison, James Essex,[1] Mark Stacey, Eric Wagner
Remote Sensing Laboratory – Nellis

This investigation aimed to design and develop a proof-of-concept Multipath Communication Device (MPCD) for handling field data telemetry. The team created a flexible, centrally configured communications platform. This platform allows static and mobile field-deployed assets to create a most-capable/least-cost configuration, based through one of several commercial or standalone communications mechanisms. Capable of multiple configurations, the device can accept data from multiple sources. It then autonomously receives, packages, buffers, archives, and transmits data to a mobile base station or to fixed Web assets via the Internet. Transmission-capable up to Unclassified Controlled Nuclear Information (UCNI), the device meets all government-approved security doctrines for data transmission.

Background

Real-time data requirements exist for most emergency response–related activities. This is true for crisis response and consequence management, where operational scenarios require a configurable communications platform allowing static and mobile field-deployed assets to create a communication path through a commercial or standalone communications mechanism. Integrating this technology into the existing RSL real-time data acquisition and dissemination (RDAD) architecture will provide a capability for real-time data acquisition, data transmission, and server-based dissemination beyond the capabilities of current standalone infrastructure communication scenarios (Figure 1).

Project

This investigation focused on design and development of a communication system for vehicle-based field data telemetry using custom software for original equipment manufacturer (OEM) technologies. We initially investigated OEM technologies for Internet protocol (IP) data transmission and selected six modules to incorporate into our device. Each communication module was tested independently and met all requirements for coverage, cost, and performance (Table 1).

Commercial off-the-shelf OEM hardware technologies were also chosen for central processing unit (CPU), global positioning system (GPS), and system power components (Figure 2). The design's single board computer (SBC) met requirements for expansion options, CPU speed, and operational specifications. The device runs a customized, embedded Microsoft Windows XP operating system.

[1] essexjj@nv.doe.gov, 702-295-8714

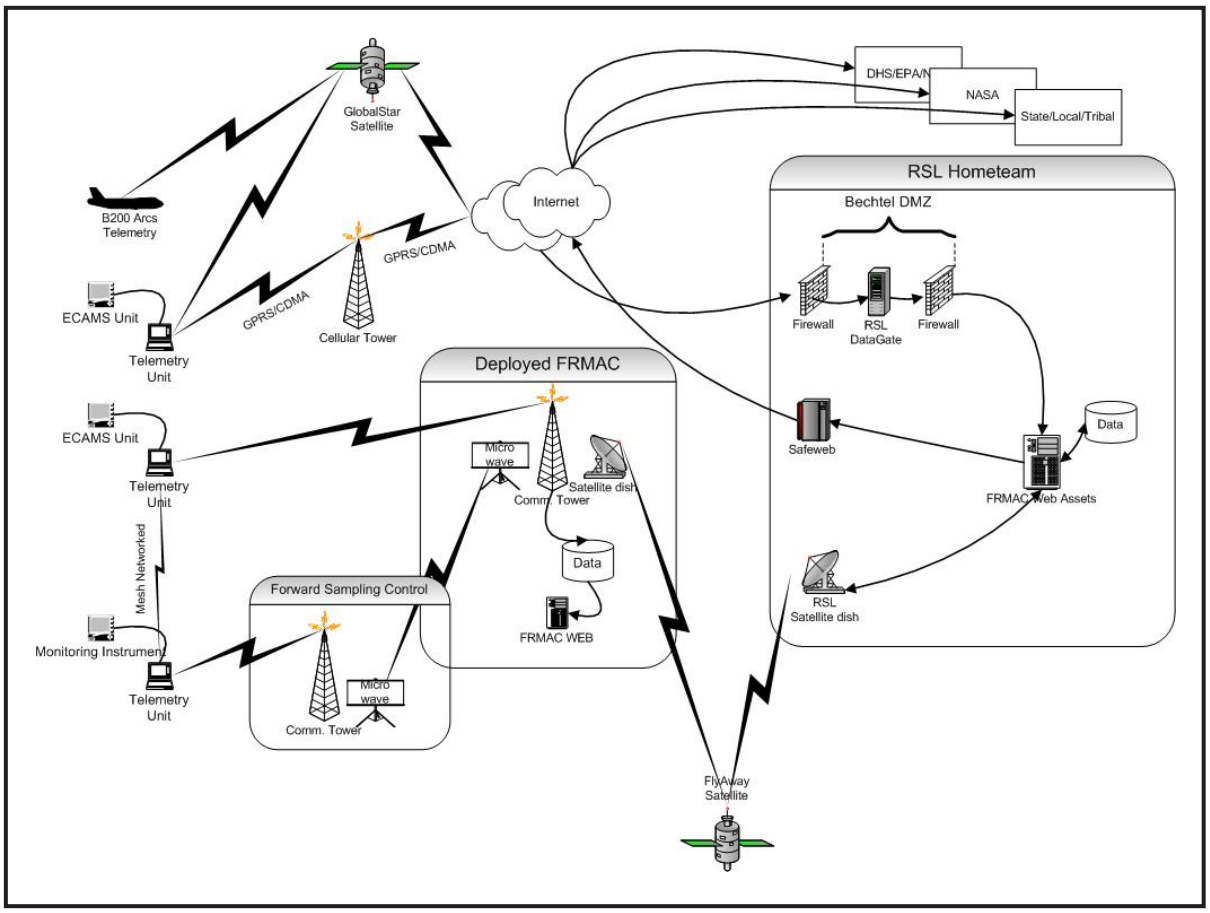

Figure 1. Existing and proposed assets for full implementation of the RDAD network

Software Development

Based on operational requirements, both manual and least-cost configuration control modes were required. We investigated multiple, nonlinear, decision-making algorithms capable of fusing past experience, situational data, and module characteristics. A fuzzy logic algorithm was chosen over neural networks, genetic algorithms, and reinforced learning due to its ability for fast, approximate reasoning, ease of training, and unmodified incorporation of additional plug-and-play communication modules.

Table 1. Communications modules used in MPCD

Module	Carrier	Bandwidth	Procurement Cost	Operation Cost	Coverage / Range
CDMA	Verizon	153 kbps	$300	Plans vary; $59/month for service, $0.25/ minute for data (Quick 2 Net[sm])	US Metro
GSM/GPRS	Cingular	85 kbps	$300	Plans vary; $20/month for 5 MB, additional $0.008/k	US Metro
Globalstar GSP 1620	Globalstar	9.6 kbs	$1,000	Plans vary; effective rate approx. $1.00/ minute	All regions except Sub-Sahara Africa, China, and these Central American countries: Belize, Costa Rica, El Salvador, Guatemala, Honduras, Nicaragua, Panama, and surrounding coastal waters
NovaRoam	N/A	100/400 kbps	$1,800	N/A	Up to 25 miles line of sight with proper installation
802.11g	N/A	1 to 23 Mbps	$60	N/A	Up to 1 mile with high-gain antenna; typically 1000 feet line of sight
BlueTooth	N/A	1 Mbps	$50	N/A	32 feet

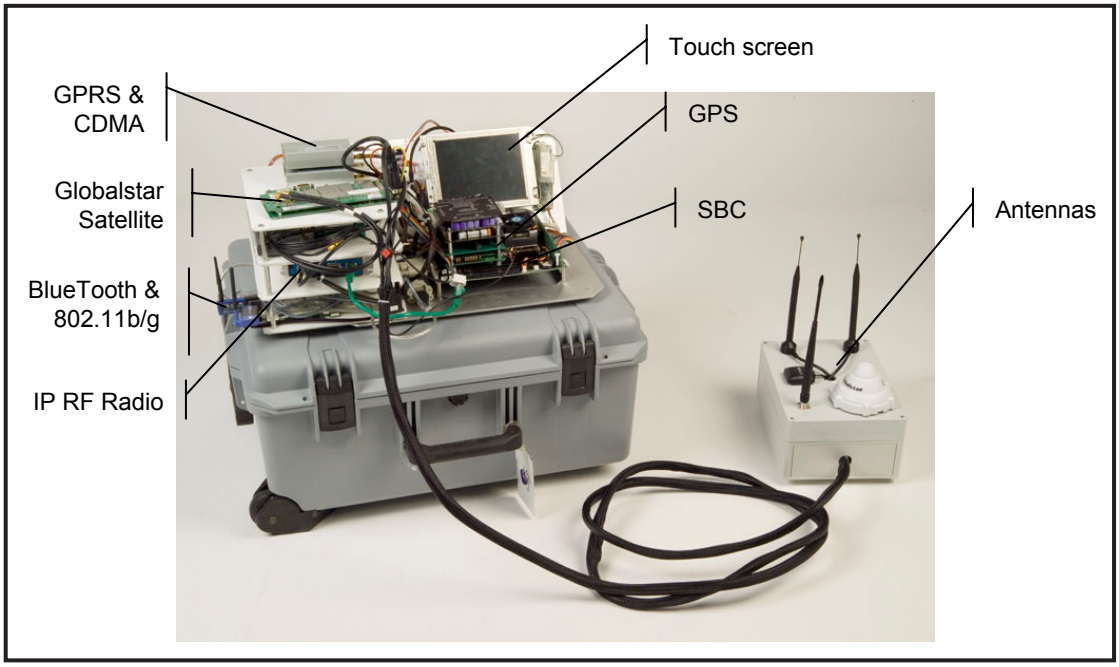

Figure 2. Prototype Multipath Communication Device (MPCD)

The fuzzy logic algorithm used creates the most capable communication configuration based on cost and performance. It requires assembling a fuzzy set for each of five parameters and creating two separate rule sets for determining membership within the sets. Initially, each parameter, including module use cost, percent spent, bandwidth, past reliability, and recent connection attempts, have equal weighting. However, as parameters vary, weighting may also change.

Operations costs are initially estimated by entering the number of MPCD devices, transmit model, and total hours of operation. Based on these inputs, the range is estimated and displayed for the coordinator to determine cost tolerance. Cost tolerance is then used together with percent spent for the scenario and costs per module, to dictate the weighting coefficients used to determine the relationship between cost and performance.

Performance parameters are calculated in real time, using data stored locally on the MPCD device, including successful connection attempts, duration connected, and dropped connections for each module. Data about connection duration and cost is also collected, to be forwarded to the central location for cost data coordination (Figure 3).

Ranking results are obtained for each module by calculating the crisp usability value (Figure 4). This value is determined by applying the known characteristics of the device and data requirements into the fuzzy logic algorithm. The fuzzification process takes these crisp inputs and applies them

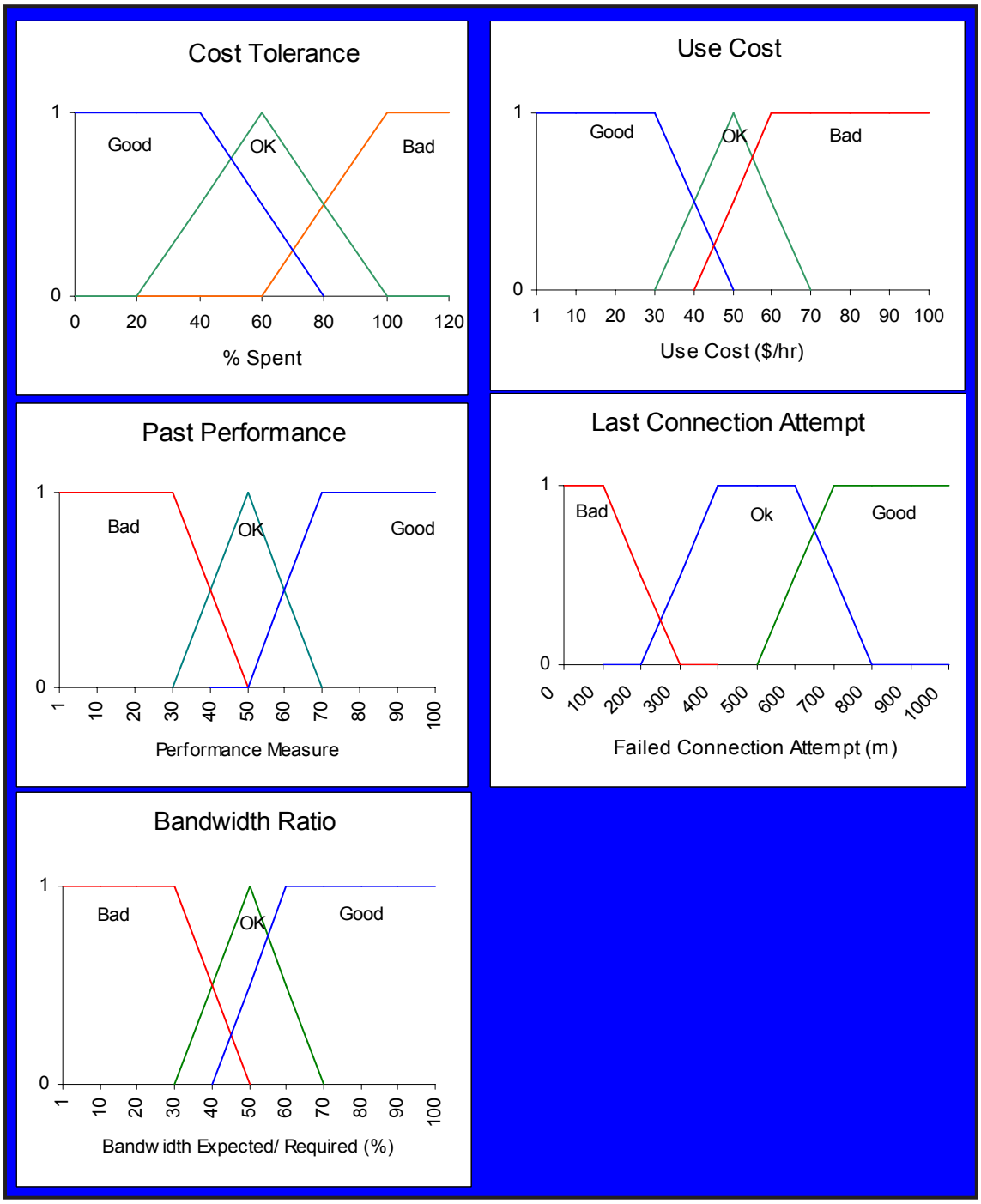

Figure 3. Fuzzy parameters for cost and performance used to provide data to the rule sets

to the corresponding membership function to determine the degree of membership in each fuzzy set. Membership is also used to establish rule execution, which determines the correlation to output membership. Min-max inferencing is used to calculate a single degree of membership for each fuzzy output member. The final defuzzification process then translates the fuzzy outputs into a crisp usability rank. This is performed using centroid defuzzification, represented by Equation 1.

$$X0 = \sum_{i=1}^{N} wici Ii \Big/ \sum_{i=1}^{N} wi Ii, \quad \textbf{(1)}$$

where X0 is the crisp output, w is the degree of membership, c is the centroid, and I is the area.

The manual configuration mode requires both an event session and device session. Once session data is chosen, the device can be powered off and will resume with the last session configured. The session determines the type of data sources connected to the MPCD and whether or not the device will use an existing or new communication module configuration. Setup occurs either via a commercial telemetry connection, where the device receives a configuration via database access, or manually, over a stand-alone wireless connection.

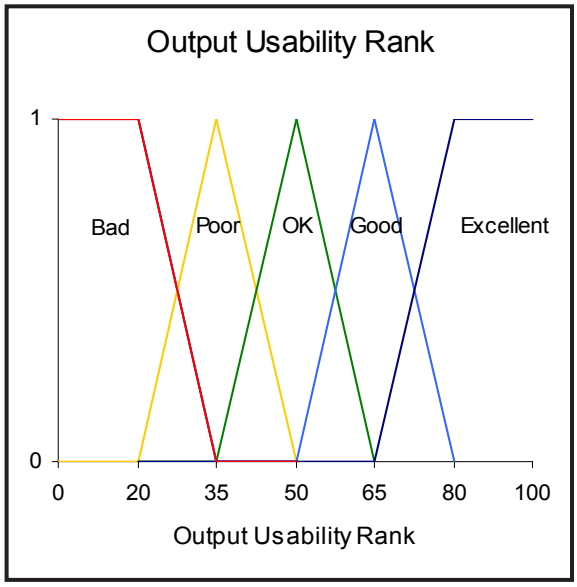

Figure 4. Crisp output used to calculate the usability rank, based on membership of cost and performance, defined by the two rule sets

Field tests were run on several modes of operation, including continuous, distance interval–based, time-based, or event-based connection scenarios. The results of preliminary tests met or exceeded expected results for outdoor benchtop testing. Additional data will be collected during the testing and evaluation phase in an NA-42 Technical Integration Program.

Conclusion

This investigation has demonstrated the feasibility of programmatically controlling multiple IP communication modules to allow connectivity through available communication modules, meeting specifications for cost, mobility, bandwidth, and performance. Project results have piqued the interest of multiple emergency programs that desire a highly reliable data communication mechanism. Testing and evaluation are currently occurring under the NA-42 program for Technical Integration (TI), and we plan to have a device ready for small-volume production (50–100 units) by the end of FY 2006.

Acknowledgments

This project was an RSL–wide collaboration that involved participants from Communications, Engineering, GIS/Data Management, Technical Operations, and the Radiation Sciences.

Reference

Internet FAQ Archives, "An Introduction to Fuzzy Control Systems," http://www.faqs.org/docs/fuzzy, accessed July 11, 2005.

this page intentionally left blank

DOE Complex Universal Trigger Distribution System

Lorrie Capitanelli, Cody Christensen, Heath Fullmer, David Good, Rudolpha Jorgensen (former employee), Tim Ploeger, Robin Robinson[1]
North Las Vegas

This project sought to develop a prototype universal trigger distribution system for use throughout the DOE test complex, including the NTS. The system will replace 20- to 30-year-old legacy pulse-generation and discrimination systems at the NTS. The new system utilizes fiber optics for transmission of trigger pulses as well as interfacing to legacy trigger systems.

Background

Current NTS trigger systems are based on 20- to 30-year-old designs. Due to parts availability, it is unknown how long these systems can be maintained. An ideal replacement trigger system would interface with existing hardware at the NTS, add the capability of trigger distribution via fiber-optic cable, and be designed for high reliability and easy customization to experiment requirements.

Project

A prototype universal trigger system (UTS) was designed to interface to existing legacy trigger systems, as well as provide triggers via fiber-optic cable. Each UTS interface function, input or output of signals, is performed by custom-printed circuit boards installed into a general-purpose backplane. The system may be quickly reconfigured by adding or removing boards (Figure 1).

Interface capabilities include ±5.0-V analog signals and fiber-optic pulses at 1320 nm or 820 nm. Output signals are 75-V tail pulses, transistor-transistor-logic (TTL) 50-Ω pulses, and fiber-optic triggers. The system is highly configurable, expandable, and easily customized to the needs of a particular experiment. The only limitation on chassis configuration is the system's card-holding capacity, with a full chassis comprising 19 cards. Although typically configured as two identical, fully redundant card sets, it may be configured with any combination of cards.

The bulk of our research was the development of the fiber-optic trigger board (Figure 2). The board utilizes a bidirectional transmitter/receiver module using an integral dichroic beamsplitter. The fiber-optic modules are designed to be used in pairs: one transmits/receives at 1320 nm/820 nm, the other at 820 nm/1320 nm.

[1] robinsra@nv.doe.gov, 702-295-2523

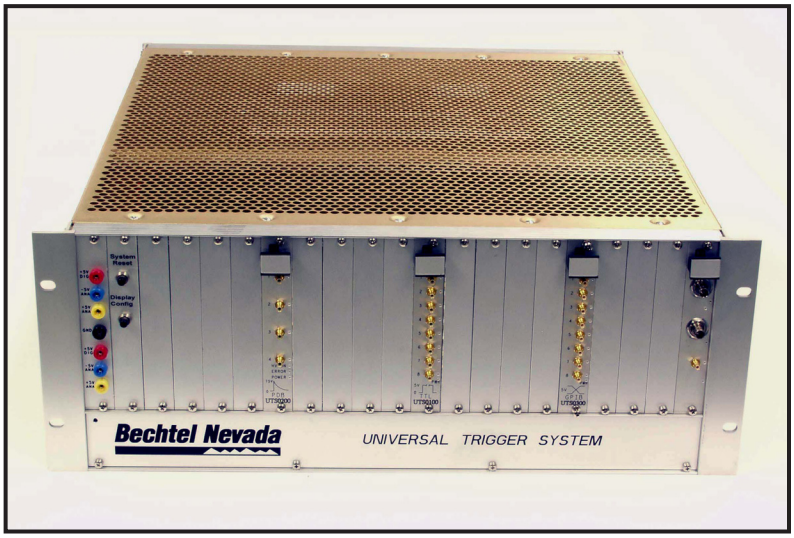

Figure 1. Universal trigger system chassis, featuring two independently powered backplanes with diode-mixed power to the bus termination. Signal lines, common across both backplanes, are available to all boards. Installed boards (L to R): pulse driver (75-V tail pulse), TTL output, general-purpose input, fiber-optic transmitter/receiver.

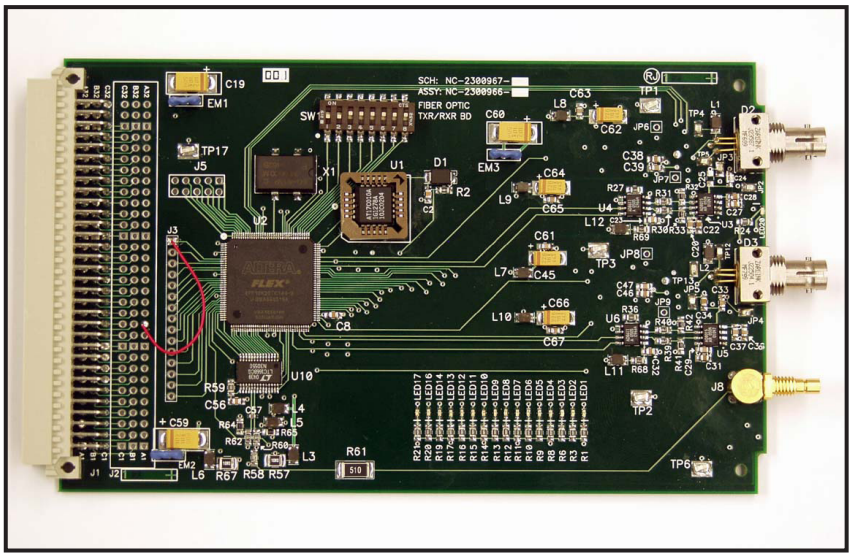

Figure 2. Two-channel, bidirectional fiber-optic transmitter/receiver board. J8 gold connector (bottom R) is the output from a 16-bit digital-to-analog converter (DAC) used to support NLV-013, optical transducer for underground testing.

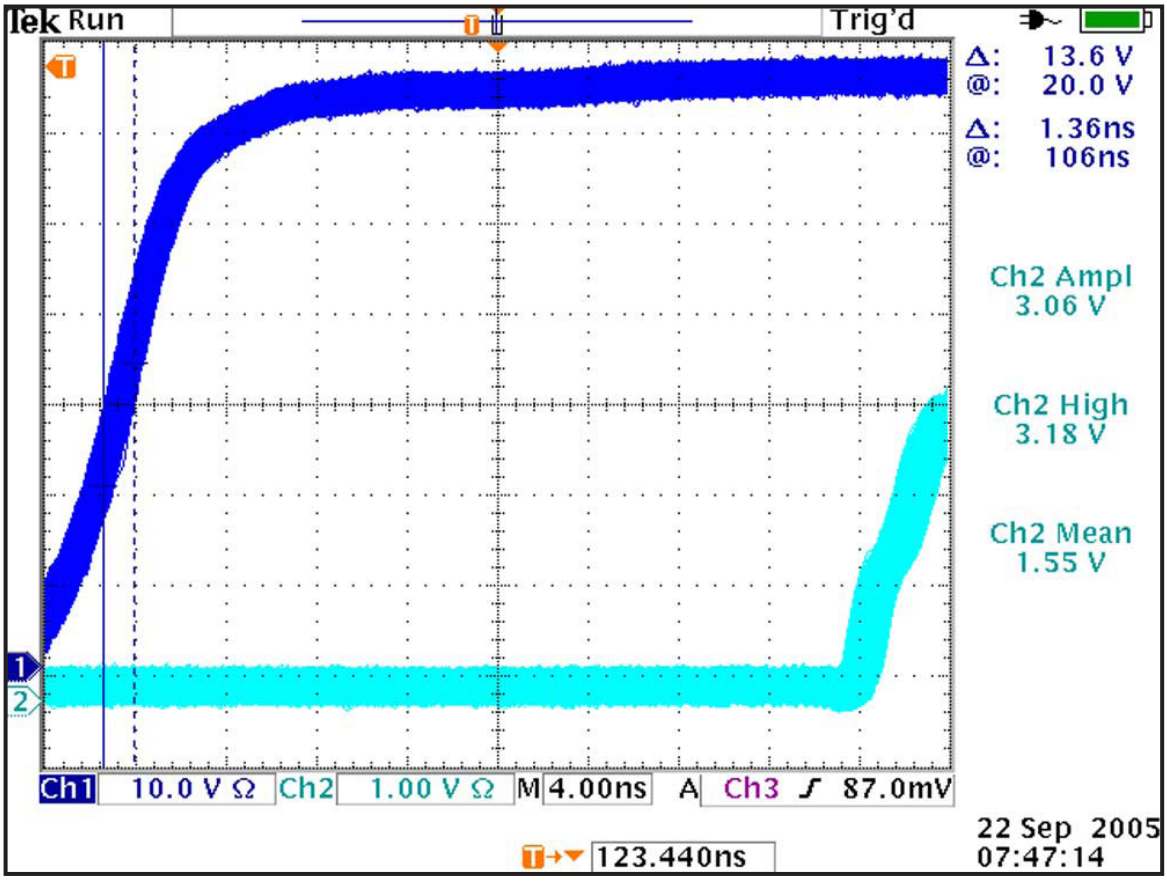

Figure 3. Infinite persistence scope display of jitter on output 75-V tail pulse and 50-Ω TTL output. Note: Trigger signal is not displayed. Figure shows long-term jitter on output triggers through the system. Data collection time = >10 hours.

We used commercially available integrated circuits for the light-emitting diode (LED) drive and pin diode receiver functions. The LED drive circuit performed very well, providing sufficient LED output intensity and excellent output shape. The first receiver designed performed poorly in this application, though we do not yet understand why. Another receiver design, developed in-house, is operating very well. The prototype's overall system performance is close to the original design specifications. Output tail pulse jitter is ~1.36 ns over a 12-hour test period, while TTL output jitter is ~2 ns (Figure 3). Both jitter values reflect hours of pulses being generated at 1 Hz and displayed on a digital scope set to infinite persistence. Shorter tests, on the order of an hour, show jitter to be <900 ps for the tail pulse and <1.5 ns for the TTL output. Both jitter measurements can be reduced by additional system tuning, though time constraints at the fiscal year-end did not allow us to do so. Measured propagation delays were higher than anticipated, with the tail pulse delay at 86 ns and TTL output delay at 121 ns. These values can also be reduced by additional system tuning.

Conclusion

A prototype universal trigger distribution system was designed, fabricated, and tested. The trigger distribution system was designed to operate in a variety of experimental locations throughout the DOE complex and to functionally replace legacy trigger distribution systems. The prototype performed very close to design targets. With minimal additional work, the system performance could easily exceed targeted design specifications. The fiber-optic transmitter/receiver board requires minor revisions to improve jitter and propagation delay values. Other modifications might include increasing channel density from two to four fiber-optic channels and removing the 16-bit DAC. Currently, the project only utilizes one-way transmission, but future development could employ bidirectional capability for diagnostics, fiber status, and communication between distributed trigger systems.

Variable Temperature and Flow Stack for Reactive Fugitive Releases

Charles Lohrstorfer[1]
Nevada Test Site

James Capelle, John DiBenedetto, Thomas Keenan
Special Technologies Laboratory

This project hoped to advance the chemical release technology used at the NTS. It has focused on expanding capabilities at the Nonproliferation Test and Evaluation Complex (NPTEC) to include additional system variables, specifically variable flow rates and exit temperatures. After identifying the benefit of providing variable temperature and airflow rates, our team proposed creating a capability for modeling existing and future chemical release apertures.[2] A secondary benefit would be the ability to study chemical reactions under stacklike conditions. Incorporating optical ports at each end, the two-man-portable design would provide a simple, rapid method to study reaction kinetics. The critical path was to model a simple portable release aperture, build a prototype, create a variable flow/temperature source, and verify the model. After design, a custom, commercially available heater/blower unit with controllable temperature and flow rate was specified, and the unit was procured. In parallel, a portable stainless steel portable stack was designed at STL and fabricated by an outside shop. The heater/blower and mini-stack were integrated at the STL 226 test complex, and a series of preliminary tests was performed.

Background

Nonproliferation technologies (NA-22, IWFO) and environmental monitoring programs require more variable release rates and conditions. While the NPTEC currently provides accurate chemical releases, the facility has no method to continuously vary system temperature or total discharge rate. Aircraft "start carts" are used as reliable sources of flow and heat but at single settings of flow and temperature. Figure 1 shows an NPTEC C-130 start cart attached to the 10' mini-stack used at NPTEC during the FY 2005 Shrike Test Campaign, sponsored by the DOE/NNSA, NA-22, Office of Nonproliferation. While NPTEC is recognized as a national leader in chemical releases from stacks, no American chemical release systems can provide variable temperature and overall flow rates to fully simulate the required scenarios for liquids. NPTEC, its users, and other U.S. facilities would adopt these advances in release technology.

[1] lohrstcf@nv.doe.gov, 702-295-5688

[2] NPTEC refers to release systems as the chemical release instrumentation and hardware (valves, meters, nozzles, etc.). We will refer to the physical stacks and other release mechanisms as "apertures."

Project

The project's main components were to:

1. Develop a specification and procure a heater/blower unit that would meet or exceed current NPTEC equipment capacity (single start cart) but with controllable temperature and flow variation. The heater/blower must be able to produce 1250 SCFM air flow at temperatures of up to 200°C. As a lower limit, STL designed the system function at 625 SCFM and ambient temperature.
2. Design and procure a two-man-portable stack for use with the heater/blower during evaluation.
3. Model the proposed system using state-of-the-art, computational fluid dynamic (CFD) software and optimize design based on the results.
4. Integrate the blower/heat exchanger with the portable stack, instrument and test the system to verify specified performance, and compare with performance predicted by the CFD model.

Figure 1. C-130 start cart and existing NPTEC mini-stack

Results

The original project proposal envisioned the design and construction of a manifold system that would mix ambient air with hot air from the start carts, thus providing controllable variation of temperature and flow rate in the stack. However, early on, we discovered a custom, commercially available heater/blower system that would meet or exceed the capacity of a C-130 start cart, but with variable temperature and flow capability. As this heater/blower unit would also eliminate the problem of acoustic transmission through the flow system, optical and chemical diagnostics on the stack would not experience the strong vibrations from the start carts. Considering the added benefit of complete remote control of system functions, we decided to procure and integrate the custom unit.

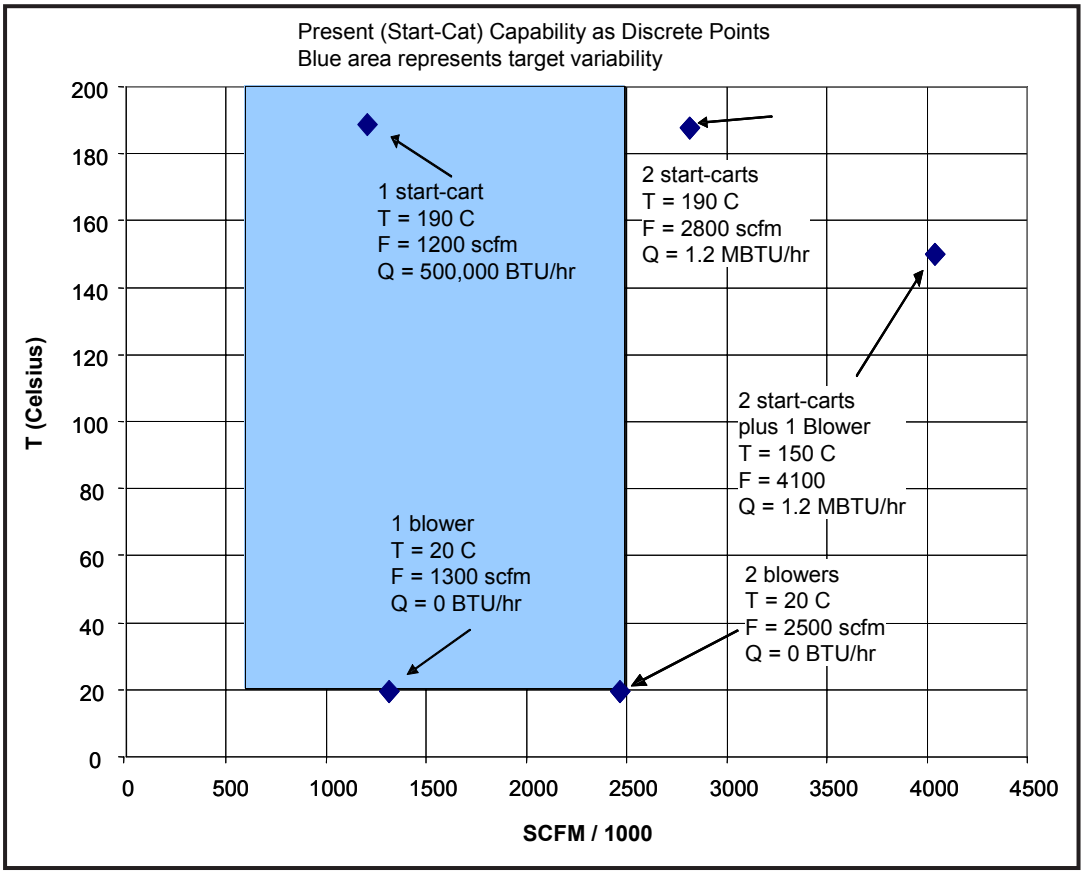

Figure 2. Existing flow/temperature options (points) and variable system (blue square)

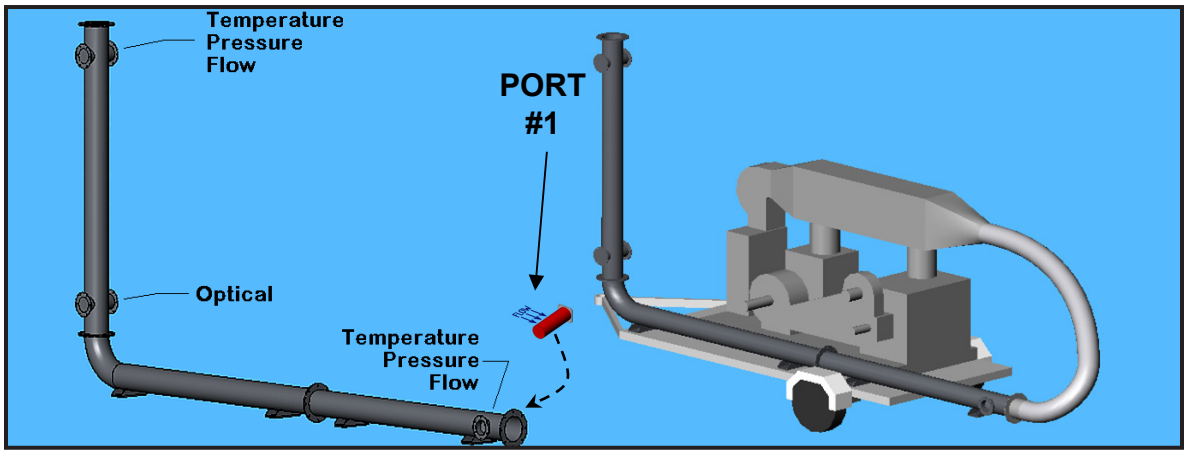

Figure 3. (left): A SolidWorks rendering of the heater/blower as tested. Note Port #1 at the input. (right): Same release aperture attached to the blower on a trailer. One obstruction shown in red.

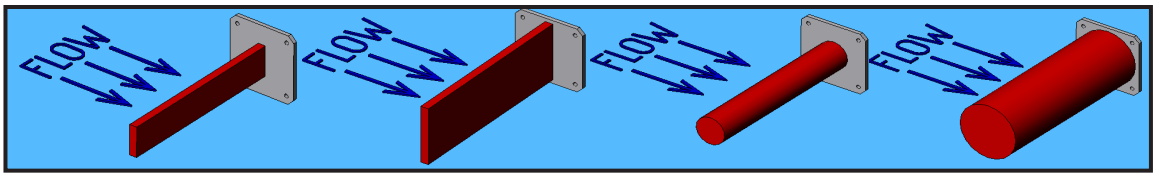

Figure 4. Obstructions used in modeling and physical tests

Figure 2 shows some of the existing discrete temperatures and flows achievable with a pair of start carts and ambient temperature blowers used at NPTEC. The final SDRD design specification is a compromise in total range, as it does not completely replace two carts. However, the custom, commercial unit provides a wide range of variability in a single heater/blower unit that can be remotely controlled and more quietly operated on 220-V power and propane heat.

Figure 3 demonstrates a model release aperture designed in the SolidWorks computer-aided design (CAD) software package. We specified components that could be easily transported and assembled by two individuals at a release site. After weight and strength were considered, the stack components were fabricated from standard stainless steel pipe that could be easily replicated. The heater/blower and release aperture could be mounted on a standard 20' trailer as rendered. If fielded, this configuration could provide rapid, complex-wide versatility.

Flow modeling was performed using COSMOSFloWorks. The module couples directly to the SolidWorks CAD software purchased specifically for this project. Using FloWorks model shapes, obstructions were designed in SolidWorks and fabricated at a local machine shop. The obstruction concept is an initial test for modeling nozzles and other chemical release components located in the flowing gas. Figure 4 shows the model obstructions, and Figure 5 depicts the model's graphical output for a

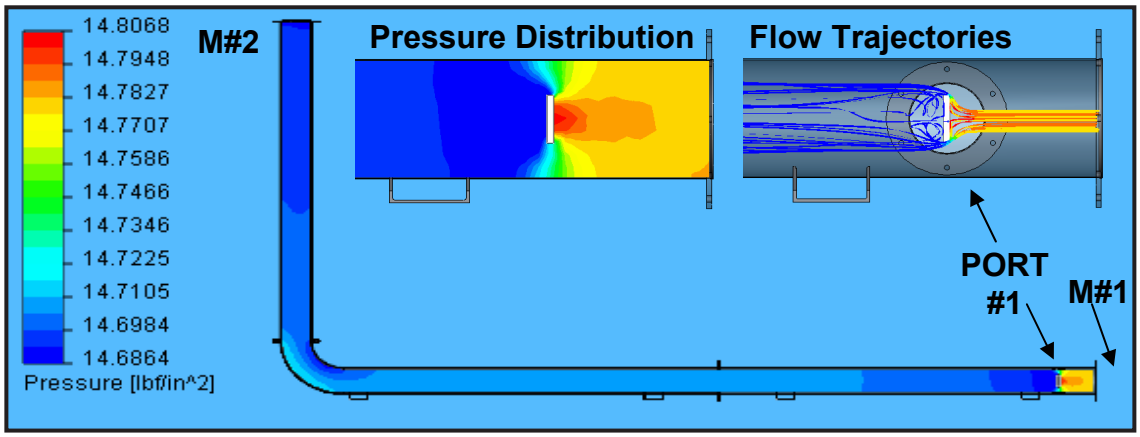

Figure 5. Model output obtained for the 4" flat plate obstruction. Inserts show magnification of area near Port #1.

Table 1. COSMOSFloWorks simulation results. Conditions: 200°C, 1250 SCFM (2050 ACFM).

Modeled Restriction	System pressure drop (w.c.) between M#1 and M#2	Model difference in pressure compared to open pipe
None (open pipe)	0.908	0
2" plate	1.212	0.304
4" plate	2.666	1.758
2" OD rod	1.116	0.208
4" OD rod	1.384	0.476
Air foil	0.913	0.005

4" plate, both inserted at Port #1. In Table 1, calculated effects on flow are shown as growth in back pressure with increasing restriction. The model back-pressure values are calculated at constant flow and temperature (1250 SCFM and 200°C, respectively).

The vendor specification for maintaining flow requires that back pressure not exceed 2.3" of water. While a 4" obstruction is a severe case, the modeling shows that the back pressure generated is greater than 2.7" of water at 200°C and could impact the blower's ability to generate sufficient flow.

Figure 6 shows the actual system during tests at STL 226. Under these conditions, the system was not obstructed enough with the 4" plate to create a back pressure exceeding the specification for linear performance (2.3" w.c.). Given the cross section of the plate, it is unlikely that a future nozzle system will create more drag or flow blockage than when tested here.

Figure 6. Variable temperature and flow system under test at STL

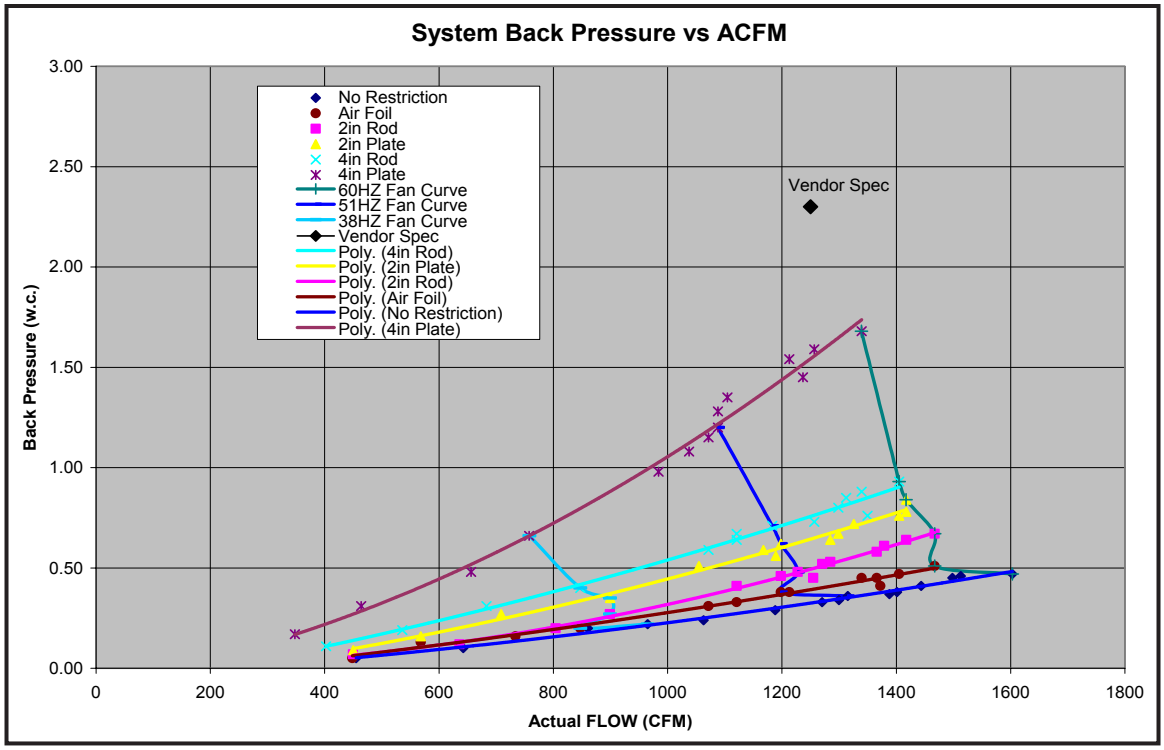

Figure 7. Flow versus system back pressure measured at Port #1. Actual flow (ACFM) measured at Port #1. Measurements made at ambient temperature (no heater).

The relationship between back pressure and blower flow is often depicted using a fan curve (Recktenwald, 2006). We tried to establish this curve for the complete system by determining a number of system performance curves. In this work, some system curves resulted from placing obstructions in the pipe at Port #1. Fan curves are derived from the experimental data. (A more comprehensive set of performance curves might be generated by inserting a flow valve in the pipe.) Figure 7 shows curves generated from the measurements. Since these measurements were made at ambient temperature, and the modeling was originally completed at elevated temperature (200°C), only a limited comparison to model data is possible. Additional modeling at ambient temperature, required for a direct comparison, would be valuable.

Conclusion

A fully operational release system with accurate and repeatable temperature and airflow control has been developed. We expect this system to meet release requirements for a multitude of scenarios, and it will prove useful for environmental monitoring and nonproliferation evaluation and testing at NPTEC.

At this time, modeling results are preliminary. As Figure 7 shows, the system appears to be operating in a linear range of the fan curve (meeting vendor spec). Reasonable agreement was found for trends with larger obstructions, such as the 4" plate and round shapes. The model overestimated the effects of the small airfoil. Observed back pressure was less than 50% of the predicted 0.913" of water. This comparison was only made for the 200˚C data. Additional tests in which the model variables for temperature and flow are set closer to the actual test values are needed. Modeling must be performed at ambient temperature to complete the comparison with STL test data. One important additional system test would be to create an obstruction that will generate at least 2.3" of back pressure to verify the vendor specification.

Reference

Recktenwald, G., "A Flow Bench for Measuring Fan Curves and System Curves for Air-Cooled Electronic Equipment," Portland State University, Portland, Oregon, www.me.pdx.edu/~gerry/epub/pdf/flowBenchManual.pdf, accessed April 21, 2006.

this page intentionally left blank

Optical Transducer Development for Underground Testing

Heath Fullmer, Rudolpha Jorgensen, Tim Ploeger,[1] Robin Robinson
North Las Vegas

To better understand the need for a more modern data transportation medium, this project researched containment metrology for subcritical experiments and past underground testing. Our team designed a device capable of transforming an analog transducer producing electrical signals from DC to 1 MHz into a 16-bit digital data stream to be sent through a single multimode fiber-optic cable.

Background

High data resolution and accuracy in inaccessible experimentation environments has previously been challenging, at best. Harsh environments placed data acquisition systems many meters, even kilometers, from their data-producing transducers. Another engineering dilemma was the need for data dissemination under high electromagnetic interference (Glenair, 1999). To address these challenges, we proposed digital sampling at 16 bits of analog transducer data and transmitting this data via fiber optics (Pirkl, 2005).

Project

The approach taken by our team was to design a single multimode fiber-optic data cable to transmit analog data and receive command information (Figure 1).

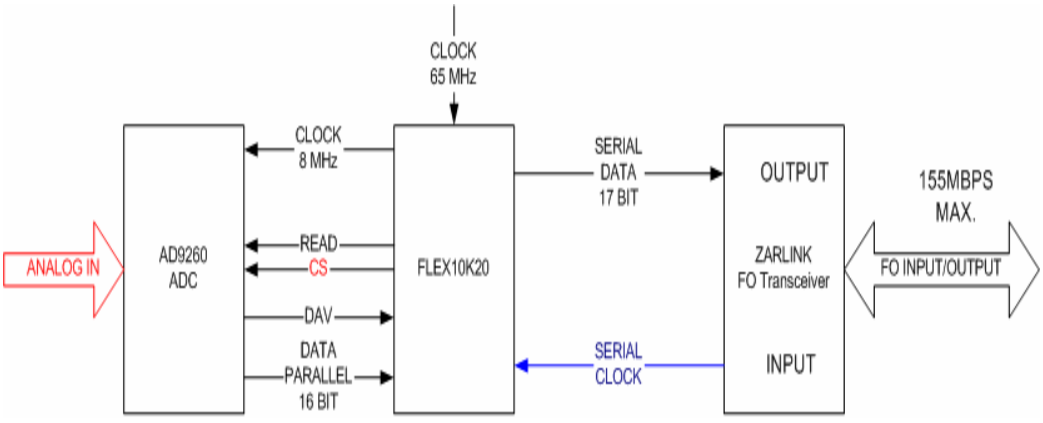

Figure 1. Analog-to-fiber-optic transmitter signal flow

[1] ploegetr@nv.doe.gov, 702-295-0138

The crux of the project was the electrical-to-optical digital data conversion. Analog signals were injected and subsequently digitized using an Analog Devices analog-to-digital converter (ADC), capable of sampling DC to 1.01-MHz input (Analog Devices, 2005). The input voltage was chosen to be a differential signal with a full-scale input of 4 Vpk-pk (±2 V), to reduce errors from floating reference conditions. This ADC produces a 16-bit binary equivalent of the sampled signal with a full-scale output of 65535 counts (Pirkl, 2005). After preliminary examination, we determined the effective bit count to be 12, leaving the last four bits to be in possible error. This allows for an error of 0.916 mV at 61 µV/count and an advantage over 8-bit systems with a 59-mV error at 19.5 mV/count. The effective bit count is a natural measurement made for ADCs with 12 effective bits out of 16 to be very good. With 12 effective bits, the precision is still an improvement over available 12-bit systems.

Conversion from parallel to serial data was accomplished by an Altera Flex 10K20. The parallel data emitted from the ADC (transmitter card) was derived by a clock generated on the receiver card at the other end of the fiber-optic cable. The resultant data was shifted into a serial stream at 1.01 megasamples/sec out of the transmitters' fiber-optic interface.

The signal was monitored by Tektronic scopes, using both electrical and optical probes. A ramp was supplied to the front end of the transmitter board, digitized, optically transmitted, then reconstructed. Two measurements were made to test the link: 1) optical data signature and power, and 2) receiver signal-to-noise ratio (SNR). Cross talk was found to exist between the transmitter and receiver portions of the fiber-optic circuit. The scope captures appear in Figures 2 and 3. Cross talk was found to result from inconsistent amplifier specifications, and should be researched and replaced with a more apt transimpedance amplifier.

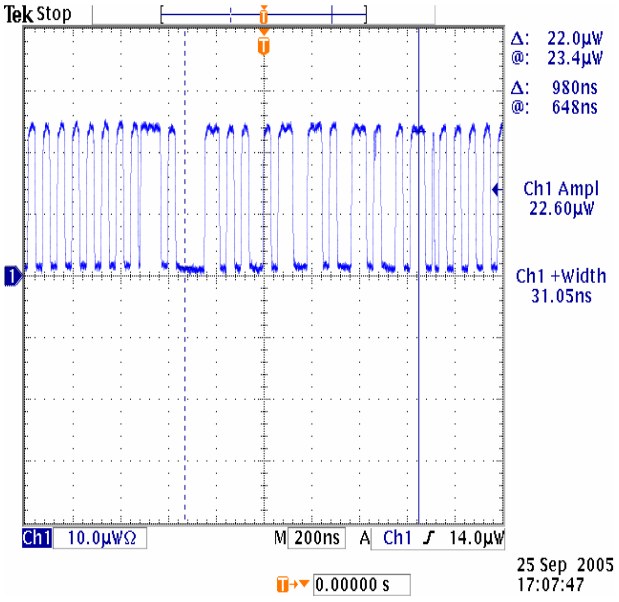

Figure 2. Power measurement and waveform of optical transmitter (coded digital data shown)

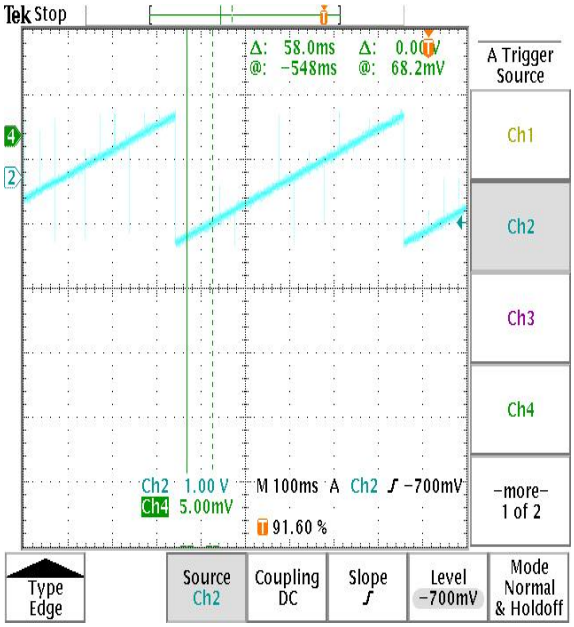

Figure 3. Ramp signal injected showing the signal-to-noise ratio of the receiver (note spikes on ramp)

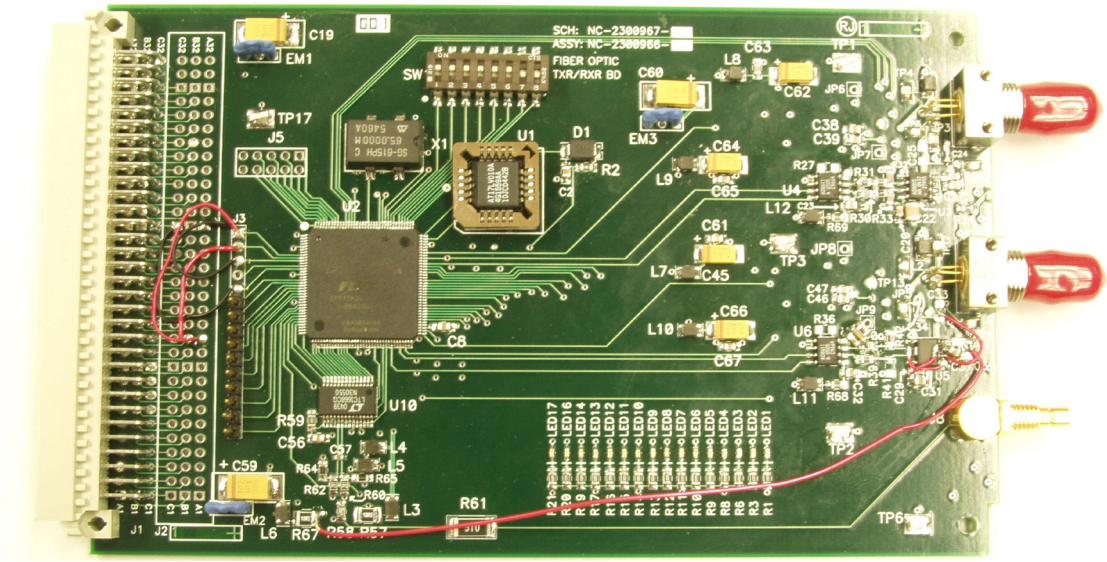

Figure 4. Receiver board

Figure 5. Transmitter board

Constructed and tested hardware appears in Figures 4 and 5. The transmitter was implemented in a Versa Module Eurocard (VME) card configuration. The VME chassis was used as a power supply only during final system testing. With the test module shown in Figure 4, an eight-channel system can be easily constructed utilizing a VME backplane. The amount of real estate taken for signal traces was minimized for the final production of the signal conditioner. This design features the latest Altera FPGA with digital signal processing. The FPGA can package transmitted data at 40 MHz.

Conclusion

Integrating fiber-optic technology into the data acquisition model would reduce cost and dampen the amount of error injected into data. Such an approach would be novel because the analog signal would be digitized at the transducer location and sent digitally. Analog voltage levels would not be loosely interpreted to wave-division multiplexing. This design would benefit from further investigation into the transimpedance amplification and alternate transceiver components.

Acknowledgments

Thanks to Michael Bridenburg, John Pelles, Lorrie Capitanelli, Cody Christensen, Michael Clark, and David Good for their hard work and dedication on this endeavor.

References

Analog Devices, http://www.analog.com/analog_root/static/designCenter/index.html, application notes AN-214, 282, 347, 352, 359, 417, 589, accessed June 14, 2005.

Glenair, "Turn Off Your Radio," *QwikConnect* newsletter **6**, 2 (April 1999), http://www.glenair.com/qwikconnect/vol6num2/coverstory.htm, accessed July 2, 2005.

Pirkl, L. A., "One-Gigasample-per-Second Remote Digitizer, *Nevada Test Site–Directed Research, Development, and Demonstration,* FY 2004 Report, Bechtel Nevada, Las Vegas, Nevada, 2005, 203–206.

this page intentionally left blank

Integration of DSP Technology into VISAR Receiver

Eduardo Rodriguez, Araceli Rutkowski, Michael Rutkowski[1]
Los Alamos Operations

The use of digital signal processing (DSP) in telecommunications, audio compression, echo location, and image processing has been steadily increasing. Our project's goal was to integrate DSP technology into an optical receiver used in the velocity interferometer system for any reflector (VISAR) and to improve the receiver's functionality. Project development engineers gained valuable experience in working with DSPs and learning integration concepts, while simultaneously improving VISAR receiver design. Testing showed that the circuitry currently used to provide the optical power meter reading can result in an error of up to 20%, especially at lower power input values. Using DSP technology, we sought to improve this circuitry by decreasing the maximum error to 5%. Presently, we have reduced this error to a maximum of 7%. With continued work, we believe we could further diminish the error while enhancing other VISAR receiver functionality.

Background

Optical power meter circuitry is calibrated during assembly. This circuitry produces an output voltage (1 mV per 1 μW) proportional to the optical power present at the optical receiver's input. Testing has shown that at lower input power levels, environmental factors can produce an output voltage error of up to 20%.

The project's mission was to integrate DSP technology into the VISAR receiver design, in order to reduce the magnitude of error in the optical power meter circuitry, while investigating DSP capabilities and integration. DSPs provide faster processing response times than do traditional microprocessors. Their ability to perform a greater number of MAC (Multiply and Accumulate) operations than traditional microprocessors results in superior performance, by enabling real-time signal processing in many designs. Incorporating DSPs into existing designs enhances overall design capabilities, which, in turn, will lead to improvements in future company products.

Project

In Figure 1, a block diagram denotes VISAR receiver operation. In the lower portion of the figure, a multimode optical signal at 530 nm, ranging from 1 μW to 100 μW, is detected using 100/140-μm fiber. This signal is utilized by two distinct paths. The main path (RF) transforms optical interference patterns from the VISAR to a voltage signal whose voltage level is great enough to overcome system

[1] rutkowms@nv.doe.gov, 505-663-2074

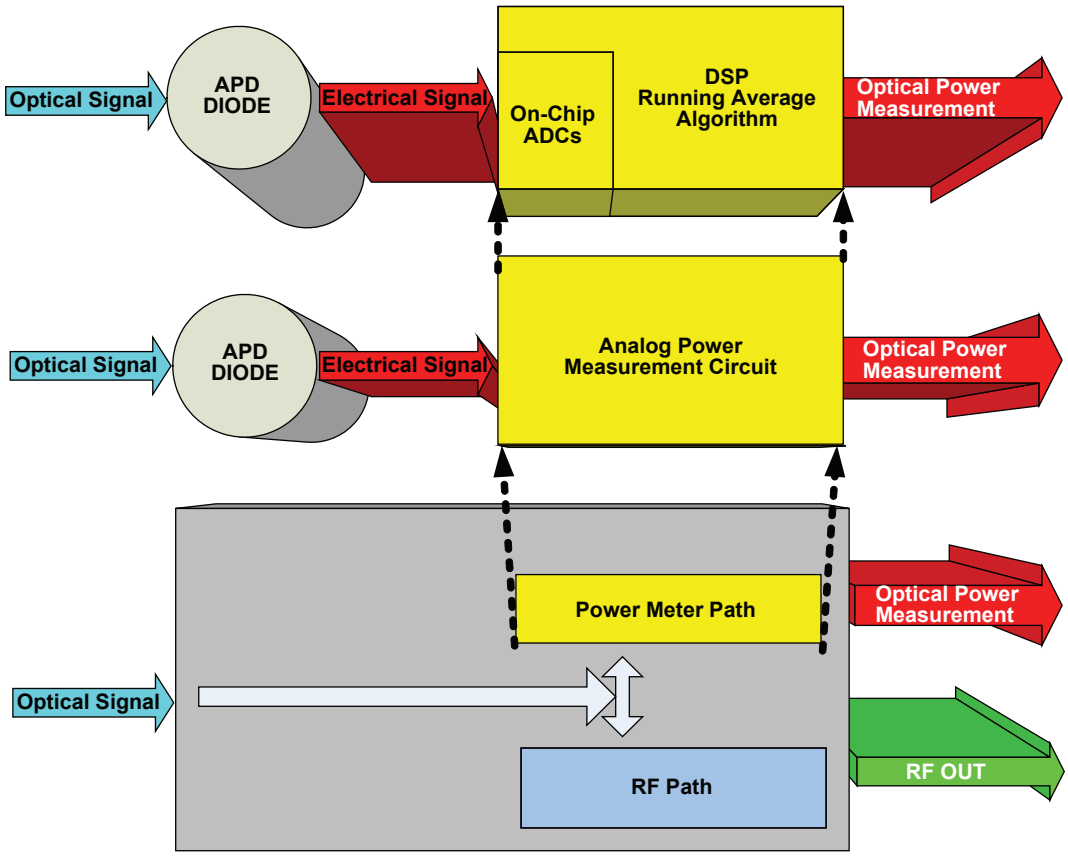

Figure 1. VISAR receiver

noise and provide the dynamic range to drive an oscilloscope. The other path (Power Meter) detects avalanche photodiode (APD) current proportional to received incident light. This project aimed to replace analog circuitry used for the Power Meter path with DSP circuitry to reduce signal error to a 5% maximum.

The project team replaced the bulk of this circuitry (operational amplifiers and trim resistors) with a DSP containing on-chip analog-to-digital converters (ADCs).

In using ADCs for this purpose, the team overcame noise on the signal lines by using an oversampling, averaging, and decimation algorithm. Figure 2 illustrates how this approach filtered out noise (Texas Instruments, 1998).

Figure 2 illustrates how the noise power present in a signal can be spread out over a larger bandwidth by oversampling. DSP filtering techniques are performed on this signal, which then yield a reduction in noise signal contribution. When this technique is used, the original sampling frequency must be at

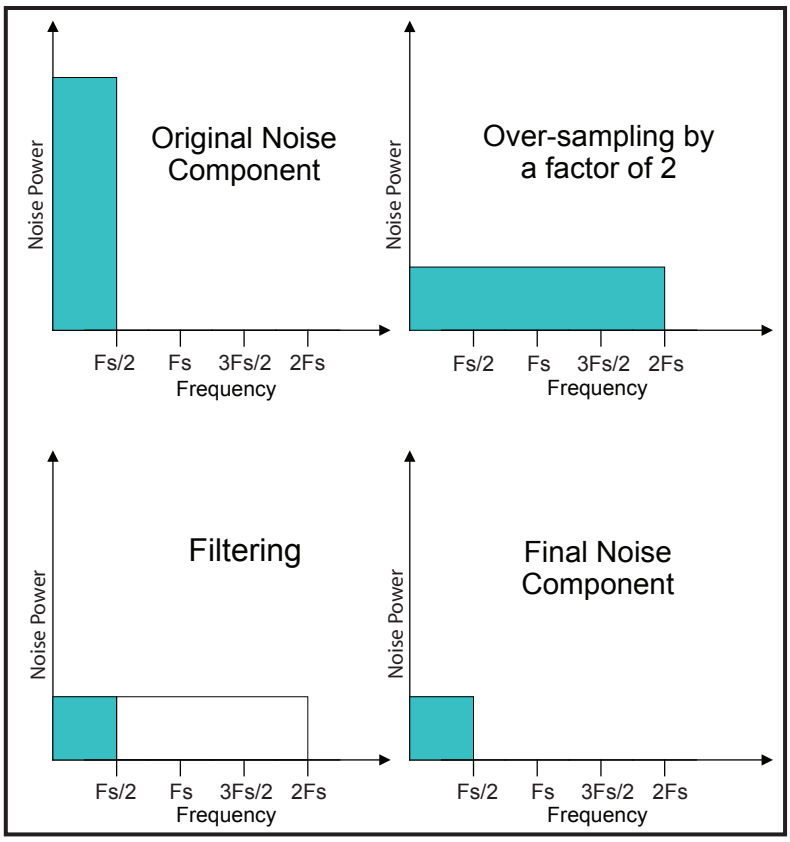

Figure 2. Oversampling and filtering effects on noise power. The blue-shaded portion represents noise contribution to the signal being sampled. Oversampling and filtering reduce the noise power contribution to the signal, increasing the signal-to-noise ratio.

least twice that of any frequency in the signal of interest (Nyquist's theorem), and the noise present must be random. Random noise appears as a Gaussian bell curve on a probability density function (PDF) (Texas Instruments, 1998). In Figure 3, a DC signal sampling appears as a PDF, confirming that the noise present is indeed random.

Figure 4 shows a signal being sampled at a certain frequency, F_s (red trace). The blue trace shows the same signal oversampled at a frequency of 16 × F_s, that is, 16 times faster than the original sampling frequency. The black trace shows the result of averaging and decimation (16 samples were averaged and down-sampled) on the sampled values from the blue trace. Using Figure 4, one can easily compare the original signal (red trace), sampling at a frequency of F_s, with the oversampled, averaged, and decimated signal (black trace).

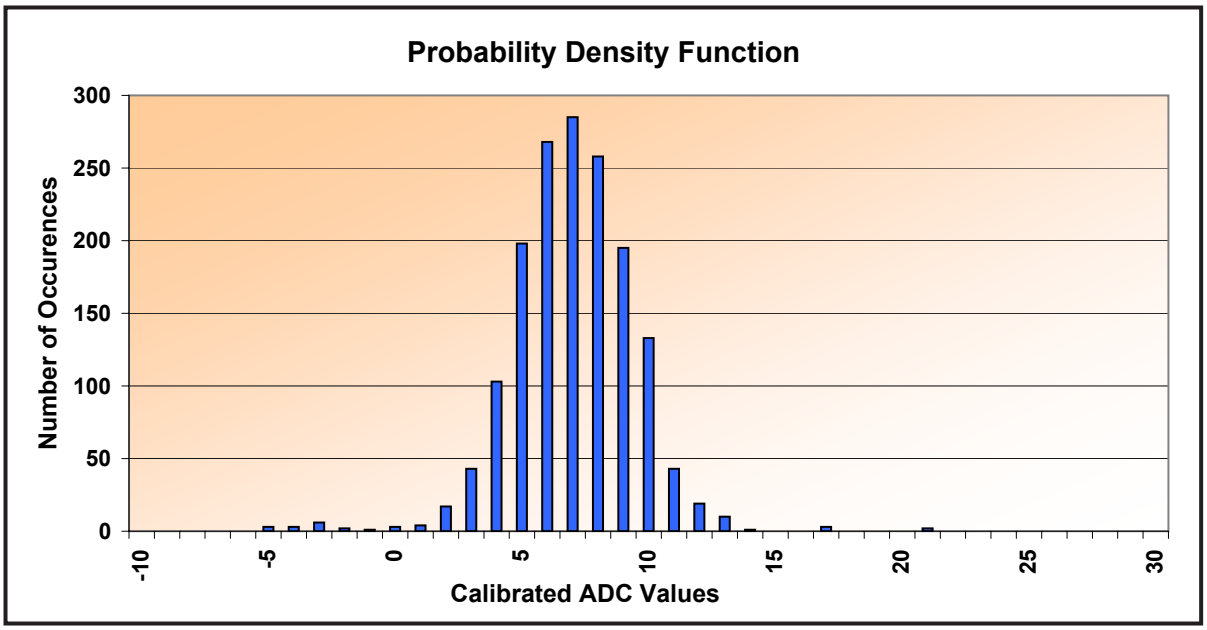

Figure 3. Probability density function of typical sampled signal

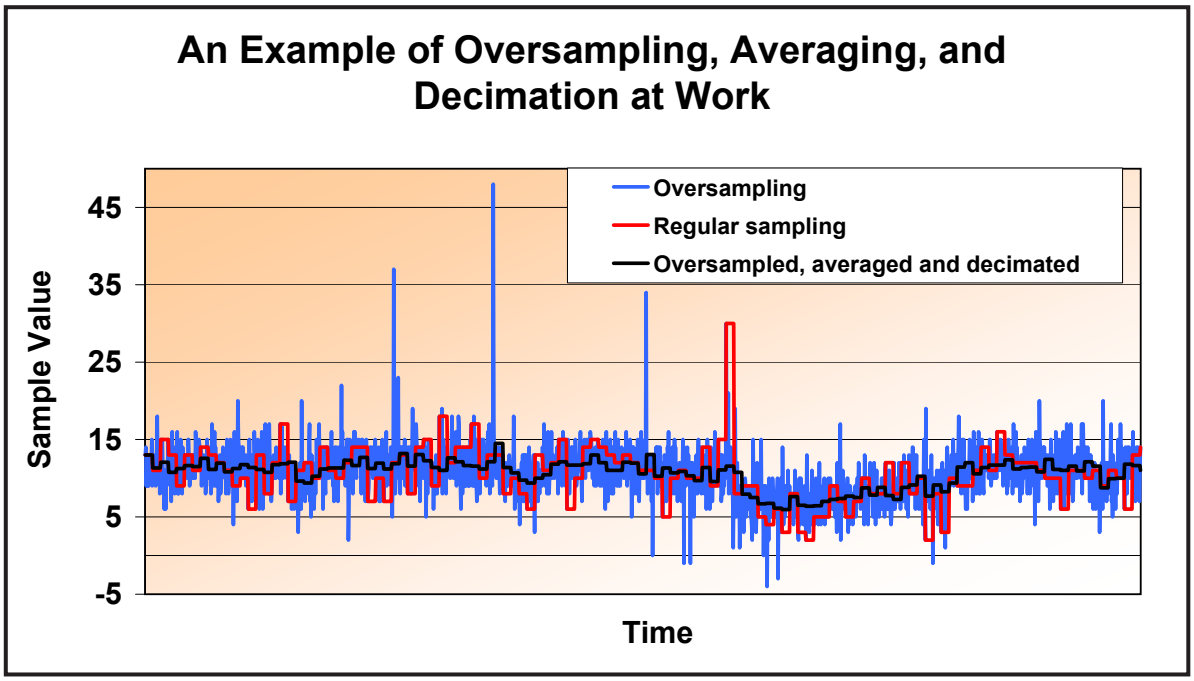

Figure 4. Oversampling algorithm at work, demonstrating how noise is removed from a transient signal

The original sampling (red trace), at a sampling of F_s, contained quantization levels ranging from 2 to 30. During oversampling (blue trace) at a frequency of 16 × F_s, quantization levels ranged from –4 to 48. Observe that the value range was reduced after averaging and decimation (black trace) to between 6 and 14, a vast improvement over the original sampling. The resulting trace (black) produces with a signal at the same frequency as the original trace (red), but with the noise contribution removed.

In addition, oversampling can improve ADC bit resolution when the following formula (Cygnal Integrated Products, 2001) is used to calculate the oversampling frequency:

$$F_{os} = 4^{w} \times F_s, \quad (1)$$

where

w = desired number of additional resolution bits,

F_s = original sampling frequency, and

F_{os} = oversampling frequency.

For this project we increased bit resolution by 6 bits, w = 6 (from 12 to 18 bits), and since close-to-DC values exist, we selected F_s = 1 Hz, resulting in an oversampling frequency of 4.096 kHz. The team decided to increase the oversampling rate to 130 kHz, to see how far we could extend the improved precision.

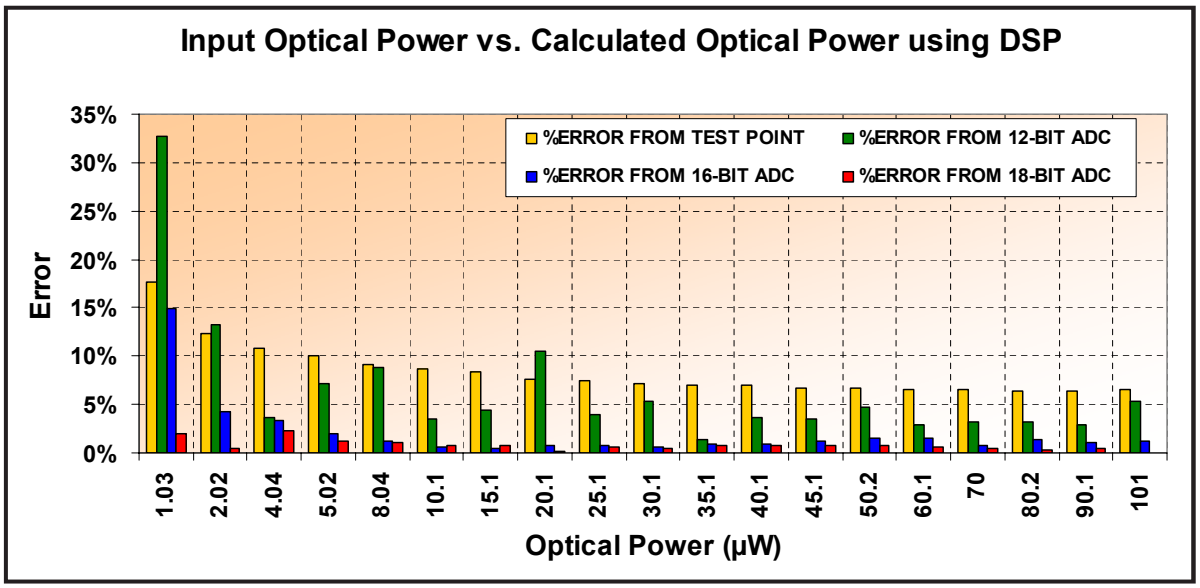

Figure 5. Comparison between present design and alternate designs using DSP

Figure 5 compares the analog circuitry (yellow bars) and three DSP alternatives. The green bars represent 12-bit values obtained from the on-chip ADCs, with no oversampling algorithm having been performed. Results were comparable to those obtained by the current analog circuitry used. Three of the 19 power levels generated a larger error than the analog circuitry, while the remaining 16 yielded a smaller error than the analog circuitry. The blue bars show results from a 16-bit oversampling, averaging, and decimation algorithm, which produced better outcomes for all power levels tested. Finally, the red bars represent results from an 18-bit oversampling, averaging, and decimation algorithm, which yielded the best results for all power levels tested. Figure 6 shows the outcomes from applying the 18-bit algorithm to another set of data points.

While this data set is not as good as the previous 18-bit set, all error readings are below 6%. This data was collected from a prototype of two PCBs. We believe that if we were to place all circuitry on one PCB, the error would decrease by an additional percentage point or more.

Conclusion

Using DSP and the oversampling, averaging, and decimation algorithm, the project team reduced the power meter error significantly, from a maximum of 20% to 7%. These results were achieved using a two-PCB prototype. Placing all circuitry on a single PCB would reduce the error even more, by removing noise contributions associated with board-to-board connections.

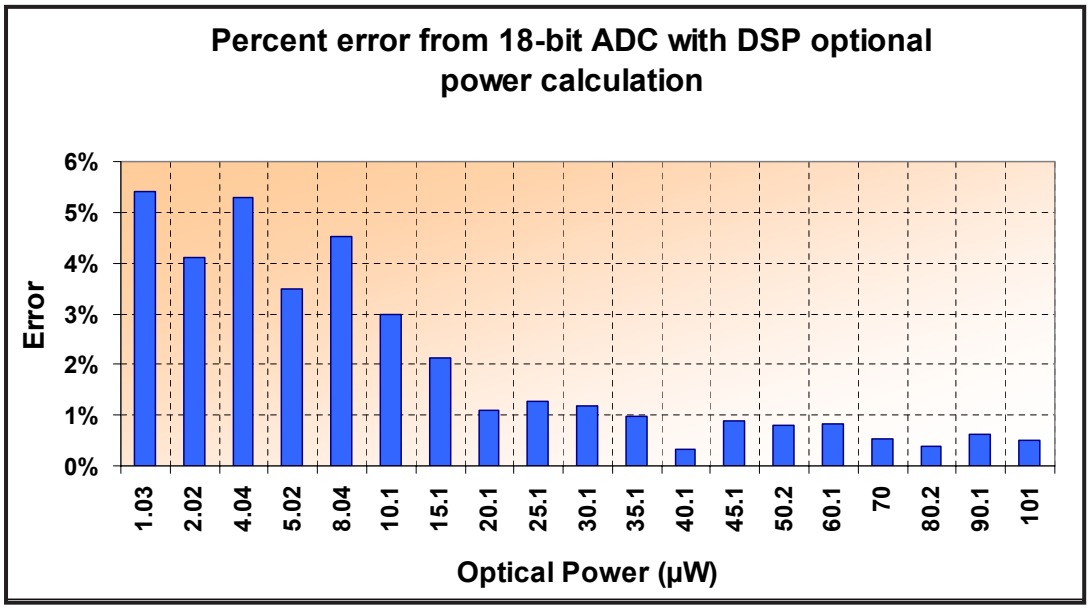

Figure 6. 18-bit, DSP design power-meter error

The fact that the DSP can also function as a general-purpose microprocessor could prove useful to enhancing product performance; it may provide a better user interface, storage of manufacturing information for traceability, auto calibration, and error checking.

DSPs can provide considerable product enhancements but require significant support resources to fully integrate them into products.

Acknowledgments

We would like to acknowledge the assistance of Heather Leffler and Frank Martinez of Bechtel Nevada, as well as that of Tim Love at Texas Instruments. Their support was vital to the advancement of this project.

References

Cygnal Integrated Products, Inc., "Improving ADC resolution by oversampling and averaging," Cygnal Application Note AN018-1.1, May 2001.

Texas Instruments, "Oversampling techniques using the TMS320C24X family," Texas Instruments Europe, Literature Number: SPRA461, June 1998.

this page intentionally left blank

Photonics

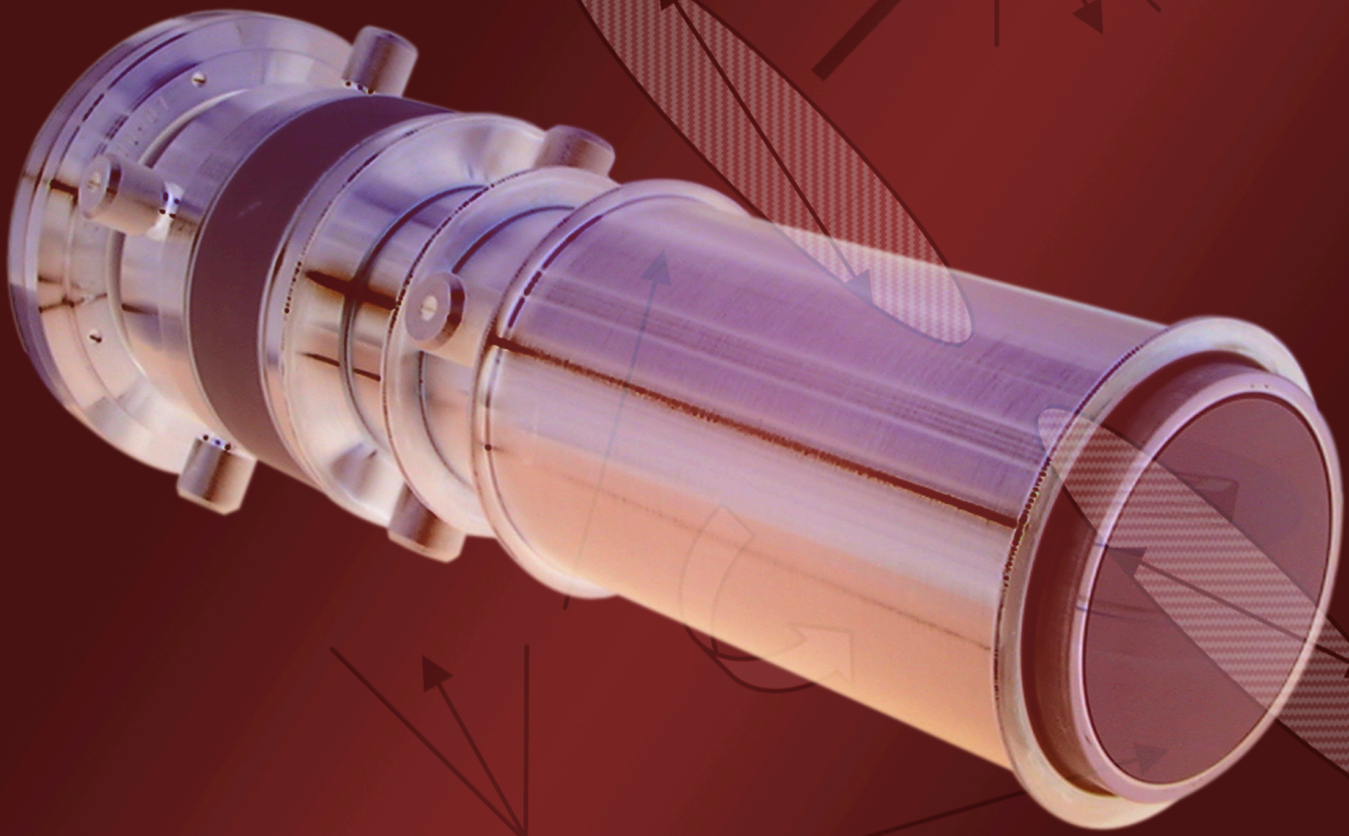

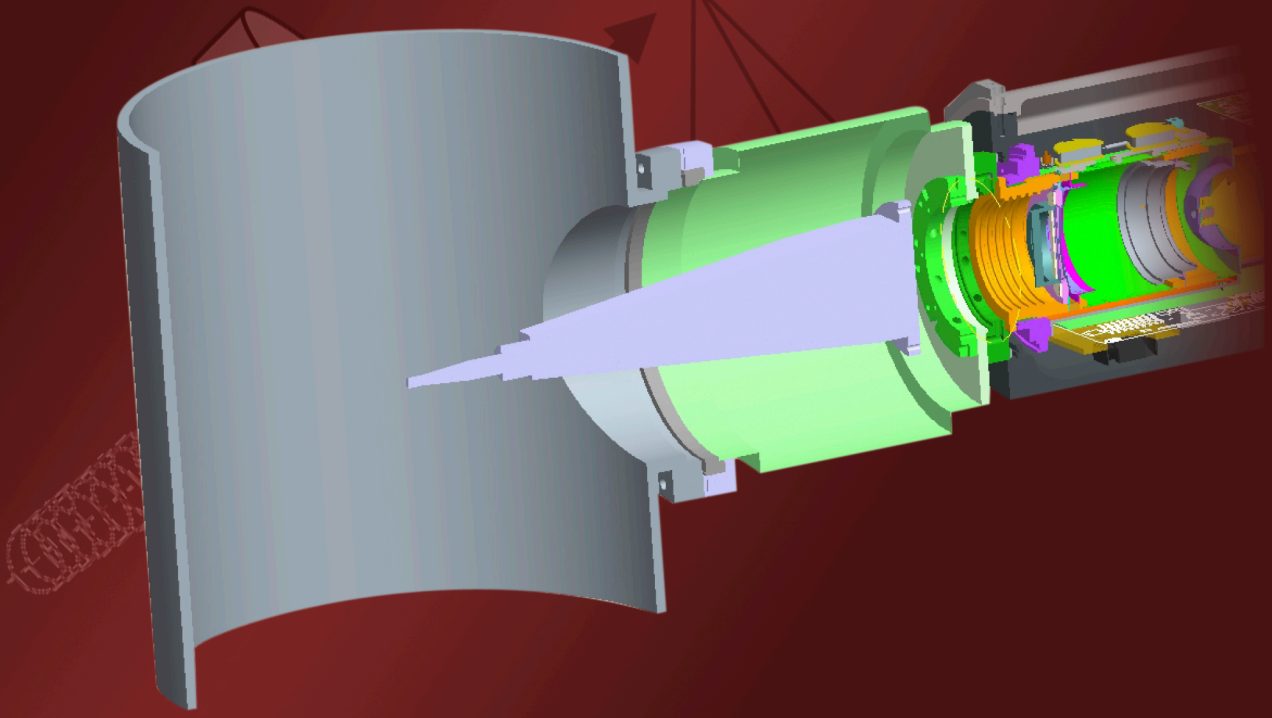

Laser Ablation Phase Diagnostic

Gene Capelle,[1] *Roderick Tiangco*
Special Technologies Laboratory

This effort intended to investigate laser ablation/plume detection as a potential new technique for detecting phase changes at material surfaces. An experimental measurement system was built, and some initial measurements were made. While a definitive answer has not yet been obtained, indications to date show that the technique is currently not worth pursuing further because of the small magnitude of the observed effect and the difficulties of measurements performed on a moving surface.

Background

Understanding the physics of materials, especially shocked metals and the subsequent changes of state produced, is a high priority in the Stockpile Stewardship Program. However, demonstrated measurement techniques for detecting phase change information are lacking. (A new phase diagnostic using spectral reflectivity to probe the phase of shocked metal is currently under investigation at STL.) This project planned to investigate a laser ablation technique as a possible melt diagnostic. Specifically, a small cloud of material would be ablated from the surface of the shocked material under study. The resulting plume would then be monitored optically and analyzed for quantity of material, which should be different for different phases of the shocked surface.

To our knowledge, this technique has not previously been investigated, both because of the expense of the capital equipment (laser, high vacuum system, etc.) required and the uncertain prospects for success. Because we possessed all the necessary capital equipment in-house, and since both the literature and calculations made by the Principal Investigator of this project suggested a small but possibly measurable effect, we undertook an investigation.

Project

Literature and Preliminary Decisions

The first step was to conduct a literature search on laser ablation, a removal of material by laser energy incident upon the surface. Material removal can be achieved by combining material vaporization due to heat and explosive drive-off from the surface. The resulting plume will be a plasmalike substance that may consist of molecular fragments, neutral particles, free electrons and ions, and chemical reaction products. For short laser pulses (on the order of nanoseconds long) in which irradiance is

[1] capellga@nv.doe.gov, 805-681-2252

>109 watts/cm^2, the laser interaction with the surface is explosive, not thermal. In addition, the interaction is generally not well defined nor very consistent from pulse to pulse. The literature agrees that to be safely in the thermal vaporization regime, the irradiance must be less than 0.3 to 1.0 GW/cm^2 (values in the literature span this range). Ablation depth, and hence quantity of material removed per laser pulse, depends on laser energy absorbed (i.e., surface reflectivity) and also by the heat of material vaporization, which is a function of material phase. The experimental technique is based on these properties.

The surrogate used in this work was tin metal (Nesmeyanov, 1963). In the vaporization regime, there is not complete agreement on the form in which tin evaporates (e.g., Sn, Sn_2, etc.), though in our case it would be primarily Sn. Since the reflectivity of tin does not change greatly with wavelength over the visible region, 532 nm was chosen as the excitation wavelength because it is visible.

For several reasons, we decided to conduct this experiment in a modest vacuum (a few $\times 10^{-5}$ torr). First, many Stockpile Stewardship shock physics experiments are performed in such a vacuum. Second, the mean free path of a tin particle is less than 1 μ at atmospheric pressure but is 10 mm or more at pressures below 10^{-4} torr. This makes a better, taller plume. It also results in fewer collisions. Hence, there is less likelihood of Sn atoms in the plume being destroyed by formation of Sn_2, SnO, or other species.

For detecting the ablation-produced plume of tin, we considered many potential techniques, all but one of which were dismissed. There was probably not enough material in the plume for either shadowgraphy or fluorescence techniques to work. Because of the relatively low Sn concentrations, resonance techniques (i.e., using absorption lines corresponding to allowed transitions from the ground state of tin atoms) were deemed best. Use of a tunable laser tuned to one of the tin lines was dismissed due to the complexity of the technique.[2] It was therefore decided to use a tin, hollow-cathode resonant lamp as the source of resonant Sn-atom emission.

Experimental Setup

For the ablation, we used a pulsed laser with a pulse width of approximately 7 ns full-width at half-maximum (FWHM) and a 532-nm output. It was typically operated at a 65-mJ/pulse and focused onto the sample to a spot size adjusted to keep irradiance at or below 0.3 GW/cm^2. The small, high-purity tin sample was mounted in an aluminum sample block (originally copper, but changed to avoid alloying with the tin sample). The block, and hence the sample, could be heated to well above the tin melting point of 231.9°C (monitored by thermocouple) by means of two electrically powered heating elements. This sample unit was mounted inside a vacuum system (driven by a mechanical pump plus turbo pump) and typically pumped to a few $\times 10^{-5}$ torr. A quartz window above the sample allowed

[2] Because tin resonance lines are in the ultraviolet, at 224.6 nm and 286.3 nm, reaching these wavelengths with a laser would make for a rather complex system. A wavelength doubling system would have to be built and added to the in-house excimer and dye laser combination.

the laser to enter the vacuum system to strike the sample perpendicularly. Quartz windows on center line left and right permitted an optical line of sight across the top of the sample for the detection system (Figure 1). The detection system consisted of a tin, hollow-cathode resonance lamp shone into the vacuum system and across the area above the sample (irises and beam stops limited the field of view). On the opposite side was a 0.5-m monochromator set to pass the 286.3-nm tin line in second order (i.e., set to 572.6 nm, with a UG-5 prefilter to block visible light, especially laser and plasma light). This is shown in Figure 2. A photomultiplier tube (PMT) was located at the output slit to detect transmitted light. It was first connected to a picoammeter to allow wavelength calibration and to tune to the tin line. The PMT was then connected through a preamplifier to a digital oscilloscope for readout. The oscilloscope trigger was synchronized with output light from the laser.

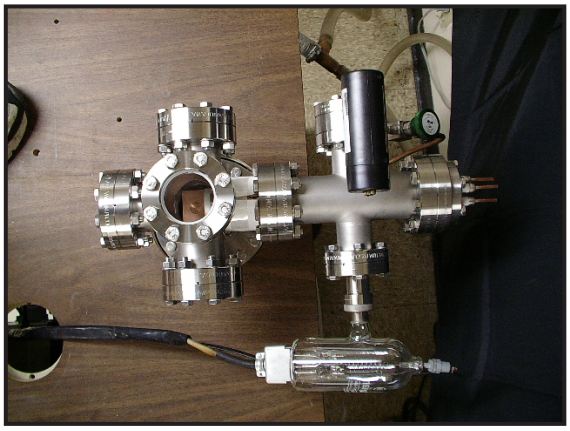

Figure 1. Vacuum system showing original copper heating block with well for tin sample

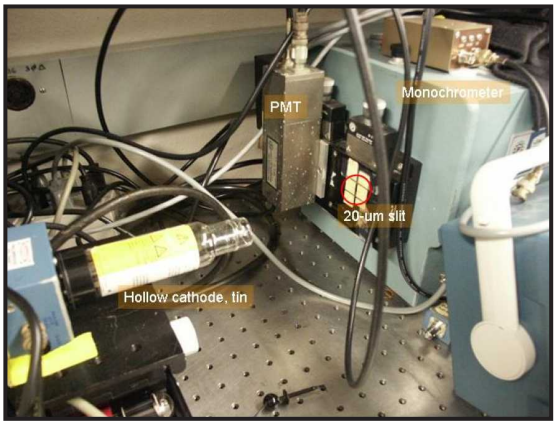

Figure 2. Detection system showing UG-5 color glass filter normally mounted at input slit

Results

The laser ablation/detection system was first tested in air. Using the resonance lamp but no laser, the system was aligned (optically, and for exact wavelength). Then using only the laser, the laser axis was aligned. In air, the tin resonance line appeared strongly in the signal channel when the laser was fired, due to emission from excited tin atoms in the laser ablation–produced plasma.

A measurement was made to determine the amount of tin removed per laser pulse. The crater size created by 10 laser pulses allowed us to calculate a value of approximately 8 μg of tin removed per pulse. Alternatively, assuming 25% of the laser pulse energy goes to vaporization and using known properties of tin (heat of fusion, heat of vaporization, etc.) yields a calculated value of 5 μg of tin removed per pulse, in good agreement. This corresponds to a few $\times 10^{16}$ atoms of tin removed per laser pulse, which should be quite detectable in a plume.

The ablation/detection system was then mated with the vacuum system and operated at pressures below 10^{-4} torr. We intended to monitor the signal from the hollow-cathode lamp and look for a transient change after the laser pulse due to absorption by tin atoms. We would do this for both liquid and solid tin, and seek a measurable difference. On the first measurement attempts, the atomic tin emission from the laser-induced plasma was still so bright that the desired signal was largely obscured. Figure 3 shows the PMT response at the tin resonance line following a laser pulse striking molten tin (at about 300°C). This light is due primarily to tin emission from the laser-generated plasma and completely overwhelms the hollow-cathode resonance lamp output. An absorption feature can be seen at ~4 μs from the beginning of the light; this, we believe, is due to the absorption of tin light occurring at the time of highest density of ground state tin atoms in the optical path. Unfortunately, there was no time to continue to study this signal.

Further steps would be to confirm that the extremely bright plasma was not caused by exceeding the vaporization regime threshold (i.e., too tight a focus), then to install carefully placed irises and baffles to allow observing the plume region beyond the plasma zone (which extended a few millimeters above the sample surface).

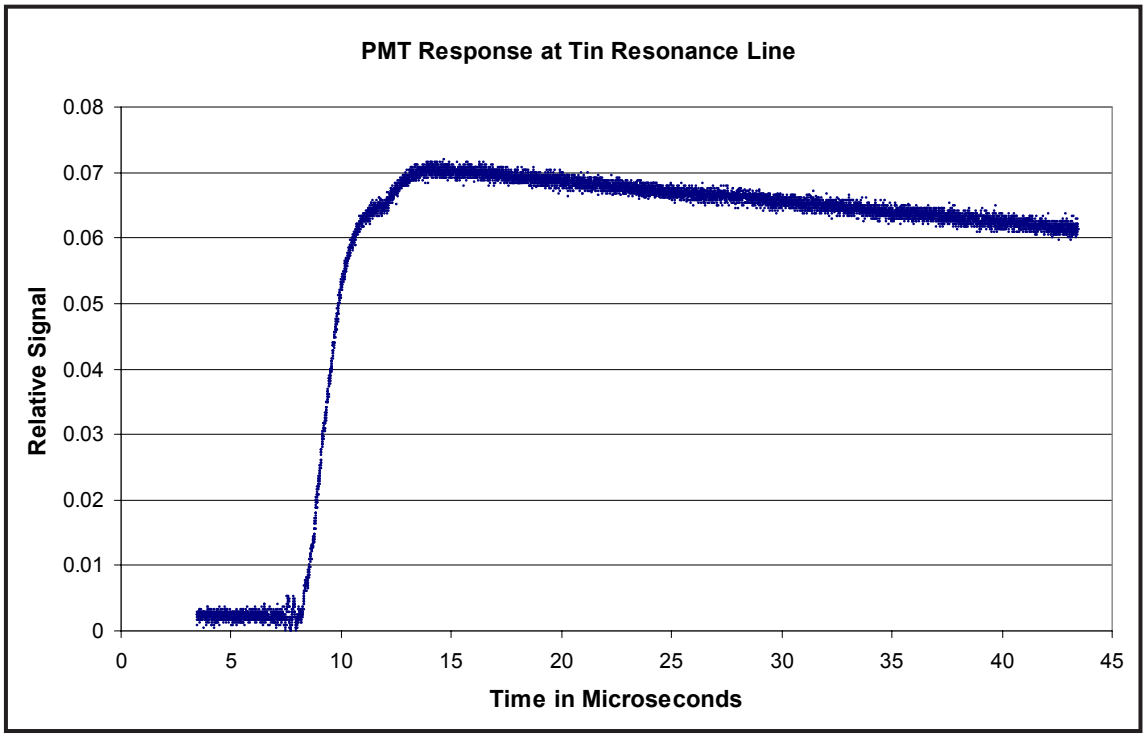

Figure 3. Absorption signal following laser ablation pulse by ~4 μs

Conclusion

Based on the observed results, many factors are working against the success of this technique, and further pursuit is probably not worthwhile at this time.

First are problems inherent in the experiment. There is the larger-than-expected tin emission from the laser-generated plasma in vacuum. Baffling may not be sufficient, in view of the few-percent change we would expect to measure. Also, the hollow-cathode lamp output was weaker and noisier than expected, making a single-pulse measurement difficult. A tunable laser (to allow large standoff) might be necessary to solve these problems.

Second are yet-to-be-encountered problems associated with making measurements in an actual shock experiment scenario. Even if the laser ablation system functioned as originally hoped, it is a complicated system and requires more real estate (access windows) around the target than is normally available, due to competition among experiments for up-close space. Also, since alignment is critical, it would be challenging to make measurements on a quickly accelerating surface. Furthermore, the laser-generated plume would be coming from a moving surface, and the motion would cause a difficult-to-correct-for density variation in the plume. Also, in a test scenario, it would be important to probe the surface often during a short window (on the order of 100 μs), beginning when the shock wave reaches reached the surface. However, we found that plasma light and hence, the plume, persist for a relatively long time (hundreds of μs). This would effectively limit this probe technique to only one measurement, which is insufficient.

Acknowledgments

The authors wish to recognize Mike Grover for his invaluable assistance in preparing the vacuum system.

Reference

Nesmeyanov, A. N., *Vapor Pressure of the Elements*, Academic Press, New York, 1963.

this page intentionally left blank

Velocimetric Probe Development for Optical Pin Dome Experiments

Jon Becker, Edward P. Daykin,[1] Raymond W. Eichholz
North Las Vegas

This project intended to develop fiber-optically coupled velocimetric (optical) probes compatible with the velocity interferometer system for any reflector (VISAR), Fabry-Perot, or photonic Doppler velocimetry (PDV), for use on pin dome experiments. Two design concepts were pursued: 1) a refractive system based on existing approaches and suitable to PDV, and 2) a reflective system allowing for a more compact optic and an extended depth of field, compatible with all three velocimetry systems. Our team successfully built, tested, and installed the refractive probe into a pin dome experiment scheduled for spring 2006. We also completed a ZEMAX-based optical design for a prototype reflective probe. Both these miniaturized probes provide a collection efficiency of approximately 1×10^{-4} or better under typical experimental conditions. Constructed entirely of glass (or acrylic), they may be mounted directly onto the pin dome with minimal modification of experimental hardware or assembly procedures.

Background

Pin dome experiments are high-value, high-cost experimental programs within both Lawrence Livermore and Los Alamos National Laboratories (Clark, 2004), as well as in other countries (AWE, 2005). These experiments have relied exclusively on electrical pins for data. However, recently developed techniques allowing velocimetric measurements within the pin dome geometry have attracted great interest. A fundamental limitation to applying velocimetry to these experiments is the fiber-optic probe, particularly its physical size, collection efficiency, and ability to integrate into severe mechanical constraints. Our team pursued development of two types of velocimetry probes, which were sized according to pin dome geometry. These relatively robust probes could be readily installed into the pin dome and yielded collection efficiencies comparable to that of our standard velocimetry probes.

Project

We divided probe development into two phases. The first phase would yield a relatively straightforward, refractive (lensed) probe, which would provide a test case for integration into the pin dome. The second phase would involve the design and eventual fabrication of a more complex reflective probe. This phased approach allowed us to initially focus on engineering and assembly measures for installation

[1] daykinep@nv.doe.gov, 702-295-0681

that would avoid perturbing pin dome mechanical design or pin measurement scheme. Potential mechanisms for pin failure (data loss) due to design and assembly were the topic of much discussion and, ultimately, the cause for a probe redesign early in this project.

A first-generation PDV probe, approximately 1 mm in diameter and constructed of glass and steel, was designed and built to extend in length to near the surface of interest, and to observe surface jump-off. It was then successfully tested as an add-on to an unrelated experiment. Interface hardware and assembly techniques were developed over several months, but there was still concern about "punch-through," that a probe constructed of high-mass material and located near the surface of interest might punch a hole through the surface and allow hot gasses and/or matter to inject into a region of electrical pins. If the pins had yet to make their measurements (be contacted), this matter expansion could potentially cause data loss or otherwise perturb the electrical measurements. LLNL conducted code simulations that validated this concern and led to a probe redesign.

The redesigned probe—shorter than neighboring pins and built entirely of glass to reduce mass—is currently installed into a pin dome awaiting execution. Code simulations run at LLNL indicate that punch-through will likely not occur, almost certainly not within the measurement timeframe. Since this probe is further from the target surface (closer to the pin dome), its diameter was increased to allow for an approximately 10^{-4} collection efficiency. We also developed a detailed design and method for interfacing this probe and associated fiber optics with pin dome experimental hardware. (See the "Refractive Probe" section, below.)

In the project's second phase, we pursued a potentially more capable but significantly more complex design. Conceptually, our approach was to design a robust, single-component reflective optic that could be fabricated via injection molding—a fiber-optically coupled "plug" to be inserted directly into the pin dome. A reflective optic allows for the beam path to be folded onto itself to reduce probe size, i.e., a reflective telescope. We also desired separate launch-and-receive fibers, ensuring compatibility with Fabry-Perot or VISAR systems. And finally, we sought a probe that would allow for independent optical power to act on the launch-and-receive fibers (two-fiber case), thus permitting an increase in the probe's depth of field. A preliminary optical design was accomplished with ZEMAX ray-tracing software. Further details appear below, in the "Reflective Probe" section.

Refractive Probe

Designed for use with PDV, this probe (see Figure 1) allows for an approximate peak collection efficiency of several parts in 10^4 (target surface distance 37 mm from the probe lens, tantalum surface, ball-rolled preparation). Probe specifications are as follows:

1. Probe uses a commercially available lens designed for diffraction-limited performance at 1550 nm.

2. An 8° angle polish minimizes Fresnel reflections from the fiber end-face. It aids in accurately determining the probe efficiency curve by eliminating intensity drift due to interference with Fresnel reflections.

3. Materials: Corning single-mode fiber (SMF-28R, 0.009-mm core, 0.126-mm OD), glass "stalk" (0.251-mm ID, 0.669-mm OD, Polymicro Technologies, P/N 2001817), glass ferrule (0.126-mm ID, 1.8-mm OD, ~5-mm length, Polymicro Technologies, P/N 6600847), glass tube (1.8-mm ID, 2.8-mm OD, ~10-mm length, Polymicro Technologies, P/N 6600887).

4. Semirigid support "stalk" constructed of glass coated with polyimide. Robustness and flexibility is similar to that of standard fiber optics; however, short lengths provide sufficient mechanical strength to support probe body mass.

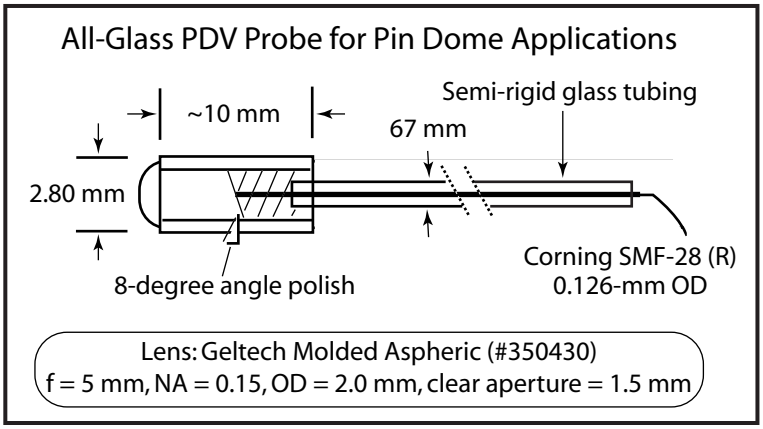

Figure 1. An all-glass PDV probe (1550 nm), as installed into a pin dome experiment

The measured efficiency curve for a refractive probe is shown in Figure 2. A mock-up pin dome with this probe installed appears in Figure 3.

Two additional probe performance parameters were investigated: 1) the probe pointing stability as a function of time was measured, since it is suspended on a semirigid stalk, and 2) lens adhesion was verified as sufficient for a differential pressure of one atmosphere, since the inside of the probe is at approximately one atmosphere and sealed, while the external environment will be under vacuum.

To address the pointing stability, we mounted a probe onto a test fixture, injected visible light into it, and used a charge-coupled device (CCD) camera to record the spatial position of the probe's focal spot as a function of time. We noted this position over three days with no discernable movement to within our measurement resolution of 1 Mrad. To address the second concern, we placed three fully

constructed probes into a vacuum chamber pumped down to approximately 10 torr. This provided a differential pressure of approximately 1 atm between the external environment and the probe's internal volume (sealed at 1 atm). No lens adhesion loss was observed.

Reflective Probe

A ZEMAX-based drawing for a prototype reflective probe design appears in Figure 4. The optical design prescription is provided in Table 1. The general idea was to design a compact, robust, all-acrylic optic that could be fabricated via injection molding. This optic could then be "plugged"

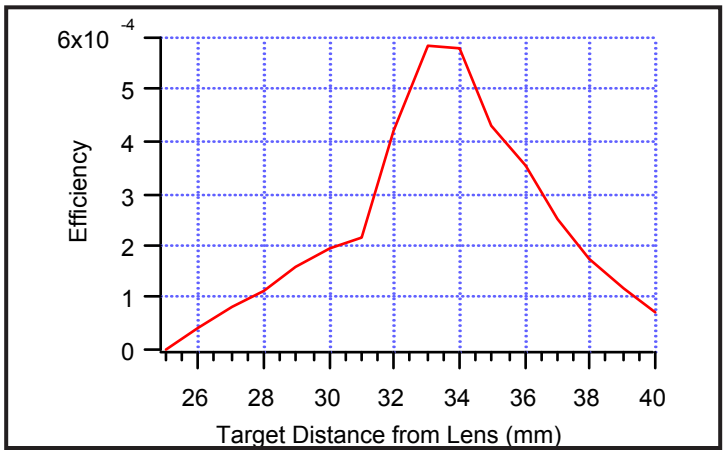

Figure 2. Efficiency curve for an all-glass, PDV pin dome probe. Target surface was ball-rolled tantalum.

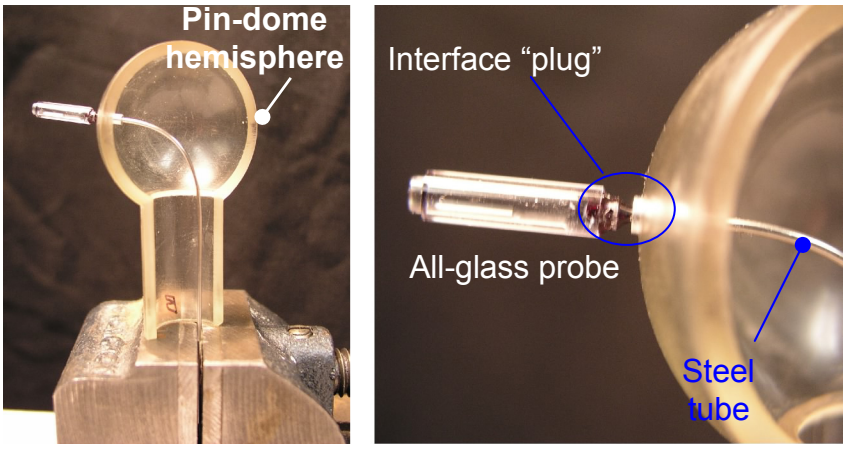

Figure 3. Refractive, all-glass probe installed into a pin dome mock-up

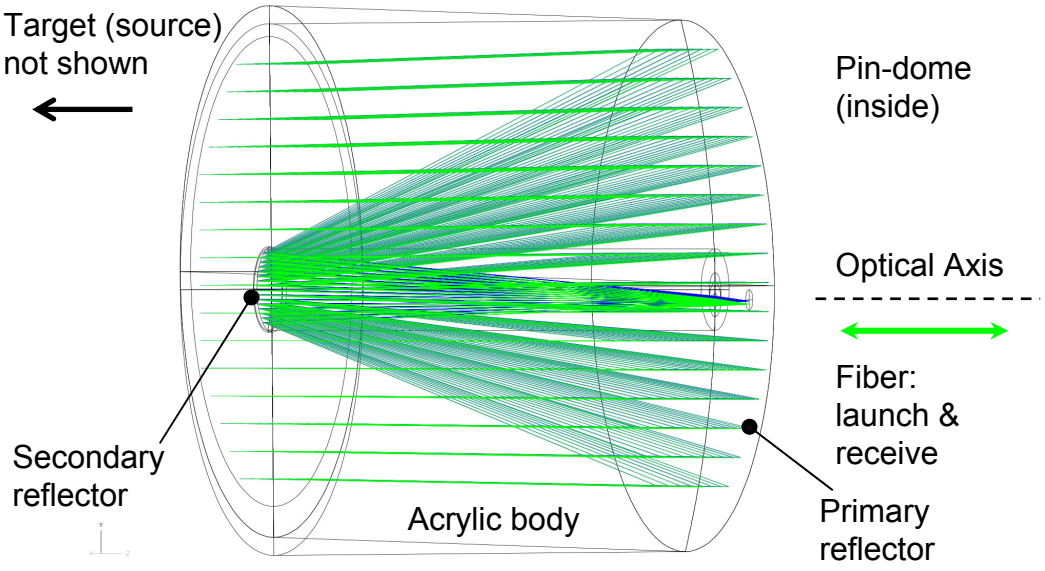

Figure 4. A single-fiber, "plug"-type reflective probe design. Design is for an all-acrylic optic, allowing for injection molding, with reflective coatings to provide the elliptical (primary) and spherical (secondary) reflective surfaces. This 6.5-mm-long probe has a clear aperture of 6.5 mm (including a 1.1-mm obscuration). A slight off-axis decenter has been introduced to demonstrate the ability to maintain high optical performance for possible two-fiber designs.

Table 1. ZEMAX-based optical design prescription for a single-fiber, reflective "plug"-type probe

#	Type	Radius (mm)	Thickness (mm)	Glass	Semi-Diameter (mm)	Conic	Dec X (mm)	Dec Y (mm)	Tilt X (deg)
0	STANDARD		73.500	AIR	0.100				
1	STANDARD		6.500	ACRYLIC	3.250				
2	COORDBRK		0.000		0.000			–0.250	
3	STANDARD	–14.500	–6.500	MIRROR	3.678	–0.623874			
4	COORDBRK		0.000		0.000				
5	STANDARD		0.000	ACRYLIC	0.591				
6	COORDBRK		0.000		0.000				0.498
7	STANDARD	–2.968	6.500	MIRROR	0.565				
8	STANDARD		0.000	ACRYLIC	0.234				
9	COORDBRK		0.000		0.000			–0.143	
10	STANDARD		0.500	AIR	0.091				
11	STANDARD		0.000		0.143				
			INDEX @	532 nm:	1.49463171				

directly into the pin dome to ease installation. Attributes of this approach allow for the following: 1) a physically shorter probe, due to the folded beam path, with a relatively large, clear aperture for a collection efficiency of approximately 10^{-4}, 2) the ability to be designed as either a two-fiber (Fabry or VISAR) or single-fiber (PDV) probe, 3) performance at either 532-nm or 1550-nm light, and 4) the ability to be designed with independent optical power applied to the launch-and-receive fibers (two-fiber case), allowing for an approximately collimated launch beam that, in turn, gives the probe an extended depth of field.

Depth of Field

For the purposes of this report, "depth of field" refers to the full-width at half-maximum (FWHM) of a probe's collection-efficiency curve. Modeling and laboratory measurements were conducted to quantify the depth-of-field dependence on illumination spot size. Probe collection efficiency was measured with a standard "nested lens" probe under normal conditions (illumination and return beam paths both pass through a common optic). It was also measured under an "alternate launch" condition, in which the illumination beam was collimated to a diameter of ~1 mm and launched independently from the return beam (through an aperture drilled into a mirror). Measured probe efficiency curves appear in Figure 5.

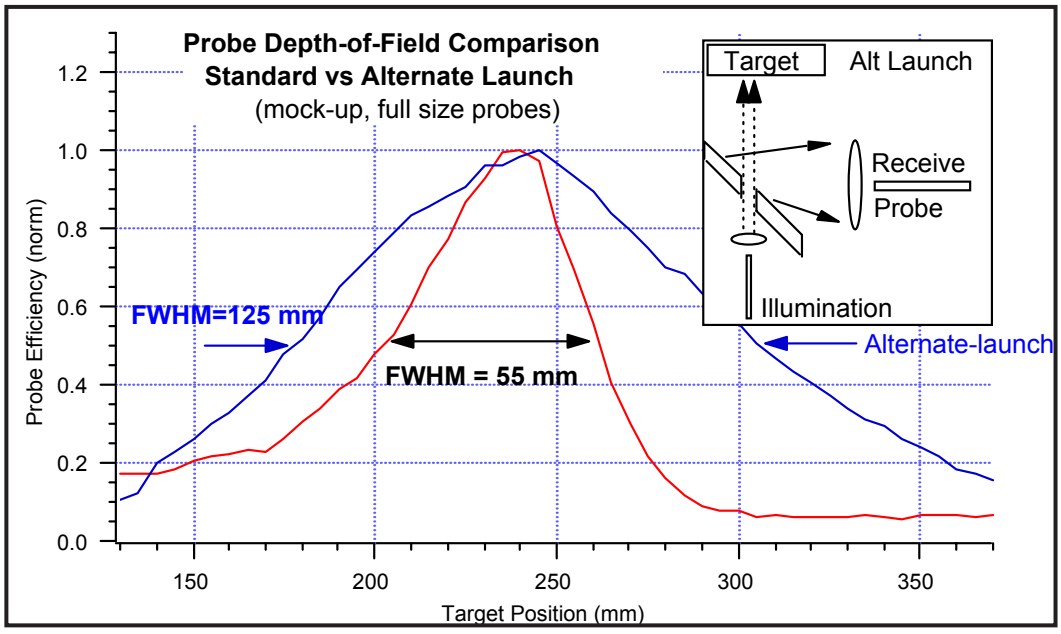

Figure 5. Comparison of probe efficiency curves. An "alternate launch" approach yields an approximately constant illumination spot size on the target, allowing for an increased depth of field as compared to a standard "nested lens" probe, which produces a varying illumination spot size.

Conclusion

We have successfully designed, fabricated, and tested a miniature, all-glass, PDV-type refractive probe. We have also developed interfacing hardware and methods, and installed one such probe into a pin dome experiment (as an experimental "add-on") scheduled for spring 2006. From this probe we anticipate a successful velocimetric data record, without any perturbation to existing pin measurements. This would represent the first velocimetric data from an LLNL pin dome experiment. Further development of a reflective probe will require programmatic funding. However, we believe that this approach offers potential for significant performance improvements as well as the flexibility for using different velocimetry diagnostics. Programmatic interest has already been expressed in applying several refractive probes to upcoming pin dome experiments, enabling future development of probes and velocimetric measurement techniques on pin dome experiments.

Acknowledgments

Special thanks to Ted Strand, David Hare, Tony Whitworth, Lance Buckley, David Edick, and Fred Ellsworth of LLNL, for their many discussions and contributions in time, expertise, and experimental and computer modeling resources.

References

Clark, D. A., V. T. Romero, "Krakatau VISAR Probes," VISAR Conference, Special Technologies Laboratory, Santa Barbara, CA, February 18, 2004.

United Kingdom's Atomic Weapons Establishment (AWE), http://www.awe.co.uk/main_site/scientific_and_technical/featured_areas/hydrodynamics_contents/esr-contents/esr-c/esr-c2/esr-c4/index.html, accessed on January 4, 2005.

this page intentionally left blank

Electron Beam CCD Camera Readout

D. Taner Bilir, Jerald Cradick, Charles E. Diamond[1]
Livermore Operations

This research studied the feasibility of directly recording/bombarding 20-keV electron images from a streak tube onto a charge-coupled device (CCD) chip to improve the dynamic range and resolution of streak camera systems. A study of past issues/problems with direct electron bombardment and improvements to CCD chip technology was applied to this project to formulate a test plan. An open-frame/x-ray streak tube was modified by the removal of the phosphor, and a vacuum-tight flange was designed and fabricated to allow for testing both 1K × 1K and 2K × 2K CCD cameras. Both CCD cameras successfully recorded images while the streak camera was set up in both the static and dynamic modes of operation.

Background

X-ray streak cameras currently use lens- or fiber optic–coupled CCD cameras to acquire data from an electron-excited phosphor deposited on a fiber-optic faceplate. System losses start at the efficiency of the electron-to-photon conversion at the phosphor, transmission through the phosphor fiber-optic faceplate, the interface (Moiré) loss of the phosphor/CCD fiber-optic faceplates, transmission through the CCD fiber-optic faceplate, and the efficiency of the CCD chip's photon-to-electron conversion. It takes approximately 100 photoelectrons to generate 1 electron in the CCD well, whereas direct electron detection (at 20 keV) generates approximately 3000 electrons in the CCD well for each photoelectron (Horacek, 1995). In some cases, a sealed microchannel plate intensifier (MCPI) is used to overcome the losses, but the signal-to-noise ratio (SNR), dynamic range, and overall system resolution suffer significantly. Early attempts to use CCDs as electron detectors showed that irreversible damage occurred with accumulated exposure due to the creation of charge defects at the Si-SiO2 interface (Stearns, 1989). Current CCDs employ a Multi-Pinned Phase (MPP) technology, which alleviates this problem by eliminating surface states at the Si-SiO2 interface (Janesick, 2001). A diagnostic with an order of magnitude improvement in performance should allow the experimenter to cover a larger range of energies. Increased SNR, dynamic range, and resolution can reduce the time required to complete a set of experiments. Diagnostics using x-ray streak cameras to collect data could resolve events from a single x-ray photon through the entire dynamic range of the 16-bit, electron-beam CCD camera. This technology may be adapted for an optically sealed streak tube.

[1] diamonce@nv.doe.gov, 925-960-2540

Project

This project was divided into three phases. First, we modified an existing x-ray streak tube by removing the P-20 phosphor. Then we designed and fabricated the flanges required to mount the CCD chip in the same focal plane as the P-20 phosphor (Figure 1).

To complete the second phase, we used an existing 1K × 1K CCD camera with 24-µm pixels that had a back-thinned CCD with an antireflective (AR) coating. While the AR coating is not ideal for direct electron detection, the 1K × 1K CCD camera was chosen to reduce the overall risk of the initial power-up procedure of the x-ray streak tube's high-voltage section. A low vacuum chamber was modified to a high vacuum chamber, and an ultraviolet (UV) penlight source was installed as the excitation source to the streak tube (Figure 2).

Once the vacuum leaks and the high-voltage arcing problems were brought under control, direct electron static (unswept) resolution images were recorded on the 1K × 1K CCD camera. Static direct electron resolution images were also recorded using a Manson x-ray source as the excitation source to the streak tube. Dynamic (swept) resolution images were recorded with the 100-fsec UV laser in LO's Short Pulse Lab (SPL). Images from all three experimental setups appear in Figure 3.

The data in Figure 3 was compared to data acquired from the x-ray streak camera's original configuration (P-20 phosphor, 40-mm MCPI, and a fiber-optically coupled 4K × 4K, 9-µm pixel size CCD camera). The data from the electron beam CCD camera readout system dramatically improved the sensitivity, dynamic range, dynamic resolution, and SNR. Sensitivity, dynamic range, and SNR improved by a factor of 10, while the dynamic resolution improved by a factor of 4. The dynamic resolution limit was determined to be the Nyquist limit of the electron beam CCD camera's pixel size; thus, the project's third phase was implemented. The final test for the 1K × 1K CCD camera was to intentionally cause the streak tube to arc multiple times, in order to send a high dose of 20-keV electrons at the CCD chip. No detectable pixel well-spreading was observed in the resolution images taken after intentionally arcing the streak tube multiple times. The background images taken before and after arcing also showed no change in the offset.

The final project phase consisted of mounting a 2K × 2K back-thinned, 13-µm pixel-size electron beam CCD camera with no AR coating onto the x-ray streak tube. Again, to minimize risk, an engineering-grade CCD chip was tested first, and then a Grade 2 CCD chip was also tested. The same tests that were performed on the 1K × 1K CCD camera were performed on both 2K × 2K CCD chips. An additional test on the 2K × 2K CCD chip was also run in LO's Long Pulse Lab (LPL). The smaller pixel size of the 2K × 2K CCD chip did improve the static and dynamic resolution (see results in Figure 4).

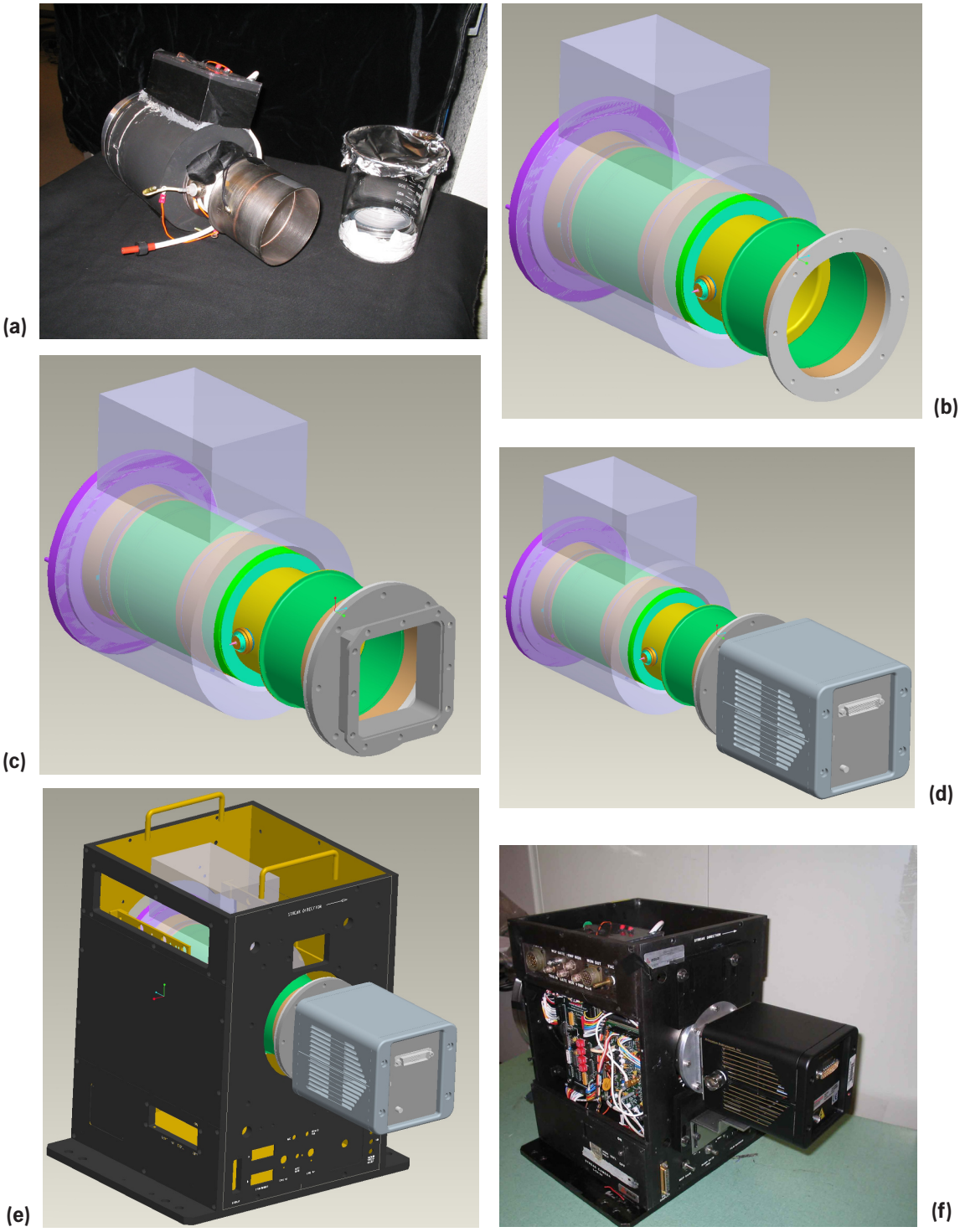

Figure 1. X-ray streak camera modification process: a) P-20 phosphor removal, b) welded flange design, c) welded flange to 2K × 2K CCD camera adaptor design, d) assembly of x-ray streak tube and 2K × 2K CCD camera, e) x-ray streak tube chassis design, f) fabricated and assembled finished product

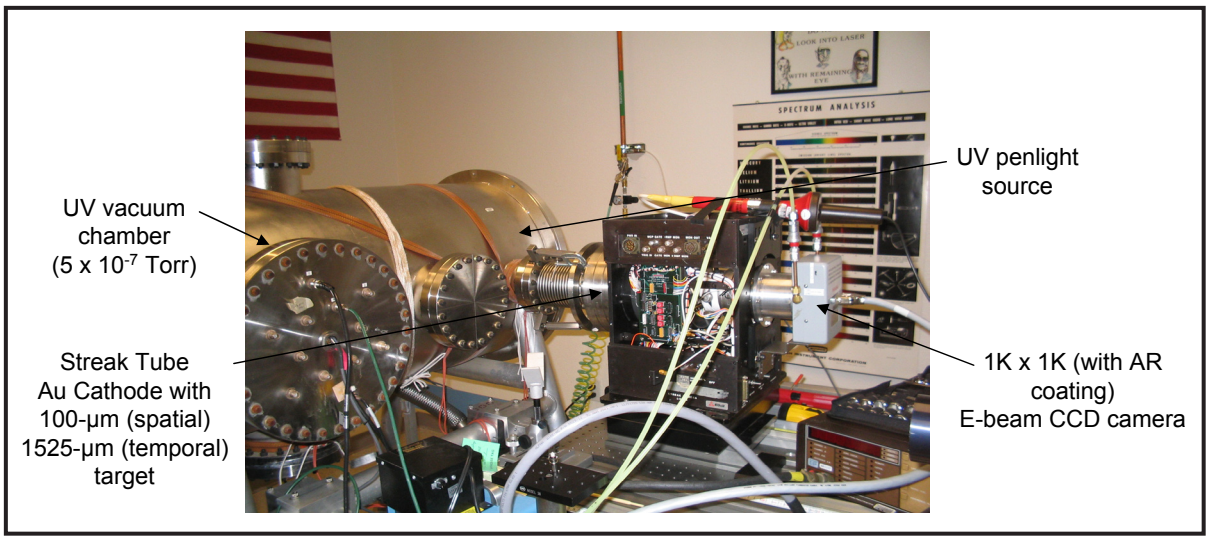

Figure 2. Initial power-up and UV static test setup

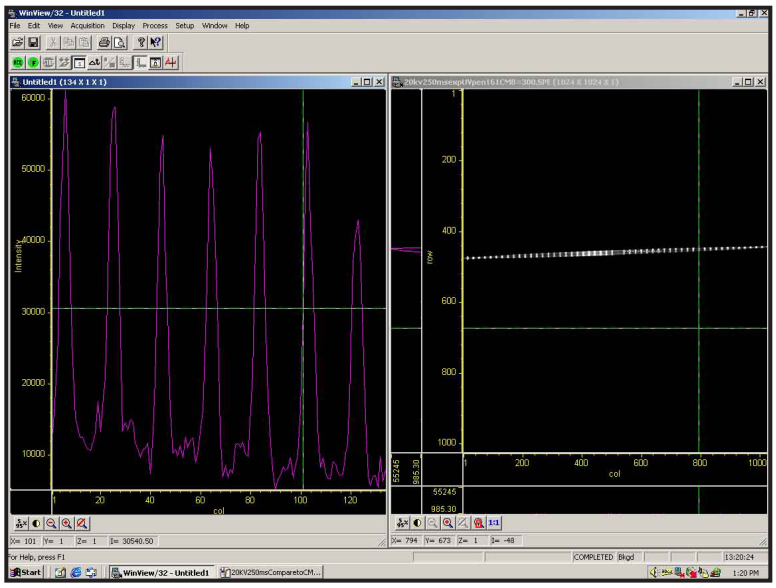

Figure 3(a). Direct electron resolution images: UV penlight 100-µm target resolved to 125 µm

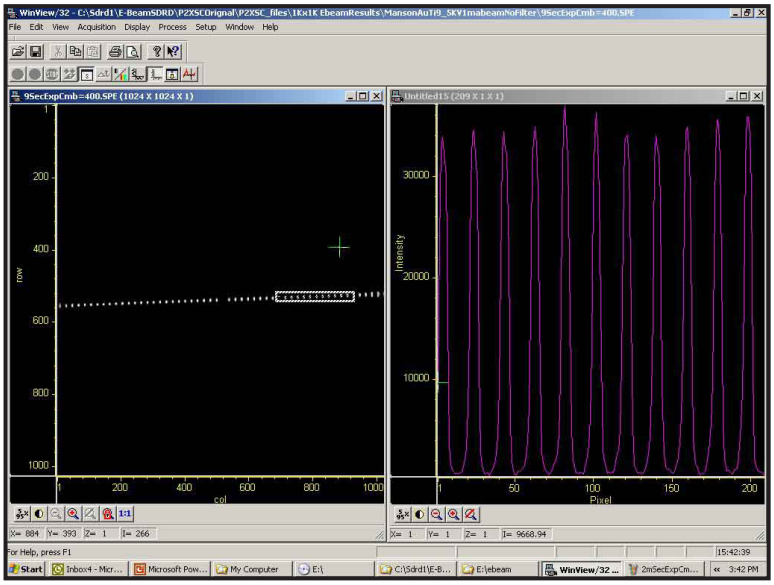

Figure 3(b). Direct electron resolution images: Manson x-ray 100-µm target resolved to 100 µm

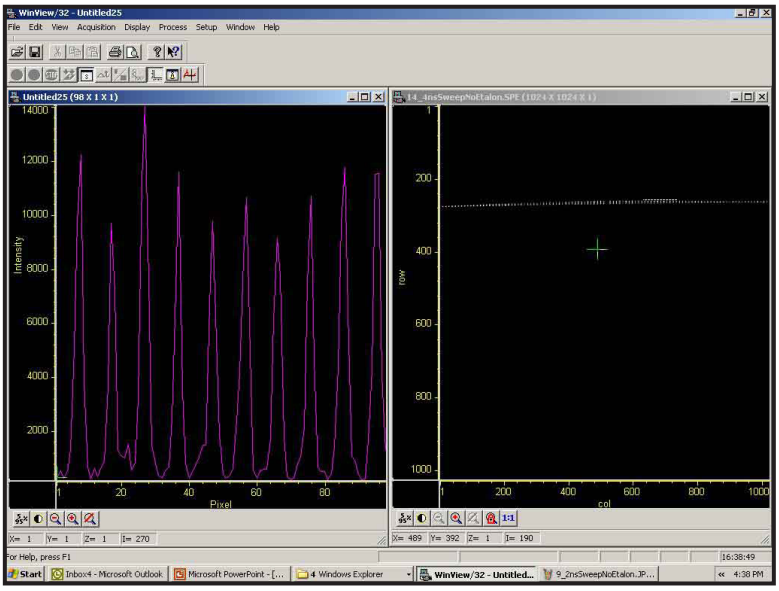

Figure 3(c). Direct electron resolution images: SPL 50-µm target resolved to 63 µm at a sweep rate of 10 ns/40 mm

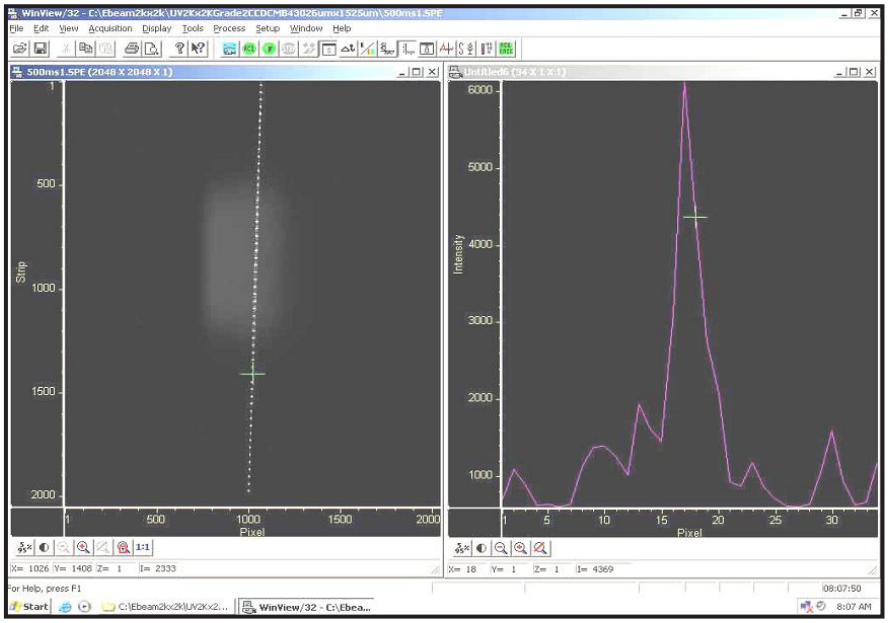

Figure 4(a). 2K × 2K CCD test results: UV 26-µm target resolved to 33 µm

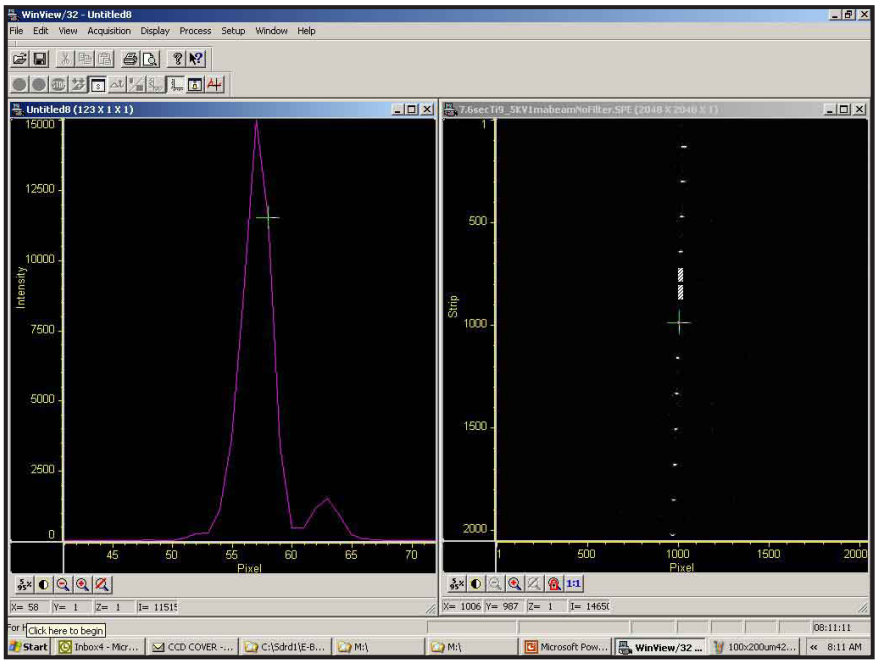

Figure 4(b). 2K × 2K CCD test results: Manson x-ray 14-µm target resolved to 33 µm

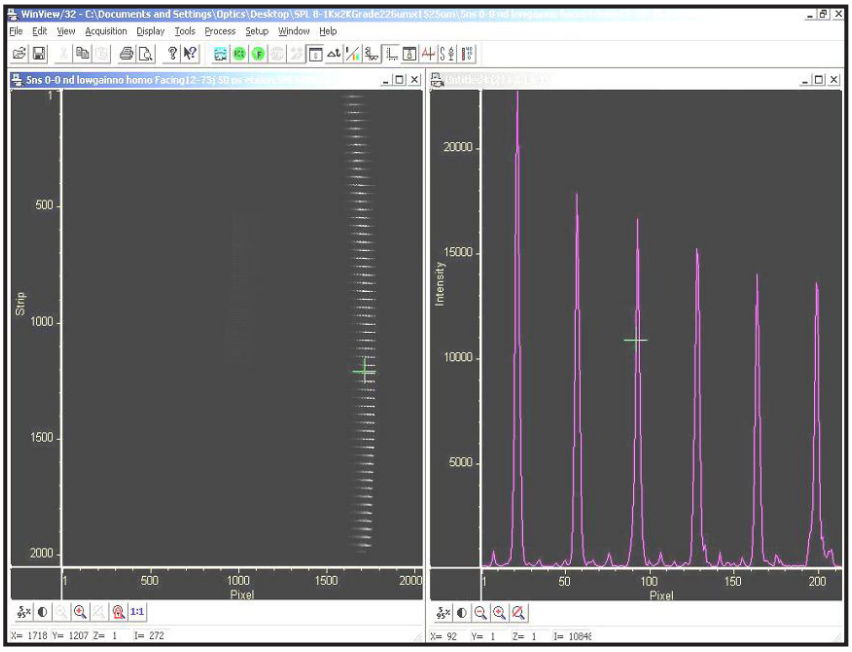

Figure 4(c). 2K × 2K CCD test results: SPL 26-µm target resolved to 39 µm; temporal resolution easily resolves 50-ps etalon spacing (5-ns/40-mm sweep rate)

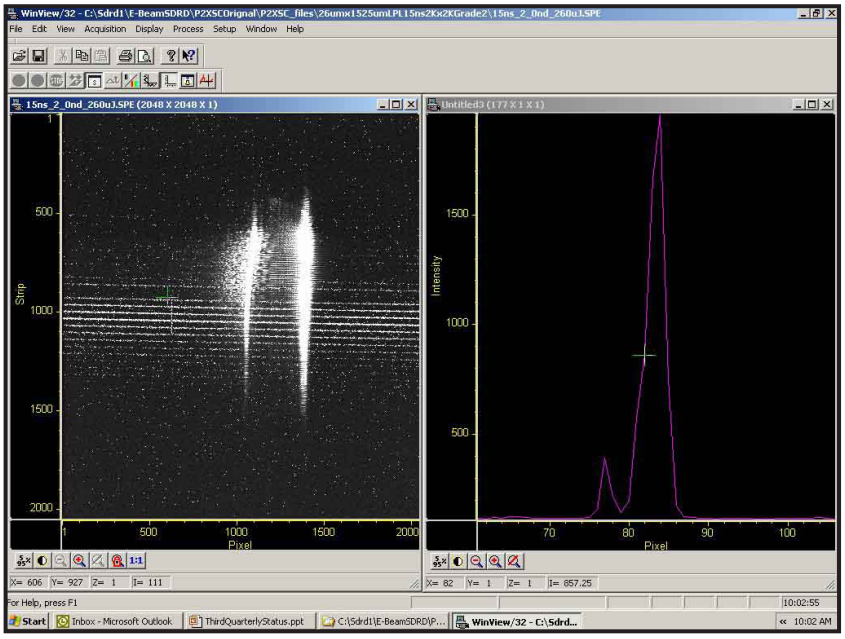

Figure 4(d). 2K × 2K CCD test results: LPL 26-µm target resolved to 33 µm (15-ns/40-mm sweep rate)

The final step in the third phase would have been to apply an aluminum coating to the face of the 2K × 2K CCD chip and repeat the same tests. We intended to match the streak tube's dynamic range to the CCD camera's dynamic range and also eliminate the CCD chip's response to the UV light, thus further increasing the SNR. For example, the two bright spots in Figure (4d), which are caused by unconverted UV light striking the CCD chip, would likely have been eliminated with the aluminum coating on the chip. This task was not completed by project end but remains an interesting topic for further research.

Conclusion

The primary goals of this project were to determine that the current CCD chip technology is capable of withstanding direct detection of 20-keV electrons, and to gain an order of magnitude improvement in the x-ray streak camera system dynamic range, resolution, and SNR. These goals have been achieved by empirical testing methods and comparison to data taken from an x-ray streak camera with a phosphor, MCPI, and fiber-coupled CCD camera. This project has produced a usable, fieldable x-ray streak camera with an electron-beam CCD camera readout system with a high sensitivity to both UV and x-rays, while maintaining a high dynamic range, resolution, and SNR.

In order to implement this technology into a BN50 optical streak tube, we must resolve many issues. The most pressing are: 1) the streak tube processing temperatures (375°C) and hence, CCD survivability; and 2) modifying the electron optics (or curving the CCD array) to allow the electrons to land in focus over the entire surface area of the array. Preliminary discussions with the BN50 streak tube manufacturer indicate that the process may be changed to accommodate the CCD chip, along with obtaining a CCD chip without the chip carrier. Electron optics modification also seems possible; however, it will require extensive electron ballistic modeling to verify this assumption.

Acknowledgments

The authors would particularly like to thank Franz Weber of LLNL for his innovative ideas and support during this program, which expanded upon his original work. All LO departments assisted the Electro-Optics Group with this project. We would like to especially acknowledge the following individuals: A. Shellman for his delicate removal of the phosphor, and M. Karrick and D. Max for outstanding work in the assembly, vacuum-sealed welding, and repair of the CCD adaptor flange. M. Haugh, P. Torres (Manson x-ray source), M. Griffin, T. Pond (SPL), S. Hampton, and K. Larson (LPL) offered invaluable assistance in the setup and testing phases. R. Knight, M. Kucher, and E. Silbernagel provided excellent mechanical designs and fabrication support. M. Ramsey offered his expertise in vacuum systems, and K. Loughman provided fast fabrication work. We also obtained technical expertise from R. Rohde of Las Vegas Operations (LVO).

References

Horacek, M., "Direct Detection of Electrons by Area Array CCD," *J. Instit. Sci. Instrum.*, Academy of Sciences of the Czech Republic Kralovopolska, Brno, Czech Republic, 1995.

Janesick, J. R., *Scientific Charge-Coupled Devices,* SPIE Press, Bellingham, Washington, 2001, 310–318.

Stearns, D. G., J. D. Wiedwald, "Response of Charge-Coupled Devices to Direct Electron Bombardment," UCRL-100782, Lawrence Livermore National Laboratory, Livermore, California, 1989.

this page intentionally left blank

Digital Streak Camera

Wendi Dreesen[1]
Los Alamos Operations

The initial phase of a plan to fabricate a digital streak camera complementary metal oxide semiconductor integrated circuit (CMOS IC) has been completed. The preliminary design, which has been demonstrated to meet project requirements, was completed with the help of Rockwell Scientific Company. The imager design contains two rows of 256 pixels, can store 512 frames, and offers a frame rate of up to 10 ns. The pixel size and spacing is ideal for coupling to 512 strands of 100-µm diameter optical fibers. The system has 12 bits of resolution and more than 11 bits of dynamic range. Each row of pixels has a programmable gain adjustment.

Background

High-speed imaging is a core Stockpile Stewardship diagnostic. These systems utilize current high-speed imaging technologies that have a limited number of channels due to the size and expense of currently available equipment. They frequently use analog streak cameras, which tend to be bulky, expensive, and sometimes difficult to maintain. To replace the analog streak camera and associated support equipment, we proposed the development of a stand-alone complementary metal oxide semiconductor (CMOS) chip.

Although the initial cost of the development effort was substantial because of our partnership with industry experts, a high probability of success existed. Once a prototype device is developed, the cost per system will decrease considerably. In addition, this system will be more flexible, programmable, and small enough to package into systems with thousands of channels.

This project addressed the first of three development phases. This phase developed the conceptual design, schematics, preliminary layout, and modeling of the imager. Specific deliverables included circuit simulation outputs, preliminary IC layouts, system block diagrams, and preliminary performance predictions.

[1] dreesewm@nv.doe.gov, 505-663-2050

Project

This work was a continuation of an FY 2004 SDRD project begun with Stuart Kleinfelder (University of California, Irvine), who has a considerable background in high-speed imaging systems research. When consensus could not be reached about the project's direction, a new partnership was sought for the CMOS design. After completing an extensive search, the contract was awarded on June 15, 2005, to Rockwell Scientific Company, a research, development, and production company specializing in electronics, imaging sensors, and optics. Its customer base includes SNL, the Jet Propulsion Laboratory, the National Aeronautics and Space Administration (NASA), and Northrop Grumman.

The design requirements were:

- (2 × 256) pixel array × 512 samples per pixel
- 100 μm × 100 μm pixel size
- 10-ns frame rate
- 12-bit digital output, >11-bit dynamic range, with at least one output in which readout rate is sufficient to maintain dynamic range
- Pixel arrangement that allows a coupling of 100-μm-diameter core optical fiber with 140-μm outer diameter size to each pixel
- Allowance for adjustable gains on each of the two pixel rows
- System-on-chip design.

CMOS design tasks were physical layout, data acquisition sequence, input cell design, input and storage cells layout, design performance, and frame timing.

The general design concept was to couple a silicon photodiode array to a readout integrated chip (ROIC) on one CMOS chip. To begin, the designers explored the chip's physical limitations by creating a general mechanical layout. Since two rows of 256 channels could not physically fit on their maximum reticle size, the designers developed a reticle with two sets of a 2 × 128 array that could be stitched together with an identical reticle to form the 512-pixel device (Figure 1).

The basic floor plan appears in Figure 2. The second requirement, maximum current per pixel, depended on the pads that could be physically placed into the device. A timing scheme of how the chip acquires and sends data to the controller was developed; basic timing includes a trigger at least one clock pulse wide that will signal the chip to begin capturing signals into the pixels. When the 512 storage devices are full, the user can employ optional signal lines to control the chip's data readout.

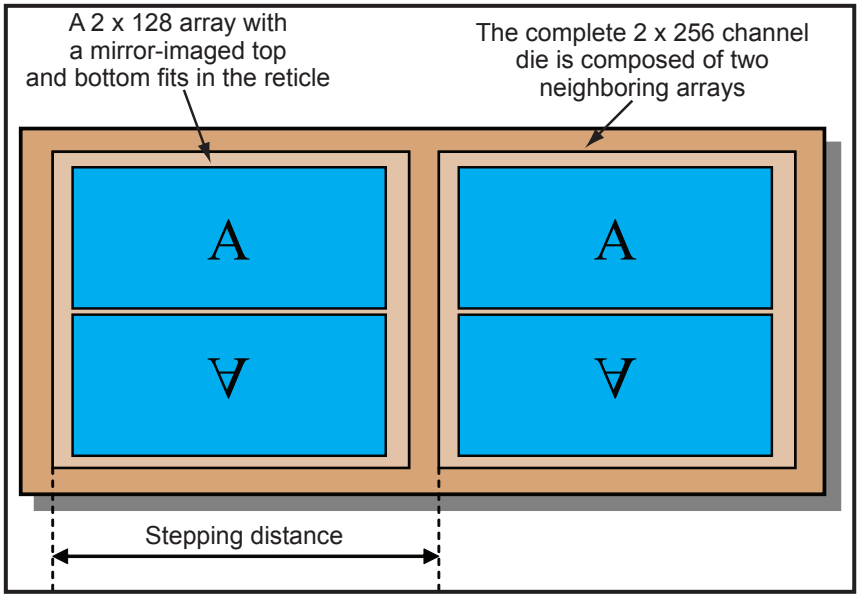

Figure 1. Conceptual layout for four sets of 128 pixels

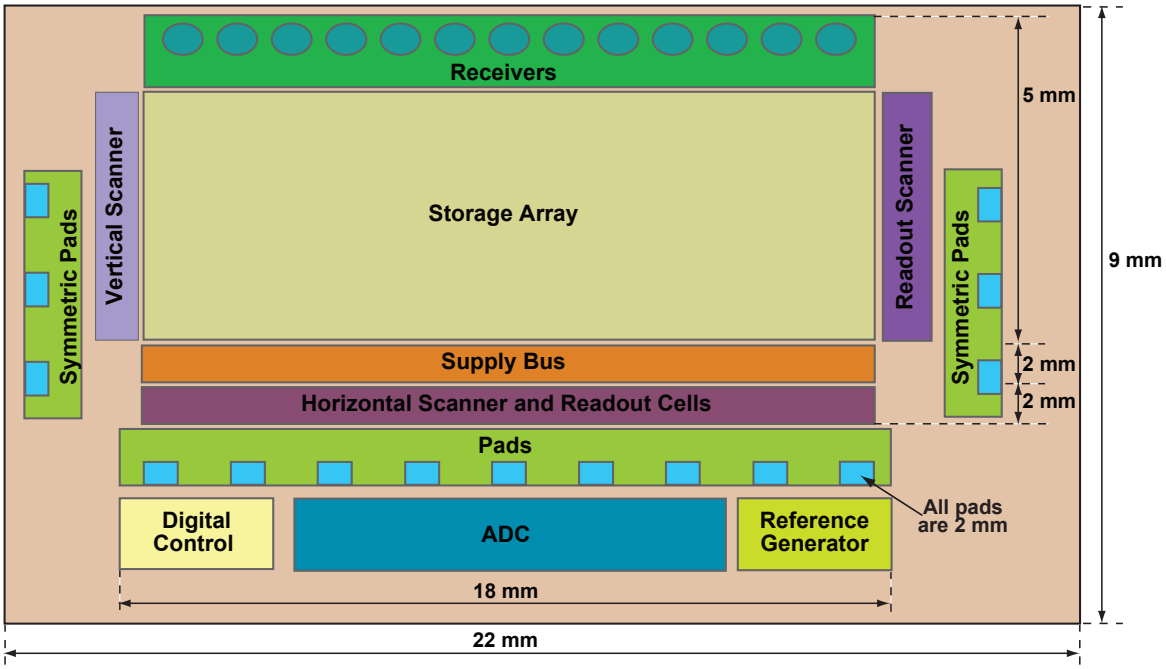

Figure 2. Conceptual layout of 128-pixel CMOS floor plan

Once the maximum current per pixel was determined, the designers could complete the input cell receiver design. Four options were developed: source follower, capacitive transimpedance amplifier (CTIA) with pixel division, CTIA with a biased current buffer, and a resistive transimpedance amplifier (RTIA). Only the RTIA design satisfied both the chip requirements and maximum-current-per-pixel constraint. The three-staged RTIA design (Figure 3) is a front-end amplifier where most of the gain is achieved, a second-order shaping and small gain stage, and a high-speed buffer stage that efficiently transfers charge onto the storage capacitors.

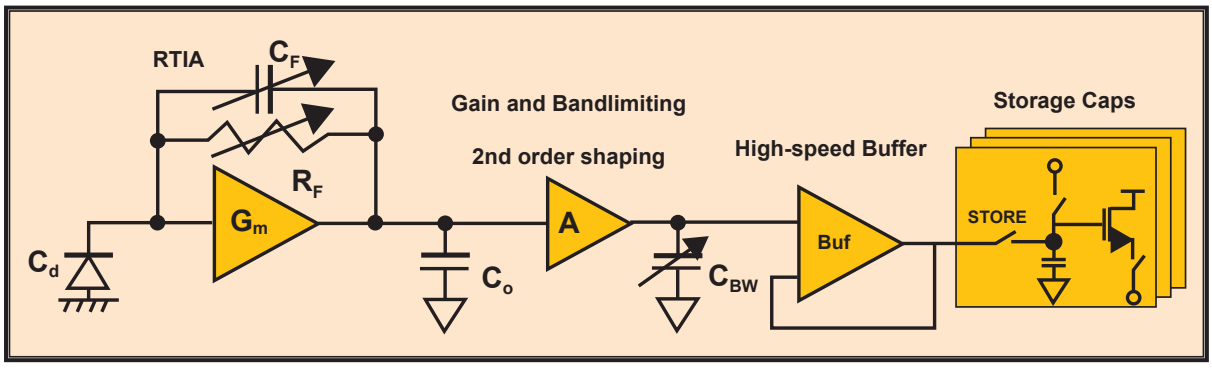

Figure 3. RTIA block design

The RTIA input cell is programmable such that the amplification stages and timing can be altered, and consequently, the bandwidth is changed. The gain stage can be altered from a gain of unity to three. Usable bandwidths can vary within 7 to 30 MHz. Figure 4 shows the device's frequency performance.

Simulations of the input cell showed that the data could settle within the 10-ns frame rate requirement, parasitic coupling was smaller than the anticipated noise level, the bandwidth was maintained, and the data output level reached 1.8 V_{pp}, maintaining the dynamic range. The receiver and buffer layouts were checked to ensure correct fit on the approximately 22 mm × 9 mm chip size.

Frequency and noise analyses, shown in Figures 6 and 7, respectively, indicated that a star connection bus and low-resistive paths would minimize crosstalk. The noise is dominated by the feedback resistor in the RTIA. For small input signals, the input receiver will dominate the noise, while for large signals, shot noise will dominate.

Capacitive loading was another issue to consider. Parasitic capacitance deteriorates chip performance by increasing the load on a line that we need to stabilize in less than 10 ns, as determined by the 10-ns frame rate requirement. It also adds crosstalk components as well. Figure 7 shows the analog noise analysis completed on the models; thermal noise apparently dominates the noise floor. Table 1 shows the final summary of analog design performance.

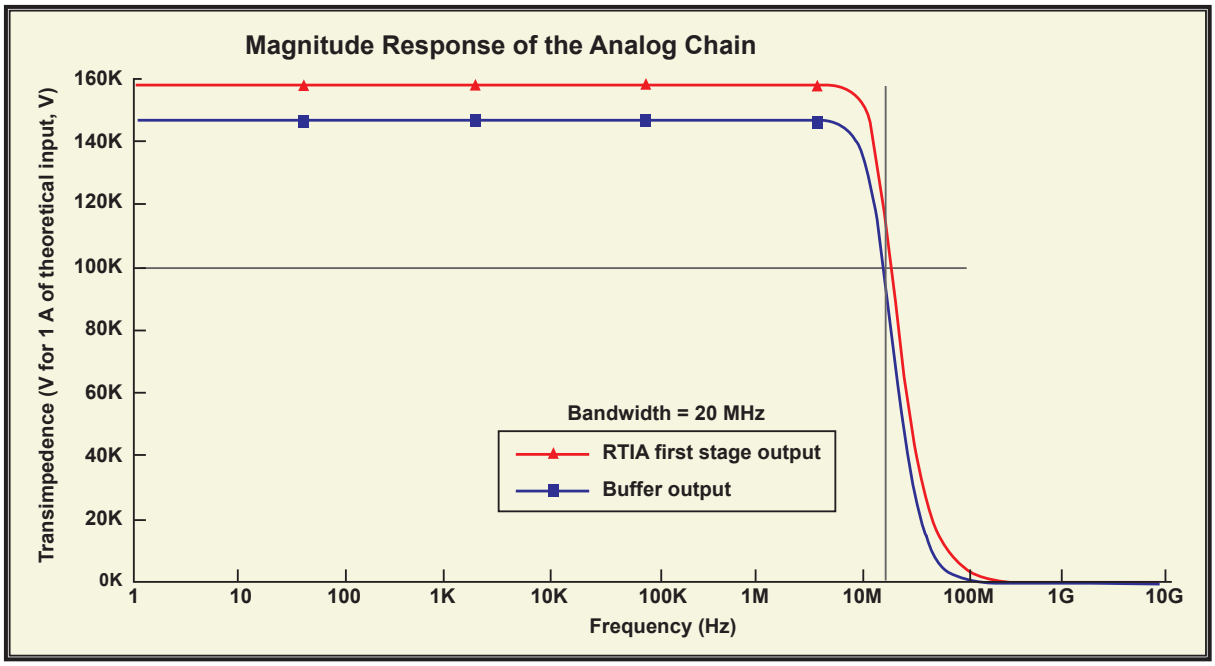

Figure 4. Verification of desired bandwidth

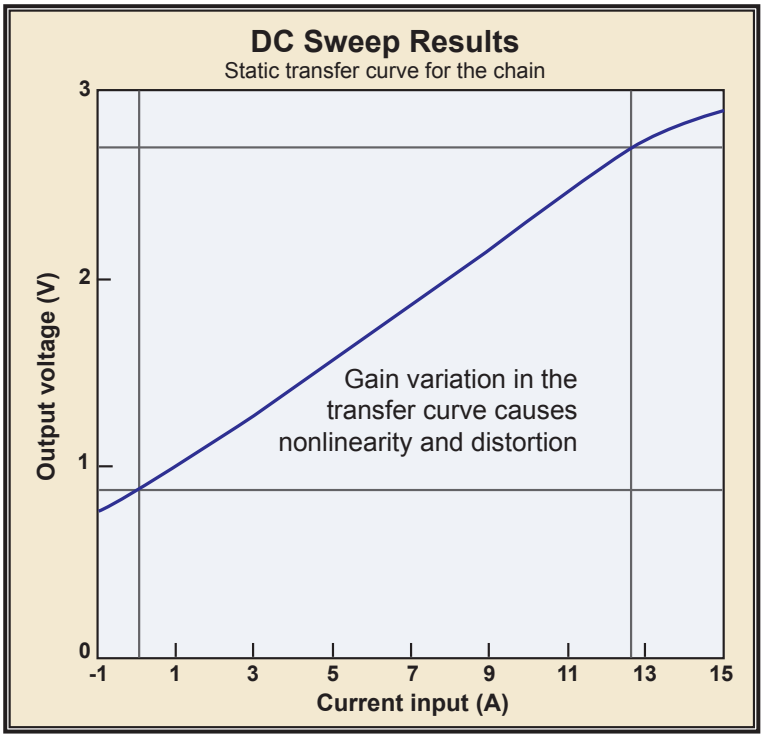

Figure 5. DC sweeps verify transimpedance amplifier results

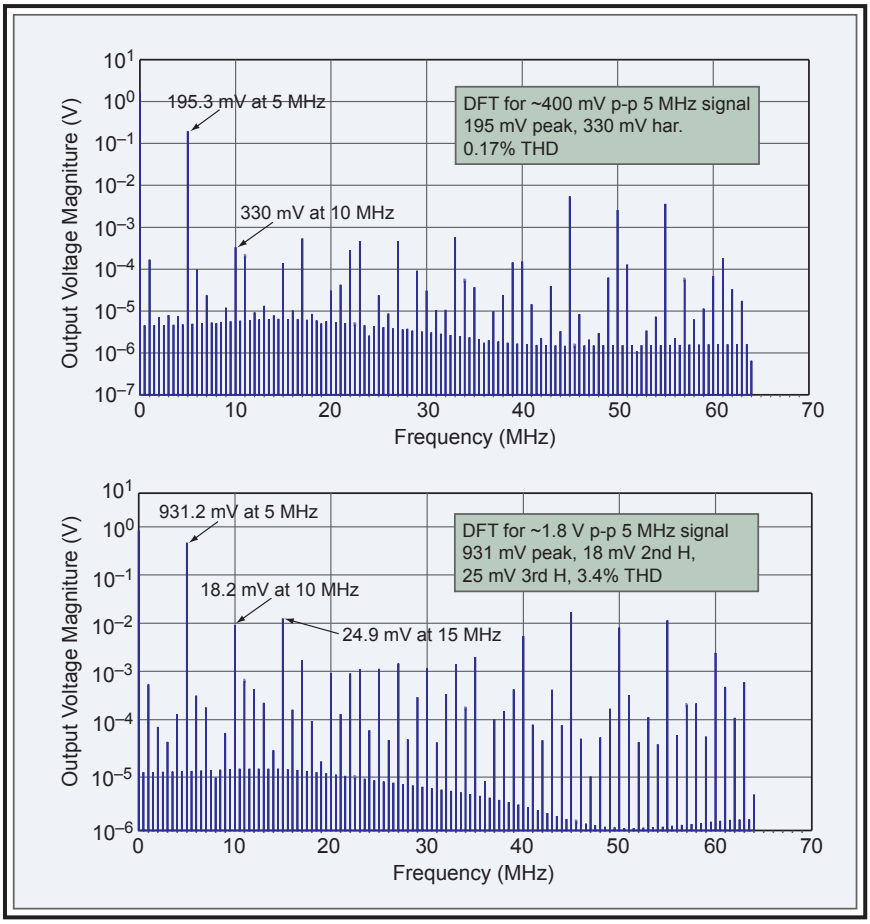

Figure 6. Frequency spectrum of output shows predicted distortion

The next consideration was that the timing of the pixel frames traveling through the chip was correct and did not lead to erroneous data. After a conceptual design for the chip's vertical scanner was realized (Figure 8), a smaller test circuit was simulated. In the circuit, four rows of 128-pixel columns were modeled. In the model, the designers incorporated programmable capacitors such that the delay lines in the vertical scanner could be changed to optimize capacitor array information readout. Several different simulations were modeled. After careful analysis of the simulations, the designers determined the clocking pulses to be skewed up to 2.1 ns, and that the skew is deterministic.

A clock jitter analysis performed on the simulation showed a worst-case maximum of 390 fsec root-mean-square jitter. Jitter sources are clock-path noise (including thermal and shot noise), external

clock jitter, and noise from a power supply–induced jitter. Based on a 10-ns sample period with a 12-bit analog-to-digital converter resolution, the jitter budget was determined to be 1 psec. The final design specifications are summarized in Table 2.

Table 1. Analog design performance specifications

Characteristic	Performance
Programmable transimpedance (Ω)	25 K, 50 K, 75 K, 100 K, 125 K, 150 K, 175 K, 200 K
Programmable bandwidth	7–30 MHz
Programmable gain	0.93 degrees (1, 1.22, 1.25, 1.28, 1.33, 1.66, 2, 3)
Maximum output swing	1.8 V
Noise at 150-K transimpedance (150 K, gain 0.93) and 20-MHz bandwidth with 2.7-pF diode capacitance	500 µV (receiver) + readout noise (450 µV) 673 µV ≥ input referred : 4.83 nA
Dynamic range for above case in case of 10.7 mA of maximum input current (output voltage : 1.5 V)	Ratio 2215:1 or 11.1 bits
Output nonlinearity with 5-MHz signal	0.17% with 400-mV peak-to-peak signal 3.4% with 1.8-V peak-to-peak signal

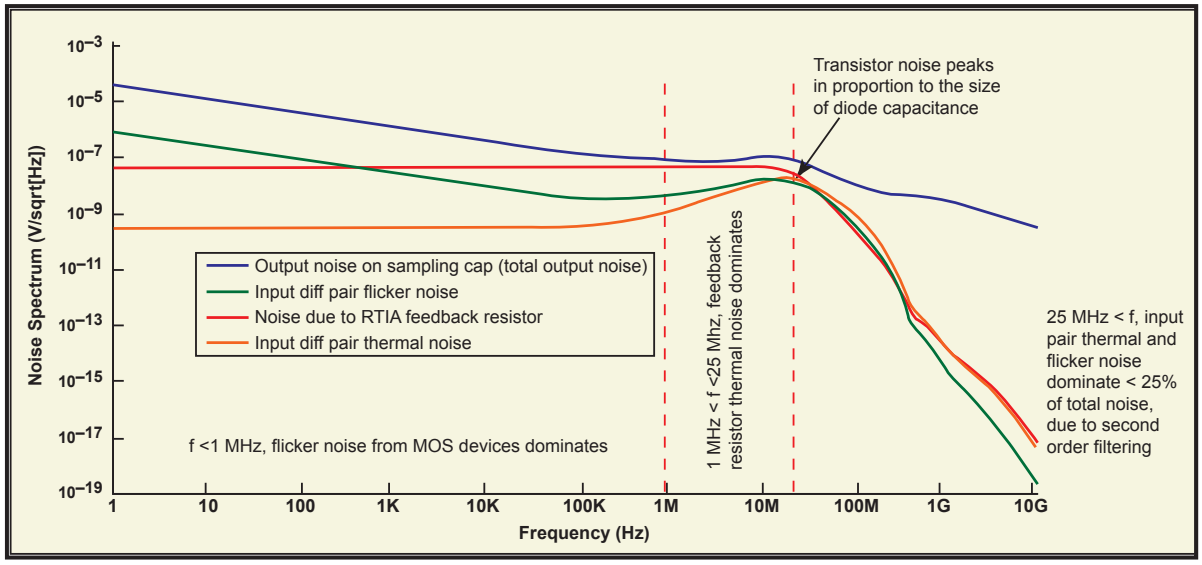

Figure 7. Noise analysis of RTIA design. Transimpedance = 150 KΩ, current = 0.93 A, which gives $V_{out\ rms}$ = 500 µV, and the input referred noise current is 3.6 nA.

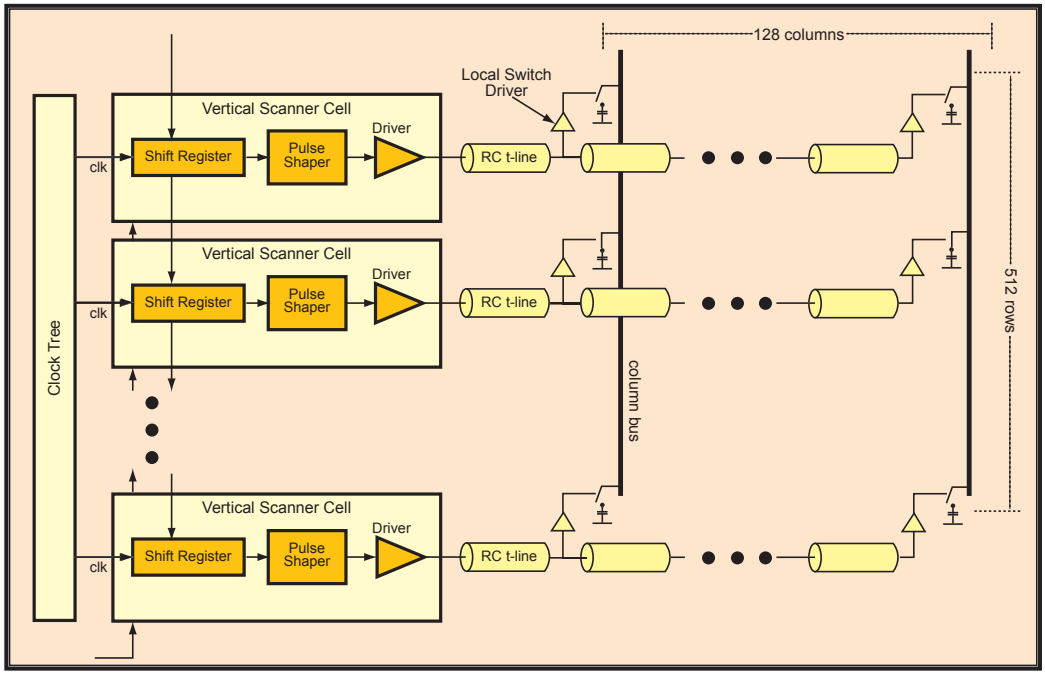

Figure 8. Vertical scanner concept design

Table 2. Final design specifications summary

Characteristic	Specifications	Design
Array size	(2 × 256) pixel array × 512 samples per pixel	By design
Allow for adjustable gains on each of the two rows of pixels	Allow for adjustable gains on each of the two rows of pixels	By design
Pixel size – multimode fiber core	100-μm diameter	By design
Pixel pitch – multimode fiber cladding	140-μm diameter	By design
Frame rate	10 ns	10 ns
Maximum illumination	133,000 photons/ns	625,000 photons/ns @ RF = 25 k 78,125 photons/ns @ RF = 200 k
Data output	12-bit digital	12-bit ADC
Dynamic range with one or more outputs where readout rate is sufficient to maintain dynamic range	>11 bits	~11.1 bits
System on chip design	System on chip design	By design

Conclusion

A design for a digital streak circuit was developed that satisfies mechanical requirements. It was determined that the system's initial floor plan is approximately 22 mm × 9 mm of die area. Streak camera acquisition of images was defined. The input cell was modeled for the required specifications, and it was verified that the circuitry performs as requirements have specified. Input and storage cell layouts have been realized and modeled, and system performance has been reverified with simulation data extracted from the layout. The designers have confirmed that frame timing for individual channels is consistent and uniform. The final design summary is given in Table 2. In addition to achieving the objectives listed in the project statement of work, the layout engineers also almost finalized IC layouts. Post-layout simulations for the input cells were also completed.

Future development will include IC layout designs, models, parasitic extractions, post-layout simulations with parasitics, and final performance predictions, followed by IC fabrication and packaging, and completion of the full functional test to verify that the IC chips can meet target requirements in addition to the data sheets. We will start the second design phase as soon as BN funding becomes available.

Acknowledgments

I would like to thank the Rockwell Scientific Company team on their efforts in realizing this project. Their contribution and expertise in CMOS imager design made this a great success. The members include: Hakan Durmus, Anders Petersen, Vincent Douence, Atul Joshi, and John Auyeung.

this page intentionally left blank

Streak Pyrometer

Cenobio H. Gallegos[1]
Los Alamos Operations

The spatially integrated, temporally resolved pyrometers developed to analyze shock properties of different materials consist of discrete spectral channels operating in the near-infrared and infrared (IR) spectral regions. Our project goal was to build a dynamic pyrometer with a continuous spectral record, over time, in the IR. This was accomplished by enhancing the quantum efficiency (QE) of an existing streak camera by placing a microchannel plate (MCP) at the input and focusing a spectrometer on the input of the MCP with a spectral range from 600 nm to 1100 nm.

Background

Dynamic (discrete-channel) pyrometers can record output from five photomultiplier tubes on 8-bit digitizers, each with a narrowband filter calibrated to a blackbody source. Essentially, the pyrometer records five discrete points on the blackbody spectrum (500 nm to 1.7 μm).

By measuring a continuous light spectrum, two physics questions may be answered. First, recording the temporal resolution of a continuous spectrum would enable detection of hot spots (multiple temperatures) that occur in time where discrete-channel pyrometers cannot resolve the multiple temperatures. Second, the streak pyrometer could also be used to analyze postshot breakout melt, a theoretical phenomenon that a discrete-channel pyrometer cannot measure. These dynamic temperature measurements could be conducted on P-Rad, DARHT, Z-pinch, Saturn, and the subcritical experiments.

Project

Our team built a streak pyrometer capable of recording a continuous spectrum from 475 to 900 nm. This was accomplished by mounting a DEP, Inc., MCP at the input of a streak camera, with a spectrometer focused on the MCP. The MCP has an extended red photocathode, a fiber-plug output, and a quartz input window.

The BN streak camera used (ser. #556) has a QE that peaks at 17% at 460 nm and is 0% at 875 nm. The DEP-manufactured MCP's QE peaks at 10.54% at 540 nm and is about 0% at 950 nm (Figure 1). The MCP's gain and QE at the input of a streak camera will yield the sensitivity and dynamic

[1] gallegch@nv.doe.gov, 505-663-2056

range (16-bit) required to measure temperatures as low as 700°C, with a dynamic sweep of 20 µsec. Our team performed spectral calibrations with different low-pressure gaslight sources, a xenon strobe lamp, and a krypton flashlight.

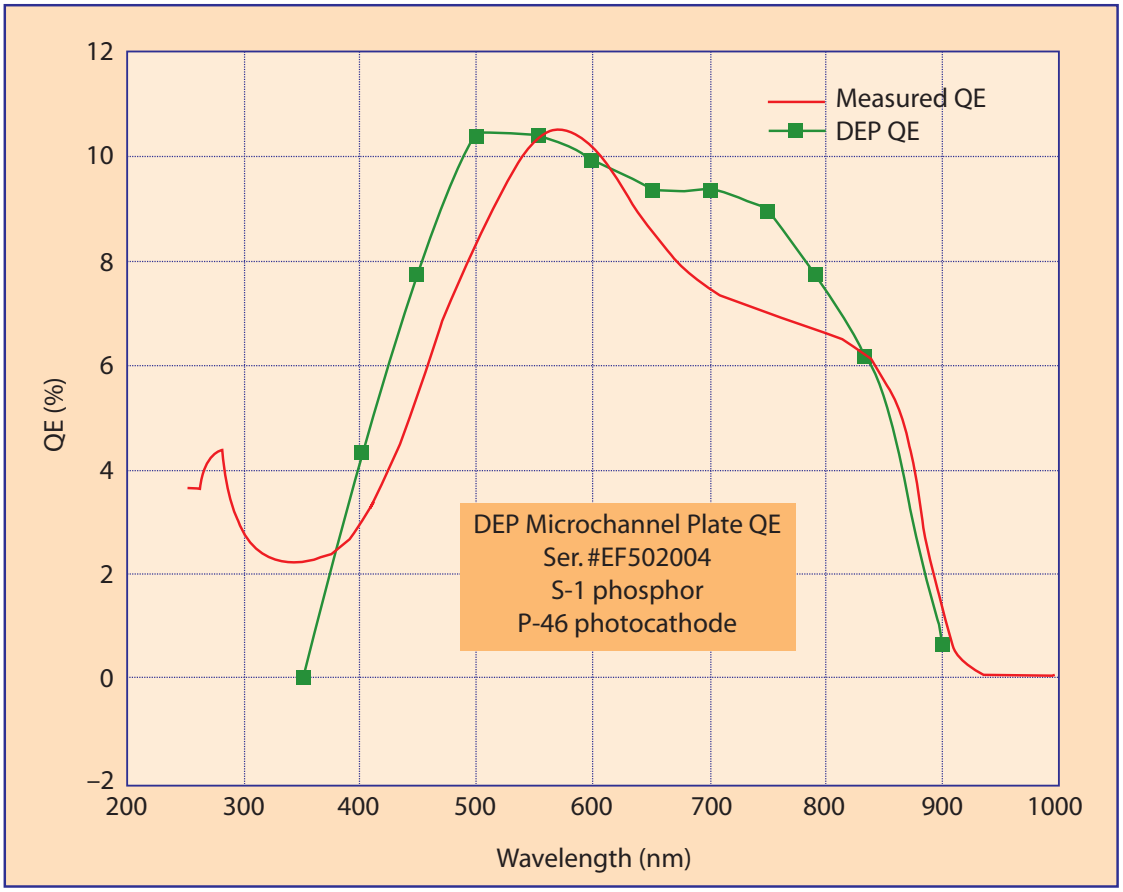

Figure 1. Comparison of measured vs. manufactured QE

We used blackbody sources from temperatures ranging from 500°C to 900°C. Calibrations were performed with both blackbody sources and the lens system. One calibration was conducted with the extended blackbody and a bare fiber, with the fiber close enough to take advantage of the numerical aperture. Figure 2 shows the system setup (only one source at a time was used).

The cavity blackbody produced the best results. All dynamic data shown is from this calibration series.

Figure 3 is the static image (the streak image shows a 140-µsec sweep) and graph of a xenon strobe.

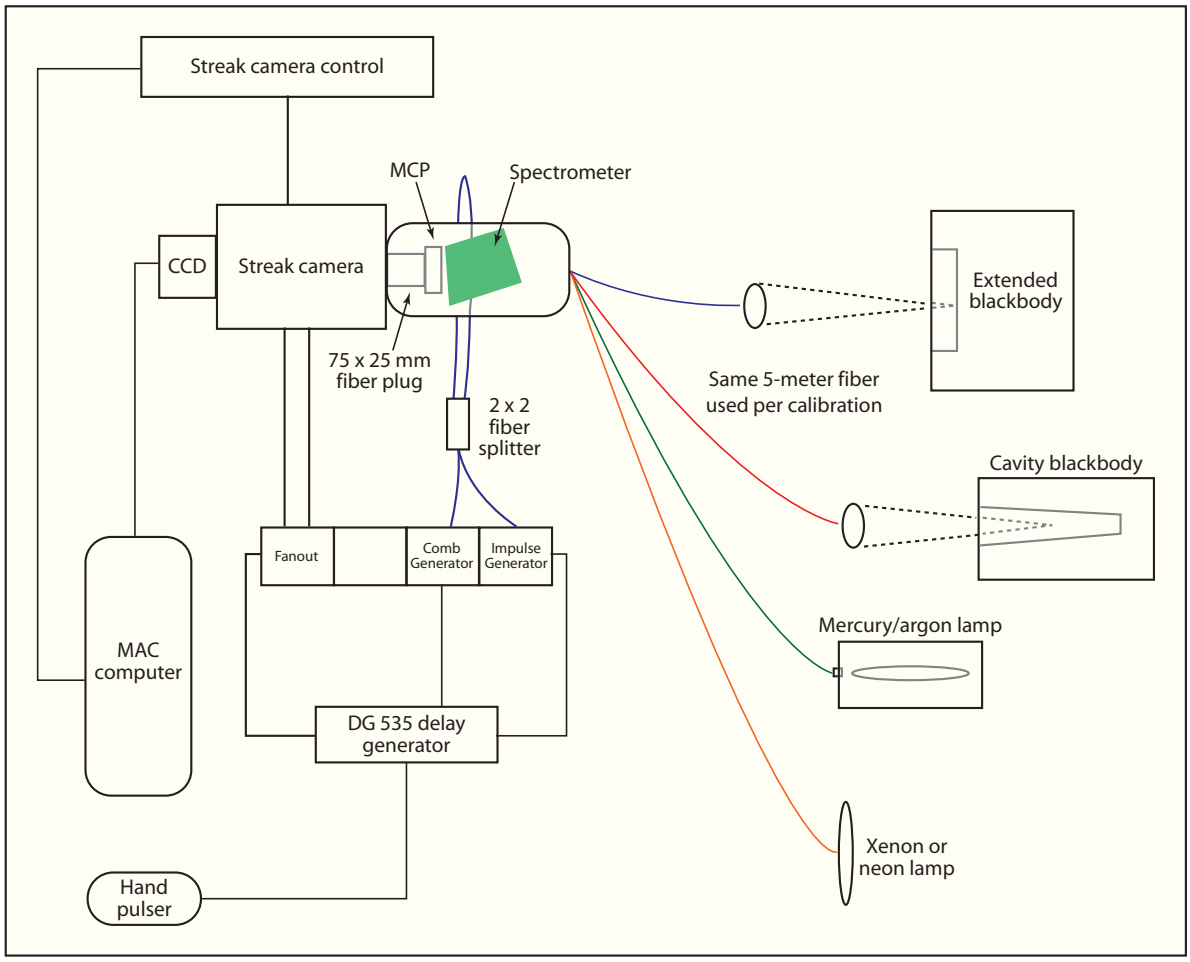

Figure 2. Streak/pyrometer block diagram

Figure 4 depicts a streak image of 140-µsec sweep with the Grasby cavity blackbody at 700°C. The graph is the collapse of 16 pixels wide between the combs (boxed area). More light is present throughout the sweep, enabling a decent temporal reading.

The ideal MCP (manufactured by ITT) has a QE curve that peaks at about 45% at 575 nm and drops off at the longer wavelengths as follows: 35% at 825 nm, 20% at 875 nm, and 5% at 900 nm. This MCP may have performed better; however, ITT was not interested in manufacturing it with a faster decay-time phosphor. The P-20 decay time is much too slow for useful temporal resolution.

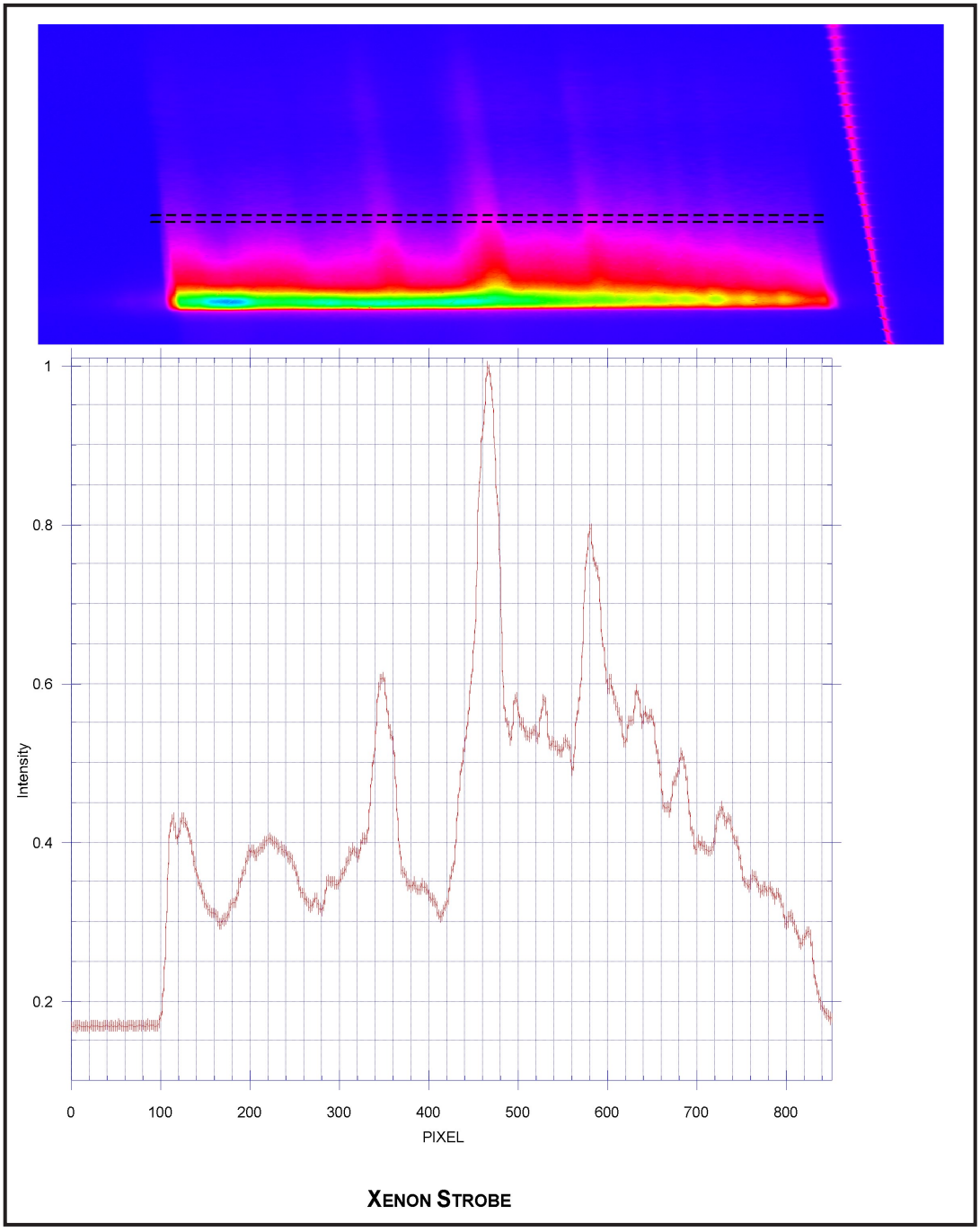

Figure 3. Xenon calibration image and digital collapse

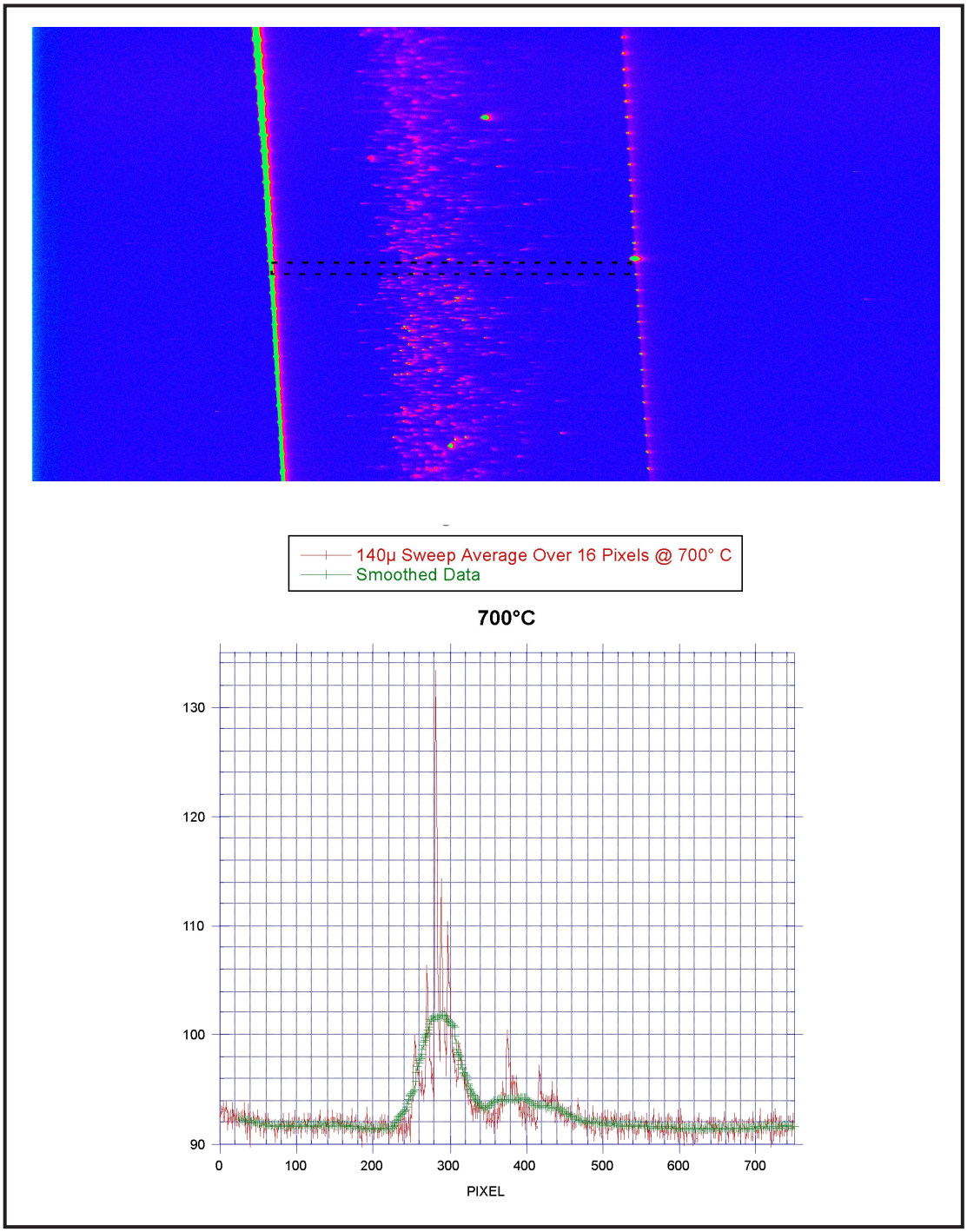

Figure 4. 140-µsec sweep streak image and digital collapse

Conclusion

The system did not perform as well as expected with the DEP MCP (S-25 photocathode, P46 phosphor). Due to the large fiber used (100/140μ), the spectrometer lines were wider than anticipated. The lowest dynamic temperature that could be measured with this system was 700°C, as the calibration data indicates.

A marked improvement is expected with the S-1 photocathode because of the QE out to 1 μm and MCP gain. However, the system is usable as is. With a few improvements in the spectrometer and better QE in the infrared, a decent dynamic measurement of 600°C is attainable.

Acknowledgments

We would like to thank Brent Frogget for his assistance with the optical design; Paul Flores for his help with the mechanical design, manufacture, and assembly; and Sheri Dance for her assistance with the system setup.

Displacement Interferometry System

Bruce Marshall[1]
Special Technologies Laboratory

In a displacement interferometry system, the use of single-mode fiber causes the optical power collected from a target surface to be very low and yields large variations in fringe amplitude. This project hoped to determine the source of these variations and explore ways to reduce their magnitude. Two test stands were built for use in studying the problem. Our team made several measurements and observations supporting the hypothesis that signal variability is due to dynamic speckle patterns produced by the moving target. Observations further indicate that depolarization is not a significant cause of signal variability for targets that lack linear surface structure. The team also demonstrated a two-fiber arrangement for photonic Doppler velocimeter (PDV) experiments that provides coverage during dropouts in any one channel. This system additionally offers a means to generate fringes during setup and makes the reference beam power independent of the power launched from the probe.

Background

Interferometry has long been used for noncontact distance and velocity measurement, and several systems of this sort are commercially available. Distance-measuring systems, such as Doppler lidar, use phase- or fringe-counting techniques to measure changes in position with subwavelength accuracy. For velocity measurements, a displacement interferometer, generally known as a PDV, consists of an interferometer in which motion of one cavity mirror produces fringes at a rate of one per each half-wavelength of travel. Continuous motion results in a sinusoidal output from the interferometer with frequency proportional to velocity. Direct interferometric measurement of shock velocity has only recently been used because, until now, the fringe rates exceeded recording-system bandwidth and record-length capabilities. As developed by Ted Strand of LLNL, PDV is a very simple, robust, and accurate means of measuring shock velocity. The power of frequency domain analysis allows good velocity measurements to be obtained with signal levels that other techniques could not achieve.

This project addressed one of the problems observed with PDV: the fringe contrast can vary on a microsecond time scale. We hypothesize that elimination of data dropouts might facilitate improvement in PDV velocity resolution.

[1] marshabr@nv.doe.gov, 805-681-2266

Project

An initial literature study yielded several articles on lidar that are relevant to PDV (Leeb, 1998; Winzer, 1998). To investigate the fringe fluctuations in PDV measurements, we purchased components to allow construction of a conventional PDV and several variations. We also built several test fixtures to provide an easy means of evaluating our ideas.

One article regarding lidar is particularly relevant (Winzer, 1998). The authors analyze the lens-coupling efficiency of random coherent light into single-mode optical fiber. They evaluate the overlap integral between the incoming, random optical field and the back-propagated Gaussian fiber mode to show that the coupling efficiency depends on the number of speckles within the receive aperture.

To test this concept, we set up an interferometer using 532 nm of light and projected the Gaussian fiber mode along with the speckle pattern from the target surface. As seen in Figure 1, the fiber mode field is comparable in size to the spatial period of the speckle pattern. If the speckle pattern shifts, which can occur from a number of causes, coupling into the fiber will change significantly.

Using the basic PDV system (see Figure 2) we assembled several variations. Using a simple rotating metallic disk to simulate the moving surface (the "target"), the data shown in Figure 3 were collected. Typical envelope fluctuations can be seen on the amplitude data at the bottom of the figure.

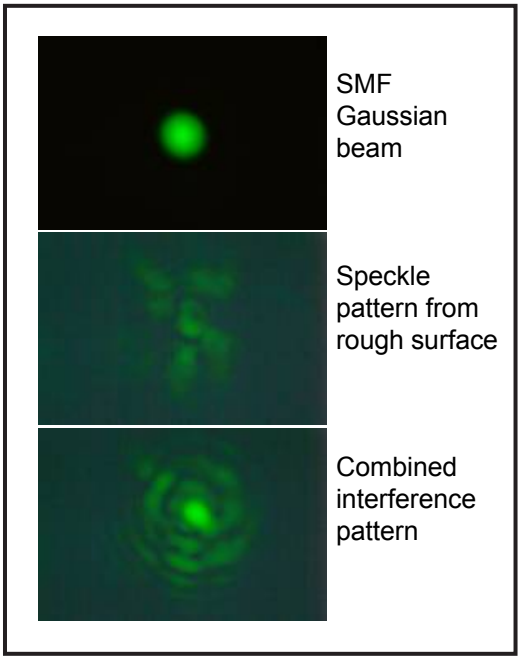

Figure 1. Interference patterns projected from a Michelson interferometer

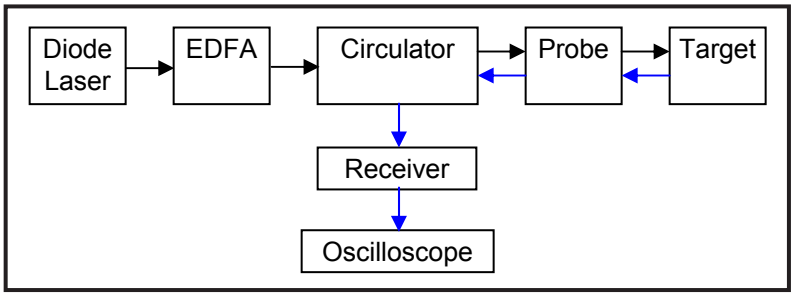

Figure 2. Basic PDV system

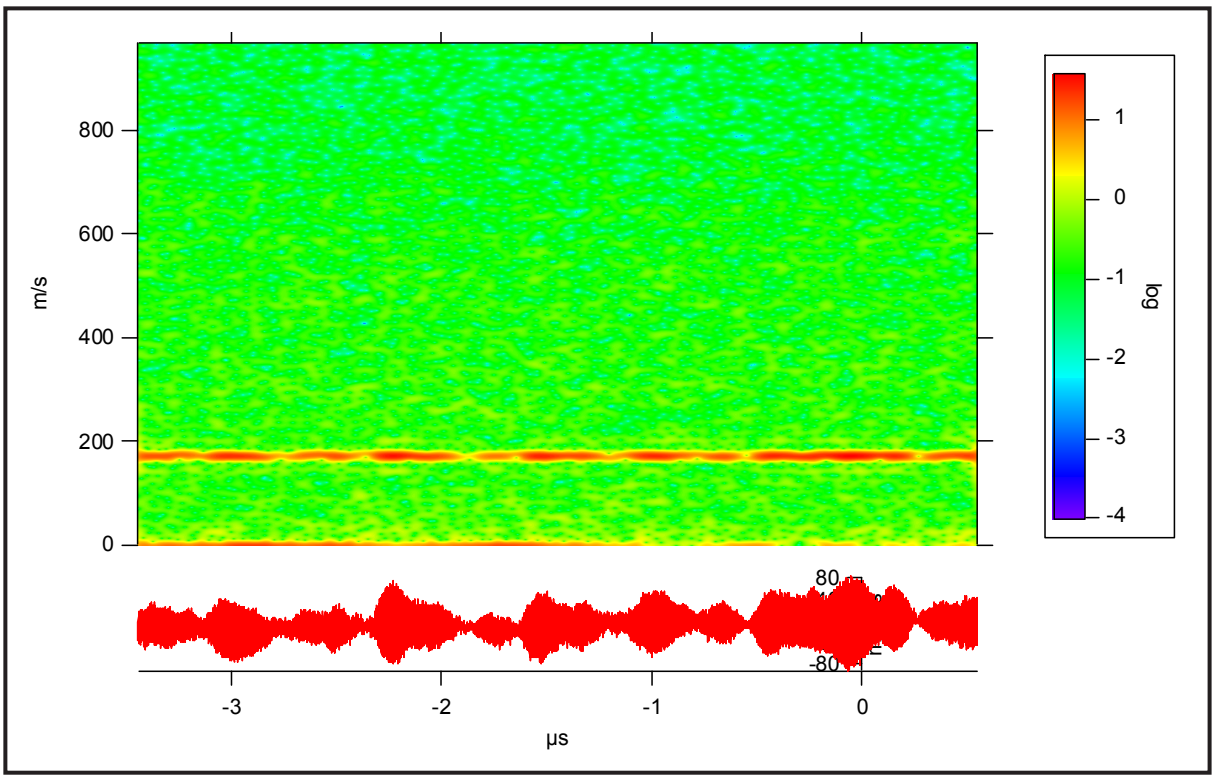

Figure 3. Single-fiber PDV data from rotating disk

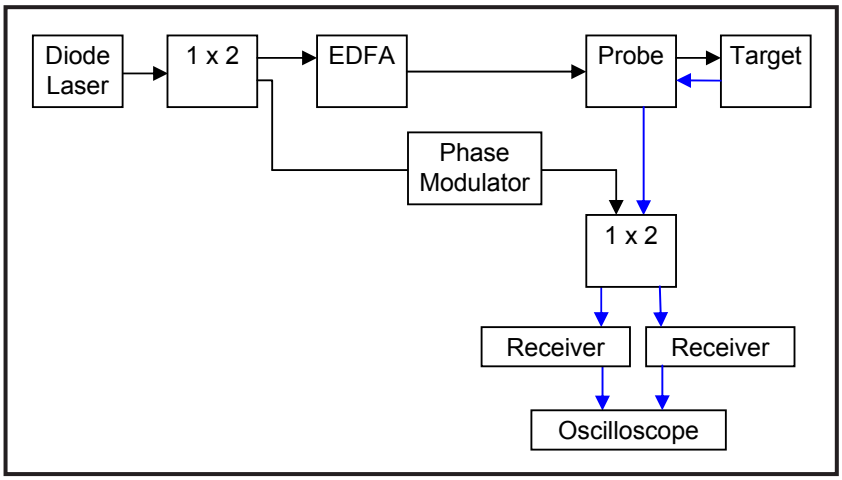

Figure 4. Two-fiber PDV system

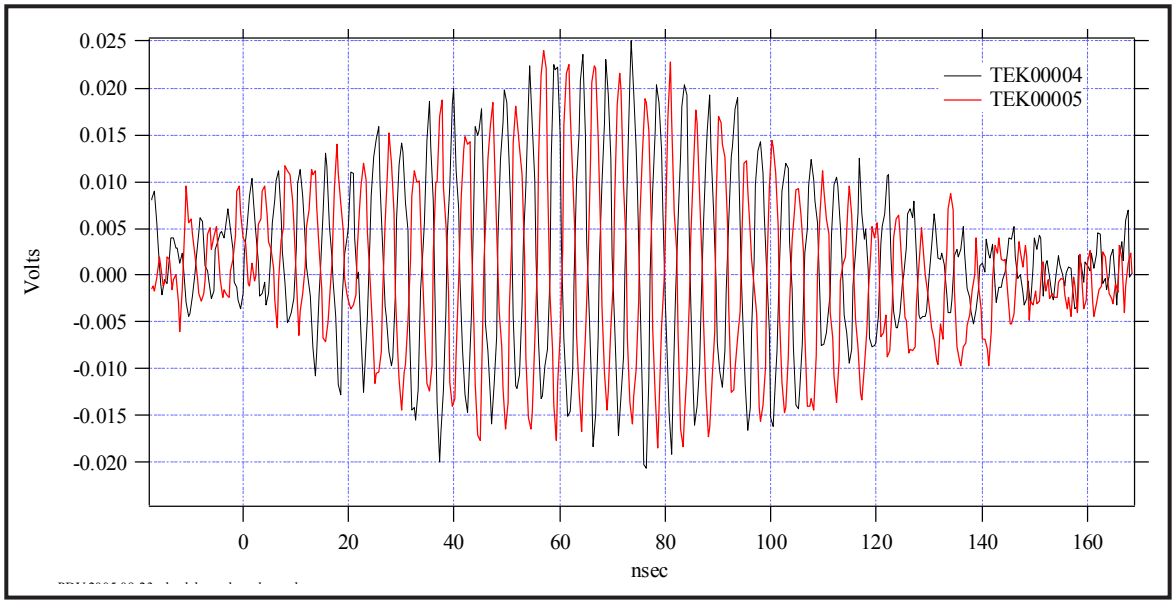

Figure 5. Expanded portion of complementary fringes from two-fiber PDV system

The two-fiber PDV system shown in Figure 4 uses separate send and receive fibers to provide a simple way to generate fringes during setup and to allow amplitude control of the reference beam. Figure 5 gives a time-expanded portion of the data from the two-fiber system and shows the complementary fringes, which may help enhance data quality.

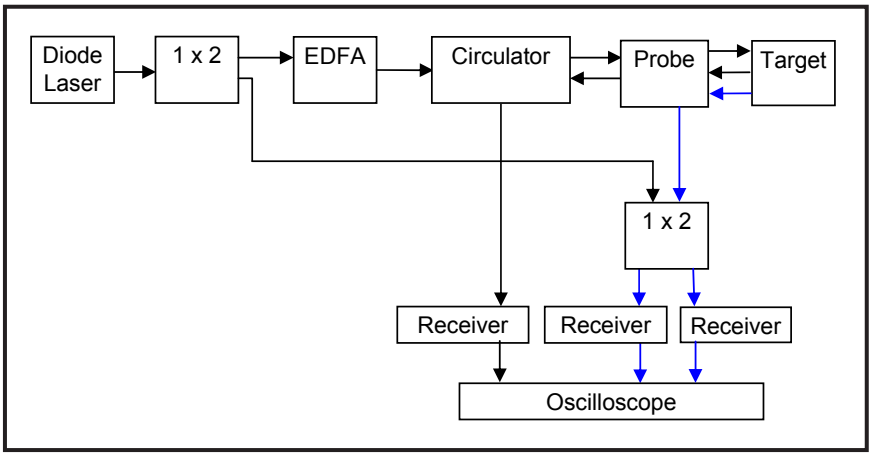

Figure 6. PDV system with dual receiving fibers

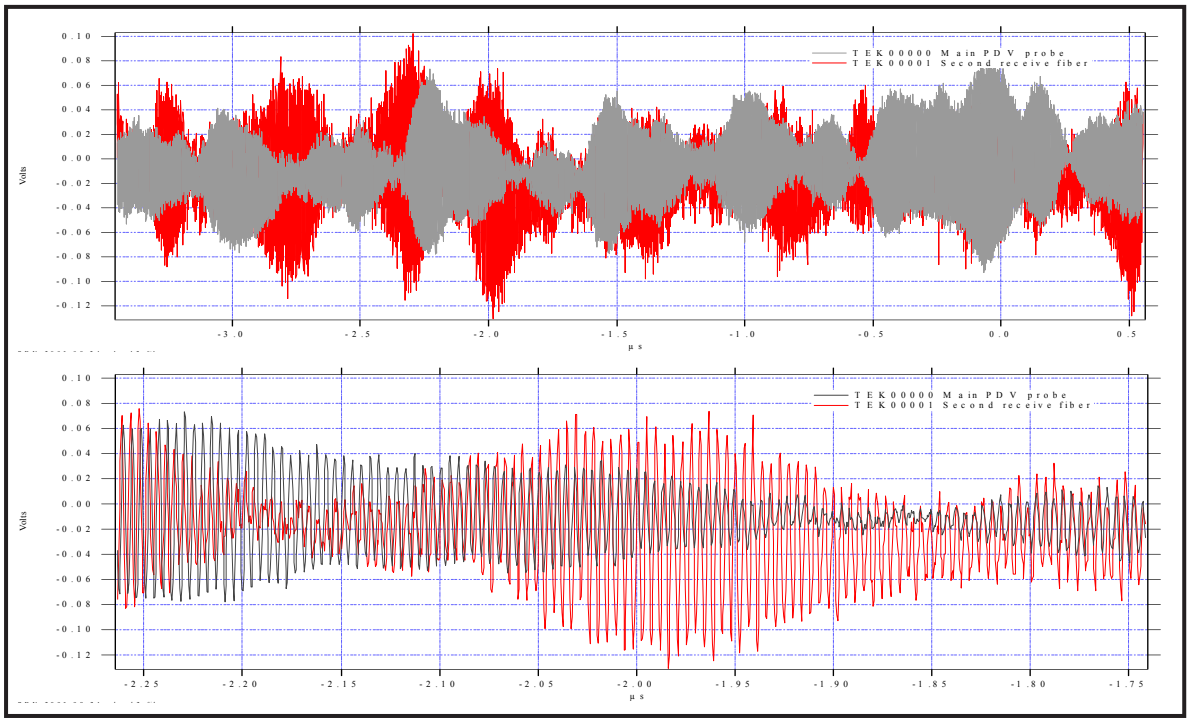

Figure 7. Dual-receive-fiber data from rotating disk showing overlap of fringe envelopes

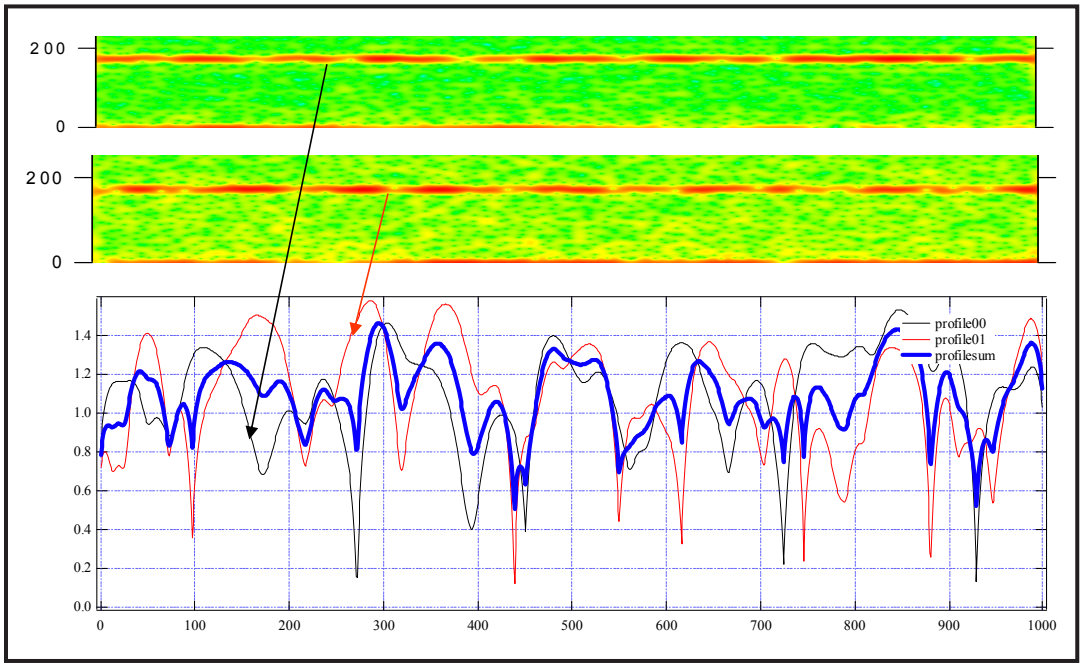

Figure 8. Dual-receive-fiber data from rotating disk showing reduction in dropouts for combined data

The two receiving fibers shown in another variation of the basic PDV system in Figure 6 give overlapping coverage on two channels so that the dropouts are reduced. Data from this system appear in Figures 7 and 8. The blue curve in the lower part of Figure 8 is the combined data, which has much less variability than either of the raw data records. We also examined systems that include multimode receiving fibers and heterodyne detection. Both techniques look promising and warrant further investigation.

A simple calculation model was started, based on a noncollimated probe and a small number of scattering points. It yielded results that were in reasonable agreement with observations. Additional work is planned in FY 2006, both to test new PDV systems concepts and to refine the optical model.

Conclusion

Fluctuations can be explained in terms of the overlap of the dynamic speckle pattern with the mode field of the single-mode fiber. Depolarization is not a likely factor unless significant amounts of multiple scattering are present. The probe optics determine the area that is illuminated as well as the way in which the return light is mixed with the reference beam. Speckle pattern fluctuation is determined by:

- divergence of PDV illumination and collection fibers
- distribution of scattering points on the target
- varying distance from the fiber to the target
- changing area of illumination
- alterations in the surface topography and tilt
- presence of multiple velocities in the field of view.

References

Leeb, W. R., P. J. Winzer, K. H. Kudielka, "Aperture dependence of the mixing efficiency, the signal-to-noise ratio, and the speckle number in coherent lidar receivers," *Appl. Opt.* **37**, 15 (May 20, 1998) 3143–3148.

Winzer, P. J., W. R. Leeb, "Fiber coupling efficiency for random light and its applications to lidar," *Opt. Lett.* **23**, 13 (July 1, 1998) 986–988.

Laser Diode VISAR

Bruce Marshall[1]
Special Technologies Laboratory

The velocity interferometry system for any reflector (VISAR) is widely used in the Stockpile Stewardship community for measurement of shock velocity. A VISAR consists of a wide-angle-delay Michelson interferometer. Because of the delay, which can range from a few millimeters to several meters, a laser with long coherence is required for the VISAR system. These lasers are expensive and bulky. As an alternative, we built a self-compensating VISAR that generates a coherence echo in the beam, so that a short-coherence-length diode laser can be used as the optical source. We also packaged a high-power, fiber-coupled diode laser in a battery-powered box to use with the VISAR. There are several technical challenges involved in this project. These include building a stable, matched pair of VISAR cavities and finding a diode laser with low enough coherence. We succeeded in both aspects, but have concluded that the optical inefficiency and excessive system noise probably make it of interest only in situations where a conventional VISAR cannot be used. It should be noted that a spin-off of this project was a compact, stable, air-delay VISAR that is now being used in programmatic applications.

Background

A VISAR system uses a wide-field-delayed Michelson interferometer to measure the Doppler shift of laser light reflected from a moving target. From the VISAR signals the target velocity can be determined with high accuracy. The light source for the VISAR system must have long coherence length relative to the interferometer delay. Typical VISAR delays range from a few millimeters to several hundred millimeters or more.

The lasers most commonly used for VISAR are frequency-doubled, diode-pumped YAG lasers, which are available at up to 10 W continuous wave (CW) and have very good stability and coherence. These are also fairly large, heavy, and fragile lasers, weighing ~100 lb and requiring long warm-up and cool-down times. External cooling is required at the higher powers for stability. A large, doubled, diode-pumped YAG is not practical for highly portable, battery-powered applications.

High-power diode lasers are multimode devices with applications that do not require good coherence, such as dentistry, soldering, and optical pumping. The diode consists of one or more bars that are stacked to achieve the required power. With careful design, the emission from a high-power diode

[1] marshabr@nv.doe.gov, 805-681-2266

laser can be coupled efficiently into a 100-µm- or 200-µm-core multimode fiber. The emission spectrum consists of several lines, each of which is fairly narrow and has a long coherence length. If there are enough lines, the sum will approximate an incoherent source.

An incoherent source can be used for interferometry if a coherence echo is imprinted on the beam by splitting the beam, delaying it, and then recombining the two beams while maintaining the wavefronts. A block diagram of this concept is shown in Figure 1. The use of coherence echoes has been reported several times over the past 15 years. A VISAR system using a short-coherence laser diode with single-mode optical fiber, which could measure motion over distances of about 10 µm, was described by Levin (1996). David Erskine at Lawrence Livermore National Laboratory (LLNL) developed a white light–imaging velocity interferometer using coherence echoes (1995). However, neither group used partially coherent light from a high-power diode laser to make a VISAR that could detect motion over the longer distances often required in the Stockpile Stewardship Program.

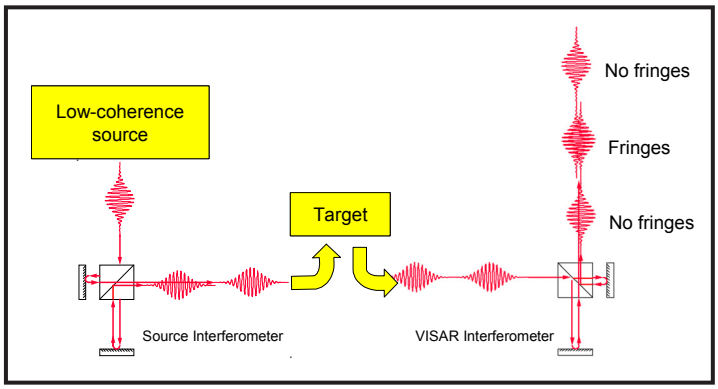

Figure 1. Tandem VISAR system

If the diode laser is too coherent, laser phase noise will be converted into amplitude noise when it passes through the first interferometer, reducing data quality. Operating the laser below threshold eliminates any modulation by the interferometer when one leg is blocked (Figure 2).

Project

During FY 2004, we built a breadboard version of a dual, matched-cavity VISAR and demonstrated that the optical design was practical and that cavity delays could be matched accurately enough to obtain fringes. During FY 2005, we completed VISAR assembly, including the four complementary and quadrature outputs, with all components permanently fixed in place. We also built a battery-powered laser source box and a test stand for Doppler shifting light. The completed VISAR (Figure 3) has a fringe constant of 303 m/s per fringe. The VISAR is constructed in a single block of aluminum that measures 15 × 18 × 2 in. Each cavity has a mirror mounted on a piezo actuator to generate fringes for setup purposes. Fine adjustment is provided by steering plates in the collimated beams.

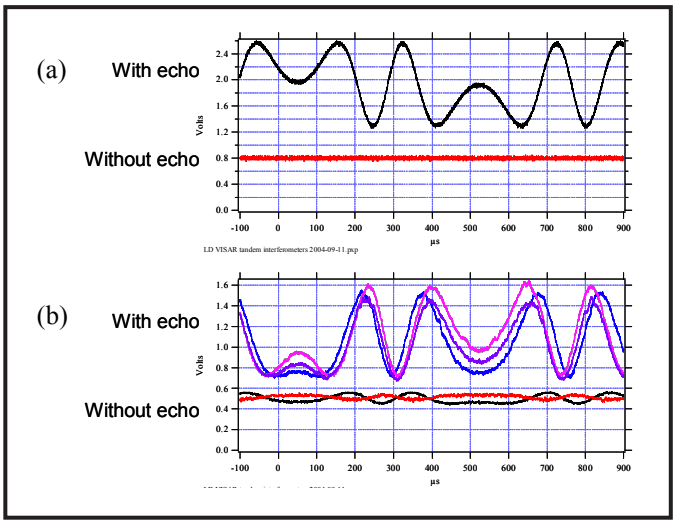

Figure 2. Interferometer signals showing coherence effects: (a) laser diode below threshold (incoherent); (b) laser diode above threshold (partially coherent)

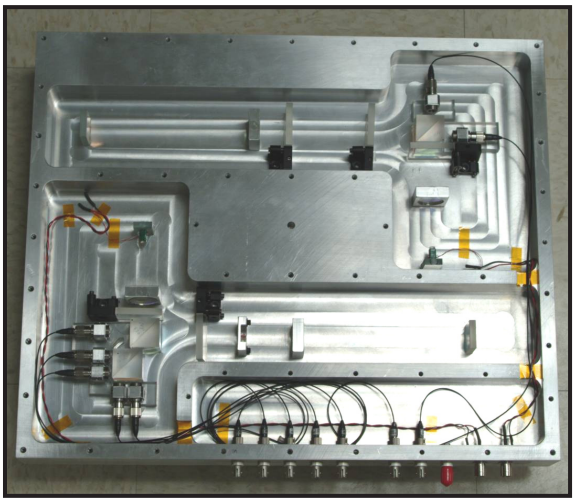

Figure 3. Laser diode VISAR cavity

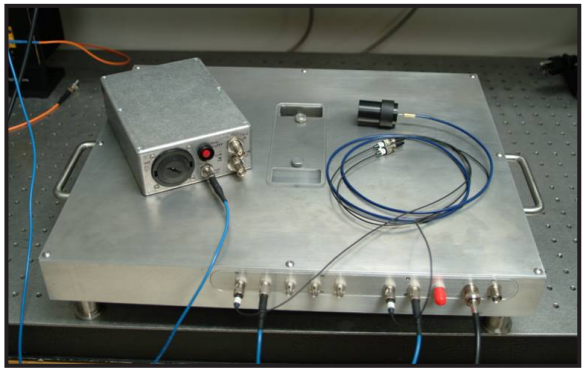

Figure 4. Laser diode VISAR system with laser source box and BoomBox probe

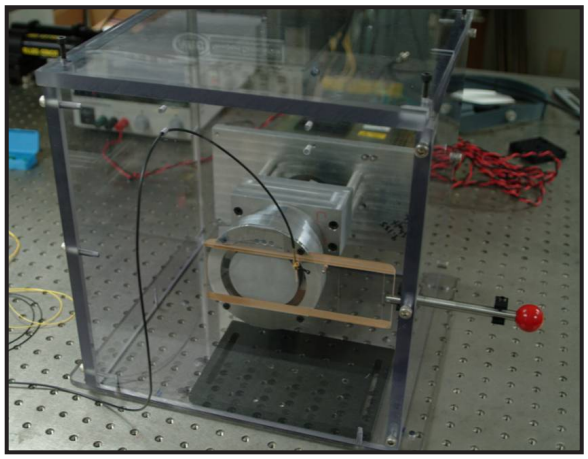

Figure 5. Rotating disk test stand

The fiber-coupling efficiency in each cavity is ~44%. The VISAR, along with the laser source box and a BoomBox target package, are shown in Figure 4.

The laser source box supplies approximately 1.5 W at 808 nm from a 100-μm-core fiber. It is based on the Analog Modules model 781 laser diode driver board that is powered by two D cells and can deliver up to 5 A in an 8-ms rectangular pulse.

The rotating disk test fixture (Figure 5) consists of an air bearing with a 70-mm-diameter aluminum disk rotating at 50,000 rpm. By scanning the probe across the surface while maintaining an 80° angle of incidence, the velocity can be varied from –175 m/s to +175 m/s. This device has the limitation that the spot size must be small, or a range of velocities will be observed simultaneously.

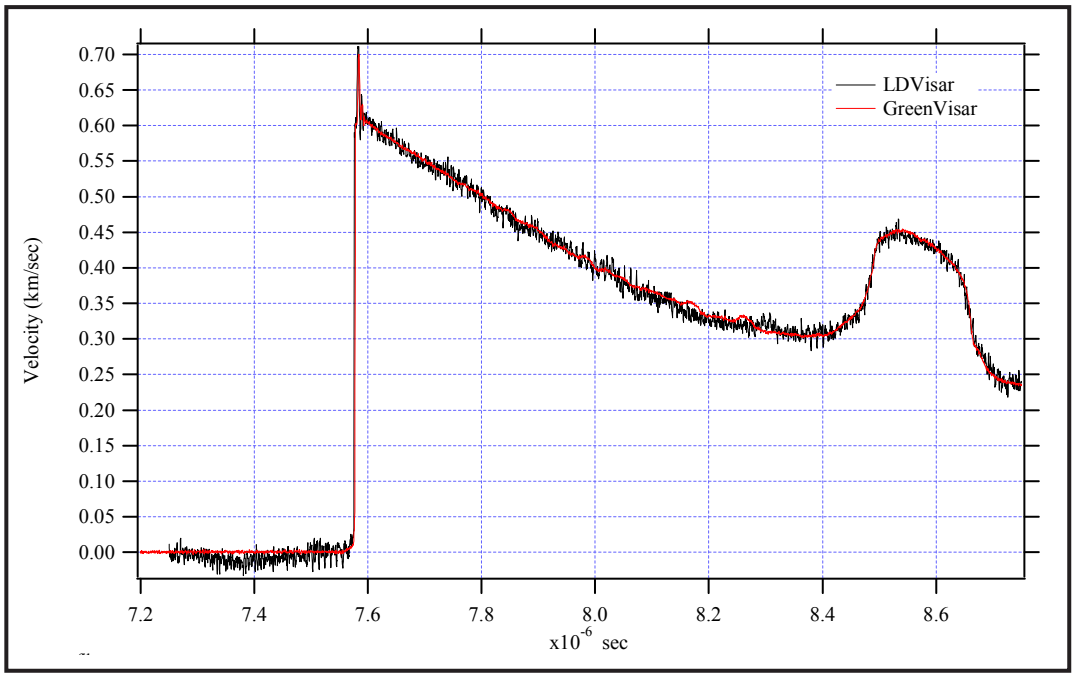

Figure 6. Velocity data from BoomBox experiment comparing conventional greem VISAR with laser diode VISAR. No smoothing was applied.

The laser diode VISAR system was used to measure the velocity of a copper flyer plate with an LiF window at the STL BoomBox. The digitizer signals were noisy, partially because the photomultiplier tubes available had poor response at 808 nm. (Quantum efficiency of the S-20 tubes is about 0.5% at 800 nm, compared to about 10% at 532 nm.) The analyzed data (Figure 6) are overlaid with data from a conventional VISAR. Note that agreement is very good.

Conclusion

A VISAR system using a laser diode source was built and demonstrated. Stability of the interferometers was shown to be good. A pulsed, battery-powered laser source box was also proven to work well. However, some fundamental problems show that this is probably not a practical alternative to conventional VISAR because of the optical power cost of imposing the coherence echo on the laser diode beam. The source interferometer had an overall efficiency of about 22%, which resulted from an inherent 50% split and an observed 44% coupling efficiency. In addition, since only half of the light interferes when recombined in the second interferometer, another 50% of the power is effectively lost. Therefore, for comparable fringe amplitude, the laser-diode VISAR has about 11% of the efficiency of a conventional VISAR and would require nine times as much laser power to achieve the same signal-to-noise ratio. Also, the contrast is reduced because the fringes are riding on top of a 50% incoherent

baseline. Although higher power, fiber-coupled laser diodes are available, they are expensive and require high-power drivers, defeating some of the purpose of the project. This system also requires the construction of a pair of matched interferometers, which adds to the expense. One must also consider the use of photonic Doppler velocimetry (PDV), which would probably be a better replacement for VISAR in those places where compactness, portability, and stability make VISAR impractical. The performance demonstrated in the BoomBox experiment was good except for the noise. It might be worth revisiting the laser-diode VISAR concept and testing it with better receivers.

References

Erskine, D., "White light velocity interferometry," UCRL-JC-121520, Lawrence Livermore National Laboratory, Livermore, California, 1995.

Levin, L., D. Tzach, J. Shamir, "Fiber optic velocity interferometer with very short coherence length light source," *Rev. Sci. Instrum.* **67**, 4 (April 1996) 1434–1437.

Optically Sampled Mach-Zehnder System

Bruce Marshall, E. Kirk Miller[1]
Special Technologies Laboratory

This project sought to research and demonstrate, if feasible, an extended-bandwidth data transmission and recording system based on a fiber-optic Mach-Zehnder (M-Z) modulator. Available technology options were researched, and a "photonic time-stretch" digitization technique was selected and mostly demonstrated. Included was a novel pulse-switching scheme that will allow long records to be captured by multiplexing digitizer channels at their full recording bandwidth.

Background

Data recording for single-shot events, such as underground nuclear tests and experiments at pulsed-power facilities including Sandia National Laboratories' Z machine, requires high-bandwidth capability and remote recording that can currently only be simultaneously realized with fiber optics. Using off-the-shelf components, present technology allows assembly of a system capable of up to 10–12 GHz, limited primarily by a digitizer sampling rate of 40 GS/s and 12 GHz analog. In these state-of-the-art systems, the electrical signal from a suitable detector (e.g., a Compton diode) drives a fiber-optic M-Z modulator, varying the transmitted light intensity from a continuous-wave (CW) laser. This device can simultaneously modulate light of different wavelengths (typically 1525–1605 nm for telecom devices) at frequencies well above digitizer bandwidths. Thus, we sought to extend bandwidth by using multiple wavelengths to sample the M-Z transmission, reading out the different wavelengths at various times on different digitizer channels. This capability could also be employed in high-frequency signal applications, such as radar and electronic warfare.

Project

We considered two potential approaches: photonic time-stretch conversion (method A) and wavelength-multiplexed pulse train (method B). In method A, a short, spectrally broad pulse is stretched in time by dispersion in an optical fiber before being modulated by the M-Z. After modulation, it is stretched further by dispersion prior to being digitized. The ratio of the second to the first stretch yields the factor by which the effective sampling rate is multiplied. For example, if a pulse is stretched to 1 ns before modulation, then to 10 ns before digitization, the stretch ratio is 10, and a digitizer at 40 GS/s will effectively sample at 400 GS/s.

[1] millerek@nv.doe.gov, 805-681-2237

Using method B, four CW wavelengths are sampled by the M-Z, then delayed relative to one another by dispersion in a fiber. Before digitization, they are "gated" into ~10-ps pulses by another fast modulator to create snapshots of the M-Z transmission at different times in the past. The pulses formed by gating could then be demultiplexed by wavelength and routed to four digitizer channels for recording. Each digitizer channel would then see every fourth pulse. A similar scheme was reported in the literature by Ng (2004).

Method B suffers a fatal flaw of conventional digitizers in that, to effectively determine the amplitude of each pulse, approximately three samples must be made to satisfy the Nyquist criterion. (If a given scheme samples three times within one cycle, and thus satisfies the Nyquist criterion, one can ensure against aliasing of high frequencies on shape reconstruction.) Hence, using four scope channels to extend the bandwidth only increases it by 4/3, which does not justify system complexity and cost. For this reason, we selected method A.

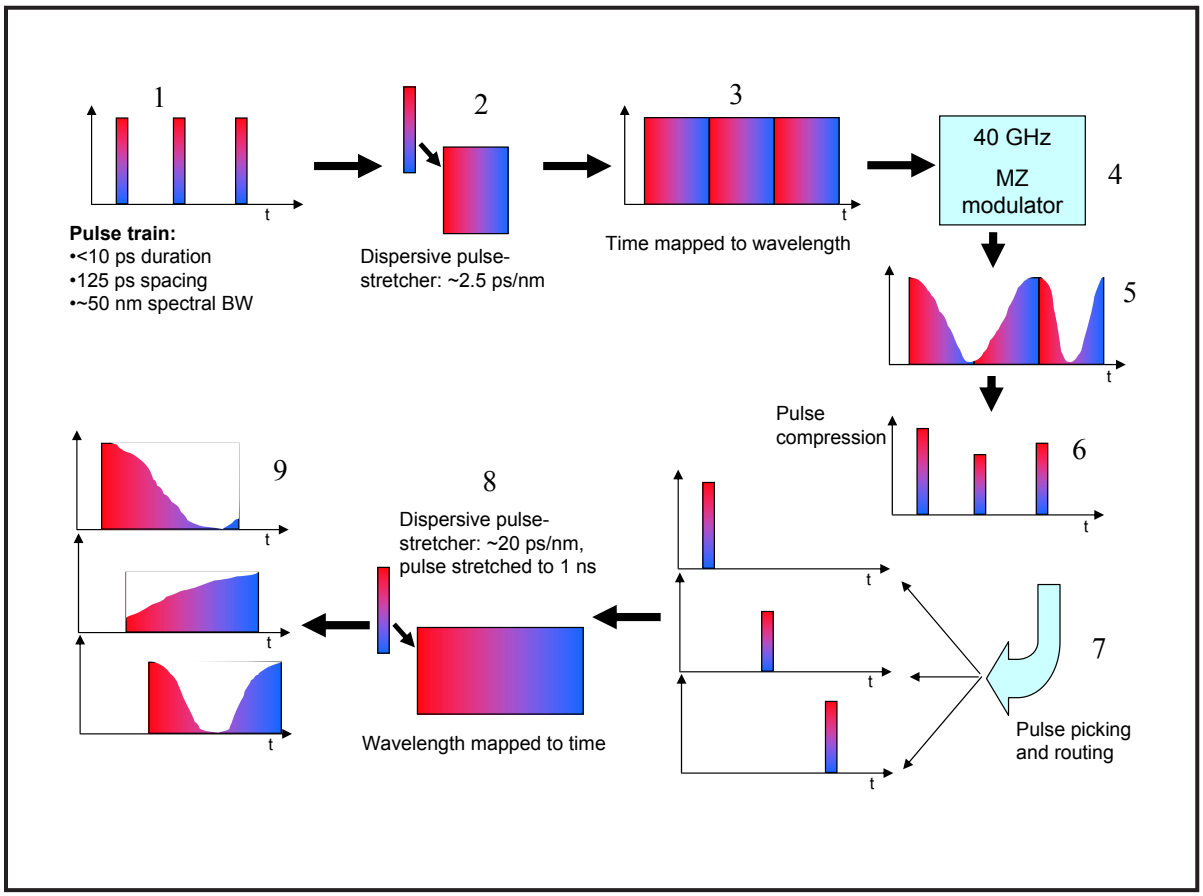

Figure 1. Photonic time-stretch digitization (method A)

A schematic diagram of method A appears in Figure 1. The majority of publications on this technique derive from Bahram Jalali's group at the University of California, Los Angeles (UCLA), and include an especially good summary article published by Han (2003). This group has implemented a single-channel version of this scheme, but apparently one that does not have the pulse picking and routing (required to cycle through digitizer channels and extend record length using available deep memory). In addition, Thomas (1995) proposed a single-shot version of this technique, with the wavelength-encoded signal later dispersed and recorded on a multichannel spectral system.

The novel part of this scheme is the pulse-switching and routing function (Step 7 in Figure 1), the subject of a technology abstract for time-domain pulse routing. A small fraction of the clock (sine wave) that generates the pulse train is coupled out to generate a square wave at 1/8 the initial frequency with ~50% duty cycle (using a Picosecond Pulse Labs 8x trigger countdown). The rising and falling edges of the square wave (one edge for every four sine-wave periods) are then employed to generate positive and negative impulses using an impulse-forming network. These impulses are amplified, split into four channels, and time-delayed to yield four interleaved pulse trains. These trains then are routed to optical switching modulators, which open briefly to allow one pulse to pass through, then close until the next electrical impulse arrives. Plots of such signals, for one of the four pulse trains, appear in Figure 2.

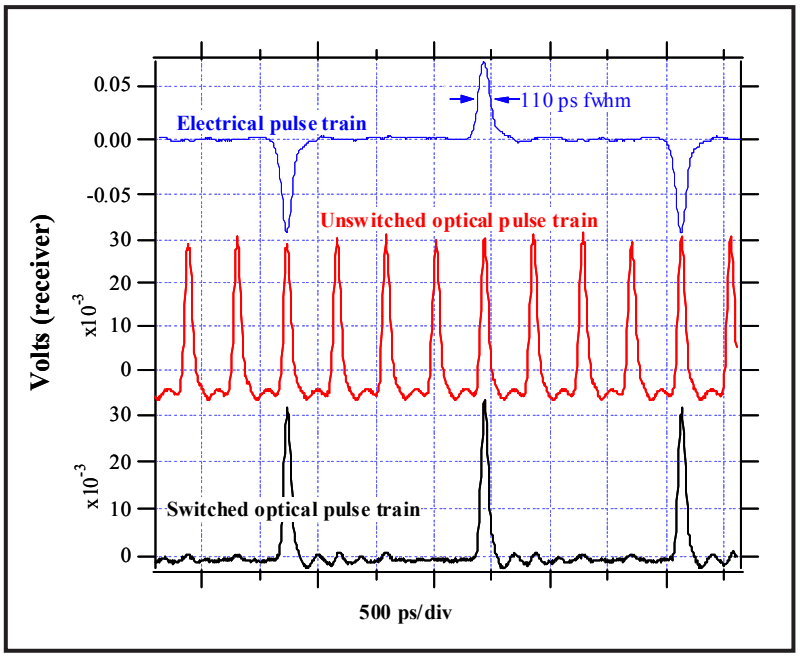

Figure 2. Electrical and optical signals from one channel of the pulse-switching scheme

A key design point is that the electrical pulse train shown in Figure 2 is amplified to ~1 V, so that after being divided in a 1 × 4 power divider, the amplitude is >500 mV. This voltage, when output to the driver amplifiers for the switching modulators, will run the drivers in saturation. This causes the pulses to have a flat top, thus reducing pulse-timing sensitivity, since the switching modulators will stay fully open longer. Figure 3 shows the box that generates the electrical pulse train for output to the modulator drivers.

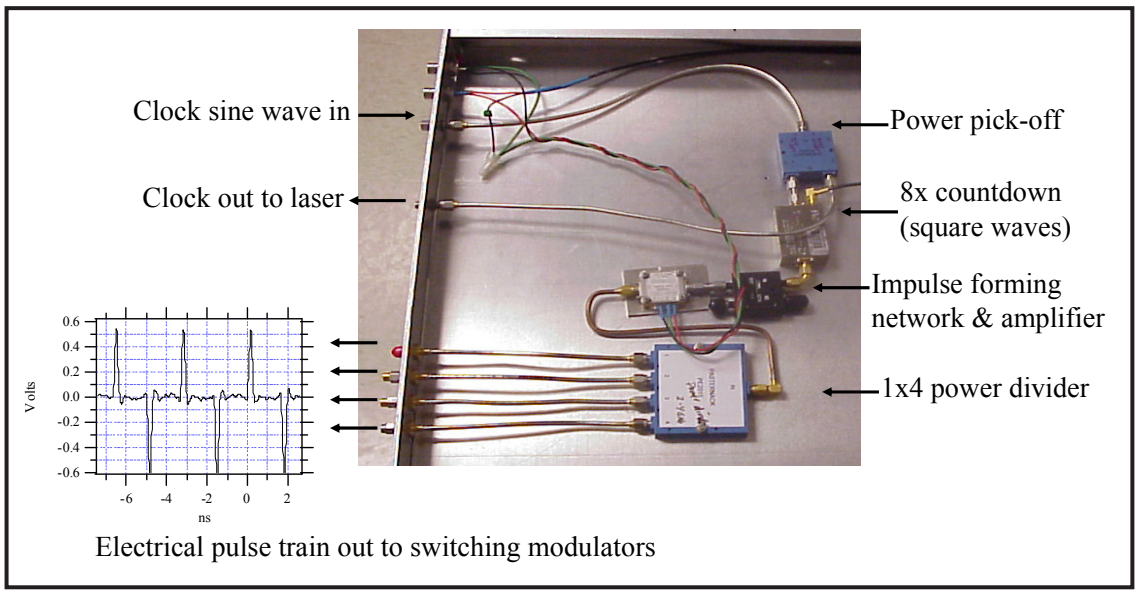

Figure 3. Electrical pulse-generation hardware

Conclusion

While the core demonstration of time-stretch digitization awaits the arrival of a specialty photonic crystal fiber for the continuum generation, the key technological hurdle of switching pulses to different channels has been achieved and is ready for integration. The Underground Test Readiness program has demonstrated interest in picking up this project for completion and demonstration in FY 2006, as part of a collaborative effort to survey and assess advanced data transmission and recording techniques to extend bandwidth and dynamic range. If long record length can be demonstrated with bandwidth greater than 25 GHz, this work will be submitted for publication in a scientific journal.

Acknowledgments

We would like to thank Dale Turley, Terry Davies, Ron Justin, and Jerry Stevens of STL for valuable discussions. John Galbraith and Monty Wood of LANL, and Craig Halvorson of LLNL provided encouragement and timely advice on digitizer performance.

References

Han, Y., B. Jalali, "Photonic Time-Stretched Analog-to-Digital Converter: Fundamental Concepts and Practical Considerations," *J. Lightwave Technol.* **21**, 12 (December 2003) 3085.

Ng, W., L. Luh, D. Persechini, D. Le, Y. M. So, M. Mokhtari, C. Fields, D. Yap, J. Jensen, "Ultra-high speed photonic analog-to-digital conversion technologies," *Proc. SPIE* **5435** (2004) 171.

Thomas, M. C., "1.5 GHz time-to-wavelength converter," *Rev. Sci. Instrum.* **66**, 5 (May 1995) 3355.

this page intentionally left blank

Circular Polarizing Flake Material for Optical Tagging and Tracking

Mark Morey,[1] *Roderick Tiangco*
Special Technologies Laboratory

A material for Optical Tagging and Tracking (OTT) applications has been identified and developed. This material is a cholesteric liquid crystal that can be cast as a thin film or processed into a flake, then applied to a target surface. The material is passively or actively illuminated and reflects circular polarized (CP) light, providing a unique optical signature. A breadboard viewer was assembled using a quarter-wave plate in conjunction with a linear polarizer (LP) filter. An electrically modulated liquid crystal version of either of the above filters can be incorporated to make the film appear to "blink."

Background

STL has had an ongoing program of developing new materials with unique optical signatures for potential OTT applications, such as nuclear smuggling or anticounterfeiting. Contrast is achieved by selecting and applying a material to a surface with the opposite spectral characteristics to produce a "white-on-black" or "black-on-white" optical effect at a chosen wavelength. These materials can be passively (solar) illuminated and require no batteries to drive an active source.

Essentially unpolarized light from the sun penetrates our atmosphere and picks up a slight polarization by the time it reaches the earth's surface. In the terrestrial world, the horizontally polarized fraction of light tends to scatter off a specular surface, while the vertical portion will penetrate an object's surface, giving it color and transparency. Both of these effects can be easily observed most effectively during midday, by rotating a linear-polarized filter by hand and observing the changes in intensity of lighted objects or the sky.

One focus of the present work was on minimizing this natural residual linear polarization's effect on image quality. The LP filter is made of a thin plastic sheet sandwiched between two glass plates. In the thin film are tiny parallel slits that allow polarized light to pass when it is parallel with the filter's slit orientation, while orthogonally polarized light is blocked.

Light can also be circularly polarized (CP). Because generating CP light is more complicated, it is nearly absent in nature, with only a few exceptions, such as reflections from a particular beetle (Kattawar, 1994). More important, the near absence of CP light in our general surroundings would lead to a high degree of contrast if a CP light signal could be generated.

[1] moreyms@nv.doe.gov, 805-681-2206

As light travels through a solid, its speed is reduced in relation to the material's refraction index. Some crystalline materials are birefringent, with different indices of refraction on two crystal axes, so that the electric field component of light parallel to one axis moves at a different speed from that parallel to the other axis. In the case of LP light entering a birefringent material at 45° to the crystal axes, the electric field components become out of phase, and the electric field vector will "corkscrew," leading to a circular polarization state of the light. A birefringent material has the reverse effect for incident CP light, generating LP light at 45° to the two optical axes (Figure 1). Such birefringent materials are sold commercially as "quarter-wave plates," or retarders, in which the layered crystal structures are tailor-made to choose wavelengths based on crystal thickness.

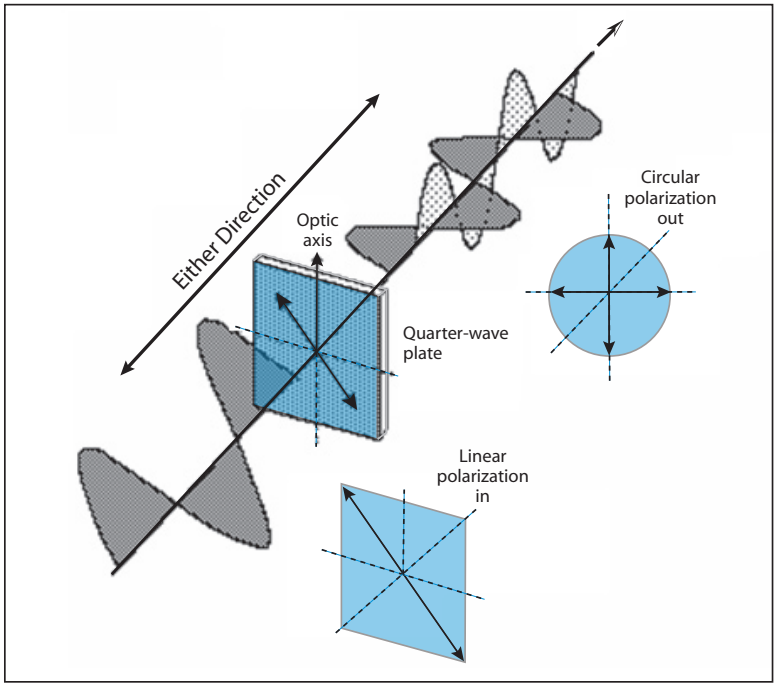

Figure 1. Circular polarized light generated with a quarter-wave plate. Image from hyperphysics.phy-astr.gsu.edu.

Project

Cholesteric liquid crystals (CLC) were discovered many years ago (Reinitzer, 1888; Korenic, 1998) but were only recently incorporated into a commercial product designed for circular light creation. STL identified a company that produces a CLC material as a thin film on a variety of substrates or as a pulverized flake. A CLC thin film consists of large molecules that have been polymerized as coils and aligned. When unpolarized light strikes the surface, half its intensity is reflected as left-hand cir-

cularly polarized light, while the other half is transmitted as right-hand circularly polarized (Figure 2). Additionally, the coil pitch and film thickness determine the wavelength reflected, which can vary from 350–2500 nm. Both thin films and flakes of this material were custom-designed to have peak reflectances at 360, 450, 520, 610, and 850 nm. The vendor grew thin films on glass plates as well as adhesive-backed stickers for considerably less cost than prior specialty OTT materials.

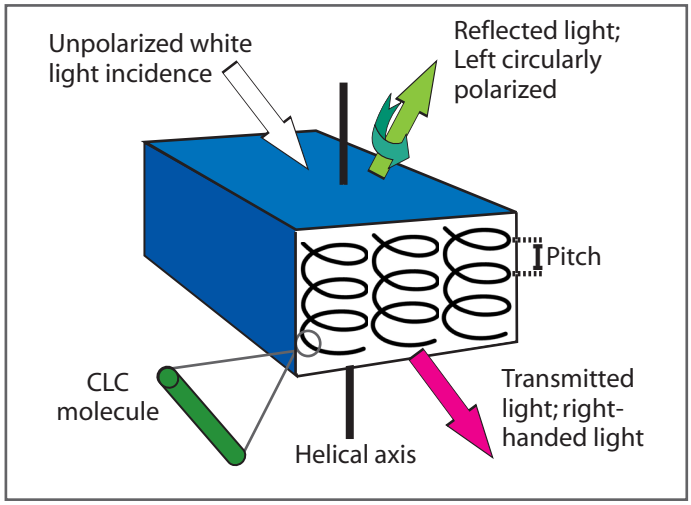

Figure 2. Optical response of cholesteric liquid crystal when illuminated with unpolarized light

Flakes from the aforementioned vendor were suspended in a soap water solution and applied to a glass slide for spectral measurement. Normal use of an organic solvent–based polymer binder was impossible due to CLC phase dissolution. On the glass slide, the flakes formed a fairly homogeneous layer with little clustering. Since the film has a maximum reflectance of 50%, and the coverage of the flakes was not 100%, the technique and formulation needed to be fine-tuned to realize the greatest contrast. For most of the tests, emphasis was placed on the thin films. Total (diffuse + specular) reflectance spectra of four of the films were measured with a Cary 5000 UV/Visible spectrophotometer (Figure 3). The results emphasize the relatively narrow spectral response of each film. The effect is most pronounced when viewed as normal with respect to the film surface. To test reproducibility of the thin film process, four samples were made of the 360-nm film. Among the samples, peak wavelength and peak width varied no more than 10%.

To specifically isolate CP light from the surrounding, essentially unpolarized light required a combination of the aforementioned LP and quarter-wave plate retardation filters. In a given scene with a CP target, light reaching the viewer will have both components. To differentiate the CP signal, light first passes through a bandpass filter and a quarter-wave plate set for the CLC film's reflected

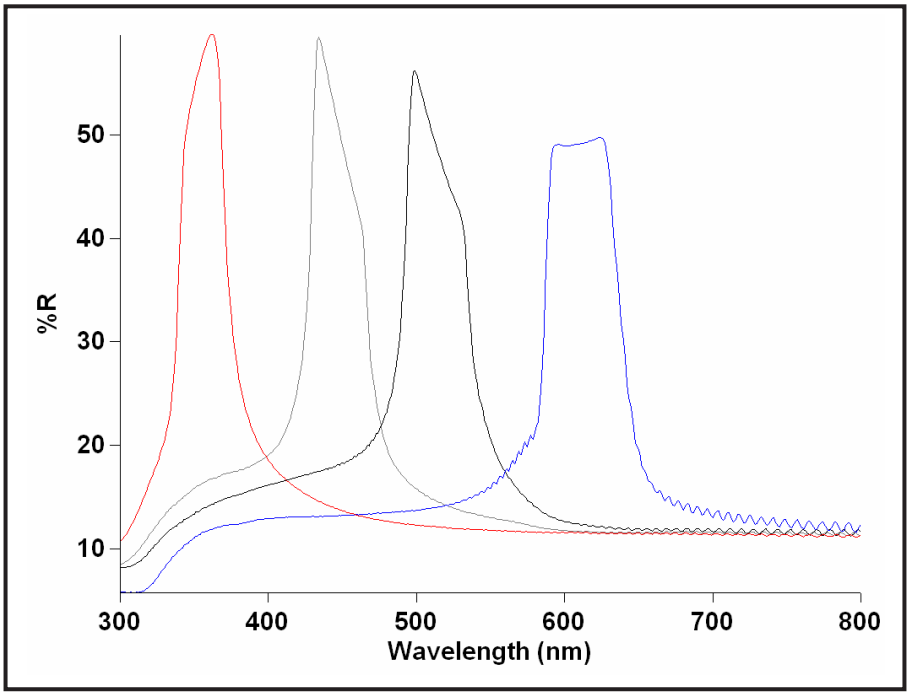

Figure 3. Reflectance of four films: 360-, 450-, 520-, and 610-nm

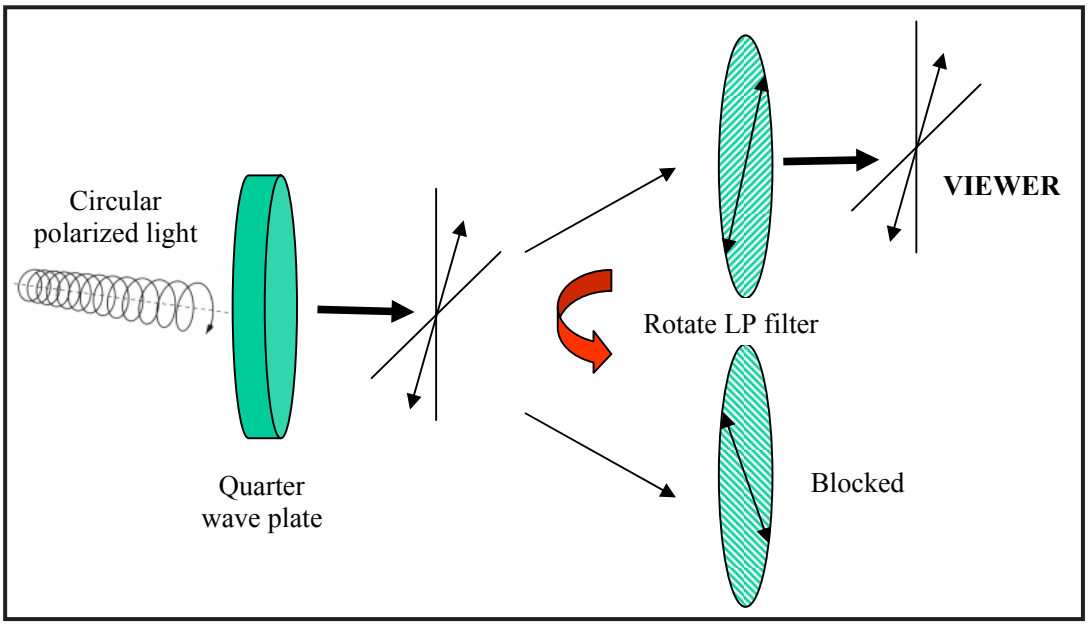

Figure 4. Schematic of viewing strategy using combination of quarter-wave plate and linear polarizer filter

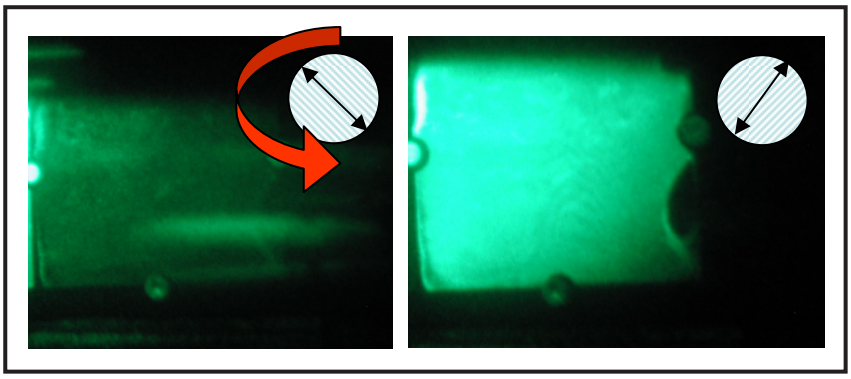

Figure 5. A 3 × 3 in. thin-film plate viewed through a rotating linear polarized filter, combined with quarter-wave plate for 360 nm. The image in the upper right-hand corner represents the relative orientation of the linear polarizer.

wavelength. This converts the transmitted light to linearly polarized light. A secondary LP filter can block or pass the resulting LP light by physical rotation (Figure 4). The unpolarized majority of light passes through the filter combination unchanged. The net effect as the LP filter is rotated is an unchanging scene with a blinking spot in the location of the CP filter. The behavior of a real CP target (Figure 5) is in this case the 360-nm thin film. The left-hand image is the thin-film target with the LP set to block the polarized light exiting the quarter-wave plate. In the right-hand image, the LP is set to pass the light. To have a blinking spot in a scene is quite helpful for passive targets in that the false positives from equally bright specular reflections can be separated optically and mentally.

The use of image processing was explored to further amplify the contrast from a CP target. In this test (Figure 6), a set of different materials was assembled along with a CP film at 360 nm. Materials consisted of metal, cardboard, marine gel coat, CP film, another 360-nm reflecting material, Teflon, and white-painted metal. A visible image of the scene was taken and converted to grayscale. Using the filter combination described above, two images of the scene were taken: one with the CP light blocked and the other with it passed, by rotating the LP filter. Using Research Systems' Environment for the Visualization of Images (ENVI) software package, the two images were registered, then the contrast between them was calculated using the following standard algorithm:

$$\frac{\text{Image } A - \text{Image } B}{\text{Image } A + \text{Image } B}. \quad \textbf{(1)}$$

In the resulting contrast image (Figure 6), any value above a set contrast calculation threshold was colored red. The threshold image was then overlaid with the first grayscale image for the final image.

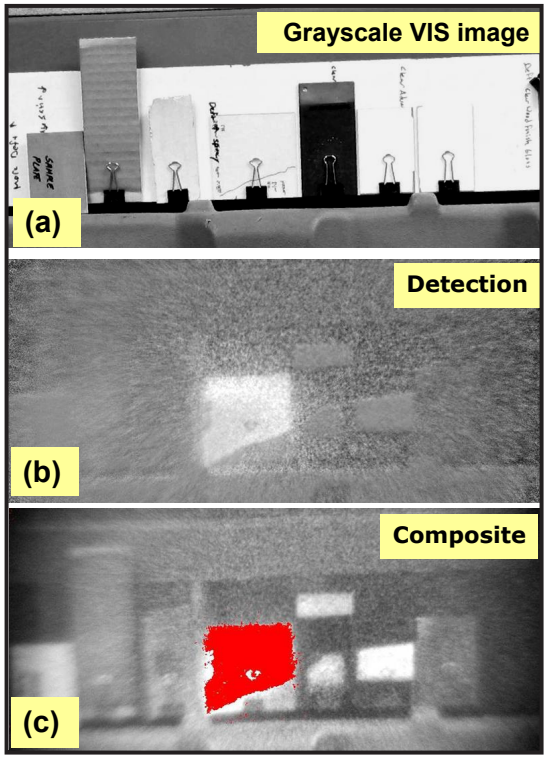

Figure 6. (a) grayscale visible image; (b) contrast image (A–B) / (A+B); (c) threshold image of contrast, overlaid with grayscale image

Conclusion

The potential of a new commercial material to generate a unique optical signature for OTT applications was demonstrated. In order to visualize the effect, a series of filters was used in conjunction with a broad-spectrum viewer that functions from the near-infrared to the ultraviolet. To increase the visual effect, the LP filter was either spun by hand or image processing was employed. Due to the positive results, the project was selected for further funding by another organization. Future work on this topic will focus on the use of electrooptical shuttering components and better methods to apply the material to a variety of surfaces.

References

Kattawar, G. W., "A Search for Circular Polarization in Nature," *Optics & Photonics News* (September 1994) 42–43.

Korenic, E. M., S. D. Jacobs, S. M. Faris, L. Li, "Color Gamut of Cholesteric Liquid Crystal Films and Flakes by Standard Colorimetry," *Color Research and Application* **23** (1998) 210–220.

Reinitzer, F., *"Beitrage zur Kenutniss des Cholesterins," Monatsch. Chem.* **9** (1888) 421.

this page intentionally left blank

Solid-State Ultraviolet Laser Diode

Curt Allen, Terry Davies, Frans Janson, Ronald L. Justin, E. Kirk Miller, Mark Morey[1]
Special Technologies Laboratory

Bechtel Nevada/STL, Sensor Electronic Technology (S-ET), and the University of California, Santa Barbara (UCSB), have collaborated to continue to improve new solid-state light sources in the deep-ultraviolet (UV) spectrum. The project's first year (FY 2004) yielded prototype devices emitting at 280 nm. In this second year, S-ET delivered super luminescent light-emitting diodes (SLLED) that generated light at 264 nm. The SLLED was incorporated into a high-speed housing and pigtailed to a fiber. The device was pulsed at 200 MHz using a high-current driver developed at STL, and its output was recorded with a Hamamatsu x-ray streak camera.

Background

For the last two years, STL has collaborated with UCSB and S-ET to develop a deep-UV, solid-state light source for calibrating an x-ray streak camera. Both the Stockpile Stewardship Program and the National Ignition Facility (NIF) have expressed a need for new calibration methods for such cameras, which led to STL's interest in this topic. The streak cameras record fast-moving events in time by detecting x-rays with a gold photocathode. Current calibrations are performed with an Nd:YAG laser that produces 5 W of light at 213 nm, but this laser is large, expensive, and cumbersome. Development of a small, solid-state, UV light source that could be pulsed at high frequencies would solve a major calibration issue.

The field of solid-state light sources, either laser diodes or light-emitting diodes (LED), is moving quite rapidly toward devices with higher output, greater efficiency, and shorter wavelengths. At the end of FY 2004, UCSB gave STL several prototypes that emitted light at 280 nm. These high-resistive (50-Ω) LEDs required custom electronics developed at STL to pulse them at high frequency. Using these new electronics, STL demonstrated that the LEDs could be pulsed to yield higher output power than in continuous wave (CW) operation. During FY 2005, the collaboration was continued via the funding of a postdoctoral researcher at UCSB. Additionally, we identified a new company, S-ET, which could produce custom LED devices emitting 264 nm.

[1] moreyms@nv.doe.gov, 805-681-2206

Project

The original goal was a laser diode that could be pulsed at GHz frequency with a wavelength output of <260 nm. While this seemed formidable, we benefited greatly from recent advancements UCSB has made on their Defense Advanced Research Projects Agency (DARPA)–funded laser diode research. A postdoctoral student worked half-time on developing a UV laser diode, while another UCSB researcher mounted newly fabricated LEDs on headers for testing. Later, we contracted S-ET to provide custom devices with components specifically made for high-frequency pulsing and emitting light at even shorter wavelengths. STL has further developed the custom electronics for diode modulation and accurate performance measurement.

Using AlGaN semiconductor materials with large band gaps usually generates deep-UV light. Light wavelength is determined by the amount of doped aluminum present, with higher levels leading to a larger band gap and shorter emission wavelengths. When an LED can be made to generate light with sufficient efficiency, it can be converted into a laser diode with a few modifications by polishing its edges to create a laser cavity. Because of the high power needed to excite the gold photocathode of an x-ray streak camera, this project sought to produce a laser diode. The limited selection of suitable semiconductor materials, difficulty in doping, prevalence of nonradiative de-excitation, and defects in layer growth lower their efficiency and provide ample room for progress in this quickly moving field. Improvements would require incremental advances in epitaxial growth of the semiconductor layers. Better control over layer crystallinity would decrease defects, improve p-n doping, increase efficiency, and enable the formation of a population inversion within the material, the main requirement for a laser diode. As we pursued more efficient devices, STL received for testing LEDs with output intensities approaching 1 mW.

Rise Time of S-ET LED Optical Output

The rise time of the S-ET 264-nm LED was measured with an S-20 streak camera. At 264 nm, S-20 photocathode sensitivity was marginal but sufficient to make a preliminary measurement. A block diagram of the system and rise time results appear in Figure 1.

A 250-V pulse with a 250-ns duration was used to drive the diode. The 400-μm-diameter output fiber from the S-ET diode and a 780-nm, 3-GHz comb output were simultaneously focused onto the S-20 photocathode. Because of optical limitations and the need to image onto a recessed photocathode, our fiber image was considerably larger than the 400-μm fiber diameter, and the rise time measurement was smeared. However, even with these limitations, the diodes did produce a rise time of >500 ps.

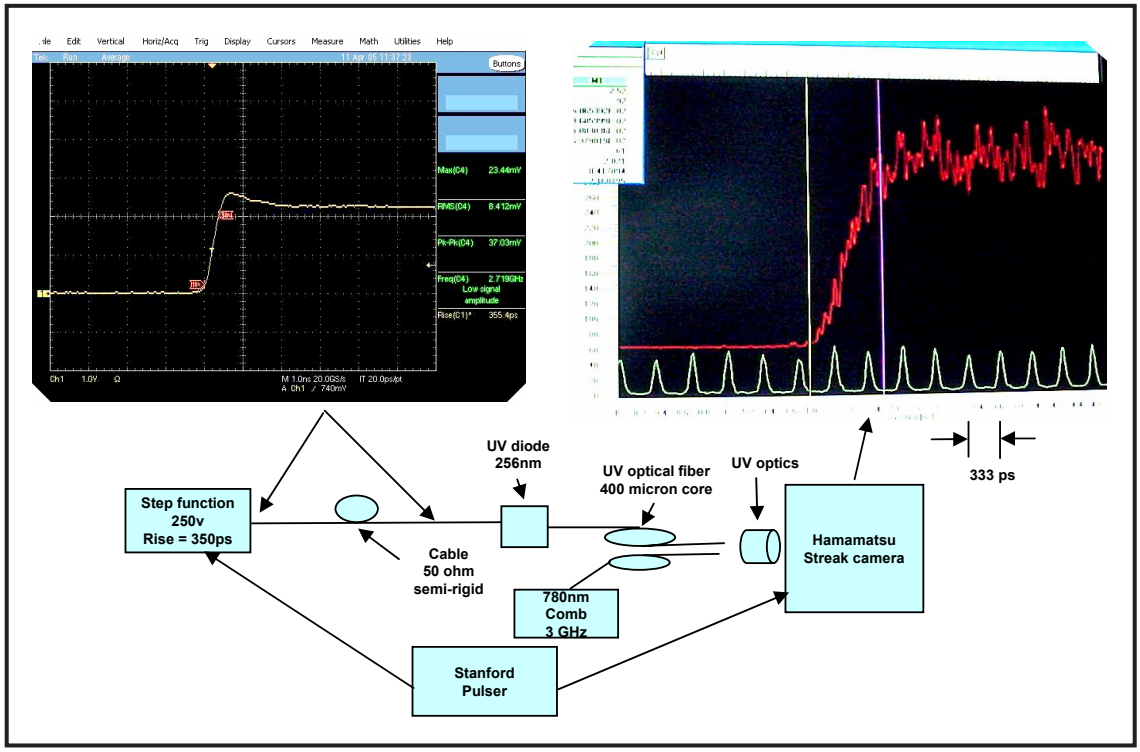

Figure 1. Rise time measurement for S-ET UV LED. Left trace is the input current drive; right trace is the streak camera record of the LED output with a 3-GHz comb calibration record on the bottom.

UV Comb Generation

The challenges of high-frequency diode modulation concern the high impedance of the AlGaN semiconductor materials. Diode impedance was measured at 50 Ω, which is quite difficult to drive at a high frequency and current. Using Bartlett's bisection theorem, which allows a resonant system to be viewed as having the same impedance from either direction, we designed and built a custom driver circuit.

This driver circuit is a simple, low-power, 200-MHz sinusoidal source mixed with a low-power, narrow-width TTL gate pulse (square wave). There is no UV output without the electronic gate pulse. The output burst duration is controlled by the gate width. Once mixed with the gate, sine amplitude increases, then is further amplified by a 50-W active amplifier that provides 45 dB of gain. This driver is AC-coupled to a passive LC tank amplifier circuit tuned to 200 MHz. This circuit not only further

amplifies the driver pulses, but also matches the dynamic impedance of the UV LED to that of the driver. This provides for maximum power transfer from source to load and is a strict necessity due to the large amount of input energy required to create milliwatts worth of UV optical output.

Figure 2 shows the drive circuit current (upper trace) for the S-ET diode and the corresponding UV optical output (lower trace), as measured by a UV-enhanced Si diode photodetector with amplification. The peak drive currents are <600 mA, sufficient to saturate the diode if drive duration exceeds 1 μs, which is long enough for almost all comb requirements.

Measurement of the optical UV output was enabled by coupling a New Focus UV enhanced silicon photodiode with four stages of fast amplification, designed at STL for the Fast VISAR receiver system. This system's frequency response broadens the pulse spikes somewhat but has still proven useful.

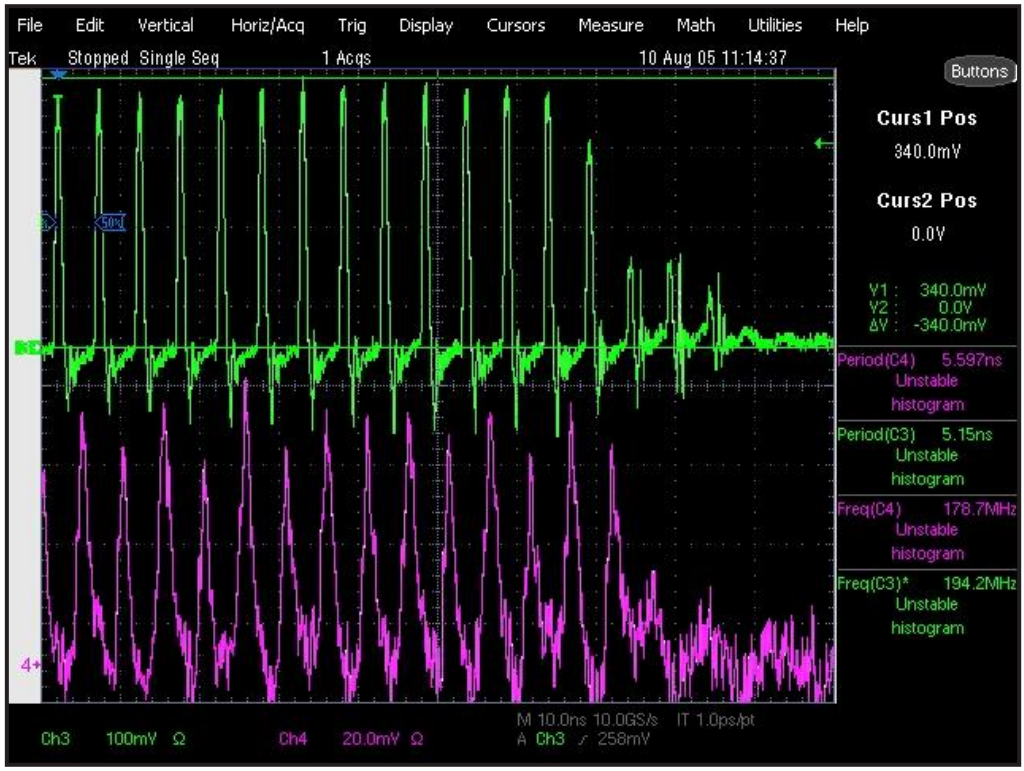

Figure 2. S-ET diode drive current (upper trace) and corresponding UV optical output (lower trace), frequency 200 MHz

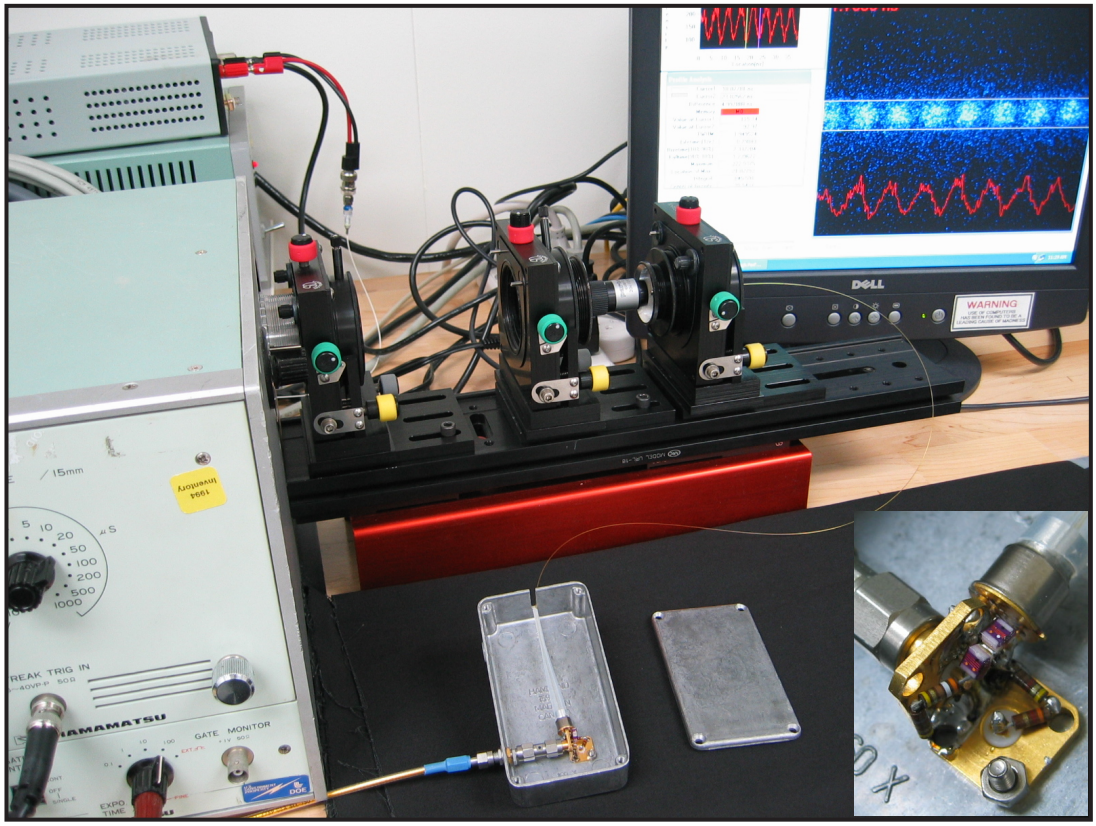

Figure 3. Streak camera recording of UV comb generation

Streak Camera UV Comb Calibration

The streak camera recording of the UV comb output may be seen on the monitor screen at right in Figure 3. The tank circuit and the fiber-pigtailed LED occupy a 1 cm^3 space in the gray box in the lower center. An expanded view of the circuit appears at right.

X-ray Detector Sensitivity to 264-nm Light

The true test of the S-ET LED's utility as a UV source for an x-ray streak camera comb generator is whether or not it produces enough power to be recordable on an x-ray photocathode. Perry Bell, of Lawrence Livermore National Laboratory (LLNL), brought equipment to STL to make that determination. His experiment and results appear in Figure 4. An x-ray microchannel plate (XMCP) was placed in a vacuum chamber associated with a Manson x-ray generator (see hardware in Figure 4). The Manson source verified proper operation of the XMCP. The 400-µm output fiber from the S-ET diode was inserted through a vacuum-tight connection into the Manson chamber (Figure 4)

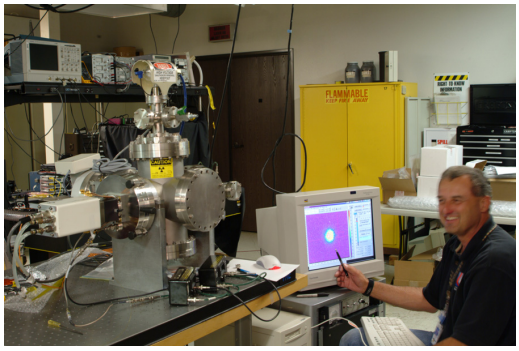

4(a)

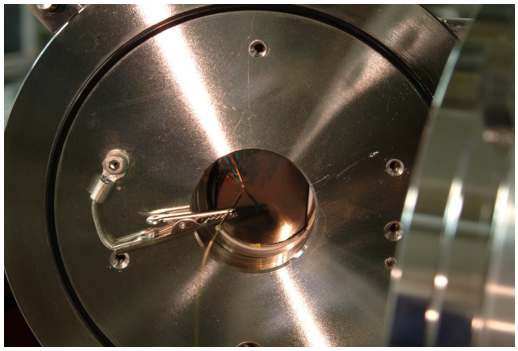

4(b)

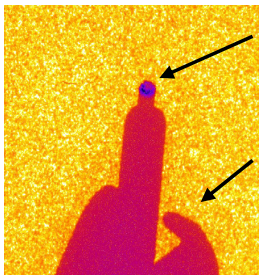

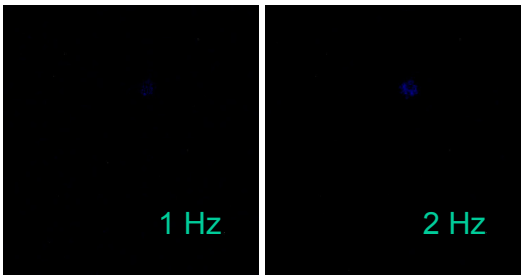

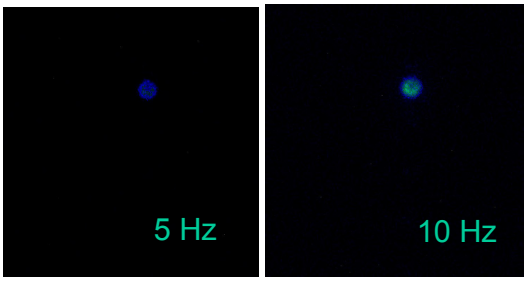

4(c)

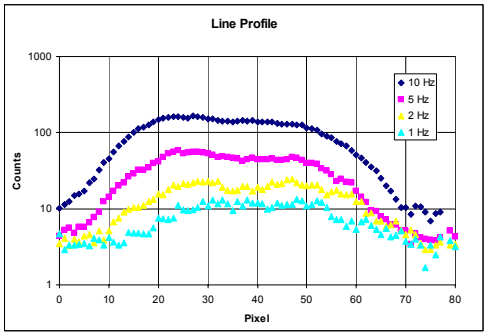

4(d)

Figure 4. (a) Laboratory setup for x-ray measurements; (b) vacuum feed-through for S-ET LED; (c) 10 sec exposures of LED on XMCP; (d) profiles through the LED beam spots from (c)

and positioned adjacent to the face of the XMCP. Pulses of variable frequency at 450 mA and 850-ns duration drove the LED for 10-sec periods. The peak UV pulse power from the diode was 0.25 mW. UV diode output images and line-out profiles appear in Figure 4. While it was encouraging to be able to detect diode output on the x-ray cathode, it was disappointing that the pulses were so long in duration. To be useful as a comb calibration source, a single UV LED pulse of 1-ns duration should be detectable by an x-ray streak camera. Clearly, higher peak power, better optical coupling, lower fiber losses, and possibly higher cathode sensitivity are needed.

Improvements that have been or can readily be made include:

- Higher power diodes: S-ET has already provided two new diodes that provide triple the output power of the 0.25-mW diode used for the above measurements
- Reduced spot size on the XMCP cathode to increase power per unit area
- Decreased length of diode fiber pigtail to reduce optical losses
- LED cooling: a 70°F cooling increased optical output by 30%.

Conclusion

Through collaborations with UCSB and S-ET, STL generated the first deep-UV calibration "comb" using a solid-state light source. A fiber-pigtailed LED at 264 nm was pulsed at up to 200 MHz. It was observed using a gold photocathode on an x-ray photodiode. LED rise time was shorter than 500 ps. Improving the optical coupling between the LED and streak camera should yield better rise times. Steady advances in AlGaN-based semiconductor devices should soon lead to the development of a deep-UV laser diode. The present S-ET UV diode technology may be adequate as a comb source for x-ray streak camera calibration.

Reference

Davies, T., M. Morey, "Solid-State Ultraviolet Laser Diode," *Nevada Test Site–Directed Research, Development, and Demonstration*, FY 2004, Bechtel Nevada, Las Vegas, Nevada, 2005, 295–298.

this page intentionally left blank

Anode Metallization

Donald Ng[1]
Livermore Operations

This project sought to investigate a replacement for the current lacquer flotation process in the manufacturing of phosphor-coated anode optics at LO. Several potential techniques were attempted, including the use of indium tin oxide (ITO), application of an alcohol-based solution of nitrocellulose, and deposition of the polymer parylene C. These techniques showed varying degrees of success, with the most promising being the nitrocellulose spin-on solution. However, none yielded the level of phosphor brightness produced by the current lacquer process.

Background

At LO, processing phosphor-coated anode optics used in phototubes involves applying lacquer on top of the phosphor to act as a sacrificial protective layer during aluminum metallization. In this process (Figure 1), the fiber-optic anode is submersed in a tank of water. A thin layer of lacquer is then applied on top of the water, which lowers onto the phosphor surface as the water is drained. The throughput for this process is low, requiring many attempts to produce a lacquer layer free of pinholes, bubbles, and tears. Any pinhole or tear in the lacquer layer will allow aluminum to embed into the phosphor during metallization and cause a dark spot in the finished phosphor screen.

To improve the throughput and reliability of phosphor anode optics, our team attempted to replace the standard lacquer drop method with a more reliable and easily applied technique. Among the experimental methods considered were spinning-on a layer of nitrocellulose dissolved in alcohol, depositing a layer of ITO on top of the lacquer, and depositing a layer of a conformal polymer coating, parylene C. Both the nitrocellulose and parylene C methods would still require baking after metallization to volatize the sacrificial protective layer in the same manner as the lacquer currently used. The ITO application would be permanent, eliminating the baking step after metallization.

Project

We prepared a solution by dissolving 1.145 gr of DLX 5/8 nitrocellulose obtained from Nobel Enterprises (UK) in 30 ml of ethanol and 34 ml of isopropyl alcohol. After 48 hours, the solution contained undissolved nitrocellulose. After heat was applied, the solid nitrocellulose remained. Four 1-ml volumes of clear liquid were pipetted out of the container and dropped onto a phosphor-coated, 75-mm anode optic spinning at 750 revolutions per minute (rpm). The coating was visibly thin, but aluminum

[1]ngdp@nv.doe.gov, 925-960-2500

deposition was performed with a 1000-A Al layer evaporated onto the nitrocellulose. The optic was baked-out in an air oven at 375°C to volatize the nitrocellulose. Another deposition of 500 A of Al followed. Testing with an electron beam at 10 kV and 20 μA produced 60 ft-L from the phosphor screen, compared to the typical 320 ft-L observed with the lacquer process.

Nitrocellulose solutions using new reagent-grade alcohol produced a clearer solution but poorer light output. We dissolved 4.048 gr nitrocellulose in a mixture of 50 ml isopropyl alcohol and 100 ml ethanol, which yielded a clear solution with no residual solids. A 2-ml aliquot of solution was spun onto a 75-mm optic, spun at 1000 rpm, and processed in the same manner as earlier optics. Testing with an electron beam at 10 kV produced 142 ft-L output from the phosphor. This represented a significant improvement over the first solution but fell far short of the 320 ft-L seen with the lacquer process.

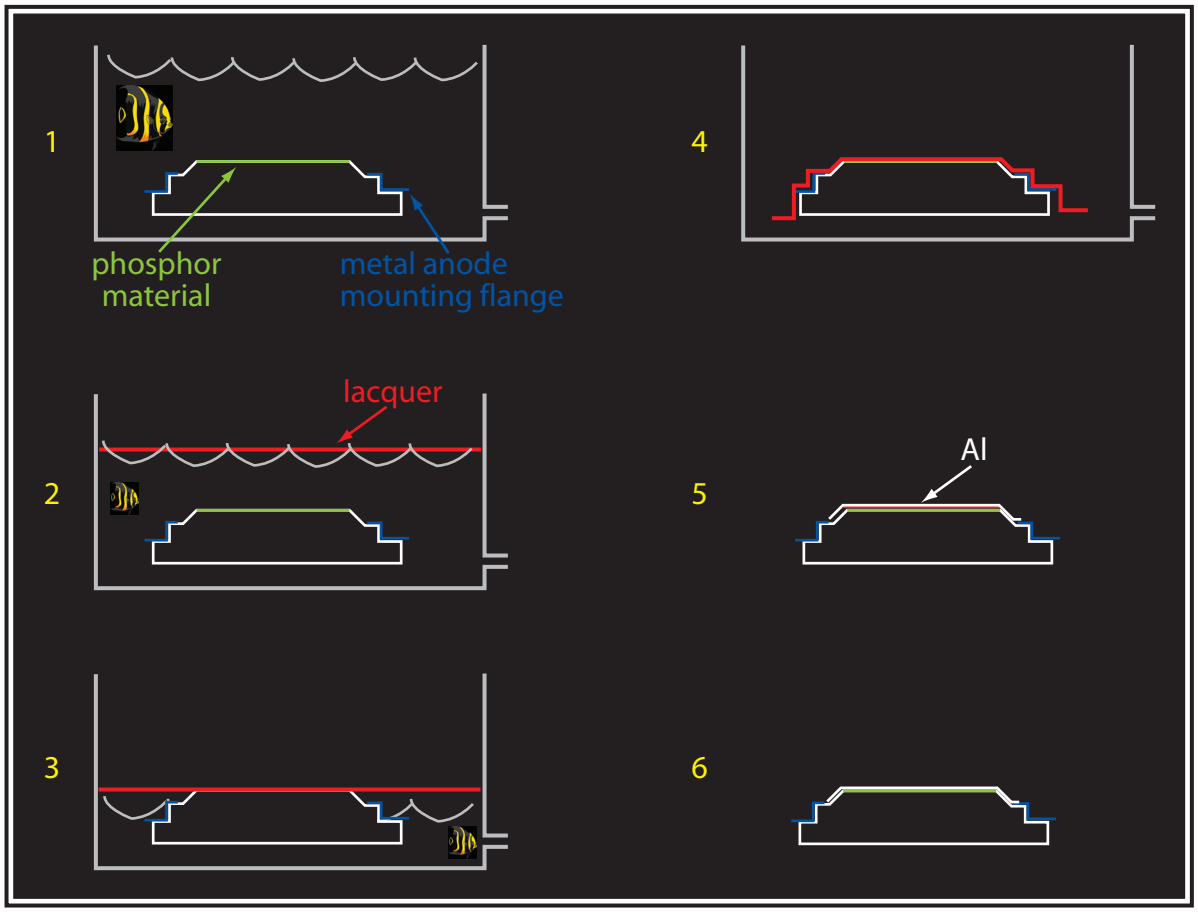

Figure 1. Flotation lacquer deposition steps (current approach)

Obtaining uniform coverage with the thin, alcohol-based nitrocellulose solutions was difficult because of the roughness of the phosphor surface and delivery from a pipette, a gravity-induced drop. Attempting to make solution delivery more uniform and repeatable, we purchased a solution dispenser (Figure 2). However, since it was designed to dispense high-viscosity photoresist onto semiconductor wafers, the dispenser proved to be too powerful for the relatively low-viscosity, nitrocellulose solutions. Thus, the issue of uniformity and thickness of the deposited nitrocellulose layer still must be addressed.

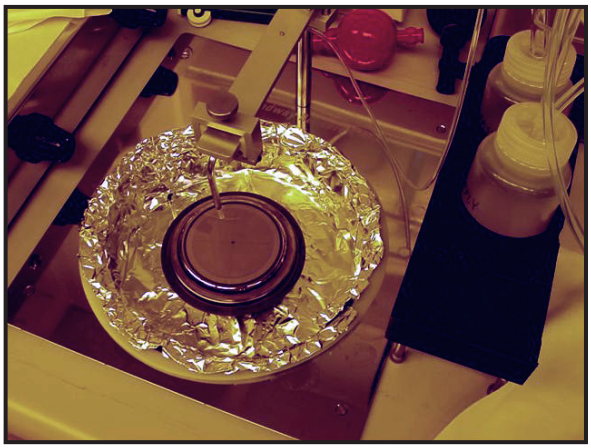

Figure 2. 75-mm anode optic under fluid dispenser

A phosphor-coated fiber optic was sent to Deposition Research Laboratory, Inc., for coating with a 40-nm ITO layer. A 1500-A Al layer was evaporated on top of the ITO for metallization, and the screen was tested in an electron beam at 10 kV. The light produced was only 43 ft-L, and we suspected that the ITO layer was too thin to be continuous. The fiber optic was cleaned and recoated with phosphor, then coated with 150 nm of ITO. After depositing 1500 A of Al, the phosphor screen produced 59 ft-L under an electron beam at 10 kV. Because of the low brightness, the ITO coating approach seemed less promising than at the project's inception. The ITO layer must be kept thin to minimize the dead voltage of the phosphor screen, but such thin layers do not sufficiently cover and protect the phosphor during the aluminum evaporation step.

A phosphor-coated, 75-mm optic was sent to Paratronix, Inc., for coating with parylene C. Parylene is a polymer that can be coated onto an object by vapor deposition. The polymerization occurs during the coating process and yields a conformal film. Because of its electrical insulation and chemical inertness, it is typically used to coat electronic components. A 720-nm-thick parylene coating was deposited onto the phosphor. 1000 A of Al was then deposited onto the parylene, and the phosphor was baked in air at 375°C for 12 hours, then baked in vacuum at 375°C for 6 hours. A 500-A layer of Al was deposited to finish the metallization. Testing under an electron beam at 10 kV produced an

output of 168 ft-L. Because of the difficulty of finding a vendor willing to vacuum-bake a parylene-coated object, which outgases in vacuum, only one trial was completed. It is unknown if either a thicker or thinner parylene layer would improve the phosphor's light output.

A summary of methods is presented in Table 1.

Table 1. Comparison of anode metallization methods

Method	Advantage/Disadvantage	Light Output (ft-L)
Current process	Has been used for 30 years, refined and developed; labor-intensive; low throughput.	320
Nitrocellulose solution	Fast deposition, no vacuum bake; uniformity, protection during Al deposition.	142
ITO	Durable, no baking required; vendor-deposited, protection during Al deposition.	59
Parylene C	Durable vendor-deposited, vacuum bake.	168

Conclusion

The thickness of a nitrocellulose layer is instrumental to the brightness of the final phosphor screen. The current solution and delivery method produces a layer of nitrocellulose too thin to provide the same amount of protection to the underlying phosphor as the lacquer method, increasing the chance of Al entering the phosphor during metallization and reducing light output of the screen. However, the nitrocellulose solution method is much easier and less time-consuming to apply than the lacquer method. Using either ITO or parylene might prove a great disadvantage because of the need to rely on vendor quality control and repeatability. However, the one parylene trial did yield higher light output than the ITO or nitrocellulose methods. Thus, if it were possible to do coating and vacuum-baking in the LO facility, parylene would be a good candidate for further investigation and development. Otherwise, alcohol-based nitrocellulose solutions spun onto the phosphor-coated optics is the most promising of these candidates to replace the current lacquer process.

Development of a Multichannel Velocity Interferometer Optical Probe

Vincent T. Romero[1]
Los Alamos Operations

This project intended to design, build, and characterize a spherical dome comprising 100 velocity interferometer probes. Design goals were to make the dome <1" diameter, while also conceiving techniques for its assembly. In addition, our team planned to develop and define spatial characterization measurements. We created several prototype domes that will support more than 100 optical probes. For spatial characterization measurements, we attempted conventional metrology characterization techniques, but these were found to have limited resolution. In addition, highly accurate (<0.0001") optical measurement techniques were considered.

Background

For many decades, the LANL Hydrodynamic Division has used a spherical dome (pin dome) consisting of hundreds of stiff wires to measure the surface arrival time within a dynamic, implosion-driven configuration. An "electrical impulse" is produced when this imploding surface physically contacts the pins. Analyses of pin data produce valuable information on dynamic symmetry and performance characterization of implosion-driven systems.

Developments in laser-based velocimetry technology, such as VISAR (velocity interferometer system for any reflector), PDV (photon Doppler velocimetry), and Fabry-Perot, have demonstrated that these techniques can produce "continuous" records of surface motion, from surface jump-off to probe impact within a convergent configuration. Velocimetry techniques not only produce thousands of times more data per channel than historical pin methods, they also yield dynamic data that pins cannot. Velocimeters have produced measurements of surface pullback, surface reshock, spallation, and ejecta. In addition, velocimetry techniques do not physically contact the surface being measured, are very accurate (1% error), and support highly accurate (<0.0001") static proximity location measurement.

Developing optical domes comprised of a large number (>100) of velocimetry channels would advance hydrodynamic diagnostic technology. It would generate high-fidelity data that would set a new baseline and higher standards for dynamic measurements of implosion driven devices for future decades.

[1] romerovt@nv.doe.gov, 505-663-2038

Project

In FY 2004, SDRD research focused on developing an optical dome using VISAR-type probes. Because of their size (0.200"), a limited number of large-depth-of-field VISAR probes could be packed into a 1" dome. Recent advancements in PDV probe development have produced a very small (0.025") probe with an almost unlimited depth of field. This project focused on developing an optical dome comprised of PDV-type probes.

We selected LightPath T1527Y PDV probes, which required no modification. Consisting of an aspheric lens fused to a single-mode optical fiber, these off-the-shelf probes are designed for telecommunication applications. For more than 200 mm, they produce a well-collimated beam, with a spot size of approximately 200 μm.

We tried several mechanical designs for domes that could hold 100 probes. The first were one-piece domes 0.875" in diameter. Using rapid-prototyping machining techniques, we produced prototype probes. These plastic models were adequate for developing assembly methods, as well as sufficient for producing metrology and proximity characterization setups with a small number of optical fibers. However, this prototype was not successful for a final design because, after approximately 30 probes were inserted, the dome core became too congested with optical fibers, making it too difficult to pull through additional fibers. Figure 1 shows one of these earlier models.

A second design, based on the same techniques used to construct hydrodynamic pin domes, was developed. This concept divides the dome into two, with each half populated with probes, then joined together. This technique proved to be successful, and prototype units were constructed and assembled without breaking the optical fibers. Several high-fidelity units were machined out of aluminum. Figure 2 shows this split-dome design.

Supporting activities associated with this project involved developing measuring techniques for determining the probes' azimuthal rays. To define a ray, our team measured two points in space relative to a given center point. We conceived a design using a conventional metrology coordinate machine (Brown and Sharp) and a set of calibration shells. This technique measured each probe at two radii to determine beam angle with respect to center. During a mock-up, several problems arose. Illuminating the single-mode fibers using a visible diode (632 nm) produced a multimode spot that made it difficult to determine an exact center point. In addition, even with magnifying glasses, visual alignment lacked the resolution necessary for an accurate measurement. Centering the dome to the coordinate machine was straightforward and not problematic. Based on the lessons learned during mock-ups, we did not build calibration shells. Figure 3 shows the dome-calibration shells concept.

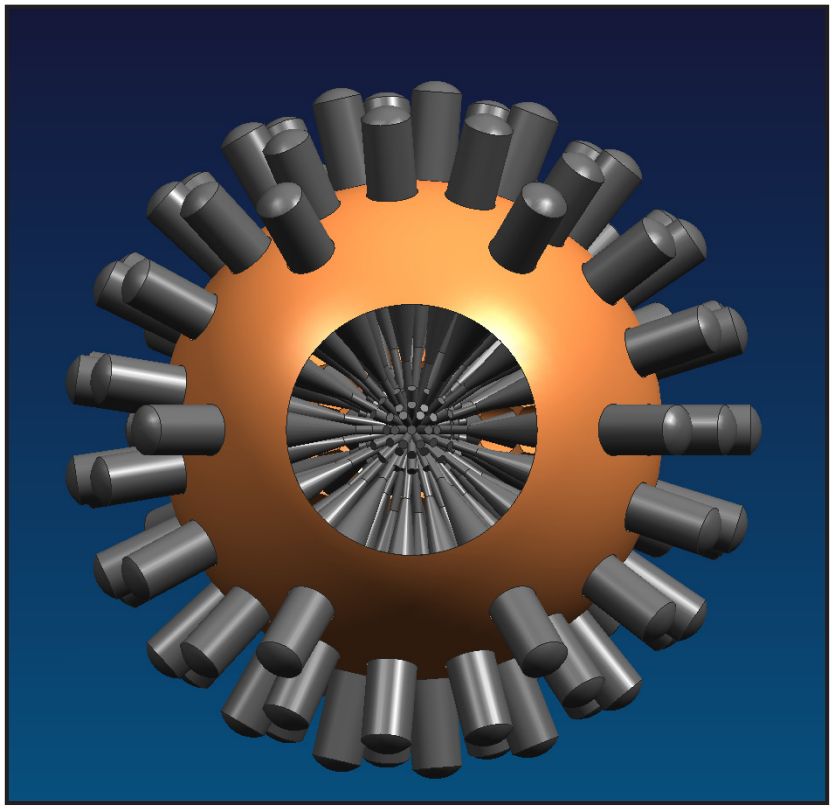

Figure 1. Early prototype

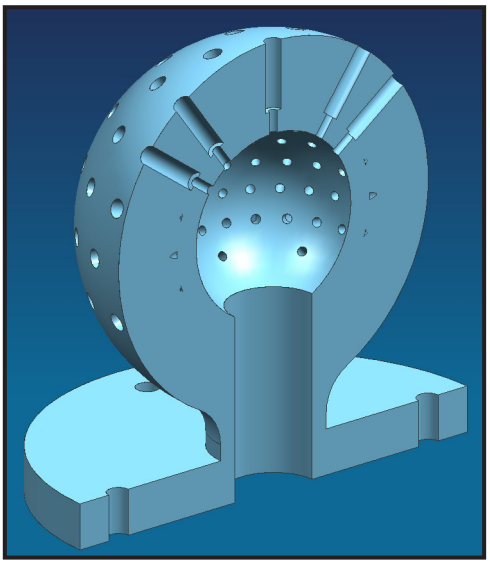

Figure 2. In the split-dome model, the two halves could be joined without breaking fibers during fabrication

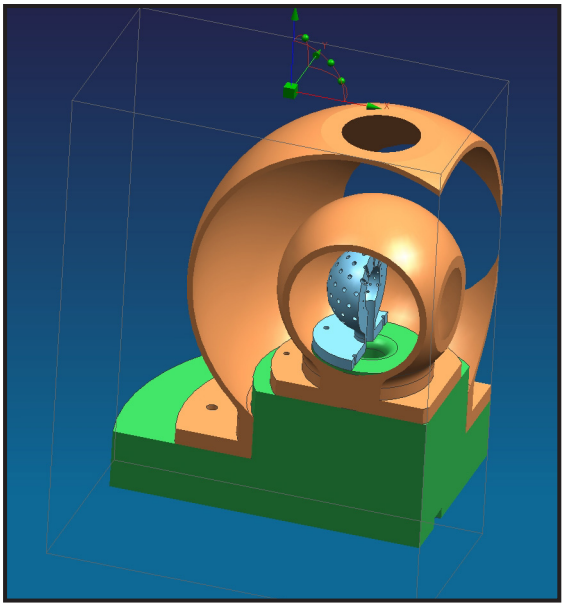

Figure 3. Dome-calibration shells concept

The team worked on developing new methods for accurately measuring the azimuthal rays that could eventually replace the coordinate machine's pointer with an infrared quadrant detector. Illuminating the probes at their designed wavelength (1500 nm) would produce a very small (<200-μm) spot size. Centering a 200-μm spot on a quadrant detector would be very accurate (±5 μm). We also tried to borrow the coordinate measuring machine developed for the LANL DX-3 hydrodynamic pin dome group with no luck, and the further development of the measurement technique was suspended.

A related supporting activity was further development of the spatial proximity measurement. The PDV probes proved to work very well with the high-resolution optical time-domain reflectometer (OTDR) (HP-8504B). Software was written both to interface with the OTDR and to automate measurement. We realized a fundamental challenge in making this precise (±1-μm) measurement that feeds back to the optical dome assembly. In assembling the optical probes into the dome, we would have to locate the probe face radii very precisely (±1 μm) or be able to exactly measure them after dome assembly. This level of precision has not been developed; it would require tools, techniques, and skills yet to be conceived. However, we do have some ideas for using powerful image-shearing microscopes or laser-based interferometers to achieve this precision. This measurement could also be reconciled by characterizing the proximity probes in a calibration setup, accurate and stable to this level of precision. Basically, the precision of proximity measurement will be limited to the metrological known position of the probes. This applies to the case of an absolute measurement using a small number (5) of probes. When using many probes, this measurement could benefit relative position versus absolute measurement.

A sample of the OTDR software appears in Figure 4.

Currently, the high-resolution proximity measurement yields a very accurate relative measurement. In this case, reference measurements are performed during initial assembly, and subsequent measurements are made to determine if the device has changed position from the final assembly steps or from being transported and relocated to experimental emplacement.

Conclusion

Our team successfully designed and fabricated an optical dome that will support a large number of PDV probes in a small area and investigated techniques for accurately measuring the position of these kinds of domes in experimental geometries

More research and development must be done in the area of probes. We selected the LightPath collimator because we were familiar with it. Many other single-mode collimators available in the telecommunications market are smaller than the LightPath and might work better. A thorough evaluation of available collimating probes would benefit not only dome designs, but also velocimetry efforts in general.

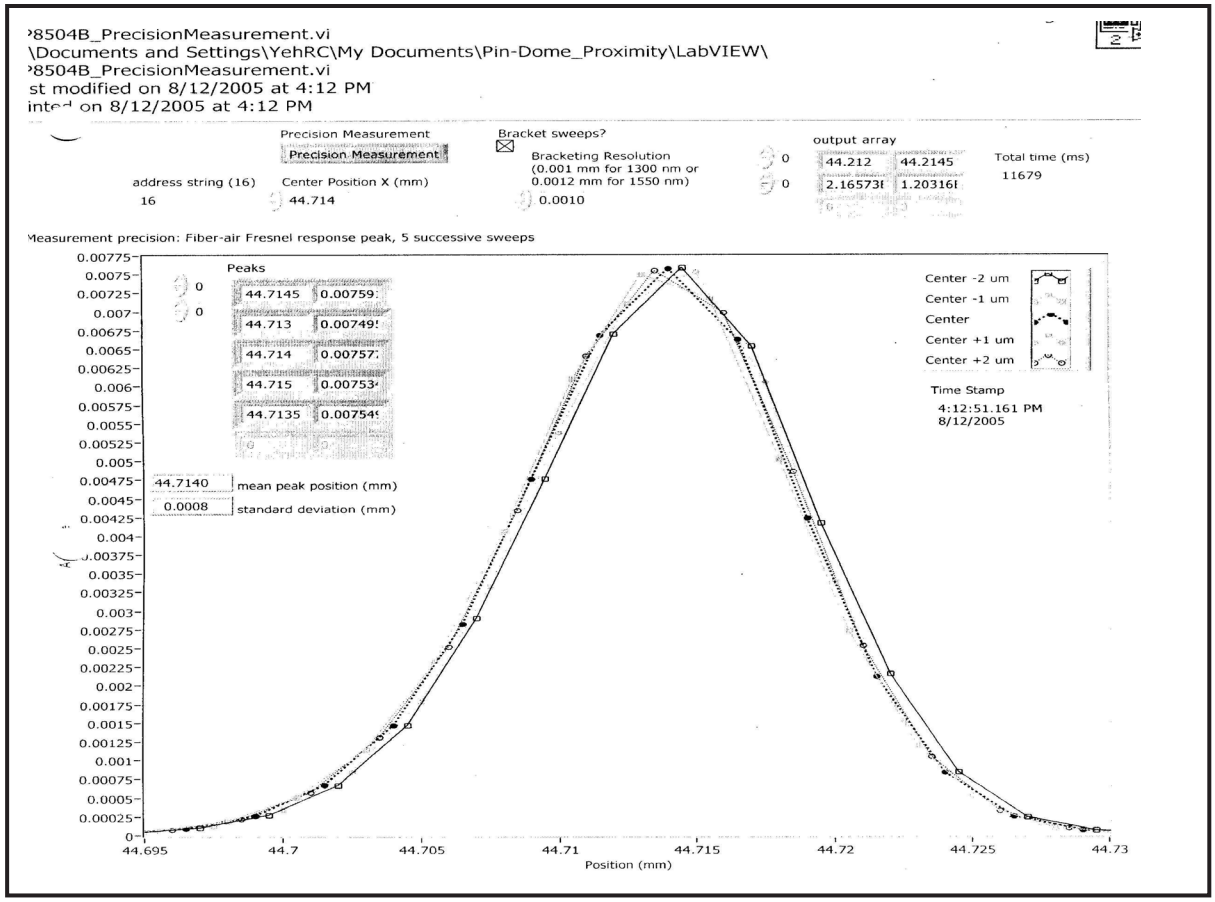

Figure 4. Results produced by the OTDR software (note the 0.8-µm deviation)

The applications of state-of-the-art microoptics technologies, developed for telecommunications such as microprisms, pitched lens, angled fiber fusion, and integrated optic circuits, could yield improved dome designs and better performance.

This optical dome research project represents just one step in developing, defining, and understanding the integration of optical technologies into a hydrodynamic configuration. It has identified a comprehensive range of resources and capabilities not currently in existence, which must be developed. Future research and collaboration of the following disciplines and technologies, along with dynamic experimentation with current and future velocimetry systems, will help produce a high-fidelity optical dome of the future.

1) Optical design and state-of-the-art microoptics technology. Develop, design, test, improve, characterize, and miniaturize optical probes.
2) Optomechanical design, micromachining, and microassembly capabilities. Assemble macroscopic optical components into diagnostic packages with high precision.
3) Precision metrology and precision optical characterization capabilities, which are critical to improving data accuracy.

Efforts are being made to develop, miniaturize, and reduce the cost of velocimetry systems. As these efforts develop, a parallel effort should be put forth into velocimetry probe development, characterization, and packaging. The performance of state-of-the-art velocity interferometer systems and the fidelity and accuracy of the data collected are directly related to optical probe quality.

Smaller optical dome versions with fewer channels could start being applied to hydrodynamic experiments. Integrating a few optical probes would enable proximity measurements—if not in the absolute measurement mode, at least in the relative measurement mode—and also could collect velocimetry data in the dynamic experiment. Hybrids of current wire pin domes and optical probes will need to be developed to link the technologies together and establish a database. An interesting configuration of optical probes would be a line covering 180° spaced in 10° increments integrated with many pins.

Optical domes could also support hybrid configurations with other types of optical diagnostics, such as visible and infrared imaging, pyrometry, holography, and surface reflectivity.

Two-Dimensional, Long-Data-Length Transient Recorder (Phase II)

Matthew LaFrancesca, Richard A. Shellman, Ke-Xun Sun,[1] John Yuhas
Livermore Operations

Our team has continued to research the conceptual framework designed in FY 2004. We have successfully developed an x-y scanning electronics system capable of delivering high-voltage, high-frequency output to deflect the electron beam. After designing and building a development platform, we designed and constructed a prototype, two-dimensional (2-D) transient recorder. During our proof-of-principle experiment, we demonstrated a 2-D camera scan using the optical framing tube. Software for raster scan imaging processing was developed.

Background

Many streak camera measurements provide temporal recording in only one or a few spatial channels, leaving unused areas on the imaging plane. For single-sweep streak cameras, high temporal resolution and long data recording length requirements are often difficult to meet simultaneously. A streak camera's typical data recording length in the temporal dimension is 2000 or 4000 pixels. Because of this short recording length, an experiment may require several cameras with different temporal resolutions and data lengths. Eliminating triggering jitter between cameras can be time-consuming, and data analysis becomes more complicated and less reliable.

Our proposed research intended to resolve these issues by designing a new camera with both high temporal resolution and long data length. The streak camera is intrinsically a 2-D recording device. Redundant spatial-dimension recording can be converted into useful temporal data tracks in a 2-D scanning camera. Our intent was to substantially improve performance over data lengths tens or even hundreds of times longer. This transient recorder would enable new measurements, such as multiple fast consecutive shots with varying time scale. For example, in the National Ignition Facility (NIF) Fast Ignitor experiment, short pulses arrive in several separated shots, at a time scale that is sparse compared with each pulse width. The long-data-length recorder with high resolution will also be a useful tool for multiple beam-timing diagnostics, to reduce the number of wasted shots caused by timing jitter.

[1] sunke@nv.doe.gov, 925-960-2514

Project

Principle of the 2-D Scanning, Long-Data-Length Transient Recorder

In FY 2004, our team designed and built an optical framing tube. We completed system design for x-y scanning electronics, generating high-voltage oscillatory output at radio frequencies (RF), and ordered key components. This year, we successfully designed and built the electronics and camera system, developed software, and conducted the first 2-D scanning experiment using the camera system.

A 2-D scanning tube has two pairs of deflection plates in orthogonal directions, to steer the electron beam in dimensions x and y. Figure 1 illustrates the concept of a 2-D, long-data-length recorder and the required electronics-scanning waveforms. Figure 1(a) depicts the sequential data tracks on the charge-coupled device (CCD) camera behind a 2-D tube. These data tracks can be obtained by applying the voltage waveforms shown in Figures 1(b) and 1(c).

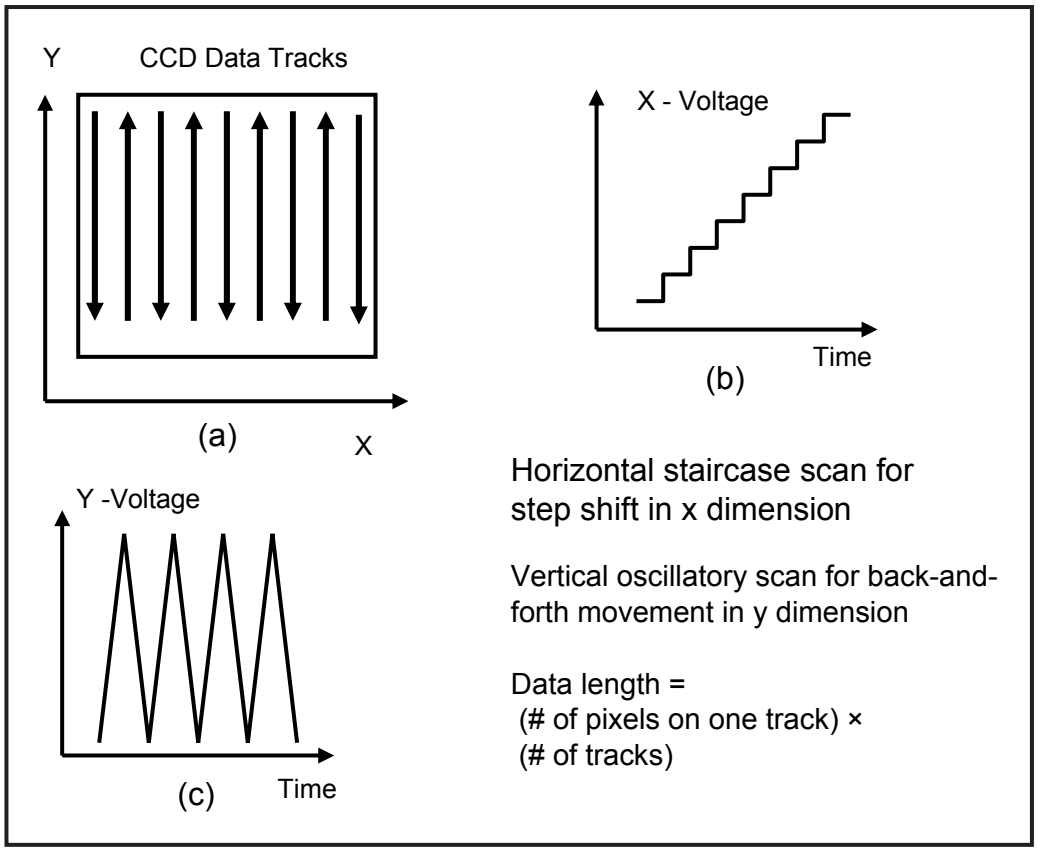

Figure 1. 2-D scanning, long-data-length transient recorder concept

The oscillatory triangle waveform voltage in Figure 1(c) is applied to the y-direction deflection plates to scan the electron beam back and forth in the y dimension. The staircase voltage waveform is applied to x-direction deflection plates to incrementally step-shift the electron beam in the x dimension. The combined electron beam movement covers the full screen via raster scan, creating sequential data stacks along the "original" spatial channel lines (Figure 1(a)). The data length is thus increased by a factor of tens or even hundreds, equivalent to the number of spatial channels.

Electronics System for Oscillatory, High-Voltage-Deflection Outputs at Radio Frequency

The main challenge in producing the 2-D camera was the development of the high-voltage RF driver for oscillatory deflection. In a practical system, the triangle waveform can be implemented by sinusoidal wave, and the nonlinearity can be corrected in image processing. We developed a pair of high-voltage drivers capable of delivering ±600 V, or a total oscillatory voltage of 1200 V at 13.56 MHz.

To accelerate the developmental process, we researched commercial vendors and purchased a high-voltage RF board as the basic unit. The original board was designed to have an effective load of approximately ~5–7 Ω and consumed 1 kW of power at high-voltage output. After conducting extensive customization and optimization, we added a pair of RF transformers, thus raising output impedance from 5 to 50 Ω and increasing cable length from minimal to practical. Power consumption at ~450 V was reduced to 40 W. These achievements allowed design and construction of the practical camera system.

For the staircase generator driving the deflection plates in the x direction, our design employed all-digital circuit configuration. The circuit uses the same crystal oscillator at 13.56 MHz as the clock

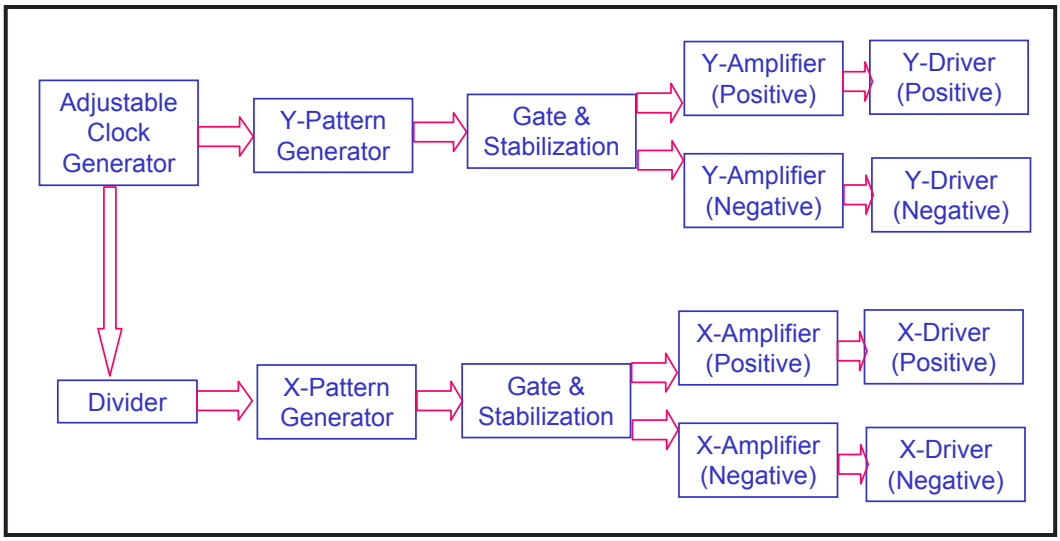

Figure 2. Electronics circuit

pulses and accumulatively increases the output voltages for each cycle. At the end of the preset counts, the circuit latches at the state of the last clock pulse. This design has several advantages: 1) It automatically synchronizes with the y driver, even at a fraction level, so that a step increase occurs for every oscillation period. Thus, no streaks overlap. 2) The circuit allows the number of streaks in the raster scan to be easily adjusted. For the initial design, the number of streaks in one staircase ranged from 1 to 256, large enough to handle many situations. 3) It enables the possibility of nonlinearity correction using both the hardware and software methods. The staircase output is fed to a commercial high-voltage video amplifier, where the staircase signal amplitude is enhanced to ~100 V. The video amplifier bandwidth is ~7 MHz.

Electronics Test

Figure 3(a) shows a typical waveform of high-voltage output at 13.56 MHz, with an amplitude of ~600 V. Figure 3(b) shows the inputs and outputs with opposite phases from the two amplifier channels. The antiphased outputs can be used to drive the pair of deflection plates and achieve 100% higher deflection sensitivity.

Figure 4 shows the construction of the electronics modules and connections into the enclosure. The enclosure is RF-shielded for better operability in a strong electromagnetic pulse (EMP) environment. Below the electronics enclosure is the tube chassis, which shields the tube from RF EMP generated from the RF boards.

Figure 5 shows single-shot staircase output at ~100 V. The voltage latches at the level when the circuit stops counting the clock pulse. In this particular waveform, approximately 200 clock pulses were counted. For clarity, the other staircase polarity is not shown.

System Development Platform

We have developed a system development platform for the 2-D camera in a short time. The platform provides chassis for the optical framing tube and shields high voltages. In addition to the original enclosure designed at LAO, five more enclosures were designed and built to accommodate the electronics boards. The entire camera assembly was placed on an optics table and mounted on a height-adjustable cart. Additional power supplies and the video amplifier were also attached to the cart. The platform and experimental setup in the Advanced Sensor Testing Lab appears in Figure 6. The platform has ensured the safety and enhanced efficiency in our experimental work. The optics table will be useful for continued development of the 2-D camera.

Software Development

A set of software programs has been developed for image processing and data extraction from the 2-D camera raster-scan recording. Since temporal information is of main interest, both the peak-

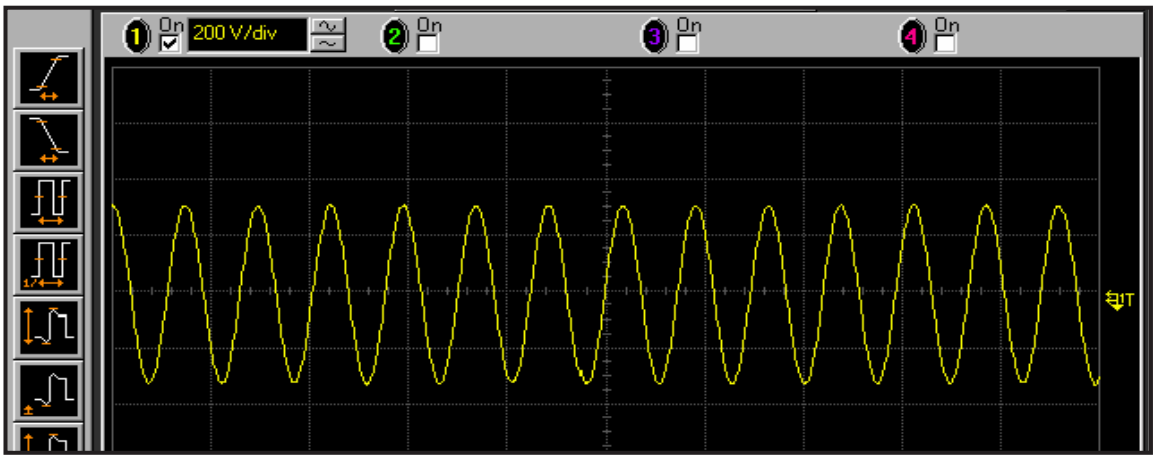

(a)

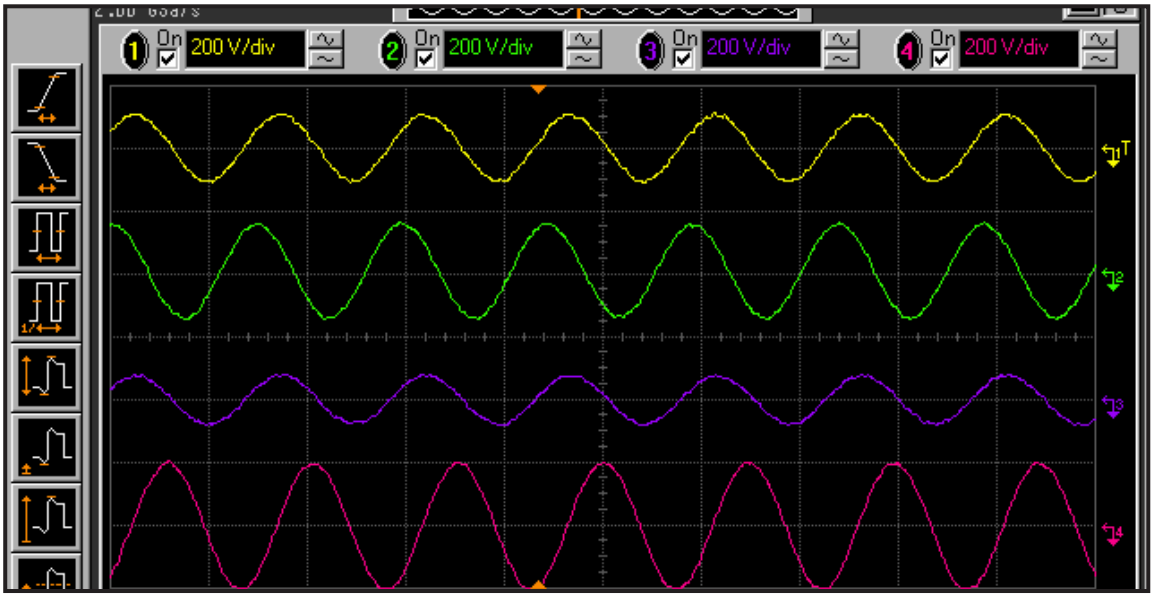

(b)

Figure 3. Oscillatory outputs from high-voltage RF amplifiers: (a) 600-V peak-to-peak, 13.5-MHz deflection voltage; (b) inputs and outputs from the two-channel RF, high-voltage amplifier after the transmission line and transformer were balanced

value sampling and geometric methods have been implemented. The program is written in MATLAB, software that contains a higher dimensional array feature that enhances code efficiency. The code can discern the tracks and flip the reading direction alternately.

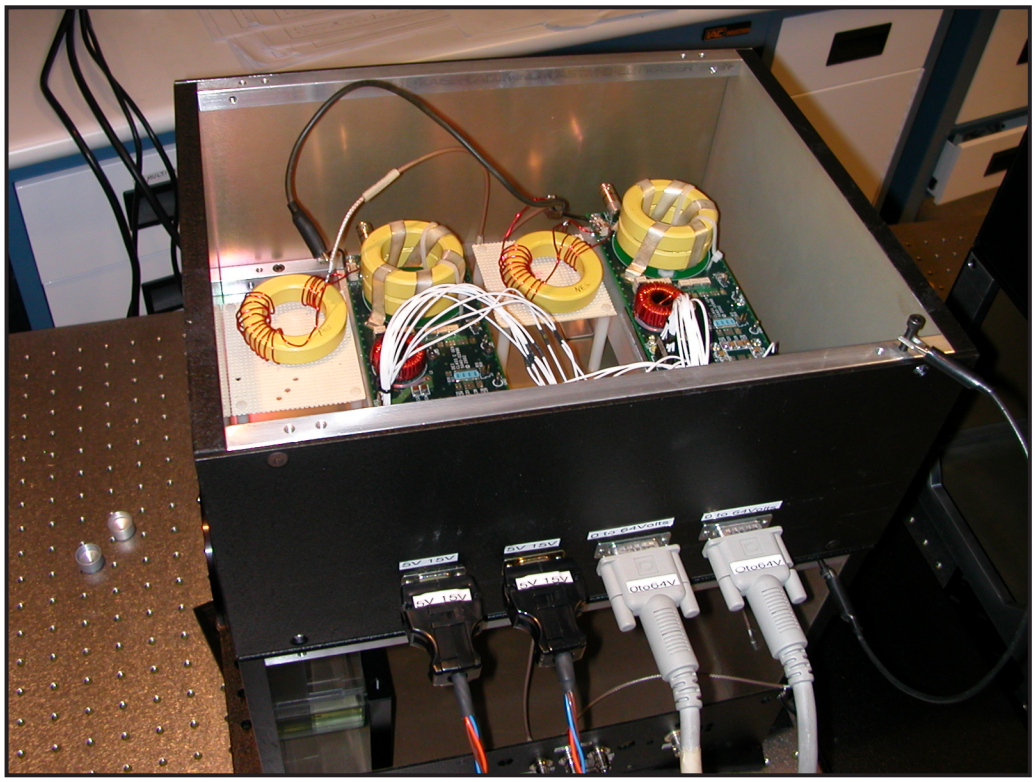

Figure 4. Electronics construction

Project

We conducted a series of proof-of-principle experiments to demonstrate the concept of a 2-D transient recorder and the electronics system performance. Figure 6 shows the experimental setup. The 2-D camera is placed on the optics table. An optical comb generator with a 200-MHz pulse rate is used as the signal source. The comb generator emits at the wavelength of 677 nm and delivers the light via an optical fiber. The output fiber tip is placed close to the framing tube photocathode. A CCD camera is positioned behind the tube's phosphor screen.

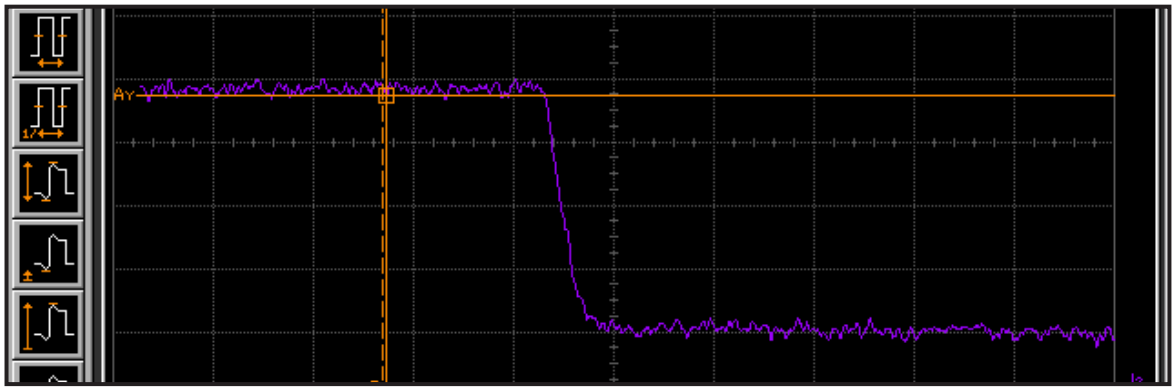

Figure 5. Single-pulse staircase wave

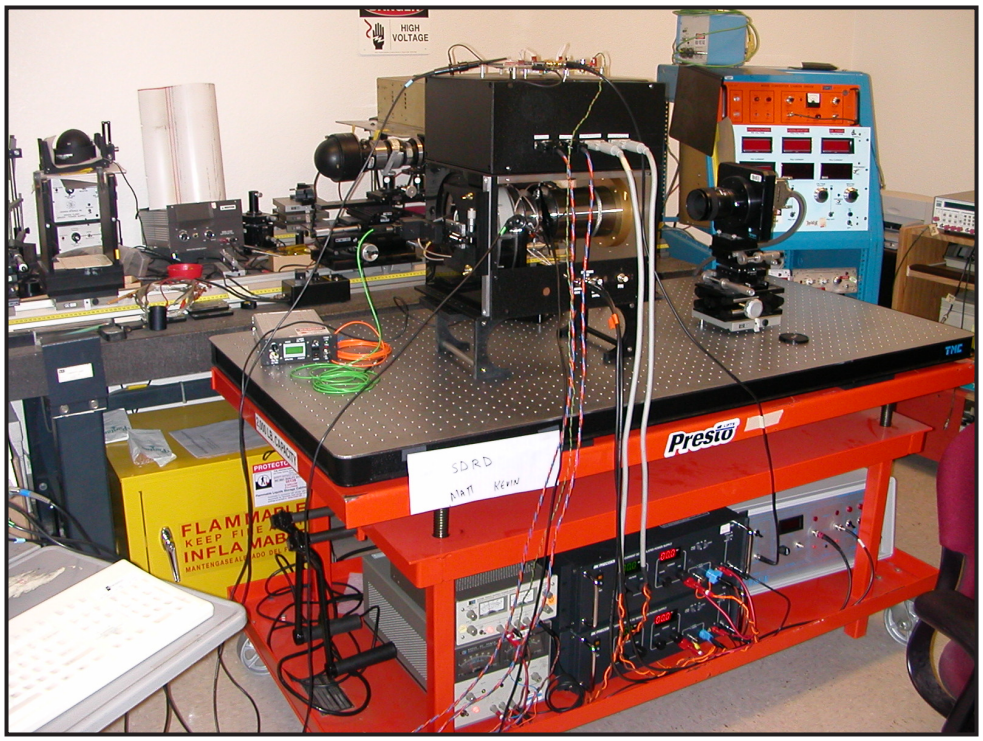

Figure 6. Development platform and experimental setup for 2-D camera tests

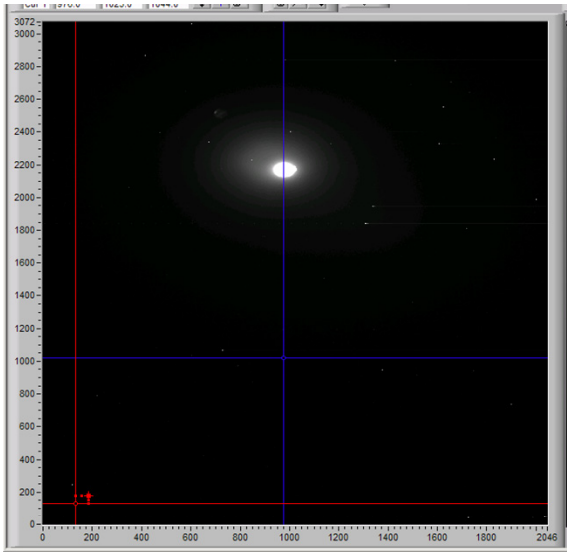

Figure 7(a). Single spot when no deflection voltage is applied

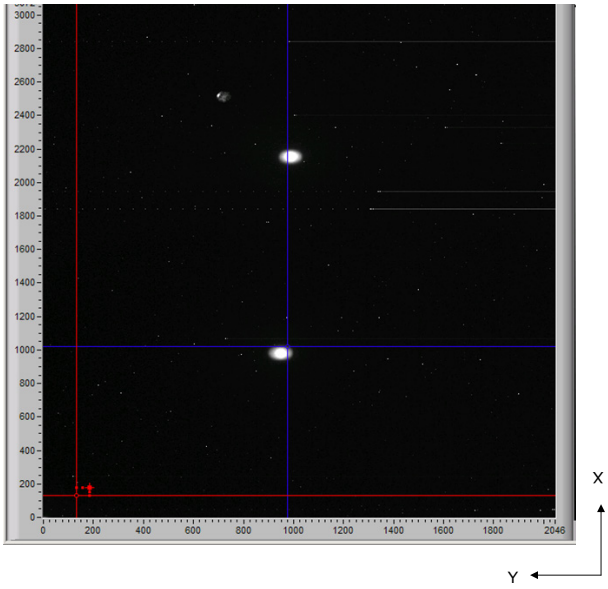

Figure 7(b). Double spots when a ~190-V differential voltage is applied in x or vertical deflection plates

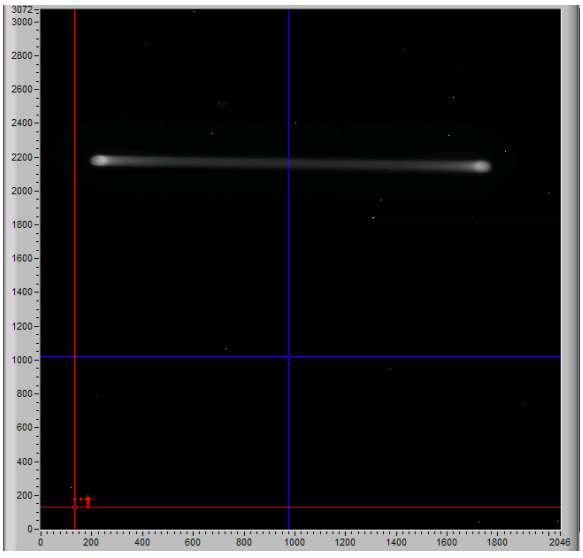

Figure 7(c). Long strip pattern when the oscillatory high voltage (~total 600 V) is applied to y axis or horizontal deflection plates

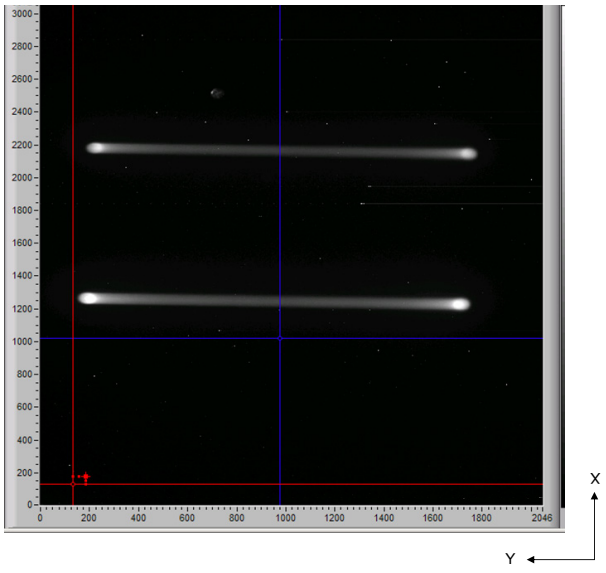

Figure 7(d). Raster scan in the region spanned by the two "strips." The oscillatory high voltage (total ~600 V) is applied to y axis or horizontal deflection plates. The frequency is 13.56 MHz. The ~190-V differential voltage is applied in x or vertical deflection plates.

Figure 7 shows the typical experimental results. The x axis is along the vertical direction, and the y axis, horizontal. Figure 7(a) illustrates the minimum spot due to fiber tip illumination.

Figure 7(b) depicts the splitting of the spot when the single-shot staircase voltage (approximately ±95 V, or total 190 V) is applied to the second pair of deflection plates (x direction). The spots correspond to the deflection voltages before and after the staircase pulse. The electron beam indeed streaks through the intermediate region. However, we did not observe the raster scan tracks in between the spots, due to the tube's limited sensitivity. This is a topic worthy of future effort. Figure 7(c) shows the pattern when the oscillatory high voltages (total ~600 V at 13.56 MHz) are applied to the first pair of deflection plates, in the horizontal y axis. No voltages were applied to the second pair of deflection plates. As expected, the single spot in 7(a) extended in the horizontal direction due to the deflection voltages. We call it a "strip," to distinguish from the single streak.

Figure 7(d) shows the pattern when both deflection voltages were applied to the deflection plates. Namely, the oscillatory high voltages (total ~600 V) were applied to y plates (shown as horizontal), and the single-shot staircase voltages (total ~190 V) were applied to the x plates (shown as vertical). The pattern on the framing tube split into two long strips. The raster scan (~200 cycles in the region) actually occurred in the area between the two strips, but tube sensitivity was too low to show the raster scan tracks. Further improvement may involve doing tube work and using a microchannel plate image intensifier (MCPI).

From Figures 7(a) to (d), we concluded that the high-voltage electronics are functioning normally, as designed. Therefore, we have accomplished the main development task for the SDRD project.

Other Developments

Several electronics boards have been made to support a versatile imager. We also identified more ambitious goals for future research and development.

Conclusion

Our team has exceeded the proposed goals in all areas of this SDRD project. We have developed a set of electronics and have overcome considerable challenges in impedance and amplitude matching, waveform quality, output magnitude, and phase antimatching. Using the electronics, we have successfully demonstrated the core concept of the 2-D raster scan and have developed the data analysis software. In addition, we have designed and built a platform for further development of this exciting camera.

this page intentionally left blank

Versatile, Higher Dimension X-ray Imager

Ruben Guzman, Mary Ann Karrick, Matthew LaFrancesca, Larry MacNeil, Don Max, Don Ng, Bill Nishimura, Jerry Richter, Al Shellman, Ke-Xun Sun,[1] John Yuhas
Livermore Operations

This project utilized LO's unique expertise in framing tube and x-ray streak cameras to develop a versatile x-ray imager for advanced high-energy density physics (HEDP) diagnostics. There are two major components to this project: the x-ray framing tube and the Multi-Imaging X-ray Streak Camera (MIXS). Our eventual goal was to combine the advantages of the two approaches, thus creating a new imaging diagnostic tool for the National Ignition Facility (NIF) and fast transient studies. However, because they have distinctively different scopes of work, we discuss the x-ray framing tube in part 1 and MIXS imaging in part 2.

Background

Imaging systems and methods that take two-dimensional (2-D), time-sequenced photos in the spatial domain are of great value in HEDP diagnostics. One promising approach is the use of a framing camera, which can yield high dynamic range and large picture size. The camera's core component is its framing tube. However, framing tubes with large photocathode areas have only been available at visible light wavelengths.

Another potential approach is using synthetic photography to reconstruct the 2-D images from temporally streaked images. In this area of research, the MIXS camera represents a new class of powerful inertial confinement fusion (ICF) diagnostics that has increasingly drawn the attention of ICF research communities at NIF and Omega, as well as in Japan. MIXS captures fast laser-implosion images in a movie-like sequence, which is extremely revealing of physical processes with complex spatial-temporal structure. Temporal separation between the two sequential images in MIXS can be as small as 10 ps. However, MIXS employs traditional streak cameras, not framing cameras.

We conducted research in two areas:

1) Extending the sensitive wavelength of the framing tube into the x-ray region by designing a new photocathode structure
2) Designing the MIXS camera, developing a software package for MIXS image processing, and designing the imaging test platform.

[1] sunke@nv.doe.gov, 925-960-2514

Part I: X-ray Framing Tube

Project

Overview

A conventional streak tube has only one pair of deflection plates for temporal sweep along one axis. In contrast, a framing tube has two pairs of deflection plates in each of the x and y directions. This added dimension in deflection enables an array of flexible functions usually unavailable in streak tubes. Examples include long-data-length recording using raster scanning, the two-direction streak camera, and the frame-shifting camera.

Figure 1 shows the conceptual design of the x-ray framing tube. A large-area photocathode is placed at the front end, followed by two grid meshes that provide initial acceleration, focusing, and gating. A high-voltage accelerator and focusing structure follow. After that, the first and second pairs of deflection plates are placed behind the aperture in orthogonal directions.

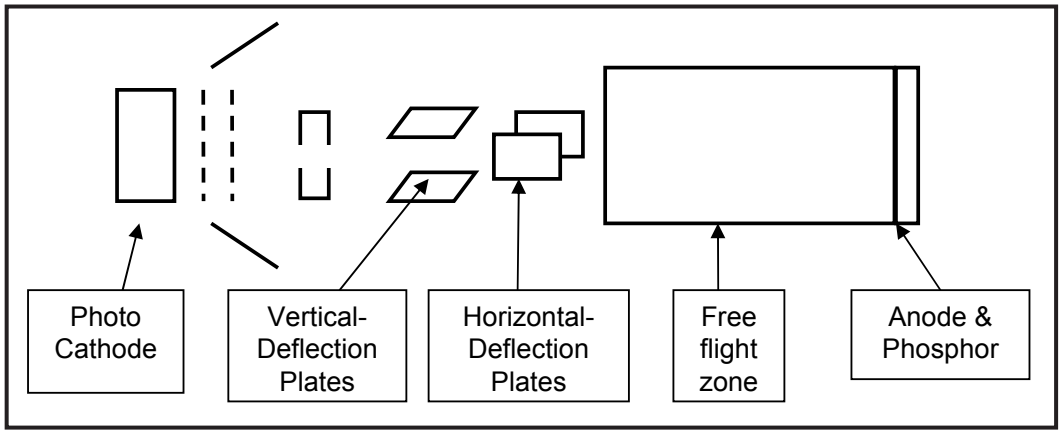

Figure 1. Conceptual design of the x-ray framing tube

Design Features

In this first-of-its-kind framing tube, flexible design allows optimization. This tube can be used to build a versatile imager and to continue optimizing the x-ray framing tube itself. The entire front assembly, including the photocathode, grid meshes, and spacing between them, is replaceable and adjustable. This flexibility allows investigation of different photocathode materials and geometries, as well as varied grid configurations.

To ensure operation under practical conditions, we used an extended insulation sleeve inside the tube, to allow it to operate in an elevated vacuum pressure of up to lower 10^{-5} torr. We added an insulation plate between the flange and the accelerator section to the external tube body. This measure permitted tube operations at 15 kV in the air without using potting.

To lower development costs, we opted to use a proven interface as much as possible. The front vacuum chamber interface was modified from the BN-50 x-ray streak tube; the imaging end was from the optical framing tube. Utilization of a proven interface allowed us to use unmodified hardware fixtures, such as charge-coupled device (CCD) mounts and the vacuum chamber interface.

Electron Optics Modeling

Our team developed a 2-D electron optics model using SIMION, a software package that numerically simulates charged particle trajectories. Model geometry appears in Figure 2. The model predicts that satisfactory focusing is achievable with a large photocathode in an open structure, such as that of an x-ray framing tube. Normal operating potential is 15 kV. The model also checks the maximum allowable deflection for the center electron beam and shows that most of the tube output area can be reached.

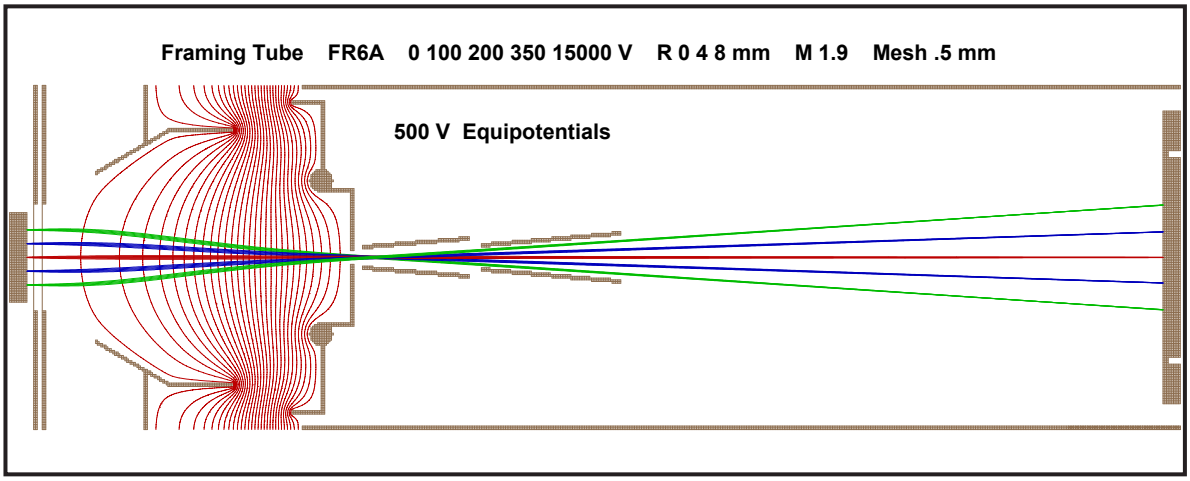

Figure 2. Electron optics modeling using the Simion program. The acceleration voltage is 15 kV.

Tube Construction

Tube construction proved to be the most labor-intensive task of this project. The complexity of two pairs of deflection plates, multiple grids, eight connectors, flanged x-ray access, vacuum port, and flexible front-end structure made the x-ray framing tube one of the most challenging tubes ever constructed by the Advanced Sensor Group at LO.

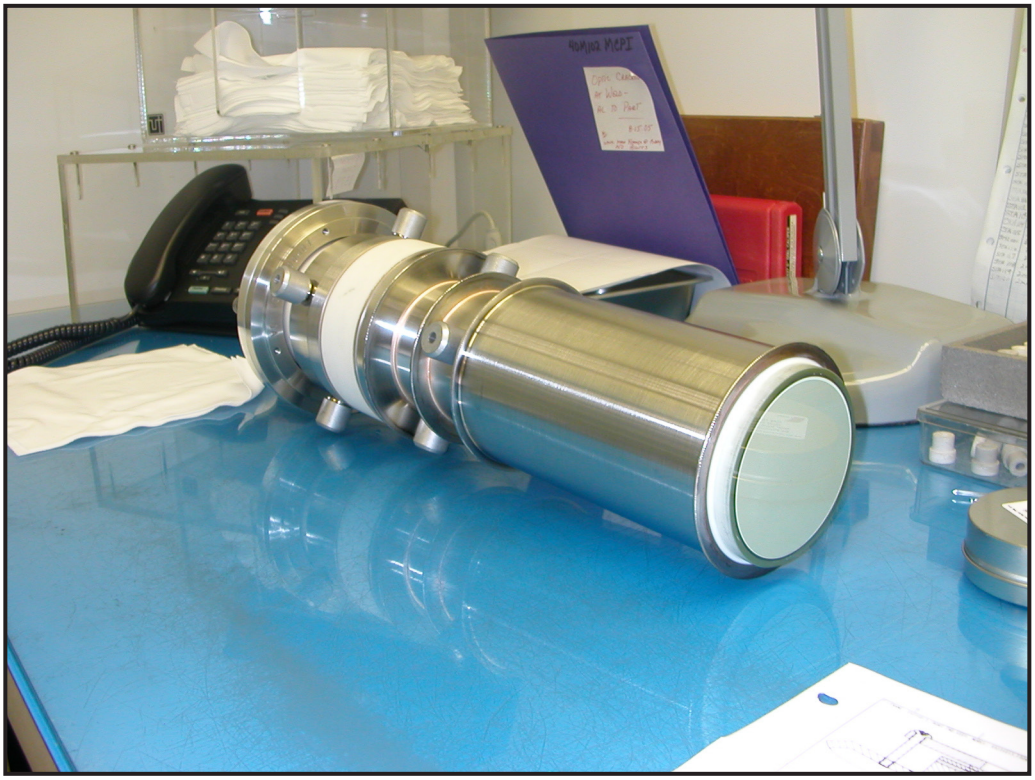

Figure 3. The assembled x-ray framing tube. The output area is shown on the right-hand side.

Laboratory Experiment

Figure 4 shows the experimental setup. The x-ray framing tube was tested using the Manson source at the LO x-ray lab. Continuous x-rays were generated by a Ti anode with a 0.5-mA, 10-kV electron beam. The x-ray spectrum was centered at ~4.3 keV. To allow maximum x-ray flux, no mask was used in the path from the Manson x-ray anode to the framing tube photocathode. An insulative disk was inserted between the tube vacuum flange and the front end of the tube to reduce the probability of electrical breakdown through air.

The photocathode is comprised of Au coated onto a ~51-μm-thick Be substrate. The Au cathode can effectively generate photoelectrons for ~2–10-keV x-rays. The combination of an Au photocathode and a Ti anode x-ray source has been tested in our previous experiments using an x-ray streak camera.

To preserve the flexibility of adjusting the tube structure, we did not apply potting to the tube exterior. This made it difficult to operate the tube at the design goal of 15 kV. However, we were able

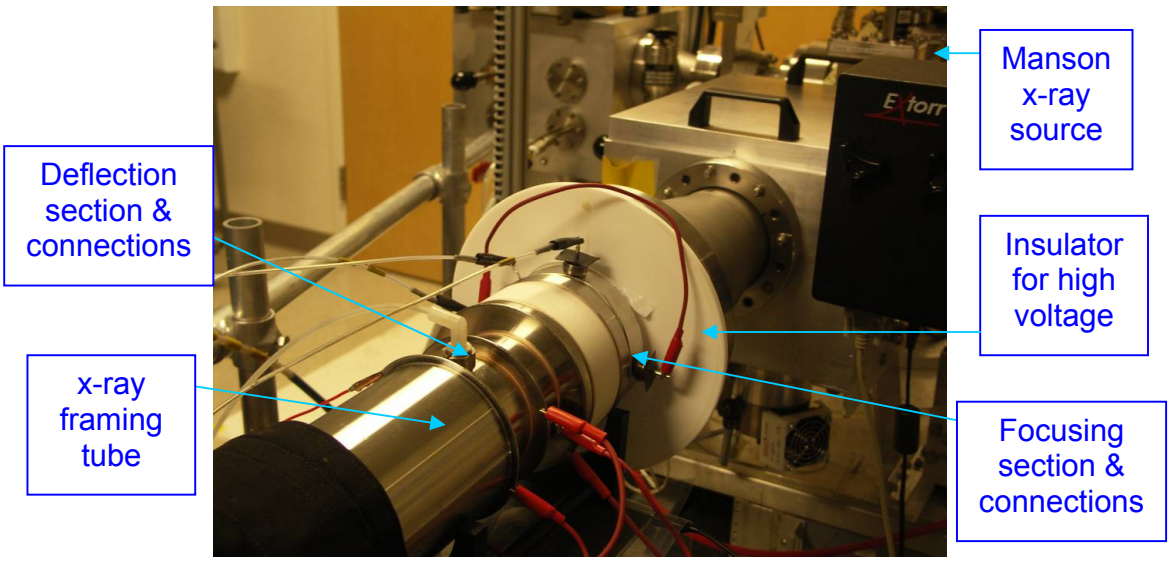

Figure 4. Experimental setup for the x-ray framing tube test

to make some improvements, including insulation between the flanges and at the connector central leads, and grounding at the connectors and tube body. We eventually succeeded in operation at 15 kV in air, without any potting of the tube.

To record framing tube output, we employed an optical CCD camera with a variable focal-length zoom lens. Because the Manson x-ray source had a low-flux output, the CCD counting rate for dark current limited the exposure time. This resulted in a high background, which prevented accurate focusing observation. Under this experimental condition, our goal was not to optimize focusing but to observe electron beam movement under different deflection voltages.

Figure 5 shows typical experimental observations. The CCD images were taken when a –15-kV potential was applied to the photocathode. Two of the grid meshes were biased ~+300 V relative to the cathode. The focusing cone was biased ~+350 V relative to the photocathode. (These voltages were taken from our experience of testing an optical framing tube with a similar acceleration structure.) DC voltages were applied to the X and Y deflection plates. In lab observation, the electron beam image spot moves in opposite directions.

Figure 5(left) shows the image when ±300-V deflection voltages were applied to the second pair of deflection plates; Figure 5(right) shows the image when reversed ±300-V deflection voltages were applied. For these two pictures, the common mode voltages were kept constant at 0. The shifting of the electron beam images due to the deflection voltages' polarity inversion is clearly demonstrated.

The field of view for Figures 5(left) and 5(right) is ~56 mm. The peaks of the two spots are ~41 mm apart in the deflection direction. Deflection sensitivity is thus ~0.034 mm/V, and the inverse measurement of deflection voltage sensitivity is ~29 V/mm.

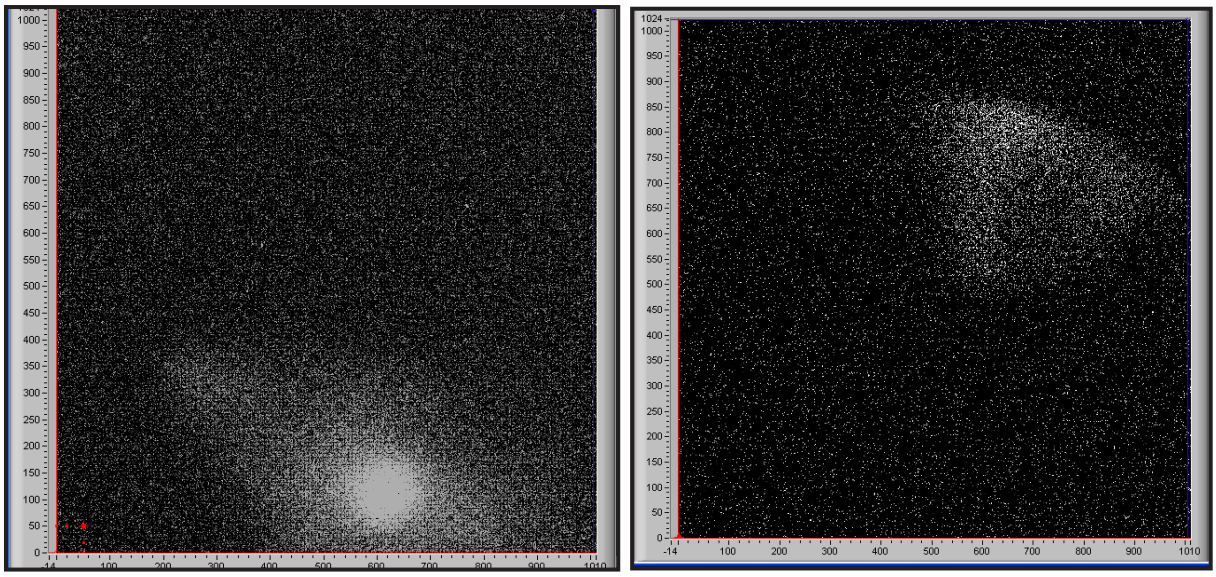

Figure 5. Electron beam images from the x-ray framing tube: (left) Downward deflection by 600 V differential deflection voltage while keeping the common mode voltage at zero; (right) upward deflection by reversing the polarity of the deflection voltages

This initial experiment clearly demonstrated the main function of the x-ray framing tube: deflection of the electron beam from a large-area photocathode. However, due to the low x-ray flux from the Manson source, the necessary long exposure time prohibited a detailed study of focusing characteristics.

Part II: MIXS

Project

Principle and State of the Art

Landen (1992) described the principle of MIXS, and here, we summarize the key steps of image processing.

1. Divided view imaging through tilted pinhole array to form a collection of multiple images from step-rotated view angles: The maximum possible number of images in the collection

depends on the total number and uniformity of spatial resolution elements on the streak camera photocathode. The imaging arrangement appears in Figure 6.

2. Streaked image collections: The streaked image contains a series of such image collections. The finest separation between each collection is limited by the camera's temporal resolution in the entire sampling temporal length.

3. Image reconstruction from the streaked images: The result is a series of temporally spaced stereographic images of the evolving target. The total number of reconstructed images depends on the quantity of clearly discernable streaks. The time separation between the images is limited only by the camera's temporal resolution, typically ~2–10 ps.

The MIXS imaging process has improved over the years. Recent results show that ~100 images can be obtained (Shiraga, 2004) when using a streak camera with ~250 total resolution elements.

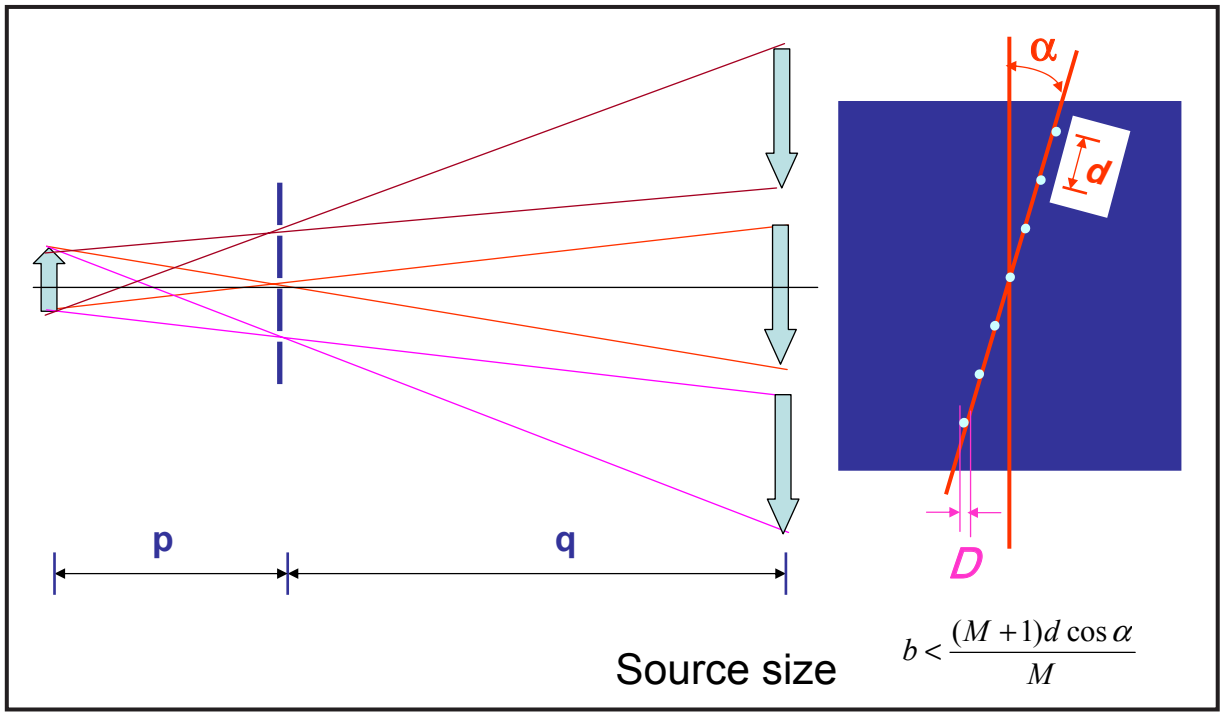

Figure 6. Imaging configuration of the MIXS experiment

MIXS Performance Enhancement

The MIXS's performance is limited by the imaging capacity of the x-ray streak camera. A streak camera with higher resolution and better uniformity has important advantages over one with lower resolution in an MIXS experiment. The number of streaks (N_{streak}) that can be simultaneously read out on a single tube is represented by:

$$N_{streak} = \frac{N_{res}}{N_w}, \quad (1)$$

where:

N_{res} = total number of resolution elements

N_w = *streak* width in resolution elements.

(Typically, N_w is determined by required details of the image.)

1. For the same N_w, a higher resolution streak camera requires less physical length on the photocathode and is therefore able to record more streaks. This, in turn, implies superior reconstructed images and a shorter temporal interval between neighboring images in the sequence.
2. The narrow streak width allows the pinhole array and thus, the camera, to be placed farther away from the target (target chamber center, or TCC). A greater distance between the instrumentation and the TCC is desirable in high-energy shots at NIF or Omega.
3. The higher resolution on the photocathode edge enables imaging with a large field of view in MIXS experiments.

This project leveraged BN's previous work on developing a high-resolution x-ray streak camera. The new generation camera (Sun, 2005) has high spatial resolution and uniformity. Experimentation has shown that this camera has ~900 resolution elements, uniformly distributed across the photocathode. The large number of resolution elements makes it ideal for MIXS imaging. Furthermore, the new camera offers ~2% temporal linearity over most of the image region.

2-D Image Sequence Reconstruction from X-ray Streak Camera Data

To implement MIXS reconstruction, we have used MATLAB to develop a set of algorithms. The higher dimensional array feature and image-processing routine in MATLAB accelerate software development. The software locates the central streak positions using either peak value sampling or the moving average methods. It identifies streak shape in the spatial dimension and determines the

minimum useful streak width for reconstruction. The software divides the image by streaks in the spatial dimension, divides the streaks into segments in the temporal domain, and reconstructs 2-D spatial images in the temporal sequence. We plan to port the code into IDL (a software package developed by Research Systems, Inc.).

Image Reconstruction Using High-Resolution X-ray Streak Camera Data

To demonstrate MIXS capability using the high-resolution x-ray streak camera, and to display the function of image reconstruction software, we have used CCD data from the x-ray streak camera to reconstruct a time sequence of 2-D spatial images, or the "movie" series of MIXS.

Actual streak data taken by the x-ray streak camera appears in Figure 7. The image was taken with the long-pulse laser at LO. While the image was not taken using the MIXS setup, the principle of reconstruction is sufficiently demonstrated.

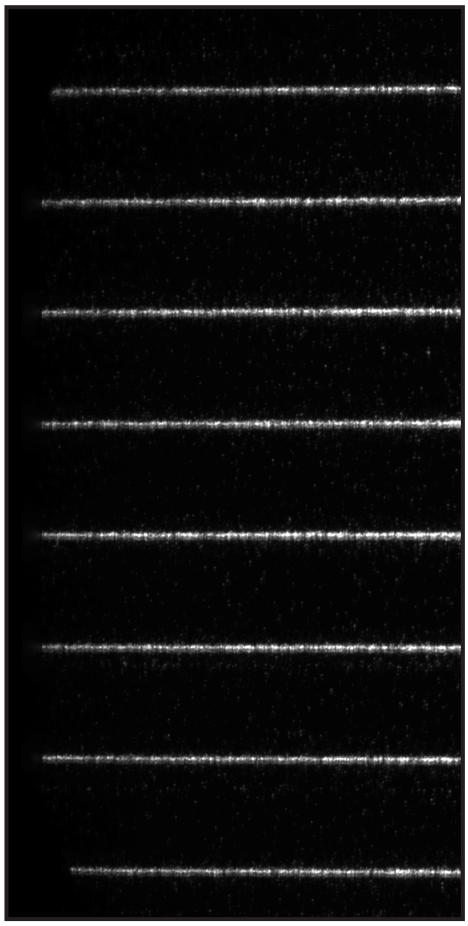

Figure 7. The sampled streak image: 2000 × 1000 pixels, 1/8 of the original image (4096 × 4096 pixels)

Figure 8 shows the reconstructed images from Figure 7. A total of 99 images are produced in this sequence. Adequate resolution is maintained in each image. If we had elected to process the image sequence using the entire 4096 × 4096 CCD data array, eight times more images (i.e., several hundred) would exist in the "movie."

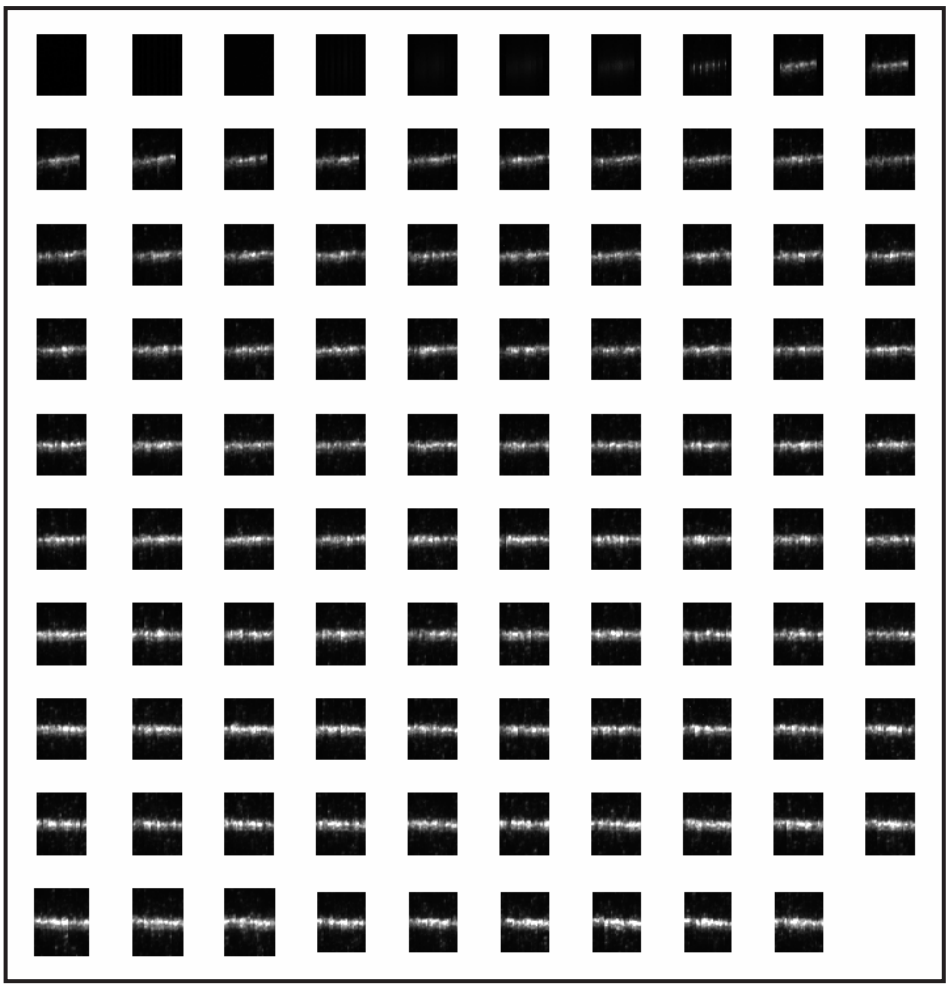

Figure 8. Reconstructed images in temporal sequence. A total of 99 images was reconstructed from 2000 × 1000, or 1/8 of the 4096 × 4096 CCD data array. Adequate resolution was maintained for each reconstructed image.

HEDP Diagnostics Applications

The high-resolution MIXS could have many applications in HEDP diagnostics. For example, because it uses a smaller target, the new polar direct drive (PDD) requires detailed spatial-temporal imaging. MIXS would provide an important means for imaging such a small, fast, and hot core.

Preparation of MIXS Lab Testing

We have designed a set of vacuum fittings that will house the MIXS experiments in LO calibration labs (Figure 9).

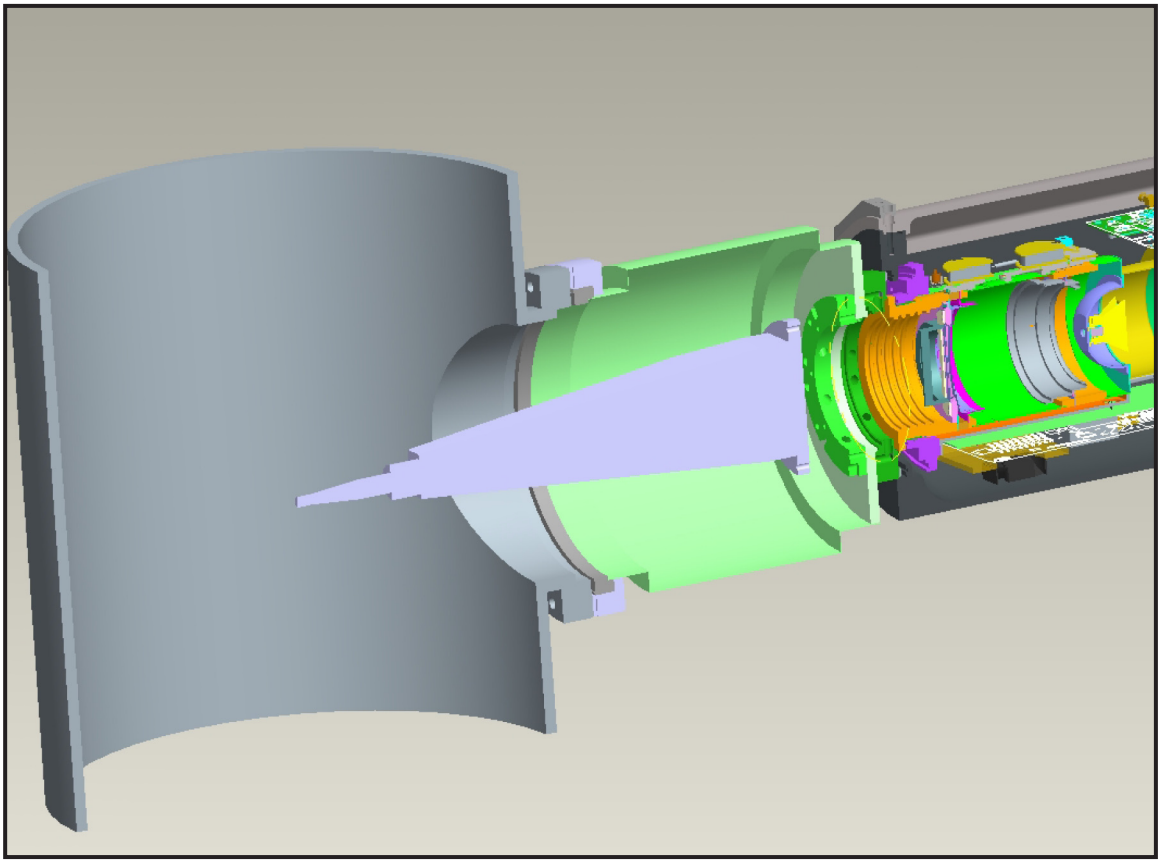

Figure 9. Design of laboratory setup

Conclusion

Our team has designed and constructed a large-photocathode x-ray framing tube. Laboratory testing of this framing tube has demonstrated fundamental operations. This tube facilitates an array of advanced imaging possibilities in HEDP experiments and is a meaningful step in serving the needs of HEDP diagnostics at such high-power x-ray generating facilities as Omega, NIF, and the Z machine.

We made good progress in the MIXS experiment design and imaging processing. The pinhole arrays for ICF experiments have been designed. We have developed the algorithm and software for image reconstruction, and the laboratory testing platform has been designed.

Path Forward

Further steps could include:

- Additional testing and characterization in the x-ray lab to improve static focusing,
- Testing at the long-pulse laser lab for dynamic focusing and linearity with UV input,
- Tube modeling effort in tube sensitivity and geometric electron optics,
- Improving tube structure, including the front-end mounting mechanism for the cathode assembly and the back-end sealing between the fiber-optic block and tube body,
- Completion of the MIXS test platform, including extending the vacuum chamber,
- Improvement of MIXS image-processing software.

References

Landen, O.L., "High-resolution time- and two-dimensional space-resolved x-ray imaging of plasmas at NOVA," *Rev. Sci. Instrum.* **63**, 10 (October 1992) 5075.

Shiraga, H., S. Fujioka, P. A. Jaanimagi, C. Stoeckl, R. B. Stephens, H. Nagatomo, K. A. Tanaka, R. Kodama, H. Azechi, "Multi-imaging x-ray streak camera for ultrahigh-speed two-dimensional x-ray imaging of imploded core plasmas," *Rev. Sci. Instrum.* **75**, 10 (October 2004) 3921.

Sun, K., W. Nishimura, T. Perry, S. Compton, "A second-generation x-ray streak camera with true large format, high dynamic range, and high reliability," *SPIE Proc.* **5920** (September 2005).

Large-Format Phosphor Imager

James R. Tinsley[1]
Special Technologies Laboratory

The purpose of this project was to investigate several methods of depositing phosphor materials onto substrates in sufficient size and thickness, to demonstrate the method as a valid replacement for scintillating tile arrays in radiation-imaging systems. Three approaches were identified as having the potential to achieve this goal. During the investigation, two were found deficient, and all subsequent effort was directed toward the third, a powder sintering technique. Powders of lutetium oxyorthosilicate (LSO) material were synthesized and sintered into solid pieces, then subjected to preliminary tests. Process optimization has begun.

Background

Radiography is a fundamental diagnostic used throughout the NNSA complex. For some radiography systems, a need exists for large-format radiation imagers (≥15 cm on a side and ≥1 mm thick) that can be read out in real time using video cameras. Systems that use penetrating radiations, such as hard x-rays and energetic protons, are becoming increasingly common as the technique is extended to larger experiments and thicker test objects. Applications include Proton Radiography and hard x-ray radiography for the subcritical experiments, DARHT, and Atlas.

In addition to suitable sources of radiation, these new systems require an image plane where the pattern of ionizing radiation is transformed into light that can be recorded using video cameras. Such imagers are currently made by tiling plates of polished scintillating crystals, principally LSO. Unfortunately, the joints between tiles and defects in the crystals themselves interfere with image quality. The resulting imperfections can be only partly cancelled by doing background subtractions. There exist other scintillating materials that are less plagued with defects, but other properties make them much less attractive for radiation imaging. Earlier attempts to mitigate these problems, such as "grouting" crystals with index-matching materials and covering crystal edges with black paint to eliminate total internal reflection, have had limited success. Efforts to maximize the tiles' optical quality by selecting the best of many different crystals have proven very expensive, time-consuming, and ultimately not completely successful.

[1] tinslejr@nv.doe.gov, 805-681-2282

Project

Initially, we proposed two methods of constructing phosphor imagers. In the first method, a phosphor slurry is "spun" onto the substrate to produce a uniform coating. This technique has been used for years at LO to produce uniform phosphor coatings. However, the coatings have always been much thinner than those envisioned for this project.

The second method is a recent development by Lexel Imaging Systems: Cataphoretic Coating. This proprietary electrodeposition technique purports to produce high-quality, virtually blemish-free coatings suitable for imaging applications. Lexel can make pieces as large as 18 × 14 cm, or larger if the demand arose. As with the LO technique, cataphoretic phosphor depositions are generally quite thin, on the order of micrometers in thickness.

With both methods, the difficulty arises in attempting to make the phosphor coatings much thicker than ever before; neither process can be extended, or just repeated, indefinitely. By contrast, increasing the areal dimensions of the imagers by less than one order of magnitude beyond what is currently done is easy to envision. However, for both techniques, even if the target thickness were achieved, the optical quality of the aggregated powder, with all of the potential scattering surfaces on the individual particles, could possibly be quite poor compared with LSO crystal tiles.

After additional discussions with LO personnel, we decided that the spinning technique likely could not achieve the desired phosphor thickness for this project. A different approach was taken. LO offered to produce compressed disks of phosphor in 1-, 2-, and 3-mm thicknesses. Previous testing had resulted in pieces with a chalklike consistency. To prevent equipment cross-contamination in the phosphor-processing facility, the disks would consist of the same phosphor used in production processes: (Zn, Cd)S:Ag, also known as P-20.

In anticipation of P-20 phosphor disks from LO, we asked Lexel to use P-20 phosphor in their cataphoretic process samples, to facilitate an equal comparison. This phosphor is not suitable for the missions discussed above. However, LSO or other materials can easily be substituted for P-20 later, since these processes are essentially mechanical and do not depend on the chemistry of the materials involved. Lexel produced seven samples, one of which had a thickness of approximately 200 μm (Figure 1). All cataphoretic samples appeared to be of very high quality.

Early in the project timeframe, a third potential option was discovered. Dr. Olivia Graeve, of the Department of Metallurgical and Materials Engineering at the University of Nevada, Reno (UNR), has sintered ceramic powders into macroscopic pieces that exhibit excellent optical qualities. Since LSO is a ceramic that has been doped with cerium to cause scintillation, we believed this technique had a very high potential for success. The remainder of this report will emphasize this approach.

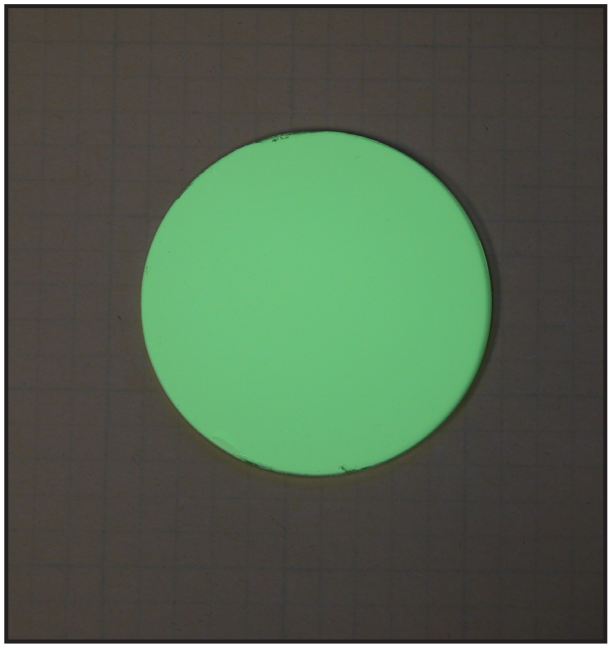

Figure 1. Sample of cataphoretic P-20 phosphor deposition illuminated with visible and UV light

Sintering ceramics with good optical properties requires a starting powder consisting of extremely fine and uniform particles. No such LSO powder, nor that of any other phosphor material, is available commercially. Therefore, it would be necessary to fabricate the material from scratch before the sintering could be attempted. FY 2005 project activities focused on solving this technological hurdle.

Our team initially thought that the LSO powder would be made using a unique synthesis process involving reverse micelles, which form microscopic reactors for the synthesis of the desired powders. We later decided to first try a more conventional combustion synthesis reaction. The reactants $Lu(NO_3)_3$, SiO_2, $Ce(NO_3)_3$, and CH_6N_4O were combined in a stoichiometric ratio with a small amount of water and placed in a furnace. The mixture decomposed, dehydrated, and ruptured into flame in less than three minutes. The powders were then annealed to "boil off" unwanted residues.

Several annealing temperatures were tried with different samples of the powder to minimize particle agglomeration, while preventing particles from fusing into larger crystals. A temperature of 1000°C proved best. The powder was then analyzed for its emission properties (using photoluminescence), phase identification (using x-ray diffraction), and particle size (using dynamic light scattering).

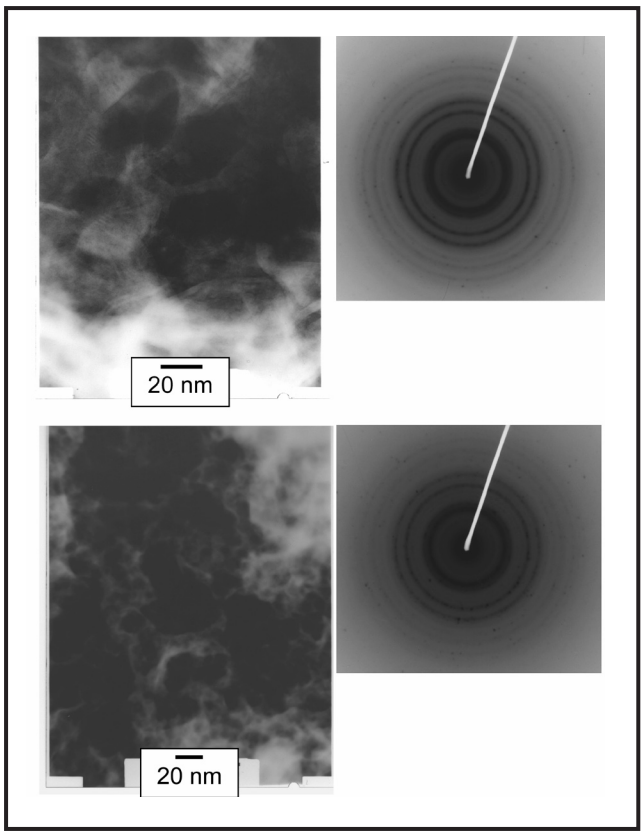

Figure 2. X-ray imaging and x-ray diffraction of two LSO powders synthesized at UNR with different annealing temperatures

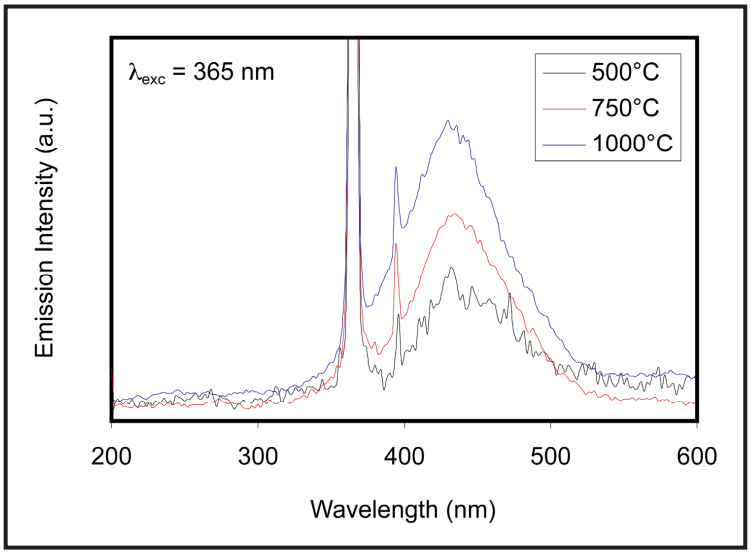

Figure 3. Photoluminescence spectra of synthesized LSO powder

As seen in Figure 2, the particle sizes after annealing were on the order of 20–30 nm in diameter, and from the diffraction patterns, the crystalline structure was quite clean.

The photoluminescence spectra (Figure 3) agree well with the measured spectra of LSO crystals found in the literature (Cooke, 1999; Cooke, 2000; Cooke, 2001).

Later, we used beta excitation to measure the scintillation response time spectrum and found it to be precisely the same as that of LSO crystals—that is, a rise time of <100 ps (greater than our apparatus can measure) and a decay time of ~40 ns.

The LSO powder exhibited all of the traits of crystalline LSO except that it was disappointingly dim. At first we suspected that the cause was small crystal size. In other phosphor powders, we have found that larger particle sizes lead to greater light output. We determined the dimness problem to be not a function of particle size, but a result of the fact that the first LSO batches contained too much cerium dopant. A literature search showed that LSO crystals are grown with less than 1% cerium dopant, despite the fact that other scintillators invariably contain 1% or more dopant (cerium in nearly all cases). However, no discussion of an *optimum* value was found. Since powder synthesis does not have the same constraints as growing crystals, it is easy to increase the cerium doping concentration, and we naively thought that increasing it to 1% might lead to higher light output. This was very wrong.

The optimum concentration of cerium in LSO is 0.05%; a greater amount leads to concentration quenching, and thus to less light production for a given amount of radiation energy deposited. Later, UNR made a batch of powder using 0.05% cerium. The new powder is being tested, as described above.

Although the first powder sintering attempts were made using the 1% cerium powder, they proved to be instructive nonetheless. The first sintering was done at 1700°C in a vacuum. The resulting disks (Figure 4) are opaque (their color is the same as that of the powder) and have areas in which the phosphorescence is completely quenched. The opacity is almost certainly due to a too-low sintering temperature, given that LSO melts at ~2150°C. The quenching derives from tungsten contamination caused by contact with the tungsten fixtures. This should be curable by replacing the tungsten with iridium or iridium-lined fixtures.

Another problem, not apparent to the naked eye, is that there is a loss of oxygen, more so in a sintering done at 1900°C, due to the sintering having been conducted in a vacuum. We have since learned that an inert atmosphere or a vacuum is overly reducing and precipitates oxygen loss, but too much oxygen will lead to tetravalent (4^+) cerium in place of the trivalent (3^+) cerium that emits light. Both conditions destroy light output.

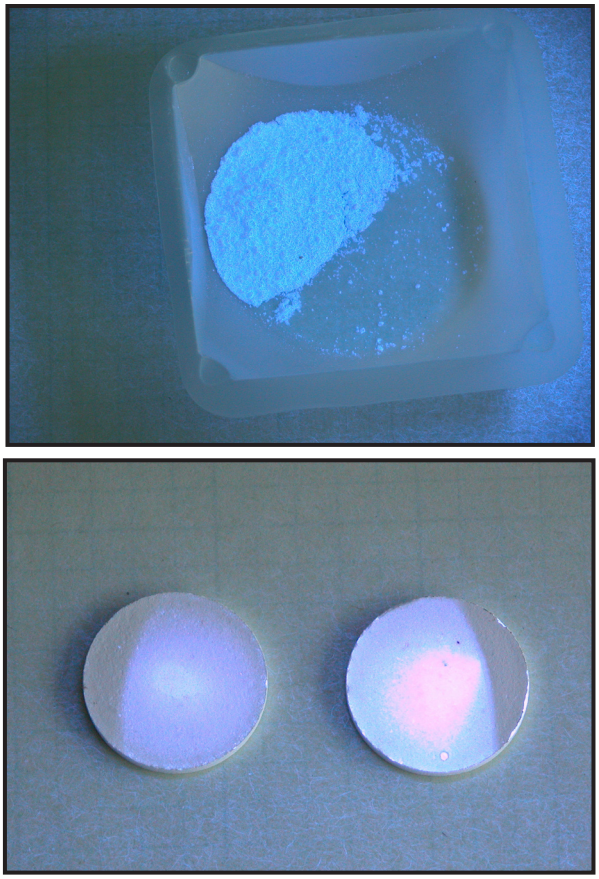

Figure 4. First sample of synthesized LSO powder (top) and first sintering attempt (bottom)

Conclusion

We have identified a new method of producing large pieces of ceramic scintillators, such as LSO. A phosphor powder that is suitable for sintering was produced. The next development challenge is to find the right conditions for a successful sintering. Further research topics might include:

- Use higher sintering temperature—closer to the LSO melting point
- Create different sintering atmosphere—start with 5000 ppm O_2 in Ar or N_2
- Replace tungsten fixtures with iridium, or at least iridium liners (iridium is expensive!)
- Modify sintering profile; increase ramp and sintering times
- Fix stoichiometry of starting materials, if necessary
- Perform Fourier transform infrared (FTIR) spectroscopy on powders to determine if surface impurities are present.

In anticipation of success in optimizing the sintering process, further research will be required on increasing piece size. This should be a straightforward process but may entail variations in procedures, such as the sintering time profile, etc. This technique might be extended to other scintillating materials that are difficult to grow in high-quality single crystals, perhaps even those that are not ceramics.

Acknowledgments

The author would like to thank Ken McClellan (LANL) for his extremely helpful input on the properties and manufacture of LSO. The author would also like to recognize the exceptional support of Wil Lewis in arranging the initial contact with UNR, and to acknowledge the contributions of Brett Pearson and other students in Dr. Graeve's lab at UNR.

References

Cooke, D. W., B. L. Bennett, R. E. Muenchausen, K. J. McClellan, J. M. Roper, M. T. Whittaker, "Intrinsic trapping sites in rare-earth and yttrium oxyorthosilicates," *J. Appl. Phys.* **86**, 9 (November 1999) 5308.

Cooke, D. W., R. E. Muenchausen, B. L. Bennett, K. J. McClellan, J. M. Roper, M. T. Whittaker, A. M. Portis, "Intrinsic trapping sites and ion-lattice coupling parameters of cerium-doped lutetium oxyorthosilicates," *Proc. SPIE, Hard X-ray, Gamma-Ray, and Neutron Detector Physics II* **4141** (2000) 111.

Cooke, D. W., B. L. Bennett, K. J. McClellan, J. M. Roper, M. T. Whittaker, "Similarities in glow peak positions and kinetics parameters of oxyorthosilicates: evidence for unique intrinsic trapping sites," *J. Lumin.* **92**, 1 (2001) 83.

NNSA/NA-116

Karen Callahan	(1)	Lucille Gentry	(1)	Jamileh Soudah	(1)

NNSA Service Center

Russell Edge	(1)	Julianne Levings	(1)

NNSA/NSO

Charlotte Carter	(2)	Laura Tomlinson	(1)

NSTec

Dennis Barker	(1)	Howard Bender	(2)	Rob Buckles	(2)
John Ciucci	(1)	Nelson Cochrane	(1)	Ken Cooke	(1)
Jim Gatling	(1)	Steve Goldstein	(1)	Chris Hagen	(2)
A. C. Hollins	(1)	Jim Holt	(1)	Steve Iversen	(2)
Warnick Kernan	(2)	Bill Kost	(1)	Ping Lee	(1)
Wil Lewis	(1)	John Manning	(1)	Michael Martinez	(1)
Masafusa Nishimura	(1)	PIs	(1 ea)	Dave Post	(1)
Carson Riland	(1)	Bob Summers	(1)	Oliver Swenington	(1)
Tom Waltman	(1)	Alan Will	(1)	B.J. Willeford	(1)
Steve Younger	(1)				

LANL

Frank Cverna	(1)
LDRD Office	(1)
(ATTN: Lisa Harris)	

LLNL

Larry Wiley	(1)
LDRD Office	(1)
(ATTN: Carl Van Bibber)	

SNL

Raymond Leeper	(1)
John Porter	(1)
LDRD Office	(1)
(ATTN: Hank Westrich)	

OSTI

Electronic copy	(1)

Resource Centers

RSL-Nellis	(1)	Technical Library	(1)

Nevada Test Site–Directed Research, Development, and Demonstration
FY 2005 Report
DOE/NV/11718--1245 and DOE/NV/25946--022
Report Date: September 2006

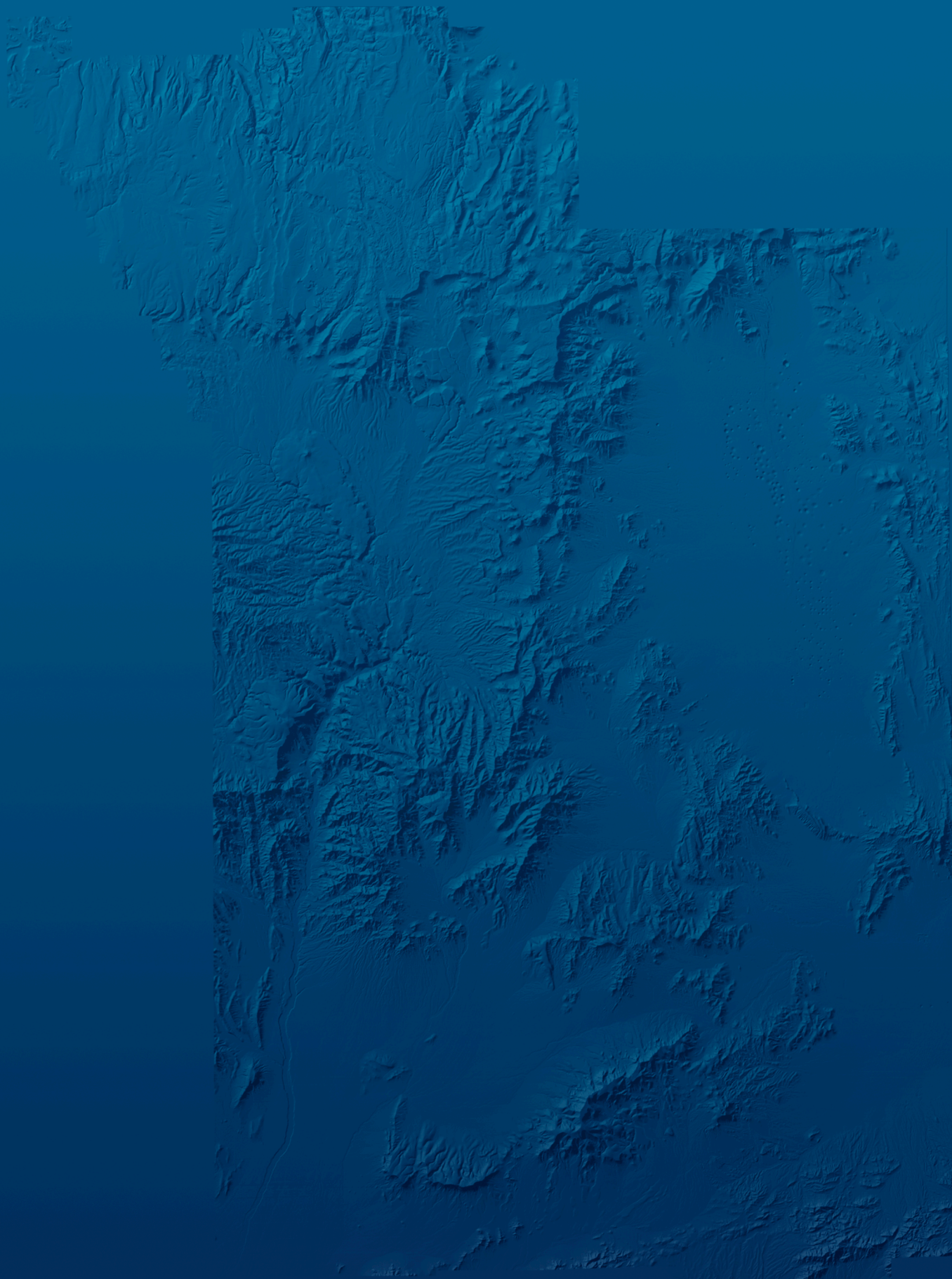
SDRD
Site Directed R & D